Impact of recrystallization and metamorphism on the mobility of germanium and related elements in orogenic Pb-Zn deposits : example of the Pyrenean Axial Zone mineralizations (France-Spain)

Alexandre Cugerone

▶ **To cite this version:**

Alexandre Cugerone. Impact of recrystallization and metamorphism on the mobility of germanium and related elements in orogenic Pb-Zn deposits : example of the Pyrenean Axial Zone mineralizations (France-Spain). Earth Sciences. Université Montpellier, 2019. English. NNT : 2019MONTG050 . tel-02578708

HAL Id: tel-02578708
https://theses.hal.science/tel-02578708

Submitted on 14 May 2020

HAL is a multi-disciplinary open access archive for the deposit and dissemination of scientific research documents, whether they are published or not. The documents may come from teaching and research institutions in France or abroad, or from public or private research centers.

L'archive ouverte pluridisciplinaire **HAL**, est destinée au dépôt et à la diffusion de documents scientifiques de niveau recherche, publiés ou non, émanant des établissements d'enseignement et de recherche français ou étrangers, des laboratoires publics ou privés.

THÈSE POUR OBTENIR LE GRADE DE DOCTEUR DE L'UNIVERSITÉ DE MONTPELLIER

En Géologie

École doctorale Gaïa

Géosciences Montpellier, UMR CNRS 5243, Université de Montpellier

Impact of recrystallization and metamorphism on the mobility of germanium and related elements in orogenic Pb-Zn deposits: example of the Pyrenean Axial Zone mineralizations (France-Spain)

-

Impact de la recristallisation et du métamorphisme sur la mobilité du germanium et éléments associés dans les minéralisations Pb-Zn orogéniques : exemple des minéralisations de la Zone Axiale des Pyrénées (France-Espagne)

UNIVERSITÉ DE MONTPELLIER

Présentée par Alexandre Cugerone

Le 15 novembre

Sous la direction de Bénédicte Cenki-Tok

Devant le jury composé de

Olivier Vanderhaeghe, Professeur, Géosciences Environnement Toulouse (GET)	**Président du jury**
Jochen Kolb, Professeur, Karlsruher Institut für Technologie (KIT)	**Rapporteur**
Fleurice Parat, Maitre de conférences, Géosciences Montpellier (GM)	**Examinatrice**
Alan Boyle, Senior lecturer, University of Liverpool	**Invité**
Kathryn Goodenough, Principal geologist, British Geological Survey (BGS)	**Invitée**
Bénédicte Cenki-Tok, Maître de conférences, Géosciences Montpellier (GM)	**Directrice de thèse**

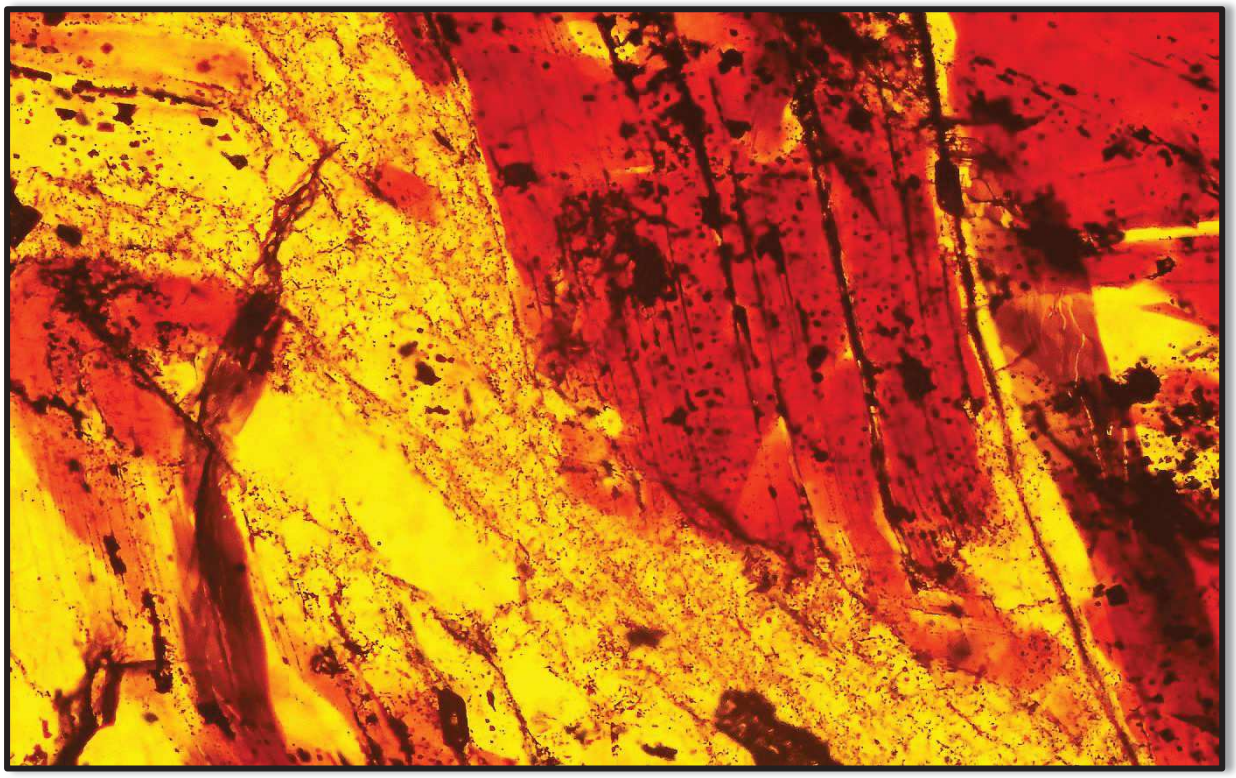

Impact of recrystallization and metamorphism on the mobility of germanium and related elements in orogenic Pb-Zn deposits: example of the Pyrenean Axial Zone mineralizations (France-Spain)

Author – Alexandre Cugerone

2019

PhD director – Bénédicte Cenki-Tok

Abstract

Rare metals are essential to the development of the green technologies that are at the core of emerging low-carbon societies. Germanium is a rare element considered critical by the European Union and the U.S. Geological Survey due to its several uses in optical and electronics devices. Non-deformed sphalerite crystals (ZnS) commonly contain Ge and other critical elements (In, Ga) which may grade up to a few thousands of ppm. Only few studies have described specific minerals with Ge contents above wt.%, because these are apparently rare in Pb-Zn(-Cu) deposits. These Ge-minerals appear to be more abundant in deformed and metamorphosed Pb-Zn(-Cu) deposits. This raises the question of the impact of deformation and metamorphism on Ge and other rare metals mobility. This type of orogenic deposits constitutes the largest known zinc concentrations on Earth and their potential for rare metal is yet to be assessed.

The Pb-Zn deposits in the Pyrenean Axial Zone are an ideal target to study the impact of deformation and metamorphism on rare metals mobility as sphalerite is only locally recrystallized. A structural field study allows to discriminate four Pb-Zn mineralization types. Type 1 is a minor syngenetic and stratiform disseminated mineralization. Type 2a is an epigenetic stratabound mineralization, concordant to the S_1 Variscan foliation. Type 2b ore are parallel to the S_2 cleavage. Sphalerite ore is highly deformed by a late cleavage sub-parallel to S_2 probably Pyrenean-Alpine in age. Fluid inclusions study shows the presence of two Type 2b fluids with a low salinity (<20 wt.% NaCl eq.) and high temperatures (200-350 °C) typical of Late-Variscan fluids whereas Mesozoic Type 2b ore exhibits high salinity (15-35 wt.% NaCl eq.) and low temperature (< 200 °C).

Germanium and related elements such as Cu, In and Ga are present in the deformed Pyrenean vein mineralizations and are heterogeneously distributed. Electron Backscattered diffraction (EBSD) analyses and chemical investigations allow to define distinct sphalerite textures with specific chemical contents: i) Dark-brown patchy or stripped zonations in coarse parent grains exhibit high Ge-content (up to 600 ppm Ge) in the lattice. ii) Light-brown zonations in coarse parent grains contain low Ge-contents mostly below 100 ppm Ge. iii) Light-brown small recrystallized daughter grains (below ~ 100 μm) present systematically low to very low Ge-contents (~ 20 ppm Ge). Copper contents (up to 1265 ppm) are highly correlated to Ge in sphalerite and Ga only occur in coarse sphalerite crystals (below ~100 ppm). Ge-minerals, such as brunogeierite, carboirite, briartite and argutite (up to ~ 70 wt. % Ge) are mainly hosted in recrystallized sphalerite domains or close to twin boundaries in coarse grains. These observations demonstrate that recrystallization of sphalerite has led to the redistribution of Ge from the sphalerite lattice into Ge-minerals. We suggest that the interactions between intra-granular diffusion and fluid assisted processes are responsible for the formation of patchy-stripped zonations and the crystallization of Ge-oxides, sulfides or chloritoids. A large variability of sphalerite chemistry and texture is frequently reported from other orogenic world-class deposits: these may have been affected by similar recrystallization and redistribution processes. The redistribution of rare metals in sulfide environments must have induced the concentration of rare metal in accessory minerals. These tiny minerals may be missed by punctual chemical analyses without prior detailed textural investigation. Understanding how rare metals concentrate through metamorphism and syntectonic recrystallization at mineral scale is essential to emphasize their spatial redistribution and localization at deposit scale. This study highlights the importance of coupling *in situ* and mapping chemical analyzes with macro- and microtextural characterization when targeting rare metals in deformed ore.

Keywords: Germanium; Pb-Zn mineralizations; Critical metals; Pyrenees; Remobilization; Recrystallization.

Résumé

Les métaux rares sont essentiels au développement des technologies vertes qui sont maintenant au cœur de nos sociétés. Le germanium est un élément rare considéré critique par l'Union Européenne et l'US Geological Survey, du fait de ses nombreux usages dans l'industrie de l'optique et de l'électronique. Les cristaux non déformés de sphalérite (ZnS) sont souvent porteurs de Ge et d'autres métaux rares (In, Ga) avec des concentrations pouvant atteindre quelques milliers de ppm. Seulement peu d'études décrivent des minéraux avec des concentrations en Ge au-dessus du % poids, du fait de leur apparente rareté dans les gisements Pb-Zn(-Cu). En fait, ces minéraux à Ge semblent plus fréquents dans les gisements Pb-Zn(-Cu) déformés ou métamorphisés ce qui soulève la question de l'impact de la déformation et du métamorphisme sur la mobilité du Ge et d'autres métaux rares. Ce type de gites contient les plus grandes ressources de zinc sur Terre and actuellement leur potentiel en métaux rares reste à évaluer.

Les gites Pb-Zn de la Zone Axiale des Pyrénées sont une cible idéale pour étudier l'impact de la déformation et du métamorphisme sur la mobilité des métaux rares car la sphalérite est seulement localement recristallisée. Une étude structurale de terrain a permis de discriminer quatre types de minéralisations Pb-Zn. La minéralisation Type 1 est disséminée, syngénétique et stratiforme. La minéralisation Type 2a est épigénétique et stratabound. Les minéralisations Type 2b tardi-Varisque et Mésozoïque sont parallèles à la schistosité S_2. La sphalérite est largement déformée par une schistosité tardive, probablement Pyrénéenne (S_p). L'étude des inclusions fluides montre la présence d'un fluide de faible salinité (<20 %poids eq. NaCl) avec de relative haute température (200-350 °C) typique d'un fluide tardi-Varisque tandis que le Type 2b Mésozoïque montre de forte salinité (15-35 %poids eq. NaCl) et des faible températures (< 200 °C). Le germanium est distribué de manière très hétérogène dans les minéralisations en veines. Des analyses texturales et chimiques permettent de définir différents domaines dans la sphalérite : i) des zonations marron sombres en patches ou rayées dans les gros grains parents présentent des concentrations en Ge élevées dans la maille cristallographique (jusqu'à 600 ppm Ge). ii) des zonations marron claires dans les gros grains parents contiennent des concentrations en Ge faibles, le plus souvent en-dessous de 100 ppmGe. iii) des petits grains clairs recristallisés (en dessous de ~100 μm) presentent de très faibles concentrations en Ge (~20 ppm Ge). Les concentrations en Cu sont corrélées à celles du Ge tandis que le Ga est zoné que dans les gros grains. Les minéraux à Ge, comme la brunogéiérite, la carboirite, la briartite et l'argutite (jusqu'à ~70 %poids Ge) apparaissent dans les domaines de sphalérite recristallisée ou plus rarement proche des limites maclées dans les gros grains. Ces observations démontrent que la recristallisation de la sphalérite a permis la redistribution du Ge depuis la maille de la sphalérite jusqu'à la formation des minéraux à Ge. Nous suggérons que les intéractions entre des fluides et la diffusion intra-granulaire sont responsable de la redistribution du Ge. Des hétérogénéités chimiques et texturales sont fréquemment reportées dans d'autres gisements et ont pu être affectés par des processus similaires de redistributions dans des minéraux accessoires. Ces petits minéraux peuvent avoir été manqués par des analyses chimiques ponctuelles sans contrôle textural préalable. Comprendre comment les métaux rares se concentrent à travers la déformation et la recristallisation syn-tectonique à l'échelle du minéral est essentiel pour surligner leur localisation à l'échelle du gisement. Cette étude met en évidence l'importance de coupler les analyses chimiques in-situ et cartographiques avec la caractérisation macro- et micro texturale lors de l'exploration des métaux rares dans des minerais déformés.

Mots-clés : germanium ; minéralisation Pb-Zn ; métaux critiques ; Pyrénées ; remobilisation ; recristallisation.

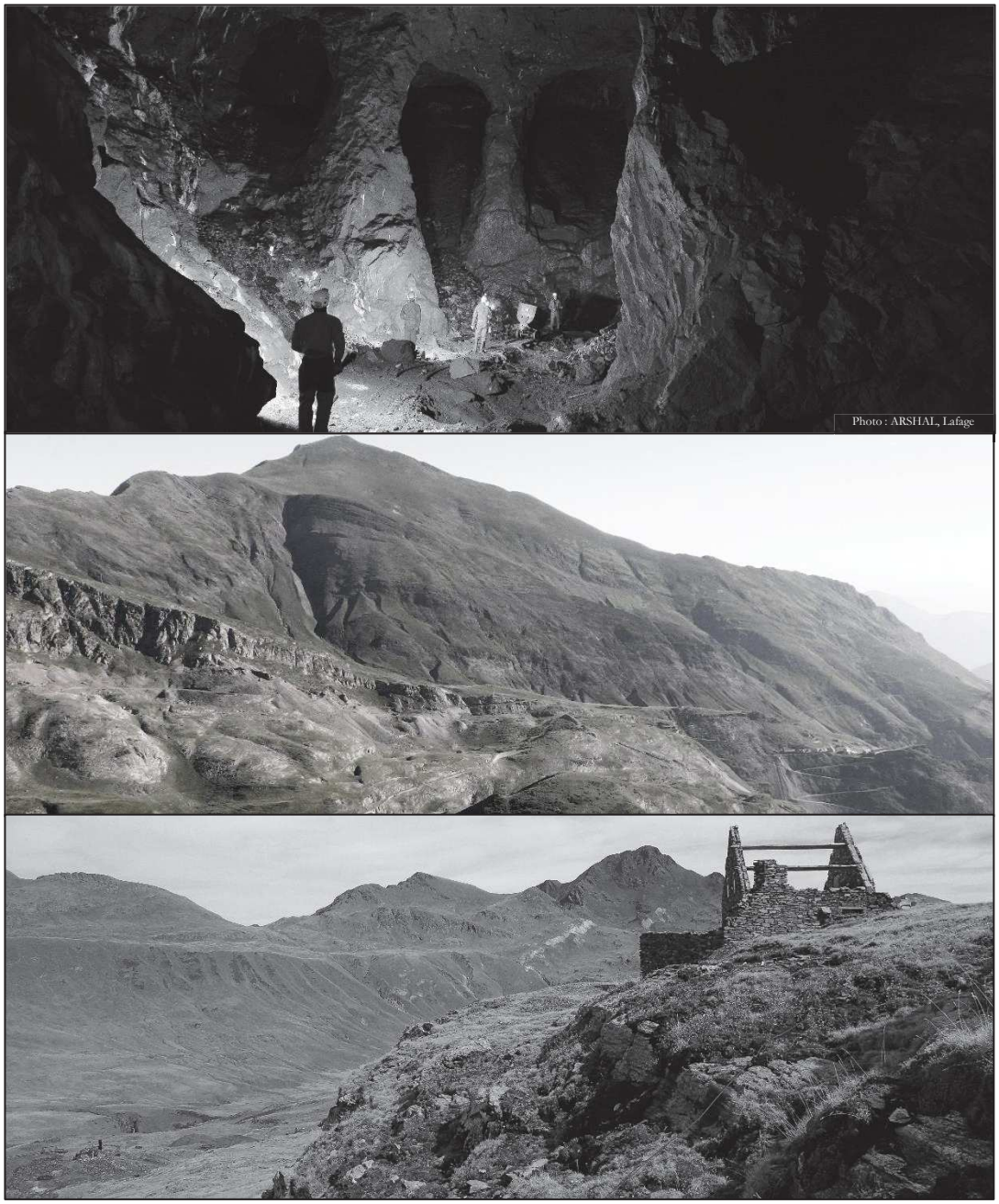

Bentaillou-Liat district

Acknowledgements/Remerciements

This study was funded through the French national program "Référentiel Géologique de France" (RGF-Pyrénées) of the French Geological Survey (Bureau de Recherches Géologiques et Minières; BRGM), Additional funding was acquired through the INSU-CNRS Tellus CESSUR program. This work was realized at Géosciences Montpellier and I acknowledge this laboratory to make available a part of the analytical techniques to achieve this work.

I am really grateful to the member of the PhD jury to have accepted to read and examine my manuscript: Jochen Kolb for his metallogenic expertise, Olivier Vanderhaeghe for his structural and geodynamic expertise on the Pyrenees, Kathryn Goodenough for her expertise on critical element geochemistry, Alan Boyle for his expertise on EBSD on sulfides and crystallography, and Fleurice Parat for her geochemistry expertise on rare elements systems.

En français, je tiens à remercier sincèrement ma directrice de thèse, Bénédicte Cenki-Tok pour sa confiance et sa disponibilité depuis mon stage de master et durant toute la thèse même si elle s'est expatriée à Sydney les derniers 10 mois de ma thèse. Elle a été une excellente directrice, toujours à l'écoute et me donnant d'excellents conseils à la fois scientifiques et de méthode qui m'ont permis de terminer à temps la thèse et avec une importante (je l'espère) production scientifique. Je voulais aussi remercier grandement Emilien Oliot, pour son engagement sans compter sur le terrain et ces nombreuses discusions sur l'aspect structural et EBSD de ma thèse. Certains terrains étaient particulièrement difficiles et nos jambes s'en rappellent encore, mentions spéciales à Crabioulès et Cierco ! Je suis très reconnaissant pour le travail d'Alain Chauvet durant ma thèse qui m'a permis d'acquérir énormément d'expériences (et pas que sur les pull-apart !). Je remercie aussi Kalin Kouzmanov pour les nombreuses discussions et manips sur l'aspect inclusions fluides, géochimie et minéralogie. Je tiens à remercier Manuel Munoz pour m'avoir transmis de nombreux conseils et savoirs sur l'analyse chimique des minéraux. Nous avons quelques discussions qui m'ont permis de grandement améliorer ma conception de l'analyse chimique des minéraux en général (ainsi que sur un certain groupe de musique !) Merci à Stefano Salvi de m'avoir donné son expérience sur les analyses inclusions fluides et de m'avoir guidé sur l'aspect microthermométrie, à Françoise Roger pour m'avoir guidé sur la datation parfois compliquée des zircons et monazites, Patrick Monié pour son implication dans la datation argon des micas et Elisabeth Le Goff pour son soutien BRGM. Merci à Jordi Gavaldà Bordes pour son implication et ses indications sur le terrain dans le Val d'Aran. Enfin je remercie Mael Alard et Angèle Laurent pour leurs assistances et leurs travails sur le terrain.

Je tiens aussi à remercier les techniciens et ingénieurs d'analyses, avec notamment Christophe Nevado et Doriane Delmas pour leurs exceptionnelles lames minces. Il en a fallu des heures pour polir cette

sphalérite et qu'elle indèxe à l'EBSD ! Je remercie aussi Fabrice Barou pour les analyses toujours parfaites à l'EBSD. Il était toujours là quand j'avais besoin d'une précision durant les nombreuses fois où je m'exporter sur l'ordinateur proche de la machine ! Je remercie aussi Vincent-Motto-Ros pour les excellentes cartes chimiques réalisées au LIBS. Je tiens enfin à remercier Bernard Boyer, ancien ingénieur de la microsonde et son excellent remplacant provisoire, Romain Lafay, Olivier Bruguier Olivier Alard et Oscar Laurent, spécialistes et ingénieurs LA-ICP-MS, et Frédéric Fernandez du MEB à Montpellier.

Je remercie grandement la participation de plusieurs spéléologues qui ont grandement contribué à la réussite du terrain dans les nombreuses localités étudiées notamment Jean Marc Poudevigne, Louis de Pazzis, et Bernard Lafage (mais aussi Véro, Roger, Bruno et j'en oublie…). Leurs précieuses aides et connaissance des lieux ont été très importantes dans l'accomplissement de l'étude de terrain. Parmis ces personnes certaines sont membres de l'ARSHAL, une association de plus d'un demi siècle vouée dans un premier temps, à protéger et explorer la grotte de la Cigalère, un immense dédale karstifié dans les Pyrénées ariégoises mais aussi dans un second temps à explorer l'ancienne mine Pb-Zn de Bentaillou, impressionnante par ces salles et son histoire. Ce lieu est magnifique à la fois sous-terre et en dehors et faire partie de ce groupe et de cette aventure durant ces deux années de suite reste un incroyable souvenir durant ma thèse.

Je remercie bien sur les amis et collègues du laboratoire, en commençant par Enora pour avoir partager ce bureau « 307 » durant ces trois ans et avoir parcouru quelques endroits sympas dans le monde le temps de quelques conférences. Merci à tous les sportifs aguérris de GM qui m'ont permis d'éliminer le stress et la charge de travail pendant la thèse, je pense à Rémi qui n'arrête jamais le sport et c'est tant mieux, Romain L. toujours partant pour faire des activités sportives et boire une bière en fait bien-sur partie intégrante, Romain H. un Grand compagnon de piscine et de trail, et Cyp un bon compagnon de vélo mais qui supporte un mauvais club de foot... Merci aussi à Clément, Asma & Camille, Nestor , Thierry, Gaëtan, Justine et j'en oublie, amis coureurs de Montpellier et d'ailleurs et anciens du Master GER notamment Julien, Flavien, Brice et Emilie.

Je me souviens de ma petite vitrine à minéraux et des nombreux bounquins sur la Terre, les océans quand je n'étais alors qu'à l'école primaire. Cette passion grandissante a été soutenue par mes parents, qui m'ont fait confiance même dans les moments de doute lorsque, par exemple, je partais seul étudier au Canada. La finalité de cette thèse est en grande partie liée à leur support indéféctible. Je tiens aussi à remercier mon frérot, Nico pour ses encouragements durant la thèse, et qui a été un modèle dans la vie pour moi durant toute mon éducation mais aussi un modèle dans le sport ! Pour conclure ces remerciements, une petite pensée à Suzanne ma grand-mère et Raymonde sa sœur qui je l'espère seront fières de moi de là où elles me regardent.

Résumé des travaux (extended abstract in french)

1.1 Introduction

Durant le dernier siècle, la proportion de ressources nécessaires à nos sociétés n'a cessé d'augmenter et de se diversifier notamment avec l'exploitation de nouveaux cortèges d'éléments comme les terres-rares, le lithium, le cobalt ou certains métaux rares comme l'indium, le gallium, ou le germanium. Plusieurs listes de métaux dits critiques sont apparues notamment dans l'Union

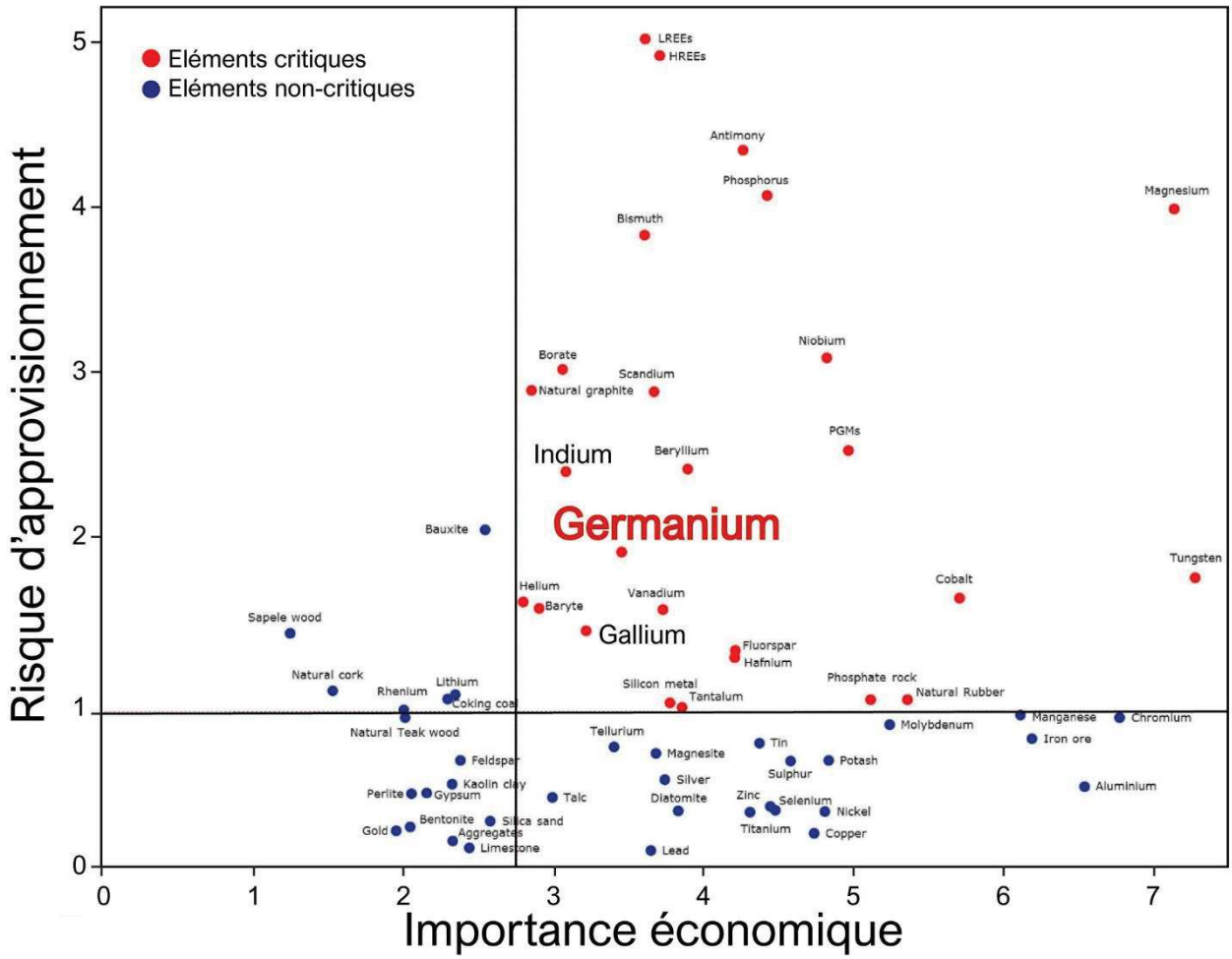

Figure 1. Comparaison de l'importance économique et du risque d'approvisionnement pour de nombreux éléments dans le cadre de l'évaluation de leurs criticités par la Comission Européenne en 2017 (*European Union, 2017*).

Européenne (Figure 1) et aux Etats-Unis principalement liées à leurs risques d'approvisionnement et leurs importances économiques. Ces éléments se trouvent en petites quantités dans la croûte terrestre et leurs modèles de concentration sont souvent mal connus.

Le Germanium est un métalloïde utilisé dans l'industrie de l'optique et de l'électronique notamment pour la fibre optique ou l'infra-rouge militaire. Son apparition ne semble pas spécialement liée à un environnement ou un type de gisement particuliers. Il est exploité le plus souvent en trace associé à la maille cristalline de la sphalérite (ZnS) ou dans des bassins houillers associé au charbon avec des concentrations n'excédant pas quelques milliers de ppm dans les deux cas. Néanmoins, le germanium ainsi que d'autres métaux rares (In, Ga) peuvent apparaitre dans des minéraux accessoires souvent portés par la sphalérite ou d'autres sulfures, avec des concentrations supérieures au % poids de Ge comme dans la brunogeierite ($GeFe_2O_4$ ~ 29% poids Ge). Ces minéraux riches en métaux rares sont souvent peu identifiés dans les minéralisations Pb-Zn-(Cu) alors qu'ils peuvent avoir une importance majeure pour l'exploration du Ge.

Les plus grandes ressources de zinc se trouvent dans des milieux déformés/métamorphisés et par conséquent peuvent avoir subi des évènements orogéniques. Cependant l'impact de ces évènements sur la concentration en éléments traces de la sphalérite est peu contraint. Des cibles idéales pour étudier l'empreinte de la déformation et du métamorphisme sur la redistribution en éléments traces de la sphalérite se situent dans les gisements Pb-Zn des Pyrénées en France et en Espagne. Ces minéralisations anciennement exploitées, ont une genèse encore débattue (*Pouit 1986; Johnson et al. 1996; Nicol et al. 1997)* et contiennent des minéraux à germanium dont certains uniquement descrits dans plusieurs gites pyrénéens (*Laforet et al. 1981; Johan et al. 1983*).

Dans cette étude, une analyse structurale sur le terrain couplée à une étude minéralogique des corps minéralisés sont premièrement présentées. Cette base de terrain a permis ensuite d'analyser la texture du minerai de zinc grâce à la cartographie EBSD (electron backscattered diffraction) couplée à l'étude chimique des éléments majeurs et mineurs (EPMA : electron probe microanalyser) et traces (LA-ICP-MS : laser ablation inductively coupled plasma mass spectrometry ; cartographie LIBS : laser induced breakdown spectroscopy). Cette méthode, assez peu conventionnelle, a permis de mieux comprendre l'arrangement des concentrations en Ge ainsi que d'autres éléments traces dans la maille de la sphalérite et dans les minéraux à Ge. Une dimension geochronologique est aussi présente, qui porte sur l'analyse de zircons dans des granites et de monazites dans des métapélites (datations U-Th-Pb), et de micas associés à la minéralisation

Pb-Zn (datations $^{40}Ar/^{39}Ar$). Enfin des analyses microthermométriques et des traces (LA-ICP-MS) portant sur les inclusions fluides associées à la minéralisation Pb-Zn sont exposées, et permettent de mieux caractériser la signature des fluides en proposant un modèle génétique complet des minéralisations Pb-Zn(-Ge).

1.2 Méthodes analytiques

L'approche analytique de cette étude est présentée dans la Figure 2 et comprend premièrement une étude structurale de terrain dans plus de dix-huit anciens gisements Pb-Zn des Pyrénées. Un échantillonage en place et orienté a été réalisé ce qui a permis la création de lames minces ou épaisses permettant de réaliser différentes analyses texturales (microscopie optique, EBSD) ou chimiques (EPMA, LA-ICP-MS, cartographie LIBS) de minéraux, essentiellement sur la sphalérite (ZnS) et les minéraux à Ge. Une analyse complète des inclusions fluides a été réalisée avec l'utilisation de la cathodoluminescence (chaude) associée à la microthermométrie et à l'analyse des traces (LA-ICP-MS). Des analyses géochronologiques U/Pb sur zircons et monazites, et $^{40}Ar/^{39}Ar$ sur micas directement porté par la sphalérite ont été réalisées pour essayer de mieux contraindre l'aspect temporel des minéralisations étudiées.

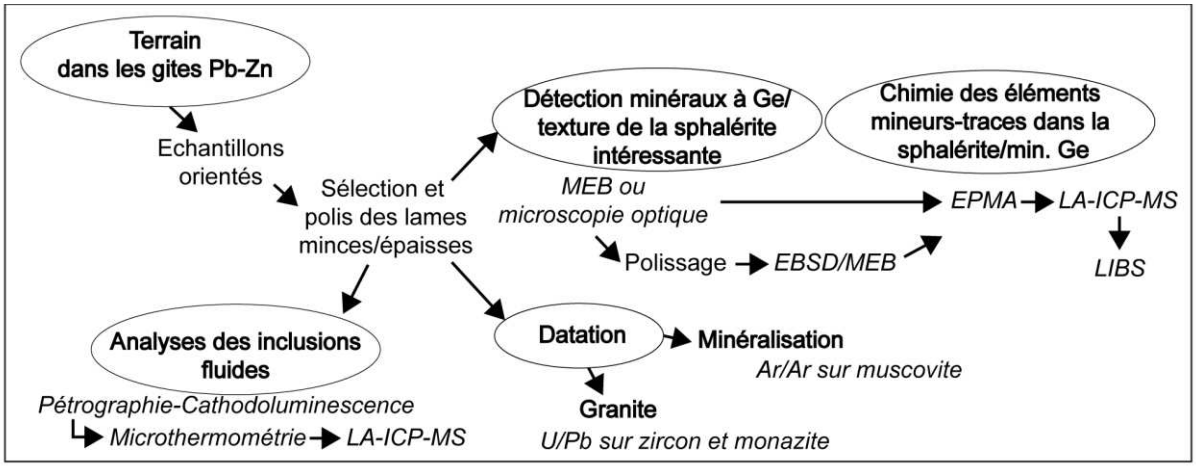

Figure 2. Approche analytique réalisée dans cette étude. Abbréviations : MEB : Microscope électronique à balayage ; EPMA : electron probe microanalyser; LA-ICP-MS : laser ablation inductively coupled plasma mass spectrometry; LIBS: laser induced breakdown spectroscopy ; Ar:

1.3 Contexte géologique

1.3.1 Structuration des Pyrenées

Les Pyrénées sont un segment orogénique E-O, et une partie de la chaîne Alpine s'étendant entre la marge Nord Ibérique et les Alpes à l'ouest (*Choukroune 1992*). Cet évènement orogénique s'étalant du Crétacé supérieur au Paléogène (*Carreras and Druguet 2014*) a permis l'exhumation d'un fragment d'une chaîne orogénique plus ancienne, du nom de Varisque (Carbonifère-Permien). Cinq grands niveaux structuraux apparaissent dans les Pyrénées du Nord vers le Sud :

-Le Bassin Aquitain est composé de roches Mésozoïque à Cénozoïque recouvert par des dépôts Oligo-Miocène post-tectoniques.

- La Zone Nord-Pyrénéenne est essentiellement composée de dépôts Mésozoiques et est bordée au sud par la faille Nord Pyrénéenne d'âge Alpin.

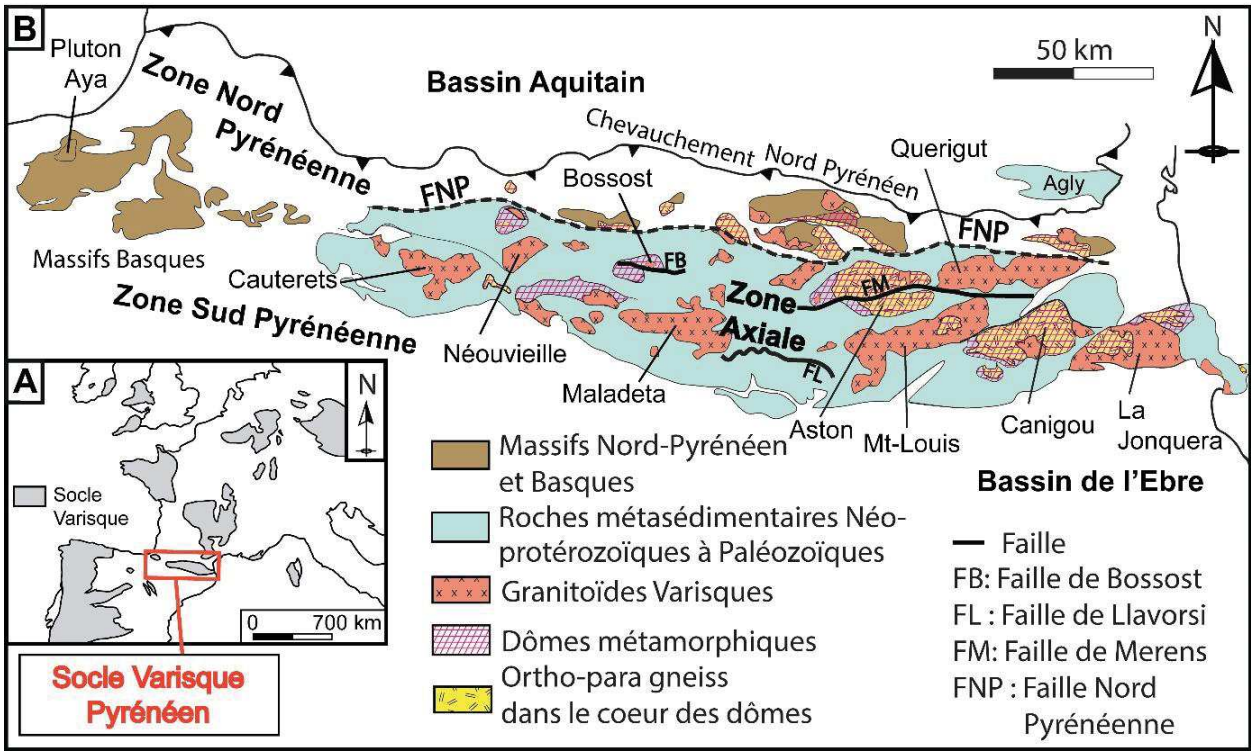

Figure 3. Localisation et composition de la zone d'étude, la Zone Axiale des Pyrénées. A. Localisation de la Zone Axiale Pyrénéenne dans la ceinture Varisque de l'Europe de l'Ouest. B. Carte géologique simplifiée du socle déformé au Varisque avec la localisation des principaux massifs de granitoïdes et des dômes métamorphiques.

-Les domaines déformés au Varisque se composent de:

i) La Zone Axiale est composée de dépôts Néoproterozoïques à Paléozoïques métasédimentaires, de roches gneissisques et granitiques d'âges Ordovicien et Varisque respectivement (Figure 3).

ii) Les massifs Nord Pyrénéens sont de petites zones de socle déformé au Varisque présents dans la Zone Nord Pyréneenne.

iii) Les massifs Basques se situent à l'Ouest de la chaîne Pyrénéenne et sont composés de roches métasédimentaires intrudées par le pluton d'Aya, datant du Permien supérieur *(Denèle et al. 2012*).

-La Zone Sud Pyrénéenne est composée de roches Mésozoïques et Cénozoïques et de plusieurs chevauchements à vergence sud.

Le bassin de l'Ebre est limité au nord par le chevauchement Sud-Pyrénéen et est composé essentiellement de roches Oligo-Miocène.

1.3.2 Evolution tectonique des Pyrénées

Un résumé de l'évolution tectonique des Pyrénéees est présenté ci-dessous.

Durant l'Ordovicien inférieur, un important magmatisme a lieu dans les roches Néoproterozoïques et Cambriennes (les plus vieilles des Pyrénées) lié à la subduction de l'Océan Péri-Gondwana sous Gondwana. L'Ordovicien Supérieur est marqué par la présence d'une discordance angulaire probablement lié à une période d'extension où à un période de déformation (*Casas and Fernández 2007).*

Le socle déformée au Varisque des Pyrénées est le résultat de la collision entre Gondwana et Avalonia durant le Carbonifère inférieur-moyen (Figure 4 ; *Matte 2001; Martinez Catalan 2011*).

Trois grands épisodes de déformation sont reconnus dans les Pyrénées selon la synthèse provenant de *Denèle et al. (2014),* la plus reconnue actuellement. Un épisode D_1 lié à l'épaississement crustal est responsable de la formation de la foliation S_1 souvent parallèle à la stratification S_0 *(Zwart 1979; Garcia-Sansegundo and Alonso 1989; Matte 2002; Vilà et al. 2007*) et probablement lié à la présence de plis couchés kilométriques F_1 *(Matte 1969; Garcia-Sansegundo and Alonso 1989; Vilà et al. 2007).* L'épisode D_2 est divisé en deux parties: premièrement un épisode de fluage crustal latéral et

horizontal (D_{2a}) directly followed by the formation of gneissic dome (D_{2b}). La schistosité S_2 souvent verticale et plan axiale de plis F_2 est reliée à cet évènement. La déformation D_3 est liée à la présence de zones de cisaillement d'ordre régional comme la faille de Bossost et de Mérens *(Carreras and Cirés 1986; Carreras 2001; Mezger et al. 2012*).

La déformation Pyrénéenne-Alpine semble minoritaire dans la Zone Axiale même si elle reste très difficile à estimer du fait de son orientation similaire au structures Varisque *(Cochelin 2016)*. Elle n'a eu probablement que peu d'inpact sur les roches Paleozoïques, à l'exception de réactivations de structures pré-existantes *(McCaig et al. 2000; García-Sansegundo et al. 2014*).

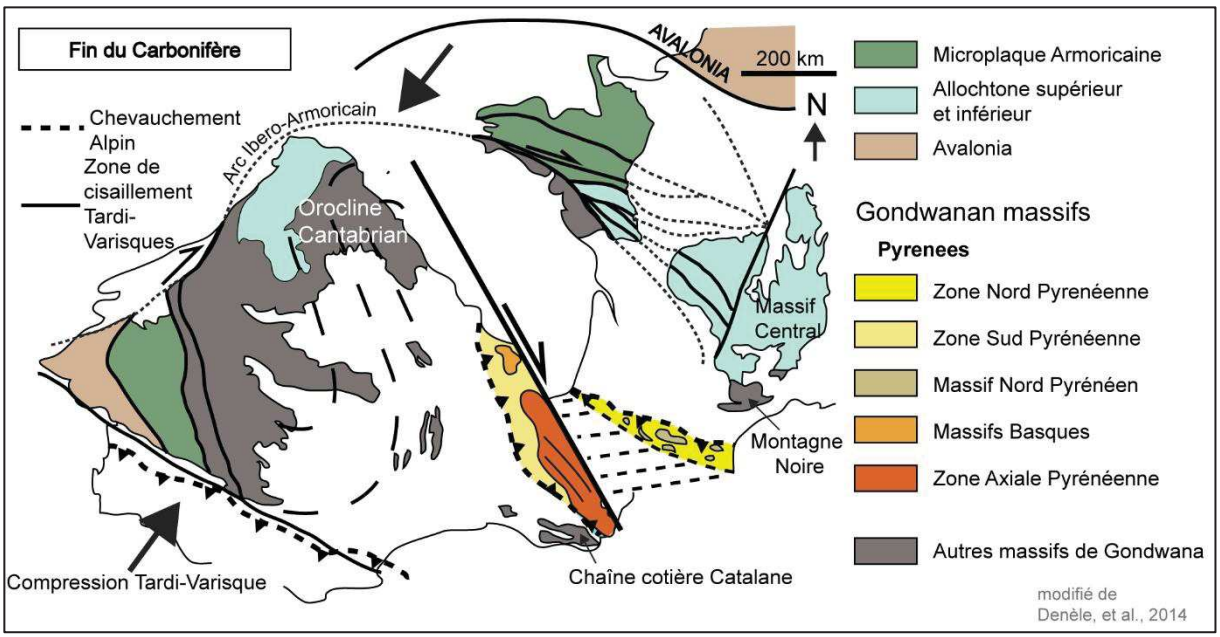

Figure 4. Représentation structurale de la ceinture Varisque de l'ouest de l'Europe, à la fin du Carbonifère (modifiée d'après *Denele et al. 2014*).

1.3.3 Minéralisations Pb-Zn dans les Pyrénées

Les minéralisations Pb-Zn dans les Pyrénées sont essentiellement localisées dans la partie centrale et ouest de la Zone Axiale des Pyrénées et dans les Massifs Basques (Figure 5), avec plus d'une centaine d'anciens gisements ou indices recensés (*Pouit 1985; Vic and Billa 2015*).

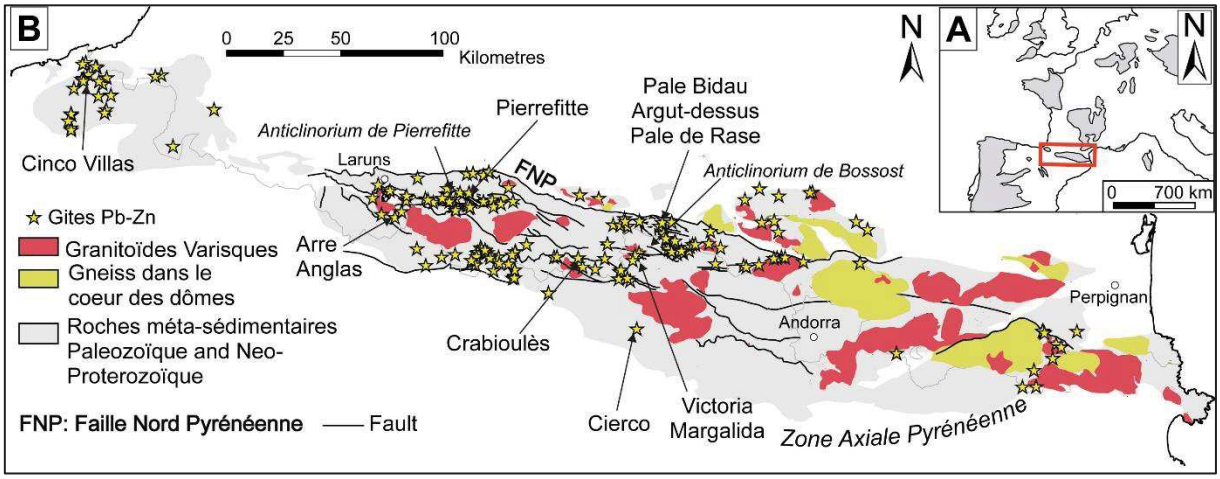

Figure 5. Carte structurale de la répartition des gites Pb-Zn des Pyrénées. Les principaux gites étudiés sont notés.

Deux grands types de minéralisations peuvent être reconnues dans les Pyrénées :

a) Les minéralisations Pb-Zn(-Fe-Cu-Ba) dans des niveaux stratiformes-stratabounds sont les plus abondantes et avec les plus forts tonnages dans les Pyrénées, notamment par la présence des anciens gisements de Pierrefitte, Bentaillou ou du Cinco-Villas (Figure 5). Ces minéralisations sont considérées SEDEX par de nombreux auteurs (*Bois et al. 1976; Pouit 1978; Cardellach and Alvarez-Perez 1979; Pouit and Bois 1986a; Pesquera and Velasco 1989; Marcoux et al. 1991b; Cardellach et al. 1996; Velasco et al. 1996)* basées sur des éléments essentiellement géométriques de terrain. D'autres auteurs montrent un important rôle de l'orogénèse Varisque avec d'importantes remobilisations dans les charnières de plis ou entre deux niveaux structuraux différents *(Alonso 1979; Nicol et al. 1997*).

b) Les minéralisations Pb-Zn(-F-Ba) en veines semblent moins répandues dans les Pyrénées. Le plus grand ancien gisement en veines des Pyrénées est celui de Cierco (*Johnson et al. 1996*), localisé en Espagne (Figure 5 ; 1.4 Mt de minerai à 4% Pb et 3% Zn). Les minéralisations de sulfures déformés en veines de Cierco sont probablement d'âge Mésozoïque (*Johnson et al. 1996)* liées au fait que la minéralisation recoupe des niveaux sédimentaires de pélites rouges Permiennes. Des veines Mésozoïques semblables apparaissent à Aulus-Les Argentières mais n'apparaissent pas déformées. A

l'est de l'anticlinorium de Pierrefitte (Figure 5), de nombreuses veines sont reconnues dans le district d'Arre et d'Anglas-Uzious (*Reyx 1973*), encaissées dans le Dévonien et interprétées comme d'âge tardi-Varisque. D'autres veines similaires sont décrites dans la littérature comme celle de Yenefrito (*Subias et al. 1999*), Parzan (*Fanlo et al. 1998*), ou La Géla (*Pouit and Bois 1980*). Ces veines sont souvent orientées E-W avec un pendage variant de 50° à vertical.

1.4 Etude structurale et minéralogique des minéralisations Pb – Zn (– Ge) des Pyrénées

L'étude structurale a été réalisée dans plus de dix-huit anciens gisements Pb-Zn des Pyrénées. Un premier type mineur de minéralisation est le Type 1 qui apparait stratiforme et disséminé dans l'encaissant schisteux ou gréseux. Le deuxième type, Type 2a est stratabound, parallèle à S_0-S_1, et peut apparaitre sur le terrain en pull-apart (Figure 6A) intimement lié à un pli F_1 couché kilométrique (Bentaillou, Figure 6A), dans des plans de chevauchement comme à Pierrefitte, ou largement plissé par la phase de déformation D_2 à Victoria. Le troisième type de structures se constitue de minéralisations en veines Type 2b (Figure 6B et C) encaissées dans des calcschistes ou des calcaires et parallèle à la schistosité S_2 Varisque. Ces minéralisations sont probablement tardi-Varisques ou Mésozoiques. Le résumé de la position structurale des différentes minéralisations est présent dans la Figure 7.

1.5 Texture et chimie des minéralisations Pyrénéennes

Les minéralisations stratabound et en veines ont été analysées texturalement (cartographie EBSD) et chimiquement (EPMA, LA-ICP-MS, cartographie LIBS). Seules les minéralisations de Type 2b présentent des enrichissements en Ge mai aussi en Cu et Ga.

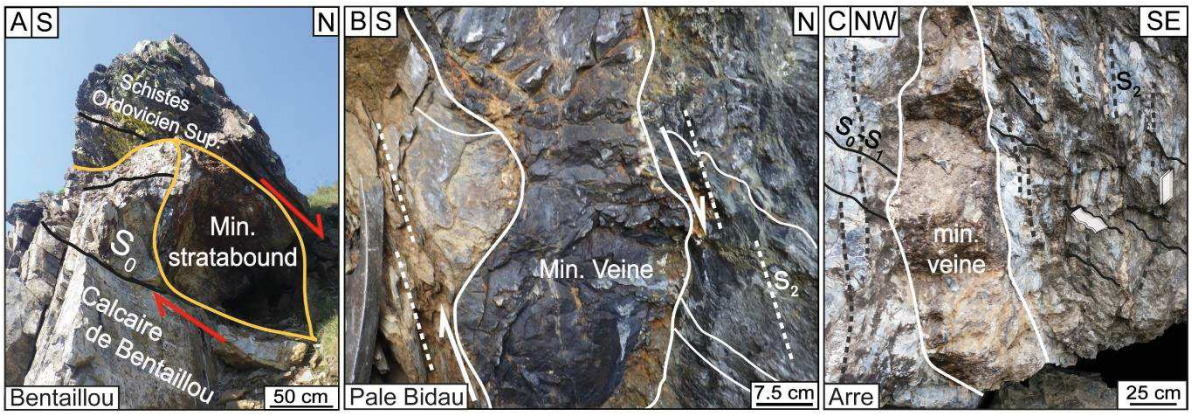

Figure 6. Photos de terrains montrant les trois principaux types de minéralisations Pb-Zn. A. Mineralisation stratabound Type 2a à Bentaillou. B. Minéralisation en veine de Type 2b (Tardi-Varisque) à Pale Bidau. C. Minéralisation en veine de Type 2b (Mésozoïque).

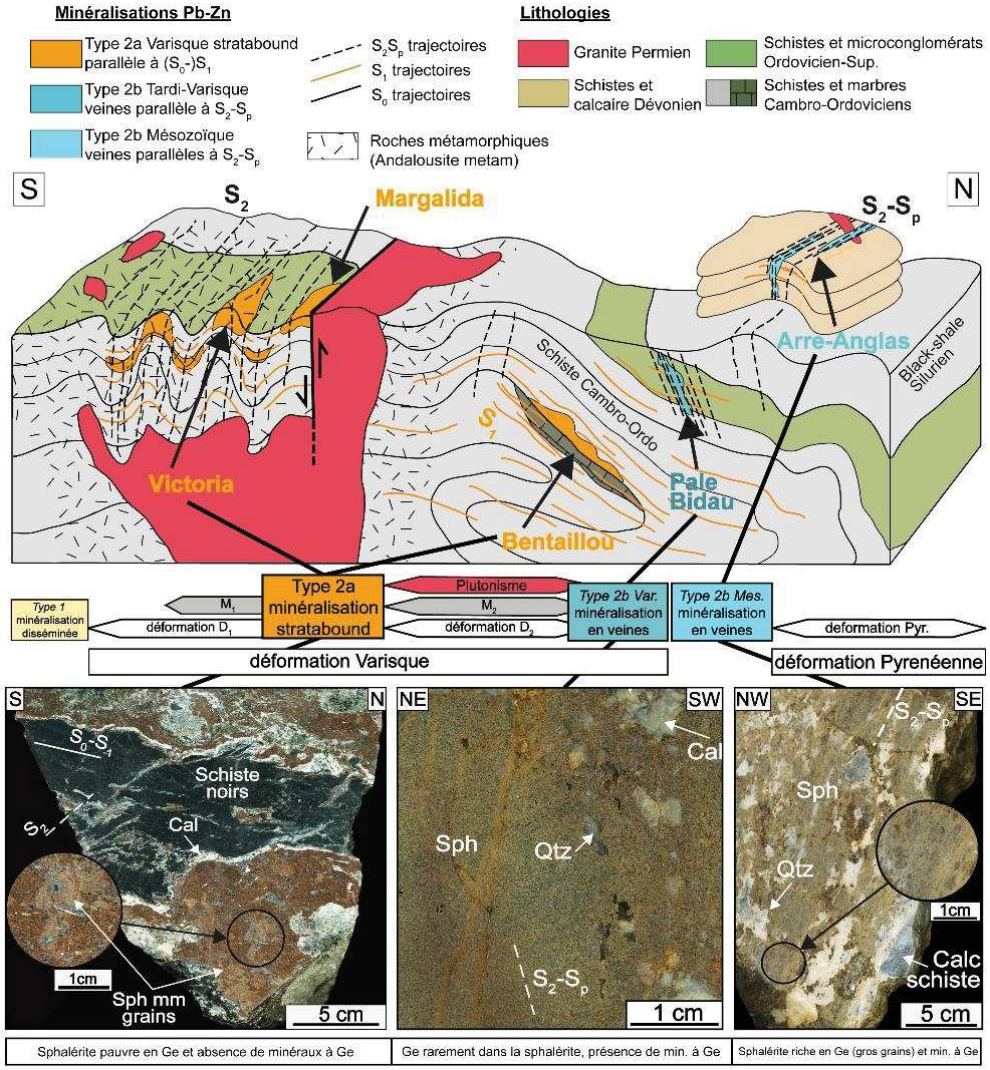

Figure 7. Modèle 3D avec la position structurale, chronologique, texturale et le contenu en Ge des trois grand types de minéralisations Pb-Zn dans la Zone Axiale des Pyrénées. Les minéralisations en veines Type 2b (tardi-Varisque et Mésozoïque) sont les uniques porteurs de la minéralisation à Ge.

Les minéralisations de Type 2a présentent des textures typiquement métamophiques avec des grains polygonaux, souvent maclés (macles de recuit, recristallisation statique). Elles peuvent présenter aussi des textures de recristallisation dynamique au cœur de plis F_2. Aucun minéral à Ge n'a été repéré et le contenu en élément traces (Ge, Ga, In, Cu) et relativement bas (<10 ppm for Ge, Ga, et In).

Les minéralisations de Type 2b contiennent une importante hétérogénéité, à la fois en termes de texture et de chimie. En visualisant la sphalérite en lumière transmise, différentes zonations de couleurs apparaissent de marron sombres à claires (Figure 8A). Avec la cartographie EBSD, il est possible de nettement visualiser les limites de grains de la sphalérite. Elle apparait largement hétérogène en termes de tailles de grains avec de gros grains (> 100 μm) et de petits grains (< 100 μm). Ces gros grains apparaissent déformés ductilement (jusqu'à 20 ° de désorientation interne progressive) et mantelés par de petits grains (Figure 8B) témoignant d'une recristallisation avec de forte désorientations ponctuelles. Chimiquement le Ge apparait différement suivant la texture analysée. Dans les zonations des gros grains nommés parents, les concentrations en Ge dans la maille de la sphalérite sont relativement élevées (jusqu'à 600 ppm Ge ; Figure 8C), contrairement aux zonations claires des grains parents qui contiennent des concentrations faibles (<100 ppm Ge). Les grains recristallisés ne possèdent que peu de Ge (<50 ppm Ge). Des minéraux à Ge portés par la sphalérite sont aussi présents (grains jaunes, Figure 8D et E) et occurrent essentiellement dans la sphalérite recristallisée ou proche de macles dans les grains grossiers. Dans la sphalérite, le Ge et le Cu sont extrèmement corrélés (Figure 9) et le Ga uniquement relativement concentré et zoné dans les grains grossiers (<100 ppm Ga). En considérant les concentrations en Ge mesurées par la cartographie LIBS, la sphalérite primaire pré-recristallisation pouvait contenir des concentrations en Ge uniformes de l'ordre de 700 ppm Ge.

Une cartographie EBSD et LIBS a été réalisée à l'échelle du grain et montrent une relation entre déformation ductile et concentration en Ge-Cu dans la maille de la sphalérite. Lorsque la déformation ductile est élevée dans la sphalérite (nombre de limites de sous grains important), le contenu en Ge et Cu est très faible comparé aux zones de grains où la déformation ductile est faible (Figure 9).

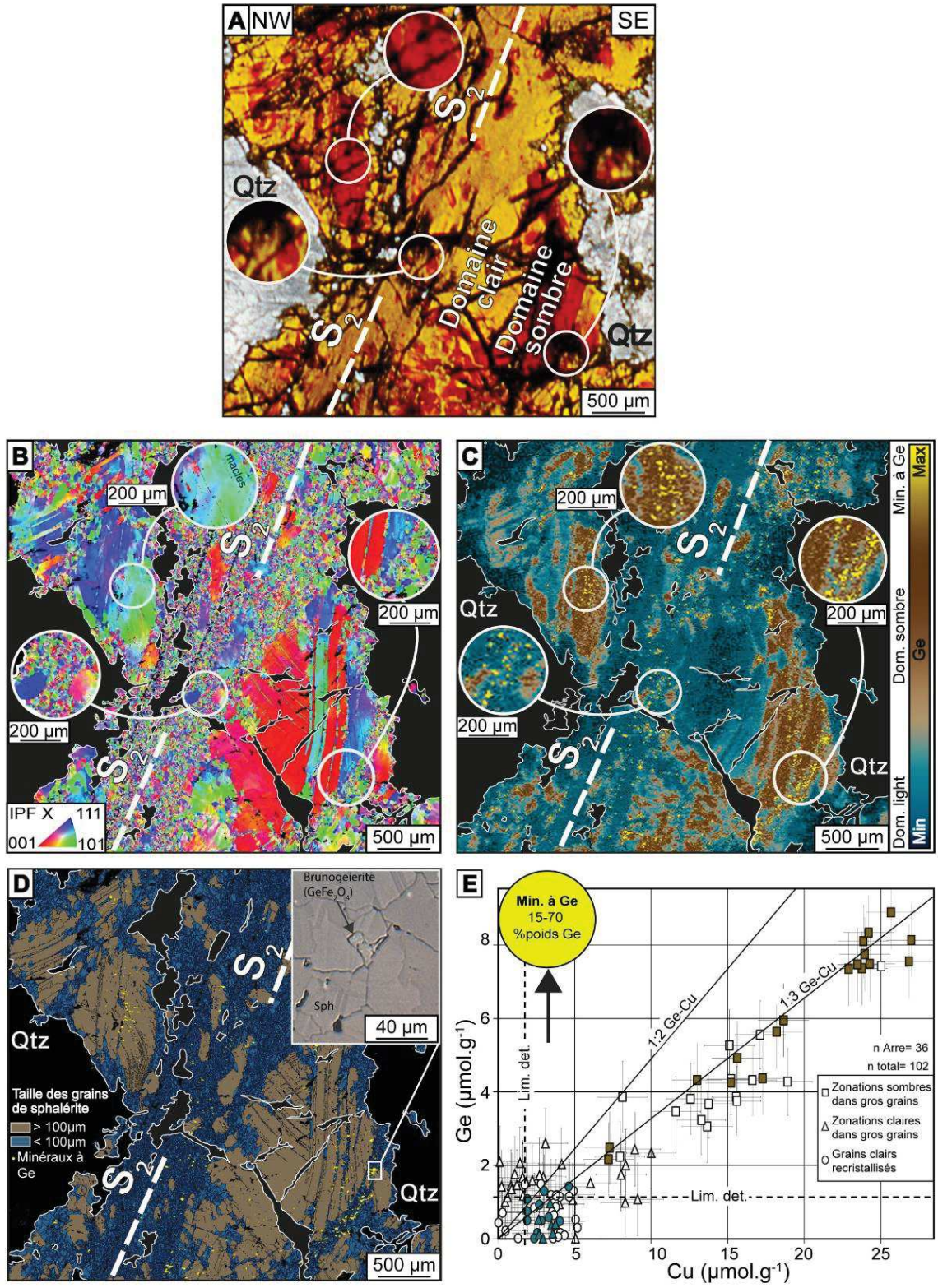

Figure 8. Sphalérite du gite Pb-Zn d'Arre analysée par des méthodes texturales (EBSD) et chimiques (cartographie LIBS et EPMA) A. Sphalérite zonée chimiquement en lumière transmise. B. Carte EBSD inverse pole figure selon l'axe X montrant l'hétérogénéité des grains et la déformation intra-granulaire. C. Carte LIBS du germanium montrant l'hétérogénéité chimique de la zone dans la sphalérite et la présence de minéraux à Ge (en jaune). D. Carte EBSD de taille de grains avec superposés, les minéraux à Ge repérés avec la carte LIBS. E. Analyses EPMA réalisées sur la sphalérite d'Arre mais aussi sur d'autres sphalérites de Type 2b à Anglas et à Pale Bidau.

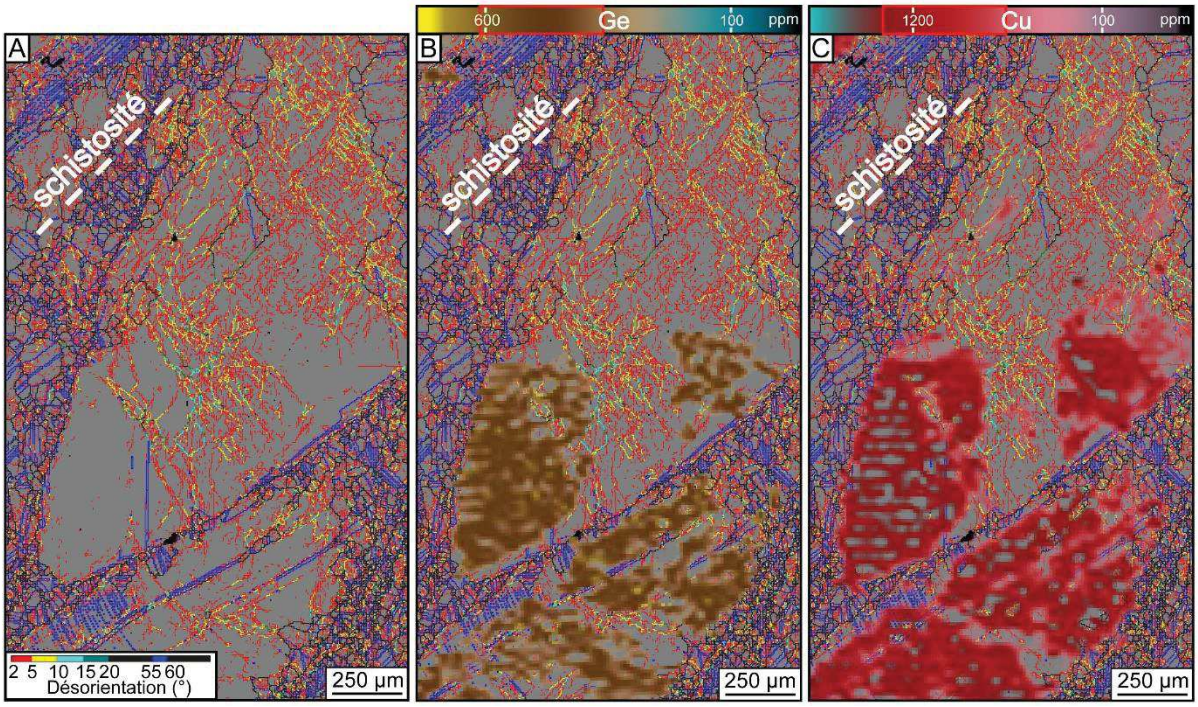

Figure 9. Répartition des concentrations en Ge et Cu en fonction de la microstructures dans deux grains parents de sphalerite. A. Carte de désorientation des limites de grains réalisée à l'EBSD avec inférieur à 20°, les limites de sous-grains, au-dessus de 20° les limite de grains et entre 55 et 60° les macles. B. Superposition des concentrations en Ge les plus élevées dans la maille de la sphalérite mesurées avec le LIBS. C. Superposition des concentrations en Cu les plus élevées dans la maille de la sphalérite acquises avec le LIBS.

1.6 Etude des fluides

Les études microthermométriques et des éléments traces dans les inclusions fluides (LA-ICP-MS) primaires et secondaires ont montré la présence de deux types de fluides. i) un fluide avec de relatives faibles salinités (<20 %poids eq. NaCl) et de hautes temperatures (200-350 °C) dans les gites de Pale Bidau, Argut-dessus et Pale de Rase (Figure 10). Des inclusions secondaires de ce type ont aussi été analysées à Margalida ii) des fluides avec de fortes salinités (15-35 %poids eq. NaCl) et de faibles températures (< 200 °C) dans les gites d'Arre et d'Anglas. Des inclusions secondaires de ce type ont aussi été analysées dans les gites de Victoria et Crabioules (Figure 10).

La comparaison de ces différents fluides avec d'autres analyses d'inclusions fluides de gite Pb-Zn dans la Zone Axiale des Pyrénées et dans la Montagne Noire, montrent que les fluides de basse salinité-haute temperature sont typiques de minéralisations Varisques *(Munoz et al. 1994, 2016;*

Johnson et al. 1996; Boiron et al. 2010). Les fluides de hautes salinités-basses températures ont par contre des caractérisques de fluides Mésozoïques (par comparaison avec les données des minéralisations en veines de Cierco, Yénefritto, etc. ; *Johnson et al. 1996; Subias et al. 1999*). La

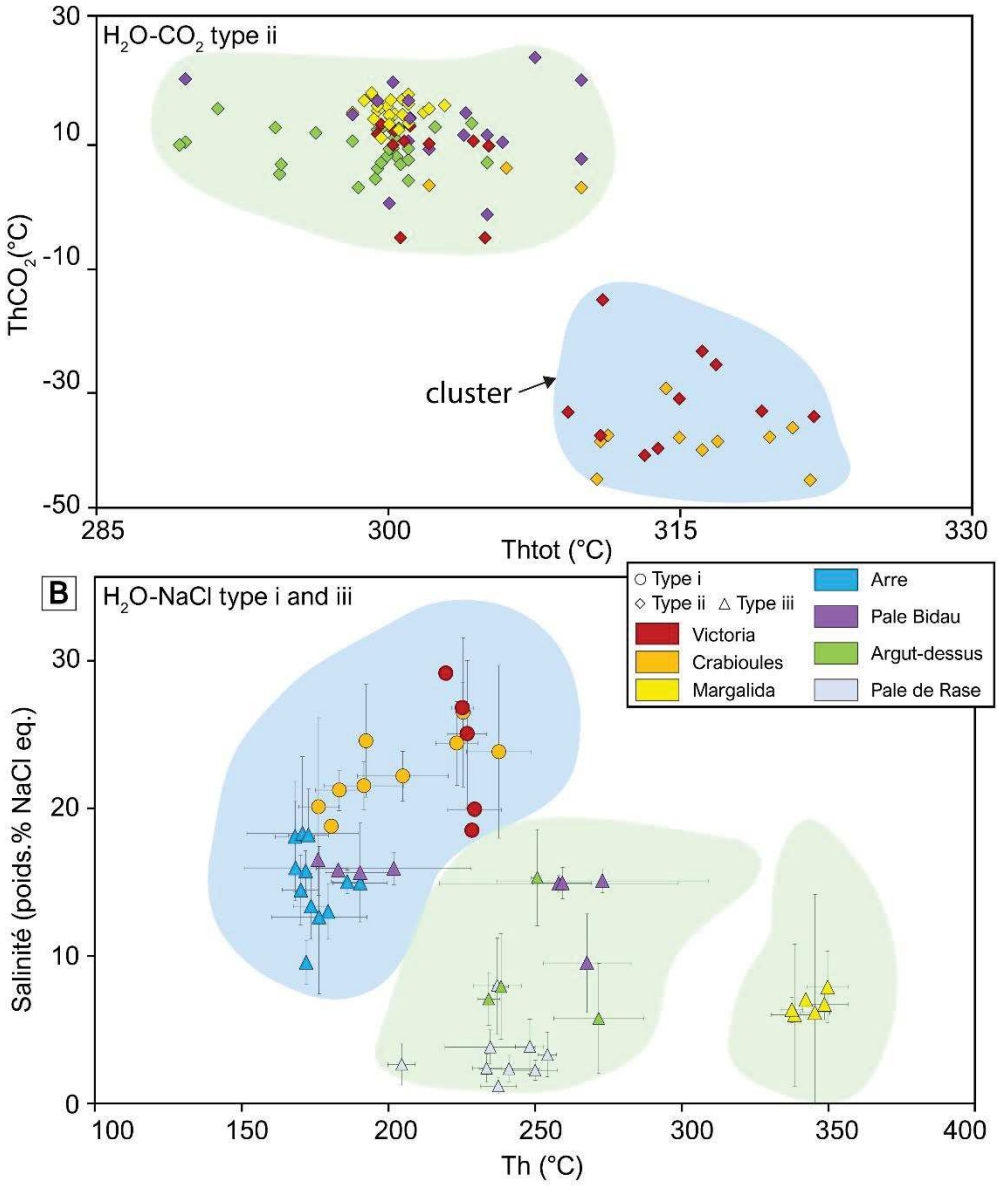

Figure 10. Résultats des analyses microthermométriques d'inclusions fluides. A. Température d'homogénéisation du CO_2 ($ThCO_2$; °C) vs homogénéisation totale (Thtot ; °C) dans les inclusions fluides carboniques. A noter l'apparition d'inclusions fluides dans les fractures à Victoria, Crabioules et Margalida (Type stratabound) proches des domaines $ThCO_2$-Thtot d'inclusions fluides de Pale Bidau et Argut-dessus (Type veine) alors que les inclusions fluides présentent dans les clusters montrent des $ThCO_2$ plus faibles. B. Salinité (% poids NaCl eq.) vs température d'homogénéisation (Th; °C) dans des assemblages à inclusions fluides à deux phases. Les analyses ponctuelles totales sont présentes en transparence.

présence de déformation dans la sphalérite est surement liée à l'action de la déformation Pyrénéenne et possiblement du métamorphisme basse-pression haute-temperature du Crétacé inférieur la précédant.

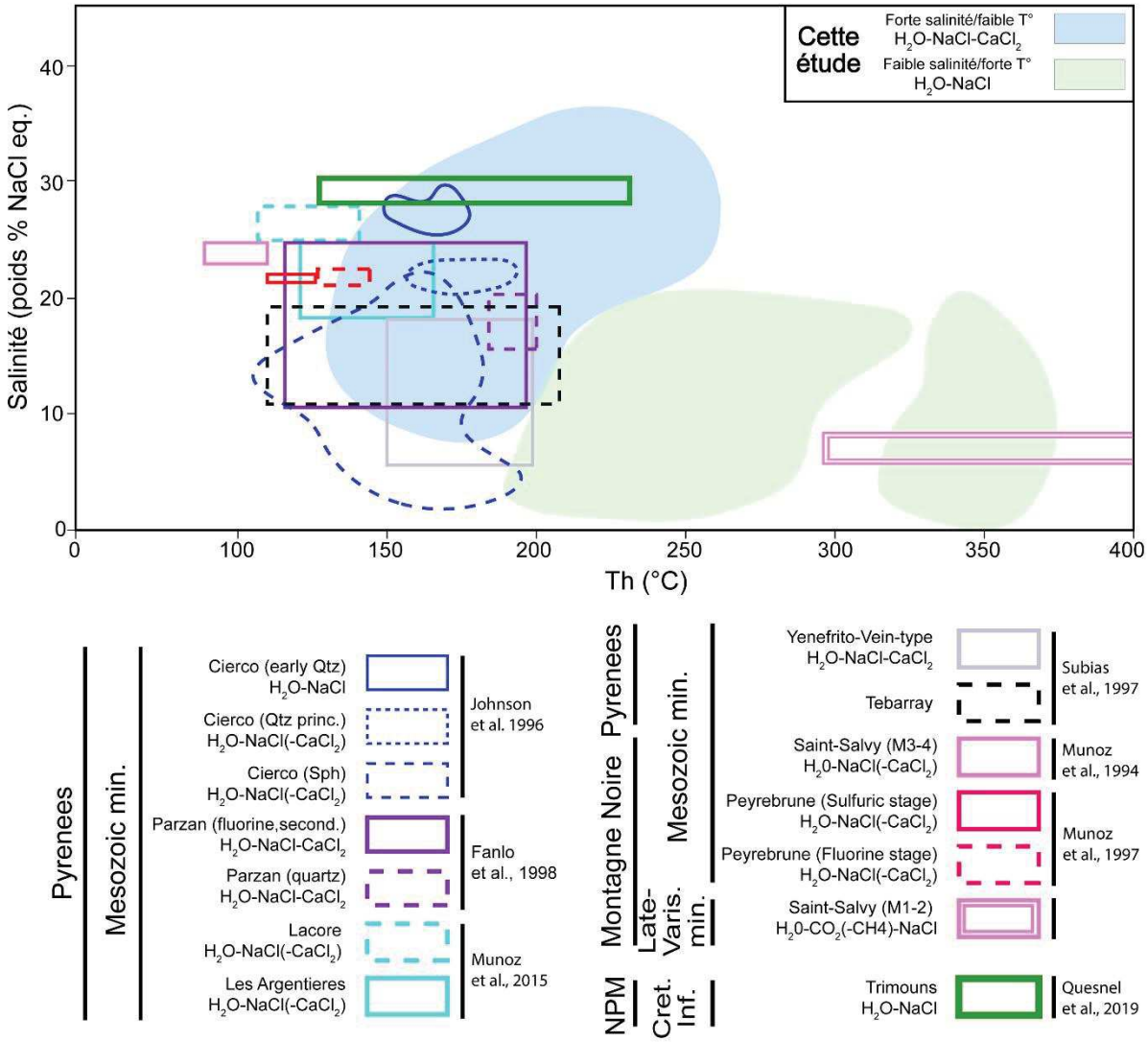

Figure 11. .Salinité (% poids NaCl eq.) vs température d'homogenéisation (Th) pour les inclusions fluides acqueuses de cette étude et d'autres gîtes étudiés dans les Pyrénées et la Montagne Noire. Le domaine de salinité-Th des fluides associés à la formation de talc dans le gisement de Trimouns est aussi exposé (abbréviations : MNP : massif Nord-Pyrénéens).

1.7 Discussion et conclusions

Une première dimension de l'étude a permis de mieux comprendre la genèse des minéralisations Pb-Zn et de cibler préférentiellement la minéralisation en veines (Type 2b) pour le germanium. Préalablement classées comme SEDEX *(Pouit 1985; Pouit and Bois 1986b; Pujals 1992*), les minéralisations de Type stratabound (Type 2a) sont intimement liées à l'orogénie Varisque en ayant été remobilisées dans les charnières de plis F_1 (Bentaillou), F_2 (Victoria) ou dans des plans de chevauchements (Pierrefitte). L'addition de l'étude des inclusions fluides a permis de différencier deux types de fluides pour les minéralisations en veines, avec des signatures en salinités-températures différentes qui sont probablement liées à deux évènements hydrothermaux régionaux (*Munoz et al. 1994; Johnson et al. 1996; Fanlo et al. 1998*) durant le Tardi-Varisque et le Mésozoïque.

En couplant des méthodes d'analyses texturales et chimiques (in-situ et cartographique), cette étude a permis de mieux comprendre la formation de concentrations de Ge dans des petits minéraux accessoires portés par la sphalérite en veines. Primairement présent dans la maille de la sphalérite (Figure 12), les concentrations en Ge ont ensuite été impactées par la recristallisation dynamique de la sphalérite, qui a induit la redistribution et la remobilisation de ces concentrations, probablement assistée par l'action de fluides. La genèse de ces fluides pourrait être liés au métamorphisme LP-HT du Crétacé inférieur et à l'orogénie Pyrénéenne, seuls évènements notables présent après le Mésozoique et ses dernières minéralisations en veines (type Arre). Le Ge mais aussi d'autres éléments comme le Cu porté dans la maille de la sphalérite ont ensuite été reprécipités dans des minéraux accessoires pour former les minéraux à Ge tels que des oxydes, des sulfures ou des chloritoïdes.

Ce processus pouvant être nommé redistribution du germanium, semble important et fréquemment présent dans les minéralisations impactées par la déformation/métamorphisme. Il est important de noter qu'aucune perte ou aucun apport externe en Ge ne sont considérés si la sphalérite primaire avant recristallisation possédait une teneur en Ge de l'ordre de 700 ppm (après calcul de masse sur carte LIBS). La présence d'importantes hétérogénéités notamment en Ge dans la sphalérite peuvent montrer la présence de ce processus et indirectement de minéraux à Ge comme dans certains gisements Pb-Zn au Brésil, au Portugal ou en Chine *(Monteiro et al. 2006; Reiser et al. 2011; Ye et al. 2011*). De plus ces minéraux à Ge ne sont pas faciles à repérer en optique et peuvent être facilement négligés, ce qui montre l'importance d'utiliser des techniques adaptées comme le MEB-EBSD ou la cartographie LIBS lors de l'étude de minerais sulfurés déformés. La

remobilisation du Ge en minéraux à Ge pourrait représenter une importante ressource en métaux rares (Ge, In, Ga) dont la faisabilité économique reste à démontrer, notamment pour certains gisements déformés qui correspondent aux plus grandes ressources actuelles en zinc.

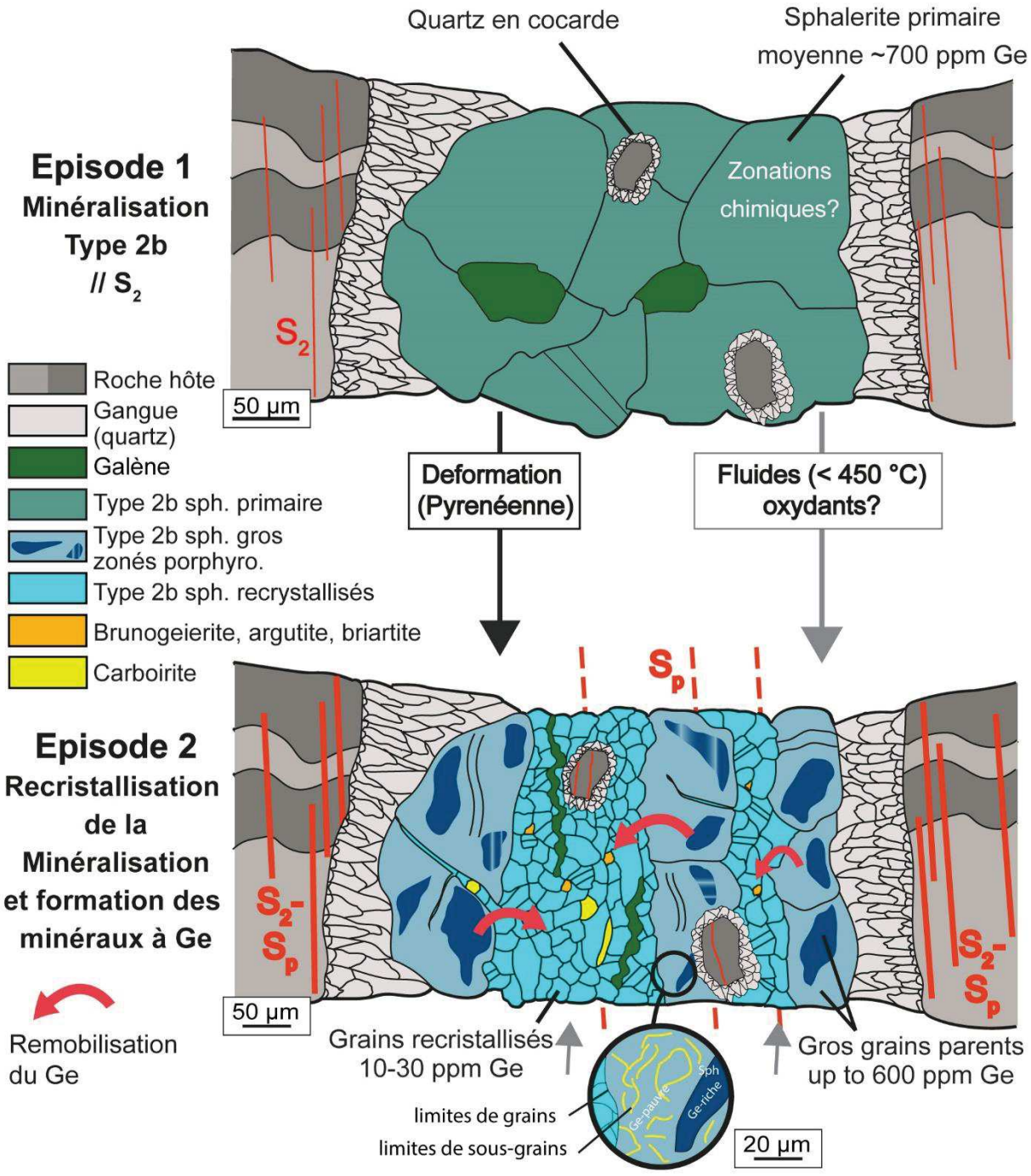

Figure 12. Modèle de remobilisation du germanium dans la sphalérite en veines de Type 2b. Abbréviations : S_2 : schistosité Varisque de l'évènement D_2 ; Sp : Schistosité supposée d'âge pyrénéen.

Table of Contents

RESUME DES TRAVAUX (EXTENDED ABSTRACT IN FRENCH) ..... **XI**

1.1 INTRODUCTION XI

1.2 METHODES ANALYTIQUES XIII

1.3 CONTEXTE GEOLOGIQUE XIV

1.3.1 Structuration des Pyrenées ..... *xiv*

1.3.2 Evolution tectonique des Pyrénées ..... *xv*

1.3.3 Minéralisations Pb-Zn dans les Pyrénées ..... *xvii*

1.4 ETUDE STRUCTURALE ET MINERALOGIQUE DES MINERALISATIONS PB – ZN (– GE) DES PYRENEES XVIII

1.5 TEXTURE ET CHIMIE DES MINERALISATIONS PYRENEENNES XVIII

1.6 ETUDE DES FLUIDES XXII

1.7 DISCUSSION ET CONCLUSIONS XXV

TABLE OF CONTENTS ..... **XXVIII**

LIST OF FIGURES ..... **XXXIII**

LIST OF TABLES ..... **XLII**

1 INTRODUCTION **1**

1.1 GENERAL INTRODUCTION AND AIM OF THIS STUDY 1

1.1.1 Notion of critical metals *1*

1.1.2 Aims of the study *2*

1.2 GERMANIUM – STATE OF THE ART 4

1.2.1 Economic and scientific interests for Ge *5*

1.2.2 Fluids associated to Ge-enrichment and base-metals (Pb-Zn) *8*

1.2.3 Germanium-minerals and Ge-bearing sulfides *11*

1.2.4 Germanium-hosts relative to geology *17*

1.3 DEFORMATION OF THE SPHALERITE AND OTHER SULFIDES 11

1.3.1 Sphalerite crystallography *11*

1.3.2 Mechanisms of deformation *12*

1.3.3 Deformation of sphalerite and related sulfides. *14*

1.3.4 Impact of recrystallization on the trace element contents in sulfides. *17*

2 ANALYTICAL METHODS **20**

2.1 ANALYTICAL APPROACH 20

2.2 FIELD WORK AND SAMPLING 20

2.3 MINERALOGICAL AND TEXTURAL INVESTIGATIONS 21
2.3.1 Microscopic observations 21
2.3.2 Quantitative Evaluation of Minerals by Scanning Electron Microscopy (QEMSCAN) analyses 21
2.3.3 Electron BackScattered Diffraction (EBSD) mapping 23
2.3.4 Chemical investigations (EPMA-LA-ICPMS-LIBS mapping) 25
2.3.5 Fluid Inclusion analyses 27
2.4 GEOCHRONOLOGY 29
2.4.1 In-situ U-Th-Pb datation on zircon and monazite 29
2.4.2 $^{40}Ar/^{39}Ar$ step-heating 30
3 GEOLOGY AND MINERAL RESSOURCES OF THE PYRENEAN AXIAL ZONE (PAZ) 32
3.1 STRUCTURAL SETTING OF THE PYRENEES 32
3.2 TECTONIC EVOLUTION OF THE PYRENEAN AXIAL ZONE (PAZ) 33
3.2.1 Ediacaran to Lower-Carboniferous ages. 33
3.2.2 Lower-Middle Carboniferous to Permian ages: Variscan orogeny 34
3.2.3 Permian to Cenozoic ages: Pyrenean-Alpine orogeny. 38
3.3 MINERAL RESSOURCES IN THE PYRENEES 39
4 STRUCTURAL FRAMEWORK FOR THE PB-ZN DEPOSITS IN THE PYRENEAN AXIAL ZONE (PAZ) 43
4.1 SHORT HISTORIC OF THE PYRENEAN PB-ZN MINES 44
4.2 ARTICLE – STRUCTURAL CONTROL ON THE FORMATION OF PB-ZN DEPOSITS: AN EXAMPLE FROM THE PYRENEAN AXIAL ZONE 45
4.2.1 Abstract 46
4.2.2 Introduction 47
4.2.3 Geological Setting 48
4.2.4 Structural Analysis of Three Pb-Zn Districts in the Bossòst Anticlinorium 51
4.2.5 Comparison with the Pierrefitte Anticlinorium: Pierrefitte and Arre-Anglas-Uzious Districts 58
4.2.6 Ore petrology and Microstructures 60
4.2.7 Discussion 62
4.2.8 Conclusions 69
4.2.9 Acknowledgment 70
4.2.10 References 70
4.3 ADDITIONNAL FIELDWORK AND MINERALOGICAL DATAS 75
4.3.1 Stratigraphic position of the Pb-Zn deposits in the Bossost dome 75
4.3.2 Bentaillou area 76
4.3.3 Horcall (Fourcaye) area 77
4.3.4 Victoria-Margalida 78

4.3.5 Estaing-Arrouy (Pierrefitte anticlinorium) 80
4.3.6 Crabioulès 81
4.3.7 Arre-Anglas-Uzious area 82
4.3.8 Cierco 83
4.3.9 QEMSCAN (Quantitative Evaluation of Minerals by Scanning Electron Microscopy) datas 84

5 GERMANIUM REDISTRIBUTION IN SPHALERITE FROM THE PYRENEAN AXIAL ZONE 88

5.1 ARTICLE – REDISTRIBUTION OF GERMANIUM DURING SPHALERITE DYNAMIC RECRYSTALLIZATION 89
5.1.1 Abstract 90
5.1.2 Introduction 90
5.1.3 Geological setting and samples 91
5.1.4 Methods 93
5.1.5 Results 93
5.1.6 Interpretation and discussion 97
5.1.7 Deformation and dynamic recrystallization of sphalerite 97
5.1.8 Mechanisms for internal Ge remobilization 97
5.1.9 Rare element redistribution in other world-class deposits 98
5.1.10 Conclusions 98
5.1.11 Acknowledgments 99
5.1.12 References 99
5.2 ARTICLE – BEHAVIOR OF GERMANIUM AND ASSOCIATED CRITICAL ELEMENTS IN RECRYSTALLIZED PB-ZN ORE DEPOSITS: EXAMPLE FROM THE PYRENEAN AXIAL ZONE 104
5.2.1 Abstract 105
5.2.2 Introduction 105
5.2.3 Sampling and analytical methods 107
5.2.4 Geological setting 109
5.2.5 Results 111
5.2.6 Discussion 123
5.2.7 Conclusions 132
5.2.8 Acknowledgements 133
5.2.9 References 133

6 GEOCHRONOLOGY OF THE BOSSOST GRANITE, METAMORPHISM AND PB-ZN MINERALIZATION 141

6.1 ARTICLE – RELATION BETWEEN MAGMATISM, METAMORPHISM AND PB-ZN-(GE) MINERALIZATION EVENTS IN THE PYRENEAN AXIAL ZONE 142
6.1.1 Abstract 143

6.1.2 Introduction 143
6.1.3 Geological setting 144
6.1.4 Samples 148
6.1.5 Instrumentation and analytical method 151
6.1.6 Results 154
6.1.7 Interpretation and discussion 162
6.1.8 Conclusion 166
6.1.9 References 167

7 PLASTIC DEFORMATION OF NATURALLY DEFORMED SPHALERITE 175

7.1 ARTICLE – PLASTIC DEFORMATION OF NATURALLY DEFORMED SPHALERITE 176
7.1.1 Abstract 177
7.1.2 Introduction 177
7.1.3 Tectonometamorphic setting 178
7.1.4 Sampling and methods 180
7.1.5 Macroscopic sample study 181
7.1.6 Microstructural study 183
7.1.7 Chemical mapping in deformed sphalerite 194
7.1.8 Discussion 197
7.1.9 Conclusion 201
7.1.10 Acknowledgment 202
7.1.11 References 202

8 FLUID INCLUSION ANALYSES ON THE PYRENEAN SPHALERITE 207

8.1 ARTICLE – GEOCHEMICAL SIGNATURES OF MINERALIZING FLUIDS IN METAMORPHOSED PB-ZN ORE BODIES IN THE PYRENEAN AXIAL ZONE: CONSTRAINTS FROM FLUID INCLUSION MICROTHERMOMETRY AND LA-ICP-MS ANALYSIS 208
8.1.1 Abstract 209
8.1.2 Introduction 209
8.1.3 Regional geology and Pb-Zn ore setting 211
8.1.4 Samples 215
8.1.5 Analytical methods 215
8.1.6 Results 217
8.1.7 Discussion 226
8.1.8 Conclusion 232
8.1.9 Acknowledgment 233
8.1.10 References 233

9 DISCUSSION AND CONCLUSION 241

9.1 New genesis model of Pb-Zn(-Ge) mineralization 241
9.2 Mode of concentration of Ge and other related rare metals in sulphide environment 243
10 BIBLIOGRAPHY 246
11 SUPPLEMENTARY MATERIALS 280
11.1 ARTICLE – Relationships between the occurrence of accessory Ge-minerals and sphalerite in Variscan Pb-Zn deposits of the Bossost anticlinorium, French Pyrenean Axial Zone: Chemistry, microstructures and ore-deposit setting – a first order textural and chemical approach 281
11.1.1 Abstract 283
11.1.2 Introduction 284
11.1.3 Geological and structural setting 286
11.1.4 Methods 288
11.1.5 Structural and petrological study of the PAZ Pb-Zn(-Ge) deposits 289
11.1.6 Mineral chemistry 297
11.1.7 Discussion 301
11.1.8 Conclusions 309
11.1.9 Acknowledgments 310
11.1.10 References 310
11.2 Sample description 318
11.3 EPMA analytical conditions 330
11.4 EPMA Sphalerite – relative to section 11.1 330
11.5 EPMA Sphalerite – relative to section 5.1 332
11.6 EPMA Brunogeierite (in oxides) – relative to section 5 335
11.7 LA-ICP-MS Sphalerite – relative to section 11.1 337
11.8 LA-ICP-MS Sphalerite – relative to section 5.2 340
11.9 Supplementary data relative to section 5.1 355
11.10 Supplementary data relative to section 5.2 357
11.11 EBSD maps 365
11.12 Fluid inclusions – Microthermometric data in quartz 384
11.13 Fluid inclusions – LA-ICP-MS analyses (quartz host) 408
11.14 Fluid inclusions – Limit of detection of LA-ICP-MS analyses (quartz host) 422
11.15 Fluid inclusions – LA-ICP-MS analyses (sphalerite host) 436
11.16 Fluid inclusions – Limit of detection of LA-ICP-MS analyses (sphalerite host) 438
11.17 Geochronology methodology and instrumentation 440

List of Figures

Figure 1. Comparaison de l'importance economique et du risque d'approvisionnement pour de nombreux elements dans le cadre de l'evaluation de leurs criticites par la Comission Europeenne en 2017 (*European Union, 2017*)xi

Figure 2. Approche analytique realisee dans cette etude. xiii

Figure 3. Localisation et composition de la zone d'etude, la Zone Axiale des Pyrenees. xiv

Figure 4. Representation structurale de la ceinture Varisque de l'ouest de l'Europe, a la fin du Carbonifere (modifiee d'apres *Denele et al. 2014*). xvi

Figure 5. Carte structurale de la repartition des gites Pb-Zn des Pyrenees. Les principaux gites etudies sont notes. xvii

Figure 6. Photos de terrains montrant les trois principaux types de mineralisations Pb-Zn. xix

Figure 7. Modele 3D avec la position structurale, chronologique, texturale et le contenu en Ge des trois grand types de mineralisations Pb-Zn dans la Zone Axiale des Pyrenees. Les mineralisations en veines Type 2b (tardi-Varisque et Mesozoïque) sont les uniques porteurs de la mineralisation a Ge. xix

Figure 8. Sphalerite du gite Pb-Zn d'Arre analysee par des methodes texturales (EBSD) et chimiques (cartographie LIBS et EPMA) xxi

Figure 9. Repartition des concentrations en Ge et Cu en fonction de la microstructures dans deux grains parents de sphalerite. xxii

Figure 10. Resultats des analyses microthermometriques d'inclusions fluides. xxiii

Figure 11. .Salinite (% poids NaCl eq.) vs temperature d'homogeneisation (Th) pour les inclusions fluides acqueuses de cette etude et d'autres gites etudies dans les Pyrenees et la Montagne Noire. Le domaine de salinite-Th des fluides associes a la formation de talc dans le gisement de Trimouns est aussi expose (abbreviations : MNP : massif Nord-Pyreneens). xxiv

Figure 12. Modele de remobilisation du germanium dans la sphalerite en veines de Type 2b. xxvi

Figure 14. Economic importance and supply risk results for numerous elements for the E.U. in the 2017 criticality assessment (from *European Union, 2017*) 2

Figure 15. A. Growth in primary production of Germanium from 1973 to 2013 (from *Frenzel et 2017* and reference herein). B. Wheels of the relation between host metals in the inner circle and by-product metals in the outer circle. By-product elements appear at distances proportional to the percentage of their total production in the outer circle (from *Nassar et al., 2015*) 3

Figure 16. Comparison between clarke concentration (elemental content/Clarke) and metal tonnage (modified from *Laznicka et al., 1999*) for the largest deposit of each element. 6

Figure 17. Germanium processing pathway (from *Ruiz et al., 2018*) 7

Figure 18. Thermodynamic properties of Ge (IV) in hydroxide complexes (from *Pokrovski and Scott, 1998a*). A. Distribution of Ge and Si hydroxides species as a function of pH at 25 and 250°C, and Psat. 9

Figure 18. Compilation of Ge-minerals (modified and actualized from *Höll et al., 2007*) 12

Figure 19. Δ^{74}Ge compositions of 'planetesimals' core (Fe meteorites), Bulk Silicate Earth (upper mantle/crust rocks), hydrothermal fluids and sulphide minerals from various ore deposits (from *Bélissont, 2016* with references herein). 14

Figure 20. Ionic radius and positive charge for elements in tetrahedral coordination (same as sphalerite; modified from *George et al., 2016*) 15

Figure 21. Location of ore deposits with Ge contents reported in the litterature. Deposits with Ge-minerals occurrence are underligned in the legend below. Note the presence of Pyrenean Axial Zone (PAZ) deposits which will be discussed in this study (modified from *Höll et al., 2007*). 1

Figure 22. Typical examples of Ge-bearing sphalerite deposit. 3

Figure 23. Two microphotographs of coarse-grained sphalerite crystals (>100 μm). 3

Figure 24. Microphotographs of Ge-bearing sulfides (reflected light; Tn: tennantite; Gn: galena; Py: pyrite; Sph or Sp: sphalerite; Cp: chalcopyrite; Bn: bornite; cc: chalcocite: cv-dg: covellite-digenite; mal: malachite; sm: smithsonite). 5

Figure 25. Smithsonite ($ZnCO_3$) replacing directly sphalerite (BSE image; from *Mondillo et al., 2018*). Abbreviations: Sm: smithsonite; Sp: sphalerite; Gth: goethite. 6

Figure 26. A. Elemental map of Ge in coal from the Blue Gem deposit-Kentucky coal field (from *Hower et al., 2018*). B. Geological map of the Lincange coal field with noted the Ge-rich lignite areas close to the faults (from *Hu et al., 2009*). C. SXRF maps of the Belle Brooke (New Zealand) coal samples (a) lignite, red = Ge, green = Fe, blue = As and (b) wood, showing the distribution of Ge (from *Etschmann et al., 2017*). 7

Figure 27. Geological description of the Kipsuhi-deposit. 9

Figure 28. Microphotographs of different Ge-minerals occurrences and their relation with sulfide texture (Abbreviations: sp, sph or bl: sphalerite; gn or ga: galena; br: briartite; cp: chalcopyrite; tn or tnt: tennantite; rn: renierite; ger: germanite; py: pyrite; ba: baryte; col: Ge-colusite). 10

Figure 29. A. Sphalerite hextetrahedral crystals oriented with different axis (100), (110) or (111) (from *Barrie et al., 2009*). B-C. Sphalerite cubic C structures and B-D. wurtzite hexagonal H-structures (from *Boyce et al., 2015*) 12

Figure 30. The three main types of recrystallization (from Passchier & Throuw and adpated from a study of *Hirth & Tullis (1992)* on quartz recrystallization. 13

Figure 32. Two types of twins in minerals. On the left, growth twins with steps and on the right, deformation twins nucleated at the edge of the grain and less marked in the core of the crystal (from *Passchier & Trouw, 1996*). 13

Figure 32. Comparison of the strenghts of five sulfide minerals and marble (from *Cox, 1981* and references herein). 15

Figure 33. Deformation mechanism maps comparision between pyrite and galena. The deformation maps are normalized at the same temperature. Red line indicates the same stress value.. 16

FIGURE 34. INTRA-GRANULAR DIFFUSION MECHANISMS AND RELATED HIGH DIFFUSIVITY PATHWAY (PIPE DIFFUSION) OR DISLOCATION–IMPURITY PAIR (DIP). 19

FIGURE 35. FLOWCHART DESCRIBING THE ANALYTICAL PROCEDURE USED IN THIS STUDY. 20

FIGURE 36. FROM A TO D: SPHALERITE OBSERVED IN DIFFERENT CONDTIONS UNDER MICROSCOPE WITH THE SAME ZOOM AND IN THE SAME SAMPLE (BENTAILLOU, BEN12). FROM E TO F: ARRE SPHALERITE (ARR03) IN TRANSMITTED PLANE POLARIZED LIGHT. 22

FIGURE 37. CAMSCAN CRYSTAL PROBE X500FE SEM-EBSD AT GEOSCIENCES MONTPELLIER. SMALL INSETS BRIEFLY EXPLAIN EBSD ACQUISITION. 23

FIGURE 38. DETAILS OF EBSD ANALYSES 24

FIGURE 39: A: SCHEMATIC REPRESENTATION OF THE LIBS TECHNIQUE. B: SCHEMATIC COMPARAISON OF LIBS WITH OTHER TRADITIONNAL TRACE ELEMENT ANALYZER SUCH AS LA-ICP-MS OR μ-XRF (SYNCHROTRON) 27

FIGURE 40. A. LOCATION OF THE PYRENEAN AXIAL ZONE IN THE VARISCAN BELT OF WESTERN EUROPE. B. SIMPLIFIED GEOLOGICAL MAP OF THE VARISCAN DEFORMED BASEMENT WITH LOCATION OF THE MAIN GRANITOÏDS MASSIFS AND METAMORPHIC DOMES. 32

FIGURE 41. THREE-STAGE RECONSTRUCTION OF THE IBERIAN-ARMORICAN ARC DURING THE CARBONIFEROUS AND THE PERMIAN. 35

FIGURE 42. STRUCTURAL REPRESENTATION OF THE VARISCAN WESTERN BELT AT THE END OF THE CARBONIFEROUS TIME (MODIFIED FROM *DENELE ET AL. 2014*). 36

FIGURE 43. DEFORMATION EVOLUTION IN SPACE AND TIME ACCORDING TO THE TWO STRUCTURAL DOMAINS (FROM *CARRERAS AND CAPPELLAS, 1994*). 37

FIGURE 44. SKETCH REPRESENTING THE EVOLUTION OF THE DEFORMATION (D_1 TO D_2) IN THE SUPER- AND INFRASTRUCTURE (FROM *DENELE ET AL. 2014*) 38

FIGURE 45. STRUCTURAL MAP OF THE PYRENAN AXIAL ZONE (PAZ) WITH NORTH PYRENEAN AND BASQUE MASSIFS. 42

FIGURE 46. (A) LOCATION OF THE PYRENEAN AXIAL ZONE (PAZ) WITHIN THE VARISCAN BELT OF WESTERN EUROPE. (B) SCHEMATIC MAP OF THE PYRENEAN AXIAL ZONE (PAZ) AND LOCATION OF ALL RECOGNIZED PB-ZN DEPOSITS (BASED ON BRGM (FRENCH GEOLOGICAL SURVEY) AND IGME (SPANISH GEOLOGICAL SURVEY) DATABASES . NOTE THE ABUNDANCE OF THESE DEPOSITS ESPECIALLY IN THE CENTRAL AND WESTERN DOMAINS OF THE PAZ. 49

FIGURE 47. THE BOSSOST ANTICLINORIUM. 50

FIGURE 48. (A) STRUCTURAL MAP OF THE BENTAILLOU-LIAT-URETS DISTRICT BASED ON FIELD STUDY AND BRGM/IGME GEOLOGICAL MAPS. (B) STRUCTURAL NNE-SSW CROSS-SECTION OF THE LIAT-BENTAILLOU AREA. 52

FIGURE 49. FIELD OBSERVATION AND STRUCTURAL MODELS IN THE BENTAILLOU-LIAT-URETS DEPOSITS (SEE LOCATION IN FIGURE 49A). 54

FIGURE 50. MARGALIDA-VICTORIA-SOLITARIA DISTRICT (SEE LOCATION ON FIGURE 49A). 56

FIGURE 51. FIELD OBSERVATIONS AND 3D STRUCTURAL MODEL OF PALE BIDAU DEPOSIT (SEE LOCATION IN FIGURE 48A). 57

FIGURE 52. THE PIERREFITTE ANTICLINORIUM. 59

FIGURE 53. PARAGENETIC SUCCESSION OF ORE AND GANGUE MINERALS FOR ALL THE ELEVEN PYRENEAN-STUDIED PB-ZN DEPOSITS. 61

FIGURE 54. MICROPHOTOGRAPHS SHOWING CHARACTERISTICS TEXTURES IN THE THREE MINERALIZATION TYPES. 63

FIGURE 55. SCHEMATIC 3D SKETCH DISPLAYING THE THREE MAIN MINERALIZATION TYPES WHICH ARE TYPICALLY OBSERVED IN THE STUDIED AREA AND RELATED TO EACH STUDIED DEPOSIT. 64

FIGURE 56. GENETIC MODEL FOR THE FORMATION OF THE THREE MAIN PB-ZN MINERALIZATION TYPES. 67

FIGURE 57. STRATIGRAPHIC POSITION OF THE PB-ZN DEPOSITS REPORTED IN THE BOSSOST ANTICLINORIUM AREA. 75

FIGURE 58: 3D STRUCTURAL BLOC REPRESENTING THE GEOLOGY OF THE BENTAILLOU AREA AND THE KILOMETRIC SCALE RECUMBENT FOLD. POSITION OF THE TYPE 2A ORE IS REPRESENTED. 76

FIGURE 59. HORCALL AREA. 77

FIGURE 60 3D STRUCTURAL BLOC REPRESENTING THE VICTORIA-MARGALIDA AREA WITH POSITION OF THE DIFFERENT GALLERIES AND TYPE 2A MINERALIZATIONS. 79

FIGURE 61. ESTAING DEPOSIT (TYPE 2A AND/OR 2B MINERALIZATION). 80

FIGURE 62. CRABIOULES DEPOSIT (TYPE 2A). 81

FIGURE 63 3D STRUCTURAL BLOC REPRESENTING THE ARRE-ANGLAS-UZIOUS AREA WITH POSITION OF THE STUDIED TYPE 2B MINERALIZATIONS. 82

FIGURE 64. CIERCO VEIN MINERALIZATION HOSTED IN THE BONO GRANODIORITE 84

FIGURE 65. QEMSCAN MAPS FROM ARGUT-DESSUS AND PALE BIDAU ORE SAMPLES. 85

FIGURE 66. QEMSCAN MINERALOGICAL MAP OF BENTAILLOU PB-ZN ASSOCIATED TO HOST-ROCK (INDEXED AS MUSCOVITE). NO GE-MINERAL IS REPORTED. 86

FIGURE 67. (A) MAP OF VARISCAN MASSIFS IN WESTERN EUROPE, AND LOCATION OF B. (B) SIMPLIFIED GEOLOGICAL MAP OF THE PYRENEAN AXIAL ZONE (PAZ) AND LOCATION OF MAIN PB-ZN DEPOSITS (YELLOW STARS, FROM *POUIT [1985]* AND BUREAU DE RECHERCHES GEOLOGIQUES ET MINIERES DATABASE *[HTTP://INFOTERRE.BRGM.FR]* AND INSTITUTO GEOLOGICO Y MINERO DE ESPAÑA DATABASE *[HTTP://MAPAS.IGME.ES/SERVICIOS/DEFAULT.ASPX]*). STUDY AREA IS HIGHLIGHTED WITH BLUE STAR. (C) GEOLOGICAL AND STRUCTURAL MAP OF THE ARRE DEPOSIT AREA. PB-ZN ORE IS HOSTED IN N060°E–N080°E SUBVERTICAL VEINS HOSTED IN LOWER DEVONIAN MARBLE CALC-SCHIST. LOCATION OF FIGURE 69A IS INDICATED. 92

FIGURE 68. (A) OUTCROP PHOTOGRAPH OF ARRE (PYRENEAN AXIAL ZONE, PYRENEES) PB-ZN VEIN TYPE. NOTE S_2 CLEAVAGE IN THE HOST ROCK. LOCATION OF THE STUDIED SAMPLE (B) IS INDICATED (MODIFIED FROM *CUGERONE ET AL., 2018B*). (B) PHOTOGRAPH OF ORE. SPHALERITE (SPH) APPEARS LIGHT BROWN AND IS ASSOCIATED WITH QUARTZ AGGREGATE (QTZ) AND SCHISTOSE HOST ROCK. LOCATION OF THE STUDIED SECTION (C) IS INDICATED. (C) PLANE-POLARIZED (TRANSMITTED) LIGHT MICROPHOTOGRAPH OF STUDIED ORE (150-MM-THICK SECTION). 92

FIGURE 69. SPHALERITE MICROSTRUCTURES AND LOCATIONS OF GE MINERALS IN ARRE (PYRENEAN AXIAL ZONE, PYRENEES) SAMPLE. 94

FIGURE 70. GE CONCENTRATION IN SPHALERITE AND LOCATIONS OF GE MINERALS IN ARRE (PYRENEAN AXIAL ZONE, PYRENEES) SAMPLE. 96

FIGURE 71. A LOCATION OF THE PYRENEAN AXIAL ZONE IN THE VARISCAN BELT OF WESTERN EUROPE. B LITHOLOGICAL AND STRUCTURAL MAP OF CENTRAL PYRENEAN AXIAL ZONE WITH LOCATION OF PB-ZN DEPOSITS C STRUCTURAL 3D SYNTHETIC MODEL WITH LOCATION OF THE STUDIED PB-ZN DEPOSITS AND REPLACED ACCORDING TO LITHOLOGIES, STRUCTURES AND METAMORPHIC IMPRINT. 110

Figure 72. Sample photographs of the studied deposits.. 112

Figure 73. EBSD grains size map superposed onto a transmitted light microphotograph of sphalerite-quartz mineralization in F_2 fold hinge from VT deposit 113

Figure 74. Microphotographs associated to EBSD grain size map with grain boundaries and chemical contents (Sph: sphalerite; Qtz: quartz; Gln: galena). 115

Figure 75. Images of Ge-minerals hosted in recrystallized sphalerite 116

Figure 76. LA-ICP-MS data for Type 2b sphalerite, showing trace element concentration in three different textures and for three ore deposits (complete dataset available in Table 17-supp data). 119

Figure 77. LA-ICP-MS data for Type 2a sphalerite, showing trace element concentration in three different textures and for three ore deposits (complete dataset available in Table 17-supp data). 120

Figure 78. LIBS mapping on Arre Type 2b ore mineralization. Sph: sphalerite; Qtz: quartz; S_2: S_2 foliation. 122

Figure 79. Compared content in representative elements for Type 2b sphalerite mineralizations in a et b and between Type 2a and Type 2b in c and d. 124

Figure 80. Trace element comparison between Type 2b coarse sphalerite grains and Type 2a coarse sphalerite crystals. 125

Figure 81. Two stage genesis model for the formation of Ge-minerals and sphalerite textures and chemistry in Type 2b Pb-Zn mineralization. Stage 1 represent the mineralzation before deformation. Stage 2 is the mineralization representation after deformation (supposed Variscan D_2). 129

Figure 82. Ge vs Cu contents comparison between PAZ sphalerites (including Argut-dessus deposit; Cugerone et al., 2018a) and others sphalerite mineralizations in the world. 130

Figure 83. A. Location of the PAZ and other massifs in the Variscan belt of the Western Europe. B: Simplified geological map of the Pyrenean Axial Zone (PAZ) with location of the basement and metamorphic domes. The U/Pb data are in red for granites, and in green for gneiss (magmatic age except one with "*" which correspond to metamorphic age). 146

Figure 84. Geological map of the Bossost anticlinorium with the location of the collected sample for the U/Pb datations (BOS32a and BOS32b= granitic sill; BOS17 and BOS18=metapelites). 149

Figure 85. A. Metapelite (BOS17) with biotite (Bt), garnet (Gt) and staurolite (St) assemblages (plane polarized light). 149

Figure 86. Microphotographs showing muscovite and sphalerite associations in: A 150

Figure 87. A. CL microphotographs of the zircons from the BOS32B sample. B. BSE and SE microphotographs of the zircons from the BOS32A sample. 154

Figure 88. A. and B. Zircon U-Pb Concordia diagrams obtained on two granitic sills of the Bossost dome (BOS 32B and 32A, by LA-ICPMS. C. Histogram distribution diagrams for the sample BOS 32A. To avoid distorting the distribution of populations, only one date per grain is used 155

Figure 89. Back-scattered electron (BSE) images of the studied monazites (abbreviations: Mz: monazite, St: staurolite, Gt: garnet; Ms: muscovite; Ap: apatite). 158

Figure 90. U-Th-Pb Concordia diagrams for the monazites analysed in the metapelites (BOS17, BOS18 and BOS17and BOS18). 159

Figure 91. Step-heating $^{40}Ar/^{39}Ar$ results for Bentaillou muscovite. 161

Figure 92. Two sketches representing the location and the age of the in-situ $^{40}Ar/^{39}Ar$ measurements on the Bentaillou and Anglas thick sections, composed essentially of sphalerite and quartz. 161

Figure 93. U vs Th contents comparison in Bossost zircon between our study and the zircon from *Mezger & Gerdes (2016)* and *Lopez-Sanchez et al. (2018).* 162

Figure 94. Chronological succession of the magmatic, metamorphic and Pb-Zn mineralizations events in the Pyrenean Axial Zone (PAZ) and in the North Pyrenean Massifs (NPM). T 165

Figure 95. A Location of the Pyrenean Axial Zone and Montagne Noire in the Variscan belt of Western Europe. B Lithological and structural map of the Pyrenean Axial Zone and Montagne Noire with location of Pb-Zn deposits 179

Figure 96. Samples photographs and scan of the studied deposits. 182

Figure 97. A Box plot of grain size for all sphalerite samples (grain > 20° misorientation angle with consideration of twin boundaries (55-60°). B Cumulative plot of the number of grain compared to the grain orientation spread (GOS). 183

Figure 98 Saint-Salvy (SA, M4 type) sample (step of measurement: 5.7 µm). 185

Figure 99. Pale Bidau (PB) sample (step of measurement: 1.5 µm).. 188

Figure 100. Arre (AR) sample (step of measurement: 2.5 µm). 189

Figure 101. Zoom in Arre (AR) sphalerite crystals (step of measurement: 0.5 µm). 190

Figure 102. Anglas (AG) sample (step of measurement: 3 µm) 192

Figure 103. Bentaillou (BT) sample (step of measurement: 5.7 µm). 193

Figure 104. LIBS coupled to EBSD misorientation boundary maps on PB sphalerite sample. Position of Figure 100 is represented in all the map. A EBSD misorientation map superimposed to a transmitted plane polarized light sphalerite scan (step of measurement: 1.5 and 4 µm for the left and right maps respectively). B Copper LIBS map with indication of the coarse grain domains noted with the number 1. C Gallium LIBS map with contents highly correlated to Cu in sphalerite. D Germanium map with small yellow dots which represent Ge-minerals hosted in sphalerite. Areas where they are concentrated correspond to the high Cu-Ga contents in sphalerite. 195

Figure 105. LIBS coupled to EBSD maps on AR sphalerite sample (same area as the Figure 101, step of measurement: 2.5 µm). The highest Ge and Cu contents in sphalerite lattice are selected for the LIBS maps. 196

Figure 106. Synthetic sketches representing the deformational features related to chemical heterogeneities in sphalerite, from non-deformed, and deformed/recrystallized to metamorphosed crystals. 198

Figure 107. A. Location of the Pyrenean Axial Zone in the Variscan belt of Western Europe. B Lithological and structural map of Pyrenean Axial Zone with location of Pb-Zn deposits (BRGM and IGME databases). 211

Figure 108. Ore samples photographs and scan of the studied deposits 213

Figure 109. Sample description observed in transmitted plane polarized light 214

Figure 110. Synthesis of the four types of fluid inclusions analysed in quartz from the studied deposits. 218

Figure 111. Fluid inclusions in quartz (Qtz). 219

Figure 112. Fluid inclusions in quartz (Qtz) of the vein mineralization from Arre (AR). 220

Figure 113. Fluid inclusions in sphalerite (transmitted plane polarized light). 221

Figure 114. Results of microthermometric analyses on fluid inclusions. 222

Figure 115. LA-ICP-MS results related to microthermometric datas for all the fluid inclusions analyses, performed on quartz and sphalerite 225

Figure 116. A. Zn-Pb-Mn diagram of the LA-ICPMS fluid inclusion dataset. B. Na-K-Ca diagram of the LA-ICPMS dataset. 226

Figure 117. A. Na-Cl-Br systematics of measures inclusion fluids composition from CR, VT, AR and PB deposits. B. Comparison based on ratio Cl/Br vs Na/K of FI analysed in this study with the compositon of seawater, representative analyses of magmatic fluids, magmatic fluids involving an evaporite component, sedimentary formation waters, residual brines after various degrees of seawater evaporation, and halite-dominated versus anhydrite-dominated evaporite rocks 227

Figure 118. Comparison of trace element data from fluid inclusions in low and high salinity fluid. 228

Figure 119. A-B. Ca and K vs Cl plots for fluid inclusions in all deposits. 229

Figure 120. Plot of salinity (wt.% NaCl eq.) vs homogenization temperature (Th) for the aqueous fluid inclusions from this study and between the studied Pb-Zn mineralizations and other studied deposits in the Pyrenees or the Montagne Noire. 230

Figure 121. Revised model with structural position, chronology, textures and Ge-contents of the four main Pb-Zn mineralizations in the Pyrenean Axial Zone (PAZ). 242

Figure 122. Revised model of formation of Ge-minerals in the PAZ Type2b veins (Late-Variscan and Mesozoïc). 244

Figure 123. Graphical abstract describing the main purpose of the article 282

Figure 124 : a) Location of the Pyrenean Axial Zone (PAZ) within the Hercynian belt of Western Europe (modified from *Denele et al., 2014*); b) Main Pb-Zn deposits in Paleozoic rocks of the Central PAZ, with the location of the studied Pb-Zn deposits (modified from *Zwart, 1979*). Location of the cross-sections shown in Figs. 1c and 2b; c) N-S cross-section of the Bossost dome (from *Mezger and Gerdes, 2016*). 284

Figure 125. a) Regional structural map for the northern part of the Bossost anticlinorium b) NNE-SSW structural cross-section near Melles in Cambro- Silurian rocks. c) Pole figures of S0-S1 and S2 measurements. 288

Figure 126. Outcrop photographs from the three studied PAZ deposits: 291

Figure 127 : Microphotographs of different structures in thin section 293

Figure 128 Paragenetic succession of ore and gangue minerals in stratiform and vein mineralizations in the three PAZ studied deposits. 294

Figure 129 : Microphotographs showing characteristic textures in sulfide mineralization. 296

Figure 130 : Diagram showing GeO_2 and FeO contents in 28 brunogeierite grains from the three different deposits (EMPA data) and in different textural position according to sphalerite grains. 300

Figure 131 : Principal component analysis of the LA-ICP-MS log-transformed dataset of trace element contents in sphalerite from the Pale Bidau, Argut-dessus and Pale de Rase deposits. 301
Figure 132 : a) Representative single-spot LA-ICP-MS spectra for selected elements in sphalerite. 302
Figure 133 : Schematic N-S regional sketch of structural relationships between mineralization, bedding and cleavage at macroscopic scale. 303
Figure 134 : Schematic sketch showing relationships between host-rocks, type-1 and 2 mineralizations at microscopic scale. 304
Figure 135 : Synthesis of the characteristics of the four main Ge-bearing deposit-types and PAZ deposits (red frame) based on several criteria: deposit-setting, ore texture (sphalerite), metamorphic imprint, and main Ge-concentration. 307
Figure 136 : Geodynamic sketch diagrams showing the geologic environments of the main Ge-bearing ore deposits worldwide 308
Figure 137. EDS Ge-map acquirred simultaneously as EBSD mapping which reffered to Figure 70. 355
Figure 138. Sphalerite area from Figure 71. 356
Figure 139. LA-ICP-MS spectra of sphalerite measurements 357
Figure 140. LIBS additionnal maps of Zn, Si, Fe, Cd, Al, Mg, Ti 358
Figure 141. Sphalerite (brown-orange colors), quartz (white) and host-rock (grey-black at the right) from Arre in transmitted light 361
Figure 142. LIBS Ge map in sphalerite, quartz and host-rock of the same area as Figure 140. 362
Figure 143. LIBS Cu map in sphalerite, quartz and host-rock of the same area as Figure 140 363
Figure 144. LIBS Ga map in sphalerite, quartz and host-rock of the same area as Figure 140 364
Figure 145. EBSD maps of Arre sphalerite (0.5 µM = step of measurment) with band contrast and all Euler maps. 366
Figure 146. EBSD maps of Arre sphalerite with misorientation boundary and inverse pole figure according to the X axis maps. 367
Figure 147. EBSD maps of Arre sphalerite (2.5 µM = step of measurment) with All Euler map with grain boundaries (>20°) and misorientation boundary map. 368
Figure 148. EBSD maps of Arre sphalerite with inverse pole figure according to the X axis. 369
Figure 149. EBSD maps of Saint-Salvy sphalerite (5.7 µM = step of measurment) with band contrast and all Euler maps. 370
Figure 150.. EBSD maps of Saint-Salvy sphalerite with misorientation boundary and inverse pole figure according to the X axis maps. 371
Figure 151. EBSD maps of Bentaillou sphalerite (6.5 µM = step of measurment) with band contrast and all Euler maps. 372
Figure 152 EBSD maps of Bentaillou sphalerite with misorientation boundary and inverse pole figure according to the X axis maps. 373

FIGURE 153. EBSD MAPS OF PALE BIDAU SPHALERITE (1.5 μM = STEP OF MEASURMENT) WITH BAND CONTRAST AND ALL EULER MAPS SUPERIMPOSED ON REFLECTED LIGHT SCAN. 374

FIGURE 154. EBSD MAPS OF BENTAILLOU SPHALERITE 375

FIGURE 155. EBSD MAPS OF LIAT VEIN SPHALERITE (3.5 μM = STEP OF MEASURMENT) WITH ALL EULER MAP AND INVERSE POLE FIGURE ACCORDING TO THE X. 376

FIGURE 156. EBSD MAPS OF LIAT STRATABOUND SPHALERITE (6 μM = STEP OF MEASURMENT) WITH BAND CONTRAST AND ALL EULER MAP. SPHALERITE IS IN THE BOTTOM AREA OF THE MAPS PARALLEL TO S_0-S_1. 377

FIGURE 157. EBSD MAP OF LIAT STRATABOUND SPHALERITEWITH INVERSE POLE FIGURE ACCORDING TO THE X. 378

FIGURE 158. EBSD MAP OF CIERCO VEIN SPHALERITE (4 μM = STEP OF MEASURMENT) WITH ALL EULER AND INVERSE POLE FIGURE ACCORDING TO THE X. 379

FIGURE 159. EBSD MAPS OF MARGALIDA STRATABOUND SPHALERITE (5 μM = STEP OF MEASURMENT) WITH BAND CONTRAST AND ALL EULER MAP. 380

FIGURE 160. . EBSD MAPS OF MARGALIDA STRATABOUND SPHALERITE WITH INVERSE POLE FIGURE ACCORDING TO X AXIS. 381

FIGURE 161. EBSD MAPS OF ANGLAS SPHALERITE (3 μM = STEP OF MEASURMENT) WITH ALL EULER MAP AND INVERSE POLE FIGURE. 382

FIGURE 162. EBSD MAPS OF ARGUT-DESSUS VEIN SPHALERITE (1 μM = STEP OF MEASURMENT) WITH BAND CONTRAST AND INVERSE POLE FIGURE ACORDING TO X AXIS. 383

List of Tables

Table 1. Analytical conditions for each element analyzed with EMPA (Electron microprobe analyzer) 25

Table 2. Informations in Pb-Zn(-Ag) tonnages for the Pyrenean Pb-Zn deposits 44

Table 3. U-Th-Pb LA-ICP-MS data for the zircon grains in BOS32A and BOS32B samples 156

Table 4. U-Th-Pb LA-ICP-MS data for the monazite grains in BOS17 and BOS18 samples. 157

Table 5. $^{40}Ar/^{39}Ar$ data from Anglas muscovite associated to sphalerite mineralization and analyzed on thick section. 160

Table 6. $^{40}Ar/^{39}Ar$ data from A. Bentaillou separated muscovite crystals; B. Bentaillou muscovite analyzed in thick section. 160

Table 7 : Geological characteristic of the three studied Pb-Zn deposits and the two types of mineralizations. 292

Table 8 : a) EPMA analyzes of 28 brunogeierite (GeFe2O4) crystals in weight-oxide % (structural formula normalized to 4 oxides). b) LA-ICP-MS analyzes of 3 brunogeierite ($GeFe_2O_4$) crystals in weight % for different elements (Co, Cu, Ga, Ge, Ag, Sn, Sb, Pb) (PBO8 sample). 297

Table 9 : a) EPMA analyzes of sphalerite (ZnS, n=49) in weight%. 298

Table 10 Complete sample list (n=329; abbreviations: FI: fluid inclusions) 318

Table 11. EPMA analytical conditions in order to maximize detection of Ge in sphalerite (all EPMA sphalerite data) 330

Table 12. EMPA in-situ measurements on sphalerite from Pale Bidau, Argut-dessus and Pale de Rase deposits (section 11.1 – Ore Geology Review; LOD: limit of detection) 330

Table 13. EPMA in-situ measurements on sphalerite from Arre, Anglas, Pale Bidau deposits (section 5.1 – Geology; LOD: Limit of detection). Values for Ge and Cu below limit of detection are shown. 332

Table 14. EPMA in-situ measurements on brunogeierite (ideal formulae: $GeFe_2O_4$) from Pale Bidau (BO9) and Argut-dessus (BO24-BO25-BO29B) deposits 335

Table 15. LA-ICP-MS data on sphalerite from Pale Bidau, Pale de Rase and Argut-dessus (Ore Geology Review). 337

Table 16. LA-ICP-MS data on sphalerite from Anglas, Arre, Pale Bidau, Victoria, Margalida and Bentaillou (Mineralium deposita) 340

Table 17 . Mass balance calculation on LIBS map for Ge content 359

Table 18. Geothermometer results applied on trace elements in sphalerite (based on the GGIMFis geothermomether from *Frenzel et al., 2016*) 360

Table 19. Fluid inclusions microthermometric analyses in **Crabioules (CR) sample** (CRA02 sample; in green: aqueous inclusions / in red: carbonic inclusions). 384

Table 20. Fluid inclusions microthermometric analyses in **Pale de Rase (PR) sample** (BO18 sample; in green: aqueous inclusions). 387

Table 21. Fluid inclusions microthermometric analyses in **Pale Bidau (PB) sample** (BO10 and BO12 samples; in green: aqueous inclusions / in red: carbonic inclusions). 390

Table 22. Fluid inclusions microthermometric analyses in **Arre (AR) sample** (ARR06 sample, in green: aqueous inclusions / in red: carbonic inclusions). 394

Table 23. Fluid inclusions microthermometric analyses in **Argut-dessus (AD) sample** (BO25 sample, in green: aqueous inclusions / in red: carbonic inclusions). 400

Table 24. Fluid inclusions microthermometric analyses in **Victoria (VT) sample** (VIC12 sample, in green: aqueous inclusions / in red: carbonic inclusions). 403

Table 25. Fluid inclusions microthermometric in **Margalida (MG) sample** (MARG06 sample, in green: aqueous inclusions / in red: carbonic inclusions). 406

Table 26. LA-ICP-MS data on fluid inclusions in quartz (ppm) for Victoria (VIC12), Pale Bidau (BO10-BO12), Crabioules (CRA02), Arre (ARR06) deposit. 408

Table 27. Limit of detection for fluid inclusion analyses acquired with LA-ICP-MS on quartz (ppm) for Victoria (VIC12), Pale Bidau (BO10-BO12), Crabioules (CRA02), Arre (ARR06) deposit. 422

Table 28. LA-ICP-MS data on fluid inclusions in sphalerite (ppm) for Arre (ARR06) deposit. 436

Table 29. Limit of detection for fluid inclusion analyses acquired with LA-ICP-MS on sphalerite (ppm) for Arre (ARR06) deposit. 438

Table 30. LA-ICP-MS U-Th-Pb dating methodology (LMV, Univ. Clermont-Auvergne, France) 440

1 Introduction

1.1 General introduction and aim of this study

1.1.1 Notion of critical metals

During the past century the amount of mineral resources needed by our society has grown exponentially, and mineral industries become more and more focused on the exploration of green-tech elements (Rare-Earth Elements, Lithium, Cobalt, Rare metals). The emergence of our low-carbon and high-technologic society requires rare metals (Ga, Ga, In) that occur in very low concentration in the crust (ppm).

Numerous raw materials are described as critical due to the risks of supply and their economic importance (Figure 13). Their number is constantly rising especially due to the emergence of high-technologic products. Securing a sustainable access for the needed raw materials is of growing concern within the E.U. and across the globe.

Twenty-six of seventy-eight individual materials are considered critical by the E.U. (Figure 13; *European Commission 2017a*). For the U.S. Geological survey, a list of thirty-five elements are stated as critical (*U.S. Geological Survey 2019*). Among them, rare earth elements, a group of chemically similar elements (lanthanides, Scandium (Sc), and Yttrium (Y)) separated in light and heavy groups (LREE and HREE respectively) are vital for modern technology *(Goodenough et al. 2016*). In 2016, 90% of the REE were produced and controlled by China which induce potential supply risks for E.U. and U.S. societies. Another example is W which is classified as highly critical due to its major economic importance. Tungsten is related to the production of cemented carbide

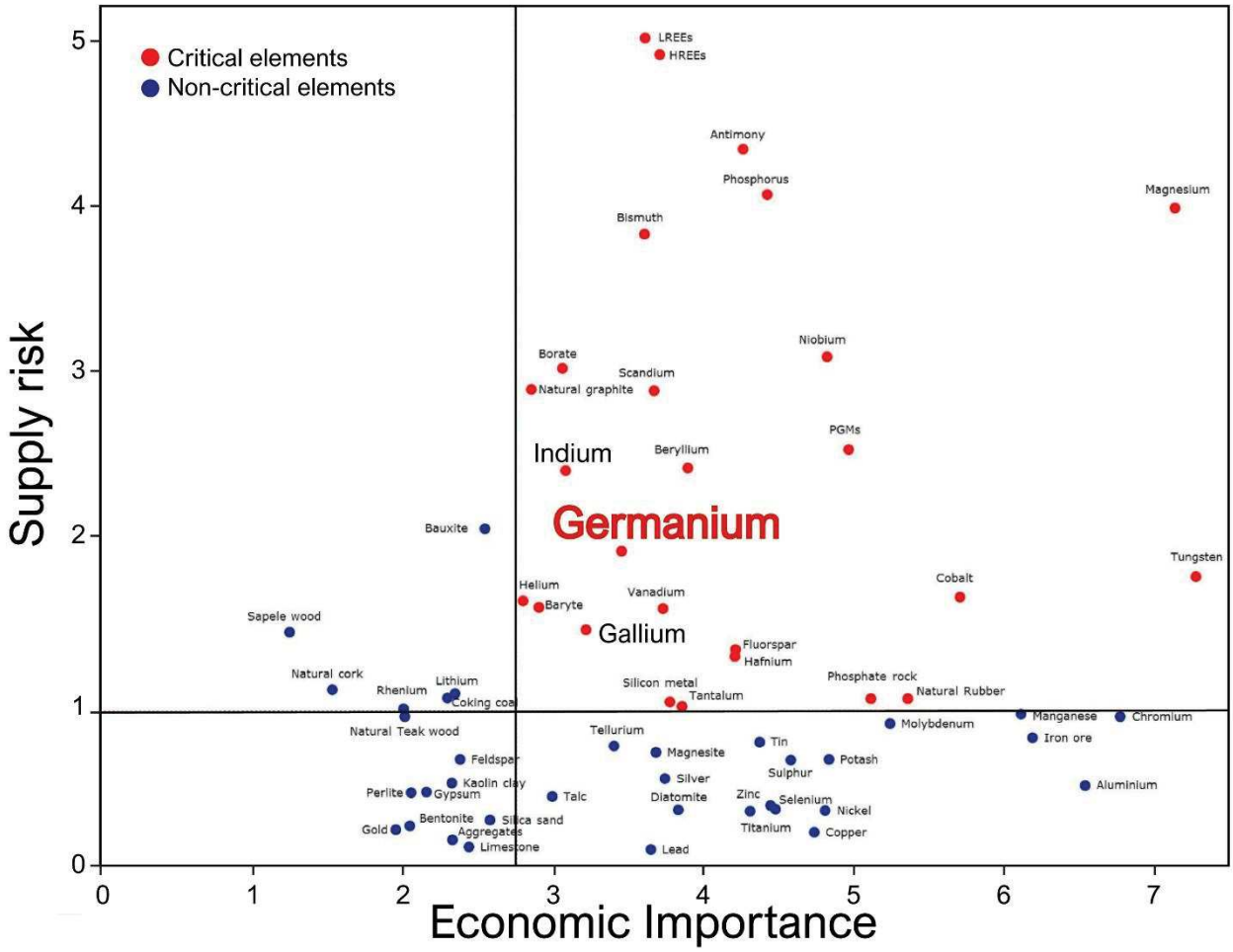

Figure 13. Economic importance and supply risk results for numerous elements for the E.U. in the 2017 criticality assessment (from *European Union, 2017*)

parts for cutting and wear-resistant applications, and is mainly exploited by China *(U.S. Geological Survey 2019*).

Rare metals such as Ge, Ga, In are essential to the development of green technologies (electronics, optical fiber, infra-red technologies) that are at the core of emerging low-carbon societies. Understanding their concentration mechanisms, is key information to their exploration.

1.1.2 Aims of the study

Germanium is an element with growing demand since the 1970 and classified as critical by the E.U and U.S. Geol. Survey. Like numerous other rare metals (In, Ga), it appears in trace content in sphalerite (zinc sulfide, ZnS) and consequently as by-product of zinc exploitation (*Frenzel et al. 2014; Nassar et al. 2015*; Figure 14). Germanium with Indium or Gallium seems to occur rarely in

major contents (>%) in specific minerals, which raises the following question: Where do these elements concentrate and why?

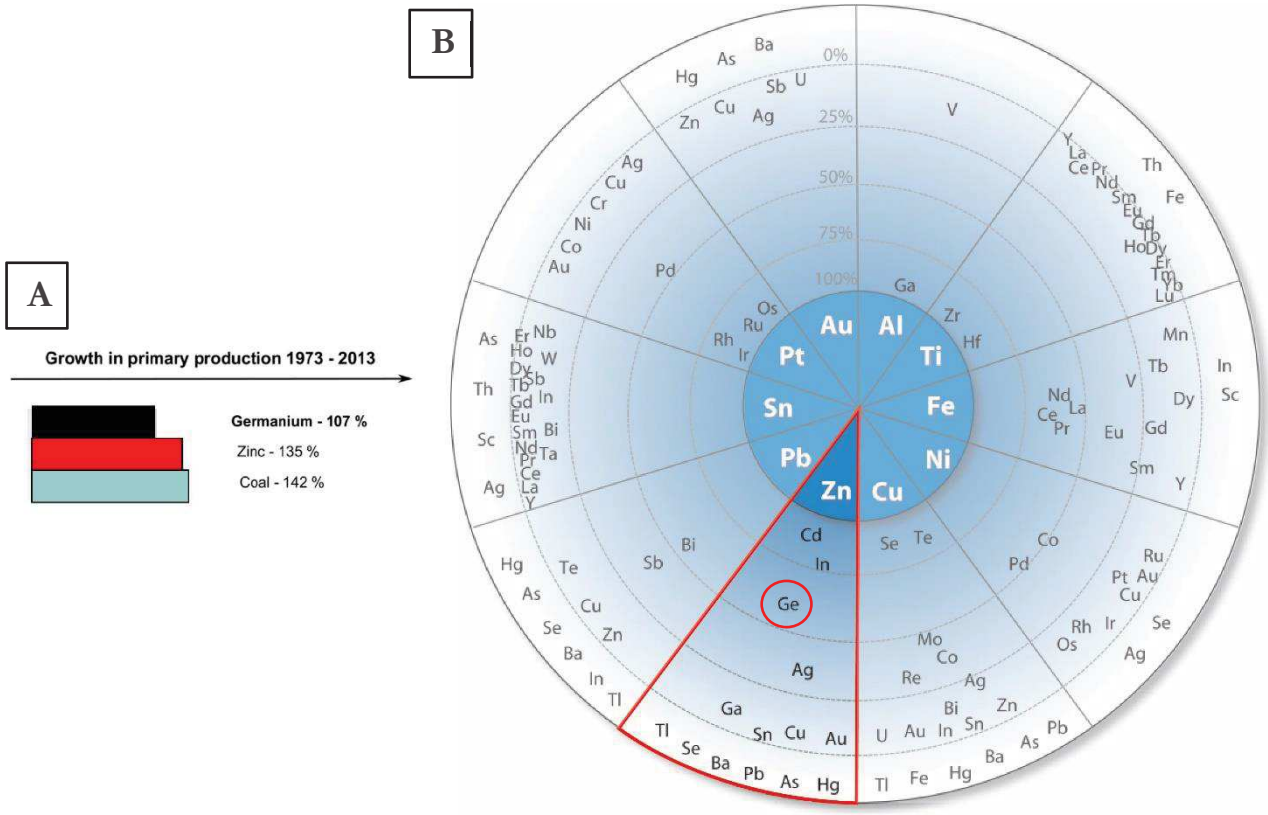

Figure 14. A. Growth in primary production of Germanium from 1973 to 2013 (from *Frenzel et 2017* and reference herein). B. Wheels of the relation between host metals in the inner circle and by-product metals in the outer circle. By-product elements appear at distances proportional to the percentage of their total production in the outer circle (from *Nassar et al., 2015*)

Appearing in a large variety of sulfide deposits, Ge, Ga, and In mining exploitation is nowadays essentially associated to zinc exploration and its chemical occurrence is considered in sulfide lattice with few hundreds of ppm. These rare metals can be found as well in accessory minerals such as brunogeierite ($GeFe_2O_4$) or in roquesite ($CuInS_2$). Investigation of Ge-minerals (Ge>%) is scarce in the literature whereas it may have major implication for the exploration of Ge (and related elements like Ga or In).

The largest sphalerite concentrations appear mainly in deformed/metamorphosed environment on Earth, and consequently may have endured orogenic events depending on the timing of mineralization (*Leach 2005; Wilkinson 2013*). Nonetheless, their impact on rare metal (Ge, Ga, In) composition and deformation mechanisms of sphalerite has been poorly studied. Excellent targets for exploring the impact of deformation/metamorphism on rare metal distribution are the

Pyrenean Pb-Zn deposits (France/Spain). Numerous Ge-minerals are reported with some of them only described in few Pyrenean localities (*Johan et al. 1983*).

My PhD thesis is organized in the following manner. Firstly, I have performed a complete and regional structural and mineralogical investigations of the Pyrenean mineralized orebodies. This is a key primary feature for the investigation of potential rare metal bearing deposits.

In a second step on my PhD, I have coupled characterization of the texture and rare elements (Ge, Ga) chemistry of deformed sphalerite mineralization. It is essential to link deformation imprint and the spatial disposition of minerals and elements to precisely track the potential remobilization processes associated to deformation. The textural method I have employed here is electron-back-scattered diffraction (EBSD) which is widely working for common minerals like quartz, olivine or even pyrite for sulfide minerals, but surprisingly not employed for base-metal textural study. Associated to precise textural mapping, I have carried out minor and trace elements chemical investigations with various methods as *in-situ* LA-ICP-MS analyses or unconventional laser-induced breakdown spectroscopy (LIBS) mapping in order to characterize the occurrence of Ge-mineralization and related elements (Cu, Ga). Additionally, I have documented the mechanisms of sphalerite deformation.

I have dated granite (zircon), monazite hosted in metapelites and hydrothermal micas (associated to Pb-Zn mineralizations) and will question the hypothesis on the timing of mineralization. Finally, I have performed a study of the fluid signature and composition associated to rare metal mineralizations. This is important to characterize the regional mineralization events and hydrothermal activity in Variscan basement is widely present in different geological massifs, such as the Pyrenean Axial Zone, Montagne Noire or Saxo-Thuringian regions. I have performed a fluid inclusion microthermometric and trace element (LA-ICP-MS) study to decipher the characteristics of the Pyrenean Ge mineralized districts which led to a new genetic model.

1.2 Germanium – state of the art

Several studies by *Bernstein (1985)*, *Höll et al. (2007)* and PhD thesis by *Belissont (2016)* report synthetic works on Ge metallogenesis based on deposit classification. This section actualizes these synthetic works and demonstrates the relation between the occurrence of Ge and its mineral host with specific emphasis to the sulfide texture related to the tectonic setting.

1.2.1 Economic and scientific interests for Ge

Germanium is a metalloid element that was discovered in the silver mine of Freiberg in 1886 in the Ge-sulphide, Argyrodite *(Weisbach 1886*). Following this discovery, other Ge-minerals were discovered, and particularly Germanite by *Pufhal (1922*).

1.2.1.1 Properties and industrial uses

Germanium is widely used in optic systems due to its transparency to the infrared spectrum and its exceptionnal refractive index. It is also used for its electrical (semi-conductor) and chemical properties (catalyst).

One of the major uses of Ge is for optical fibers. Development of semiconductor electronic devices with high sensitivity allows to exploit the photoelectric effect that converts light into electricity. Among various silicon photonic devices, germanium on silicon avalanche photodiodes (i.e. Ge/Si APDs) have attracted great attention due to their high performance properties and low cost *(Vivien et al. 2009; Soref 2010; Huang et al. 2018)*.

Another example of industrial use is associated to the capacity of Ge to be transparent to infrared spectrum with numerous military and civilian applications such as night vision goggles, satellite mapping, binoculars, gunsights, surveillance cameras, thermal imaging, or spectroscopy (*Went et al. 2006)*. Germanium is also used to form alloys in various combinations with gold, silver, copper, and palladium in dental industry and with silicon in thermoelectric devices. More often, germanium is added in very small quantities as a hardener of metals, such as aluminum, magnesium, and tin (*Butterman and Jorgenson 2005*). Additionally, Ge is employed in late stage polymerization in PET (polyethylene terephthalate) to improve transparency in bottles, films, food packaging, and many other products.

One of the most promising future uses for Ge is its incorporation in the anode of Lithium ion batteries due to high electrical conductivity and high Li-ion diffusivity *(Liu et al. 2018; Hao et al. 2019*).

1.2.1.2 Economic deposits and production

Production of pure Ge is estimated to 120 000 kg (*U.S. Geological Survey 2019*) with 75 000 kg produced by China, and is considered as critical element by E.U. and U.S.A. *(European Commission*

2017b; U.S. Geological Survey 2019). Germanium dioxide and germanium metal prices gradually increased from the beginning of 2017 to March 2018 before stabilizing, due to provisional plant closure in Canada and the hardening of environmental rules in China. The price of Ge rises of 8% compared to 2017 (*U.S. Geological Survey 2019*).

Presently, Ge is only exploited as by product from zinc or coal concentrates at low grade and tonnages (Figure 15, from *Laznicka 1999*). In the past, the Apex Mine (Utah, USA) was the only mine that operated primarily for germanium and gallium productions, because of the exceptionnal contents of these two elements in hematite and goethite (several thousands of ppm measured with *in situ* analyses; *Bernstein 1986b*). One of the greatest amount of Ge in an orebody is recorded in the Tsumeb mines (presently not-exploited) with 2100t of Ge mostly in the form of Germanite, a Ge-mineral (*Höll et al. 2007*). Saint-Salvy Pb-Zn(-Ge) mine in France was an important producer of Ge before 1993 (and its closure) with total production of 400t of Ge which represented at this time 17% of the world production.

For the U.S. market, Ge is extracted as by-product from zinc concentrates in several mines in Alaska (Red Dog district), Tennessee (Middle Tennessee mines) and Washington *(U.S. Geological*

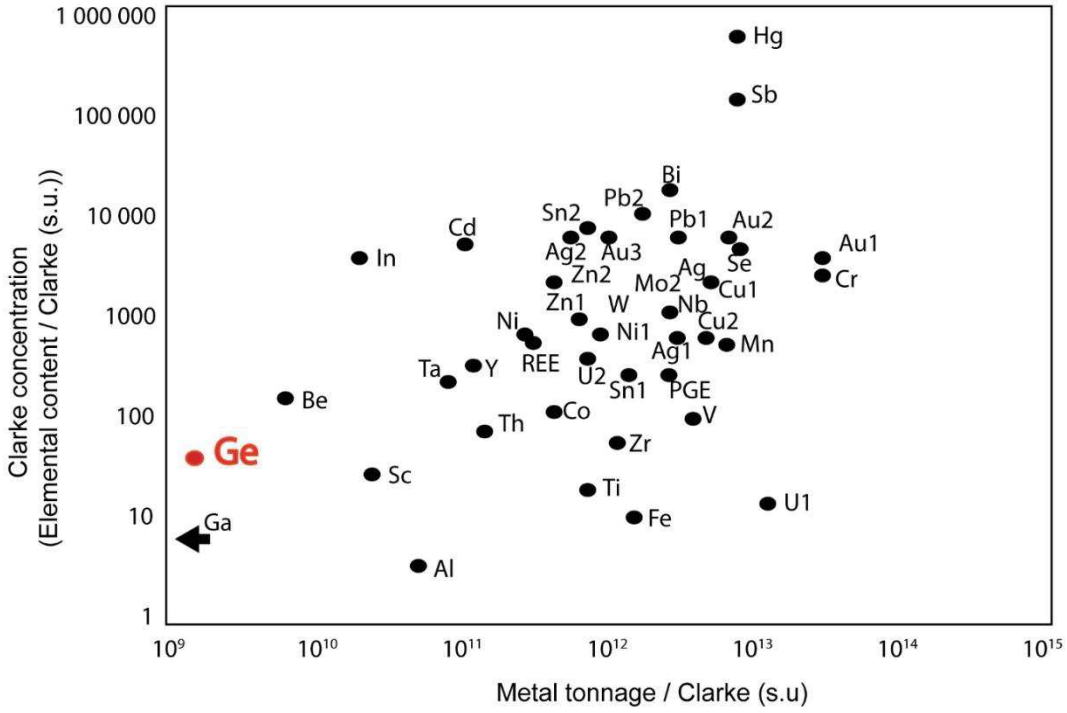

Figure 15. Comparison between clarke concentration (elemental content/Clarke) and metal tonnage (modified from *Laznicka et al., 1999*) for the largest deposit of each element. For Ge: Tsumeb (Namibie, Kipushi-type) with a mean ore bulk content between 262 et 376 ppm. For Ga : Brockman (Australie) with a mean ore bulk content of 150 ppm. For In : Mount Pleasant (Canada) with an average ore bulk content of 150 ppm.

Survey 2019). The Ge-recovery for these deposits is performed in Canada. In European Union, most of the Ge is imported from China (60%), Russia (17%) and USA (16%; *European Commission 2017*).

Ge extraction from coal began in the late 1950s and has continued successfully to present days. Coal is currently one of the main source of Ge (with Zn-sulfides) which provides half of the production of this valuable rare metal *(Seredin 2012*) and is one of few example of metal produced from coal with uranium *(Seredin 2012*), or aluminum and gallium (*Dai et al. 2006a, b*). Nowadays, the largest Ge-bearing coal deposit in the world is in Wumuchang (Yumin coal field, Inner Mongolia) with an estimated resource of 4000 t Ge *(Seredin 2012*).

Germanium is difficult to recycle from the end of life products. This recycling input rate is below 2% for Ge (*European Commission 2017b*). Nonetheless, Ge-recycling during optical devices production reach 30%.

1.2.1.3 Processing to extract Ge

Germanium-rich raw materials (only coal or zinc sulfides) are physically separated before Ge chemical processing. Hydrometallurgical processes trigger the precipitation of Ge as an hydroxide or sulphide or alternately with tannic acid *(Moskalyk 2004; Melcher and Buchholz 2013; Ruiz*

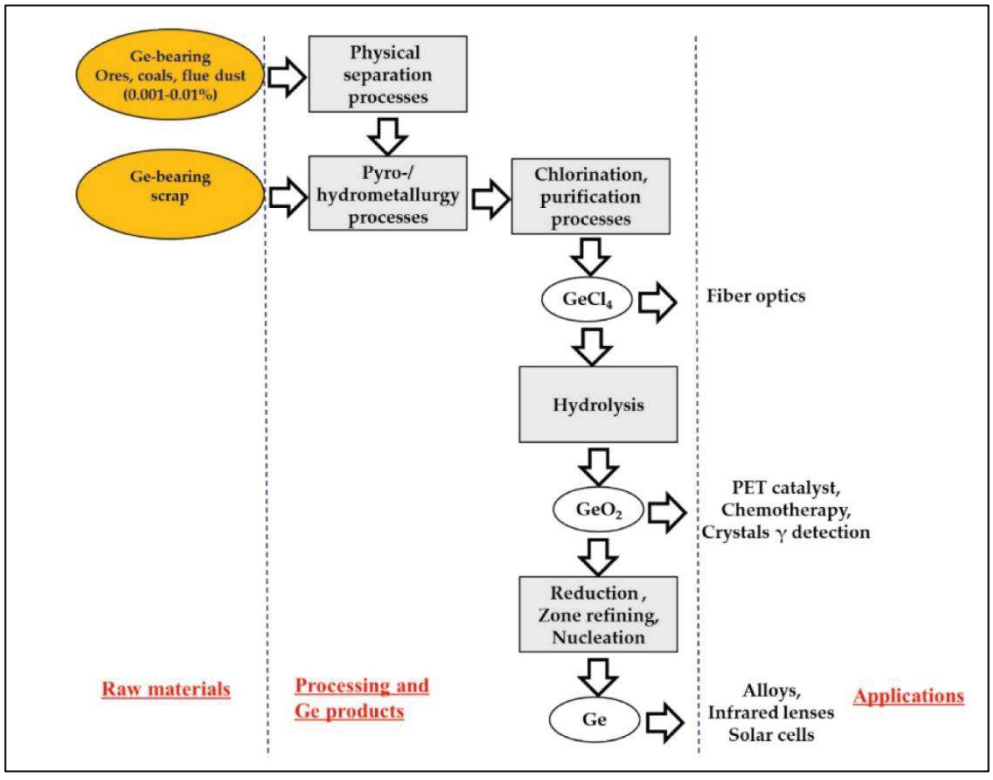

Figure 16. Germanium processing pathway (from *Ruiz et al., 2018*)

et al. 2018). A Ge concentrate is obtained with a Ge content of 30 wt.%. The metalloid is exposed to hydrochloric acid which produces $GeCl_4$ (Figure 16). This first product is directly used as primary component for fiber optics cable production. Hydrolysis may be used to obtain GeO_2 for optical lenses or catalyst industry. Additional reduction may be applied to produce alloys, infrared lenses or solar cells (*Ruiz et al. 2018*). Nowadays, as little as 3% of the Ge contained in zinc concentrates is recovered (*Licht et al. 2015; Ruiz et al. 2018; U.S. Geological Survey 2019*) due to the negative impact on Zn recovery and low Ge-refining capacities.

1.2.2 Fluids associated to Ge-enrichment and base-metals (Pb-Zn)

1.2.2.1 Aqueous Ge-fluids

In the thermal waters, Ge contents are hundreds of times higher than in other types of water. *(Mortlock and Frohlich 1987; Seredin and Finkelman 2008*). The ratio Ge/Si is often used as tracers in river or oceanic waters to determine continental weathering or oceanic hydrothermal activity (*Mortlock and Frohlich 1987; Pokrovski and Schott 1998a)*. This ratio varies according to the concentration in certain elements dissolved in water (alteration, organic matter; *Pokrovski and Schott 1998b*). Germanium-solubility in thermal water seems to increase with temperature and salinity (Figure 17A and B; *Bernstein 1985; Pokrovski and Schott 1998a; Melcher 2003*).

In most of the natural fluids, Ge is transported as hydroxide complexes ($Ge(OH)_4(aq)$ and $GeO(OH)_3^-$; *Pokrovski and Schott 1998a*) even if humic complexes may be formed with organically matter-rich waters. Germanium is also known to be enriched in high-temperature systems (i.e. granitoid system) with the occurrence of Ge enriched in topaz, fluorite or white micas *(Bernstein 1985; Breiter et al. 2013*) which suggests the probable presence of Ge-fluoride $[GeF_6]^{2-}$ complexes.

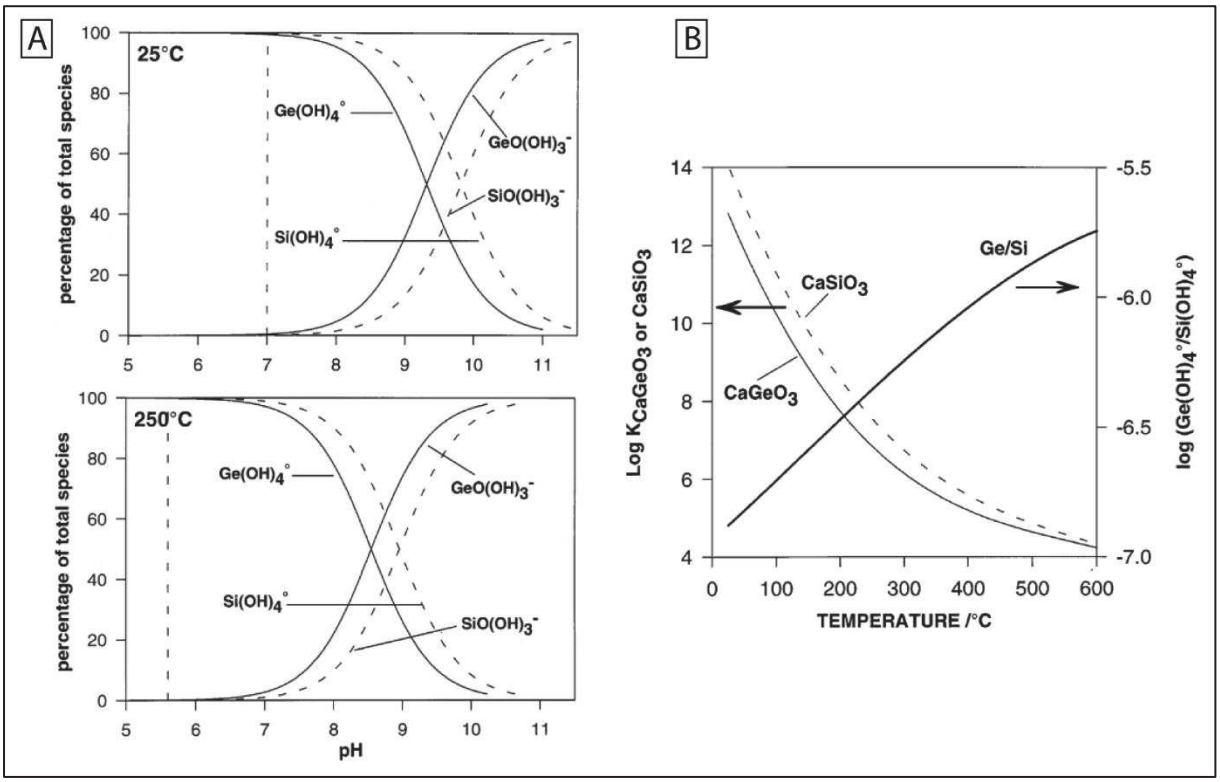

Figure 17. Thermodynamic properties of Ge (IV) in hydroxide complexes (from *Pokrovski and Scott, 1998a*). A. Distribution of Ge and Si hydroxides species as a function of pH at 25 and 250°C, and Psat. The vertical dashed lines stand for the pH of the neutrality point of water at a given temperature. B. Log K of $CaSiO_3$ (wollastonite) and $CaGeO_3$, and of $Ge(OH)_4$ °/$Si(OH)_4$ °ratio in a solution in equilibrium with a germanium-bearing wollastonite containing 1.4 ppm Ge as a function of temperature and at 1 kbar.

1.2.2.2 Hydrothermal Pb-Zn(-Ge) fluids

Germanium is often hosted in sphalerite or chalcopyrite lattices and then directly linked to the occurrence of base-metals such as Zn or Cu and their hydrothermal transport. Base metal fluids are mainly associated to chloride (Cl^-), hydrosulfide (HS^- and H_2S(aq.)) or hydroxides ($(OH)_2$ and $(OH)_3$(aq.)) complexes (*Pokrovski et al. 2008; Etschmann et al. 2010; Akinfiev and Tagirov 2014*). Temperature and to a lesser extent salinity and pH are key parameters controlling the concentrations of dissolved Zn in the fluid, especially in chloride dominated regions (*Akinfiev and Tagirov 2014*). For Ge and at high S activity, formation of thiocomplex $[GeS_4]^{4-}$ is the main reason for the precipitation of thiogermanate minerals such as germanite or briartite (*Bernstein 1985*). Several synthetic studies show relative low-temperature hydrothermal fluids related to Ge-rich deposits *(Warren and Thompson 1945; Höll et al. 2007; Belissont et al. 2014; Frenzel et al. 2016*) which is coherent with several Ge-rich vein-type deposits, Mississippi Valley-Type (MVT) or Sediment

Hosted Massive Sulfide (SHMS) deposits. For example, the Saint-Salvy deposit with Ge-rich mineralization named M4 is related to a highly-saline (23-25 wt.% NaCl eq.) and low-temperature fluid (80-140 °C; *Munoz et al. 1994*). Fluid inclusions data from MVT deposits present generally low temperatures (<200°C) and mainly ranges between 75 to 175 °C (*Bodnar et al. 2013*) with salinities generally around 20 ± 5 wt.% NaCl eq. (*Gratz and Misra 1987; Charef and Sheppard 1988; Viets et al. 1996; Xue et al. 2007; Stoffell et al. 2008; Wenz et al. 2012; Bodnar et al. 2013*). In Red Dog deposit (SHMS type) which contains substantial Ge enrichments (~ 100 ppm Ge in sphalerite lattice), primary fluid inclusions assemblages ranges between 115 to 180 °C and 14 to 19 wt.% NaCl eq. (*Leach et al. 2004*).

In the Kipushi deposit, fluid inclusions study (*Heijlen et al. 2008*) indicates primary highly-saline (halite-saturated) aqueous brines (~30-43 wt.% NaCl eq.) with homogenization temperatures around 275 °C and a younger mineralization stage with lower salinities (23-31 wt.% NaCl eq.) and temperatures (<80-170 °C). Salinities are supposedly derived from evaporite dissolution (Cl/Br ratio) and high contents in Ba, Pb, Zn and Fe are observed in fluid inclusions. At Khusib, presence of Ge-fluoride $[GeF_6]^{2-}$ complexes is supposed because of the close association of Ge-bearing sulfides and F-rich silicates (*Melcher 2003*). In Black Angel deposit, probably classified as Kipushi-type ore, unpublished fluid inclusions data report a high temperature from 400 to 450 °C for the mineralized fluid (*Horn et al. 2018*). In Radka epithermal vein-deposits with some Ge-enrichments (renierite), temperatures range between 220 to 260 °C and low salinity (2.4-3.4 wt.% NaCl eq.; *Kouzmanov et al. 2002)*. These reported variable temperatures and salinities show that these parameters do not seem to be the key parameters in the occurrence of Ge-enriched fluids.

1.2.2.3 Source for Ge enrichments

The most probable source for Ge is organic matter. In some Kipushi-type deposits, the metal source is certainly associated to the upper crust *(Schneider et al. 2007; Kampunzu et al. 2009*) with a seawater source for sulfur component (*Kampunzu et al. 2009*). Germanium origin in deposits such as Tsumeb or Khusib deposits is discussed in *Melcher (2003)* and may be related to circulation of fluids within Ge-rich rocks with a particularly rich organic component (element association, presence of organic matter in the stratigraphic succession) which is coherent with the high-organic affinity of Ge. Occurrence of organic component is also confirmed by the fluid analyses in *Heijlen et al. (2008)* which supposed reduced conditions due to the remaining high Ba contents in fluid inclusions (LA-ICP-MS data) and related to exceptionnal hydrocarbon-rich facies in the host-rocks

of the Kipushi-mine and the other regional Kipushi-type deposits. Association with hydrocarbon phases is largely described in carbonate-hosted deposits with Ge-enrichment such as Tres Maria or Tennessee Pb-Zn mineralizations *(Saini-Eidukat et al. 2009; Bonnet 2014*). The implication of the organic matter in the reduction process is also described in the Saint-Salvy Ge-rich deposit according to $\delta^{34}S$ and $\delta^{13}C$ isotopic data *(Munoz et al. 1994*).

Another probable origin for the Ge-enrichment is the hydrothermal alteration of granitoid rocks where Ge may be concentrated through fractional crystallization *(Seredin and Finkelman 2008*). The Ge-content of granitic intrusions ranges between 1-3 to 1-7 ppm Ge (*Burton et al. 1958; Breiter et al. 2013*) with a general mean content of 1.4 ppm Ge *(Taylor and McLennan 1995; Hu et al. 2009)*. In Lincang coal deposit, granitic intrusions occurrence close to coal-lignite fields appear and Ge anomalies were investigated *(Du et al. 2009; Hu et al. 2009; Qi et al. 2011*), which demonstrates a slight enrichment in Ge (ranging from 2.7 to 5.0 ppm Ge). No significant differences in Ge content between different types of granite (type A or S) are seen but an increase of their Ge concentrations appear during fractionation (*Breiter et al. 2013*). Recent study in coal deposits shows a possible extraction of Ge and other elements from granitic rocks by low temperature hydrothermal fluids and transport with $Ge(OH)_4(aq)$ complexes *(Etschmann et al. 2017*)

1.2.3 Germanium-minerals and Ge-bearing sulfides

1.2.3.1 Mineralogy

Germanium is often found in the sulfide lattice, mainly sphalerite or chalcopyrite, or in coal. But Ge can occur in major contents in specific mineral (named herein "Ge-minerals"). These minerals seem rare in Pb-Zn(-Ge) deposits (*Bernstein 1985; Höll et al. 2007; Belissont 2016*) and confirm the fact that Ge is difficult to concentrate at global scale. In few deposits, Ge-minerals may be hosted in small sizes in zinc sulfide and their reflectance close to sphalerite or chalcopyrite do not help to localize them. Nonetheless, in several deposits from the Kipushi-type (Kipushi, Khusib, Kabwe and Tsumeb Zn-Cu-Pb deposits), Ge-minerals may constitute coarse phases (>100 μm) with apparition of renierite, germanite (rare in Kipushi mine) and briartite *(De Vos et al. 1974; Hughes 1987; Melcher et al. 2006; Kampunzu et al. 2009; Belissont 2016*).

The most common Ge-minerals are Ge-sulfides (Figure 18). Germanite, renierite or briartite are frequently hosted in sphalerite even if other sulfide hosts bornite, chalcopyrite, tennantite-tetrahédrite and more rarely galena and pyrite may appear for these minerals (*Bernstein and Cox 1986; Wagner and Monecke 2005; Höll et al. 2007; Kamona and Friedrich 2007; Belissont 2016*).

Mineral group		Name	Formula	Environment	Location-type	wt.% Ge	Source
Oxides	Rutile	**Argutite**	Ge4+O2	Vein-type (deformed)	Pyrenees	69.4	Johan et al., 1983
Oxides		**Eyselite**	Fe3+Ge4+3O7(OH)	Oxidized Kipushi-type	Tsumeb	53.9	Roberts et al., 2004
Germanates		**Otjisumeite**	PbGe4O9	Oxidized Kipushi-type	Tsumeb	45.3	Keller et al., 1981
Germanates		**Bartelkeite**	PbFeGe6+(Ge4+O8)	Kipushi-type	Tsumeb	35.8	Origlieri et al., 2012
Hydroxides	Stottite	**Manganostottite**	MnGe(OH)6	Oxidized Kipushi-type	Tsumeb	35	Strunz et al., 1961
Hydroxides	Stottite	**Stottite**	FeGe(OH)6	Oxidized Kipushi-type	Tsumeb	31.5	Strunz et al., 1958
Germanates	Lepidomelane	**Ge-lepidomelane**	(K,Na,H30)2(Fe6)(Ge5Al 3)020(Cl2OH2)	Vein-type (deformed)	Pyrenees	27.8	Johan et al., 1983
Palladogermanide		**Marathonite**	Pd2Ge	Cu-Ni-PGE deposit	Marathon	25.4	McDonald et al., 2017
Germanates	Chloritoid	**Carboirite**	FeA12GeO5(OH)2	Vein-type (deformed)	Pyrenees	24.5	Johan et al., 1983
Oxides	Topaz	**Krieselite**	Al2GeO4 (F,OH)2	Oxidized Kipushi-type	Tsumeb	23.6	Schlüter et al., 2010
Oxides	Ringwoodite	**Brunogeierite**	(Fe2+)2Ge4+O4	Vein-type (deformed)/oxidized Kipushi-type	Tsumeb/Pyrenees	22.3	Otteman & Nuber, 1972
Sulfides	Stannite	**Briartite**	Cu2(Fe,Zn)GeS4	Kipushi-type	Kipushi	16.6	Francotte et al., 1965
Sulfides	Stannite	**Barquillite**	Cu2(Cd,Fe)GeS4	Vein-type	Barquilla	16.5	Murciego et al., 2014
Sulfates	Ettringite-thaumasite	**Cararaite**	Ca3Ge(OH)6(SO4)(CO3) ·12H2O	Calcite veins	Carrara basin	15	Merlino et al., 2001
Sulfates	Fleischerite	**Schaurteite**	Ca3Ge[(OH)6(SO4)2]·3H 2O	Oxidized Kipushi-type	Tsumeb	13.4	Origlieri et al., 2012
Sulfides	Stannoidite	**Omariniite**	Cu+8Fe3+2Zn2+Ge4+2 S2-12	Epithermal	Capillitas, Catamarca	11.6	Bindi et al., 2017
Sulfides	Germanite	**Maikainite**	Cu10(Fe,Cu)3MoGe3S16	Kipushi-type	Tsumeb/Maikin	10.8	Spiridonov et al., 2003
Sulfides	Germanite	**Germanocolusite**	Cu13V(Ge,As)3S16	Polymetallic hydorthermal deposit	Urup / Tsumeb / Waterloo	10.1	Spiridonov et al., 1992 / Wagner & Monecke, 2005
Sulfides	Germanite	**Ovamboite**	Cu10(Fe,Cu,Zn)3WGe3S 16	Kipushi-type	Tsumeb/Maikin	9.9	Spiridonov et al., 2003
Sulfides	Germanite	**Morozeviczite-Polkovicite**	(Pb,Fe)3Ge1-xS4	Vein-type	Polkowice	9.8	Harańczyk, 1975
Sulfides	Germanite	**Renierite**	Cu10(Zn1-xCu)Ge2-xAsxFe4S16	Kipushi-type / Epithermal	Kipushi	7.8-9.0	Vaes, 1948 / Bernstein, 1986
Sulfides	Germanite	**Germanite**	Cu13Fe2Ge2S16	Kipushi-type / VHMS	Tsumeb	6.0-11	Pufahl, 1922
Sulfides	Germanite	**Catamarcaite**	Cu2GeWS8	Epithermal	Capillitas, Catamarca	7.9	Putz et al., 2006
Sulfides	Argyrodite	**Putzite**	(Cu4.7Ag3.3)8GeS6	Epithermal	Capillitas, Catamarca	7.7	Paar et al., 2004
Sulfates		**Itoite**	Pb3[GeO2(OH)2(SO4)2]	Oxidized Kipushi-type	Tsumeb	7.6	Frondel et al., 1960
Sulfates	Fleischerite	**Fleischerite**	Pb3Ge[(OH)6(SO4)2]·3 H2O	Oxidized Kipushi-type	Tsumeb	7.2	Frondel et al., 1960
Sulfides	Argyrodite	**Argyrodite**	Ag8GeS6	Vein-type/porphyre	Freiberg	6.4	Weisbach, 1886
Sulfides	Stannite	**Calvertite**	Cu5Ge0.5S4	Kipushi-type	Tsumeb	5.6	Jambor et al., 2007
Sulfides	Argyrodite	**Alburnite**	Ag8GeTe2S4	Epithermal	Rosia Montana	5.5	Tamas et al., 2014
Silicates	Cyclosilicate	**Mathewrogersite**	Pb7(Fe,Cu)Al3Ge [(Si6O18)2|(OH, H2O)6]	Oxidized Kipushi-type	Tsumeb	2.7	Keller & Dunn, 1986

Figure 18. Compilation of Ge-minerals (modified and actualized from *Holl et al., 2007*) (*Weisbach 1886; Pufahl 1922; Vaes 1948; Strunz et al. 1958; Frondel et al. 1960; Strunz and Giglio 1961; Francotte et al. 1965; Ottemann and Nuber 1972; Harańczyk 1975; Keller et al. 1981; Johan et al. 1983; Bernstein 1986a; Keller, P., Dunn 1986; Spiridonov et al. 1992; Merlino and Orlandi 2001; Spiridonov 2003; Paar et al. 2004; Roberts et al. 2004; Wagner et al. 2005; Putz et al. 2006; Jambor et al. 2007; Schlüter et al. 2010; Origlieri and Downs 2013; Murciego et al. 2014; Tamas et al. 2014; Bindi et al. 2017; McDonald et al. 2017)*

Some examples like in Kabwe *(Kamona and Friedrich 2007*) show the presence of briartite or renierite hosted in sphalerite or galena. Briartite appears also as minute exsolution blebs in chalcopyrite. Ge-oxides seem rare and are described only in a few localities such as in Pyrenean Pb-Zn deposits where two Ge-species were discovered by *Johan et al. (1983)*: Argutite (GeO_2) and

Carboirite (Ge-chloritoid). Brunogeierite is also reported in the Tsumeb and Kipushi deposits and this Ge-spinel seems more related to supergene alteration (*Ottemann and Nuber 1972; Intiomale and Oosterbosch 1974; Lombaard et al. 1986)*.

Germanium-hydroxides and sulfates are reported in some localities and are genetically linked to the alteration of the primary sulfide phase *(Strunz and Giglio 1961; Bernstein and Waychunas 1987; Mondillo et al. 2018b*).

1.2.3.2 Distribution and chemistry

Germanium is often poorly concentrated on Earth but it exhibits numerous chemical affinities as siderophile, chalcophile or organophilic or lithophile behaviors which is certainly responsible for the occurrence of Ge in a wide variety of environments (*Bernstein 1985; Höll et al. 2007*). Siderophile behavior is associated to its relative enrichment in the iron phases of the meteorites, which is frequently used to classify iron meteorite (*Bernstein 1985; Luais 2007*). Chalcophile affinity is related to the frequent incorporation of Ge in sulfide minerals (sphalerite, chalcopyrite, etc.). High sulfidation conditions allow to the formation of the thiocomplex $[GeS4]^{4-}$ (*Belissont 2016*). Germanium organophile affinities is one of the higher in the Mendeleyev periodic table and marked by the relative enrichment of Ge in coal and lignite deposit up to few thousands of ppm Ge (*Goldschmidt and Peters 1933; Höll et al. 2007*).

Germanium is relatively enriched in the crust with values between 1.0 to 1.7 ppm (*Bernstein 1985*) or 1.5 ppm (i.e. Clarke; *Smith and Huyck 1999*) compared to elements like silver (Clarke = 0.07 ppm) which is mainly due to its affinity for Si. In silicates, Ge often occurs at low contents, with up to few tens of ppm, and is related to the isomorphous substitution with Si and their similar ionic radius (0.39 and 0.28 angström respectively; Figure 20). In this substitution, Ge and Si are tetravalent. An exceptionnal high Ge-content occur in Pyrenean quartz with up to 8700 ppm Ge measured with EPMA analyses in the Arrens, Carboire and Anglas-Uzious deposits (*Johan et al. 1983*). There is a strong tendency for Ge to be concentrated in late-magmatic and hydrothermal fluid such as pegmatitic quartz with a common high Ge/Fe ratio (*Morey 1957; Bernstein 1985; Götze et al. 2004)* or in topaz, garnet and mica *(Papise 1928; Burton et al. 1958; Johan and Oudin 1986; Breiter et al. 2013*).

Germanium has an electronic configuration of $[Ar]3d^{10}4s^{2}4p^{2}$ and forms covalent bonds with many ligands due to its high electronegativity, more important than Si or Sn for example (*Cotton and Wilkinson 1980)*. Few data are reported for Ge isotopes in the literature in upper

mantle/crust, hydrothermal or meteoritic systems *(Luais et al. 2000; Luais 2007; Belissont et al. 2014; Meng et al. 2015*). Five stable isotopes are described and classified by weight and abundance: ^{74}Ge (35.94 %), ^{72}Ge (27.66 %), ^{70}Ge (21.23 %), ^{73}Ge (7.73 %), and ^{76}Ge (7.44 %). The most common ratio used in the Ge isotopic analyses is the ratio $\delta^{74}Ge=^{74}Ge/^{70}Ge$ (35.94 and 21.23% in abundance, respectively; *Belissont 2016*). In sulfide minerals, δ^{74}Ge ranges between –5.72 ‰ to +3.67 ‰. The variations in concentrations in the sulfides (Figure 19) are certainly not directly linked to temperature but to Rayleigh fractionation effect (*Belissont 2016*).

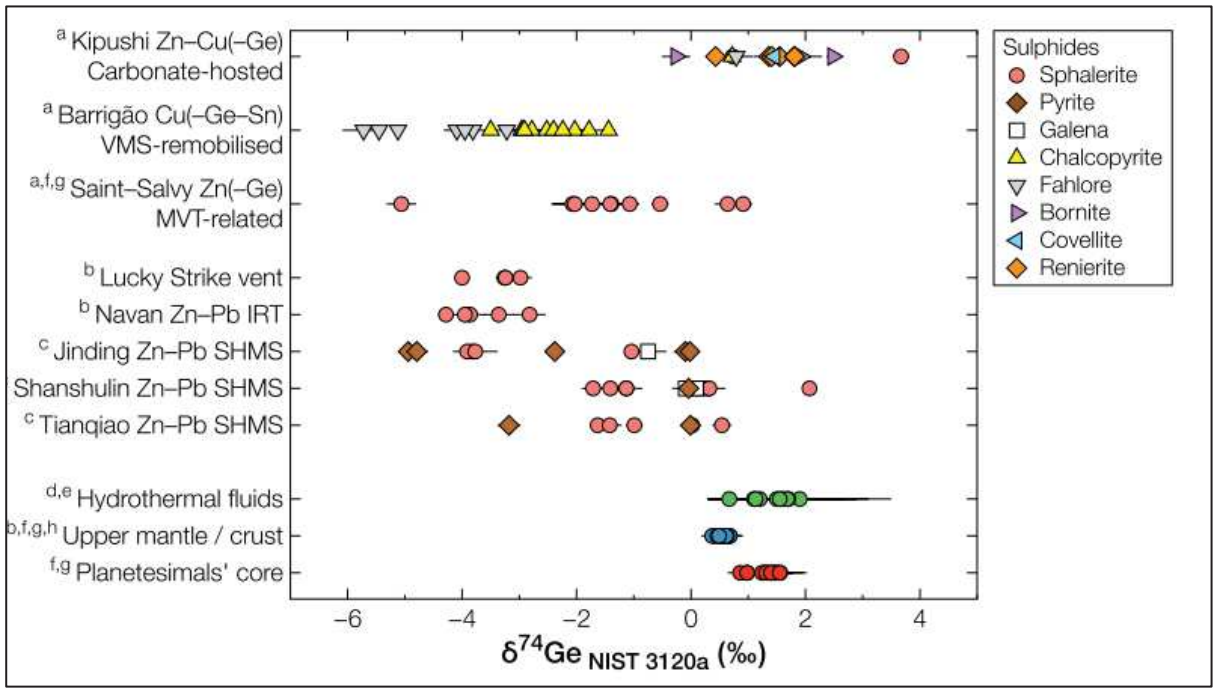

Figure 19. δ^{74}Ge compositions of 'planetesimals' core (Fe meteorites), Bulk Silicate Earth (upper mantle/crust rocks), hydrothermal fluids and sulphide minerals from various ore deposits (from *Belissont, 2016* with references herein).

1.2.3.3 Incorporation of Ge and related trace elements in sphalerite

Sphalerite may host a large numbers of trace elements in its tetrahedral sites such as common metals like Fe, Mn, Cd, Cu, Co or Ag. Rare elements such as Ga, In or Ge may be also incorporated in the sphalerite lattice (*Di Benedetto et al. 2005; Cook et al. 2009b*). These mechanisms of incorporation are chemically explained by the Goldschmidt's rules and Ringwood's subsequent modifications (*Goldschmidt 1954; Ringwood 1955*) with this visual graphic (Figure 20) modified from (*George et al. 2016*, ionic radius value from *Shannon et al. 1976)*.

Four rules describe the possible substitution in minerals: i) the ions can widely replace those of another in ionic crystals if their radii differ by less than approximately 15%; ii) if the charges

differ by more than one unit after the replacement, substitution is generally slight; iii) when two different ions can occupy a particular position in a crystal lattice, the ion with the higher ionic potential forms a stronger bond with the anions surrounding the site; iv) substitutions may be limited, even when the size and charge criteria are satisfied, when the competing ions have different electronegativities and form bonds of different ionic character. These rules are empiric and the relations between the ions are not always respected because of the influence of specific

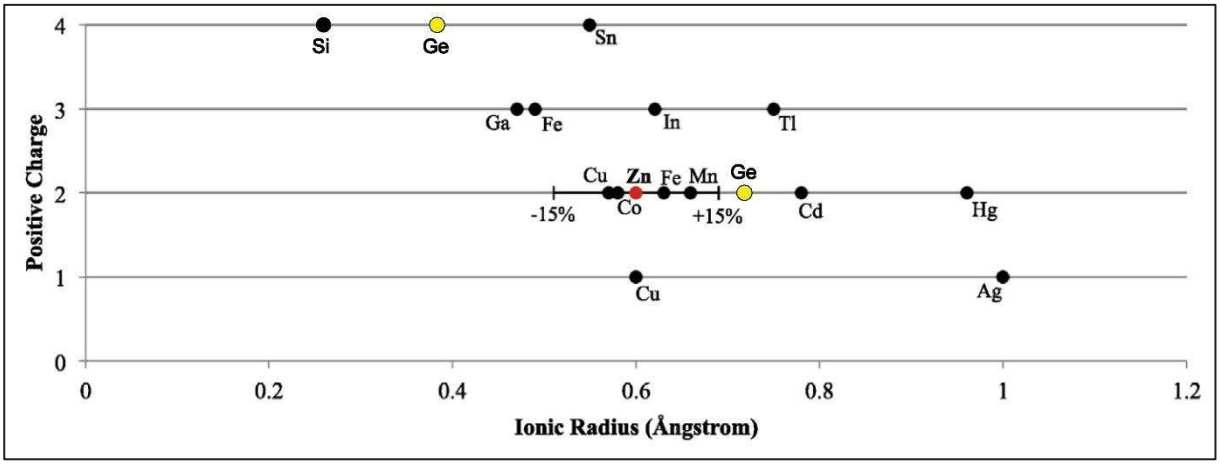

Figure 20. Ionic radius and positive charge for elements in tetrahedral coordination (same as sphalerite; modified from *George et al., 2016*)

thermodynamic conditions, especially for Ge (Figure 20).

Johan (1988) proposed a general substitution mechanism in sphalerite, which was slightly revised by *Belissont (2016)* and exclusion of divalent elements in the mechanism : $(2x + 3y)Zn^{2+} \leftrightarrow (x+2y)(Cu, Ag)^{+}+x(Ga, In, Sb)^{3+}+y(Ge, Sn)^{4+}$. In sphalerite, divalent Fe Mn, Cd ions are incorporated in the sphalerite lattice with a direct substitution with Zn (i.e. $Zn^{2+} \leftrightarrow (Fe, Cd, Mn, Co)^{2+}$ and their contents may reach few thousands of ppm (*Ye and Tiegeng 1999; Bernadini et al. 2004; Monteiro et al. 2006)*. Their incorporation seems highly dependent of their similar ionic radius with Zn *(Belissont et al. 2016; George et al. 2016*). Numerous ionic radii largely differ from Zn^{2+} even they are known to be present in solid solution in the sphalerite. This is possibly linked to temperature effects which may enhance the incorporation of elements with different radius (*George et al. 2016*).

Copper seems generally incorporated with up to thousands of ppm in sphalerite, under the monovalent state attested by numerous correlation in concentrations with Ge (*Bernstein 1985; Johan 1988; Belissont et al. 2014, 2016*), Ga (*Cook et al. 2009b; Bonnet 2014; Sahlström et al. 2017a*), or In *(Johan 1988; Cook et al. 2009b; Shimizu and Morishita 2012; Murakami and Ishihara 2013; Sahlström et al. 2017b*) and μ-XANES study by (*Cook et al. 2012*). Silver exhibits a same monovalent state and

probably participates like Cu to the incorporation of trivalent or tetravalent ions (*Johan 1988; Belissont et al. 2014; Bauer et al. 2018*)

Indium and Ga are incorporated under trivalent state attested by their correlations with monovalent ions *(Johan 1988; Murakami and Ishihara 2013; Belissont et al. 2014; Bauer et al. 2018*) involving substitution mechanisms such as $2Zn^{2+} \leftrightarrow Cu^{+} + (In^{3+}$ or $Ga^{3+})$. Tin oxidation state (which may be 2^{+},3^{+},or 4^{+}) and incorporation in sphalerite is not clear due to the lack of XANES study. *Murakami and Ishihara (2013)* describe within In-bearing sphalerite, the occurrence of substitution mechanisms with Zn associated to the correlation of the tetravalent Sn^{4+} contents and monovalent Ag^{+} and/or Cu^{+} concentrations. *Belissont et al. (2014)* define a possible correlation between Sn and In (with a vacancy), despite no evidence of the occurrence of Sn^{3+} ($3Zn^{2+} \leftrightarrow In^{3+} + Sn^{3+} + \square$).

Germanium is mainly incorporated in sphalerite with a coupled Zn substitution associated to monovalent ions such as Cu or Ag. The oxidation state is still debated even if a large amount of the actual chemical analyses (LA-ICP-MS or μ-XANES) show the occurrence of the tetravalent state in all sulfides, even in coal-lignite deposits (*Etschmann et al. 2017*). In Saint-Salvy sphalerite, μ - XANES combined to LA-ICP-MS studies show unequivocal presence of Ge^{4+} in sphalerite lattice (*Belissont et al. 2016*). In the Freiberg sphalerite (IIa type), *Bauer et al. (2018)* observe a correlation between Ge and Ag contents in sphalerite, involving the substitution $3Zn^{2+} \leftrightarrow 2Ag^{+} + Ge^{4+}$. In the Tres Maria carbonate-hosted deposit, Ge^{4+} occurrence is also demonstrated but no correlation with existent monovalent element is present (*Cook et al. 2015*) which supposed a direct Ge^{4+} substitution with (Zn^{2+}, Fe^{2+}) and vacancies in the structure to compensate charge balance. In the sphalerite from Tennessee (*Bonnet et al. 2017*), presence of divalent and tetravalent Ge ions is unexpectedly observed, surrounded by sulfur or oxygen atoms (argutite-like GeO_2). The occurrence of two different oxidation states implies changes in conditions during sphalerite formation, perhaps associated to fS_2 and fO_2.

1.2.3.4 Oxidation state in Ge-minerals and other sulfides

Germanium is hosted in a large diversity of mineral groups, but the tetravalent oxidation state is observed in a large majority of Ge-minerals as well as in chalcopyrite. In renierite (Figure 18), only Ge^{4+} cations occur, related to a continuous solid-solution between the zincian and the arsenian end-members and a coupled substitution $Zn^{2+} + Ge^{4+} \leftrightarrow Cu^{+} + As^{5+}$ (*Bernstein 1986a*). Other Ge-sulfides such as briartite and germanite (Figure 18), contain only Ge^{4+} (*Belissont 2016*) as well as argutite and carboirite (*Johan et al. 1983*), eyselite (*Roberts et al. 2004*), and omariinite (*Bindi et al.*

2017). Brunogeierite was previously considered to contain Ge^{2+} but *Cempírek and Groat (2013)* demonstrate the unique presence of Ge^{4+} with bond valence calculations. This mineral has probably a complete solid solution with magnetite *(Bernstein 1985*). One of the few exceptions for the ubiquitous occurrence of tetravalent Ge exists with the bartelkeite (Figure 18), a lead and iron germanate which contains both Ge^{6+} and Ge^{4+}. It represents the unique known occurrence of Ge^{6+}(*Origlieri et al. 2012*). In chalcopyrite and covellite from the Kipushi mine, μ-XANES study only reported the presence of tetravalent germanium (*Belissont et al. 2016*).

1.2.4 Germanium-hosts relative to geology

A classification according deposit type is generally exposed for the major elements like Pb, Zn, or Cu. This classification is constituted following well-described and known deposits and are based on their similarities such as their type of genesis, the ore geometry or their mineralized temperature. In the case of Germanium, the same classification was done in *Höll et al. (2007)* and technical classification names are referred to this article. A version of the map by *Höll et al. (2007*) is shown in the **Erreur ! Source du renvoi introuvable.**. The Ge occurrence is intimately linked to sphalerite but not only and may appear in coal, in other sulfides like chalcopyrite, tennantite-tetrahedrite or in Ge-minerals. A classification according to Ge mineral-hosts and their related geological context is done with a separated description for each in the following paragraphs.

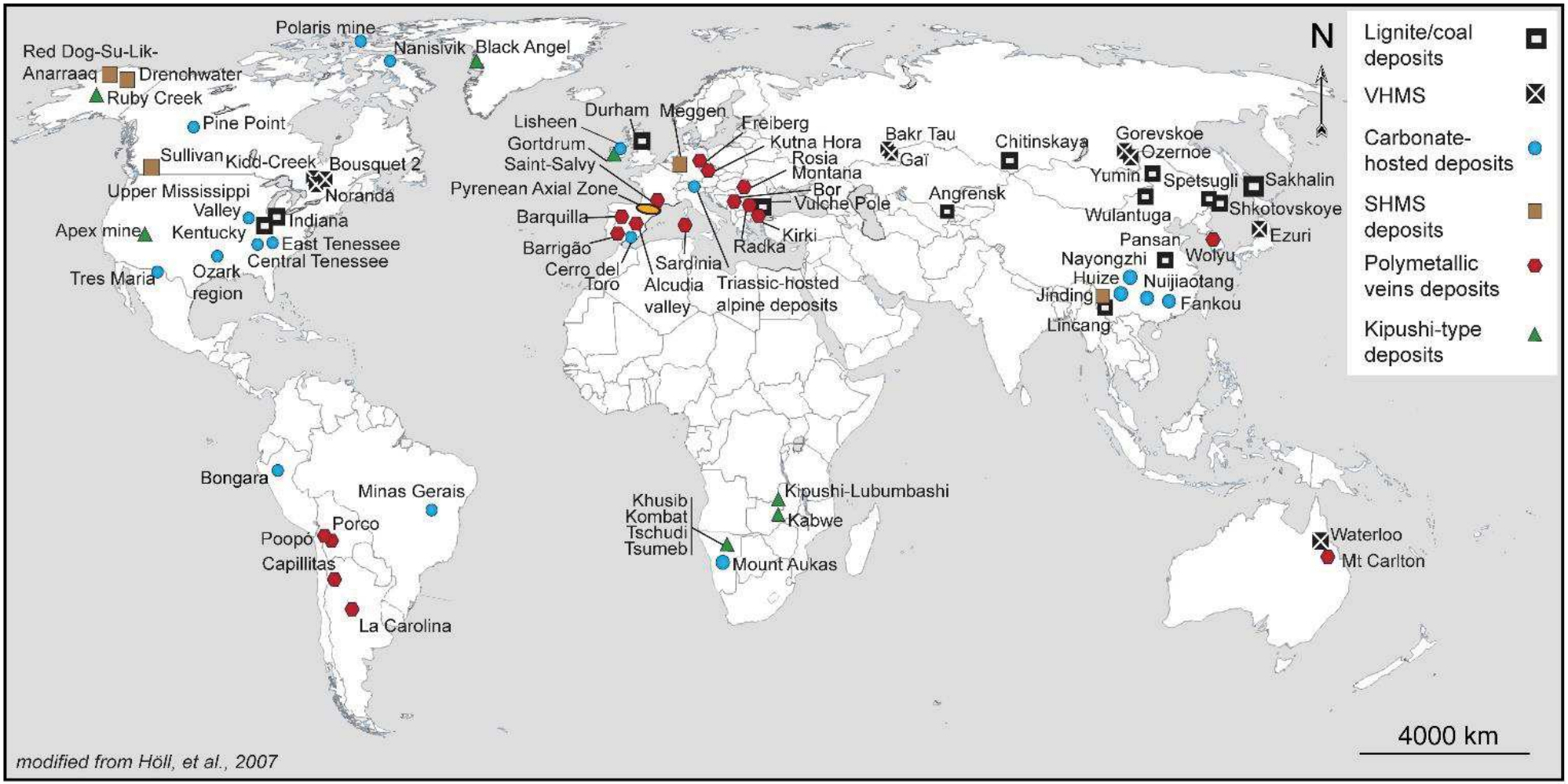

Figure 21. Location of ore deposits with Ge contents reported in the litterature. Deposits with Ge-minerals occurrence are underligned in the legend below. Note the presence of Pyrenean Axial Zone (PAZ) deposits which will be discussed in this study (modified from *Höll et al., 2007*). References below.

Figure 21 references. **Lignite and coal deposits**: Angrensk (*Seredin and Finkelman 2008*), Uzbekistan / Durham (*Bernstein 1985)*, England / Kentucky (Hower et al. 2002, 2018), USA / Indiana (Mastalerz and Drobniak *2012)*, USA / Lincang *(Hu et al. 2009; Qi et al. 2011)*, China / Pansan mine (*Chen et al. 2014)*, China / Sakhalin *(Seredin and Finkelman 2008)*, Russia / Shkotovskoye (*Seredin and Finkelman 2008)*, Russia / Spetsugli (*Seredin 2003*), Russia / Vulche Pole (*Vassilev et al. 1995a*), Bulgaria / Wulantuga (*Du et al. 2009; Qi et al. 2011*), China / Yimin *(Li et al. 2014)*, China – **Volcanic-Hosted Massive Sulfide (VHMS) Cu–Zn(–Pb)(–Ba) deposits:** Abitibi–Belt: Kidd Creek, Noranda, Bousquet 2 Mine (*Tourigny et al. 1993)*, Canada / Bakr Tau (*Prokin and Buslaev 1999*), Russia / Barrigao (*Reiser et al. 2011*), Spain / Ezuri (Kuroko-type deposits; *Komuro and Kajiwara, 2004*), Japan / Gaï *(Prokin and Buslaev 1999; Vikentyev et al. 2016a)*, Russia / Gorevskoe *(Höll et al. 2007)*, Russia / Ozernoe (*Höll et al. 2007*), Russia / Waterloo, (*Wagner and Monecke 2005*), Australia – **Carbonate-hosted base metal deposits (MVT, Alpine-type, Irish-type) Zn-Pb-Fe(-Cu)(-Ag)(-Ba) deposits** : Bongara (*Mondillo et al. 2018a*), Peru / Central-Tenessee *(Bonnet 2014*), USA / Cerro del Toro *(Morales-Ruano et al. 1996),* Spain / East-Tenesse (*Bonnet 2014*), USA / Fankou (*Song 1984*), China / Huize (*Han et al. 2006; Ye et al. 2011*), China/ Lisheen *(Wilkinson et al. 2005*), Ireland/ Minas Gerais *(Monteiro et al. 2006*), Brasil / Mount Aukas *(Emslie 1960)*, Namibia / Nanisivik *(Arne et al. 1991; Harris and Sangster 1991*), Canada / Nayongzhi (*Wei et al. 2018*), China / Nuijiaotang (*Ye et al. 2011*), China / Ozark region deposits *(Viets et al. 1992*), USA / Pine Point, and Polaris Mine *(Höll et al. 2007)*, Canada / Triassic-hosted alpine deposits *(Schroll 1996),* Austria / Upper Mississippi valley *(Hall and Heyl 1968),* USA / Tres Maria *(Saini-Eidukat et al. 2009; Cook et al. 2015*), Mexico – **Sediment- Hosted Massive Sulfide (SHMS) Zn–Pb–Cu(–Ba) deposits:** Anarraaq, Drenchwater and Su-Lik (*Heimann et al. 2013*), Alaska, USA / Jinding (*Ye et al. 2011*), China / Meggen *(Höll et al. 2007*), Germany / Red Dog *(Moore et al. 1986; Kelley and Jennings 2004),* USA / Sullivan (*Höll et al. 2007*), Canada – **Polymetallic Veins-type Ag-Pb-Zn(-Cu)(-Fe)(-Au)(-Sn) deposits:** Alcudia valley (*Palero-Fernández and Martín-Izard 2005)*, Spain / Barquilla (*Pascua et al. 1997*), Spain / Bor *(Höll et al. 2007)*, Serbia / Capillitas *(Putz et al. 2006),* Argentina / Freiberg *(Seifert and Sandmann 2006; Bauer et al. 2018)*, Germany / Kirki *(Schwarz-Schampera and Herzig 2002*), Greece / Kutna Hora *(Schwarz-Schampera and Herzig 2002*), Czech Republic / La Carolina (*Gallard-Esquivel et al. 2018*), Argentina / Mt Carlton (*Sahlström et al. 2017a*), Australia / Noailhac-Saint Salvy *(Munoz et al. 1994; Belissont et al. 2014*), France / Poopó *(Torres et al. 2019),* Bolivia / Porco *(Paar et al. 2005)*, Bolivia / Radka(*Kouzmanov 2001)*, Bulgaria / Rosia Montana *(Bailly et al. 2005)*, Romania / Sardinia *(Höll et al. 2007*), Italy / Wolyu, (*Yun et al. 1993)*, Korea – **Polymetallic Kipushi-Type (KPT) Cu-Pb-Zn deposits:** Apex Mine *(Bernstein 1986b; Dutrizac et al. 1986)*, USA / Black-Angel (*Horn et al. 2018*), Greenland /Kabwe *(Kamona et al. 1999; Kamona and Friedrich 2007; Kampunzu et al. 2009)*, Zambia / Khusib (*Melcher et al. 2006*), Namibia / Kipushi (*De Vos et al. 1974; Intiomale and Oosterbosch 1974*), Democratic Republic of Congo / Kombat (*Deane 1995*), Namibia / Tschudi *(Mckinney et al. 2006*), Namibia / Tsumeb *(Hughes 1987; Melcher et al. 2006*), Namibia / Ruby Creek *(Bernstein and Cox 1986; Hitzman 1986)*, USA.

1.2.4.1 Sphalerite lattice

Sphalerite is relativelty enriched in Ge in a large diversity of deposit-types (>100 ppm and < few thousands of ppm). Their genesis may be syngenetic-early diagenetic and in this case, Ge-enrichment in this sphalerite is relatively poor (< 50 ppm Ge) even if some SHMS sphalerite may contain unusual Ge-conconcentrations like in the Anarraaq deposit with up to 720 ppm Ge (*Graham et al. 2009*). Most of the known Ge-mineralizations associated to sphalerite are epigenetic

like in the MVT deposits (*Viets et al. 1992; Bonnet 2014*) or Vein deposits *(Belissont et al. 2014*). Their setting is often related to extensional environments and circulation of hydrothermal fluids in weakness levels, such as rock interface, porosity-karst (Figure 22A and B) or schistosity. These deposits may be hosted in a wide variety of rocks from carbonate like most of the MVT (*Viets et al. 1992; Saini-Eidukat et al. 2009; Bonnet et al. 2017*) to black-schists or granitoid-gneiss such as other vein systems (*Munoz et al. 1994; Bauer et al. 2018*). In the Saint-Salvy Zn–Ge–Ag–(Pb–Cd) deposit (Montagne Noire, France), four different Pb-Zn mineralizations were described (*Barbanson and Geldron 1983; Cassard et al. 1993; Munoz et al. 1994)*. The main mineralization (M4) is structurally controlled by competence interface between metamorphic schist due to Late-Variscan Sidobre granite and poorly metamorphosed schist (Figure 22C). Previously linked to a Late-Variscan forming hydrothermal fluid, *Munoz et al. (1994)* demonstrate a more recent age for the

mineralization emplacement which is probably Triassic-Jurassic in age and linked to the widespread Pb-Zn hydrothermal event in the western Europe (*Boiron et al. 2010; Cathelineau et al. 2012)*. Some epithermal deposits (high sulfidation) may contain substantial Ge contents like in the Mt-Carlton

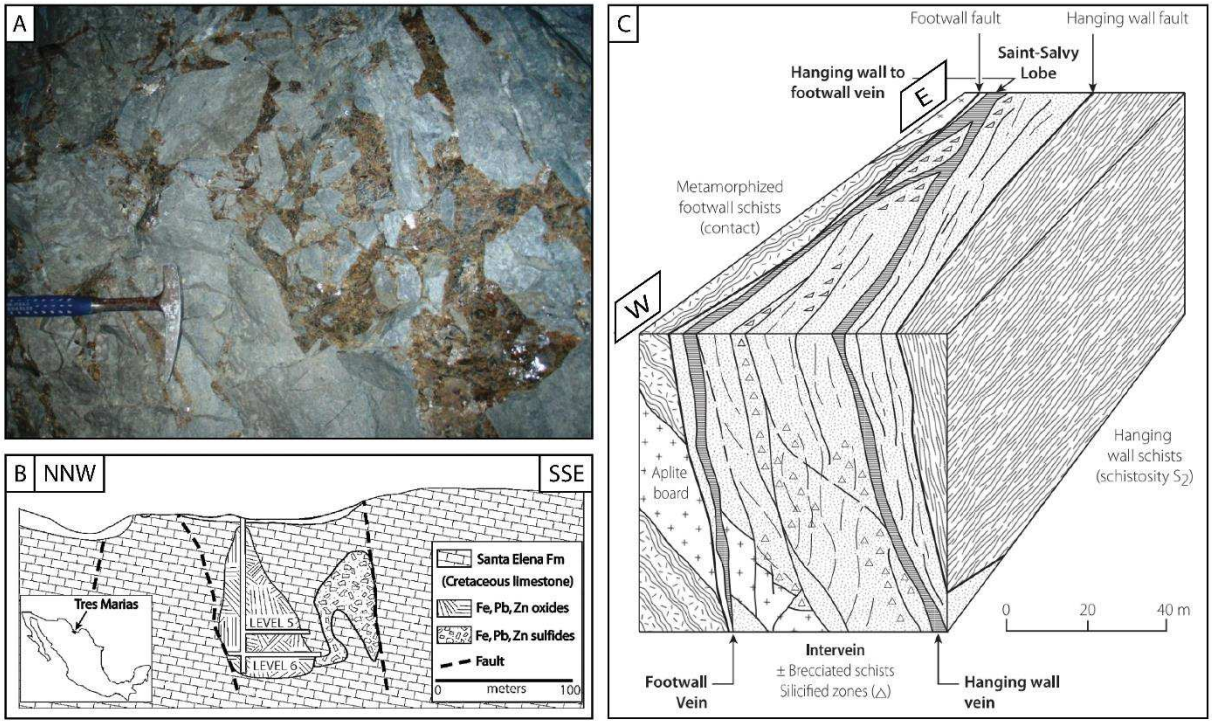

Figure 22. Typical examples of Ge-bearing sphalerite deposit. A. Outcrop photograph of sphalerite mineralization in brecciated dolomie (the Central-Tenessee deposit, from *Bonnet, 2014*). B. Cross-section in the Tres Maria deposit hosted in Mid-Cretaceous limestone (from *Saini-Eidukat et al.,, 2009*). C. Cross-section of the Saint-Salvy vein complex between metamorphic and unmetamorphosed schists (from *Cassard et al., 1994*).

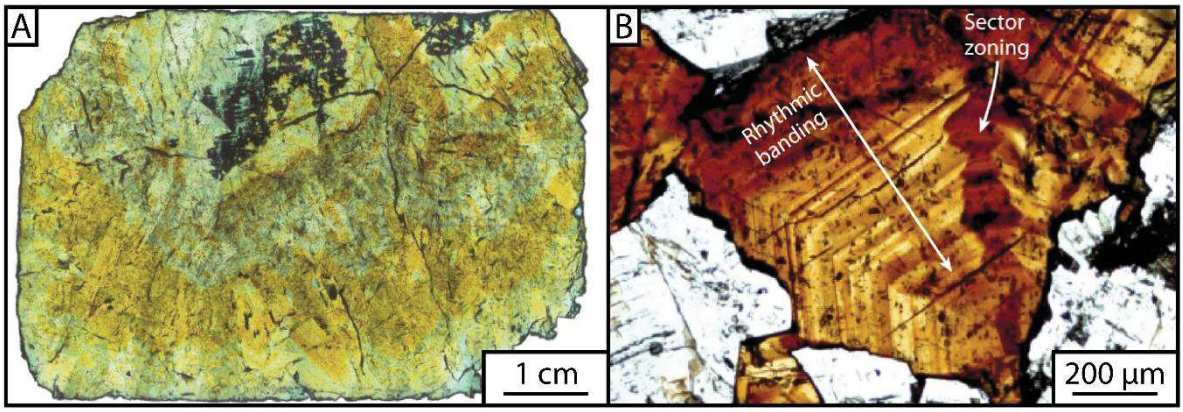

Figure 23. Two microphotographs of coarse-grained sphalerite crystals (>100 µm). A. Sphalerite with pale yellow to light orange colors from the Central Tenessee MVT deposit . Darker bands contain up to 790 ppm Ge (*Bonnet, 2014*). B. Sphalerite from the Saint-Salvy vein deposit (*Bélissont et al., 2014*). Ge enrichment is preferentially located in sector zoning, with Ge-contents up to 2580 ppm Ge.

deposit (up to 611 ppm Ge; *Sahlström et al. 2017*). Post-mineralzation imprint is often negligible attested by non-deformed and well-formed sphalerite crystals.

Sphalerite from non-deformed MVT or polymetallic vein mineralizations (Figure 23; *Johan 1988; Viets et al. 1992; Cook et al. 2009b; Belissont et al. 2014; Bonnet 2014*) are commonly enriched in Ge and exhibit coarse millimetric grains. But colloform or schalenblende sphalerite with smaller grain size (often < 100 μm; *Henjes-Kunst et al. 2017a*) may also contain reliable Ge content with up to 1720 ppm Ge in veins from the Freiberg district (*Bauer et al. 2018*). In Bleiberg (Austria), sphalerite crystals appear highly zoned and with important grains size variations *(Schroll 1996; Henjes-Kunst et al. 2017a*). Punctual EPMA analyses describe relative higher Ge contents (up to ~ 1 000 ppm Ge) in fine-grained sphalerite associated to colloform schalenblende layers. Germanium variations are relatively important *(Henjes-Kunst et al. 2017a*). Coarse grains locally occur in fine-grained sphalerite and contain lower Ge amounts (~below 500 ppm Ge). These coarse crystals may appear zoned but no clear detail on the location of these analyses are present.

1.2.4.2 Other sulfides lattices with Ge in trace content

Many other sulfides such as chalcopyrite or tennantite-tetrahedrite minerals can host substantial Ge concentrations and are often related to epigenetic deposit-type. Many of them have endured deformation/metamorphism such as the Barrigao epigenetic vein deposit (**Erreur ! Source du renvoi introuvable.**) hosted in greywackes and shales. This deposit contain deformed chalcopyrite with patchy-zoning in Ge and Sn *(Reiser et al. 2011*) and heterogeneous Ge contents up to 7100 ppm Ge (Figure 24A; *Belissont 2016*). Tennantite-tetrahedrite is also a Ge-carrier with mean content of 900 ppm. In the Kipushi-type epigenetic deposits, mineralization has endured deformed/metamorphosed imprint (*Chabu 1989; Melcher et al. 2006; Kamona and Friedrich 2007; Kampunzu et al. 2009)*. Tennantite-tetrahedrite, chalcopyrite, enargite or stannoidite crystals from the Khusib, Kabwe and Tsumeb deposits (Figure 24B-D) contain high but fluctuated Ge contents up to 2020 ppm Ge (in the Tsumeb tennantite) probably related to occurrence of Ge-minerals *(Frondel and Ito 1957; Melcher 2003; Kamona and Friedrich 2007*). In the Kipushi mine, chalcopyrite seems to contain relative homogeneous low Ge content (~ 300 ppm Ge; Figure 24D; *Belissont et al. 2019*) even if the presence of abundant Ge-minerals is recorded. In the Lisheen carbonate-hosted deposit which is non-deformed, *Wilkinson et al. (2005)* describe the presence of Ge in galena and in tennantite with contents up to 1300 and 1000 ppm Ge respectively. Enrichment in bornite (up to 1000 ppm Ge) is reported associated to the deformed VHMS deposits (*Komuro and Kajiwara 2004; Höll et al. 2007*) or to poorly deformed porphyry copper mineralizations but the association between

bornite and Ge-minerals reported in some of these deposits (the Bor deposit) is lacking (*Höll et al. 2007*). Enargite from non-deformed epithermal systems (high sulfidation) may contain abundant Ge concentrations up to 1200 ppm Ge in the Mt-Carlton deposit (*Sahlström et al. 2017a*). Remarkable high Ge content is reported in galena from the Ambrosia, Fagundes and Vazante deposits (Minas Gerais) in Brasil with up to 8470 ppm Ge (EPMA measurements; *Monteiro et al. 2006*) associated to high Ga contents (up to 4650 ppm Ga). In sphalerite Ge concentrations are lower with mean contents of 540 ppm Ge in Fagundes deposit. Recent study in the Poopó epithermal deposit (*Torres et al. 2019*) describes the presence of Ge and other elements like Ga or In in trace concentrations in unusual hosts such as rhodostannite ($Cu_2FeSn_3S_8$, up to 2100 ppm Ge) or franckeite ($(Pb,Sn)_6FeSn_2Sb_2S_{14}$; up to 1600 ppm Ge) but Ge appear depleted in sphalerite.

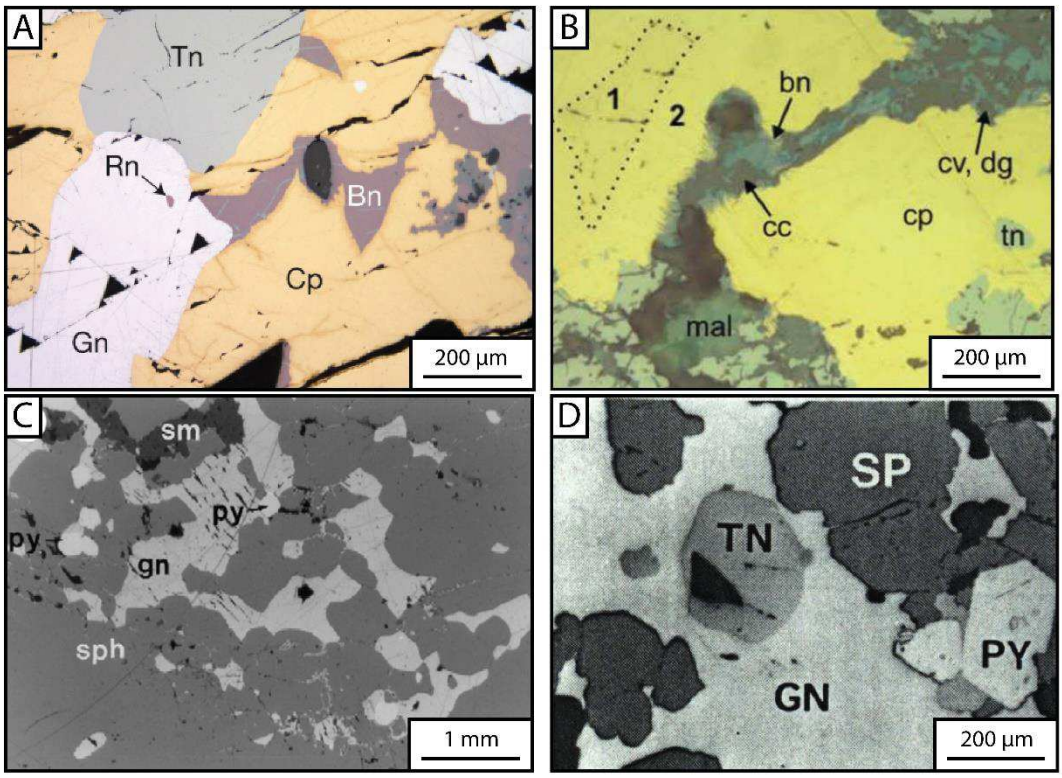

Figure 24. Microphotographs of Ge-bearing sulfides (reflected light; Tn: tennantite; Gn: galena; Py: pyrite; Sph or Sp: sphalerite; Cp: chalcopyrite; Bn: bornite; cc: chalcocite: cv-dg: covellite-digenite; mal: malachite; sm: smithsonite). A: Sulfide textures in the Kipushi mine (from *Belissont, 2016*). B. Deformed chalcopyrite from the Barrigao deposit (1: relict cp; 2: young cp; from *Reiser et al., 2011*). C: Polygonal sphalerite associated to galena and pyrite (the Kabwe deposit; from *Kamona et al., 2007*). D. Association of galena, polygonal sphalerite, tennantite and pyrite (the Tsumeb, deposit; from *Hughes, 1987*).

1.2.4.3 Non-sulfide deposit (supergene)

Supergene ore is related to the direct replacement and oxidation of sulfide in contrast to hypogene ore, which does not derive directly from sulfide deposit (*Hitzman et al. 2003*). This alteration is particularly significative in Ge-rich deposits such as Tsumeb, or Kabwe and some MVT deposits in tropical zone (*Mondillo et al. 2018a)*. Important Ge contents are described in oxidation zones of Ge-deposits related to sulfides. During alteration, germanium is remobilized in oxides (hematite, brunogeierite), hydroxides (goethite, stottite), sulfates (itoite), arsenates (olivenite) and silicates (willemite) (*Melcher 2003; Mondillo et al. 2018a*). High Ge content may be found with up to 1 wt.% Ge in hematite, 0.7 wt.% Ge in goethite (the Apex mine; *Bernstein 1986*) or up to 2.0 wt.% in willemite (the Tres Maria deposit, *Saini-Eidukat et al. 2009*). In the Apex mine, oxidation of primary Ge-sulfides like renierite or germanite is inferred *(Bernstein 1986b; Bernstein and Waychunas 1987*). Supergene alteration can lead to Ge-redistribution without apparent Ge-loss, from parent sphalerite to Zn hydrosilicates and Fe hydroxides in the Bongará district (Figure 25; *Mondillo et al. 2018a)*.

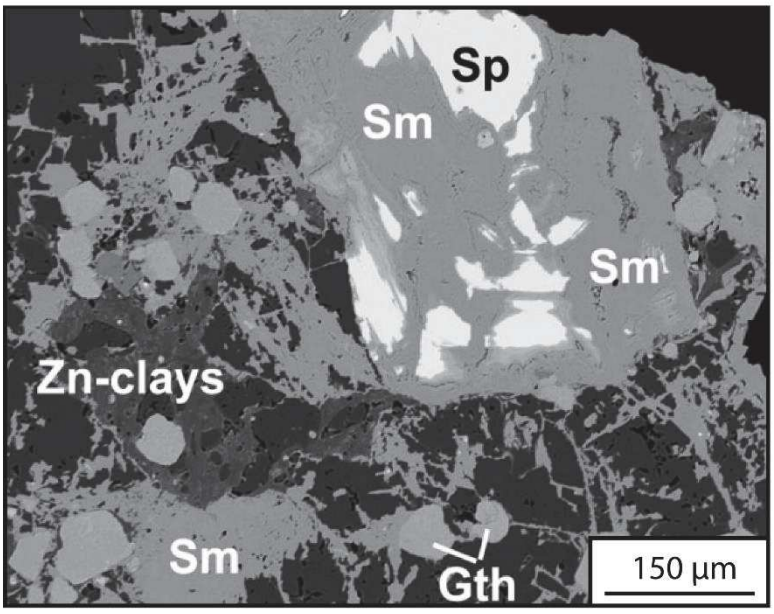

Figure 25. Smithsonite ($ZnCO_3$) replacing directly sphalerite (BSE image; from *Mondillo et al., 2018*).
Abbreviations: Sm: smithsonite; Sp: sphalerite; Gth: goethite.

1.2.4.4 Germanium-bearing coal deposits

The first discovery of Ge in coal was done by *Goldschmidt and Peters (1933*) and this enrichment is associated to its strong organic affinity (*Bernstein 1985*). In general, Ge contents in

coal are low (<1-10 ppm Ge) even if the highest Ge content reported in coal basin is 5570 ppm Ge *(Seredin and Finkelman 2008*) and may reach tens of thousands of ppm Ge in ash (*Vassilev et al. 1995b; Eskenazy 2006*). Germanium in coal is concentrated in specific macerals and organic components (*Finkelman 1983*). Recent SEM-EDS map on the Kentucky coal field shows the presence of sub-microns Ge grains in the coal matrix (Figure 26; *Hower et al. 2018*).

The origin and the spatial distribution of the Ge-enrichments are a well-debated question between Ge input from internal or external sources of the coal basin. Internal sources imply a primary Ge-enrichment in the plant material that forms the coal during burying, which is less probable due to the actual poor Ge concentrations in plants (<10 ppm; *Hu et al. 2009). S*ome authors argued for an external Ge source associated for example to the circulation of hydrothermal fluids from Ge-rich granitic rocks into faults synchronous with the coal basin development (the

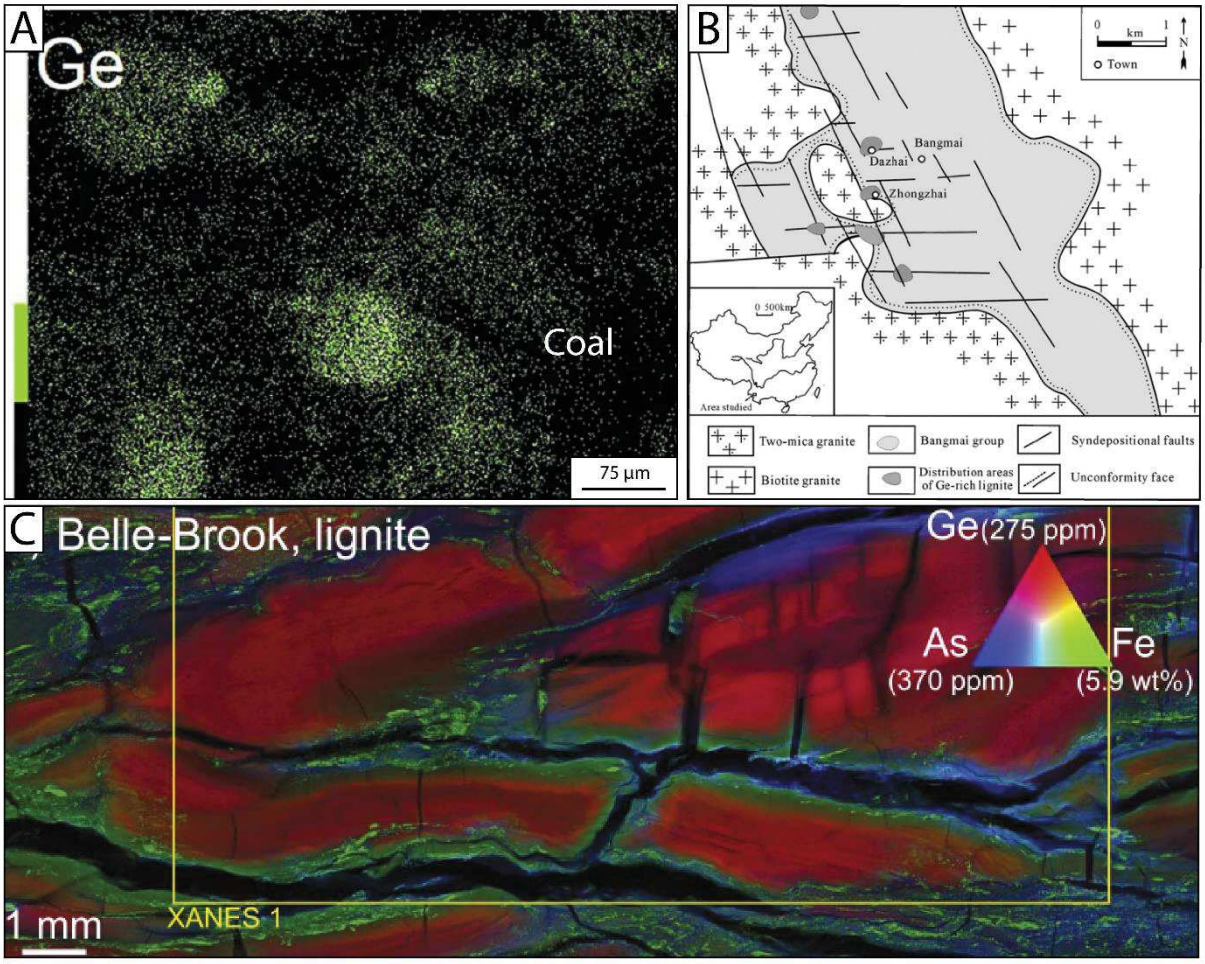

Figure 26. A. Elemental map of Ge in coal from the Blue Gem deposit-Kentucky coal field (from *Hower et al., 2018*). B. Geological map of the Lincange coal field with noted the Ge-rich lignite areas close to the faults (from *Hu et al., 2009*). C. SXRF maps of the Belle Brooke (New Zealand) coal samples (a) lignite, red = Ge, green = Fe, blue = As and (b) wood, showing the distribution of Ge (from *Etschmann et al., 2017*).

Lincang deposit; Figure 26; *Seredin and Finkelman 2008; Hu et al. 2009)*. In the Indiana coals, Ge concentrations are probably epigenetic and related to the circulation of groundwaters carrying Ge in solution (*Mastalerz and Drobniak 2012*). Hydrothermal associated to volcanic activity has probably produced extremely high Ge-enriched coals in Bulgaria *(Vassilev et al. 1995b; Eskenazy 2006*). In the Kentucky coal field, high Ge concentrations in coals are considered to be a function of seam thickness (lower Ge concentrations in thick seam) and proximity to the top and bottom margins of the coal bed (*Hower et al. 2002*). Chemical analyses in numerous coal deposits were performed by (*Etschmann et al. 2017*) which show the clear association between Ge and organic matter and the leaching of Ge close to mm fractures correlated to an enrichment of Fe and As (Figure 26C).

1.2.4.5 Germanium-minerals

Ge-minerals (>wt.% Ge) are reported in some Ge-deposits but not restricted to a deposit-type or a specific setting (**Erreur ! Source du renvoi introuvable.**). Appearance of these Ge-minerals is frequent in deformed/metamorphosed environment with relative low-grade conditions (greenschist facies). Kipushi-type are characterized by polymetallic epigenetic ore bodies, with breccia-pipe or vein-type geometries discordant in carbonate (dolomite or limestone) with irregular and elongated forms *(De Vos et al. 1974; Intiomale and Oosterbosch 1974; Lombaard et al. 1986; Hughes 1987; Deane 1995; Mckinney et al. 2006*). The typical example of this type of mineralization appears in the Zn–(Cu)–Pb–Ge Kipushi deposit which seems mainly controlled by a major sub-vertical regional fault (i.e. Kipushi fault; *Kampunzu et al. 2009; Van Wilderode et al. 2013*) but also by lithological contrasts (Figure 27A and B). The ore body is almost always parallel to this fault, which may extend on large distance and depth (up to 2000 meters for Kipushi fault) except at the contact between two different sedimentary formations where the ore mineralization becomes stratabound. The ore-forming fluids are probably genetically linked to the Late-Ordovician post-orogenic extension setting (451 Ma; Rb–Sr and Re–Os dating; *Schneider et al. 2007*).

Numerous Kipushi-type deposits show recrystallized textures (Figure 28), especially in the Kipushi, Tsumeb, Black-Angel deposits (Figure 28A-D) related to low-grade metamorphism. The Waterloo deposit in Australia hosts Ge-colusite and endured greenschist facies metamorphism (Figure 28E). The Pyrenean sphalerite, which hosts numerous Ge-minerals species, seems also metamorphosed/deformed at low-grade (Figure 28F; *Laforet et al. 1981; Johan and Oudin 1986; Oudin*

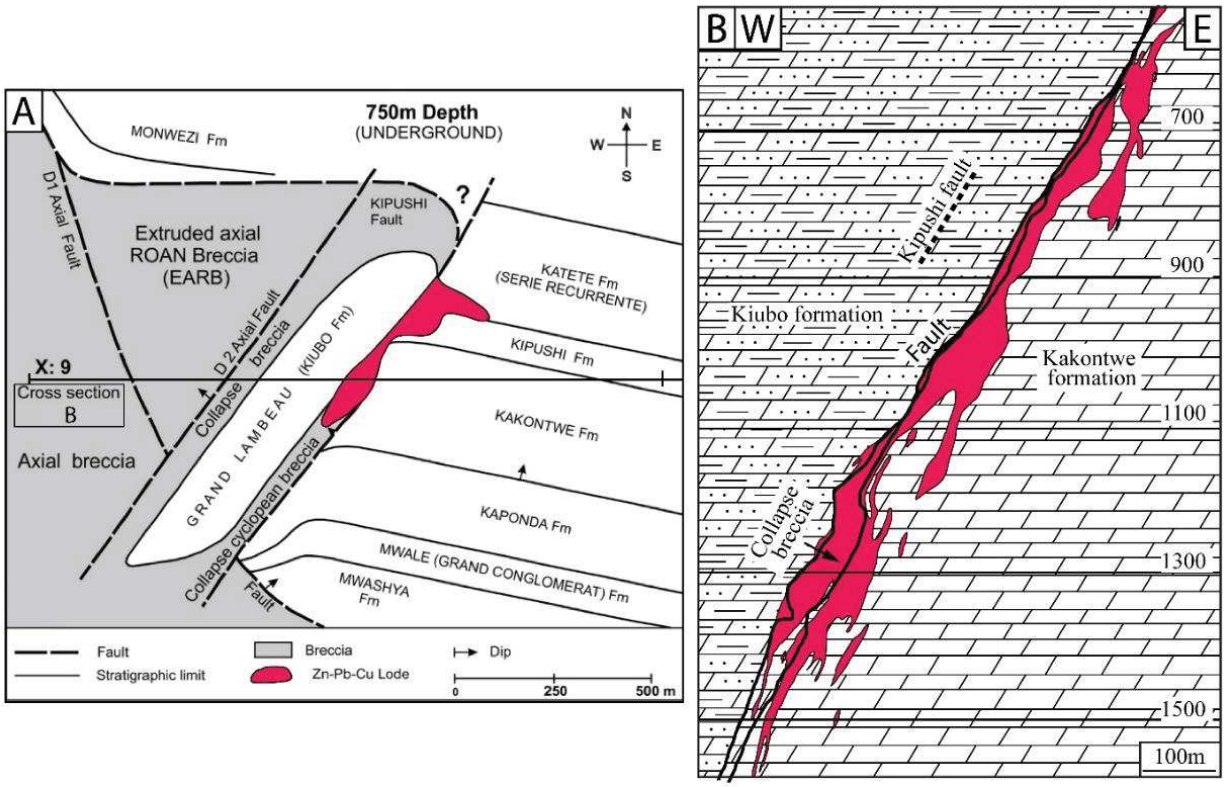

Figure 27. Geological description of the Kipsuhi-deposit. A. Schematic map view of the Kipushi deposit underground structural features at 750 m depth. B. Cross section of the Kipushi ore-body (location on A).

et al. 1988). They probably form under specific conditions, which may explain their relative scarcity in the world. Nonetheless, Ge-minerals such as renierite, argyrodite or Ge-stannoidite are also

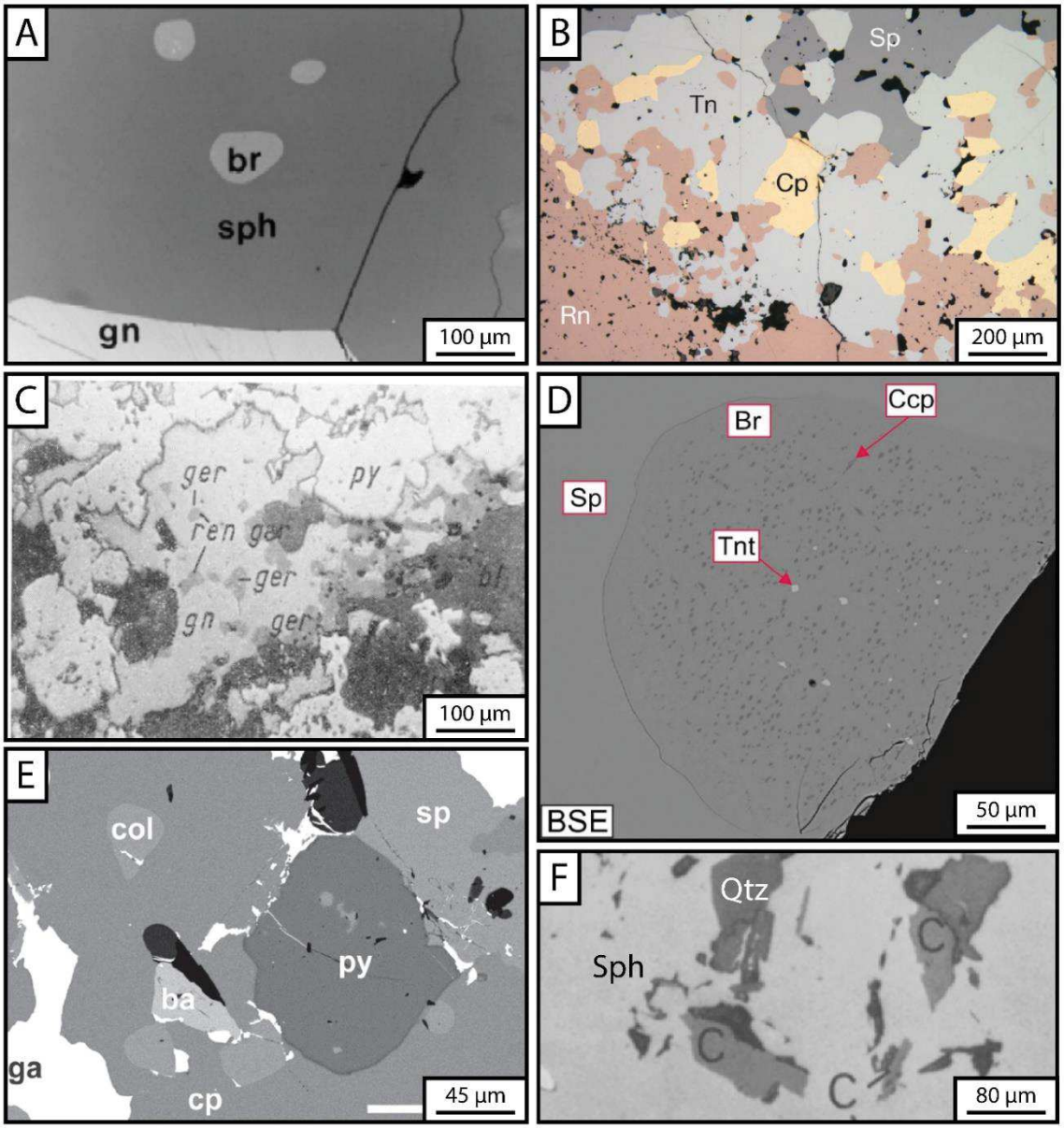

Figure 28. Microphotographs of different Ge-minerals occurrences and their relation with sulfide texture (Abbréviations: sp, sph or bl: sphalerite; gn or ga: galena; br: briartite; cp: chalcopyrite; tn or tnt: tennantite; rn: renierite; ger: germanite; py: pyrite; ba: baryte; col: Ge-colusite). A. Rounded briartite hosted in sphalerite (reflected light; from *Kamona & Friedrich, 2004*). B. Renierite associated to tennantite, chalcopyrite and sphalerite in Kipushi mine (reflected light; from *Belissont, 2016*). C. Germanite and renierite hosted in galena within Tsumeb deposit (reflected light; *Hugher et al., 1987*). D. Backscattered electron (BSE) image of a coarse rounded briartite crystal with chalcopyrite and tennantite inclusions (from *Horn et al., 2018*). E. Germano-colusite hosted in sphalerite from the Waterloo deposit (reflected light; from *Wagner & Monecke, 2005*). F. Carboirite crystals hosted in sphalerite and associated to quartz (reflectec light; from *Johan et al., 1983*).

reported in other environments such as epithermal (high-sulfidation) and porphyry systems with apparent no deformation (*Paar et al. 2004; Putz et al. 2006; Tamăş et al. 2006; Bindi et al. 2017)*.

1.2.4.6 Synthesis of the main host for Ge

Germanium may be hosted in a wide variety of minerals and environments. Ge may occur in trace content in sulfide assemblages, with a major affinity with tetrahedral sphalerite (up to few thousands of ppm Ge in carbonate-hosted deposit, *Saini-Eidukat et al. 2009*) associated to organic matter in coal seam (up to 5570 ppm Ge; *Seredin and Finkelman 2008*), reconcentrated during supergene alteration (up to 1 wt.% Ge; *Bernstein 1986b*) or even more concentrated in Ge-minerals (up to ~70 wt.% Ge; *Johan et al. 1983*). The mechanisms and processes to form these discrete Ge-minerals will be addressed in this study.

1.3 Deformation of the sphalerite and other sulfides

Sphalerite crystallography, mechanisms of sphalerite deformation and their possible impact on trace element content in sulfides are important subject to study in order to understand the probable deformation/chemical processes appearing in Pyrenean deformed sphalerite.

1.3.1 Sphalerite crystallography

Sphalerite historically known as zinc blende, is the cubic phase of ZnS (Figure 29A and B) with a 3C atomic arrangement (Figure 29B). In this combination, each sulfur atom is coordinated to four zinc atoms which usually exhibits hextetrahedral habit with development of {100} and {111} faces. Twinning is developed on {111}. A less common hexagonal form of ZnS is wurtzite (2H; Figure 29B and C; *Uenoi et al. 1996*) which seems to appear at variable fS_2 and temperature but in supersaturated solutions *(Scott and Barnes 1972; Minceva-Stefanova 1993*). Wurtzite cannot be named strictly as polymorph or polytype due to a difference of stoichiometry (slight deficiency in S) with sphalerite. Cubic sphalerite exhibits diverse textures depending on the environment of deposition such as colloform, botryoidal, schalenblende, fibrous, coarse to fine grains or massive and

commonly displays wide color variations due to its various trace element contents, from white (cleiophane) to orange or black.

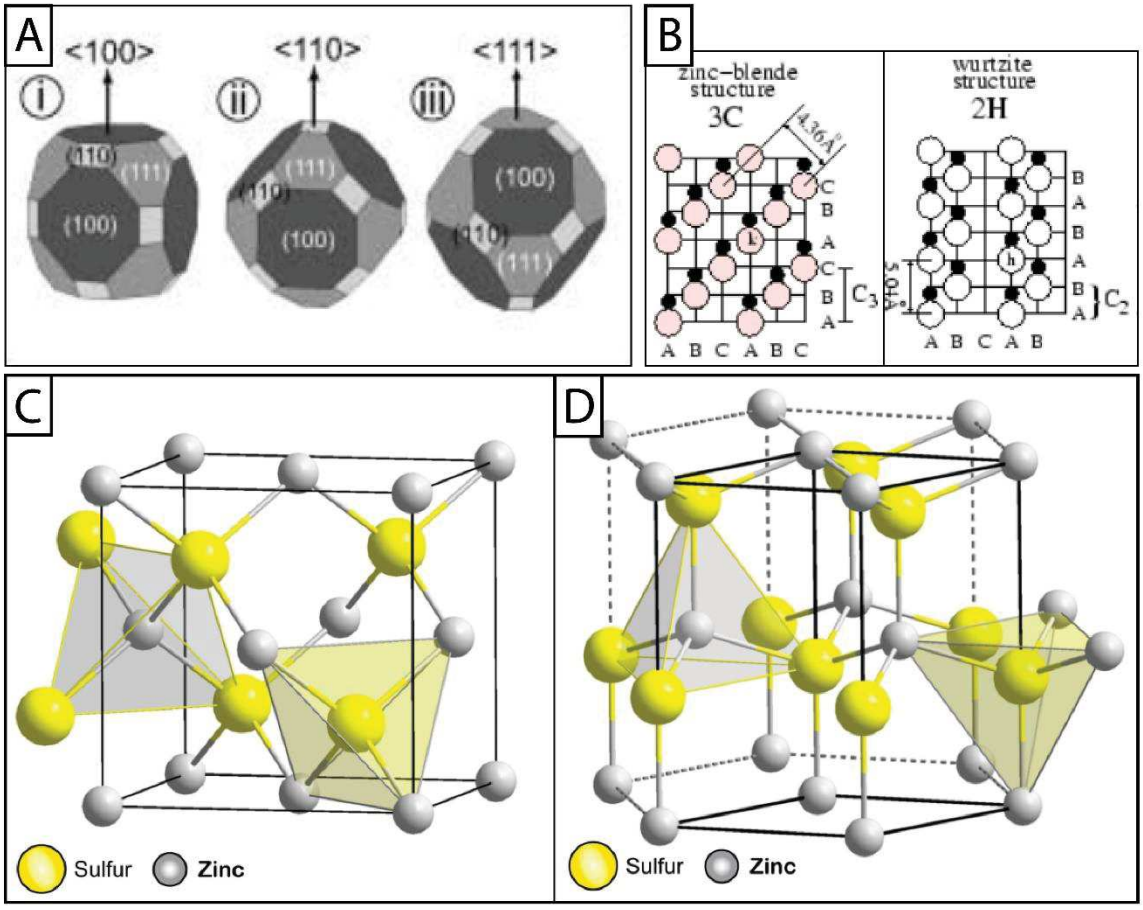

Figure 29. A. Sphalerite hextetrahedral crystals oriented with different axis (100), (110) or (111) (from *Barrie et al., 2009*). B-C. Sphalerite cubic C structures and B-D. wurtzite hexagonal H-structures (from *Boyce et al., 2015*)

1.3.2 Mechanisms of deformation

Multiple deformation mechanisms are described in this section which are related to different temperature-stress domains. At high temperature and low stress domains, diffusion creep generally appears and refers to the deformation of crystalline solids by the diffusion of vacancies (point defect or imperfection) through their crystal lattice (*Passchier and Trouw 1996)*. This mechanism results in plastic deformation rather than brittle failure of the material. There are two basic types: Coble creep and Nabarro-Herring creep. The former operates along grain boundaries, the latter by diffusion of vacancies throughout the crystal lattice *(Wheeler 1992*).

Another mechanism operating generally at higher stress domains is dislocation creep which is related to the crystal plastic deformation. Two general processes are known and are named

dislocation glide and climb. The first term refers to intra-crystalline deformation by glide of dislocations alone. The second allows dislocations to pass obstruction sites with migration of the vacancies and "climb" of the dislocation away from the obstruction (*Passchier and Trouw 1996*).

At higher stress but lower temperature domains, cataclastic flow or brittle fracturing, generally appear and may be confused with plastic deformation. A common large grain size distribution, angular crystals and polycrystalline fragments are the main distinctions.

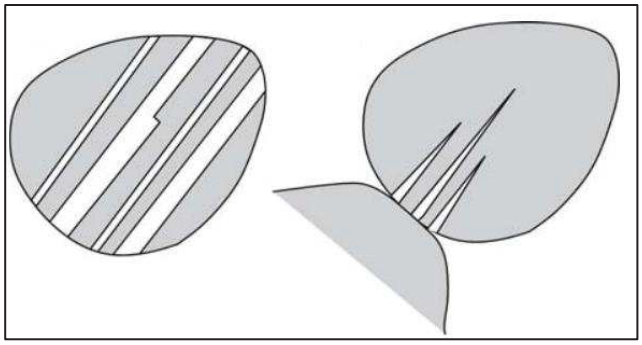

Figure 30. Two types of twins in minerals. On the left, growth twins with steps and on the right, deformation twins nucleated at the edge of the grain and less marked in the core of the crystal (from *Passchier & Trouw, 1996*).

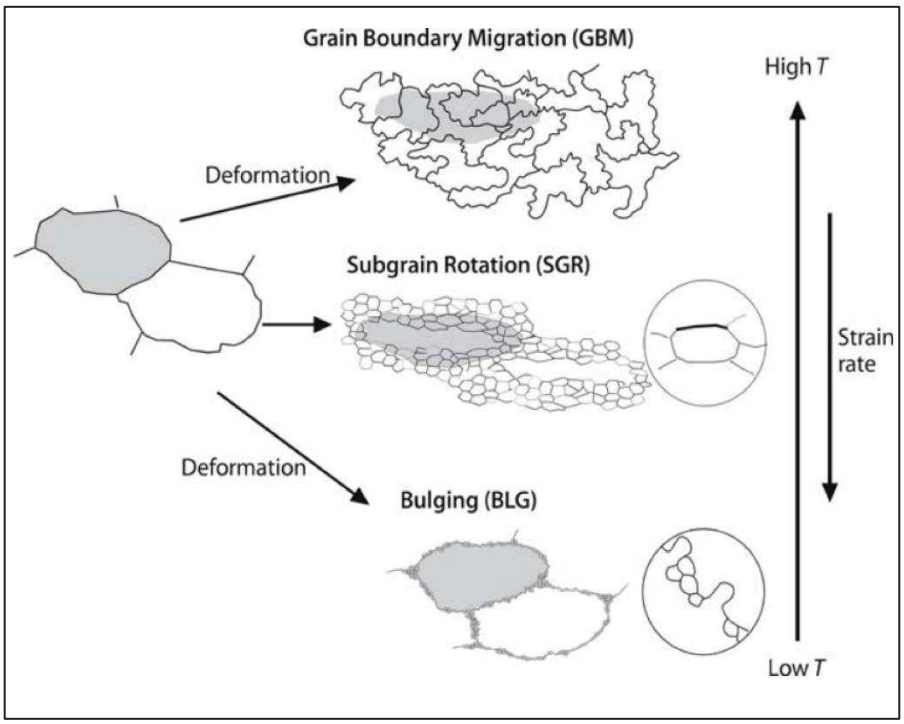

Figure 31. The three main types of recrystallization (from Passchier & Throuw and adpated from a study of *Hirth & Tullis (1992)* on quartz recrystallization.

Other structures may appear in various minerals like deformation twinning, which are commonly tapered, while growth twins are commonly straight and stepped (Figure 30; *Burkhard 1993*).

While dislocations are formed in the mineral, other processes tend to reduce and rearrange the dislocations or moving grain boundaries and are named recovery and grain boundary mobility or recrystallization. Recovery processes will reduce dislocation density and regroup these dislocations in deformation bands or at an advanced stage, in sub-grain boundaries.

Grain boundary mobility is another process which reduces dislocation density and will reorganize grain boundaries in order to improve and newly adapt grain size, shape and orientation to the new conditions of stress and temperature (*Guillope and Poirier 1979; Hirth and Tullis 1992; Passchier and Trouw 1996)*. This process is also named dynamic recrystallization and is composed of three general mechanisms (Figure 31): i) bulging recrystallization (low-temperature domains) is characterized by the grain boundary bulge into a crystal and the formation of newly small grain (pluri-μm); ii) sub-grain rotation recrystallization is the progressive increase of the misorientation compared to the parent grain until the sub-grain is too misoriented and no longer a part of the original grain. Occurrence of coarse parent grains mantled by fine recrystallized grains is a typical recognition criterion; iii) grain boundary migration recrystallization is active generally at high temperature and allow to remove dislocations with the mobility of the grain boundary. It will form lobate boundaries with no real distinction between new and old grains.

If recovery and dynamic recrystallization were produced at high temperature, additional grain boundary area reduction (GBAR) and static recrystallization will appear after deformation ceased. The first mechanism will try to reduce and modify the form of grain boundary to a more stable form, which constitute for example polygonal shape grains (*foam* texture). Static recrystallization appears when temperature is still relatively high and is related to the persistence of previous recovery, dynamic recrystallization and GBAR (*Passchier and Trouw 1996*). This mechanism may modify and destroy previous key recognizable textures. Annealing is a term used for passive heating of a previously deformed material and is referenced to a combination of recovery and static mechanism.

1.3.3 Deformation of sphalerite and related sulfides

Sulfide minerals and especially sphalerite often occur in deformed/metamorphosed terranes with numerous famous giant deposits such as the Broken-Hill, Mt-Isa, Red Dog or

Rampura deposits and question of their timing of genesis is often difficult to decipher, between a syngenetic-diagenetic model of deposition (SEDEX, review in *Wilkinson 2013*) or an epigenetic model related to the inversion periods (*Gibson and Nutman 2004; Hazarika et al. 2013; Gibson et al. 2017*).

One of the first authors to detect metamorphosed textures in sulfide like galena or sphalerite was *Stanton (1964)*. Sphalerite is commonly associated to a class of ductile sulfide minerals such as galena, chalcopyrite or pyrrhotite due to their ability to deform at low P-T *(Gill 1969; Clark*

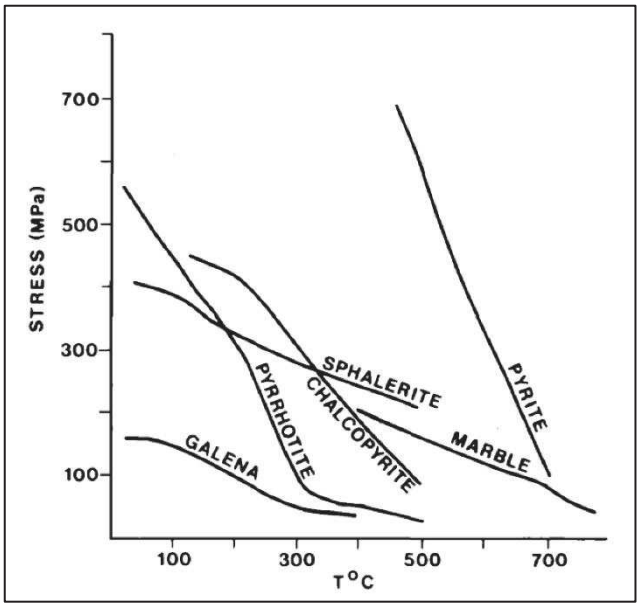

Figure 32. Comparison of the strenghts of five sulfide minerals and marble (from *Cox, 1981* and references herein). Nonetheless, these data, are inconsistent with recent works on pyrite that described plastic deformation down to ~ 250° C or lower (*Barrie et al., 2011*).

and Kelly 1973; Kelly and Clark 1975; Cox et al. 1981; Cox 1987; Siemes et al. 1991) comparatively to more "solid" minerals such as quartz, olivine or pyrite, even if recent data (*Barrie et al., 2011*) evidences plastic deformation at temperature as low as ~ 250° C. Melting point of sphalerite highly depends of its trace element content (*Hofmann 1994; Mavrogenes et al. 2001)* and may occur in temperature as low as 500 °C..

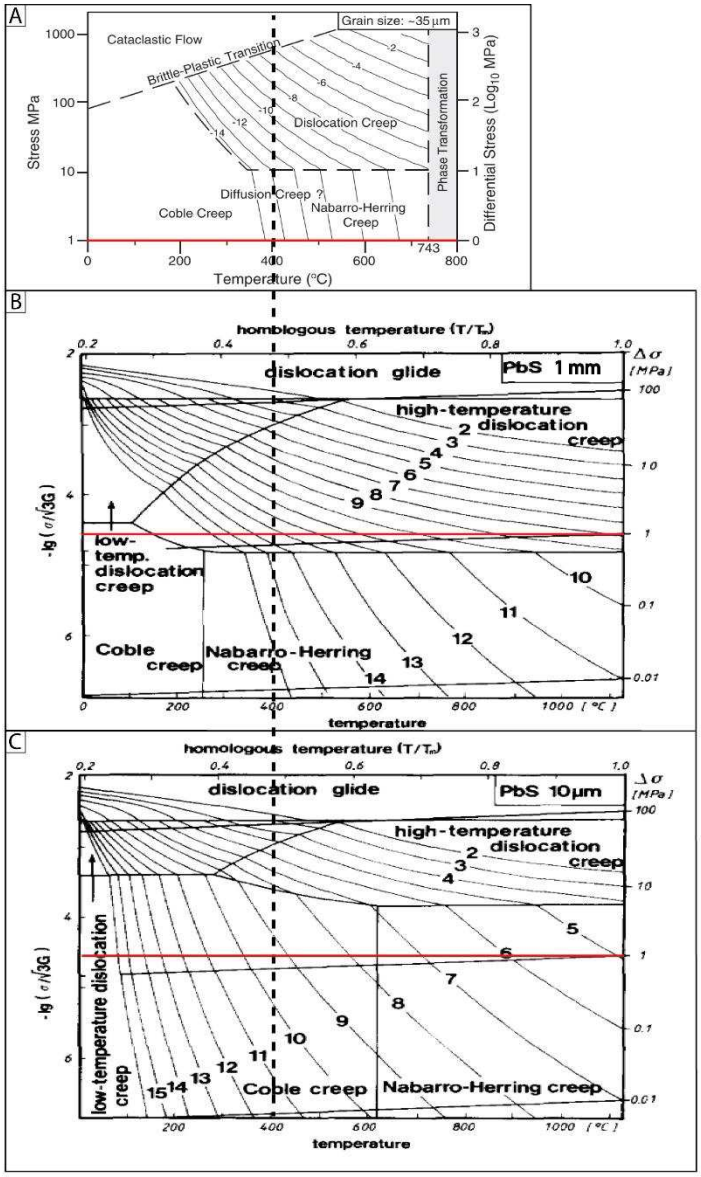

Figure 33. Deformation mechanism maps comparision between pyrite and galena. The deformation maps are normalized at the same temperature. Red line indicates the same stress value. A. Deformation map of pyrite (from *Barrie et al., 2011*). B-C. Deformation map of galena (from *Atkinson, 1976*).

Some experimental studies of deformation in the sphalerite and globally in ductile sulfide minerals was performed in the 1970's-80's essentially (*Clark and Kelly 1973; Siemes et al. 1973; Kelly and Clark 1975; Atkinson 1976; Siemes 1976; McClay and Atkinson 1977; Siemes and Borges 1979; Cox et al. 1981; Couderc et al. 1985; Cox 1987*). These experiments are key analyses to understand natural deformation and conditions in sulfides. More recent studies related to experimental and natural deformation analyses with EBSD or TEM, appear for pyrite (*Atkinson 1975; McClay and Atkinson 1977; Cox et al. 1981; Graf et al. 1981; McClay and Ellis 1984, 1983, Barrie et al. 2007, 2008, 2009, 2011; Dubosq et al. 2018*). Deformation mechanism map which report the various deformation mechanism related to strain and temperature, was initially produced by *McClay and Ellis (1983*) and

modified by *Barrie et al. (2011*) with a larger plastic deformation domain (Figure 33A). Deformation map of galena were acquired by (*Atkinson 1976)* and a comparison with pyrite respectively according temperature and stress is shown in the Figure 33. A much larger dislocation creep field for galena appears at lower temperature and stress. Unfortunately, no deformation map is yet produced for sphalerite.

The mechanisms of deformation in sphalerite are poorly known. *Clark and Kelly (1973)* describe the experimental sphalerite deformation which shows static recovery and recrystallization at 500-600 °C and may be active well-below, with occurrence of new grains containing numerous growth twins. Sphalerite slips most easily on {111} planes with a (110) directions *(Siemes et al. 1973; Siemes and Borges 1979; Couderc et al. 1983, 1985*) and twins boundaries are developed on {111}$(11\bar{2})$ (*Clark and Kelly 1973; Siemes and Borges 1979)*.

1.3.4 Impact of recrystallization on the trace element contents in sulfides.

In sulfide minerals and more specifically in pyrite or arsenopyrite minerals, mobility of trace element is well-studied associated to deformation/metamorphism, especially due to its economic interest and the remobilization-redistribution processes of elements such as gold within or out with the sulfide crystal lattice. (*Larocque et al. 1993; Marshall et al. 1998; Tomkins and Mavrogenes 2001; Wagner et al. 2007; Cook et al. 2009a; Reddy and Hough 2013; Velásquez et al. 2014; Fougerouse et al. 2016a, b, 2019; Dubosq et al. 2018; Kampmann et al. 2018*). It is commonly accepted that plastic or brittle deformation may rearrange gold or associated elements (As, Ni, Bi, Pb) concentrations located in the sulfide lattice and may for some cases redistribute these trace contents in discrete phases such as native gold or sulphosalts, with or without external element input.

In sphalerite, some studies describe its trace element content associated to later hydrothermal or deformation/metamorphism events. In W*agner and Cook (1998*), sphalerite from the Rheinisches Schiefergebirge veins endured a late hydrothermal Sb-rich event which produced sphalerite corrosion and recrystallization. Recrystallized sphalerite and corroded area are Fe-poor and Cd-rich comparatively to the primary sphalerite probably related to diffusion processes. Comparative analyses between nineteen metamorphosed sphalerites in *Lockington et al. (2014)* describes the diminution of micro-nanoscale inclusions (Pb, Bi, Cu, Ag) trapped in sphalerite with increasing metamorphic grade, due to the probable releasing of these elements during sphalerite recrystallization. Another observation is the more homogeneously distribution and lower content of Cu in the recrystallized sphalerite lattice. Lower Pb, Bi, Ag, Sn, Sb contents and higher Fe, Cd, Mn, In concentrations occur in the sphalerite with increasing metamorphic grade, even if these

absolute contents are strongly influenced by their primary concentrations in the zinc sulfide. With statistical analysis on a large trace element dataset to calculate sphalerite geothermometer, *Frenzel et al. (2016)* show that the most important effect of metamorphism will be a decrease in the value of Ga and Ge concentrations relative to the concentrations of Fe, Mn and, to a lesser degree, In. An increasing of the Ge and Ga mobilities may occur in this case.

Migration of elements may be explained by three general chemical mechanisms in the mineral lattice: i) fluid-mediated replacement occurs when elements introduced by a fluid cause a mineral phase to be replaced either by a new composition of the same phase or by an entirely new phase (*Harlov et al. 2011; Fougerouse et al. 2016b)*; ii) intra-granular diffusion is composed of different mechanisms such as volume, high diffusivity pathway (pipe diffusion) or dislocation–impurity pair (DIP) diffusion (*Klinger and Rabkin 1999; Reddy et al. 2007; Plümper et al. 2012; Vukmanovic et al. 2014)*. Volume diffusion is a mechanism that allows displace most of atoms within the crystal lattice following a chemical potential gradient at high temperatures *(Vukmanovic et al. 2014*). High diffusivity pathway (pipe diffusion) is related to dislocation walls in the plastically deformed mineral lattice which represents preferential pathways for ions migration. Occurrence of intra-granular stripe-like zonations (Figure 34A and B) may attest for substantial diffusion mechanisms (*Plümper et al. 2012*). Dislocation–impurity pair (DIP) diffusion model corresponds to the migration of large elements simultaneously with dislocations during the recovery process, resulting in increased concentration of these impurities (e.g. Pb, Bi and Ag) along the newly formed dislocation arrays (Figure 34C). Twin boundaries often contain a large amount of dislocations (*Vukmanovic et al. 2014; Piazolo et al. 2016; Dubosq et al. 2018*). iii) partial melting of the sulphide ore occurs generally in low to high grade metamorphic conditions. Occurrence of melting at low temperature is due to the low melting point for sulfide minerals, which seem dependent of their trace content *(Mavrogenes et al. 2001; Ciobanu et al. 2006*).

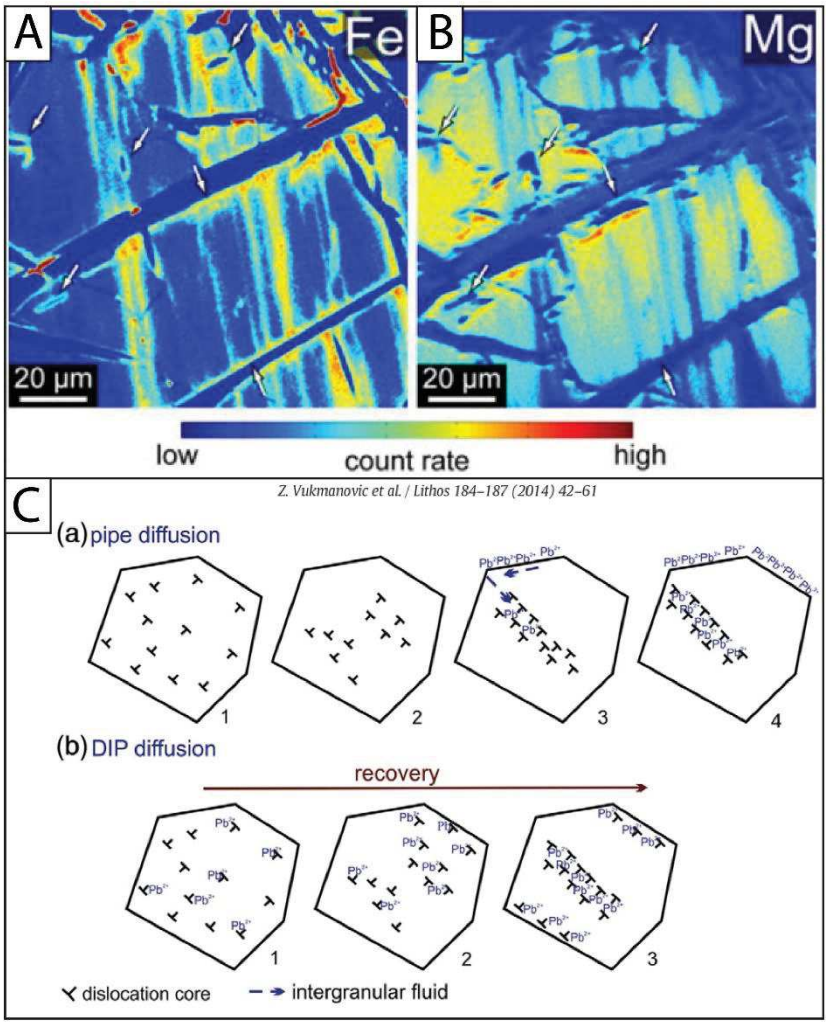

Figure 34. Intra-granular diffusion mechanisms and related high diffusivity pathway (pipe diffusion) or dislocation–impurity pair (DIP). A-B. Stripped like zonation in olivine typical of high diffusivity pathway (pipe diffusion; from *Plümper et al., 2012*). C. Difference between high diffusivity pathway (pipe diffusion) and DIP dffusion (from *Vukmanovic et al., 2014*).

2 Analytical methods

2.1 Analytical approach

The analytical method is shown in the Figure 35 and is detailed in the several sections below.

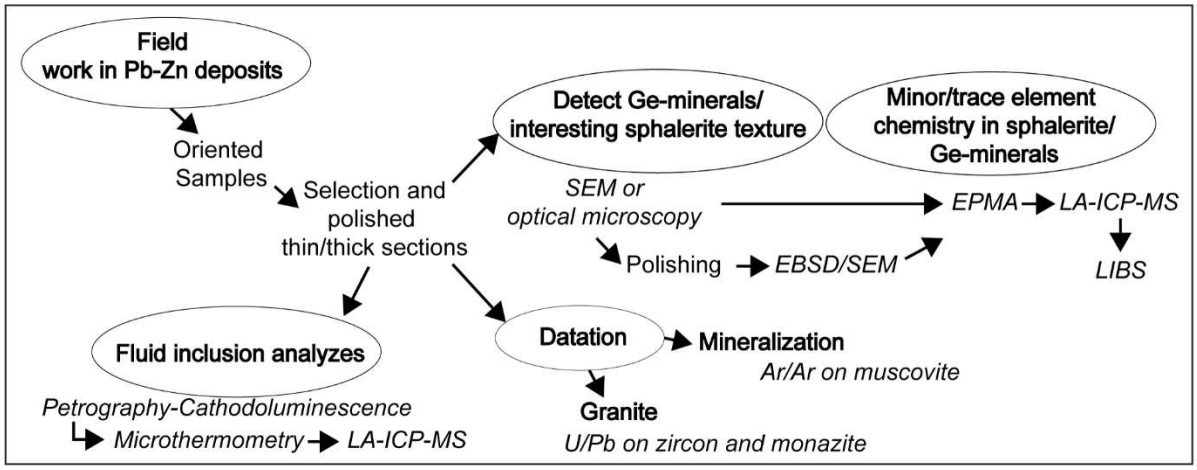

Figure 35. Flowchart describing the analytical procedure used in this study.

2.2 Field work and sampling

Numerous studies on the structural description of Pyrenean Pb-Zn deposits exist in the literature but no study presents a general structural model for these mineralizations. Field work was performed in a large number of deposits (up to twenty) related to different structural units in order to decipher and understand the genesis of these Pb-Zn(-Ge) ores. Sphalerite sampling was performed to texturally and chemically study this material, and especially their Ge content. During about 2 months of cumulative field work, three hundred and thirty rock samples were collected and studied and one hundred and sixty-five thin sections were made.

2.3 Mineralogical and textural investigations

2.3.1 Microscopic observations

Textural observation is essential to understand the ore genesis and to perform chemical or mineralogical analyzes especially in sulfides. Textural observation of minerals like sphalerite is often difficult due to the poor visualization of the grain boundaries, even at reflected or transmitted plane polarized light on microscope. Nonetheless, a better visualization of the chemical and textural contrast in sphalerite appear with thicker thin section (150μm; Figure 36). But a need to etch sphalerite with hypochlorous acid HClO (Figure 36; *Ramdohr 1969*) or to employ non-conventional techniques like eletron back-scattered diffraction (EBSD) is essential to view the grain boundaries and the textural pattern of the sphalerite.

2.3.2 Quantitative Evaluation of Minerals by Scanning Electron Microscopy (QEMSCAN) analyses

Automated mineral analysis and textural imaging of the studied samples (rock thin sections) were performed using an FEI QEMSCAN® Quanta 650F facility at the Department of Earth Sciences, University of Geneva, Switzerland. The system is equipped with two Bruker QUANTAX light-element energy dispersive X-ray spectrometer (EDS) detectors. Analyses were conducted at high vacuum, accelerating voltage of 25 kV, and a beam current of 10 nA on carbon-coated polished thin sections. FieldImage operating mode (*Pirrie et al. 2004*) was used for analyses. In total 221 individual fields were measured per sample, with 1500 μm per field, and point spacing of 5 μm. The standard 1000 counts per point were acquired, yielding a limit of detection of approximately 2wt% per element for mineral classifications. Measurements were performed using iMeasure v5.3.2 software and data processing using iDiscover® v5.3.2 software package. Final results consist of: i) high-quality spatially resolved and fully quantified mineralogical maps; ii) BSE images with identical resolution as the mineralogical maps; iii) X-ray element distribution maps.

Thirteen maps were acquired in twelve deposits in order to evaluate the presence of Ge-minerals, potential zonations (Fe, Cd, Zn) in the sphalerite or better identify the relations between the different mineralization types and the host-rock.

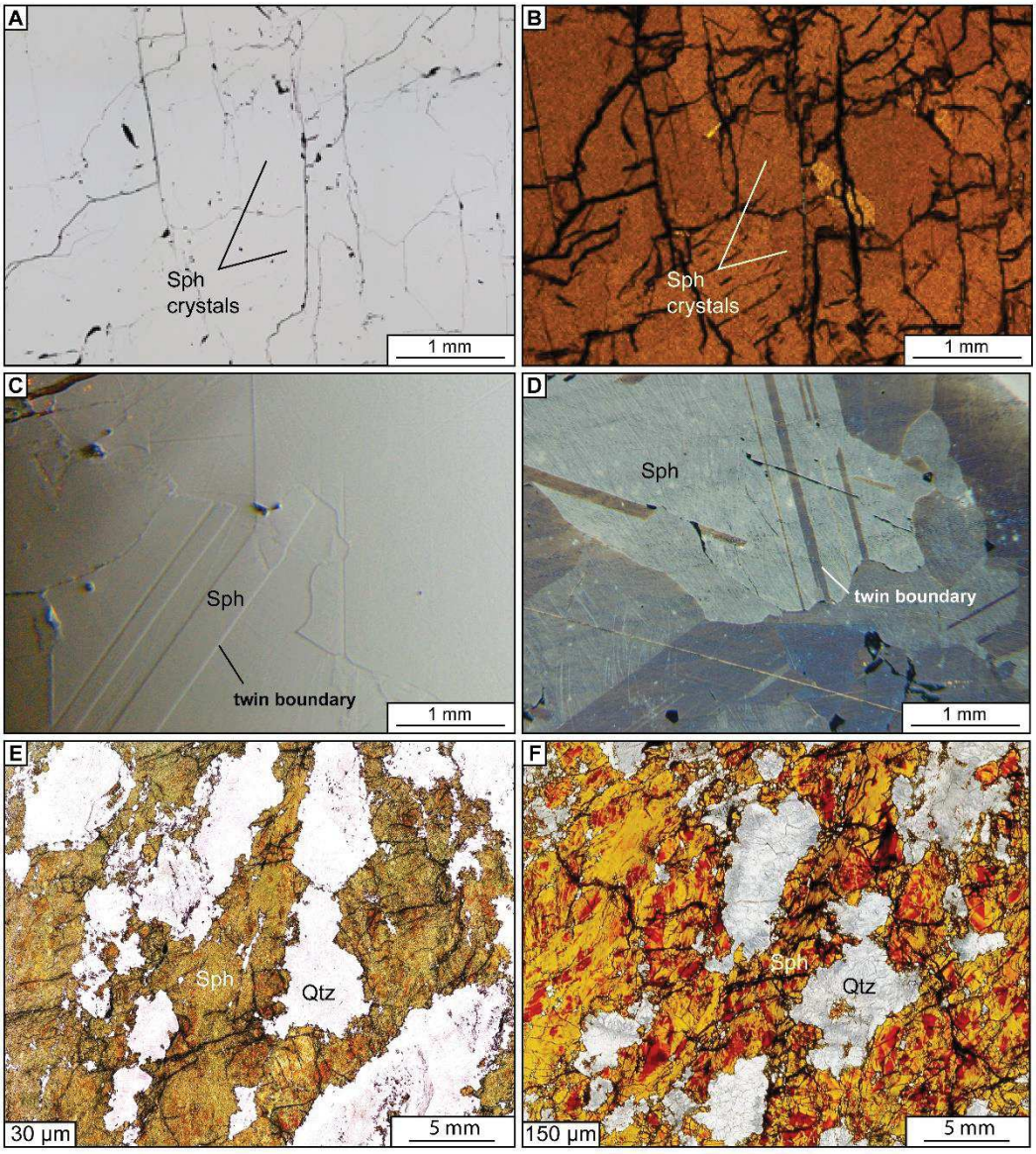

Figure 36. From A to D: Sphalerite observed in different condtions under microscope with the same zoom and in the same sample (Bentaillou, BEN12). From E to F: Arre sphalerite (ARR03) in transmitted plane polarized light. A. Sphalerite observed in plane-polarized reflected light (3-4 hours of polish). B. Same sphalerite area observed in plane-polarized transmitted light (3-4 hours of polish). C. Other sphalerite area with apparition of twins under reflected microscopy (after 15 hours of polish). D. Sphalerite grain boundary in part observable after HClO etching (~2 min). E. Arre sphalerite observed in transmitted light with a 30 µm thin section (ARR03). F. Same Arre sphalerite sample observed in transmitted plane polarized light but on a 150 µm thick section. Chemical zonations are well-visible but grain boundaries are still difficult to discern.

2.3.3 Electron BackScattered Diffraction (EBSD) mapping

Sample preparation for EBSD analysis requires an accurate polishing so that sphalerite structure can be efficiently indexed. To remove surface defects, thin section polishing was first performed with diamond polisher at four different granulometric steps (6, 3, 1 and 0.25 µm). A last step of polishing was performed using a vibrant polisher with 150 grams of pressure on a polyurethane layer with colloidal silica. During this process, cleaning with frozen colloidal silica was necessary to avoid scratches on sphalerite. Time for efficiently polishing this material can reach 28 hours for one thin section depending on the sample.

Electron back-scattered diffraction (EBSD) measures the crystallographic orientation of a well-polished surface. An electronic beam, inclined at 70° which is the best compromise between electron diffraction pattern intensity and surface roughness, hit the surface of the sample. On a crystal plane, one backscattered electron forms two lines or Kikuchi bands maps on an EBSD detector (Figure 37). All these bands constitute a diffraction diagram and after internal computation with mineral indexation (Miller index), crystallographic orientation of the analyzed area is acquired.

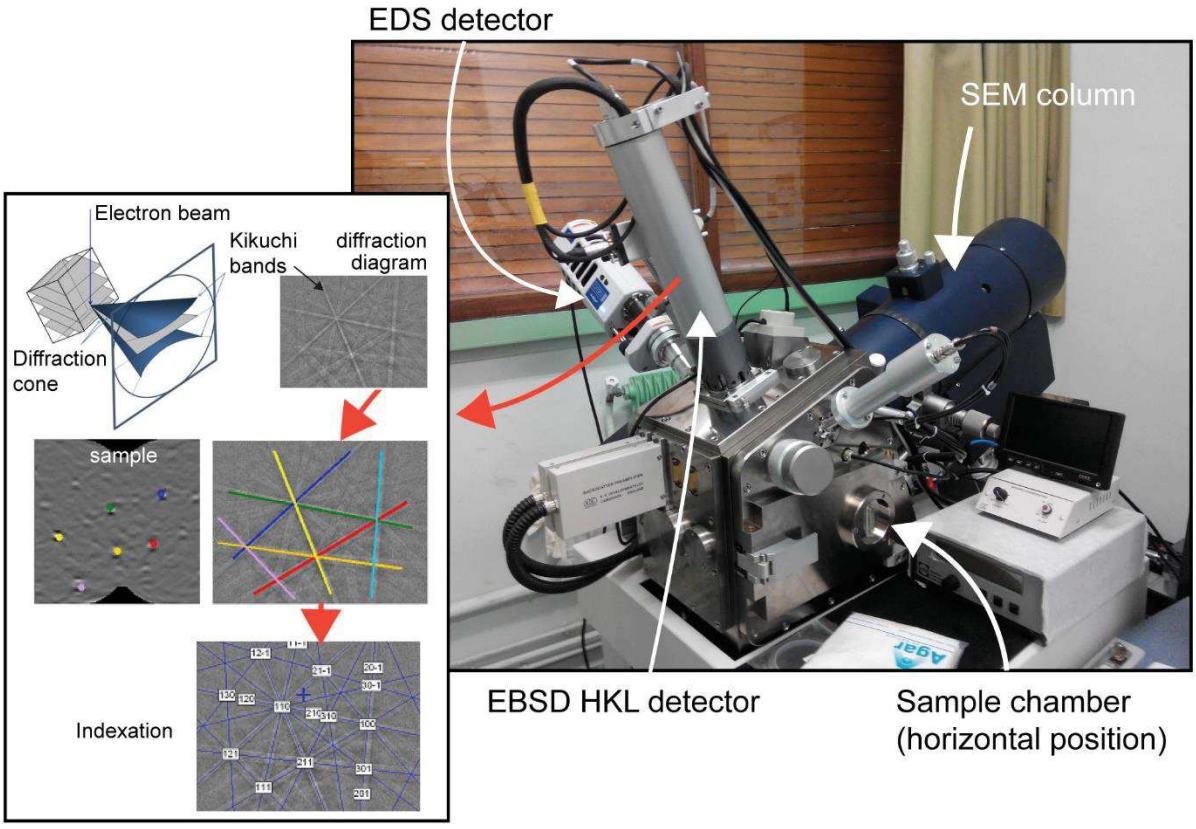

Figure 37. Camscan Crystal Probe X500FE SEM-EBSD at Géosciences Montpellier. Small insets briefly explain EBSD acquisition.

EBSD analyses were performed with a Camscan Crystal Probe X500FE SEM-EBSD at Geosciences Montpellier (CNRS-University of Montpellier, France). The specific feature of this instrument is a horizontal stage with an inclined column optimized for EBSD (Figure 37). Samples were positioned horizontally and at the standard 70° angle to the EBSD detector. Operating conditions were 20 kV and 5 nA, with a working distance of 25 mm under 2 Pa low vacuum. Element distribution maps were simultaneously acquired by measuring X-ray fluorescence with an EDS (Energy Dispersive Spectrometer) detector. Oxford Instruments softwares AZtec and Channel 5 were used to generate maps from the EDS (chemical maps) and EBSD (structural maps) detection systems.

Twenty-five maps were acquired on the sphalerite from the Pyrenean Pb-Zn deposits and one from Saint-Salvy deposit (Montagne Noire). The step size for 2D imaging was systematically below 10 μm, reaching for one map 0.5 μm (Figure 38).

Deposit	Map	Step size (μm)	Lenght (mm)	Width (mm)
Pale Bidau	BO9-1	1.5	2.33	0.99
	BO9-2	4	6.13	2.82
	BO9-3	3	3.04	2.48
	BO9-4	2.7	4.83	2.99
Saint Salvy	MO4	5.7	5.86	7.3
Arre	ARR03-site laser	2.5	3.1	5.31
	ARR03DP-1	5	5.5	6.72
	ARR03DP-2	5	7.31	5.37
	ARR03DP-3	0.5	0.63	0.82
Arre	ARR03-1	4	4.56	3.06
	ARR03-2	5	6.36	2.34
	ARR03-3	5	2.74	2.31
Bentaillou	BEN12	5.7	5.71	6.62
	BEN07	4	2.8	5.72
	BEN07	8	3.05	10.23
	BEN07	4	2.5	2.63
Victoria	VIC12	4	2.71	2.01
	VIC12	10	3.88	2.46
Liat	LIA14	6	2.96	4.76
	LIA19	3.5	5.72	2.04
Argut-dessus	BO24	1	2.12	0.9
	BO24	1	2.23	1.03
Anglas	ANG12	4	6.44	8.25
	ANG13	3	4.23	3.2
Margalida	MARG06	5	10.9	4.47
Cierco	CIE04	4	2.63	3.82

Figure 38. Details of the EBSD analyses of this study

2.3.4 Chemical investigations (EPMA-LA-ICPMS-LIBS mapping)

2.3.4.1 Electron microprobe analyzer (EPMA)

Electron probe microanalyzer (EPMA) was employed to quantify major and minor elements in sphalerite and brunogeierite ($GeFe_2O_4$). Microanalysis was carried out using a FEI Quanta FEG 100 Scanning electron microscope (SEM) and a Cameca SX100 electron microprobe analyzer (EMPA) at the Service inter-regional Microsonde-Sud, Montpellier. Major, minor and trace elements were measured with a beam current of 100nA and accelerating voltage of 20 kV. 14 elements were analyzed: standards, spectral lines, and spectrometers were as follows: Zn (Zn, Lα, TAP); S (FeS2,Kα, PET); Fe (Fe2O3,Kα, LLif); Cd(CdS, Lα, LPET); Ge (Ge, Kα, LLif); Sb (GaSb, Lα, LPET); Cu (CuS, Kα, LLif); Ga (GaSb, Kα, LLif); Ag (Ag, Lα, LPET); Mn (Mn, Kα, LPET); Sn (Sn, Lα, PET); Pb (Pb, Mα, PET); As (GaAs, Lα, TAP); Si (CaSiO3,Kα, TAP). Peak count times ranged from 30 to 240 s (240 s for Ge, Table 1). Germanium is analyzed on 2 LLif monochromators. The limit of detection for Ge, calculated by internal Cameca procedures, is reduced to 84 ppm. Gallium, As, Ag, Pb, Sn, Sb, and Mn were below detection limit and are not reported in the data tables (Table 1).

EPMA analytical conditions							
Spectrometers	Elements / Lines	Position	Reference material	Beam current (nA)	Acceleration voltage (kV)	Counting time (ms)	Mean limit of detection (LOD, ppm)
Sp4	S Ka	4 PET	FeS2	10	20	30	415
Sp1	Zn La	1 TAP	Zn	10	20	30	1151
Sp3	Fe Ka	3 LLIF	Fe2O3	100	20	30	168
Sp3	Cu Ka	3 LLIF	Cu2O3	100	20	60	123
Sp3	Ge Ka	3 LLIF	Ge	100	20	240	85
Sp2	Cd La	2 LPET	CdS	100	20	60	300
Sp2	Sb La	2 LPET	GaSb	100	20	30	165
Sp1	Si Ka	1 TAP	Wollastonite	100	20	180	30

Table 1. Analytical conditions for each element analyzed with EMPA (electron microprobe analyzer)

Two separated EPMA sessions were performed during the PhD thesis. The first allow us to analyze sphalerite (ZnS) and brunogeierite ($GeFe_2O_4$) with forty-four and twenty-eight analyzes respectively from Pale Bidau, Argut-dessus or Pale de Rase deposits. Some EPMA maps were acquired around brunogeierite to study potential concentration gradient which are not present. One hundred and two sphalerite analyses from Pale Bidau, Arre and Anglas deposits were performed on the second session (see section 11.5 for the *in-situ* analysis).

2.3.4.2 Laser-Ablation Inductively Coupled Plasma Mass Spectrometry (LA-ICPMS) in-situ analyses on solid materials

Laser ablation inductively coupled plasma mass spectrometry (LA-ICPMS) was used to determine minor and trace element concentrations in sphalerite or in brunogeierite ($GeFe_2O_4$). Analyses were carried out using an Excimer CompEx 102 coupled to a ThermoFinnigan Element XR at the OSU-OREME AETE platform (University of Montpellier, France). Laser ablation was performed using a constant 5 Hz pulse rate at 140 mJ. Each analysis comprises 180 s of background measurement and 60 s of sample ablation (signal measurement), followed by a 60 s retention time to ensure a proper cell washout. Data were processed using the Glitter 4.0 software package (*Van Achterbergh et al. 2001)*. The following isotopes were measured: ^{29}Si, ^{34}S, ^{55}Mn, ^{57}Fe, ^{59}Co, ^{61}Ni, ^{63}Cu, ^{64}Zn, ^{69}Ga, ^{74}Ge, ^{75}As, ^{77}Se, ^{95}Mo, ^{105}Pd, ^{107}Ag, ^{111}Cd, ^{115}In, ^{118}Sn, ^{121}Sb, and ^{208}Pb. MASS-1 reference was used as an external standard with a corrected 57 $\pm$ 1.75 ppm value for Ge (Dr. Stephen Wilson, personal communication). NIST SRM 610 (*Pearce et al. 1997*) was used as secondary external standard to identify possible instrumental drift. Zn or Fe concentrations was used as internal calibration in sphalerite and brunogeierite respectively. Concentrations for Ni, As, Mo, Se, Pd and Si were below detection limits in all measurements.

Two separated LA-ICPMS sessions were acquired during the PhD thesis. Twenty-nine analyses were performed on sphalerite from Pale Bidau, Argut-dessus and Pale de Rase deposits and three brunogeierite from Pale Bidau. One hundred and forty-five measurements were acquired during the second session on sphalerite from diverse mineralization types and deposits.

2.3.4.3 Laser Induced Breakdown Spectroscopy (LIBS) mapping

Laser-Induced Breakdown Spectroscopy (LIBS)-based imaging was used to image the distribution of Ge. LIBS is an all-optical analytical technique (Figure 39A), allowing the mapping of metallic elements in various type of solid matrices at a micrometric spatial resolution and with a sensitivity at the ppm level *(Sancey et al. 2014; Cáceres et al. 2017; Fabre et al. 2018*). During the analysis, the sample surface is scanned, through single laser pulses, in a pixel-by-pixel manner to induce the breakdown and sparks of the material. The light radiation emitted by the plasma is then collected by an optical system and analyzed using a spectrometer. Among other elemental imaging approaches, LIBS offers several advantages such as table-top instrumentation, ease of used, speed of operation, and detection of light elements (*Busser et al. 2018; Jolivet et al. 2019*). The sample was analyzed using Nd:YAG laser with a pulse energy of about 600 μJ operating at 100 Hz, and a lateral

resolution (i.e. distance between two consecutive laser shots) of 13 µm. The image shown in the following covers a surface of about 6 cm² (3.6 megapixels) and has been obtained in 6 hours. The spectrometer was configured in the spectral range from 250 nm to 330 nm in order to detect intense lines of Ge (265.1 nm), Cu (324.7 nm) and Ga (294.4 nm), among others. Due to an interference with an Al line, the Ge line at 269.1 nm was used in the aluminosilicate phases.

Two maps were acquired on a sphalerite sample from Pale Bidau deposit (BO9) and two other maps on an ore sample from Arre deposit (ARR03).

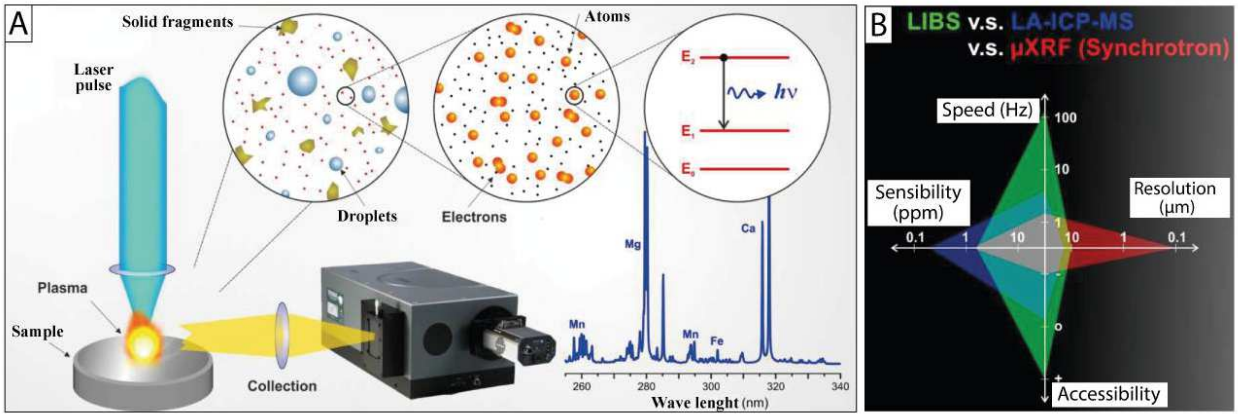

Figure 39: A: Schematic representation of the LIBS technique. B: Schematic comparaison of LIBS with other traditionnal trace element analyzer such as LA-ICP-MS or µ-XRF (synchrotron)

2.3.5 Fluid Inclusion analyses

2.3.5.1 Petrography and cathodoluminescence

Detailed petrographic studies were carried out to identify fluid inclusion assemblages (FIAs). Primary and secondary fluid inclusions were identified in doubly polished slices of 150 µm thickness using the criteria of *Roedder (1984)* and *Goldstein and Reynolds (1994)*.

Cathodoluminescence images were obtained using a HC6-LM hot cathode system by Lumic Special Microscopes, Germany, at Geosciences Environment Toulouse (GET). It was operated with a voltage of 14 kV and a current density of ca. 10 µA mm² (Neuser 1995). CL images were captured with a very-high sensitivity Olympus XC10 camera.

2.3.5.2 Microthermometry

Microthermometric measurements were performed at the University of Toulouse, following the procedures outlined by *Roedder (1984)* using a Linkam THMGS 600 heating–freezing stage mounted on a BX-51 Olympus microscope. The stage was calibrated against synthetic pure H_2O inclusions (0° and 374.1°C) supplied by SynFlinc and with natural pure CO_2 inclusions (−56.6°C) from Camperio (Ticino, Switzerland). Measurements below 0°C are accurate to ±0.1°C, whereas at the highest temperature measured (~350°C), they are accurate to ±1°C. Cryogenic experiments were carried out before heating to reduce the risk of decrepitating the inclusions. Salinity (expressed as wt.% NaCl equiv.), bulk composition, and density data were calculated for aqueous fluid inclusions using the HokieFlincs_H_2O-NaCl spreadsheet of *Steele-MacInnis et al. (2012)* and for CO_2 bearing fluid inclusions using the H_2O-NaCl-CO_2 spreadsheet of *Steele-MacInnis (2018)*.

2.3.5.3 Laser-Ablation Inductively Coupled Plasma Mass Spectrometry (LA-ICP-MS) in-situ analyses on fluid inclusions (FIs)

Laser inductively coupled plasma mass spectrometry (LA-ICP-MS) was used on FI to quantify their elemental content. These analyses were performed at ETH Zurich using the ETH-prototype GeoLas system equipped with a 193- nm ArF-Excimer Compex 102F laser ablation system (LambaPhysik-Coherent, Germany) coupled to a Nexion2000 (PerkinElmer, USA/Canada) fast-scanning quadrupole ICP mass spectrometer for multi-element analysis. Five samples were analyzed in a ca. 5-cm^3 round glass cell. Gas blanks and system contamination were minimized following the cleaning and setup procedures described in *(Schlöglova et al. 2017*). The cell was fluxed with carrier gas consisting ofhigh- purity (5.0 grade) He (1.1 L min−1), to which H_2 was added (5 mL min−1) to enhance sensitivity for heavy elements (*Guillong and Heinrich 2007*). Sample gas consisting of 6.0 grade Ar (ca. 1 $L.min^{-1}$) was admixed downstream of the ablation cell prior to injection in the plasma. The ICP-MS was optimized for maximum sensitivity on the whole mass range and low oxide rate formation (248ThO+/232Th+ <0.5%). The glass standard NIST SRM 610 *(Jochum et al. 2011*) was used as the primary reference material except for Br, Cl, and S for which we used the Sca-17 scapolite standard (*Seo et al. 2011*). Both were analyzed with 40 μm pit size, repetition rates of 10 Hz and ca. 1 min measurement consisting of 30 s gas blank + 30 s ablation. FIs in quartz were analyzed by slowly incrementing the spot size using an opening aperture to prevent cracking (*Gagnon et al. 2003*). Repetition rates of 10 Hz with laser output energies between 50 mJ (corresponding to energy densities on sample of ca. 10 $J.cm^{-2}$) were applied. Sphalerite was analyzed with a repetition rate of 10 Hz and output energies of 105 mJ (energy densities of ca. 9

J.cm^{-2}). In total, we measured 35 elements with a dwell time of 5 ms for ^{7}Li, ^{11}B, ^{23}Na, ^{25}Mg, ^{29}Si, ^{39}K, ^{55}Mn, ^{85}Rb, ^{88}Sr, ^{93}Nb, ^{133}Cs, ^{138}Ba, ^{140}Ce, ^{203}Tl, ^{208}Pb, ^{74}Ge, ^{232}Th, ^{238}U, 10 ms for ^{34}S, ^{35}Cl, ^{43}Ca, ^{57}Fe, ^{63}Cu, ^{66}Zn, ^{75}As, ^{107}Ag, ^{111}Cd, ^{115}In, ^{121}Sb and 20 ms for ^{78}Br. Magnesium, U, Th, Ce were not detected in our samples. The total sweep time was 60 ms. We subsequently reduced the data with the SILLS software (*Guillong et al. 2008*), using the salinity determined by microthermometry as internal standard for the FI and stoichiometric contents of major elements as internal standard to correct the contribution of the host mineral (Si for quartz and Zn for sphalerite).

2.4 Geochronology

2.4.1 In-situ U-Th-Pb datation on zircon and monazite

2.4.1.1 Sample preparation and petrography

For the two granitic samples, 1-2 kg was processed at the mineral separation laboratory at Geosciences Montpellier-Université de Montpellier following standard procedures of separation. The selected grains were mounted on 2.5 cm blocks with epoxy resin, polished.

Before analysis, backscatter electron (BSE) and cathodoluminescence (CL) images were acquired for all grains using a FEI QUANTA 450w (at Bourgogne-Franche Comté University) in order to check spot positions with respect to the internal microstructures, inclusions, fractures and physical defects. The monazite grains were characterized by SEM at Geosciences Montpellier.

2.4.1.2 U-Th-Pb geochronology of zircon and monazite

In situ U-Th-Pb isotopic data were obtained by laser ablation inductively coupled plasma spectrometry (LA-ICP-MS) at Laboratoire Magmas & Volcans (Clermont-Ferrand, France). The analyses involved the ablation of minerals with a Resonetics Resolution M-50 powered by an ultra-short-pulse (<4ns) ATL Atlex Excimer laser system operating at a wavelength of 193 nm. For monazite and zircon, spot diameters of 12µ and 33µm were used, associated with repetition rates of 1 Hz and 3 Hz and laser fluences of 9 /cm^2 and 4 J/cm^2, respectively. The ablated material was carried by helium and then mixed with nitrogen and argon before injection into the plasma source of an Agilent 7500 cs ICP-MS equipped with a dual pumping system to enhance sensitivity (Paquette et al. 2014). The alignment of the instrument and mass calibration were performed before

every analytical session using the NIST SRM 612 reference glass, by inspecting the signal of ^{238}U and by minimising the ThO+/Th+ ratio (< 1%). The analytical method for isotope dating is similar to that developed and reported in *Paquette and Tiepolo (2007)* and detailed in *Hurai et al. (2010, 2012)* and *Gasquet et al. (2010)*. The signals of ^{204}(Pb+Hg), ^{206}Pb, ^{207}Pb, ^{208}Pb, ^{232}Th and ^{238}U masses were acquired. The occurrence of common Pb in the sample was monitored by the evolution of the ^{204}(Pb+Hg) signal intensity, but no common Pb correction was applied owing to the large isobaric interference from Hg. The ^{235}U signal was calculated from ^{238}U on the basis of the ratio $^{238}U/^{235}U$= 137.88. Single analyses consisted of 30 seconds of background integration with the laser off, followed by 60 seconds integration with the laser firing and a 20 second delay to wash out the previous sample and prepare for the next analysis.

Data were corrected for U-Pb fractionation occurring during laser sampling and for instrumental mass discrimination (mass bias) by standard bracketing with repeated measurements of the GJ-1 zircon (*Jackson et al. 2004*) and Trebilcock monazite *(Tomascak et al. 1996*) reference material. Repeated analyses of the zircon 91500 (*Wiedenbeck et al. 1995*) and the monazite Bananeira (*Gonçalves et al. 2016*) reference materials, treated as an unknown independently control the reproducibility and accuracy of the corrections. Data reduction was carried out with the software package GLITTER® from Macquarie Research Ltd (*Van Achterbergh et al. 2001; Jackson et al. 2004)*. For each analysis, the time resolved signals of single isotopes and isotope ratios were monitored and carefully inspected to verify the presence of perturbations related to inclusions, fractures, mixing of different age domains or common Pb. Calculated ratios were exported and concordia ages and diagrams were generated using the Isoplot/Ex v. 2.49 software package of *Ludwig (2001)*. The concentrations of U-Th-Pb were calibrated relative to the values of the GJ-1 zircon (*Jackson et al. 2004*) and Trebilcock (*Tomascak et al. 1996*) reference materials.

2.4.2 $^{40}Ar/^{39}Ar$ step-heating

During this study, both in situ and step-heating $^{40}Ar/^{39}Ar$ experiments were conducted on representative samples from the studied area. After selection of the thick sections and single micas, the samples were then irradiated for 40 hours in the core of the Triga Mark II nuclear reactor of Pavia (Italy) with several aliquots of the Taylor Creek sanidine standard (28.34 ± 0.10 Ma) as flux monitor. Argon isotopic interferences on K and Ca were determined by irradiation of KF and CaF_2 pure salts from which the following correction factors were obtained: $(^{40}Ar/^{39}Ar)_K$ = 0.00969 ± 0.00038, $(^{38}Ar/^{39}Ar)_K$ = 0.01297 ± 0.00045, $(^{39}Ar/^{37}Ar)_{Ca}$ = 0.0007474 ± 0.000021 and $(^{36}Ar/^{37}Ar)_{Ca}$ = 0.000288 ± 0.000016.

Argon analyses were performed at Géosciences Montpellier (France) with an analytical system that consists of: (a) a UV laser for in situ experiments and a CO_2 laser for the step-heating experiments, (b) different lenses for laser beam focusing, (c) a steel sample chamber, maintained at 10^{-8} - 10^{-9} bar, with a drilled copper plate for individual grains, (d) an inlet line for purification of gases including two Zr-Al getters, (e) a multi-collector mass spectrometer (Argus VI from Thermo-Fisher). After loading in the sample chamber, the samples were baked at about 120 °C during 24 hours to remove atmospheric argon from the sample surface. For each *in-situ* experiment, several laser pits with a spatial resolution of 20 μm were achieved on a surface of about 200x200 μm. Step-heating experiments were conducted with a duration of heating of 30 seconds at each step.

A custom-made software was used to control the laser intensity, the timing of extraction/purification and the data acquisition. The ArArCalc software© v2.5.2 was used for data reduction and plotting. Atmospheric ^{40}Ar was estimated using a value of the initial $^{40}Ar/^{36}Ar$ ration of 295.5 (*Steiger and Jäger 1977*). Ages are reported with two sigma uncertainties.

3 Geology and mineral ressources of the Pyrenean Axial Zone (PAZ)

3.1 Structural setting of the Pyrenees

The Pyrenees is an E-W orogenic segment situated between France and Spain, including Andorra, which is a part of the European Alpine chain extending between North Iberian margin to the Alps in the East (*Choukroune 1992*). This orogenic event exhumed a fragment of the Variscan domain, the Pyrenean Axial Zone (PAZ) between the Late-Cretaceous and the Paleogene (*Carreras and Druguet 2014*).

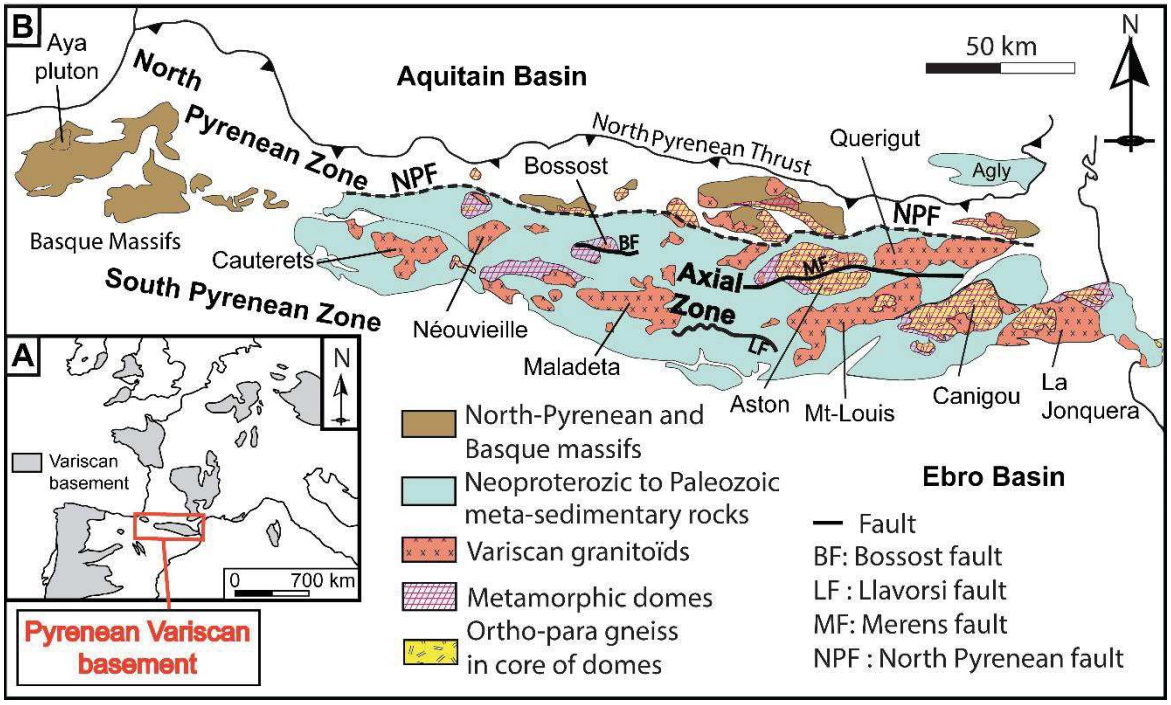

Figure 40. A. Location of the Pyrenean Axial Zone in the Variscan belt of Western Europe. B. Simplified geological map of the Variscan deformed basement with location of the main granitoïds massifs and metamorphic domes.

Five structural domains constitute this Alpine-Variscan range from north to south:

-The Aquitaine basin is composed of folded Mesozoic to Cenozoic rocks covered by post-tectonic Oligo-Miocene rocks.

-The North Pyrenean Zone is constituted of Mesozoic sedimentary rocks, associated to granitic or gneissic rocks and ultramafic lherzolitic rocks (Lherz massif), and deformed with north-verging thrust. The south of this zone is limited by the Alpine North Pyrenean Fault.

-The Variscan deformed basement is composed of three parts:

i) the Axial Zone is composed of Precambrian to Paleozoic metasedimentary rocks, Ordovician gneiss and Variscan granitoids (Figure 40; Aston, Hospitalet, etc.).

ii) the North-Pyrenean Massifs are small Variscan basement areas hosted in the North Pyrenean Zone and are composed of metasedimentary, granitic or gneissic rocks.

iii) the Basque massifs constitute the western parts of the Variscan basement and are composed of metasedimentary rocks intruded by the Upper-Permian Aya pluton (*Denèle et al. 2012*).

The South Pyrenean Zone is composed of multiple south-verging thrusts and is constituted of Mesozoic to Tertiary rocks. This zone is limited to the south by the South-Pyrenean thrust.

The Ebro basin constitutes the pro-foreland basin and is composed of Oligo-Miocene sedimentary rocks.

3.2 Tectonic evolution of the Pyrenean Axial Zone (PAZ)

The PAZ recorded two orogenic events during its geodynamic evolution, named Variscan and Alpine orogeny, and chronology of the related tectono-metamorphic events are often difficult to decipher. Herein, different sub-sections corresponding to key periods are presented to describe the geological evolution of the PAZ since the Ediacaran age.

3.2.1 Ediacaran to Lower-Carboniferous ages

The oldest rocks of the PAZ can be observed in the Eastern part of the range close to the Canigou massif (Figure 40), and are composed of Ediacaran-Cambrian volcano-sedimentary groups or series such as Canaveilles, Jujols or Olettes, (*Cavet 1957; Laumonier 2008; Padel et al. 2018*). Similar series are observed in Andorra *(Hartevelt 1970*) and in the Bossost anticlinorium (*Garcia-Sansegundo and Alonso 1989*). These formations are intruded by Early Ordovician Cadomian granitic laccoliths which occur essentially in the East part of the Pyrenees and were subsequently deformed during Variscan orogeny *(Deloule et al. 2002; Cocherie et al. 2005; Castiñeiras et al. 2008; Denèle et al.*

2009; Casas et al. 2010; Martínez et al. 2011; Mezger and Gerdes 2016; Navidad et al. 2018). The Ordovician magmatism is related to the break-up of the northern Gondwana margin associated to the opening of the Rheic Ocean *(Stampfli et al. 2007*). Cambro-Ordovician rocks, essentially composed of schists and locally of marble, are the oldest rocks in the Central and Western part of the PAZ and constitute now the core to numerous anticlinoriums such as Bossost, Pierrefitte or Lys-Caillaouas. Silurian rocks are almost exclusively constituted of black carbonaceous graptolite schist in the entire PAZ *(De Sitter and Zwart 1960; Kleinsmiede 1960; Mey 1967; Hartevelt 1970; Zwart 1979*). Devonian and Pre-Variscan Carboniferous rocks generally contrast with Silurian black-shales but are highly variable throughout the Pyrenees (*Zwart 1979*) from carbonate to black schists.

Pre-Variscan structures are often difficult to distinguish due to the superimposed Variscan deformation but several authors *(Llopis Llado 1965; Gil-Pena et al. 2001; García-Sansegundo et al. 2004; Casas and Fernández 2007*) observed evidences of unconformities in the Upper Ordovician. This is interpreted as a continental extensional event during Upper-Ordovician or linked to an Early-Mid Ordovician deformational event (*Casas and Fernández 2007)*. The first hypothesis is supported by effusive volcanism in numerous Paleozoic rocks like in Pierrefitte area (*García-Sansegundo et al. 2004)*, and presence of normal fault synchronous to Upper-Ordovician (*Casas 2010*) which may be related to the regional Sardic deformational event. A folding event recognized by (*Casas 2010*) is recorded in the Middle-Ordovician rocks without cleavage or metamorphism associated. Other authors attested the presence in Pre-Variscan formation of pennique-style folds *(Guitard 1964; Seguret and Proust 1968*) associated to the occurrence of flat-lying foliation but the new Ordovician age of the orthogneiss, basically interpreted as the Cadomian basement, now make this hypothesis unlikely.

3.2.2 Lower-Middle Carboniferous to Permian ages: Variscan orogeny

The Variscan Pyrenean range is the result of the collision between Gondwana and Laurasia-during the Lower-Middle Carboniferous *(Matte 2001; Martinez Catalan 2011; Stampfli et al. 2013*). At this time, Pyrenean terrane is probably located at the southern flank of the orogen, in the foreland basin, constituted in part by flysch sedimentation (Figure 41). During the progression of the subduction, Variscan basement of the Pyrenees will be more and more enclosed by the closure of the Cantabrian orocline, part of the Armorican-Iberian arc (Figure 41 and Figure 42), and this will lead to a quick increase of deformation mainly associated to dextral transpression and metamorphism *(Denèle et al. 2008; Mezger 2009; Cochelin et al. 2017a*). This rapid transition from a quiet foreland basin to a "hot" orogenic setting without mountain building processes is a particularity of the Variscan Pyrenean segment *(Cochelin et al. 2017a*)

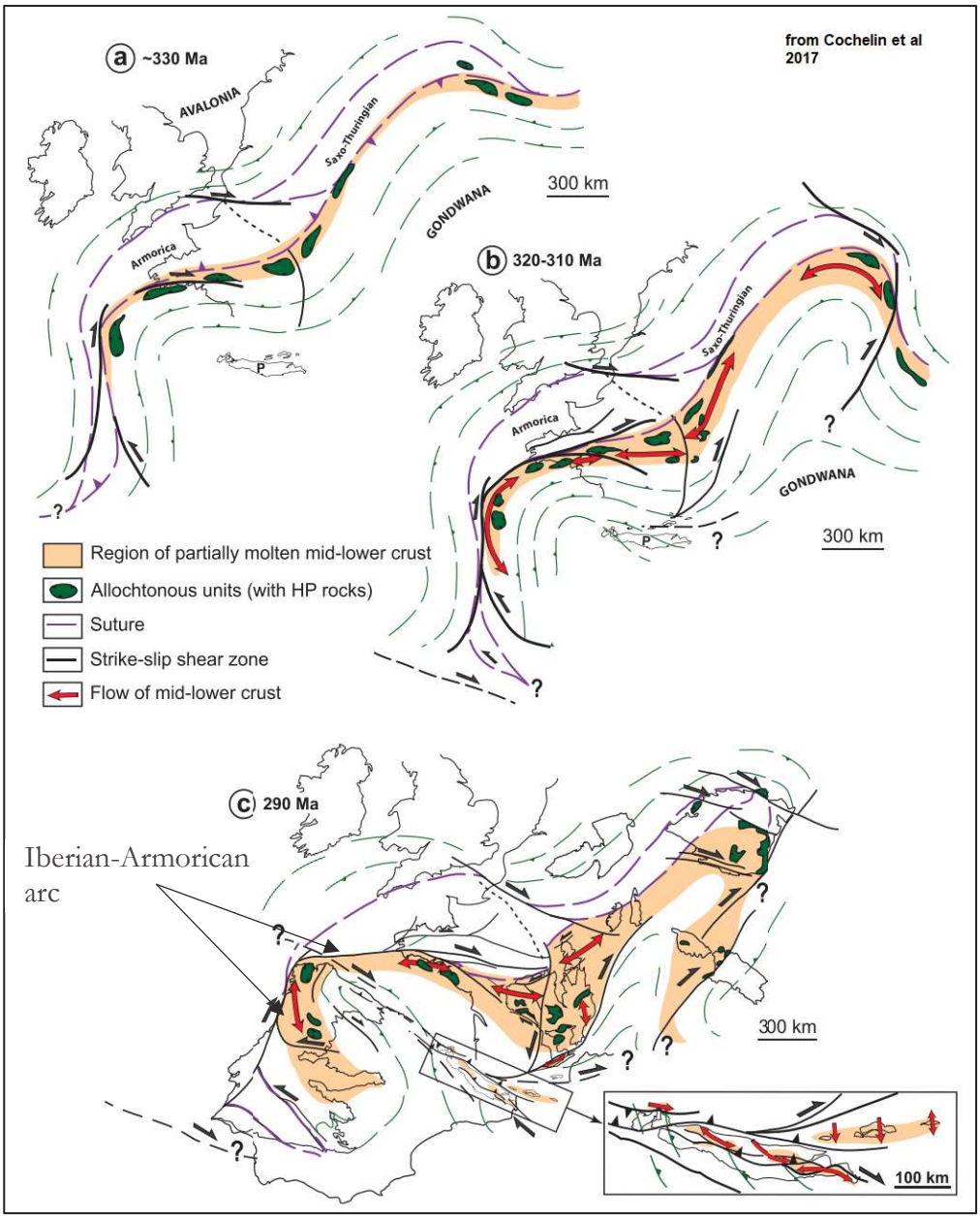

Figure 41. Three-stage reconstruction of the Iberian-Armorican arc during the Carboniferous and the Permian. (a) Late collision stage at ca. 330 Ma. (b) Syn-convergence extension of the hinterland and fold-and-thrust tectonics in the southern foreland (ca. 320–310 Ma). (c) End of orocline bending, intra-syntax HT deformation (ca. 310–290 Ma). This figure is from *Cochelin et al. 2017*.

The lower temporal limit of the Variscan orogeny is a well debated question. The beginning of the Variscan deformation is commonly considered Early-Namurian to Early-Westphalian (325-315 Ma) in age, due to the age of flysch rocks regionally named Culm (*Delvolvé et al. 1993*). But recent study by *Martín-Closas et al. (2018)* proposes the presence of two Variscan ductile deformations pre and syn flysch deposition due to biostratigraphic data at the base of the flysch interval and occurrence of strongly foliated and gneissic cobbles in these rocks. Recent study by *Mezger and Gerdes (2016)* performs age-dating on two granitic intrusions hosted in the PAZ (Bossost

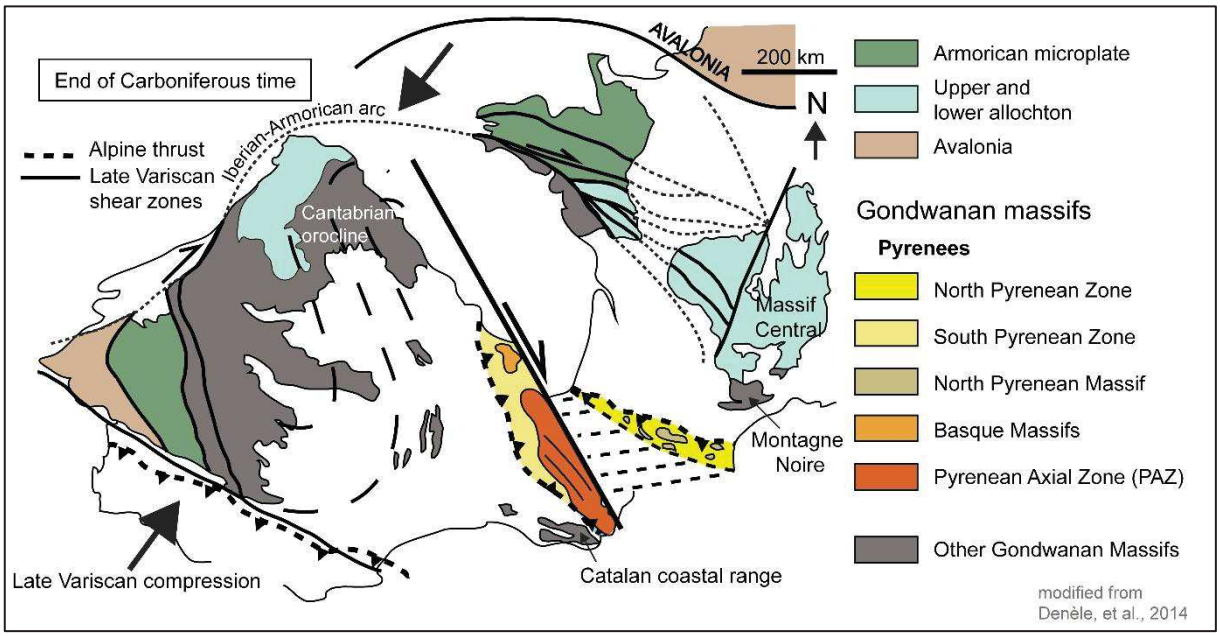

Figure 42. Structural representation of the Variscan western belt at the end of the Carboniferous time (modified from *Denele et al. 2014*).

dome) and produce a Visean (338-336 Ma) age, which demonstrates an Early-Carboniferous magmatism in the Axial Zone (330-340 Ma), different from the widespread Late-Carboniferous (320-290 Ma) magmatism (*Denèle et al. 2014*). This could imply a beginning of the deformation/metamorphism events before the ages given by the dating of the flysch. Nonetheless, the two obtained ages are questioned by *Denèle et al. (2014)* who interpret these ages as artefacts linked to an inherited component (480 and 640-620 Ma). Another recent study by *Lopez-Sanchez et al. (2018*) relate the analyses of *Mezger and Gerdes (2016)* to an Early Carboniferous component in the core of the zircons hosted in Bossost granite and in Lys Caillaouas granite (south of Bossost dome).

A commonly accepted partition of the orogen is the duality Infrastructure-Superstructure. One of the first observation of the difference of structural style according to depth was done in the Pyrenean Axial Zone by *De Sitter and Zwart (1960)* and became a classical model for the description of orogens.

According to this model, the Variscan Pyrenean crust is separated in two structural domains:

(i) a deep-seated domain called Infrastructure, which contains medium to high-grade metamorphic rocks and presents flat-lying foliations associated to recumbent folds, but highly deformed domains appear locally with steep and penetrative crenulation foliations (Figure 43).

(ii) a shallow-seated domain called the Superstructure, which is composed of low-grade metamorphic rocks and presents moderate deformation associated to a slaty cleavage (*Carreras and Capella 1994; Carreras and Druguet 2014*).

These criteria are empirical and in the field it happens that recumbent fold associated to flat-lying foliation also appear in Superstructure areas (*Carreras and Capella 1994*).

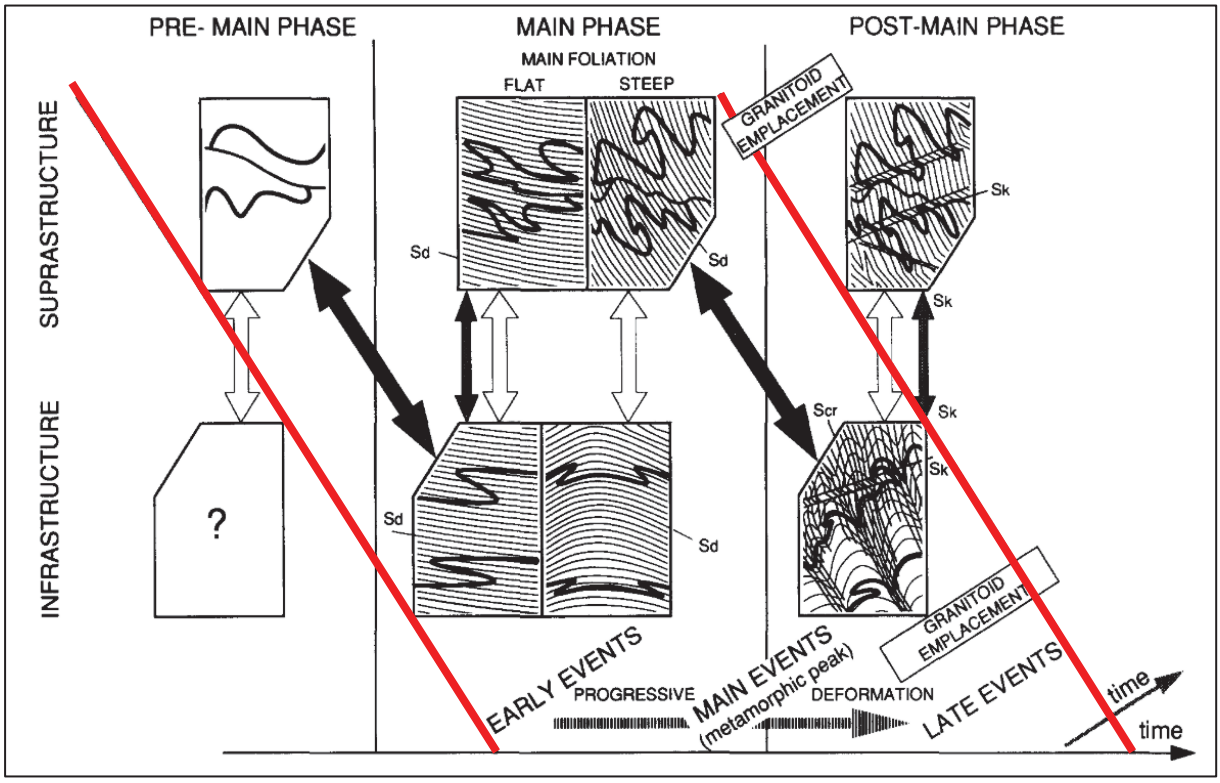

Figure 43. Deformation evolution in space and time according to the two structural domains (from *Carreras and Cappellas, 1994*). White arrows indicate proposed correlation between infra- and suprastructures. For the main phase in the suprastructure, two options are considered: dominant foliation (Sd) originally flat or steep. An alternative correlation based on the non-existence of an ubiquitous main foliation and on progression of deformation without clear breaks is indicated by the dark arrows. (Scr is a crenulation cleavage and Sk refers to axial planes of late kinks.)

In the PAZ, three deformation phases essentially Variscan in age (325–290 Ma) are recognized (Figure 44) according to the more accepted geodynamic model (*Denèle et al. 2014*). The first deformation event (D_1) related to crustal thickening is evidenced by a flat-lying foliation (S_1) that is often parallel to the stratification (S_0) *(Zwart 1979; Garcia-Sansegundo and Alonso 1989; Matte 2002; Vilà et al. 2007*). Some authors link the appearance of this flat-lying foliation to the occurrence of recumbent folds *(Matte 1969; Garcia-Sansegundo and Alonso 1989; Vilà et al. 2007)*. Regional M_1 metamorphism is of Medium-Pressure and Low-Temperature (MP/LT) and synchronous to this first D_1 deformation (*Zwart 1963a; Mezger et al. 2004; Mezger 2005; Denèle et al. 2014; de Hoÿm de Marien et al. 2019*). The second deformation event (D_{2a}) is related to horizontal and lateral crustal

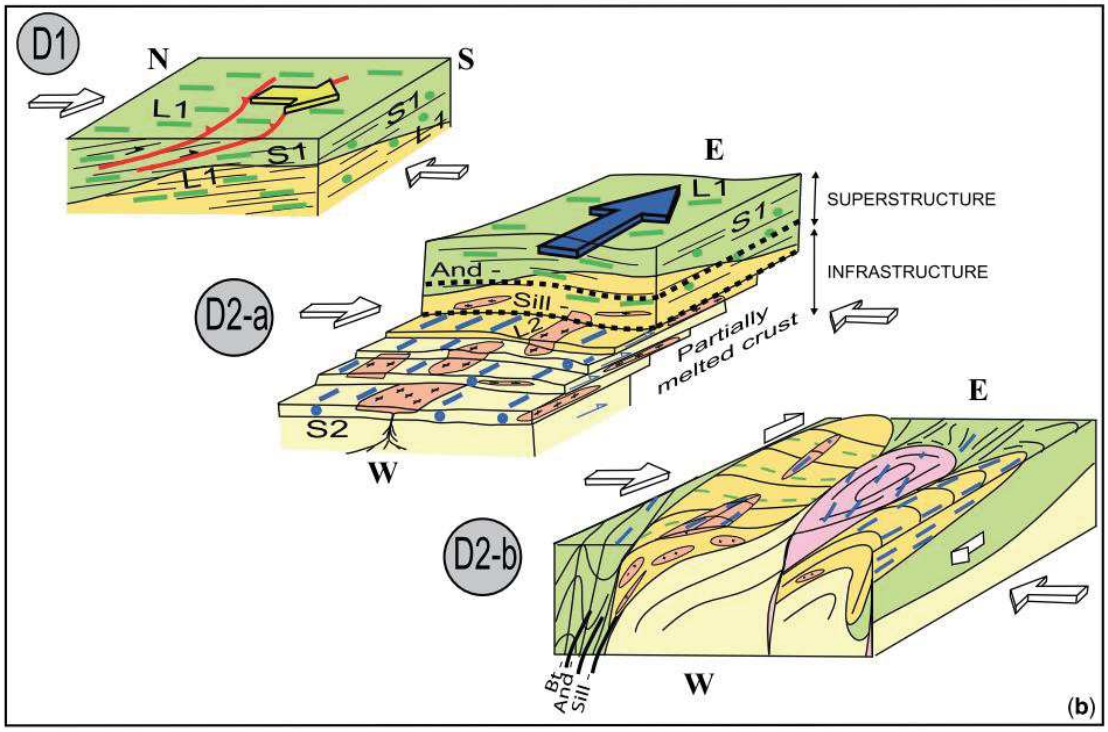

Figure 44. Sketch representing the evolution of the deformation (D_1 to D_2) in the Super- and Infrastructure (from *Denèle et al. 2014*)

flow, and is expressed by a moderate to steep axial planar (S_2) cleavage, essentially E-W. This event is directly followed by D_{2b} which corresponds to the formation of the gneissic domes. M_2 is a Low-Pressure and High-Temperature (LP/HT) metamorphism related to the intrusion of numerous Late-Variscan granitic and it is superimposed to the M_1 metamorphism *(Pouget 1991; Evans et al. 1998; Mezger 2005*). These events will form numerous metamorphic domes like the Aston, Canigou or Bossost massifs (Figure 40). Crustal ductile flow appears in Ordovician granitoids metamorphosed in gneiss *(Denèle et al. 2014; Cochelin 2016*). Numerous Late-Variscan plutons appear in the PAZ such as the Bossòst, Lys-Caillaouas, Querigut, Maladeta or Gavarnie-Heas plutons (*Kleinsmiede 1960; Evans et al. 1998; Auréjac et al. 2004; Mezger et al. 2004; Denèle et al. 2014; Cochelin 2016; Kilzi et al. 2016*) and are probably syntectonic (D_2) with an age from Late Mississippian to Late Pennsylvanian (~320-290 Ma),. Late-Variscan D_3 deformations are locally expressed as fold and E-W shear zones like the Merens and/or probably the Bossost faults *(Carreras and Cirés 1986; Carreras 2001; Mezger et al. 2012*).

3.2.3 Permian to Cenozoic ages: Pyrenean-Alpine orogeny.

Stephano-Permian extension is recorded in the south border of the Axial-Zone with formation of Late-orogenic basin filled with continental sediments and volcanic rocks *(Rodríguez-*

Méndez et al. 2016). Granitic plutons associated to this phase are also reported in the Basque Massifs (Aya pluton, *Denèle et al. 2012*).During Triassic, Jurassic and Early Cretaceous times, extensional events occurred (*Dubois and Seguin 1978; Puigdefàbregas and Souquet 1986; Joseph Canérot 1991; Choukroune 1992; Vergés et al. 2002; Lagabrielle et al. 2010*). Rifting led to the formation of an ultra-thinned northern margin during the Albian stage, which allowed the exhumation of sub-continental mantle (e.g. Lherzolite of Lherz; *Lagabrielle and Bodinier 2008; Lagabrielle et al. 2010)*. Related to this event, Na(-Ca) metasomatism with subsequent low-pressure and high-temperature metamorphism is reported mainly in the North Pyrenean Massif with the formation of albitite and talc-chlorite massifs, but also in the PAZ (*Albarède and Michard-Vitrac 1978; Golberg and Leyreloup 1990; Fallourd et al. 2014; Clerc et al. 2015*). Continental rifting is synchronous with oceanic spreading in the Bay of Biscay and associated to the rotation of the Iberian plate relative to European plate *(Le Pichon et al. 1970*). Beginning of the Pyrenean orogeny (~85-20 Ma) is evidenced by the sedimentation of terrigenous flysch rocks related to the uplift of the first terranes (*Dubois and Seguin 1978; Joseph Canérot 1991*). North-South convergence appear between the Iberian and European plates which induced their collision between Late Cretaceous and Eocene times (*Choukroune 1992*). Due to this shortening event, flexural forelands are formed in Aquitaine basin from the Late Cretaceous to Eocene and in Ebro basin from the Eocene to Early-Miocene.

Alpine deformation is difficult to distinguish in the Paleozoic PAZ due to the relative poor relation with Mesozoic sediments. In the literature, some authors demonstrate a relative low impact of alpine structures with no real penetrative deformation on the Paleozoic basement (*Munoz 1993; Cochelin 2016; Cochelin et al. 2017b*). Nonetheless, some Alpine movements or reactivation of pre-existing structures are demonstrated along the North Pyrenean fault, in multiple regional thrust such as the Rialp thrust (*Cochelin et al. 2017b*), the Gavarnie thrust *(McCaig et al. 2000; García-Sansegundo et al. 2014*), in shear zones *(Carreras and Cirés 1986; Mezger and Passchier 2003; Ostkamp et al. 2019*) or in Permo-Triassic sediments (*Cochelin 2016*).

3.3 Mineral ressources in the Pyrenees

Four main types of mineralization are reported in the Pyrenees:

i) Lead-Zinc(-Iron-Copper-Barite-Fluorite) mineralizations are widespread in the Pyrenees with more of one hundred deposits but are less abundant in the Eastern part of the PAZ (Figure 45). In the literature, two major mineralization events are described and synthesized below:

a) Lead-Zinc(-Iron-Copper-Barite) mineralizations in stratiform-stratabound bodies are the more abundant in the Pyrenees with major districts like the Pierrefitte, Bentaillou or Cinco-Villas (Figure 45). These mineralizations are hosted in a large diversity of rocks from carbonate to schist or micro-conglomerate and at different levels of the stratigraphic sequence, from Cambro-Ordovician to Devonian. Some deposits are richer in magnetite (such as Estaing) or richer in gangue mineral like the Arrens deposit where barite was exploited (*Bois 1981*). A recent BRGM report describes this last deposit as an important exploration target for zinc and barite (*Pouit and Bois 1986a; Vic and Billa 2015*).Many authors explain the genesis of these mineralizations as SEDEX(s) event(s) during Ordovician and Devonian ages with only poor remobilizations during Variscan orogeny (*Bois et al. 1976; Pouit 1978; Cardellach and Alvarez-Perez 1979; Pouit and Bois 1986a; Pesquera and Velasco 1989; Marcoux et al. 1991b; Cardellach et al. 1996; Velasco et al. 1996)*. Their arguments are primarily based on geometrical analyses of the ore bodies, which are essentially stratiform to stratabound. Other authors describe an important role of Variscan orogeny *(Alonso 1979; Nicol et al. 1997*) in the Pierrefitte and Urets-Liat districts with major remobilizations in fold hinges or between structural levels. Lead isotopic data show the same signature between Ordovician and Devonian Pb-Zn ore *(Marcoux et al. 1991b; Cardellach et al. 1996*). Age calculations give an Ordovician age based on the *Cummings and Richards* evolution model. Sulfur isotopic data were also performed on different Central Pyrenean deposits (*Cardellach et al. 1996*) and evidenced two different sources of sulfur.

b) Lead-Zinc(-Fluorite-Barite) Vein mineralization are less widespread in the Pyrenees (Figure 45). The largest exploited vein deposit in the Pyrenees is Cierco, located in Spain, at the south of the Maladeta granitoid (Figure 45). The production is estimated at 1.4 Mt of ore with average grade of 4 % of Pb and 3 % of Zn (*Johnson et al. 1996*). The mineralization, hosted in granitoid, in schist or in Permian red-beds, is probably Mesozoic in age, associated to an extensional event (*Johnson et al. 1996*) even if *Castroviejo Bolibar and Serrano (1983)* describe Late-Variscan mineralization. Pyrenean-Alpine orogenic event has probably deformed the mineralization (*Johnson et al. 1996*). Similar Mesozoic veins occurred in the Aulus-Les-Argentieres deposit (Munoz et al. 2016) but the mineralization is poorly deformed. At the East of Pierrefitte anticlinorium (Figure 45), numerous vein mineralizations are recognized and belong to the Arre-Anglas-Uzious district. These veins are hosted in Devonian schists or limestone and are interpreted as Late-Variscan in age (Reyx 1973). Other vein-deposits are described in the literature such as Yenefrito (*Subias et al. 1999*) Parzan (*Fanlo et al. 1998*) or La Gela (*Pouit and Bois 1980*) and are hosted in Late-

Variscan granitoids or in Paleozoic schists. These veins are oriented E-W or N110°E with a dip generally varying from 50° to vertical.

One of the particularities of the Pb-Zn mineralizations of the PAZ is the occurrence of Ge-minerals in sphalerite (ZnS). Some of them were discovered in the Pyrenean deposits like argutite (Argut-dessus deposit, GeO_2) and carboirite (Carboire deposit, $GeFeAl_2O_5(OH)_2$) (*Johan et al. 1983*). Their genesis is poorly constrained even if *Johan and Oudin (1986)* supposed a probable link with metamorphism.

ii) Tungsten mineralizations are linked to skarn or skarnoid deposit-type which is related to an intense metasomatism close to plutons, in carbonate or in silicoclastic rocks. Mineralogy is mainly constituted of scheelite ($CaWO_4$) and wolframite ([Fe, Mn]WO_4) and presence of Au. Fe, Zn, Sn and Mo are not rare. Between 1971 and 1986, the Salau Pyrenean deposit, hosted in Devonian rocks, was exploited with a production of 930 kt of ore with 1.5 % WO_3 eq. to ~14000t WO_3 (*Fonteilles et al. 1989; Poitrenaud 2018)*. Another major tungsten deposit in the Pyrenees is Costabonne located in the Eastern part of the Pyrenees with probable ressources of 4300t WO_3.

iii) Auriferous mineralizations are known essentially in the Eastern part of the Pyrenees with the Glorianne, Aspres and Nohédes mineralizations. No genetic model exist for these mineralizations (*Vic and Billa 2015*).

iv) Talc, magnesite or fluorine (industrial minerals) mineralizations are important ressources in the Pyrenees with presence of a giant talc deposit in Trimuns within the Saint-Barthelemy North Pyrenean massif, which represents 15% of the talc in the world (*Boutin 2016*). Herein, talc is originated from the alteration of dolomitic rocks and may be altered during several phases *(Boutin et al. 2016*). Eugui magnesite ($MgCO_3$) deposit is situated in Navarra, in the Basque Massifs (*Velasco et al. 1987*), is hosted in Carboniferous dolomite and produced 170 000t/y of magnesian oxide (MgO; *Coullaut Sáenz de Sicilia 2013*). Escaro fluorine (CaF_2) deposit is hosted in the Canaveilles carbonated levels (*Pouit and Fortuné 1980*) close to the Canigou massif. It was exploited from 1955 to 1991 and produced 2 Mt of fluorine.

1

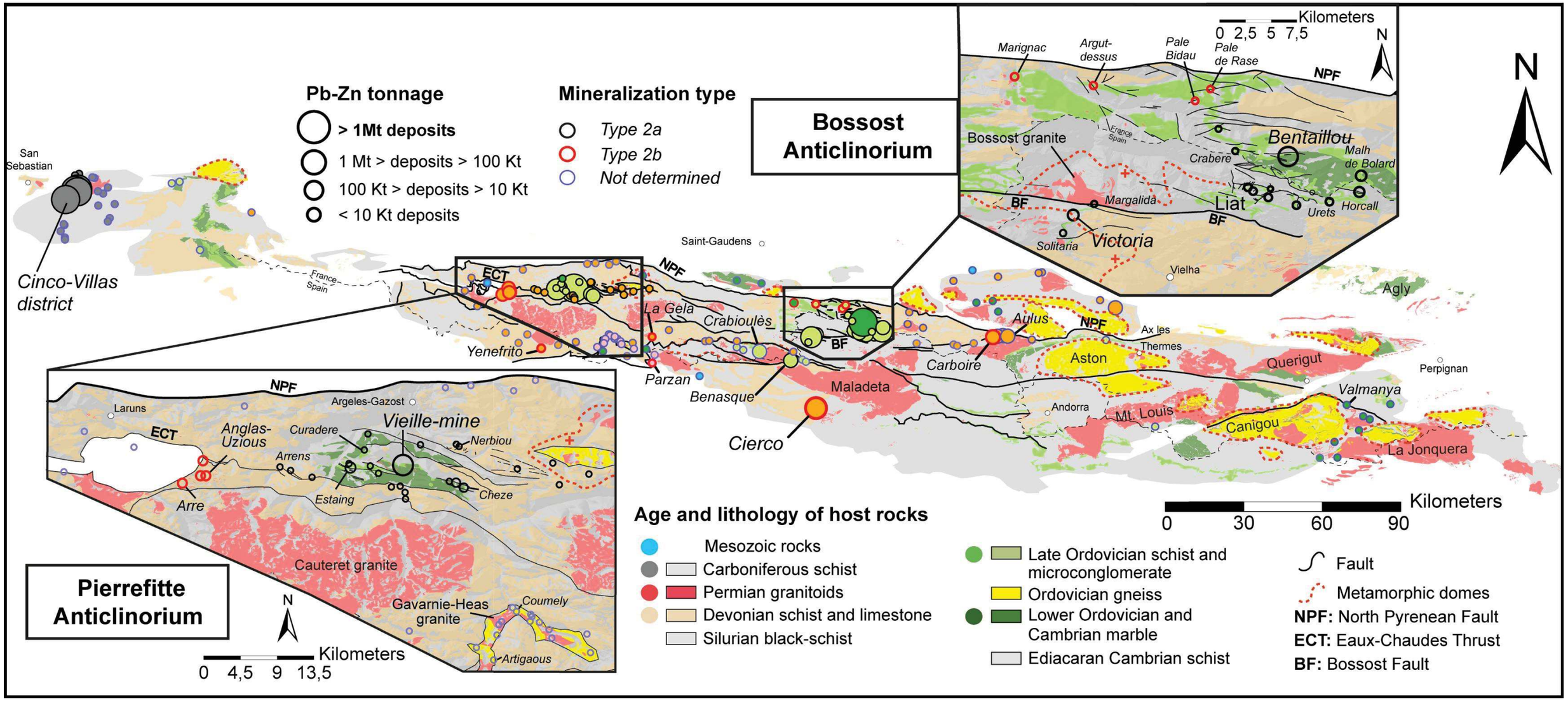

Figure 45. Structural map of the Pyrenan Axial Zone (PAZ) with North Pyrenean and Basque massifs. The distincion between the two main types of Pb-Zn mineralization referred to the chapter *4-Structural framework for the Pb-Zn deposits in the Pyrenean Axial Zone (PAZ).* Two types may occur in the same deposit so in consequence only the main exploited type is considered in the legend. This map was completed with BRGM and IGME 1/50 000 maps. The tonnage data referrred to different publications given in the Table 2.

4 Structural framework for the Pb-Zn deposits in the Pyrenean Axial Zone (PAZ)

This chapter is devoted to the fieldwork study in a large diversity of Pb-Zn mineralizations in the PAZ. The main question of this fieldwork was the temporality of the mineralization emplacement. Numerous authors argued that the mineralizations were Pre-Variscan in age (Ordovician or Devonian) and probably syngenetic with only few remobilization during Variscan deformation *(Bois et al. 1976; Pouit and Bois 1986a; Pujals 1992; Cardellach et al. 1996*). Others authors suggest that Variscan deformation greatly impacted this ore (*Alonso 1979; Nicol et al. 1997*). Before this study, no regional structural investigation was completed on these numerous Pb-Zn deposits (about 150 deposits) to answer to the ore genesis question. This problem is not only studied in the Pyrenees but seem widespread in a majority of deformed/metamorphosed Pb- Zn(- Cu) mineralizations like the Australian Pb-Zn deposits of Broken Hill or Mt-Isa *(Gibson et al. 2017*) or in Moroccan VMS *(Essaifi et al. 2019*).

4.1 Short historic of the Pyrenean Pb-Zn mines

Numerous Pb-Zn mineralizations are reported in the Pyrenees (Figure 45) but a large part of the Pb-Zn Pyrenean deposits was only exploited until the end of the 20th century or during the first half of the 21st due to relative weak tonnage or concentrations. Nonetheless, in the French part, the last exploited Pb-Zn deposits were the Bentaillou mine closed in 1955 (*Dubois 2015*) and the Pierrefitte mine closed in 1969. This last deposit was the most productive with 2 600 000t of ore with 180 000t Zn and 100 000t Pb (Table 2). In the Spanish, only few Pb-Zn mineralizations are described but the last Pb-Zn deposits closed later: in 1981 for the Cierco deposit (Alta Ribagorça, Catalonia) and in 1984 for the Arditurri Pb-Zn district (Cinco-Villas massif, Basque massif).

Anticlinorium	Deposits	Closure	Ore (t)	Metal (t)			Source
				Zn	Pb	Ag	
Bossost	Mall de Bulard		50000	14400	96		BRGM Internal report / Ovejero, 1991
	Bentaillou	1955	1 300 000	99 000	33 000		BRGM Internal report / Ovejero, 1991
				110 000	40 000		Dubois, 2015
	Liat		60 150	12 030	600		BRGM Internal report / Ovejero, 1991
	Victoria	1953	504 170	53 800	6 352		BRGM Internal report / Ovejero, 1991
	Margalida-Solitaria-Horcall-Reparadora	1953	50 000	5 000	500		BRGM Internal report / Ovejero, 1991
	Marignac		56 000	5 000	200	2	BRGM report, 1984
	Argut			2 000	2 000		BRGM report, 1984
	Pale de Rase			2 000	200		BRGM report, 1984
	Pale Bidau			3 000	900		BRGM report, 1984
Pierrefitte	Pierrefitte secteur	1969	2 600 000	180 000	100 000	150	BRGM report, 1984 ; Ovejero, 1991; Bois, 1983
	Pierrefitte mine – Vieille Mine		2 000 000				Nicol, 1997, Cadarso, 2000
	Pierrefitte mine – Garaoulère		325 000				Cadarso, 2000
	Pierrefitte mine – Couledous		250 000				Cadarso, 2000
	Estaing-Arrouy		250 000	51 000	41 000		Cadarso, 2000
	Meyabat-Heches		52 000	5 500			Ovejero
	Curadère		5 000	550			Ovejero
	Arrens	1914 (Ba)		450	50		BRGM report, 1984
	Arre	1916		6 500			BRGM report, 1984/ Geolval, 2010
	Anglas	1916					BRGM report, 1984/ Geolval, 2010
Cinco-Villas	Arditurri district	1984	120 000 000	6 000 000	600 000	6 000	Pesquera & Velasco, 1989
Pallaresa	Aulus	16th century		4 000	1 000	40	Rapport BRGM, 1977), Munoz et al., 2015
	Carboire			500	300		Rapport BRGM, 1977), Munoz et al., 2015
Others	Crabioules			2 400			BRGM report, 1984
	Cierco	1981	1 400 000	42 000	56 000		Mey, 1968 / Johnson et al., 1996
	Parzan	1923	60 000		9 000	240g/t	Fanlo et al., 1998

Table 2. Informations in Pb-Zn(-Ag) tonnages for the Pyrenean Pb-Zn deposits

4.2 ARTICLE – Structural control on the formation of Pb-Zn deposits: an example from the Pyrenean Axial Zone

This section is devoted to the article "Structural control on the formation of Pb-Zn deposits: an example from the Pyrenean Axial Zone" published on October 26, 2018 in *Minerals*, and in the Special Issue "Structural Control of Mineral Deposits: Theory and Reality". The fully edited and open-access version of this article is available at the following link: https://www.mdpi.com/2075-163X/8/11/489.

This article is based on structural field evidences which aim to demonstrate a genetic model for the entire Pb-Zn mineralizations in the Pyrenean Axial Zone (PAZ). Deciphering the link between Pb-Zn mineralizations and host-rock is often difficult in the field, and the macroscopic geometrical criteria is not always an absolute argument to demonstrate a syngenetic or epigenetic origin of the ore (formation of the ore synchronous or posterior to the formation of the host rock respectively). Especially when these arguments and the study are located only in one deposit and no relation to the geodynamic environment is inferred. Herein, a regional study based on structural interpretation of eighteen deposits and mineralogical analyses is performed. This strategy allows us to demonstrate a clear polyphased genesis of these Pb-Zn mineralizations essentially interpreted as epigenetic and intimately controlled by Variscan tectonics. It is based on cross-cutting evidences and geometry of the ore bodies, positions of the mineralizations in the stratigraphy and its texture, and relations between metamorphic mineral and Pb-Zn ore. A genetic structural model for the formation of the three main Pb-Zn mineralization types is shown in the last part of this article.

minerals

MDPI

Alexandre Cugerone[1,*], Emilien Oliot[1], Alain Chauvet[1], Jordi Gavaldà Bordes[2], Angèle Laurent[1], Elisabeth Le Goff[3] and Bénédicte Cenki-Tok[1]

[1]Géosciences Montpellier, UMR CNRS 5243, Université de Montpellier, Place E. Bataillon, CC 60, 34095 Montpellier, France; emilien.oliot@umontpellier.fr (E.O.); alain.chauvet@umontpellier.fr (A.C.); angele.laurent@etu.umontpellier.fr (A.L.); benedicte.cenki-tok@umontpellier.fr (B.C.-T.)

[2]Conselh Generau d'Aran, Vielha, 25530 Lleida, Spain; j.gavalda@aran.org

[3]Bureau de Recherches Géologiques et Minières (BRGM), Territorial Direction Languedoc-Roussillon, 1039 Rue de Pinville, 34000 Montpellier, France; e.legoff@brgm.fr

*****Correspondence: alexandre.cugerone@umontpellier.fr; Tel.: +33-643983585

Received: 21 September 2018; Accepted: 23 October 2018; Published: date: 26 October 2018

Keywords: Pb-Zn deposits; Pyrenean Axial Zone; SEDEX; remobilization; structural control; sphalerite.

4.2.1 Abstract

Pb-Zn deposits and specifically Sedimentary-Exhalative (SEDEX) deposits are frequently found in deformed and/or metamorphosed geological terranes. Ore bodies structure is generally difficult to observe and its relationships to the regional structural framework is often lacking. In the Pyrenean Axial Zone (PAZ), the main Pb-Zn mineralizations are commonly considered as Ordovician SEDEX deposits in the literature. New structural field analyzes focusing on the relations between mineralization and regional structures allowed us to classify these Pb-Zn mineralizations into three types: (I) Type 1 corresponds to minor disseminated mineralization, probably syngenetic and from an exhalative source. (II) Type 2a is a stratabound mineralization, epigenetic and synchronous to the Variscan D_1 regional deformation event and (III) Type 2b is a vein mineralization, epigenetic and synchronous to the late Variscan D_2 regional deformation event. Structural control appears to be a key parameter in concentrating Pb-Zn in the PAZ, as mineralizations occur associated to fold hinges, cleavage, and/or faults. Here we show that the

main exploited type 2a and type 2b Pb-Zn mineralizations are intimately controlled by Variscan tectonics. This study demonstrates the predominant role of structural study for unraveling the formation of Pb-Zn deposits especially in deformed/metamorphosed terranes.

4.2.2 Introduction

The world's most important Pb-Zn resources consist in Sedimentary-Exhalative (SEDEX) mineralizations (*Wilkinson 2013*). These types of ore deposits are syngenetic sedimentary to diagenetic. Occurrence of laminated sulfides parallel to bedding associated to sedimentary features (graded beds, etc.) are the key geological argument (*Leach 2005*). These important deposits occur often in ancient metamorphosed and highly deformed terranes for example in Red Dog, Alaska (*Moore et al. 1986; Kelley and Jennings 2004*); Rampura, India (*Hazarika et al. 2013*); or Broken Hill, Australia (*Lawrence 1973*). In these cases, the processes of ore formation are still largely debated. In consequence, unraveling the relationships between mineralization and orogenic remobilization(s) is essential in order to understand the genesis of Pb-Zn deposits in deformed and metamorphosed environments. For example, in Broken Hill (*Lawrence 1973; Hobbs et al. 1998; Gibson and Nutman 2004*) and Cannington (*Walters and Bailey 1998*) deposits in Australia some authors argued for a metamorphogenic and epigenetic mineralization as large metasomatic zones may have refined pre-existing Pb-Zn rich rocks. Other authors consider a pre-metamorphic and syngenetic origin with only limited remobilization linked to tectonic events (Haydon and Mcconachy 1987; Bodon 1998a; Webster 2004). In the world-class Jinding Pb-Zn deposit, the host rock has undergone a complex tectonic deformation (*Yalikun et al. 2018*). Some authors proposed a syngenetic origin of the deposit (*Shi et al. 1983; Wang et al. 1992*) whereas others argued for an epigenetic genesis of the deposit based on field study, textural evidences *(Kyle and Li 2002; Xue et al. 2007; Chi et al. 2012; Leach et al. 2017*), fluid inclusion (*Chi et al. 2005; Xue et al. 2007*), and paleomagnetic age (*Yalikun et al. 2018*). Nowadays, these high-tonnage Pb-Zn deposits are the preferential target of numerous academic and industrial studies also for the presence of rare metals like Ge, Ga, In, or Cd associated with sulfides.

The Pb-Zn deposits hosted in the Pyrenean Axial Zone (PAZ) area that has suffered Variscan tectonics (*Zwart 1979; Mezger and Passchier 2003; Denèle et al. 2014*) are usually considered to be SEDEX. As an example, due to their geometry and the presence of distal volcanic rocks, *Bois et al. (1976)* and *Pouit and Fortuné (1980)* considered as SEDEX the Pb-Zn mineralizations located in the Pierrefitte anticlinorium. In Bentaillou area, *Fert (1976)* and *Pouit (1978, 1986)* demonstrated that the stratigraphic and sedimentary controls were dominant processes during the genesis of these

mineralizations. In the Aran Valley, deposits (Liat, Victoria-Solitaria, and Margalida) have been studied by *Pujals (1992)* and (*Cardellach 1977; Cardellach et al. 1982*). These authors concluded on a stratiform and possibly exhalative formation of Pb-Zn mineralizations associated with a poor remobilization during Variscan deformation. Only few authors have documented the impact of Variscan tectonics on the genesis of these mineralizations. These are *Alonso (1979)* in Liat, Urets, and Horcalh deposits or *Nicol (1997)* for Pierrefitte anticlinorium deposits. In the Benasque Pass area, south of the Bossòst anticlinorium, *García-Sansegundo et al. (2014)* indicated probable Ordovician stratiform or stratabound Pb-Zn mineralizations intensely reworked during Variscan tectonics. The Pb isotopes study realized by *Marcoux (1986)* showed a unique major event of Pb-Zn mineralization interpreted as sedimentary-controlled and Ordovician or Devonian in age. Remobilization processes of Pb isotopes seem however poorly constrained and a complete structural study related to these analyzes is lacking.

Pyrenean sulfide mineralizations are an excellent target for investigating the links between orogenic deformation(s) and the genesis of associated mineralization(s), as well as finding key arguments to make the distinction between strictly syngenetic or rather epigenetic mineralizations and structurally remobilized mineralizations. In this work we will demonstrate that Pb-Zn deposits from five districts in the PAZ, previously largely considered SEDEX, were actually formed through processes involving a strong structural control.

4.2.3 Geological Setting

The Pyrenean Axial Zone (PAZ, Figure 46A) is the result of the collision between the Iberian and Eurasian plates since the Lower Cretaceous. Deep parts of the crust were exhumed during this orogeny. The PAZ is composed of Paleozoic metasedimentary rocks locally intruded by Ordovician granites deformed and metamorphosed during the Variscan orogeny, like the Aston or Canigou gneiss domes (*Zwart 1963a; Denèle et al. 2014*).

The PAZ is generally divided in two domains *(De Sitter and Zwart 1960; Kleinsmiede 1960; Zwart 1963a, 1979; Cochelin et al. 2017b*): (i) a deep-seated domain called Infrastructure, which contains medium to high-grade metamorphic rocks and (ii) a shallow-seated domain called the Superstructure, which is composed of low-grade metamorphic rocks. The Infrastructure presents flat-lying foliations, but highly deformed domains appear locally with steep and penetrative crenulation foliations. Alternatively, the Superstructure presents moderate deformation associated to a slaty cleavage *(Carreras and Capella 1994; Carreras and Druguet 2014*) These two domains are

intruded by Late-Carboniferous granites, like the Bossòst and the Lys-Caillaouas granites *(Kleinsmiede 1960; Cochelin 2016; Mezger and Gerdes 2016)*.

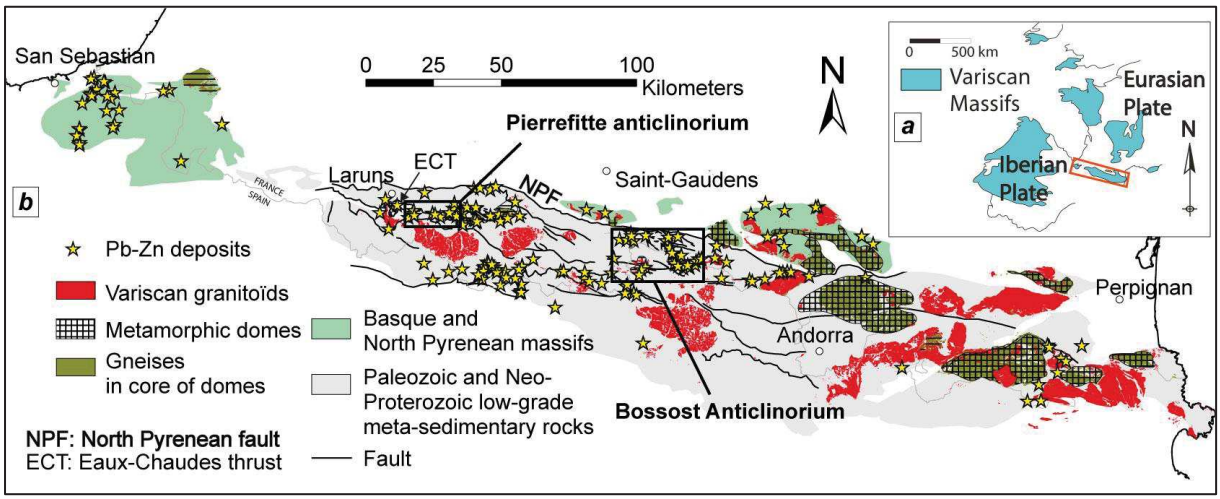

Figure 46. (**a**) Location of the Pyrenean Axial Zone (PAZ) within the Variscan belt of Western Europe. (**b**) Schematic map of the Pyrenean Axial Zone (PAZ) and location of all recognized Pb-Zn deposits (based on BRGM (French geological survey) and IGME (Spanish geological survey) databases . Note the abundance of these deposits especially in the central and western domains of the PAZ.

In the PAZ several deformation phases essentially Variscan in age (325–290 Ma) are recognized. The first deformation event (D_1) is marked by a cleavage (S_1) that is often parallel to the stratification (S_0). Regional M_1 metamorphism is of Medium-Pressure and Low-Temperature (MP/LT) and synchronous of this first D_1 deformation (*Mezger and Passchier 2003*). The second deformation event (D_2) is expressed by a moderate to steep axial planar (S_2) cleavage. M_2 is a Low-Pressure and High-Temperature (LP/HT) metamorphism linked to the Late-Variscan granitic intrusions, and it is superposed to the M_1 metamorphism (*Pouget 1991; Mezger 2005*). Late-Variscan and/or Pyrenean-Alpine D_3 deformations are locally expressed as fold and shear zones like the Merens and/or probably the Bossòst faults *(Carreras 2001; Mezger et al. 2012; Carreras and Druguet 2014)*.

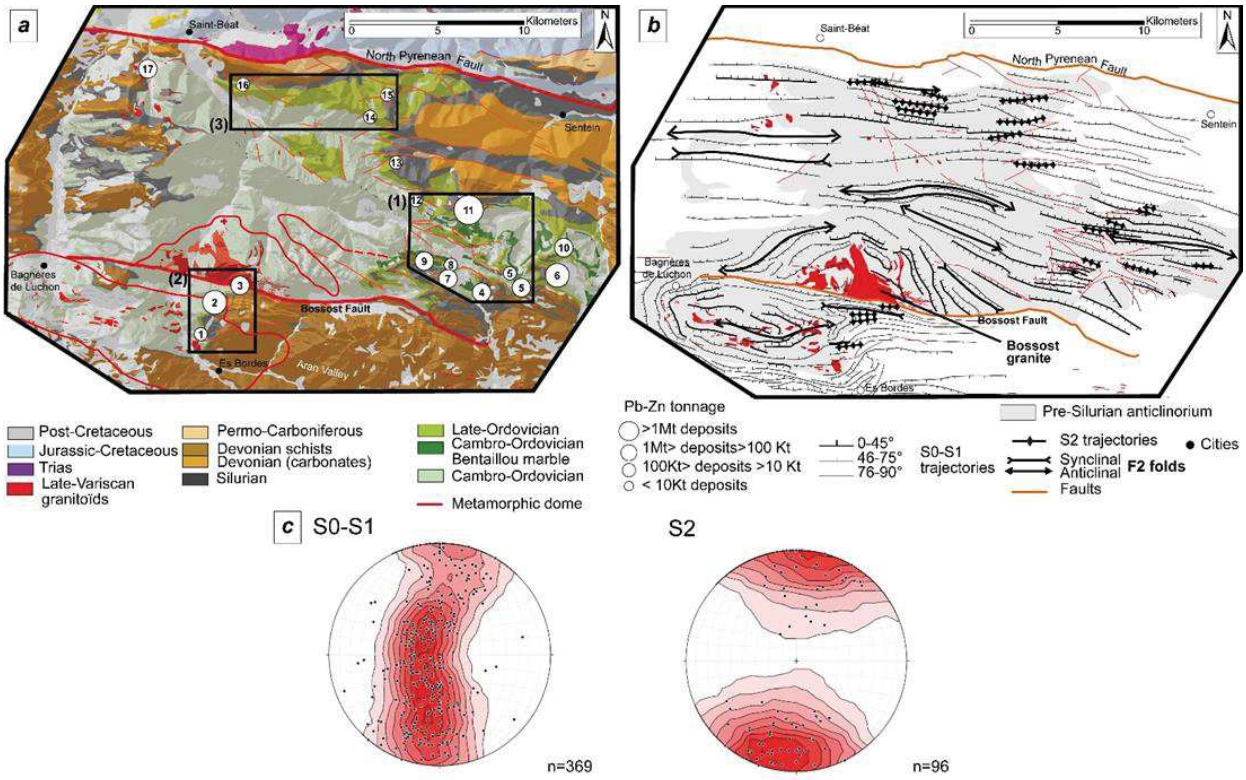

Figure 47. The Bossòst Anticlinorium. (**a**) Geological map with positions of the three districts: (1) Bentaillou-Liat-Urets district, see Figure 48 and Figure 49. Margalida-Victoria-Solitaria district, see Figure 50; and (3) Pale Bidau-Argut-Pale de Rase district, see Figure 51. Pb-Zn deposits are numbered as follows: 1: Solitaria; 2: Victoria; 3: Margalida; 4: Plan del Tor; 5: Urets; 6: Horcall; 7: Mauricio-Reparadora; 8: Estrella; 9: Liat; 10: Malh de Bolard; 11: Bentaillou; 12: Crabere; 13: Uls; 14: Pale Bidau; 15: Pale de Rase; 16: Argut. Lithologies are based on geological map of BRGM (France, (BRGM 1972; Barrère et al. 1984; Clin et al. 1989) and IGME (Spain, Aran Valley; (*García-Sansegundo et al. 2013*). Metamorphic dome boundaries are related to andalousite isograd presented by Zwart; (**b**) Structural map with foliation trajectories of S_0-S_1, subvertical S_2, and related F_2 folds. Note preferential apparition of Pb-Zn deposits when S_2 cleavage is well-expressed. (**c**) Schmidt stereographic projections (lower hemisphere) of poles to S_0-S_1 and S_2 subvertical foliation planes.

The Pyrenean Pb-Zn regional district is the second largest in France with ~400,000 t Zn and ~180,000 t Pb extracted (*BRGM 1984; Ovejero Zappino 1991*). These sulfides deposits are localized in the PAZ in the Pierrefitte and Bossòst anticlinoriums (Figure 46B). Sphalerite (ZnS) and galena (PbS) are essentially present in Ordovician and Devonian metasediments. Few Pb-Zn deposits are hosted in granitic rocks (*Castroviejo Bolibar and Serrano 1983*).

This study focuses on Pb-Zn deposits located in the Bossòst anticlinorium (Figure 46) *(Pouget 1991; Aerden 1994; Cochelin 2016)* and includes a comparison with Pb-Zn deposits occurring in the Pierrefitte anticlinorium. The southern part of the Bossòst anticlinorium forms the Aran

Valley synclinorium. The northern part is limited by the North Pyrenean fault (Figure 47A). It is mostly composed of Cambrian to Devonian rocks and an intruding Late-Variscan leucocratic granite named the Bossòst granite.

Three main Pb-Zn districts are recognized in the Bossòst anticlinorium (Figure 47): (I) The Bentaillou-Liat-Urets district is located in the eastern part of the anticlinorium and was the most productive in the Bossòst anticlinorium, ~1.4 Mt at 9% of Zn and 2% of Pb metals *(Alonso 1979; Nicol et al. 1997*). (II) The Margalida-Victoria-Solitaria district is located in the southern part of the anticlinorium, close to the Bossòst granite. Production reached ~555,000 t with 11% Zn and 0.1% Pb (*BRGM 1984*). (III) The Pale Bidau-Argut-Pale de Rase district is located in the northern part of the anticlinorium. Pb-Zn production did not exceed ~7000 t of Zn and ~3000 t of Pb (Cugerone et al. 2018a).

Pierrefitte anticlinorium is located north of the Cauteret granite and intersected by the Eaux-Chaudes thrust (ECT; Figure 46). It is essentially composed of Ordovician rocks in the West and Devonian terranes in the East. Two districts are studied: (I) Pierrefitte mines is the largest district in the PAZ which produced ~180,000 t of Zn, ~100,000 t of Pb and ~150 t of Ag (*BRGM 1984*). (II) Arre and Anglas mines are located west to Pierrefitte mines. Pb-Zn production did not exceed ~6500 t of Zn (*BRGM 1984*).

4.2.4 Structural Analysis of Three Pb-Zn Districts in the Bossòst Anticlinorium

The Bossòst anticlinorium is a 30 × 20 km E-W-trending asymmetric antiform hosting a metamorphic dome (Figure 47A). Pre-Silurian lithologies are dominated by Cambro-Ordovician schists. Locally, other lithologies are present like the Cambro-Ordovician Bentaillou marble or the late-Ordovician microconglomerate and limestone (Figure 47B).

Two distinct cleavages can be observed in the Bossòst anticlinorium. S_1 transposes the S_0 stratification and is roughly oriented N090–N120°E with varied dip angles both to the north and to the south (Figure 47B and C). S_0-S_1 dip angles are low in the metamorphic dome (Figure 47B) but this pattern is not restricted to the core of the anticlinorium. In the eastern part of the

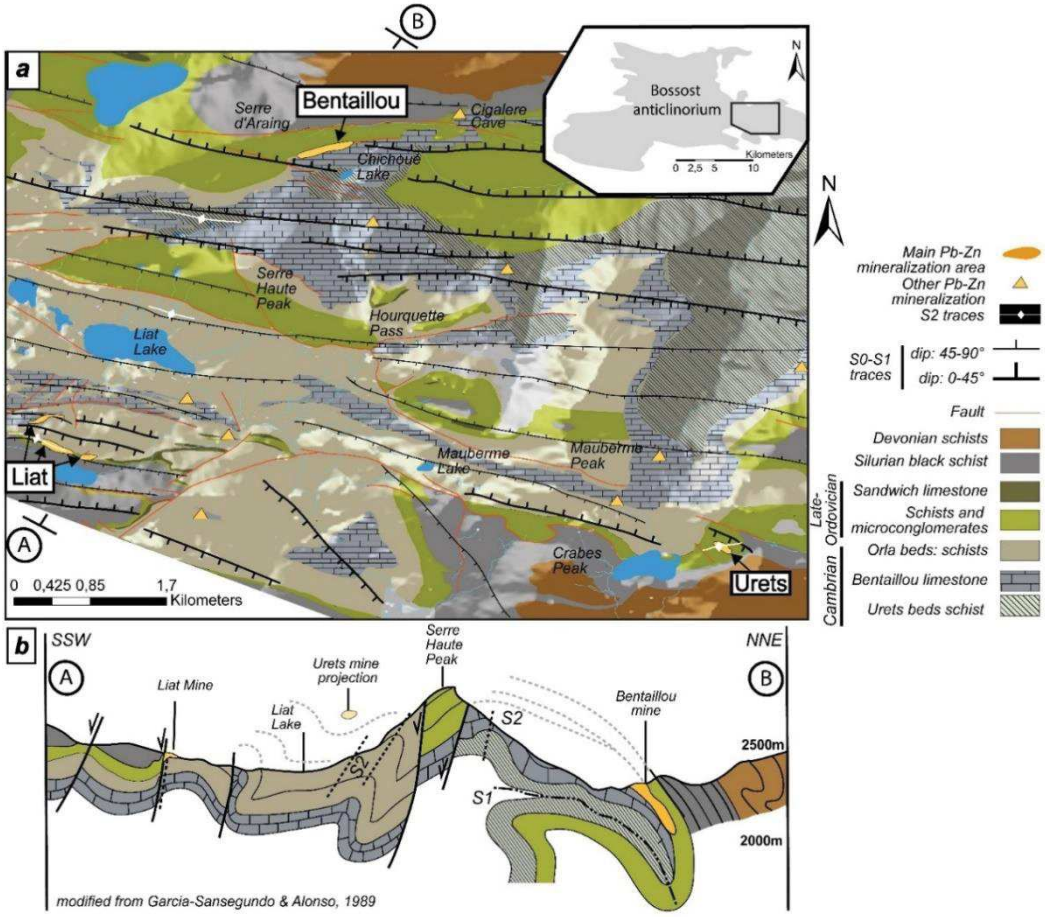

Figure 48. (**a**) Structural map of the Bentaillou-Liat-Urets district based on field study and BRGM/IGME geological maps. Location in Bossòst anticlinorium is indicated in the small sketch map (see also location on Figure 47A); (**b**) Structural NNE-SSW cross-section of the Liat-Bentaillou area. Location of the cross-section is indicated in the Figure 48A (modified from *Garcia-Sansegundo and Alonso, 1989*). Note presence of Pb-Zn mineralization at rock competence interface and close to F1 fold hinge in Bentaillou mine.

anticlinorium, foliation is generally low to moderately dipping (0–45° N or S, Figure 47B) and *Garcia-Sansegundo and Alonso (1989)* supposed the presence of large recumbent F_1 folds in the Bentaillou and Horcalh-Malh de Bolard areas. The presence of a Late Ordovician microconglomerate at the base of Bentaillou limestone is described by *Garcia-Sansegundo and Alonso (1989)* and confirms this hypothesis. Furthermore, the presence of these folds is inferred by the observation of dm- to pluri-m north-verging recumbent F_1 folds in Bentaillou marble in the underground levels of the mine and also by their presence in the Devonian schists.

Close to the southern boundary of the Bossòst granite, S_0-S_1 foliation in high-grade schists is steeply dipping (Figure 47B). The S_2 cleavage trends N080–120°E and is generally sub-vertical (Figure 47C) as axial plane of F_2 south-verging folds. S_2 cleavage and related F_2 folds are particularly well developed in the southern part of the Bossòst anticlinorium (Figure 47B).

In the PAZ districts, three Pb-Zn mineralization types are commonly observed and two of these will be described below: Stratabound mineralization is subparallel to S_0-S_1 and Vein mineralization is parallel to S_2. Disseminated mineralization is not a key mineralization type and is spread in the host rocks.

4.2.4.1 District of Bentaillou-Liat-Urets

This district is located in the southeastern part of the Bossòst anticlinorium. Three main extraction areas are present in this district: (i) Bentaillou mine is located in the north of the district (Figure 3a). Exploitation finished in 1953 and produced ~110,000 t of Zn and ~40,000 t of Pb. At that time, it was the second largest mine in the Pyrenees (*Dubois 2015*), (ii) the Liat mine lays southwest of the district and (iii) Urets is located southeast of the district (Figure 48A). Both produced ~60,000 t of Zn (*Ovejero Zappino 1991*). Mineralization occurrences will be described in the following parts.

4.2.4.1.1 Bentaillou Area

Mineralization lays close to the hinge of a N090–110°E kilometer-size F_1 recumbent fold (Figure 48B) and is essentially located at the top of the Cambro-Ordovician marble, below the Late-Ordovician schists (Figure 49A). Mineralized stratabound bodies are broadly parallel to S_0-S_1 which is sub horizontal with a progressive increase of the dip from 45°N to 80°N to the lowest underground mine levels in the north (Figure 49B). Relicts axial planar S_1 of F_1 recumbent isoclinal folds are locally underlined by recrystallized calcite in N090–100°E axial planes (Figure 49B).

Pb-Zn stratabound mineralizations are present in centimetric- to pluri-metric N-S open-filling structures which can be assimilated to pull-apart features (Figure 49C) that were formed in association with a dextral top to the north kinematic. These mineralized bodies show typical impregnation textures (Figure 49D) and sphalerite presents millimetric to centimetric grain sizes.

Pb-Zn mineralization is absent in weakly D_1 deformed areas whereas it occurs in highly deformed domains associated to the appearance of S_1 cleavage in F_1 fold hinges (Figure 49E and F).

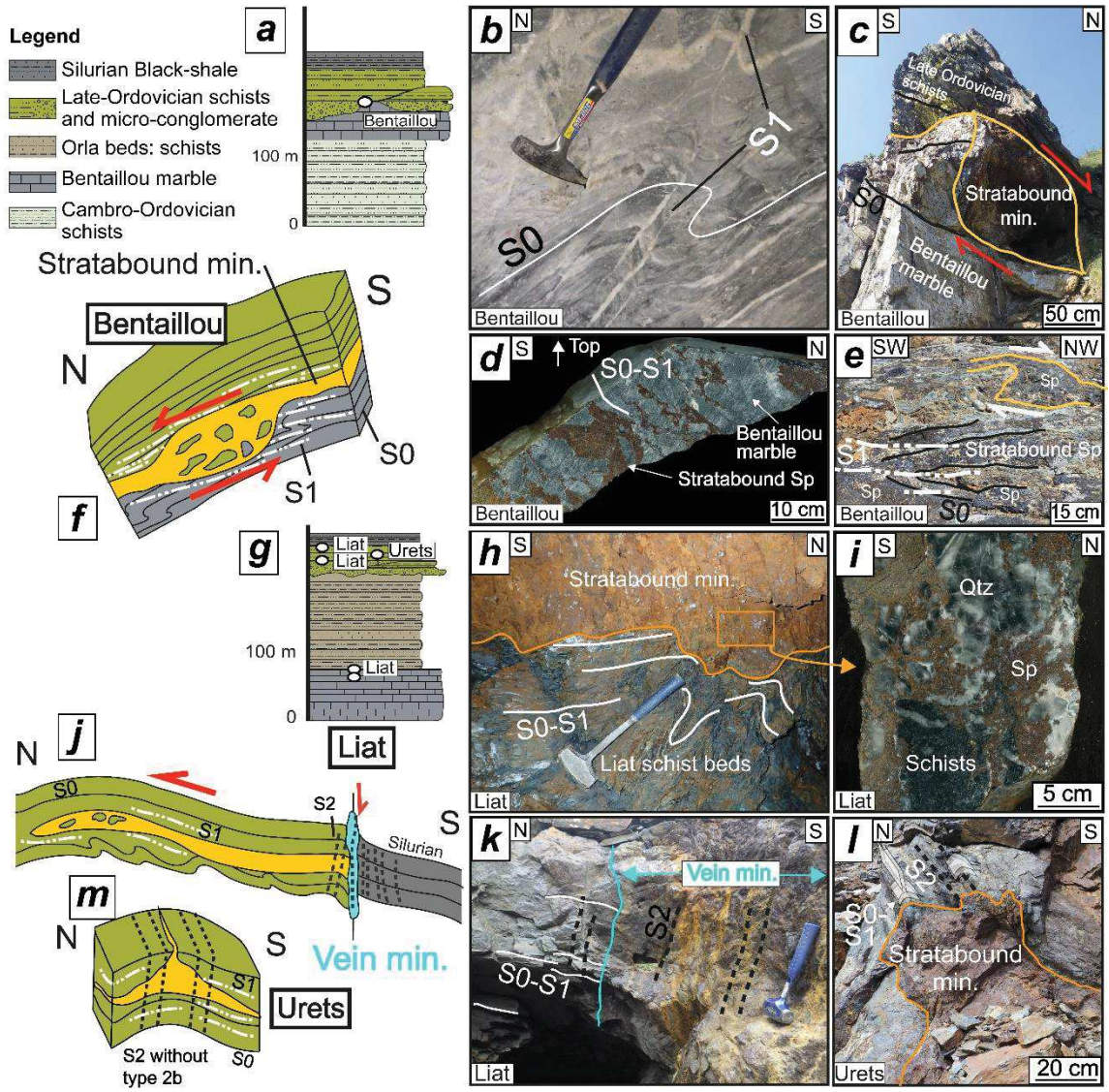

Figure 49. Field observation and structural models in the Bentaillou-Liat-Urets deposits (see location in Figure 48a). (a) Stratigraphic log of Bentaillou areas with position of the Pb-Zn deposits; (b) F1 fold in Bentaillou marble with S1 cleavage marked by calcite recrystallization; (c) pull-apart geometry of Pb-Zn mineralization in Bentaillou area; (d) oriented sample of typical mineralization in Bentaillou marble; and (e) relationship between sphalerite mineralization and host rock structure. Note that sphalerite is not folded by F1 folds and intersect S0 stratification; (f) 3D structural model of Bentaillou deposits with Pb-Zn mineralization in centimetric to pluri-metric pull apart geometry; (g) stratigraphic log of Liat-Urets area with position of the Pb-Zn deposits; (h) stratabound mineralization in top of folded schist beds in Liat area; (i) brecciated Pb-Zn mineralization in Liat area with clast of schist and quartz in sphalerite matrix; (j) 3D structural model of Liat deposit with dm to m stratabound and vein mineralizations; (k) vein Pb-Zn mineralization in Liat deposit; (l) stratabound mineralization in F2 fold hinge in Urets deposit; (m) 3D structural model of Urets deposit with pluri-dm to m Pb-Zn mineralization in F2 fold hinge. Mineral abbreviations: Qtz-quartz; Sp-sphalerite.

4.2.4.1.2 Liat Area

Pb-Zn mineralization is located at the rock interface (Figure 49G) and can be hosted in Bentaillou marble, especially on top of the marble, between the microconglomerate and Liat beds or between Liat beds and the Silurian black-shale. The large hm-size open F_2 fold is bordered to the south by a Silurian synclinorium (Figure 48A and B). S_1 cleavage is strictly parallel to S_0 in the area. D_2 deformation is well expressed in the south at the contact between Silurian black-shale and Late Ordovician schists.

Mineralized stratabound bodies with pluri-dm to m-thickness appear parallel to the shallow dipping S_0-S_1. Folds in Liat schists are present locally at the base of the mineralization (Figure 49H). It presents a brecciated texture (Figure 49I) with clasts of quartz and schists. Sphalerite presents centimetric grain sizes. At the contact with the Silurian black-shale the dip of Late Ordovician schist increases, and a normal fault is inferred. Vertical Pb-Zn vein mineralization parallel to S_2 is present in this fault. It intersects S_0 stratification, S_1 cleavage as well as stratabound mineralizations (Figure 49J and K). Vein mineralization also presents a brecciated texture and sulfide grains are oriented parallel to S_2. Sphalerite presents an infra-mm grain size.

4.2.4.1.3 Urets Area

This Pb-Zn mineralization is hosted in Liat schist. D_2 deformation is intensively present in this area, with numerous N100–130°E F_2 open to isoclinal folds associated to a subvertical N90–120°E S_2 cleavage. Stratabound pluri-dm to m Pb-Zn mineralization is mainly located in F_2 fold hinges (Figure 49L) and can locally intersect S_0 stratification (Figure 49M). Pb-Zn mineralization has a brecciated texture with mm sphalerite grains and millimetric to centimetric quartz clasts.

4.2.4.2 District of Margalida-Victoria-Solitaria

This district is located south of the Bossòst anticlinorium (Figure 47A and B). Three main extraction areas are present in this district from north to the south (Figure 50A): (i) Margalida mine is located close to the Bossòst granite next to the Bossòst fault, (ii) Victoria mine, and (iii) Solitaria mine lays south of the granite and north and west to Arres village. Margalida and Solitaria mine produced less than 50,000 t of ore with ~10% of Zn and 1% of Pb (*Ovejero Zappino 1991*). Victoria produced ~504,000 t with 11% of Zn and 1% of Pb (*Ovejero Zappino 1991*).

4.2.4.2.1 Margalida Area

Pb-Zn mineralization is located in Late-Ordovician sandwich limestone (Figure 50A and B) which forms the core of an anticlinal presenting a vertical N100°E-trending axial plane (supposed F_2 fold). Mineralization is located in the damaged zone of the Bossòst N090°E-trending fault. Mineralization appears as pluri-dm lenses generally parallel to S_0-S_1. Still mineralization is not always concordant to S_0-S_1 (Figure 50C). The texture of sulfide mineralization in Margalida area is different to this in Victoria-Solitaria area as sulfide grain size is infra-mm.

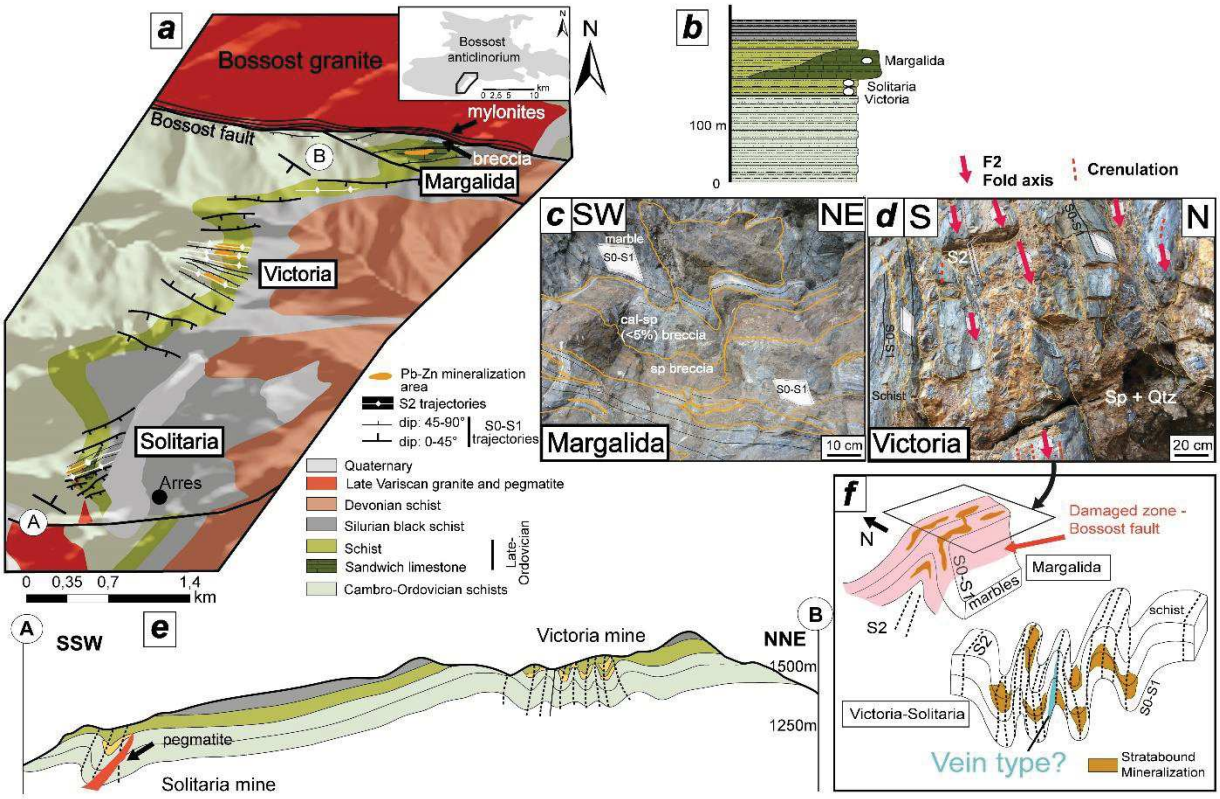

Figure 50. Margalida-Victoria-Solitaria district (see location on Figure 48a). (**a**) Structural map (lithologies are based on IGME geological map (Spain, Aran Valley; *García-Sansegundo et al. 2013*) and location on the Bossòst anticlinorium (pre-Silurian rocks); (**b**) stratigraphic log; (**c**) stratabound Pb-Zn mineralization in Margalida mine hosted in Sandwich limestone level; (**d**) typical stratabound folded mineralization (F_2 isoclinal folds) in Victoria; (**e**) structural NNE-SSW cross-section of Victoria-Solitaria area; and (**f**) structural model of Margalida and Victoria-Solitaria mines. Mineral abbreviations: Cal—Calcite; Qtz—Quartz; Sp—Sphalerite.

4.2.4.2.2 Victoria-Solitaria Areas

Pb-Zn mineralization is hosted by Late Ordovician schists (Figure 50A, B and D) and generally parallel to S_0-S_1. Locally S_0-S_1 is intensively folded by F_2 asymmetrical isoclinal N090–N120°E folds and a vertical S_2 N070–110°E axial planar cleavage can be observed. Stratabound

mineralization appears only in domains where F_2 folds imprint is intense (Figure 50E). Furthermore, in Victoria and Solitaria mines exploitation was preferentially undertaken in F_2 fold hinges. Pb-Zn mineralization is thicker in fold hinge (dm to m in thickness) and probably reworked during this D_2 deformation phase (Figure 50E and F). Sphalerite grains are often sub-millimetric. The presence of vein mineralization cannot be completely excluded as vertical galleries are present.

4.2.4.3 District of Pale Bidau-Argut-Pale de Rase

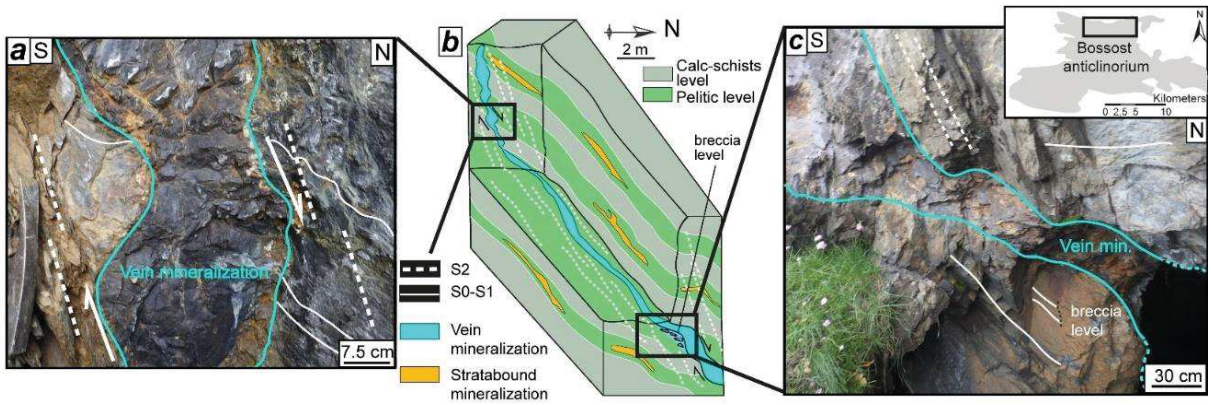

Figure 51. Field observations and 3D structural model of Pale Bidau deposit (see location in Figure 47a). (**a**) Vein Pb-Zn mineralization that occurs in pull-apart geometry; (**b**) 3D model presenting the relations between stratabound and vein Pb-Zn mineralizations; and (**c**) vein mineralization with presence of breccia at the base of a pull-apart mineralized structure.

The general structural description of the district is given in (*Cugerone et al. 2018a*). In this section, more details are given on the structural features of the Pale Bidau area (see location on Figure 47A). Two different Pb-Zn mineralization geometries appear: a first stratabound mineralization is hosted only in F_2 fold pelitic level and concordant to S_0-S_1, marked by centimetric to pluri-metric box-work texture. The second mineralization consists of veins oriented N090–120°E and consists of dm to m veins largely developed when D_2 deformation is important. Various dips are present for this mineralization but is mainly subvertical. Geometry of this mineralization can be interpreted as a pull-apart (Figure 51A) opened in a dextral top to the north movement and controlled by S_2 cleavage. Where S_2 cleavage is less pronounced, mineralization is thinner and seems to present in the sub-horizontal to 45°N S_0-S_1 cleavage (Figure 51B and C). Sphalerite crystals did not reach mm grain size.

4.2.5 Comparison with the Pierrefitte Anticlinorium: Pierrefitte and Arre-Anglas-Uzious Districts

The Pierrefitte anticlinorium is a 25 × 10 km NNW-SSE anticlinorium located in the western part of the PAZ (Figure 46B and Figure 52A). Its core is composed of Ordovician schists and Late-Ordovician carbonated breccias. Upper stratigraphic levels are made of Silurian black-shales and Devonian rocks. In western parts km-scale Valentin NNW-SSE anticlinal is included in the Pierrefitte anticlinorium. Compared to the Bossòst anticlinorium, the volume of late-Variscan granite or pegmatitic rocks outcropping is smaller and there is no metamorphic dome in the core (Figure 52A).

The Pierrefitte anticlinorium is structured by several thrusts within Silurian levels (Figure 52B and C) associated to D_1 deformation. S_2 vertical N090–100°E cleavage is well expressed in Devonian levels at the rim of the anticlinorium but is less visible in the Ordovician core.

Numerous Pb-Zn mines are present in Late-Ordovician and Devonian terranes. These have produced ~3 Mt (average 9% of Zn and 5% of Pb).

4.2.5.1 Pierrefitte District

The Pierrefitte mines (Garaoulere, Couledous, Vieille-Mine) are located at the contact with Late Ordovician rocks mainly carbonate breccia. N100–110°E S_0-S_1 foliation moderately dips (20° to 60°) to the south (Figure 52D).

Stratabound mineralization lays at the top of the Late Ordovician series at the contact or within the Silurian black-shales (Figure 52C), which follows a regional thrust parallel to S_0-S_1. The presence of a thrust in Pierrefitte area is reported in (*Zwart 1979; Calvet 1988; Nicol et al. 1997*) and this observation is supported in galleries by the occurrence of dm-scale dextral shear bands with a top-to-the-north-east kinematic. The mine galleries and the main exploited ore follow this regional thrust zone. S_1 cleavage often transposed S_0 stratification and corresponds to axial planes of isoclinal recumbent F_1 N090–120°E folds.

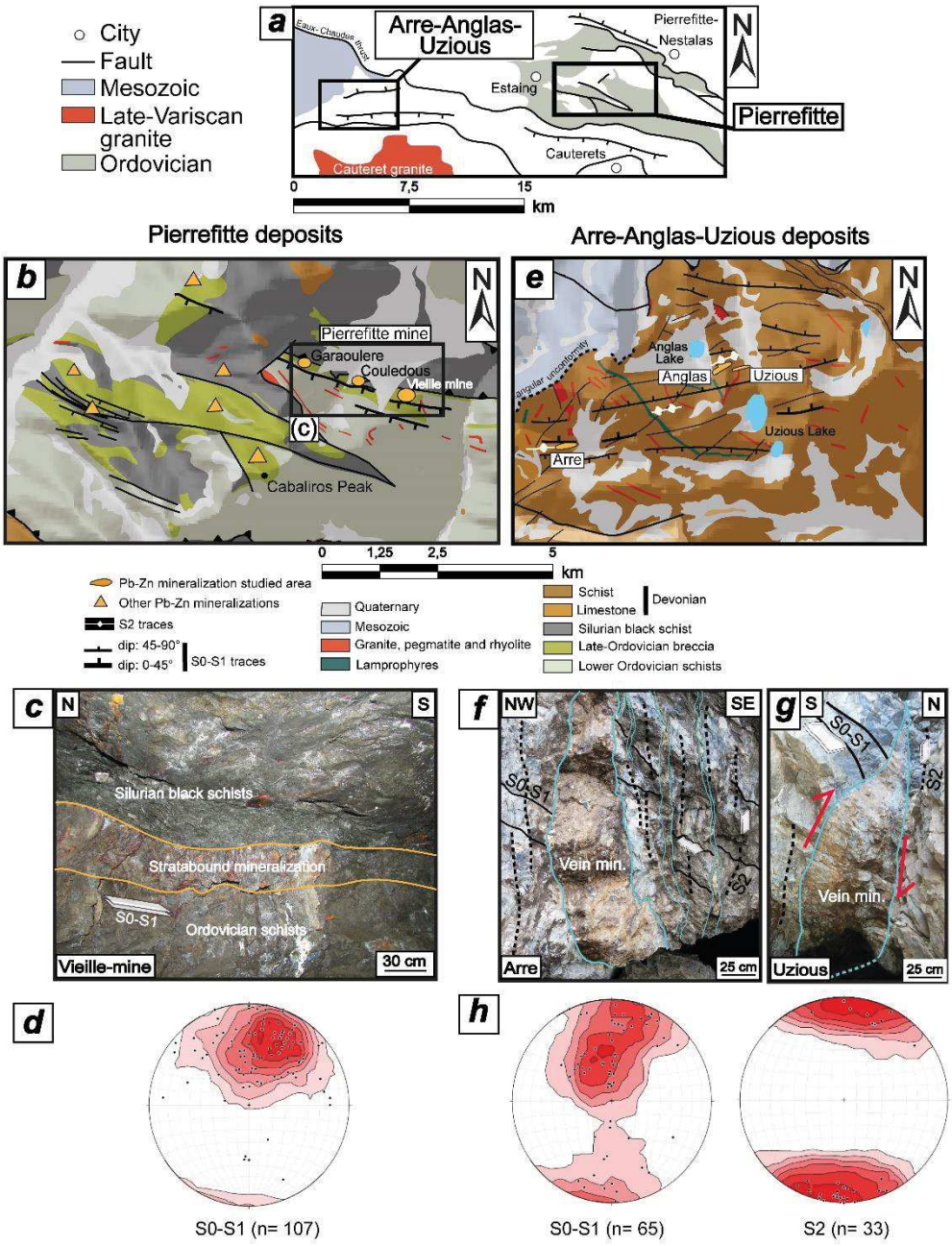

Figure 52. The Pierrefitte anticlinorium. (**a**) Simplified structural map showing the location of (**b**) and (**e**); (**b**) structural map zoomed on Pierrefitte mine (Lithologies are based on BRGM geological maps; *Barrere et al., 1980*); (**c**) photograph of typical stratabound Pb-Zn mineralization in Pierrefitte mine; (**d**) Schmidt stereographic projections (lower hemisphere) of poles to S_0-S_1 foliations measured in the Pierrefitte anticlinorium; (**e**) structural map of the Pierrefitte-Valentin anticlinorium zoomed on Anglas-Uzious and Arre mines (Lithologies are based on BRGM geological maps); (**f**) photograph of Arre vein mineralization parallel to S_2 cleavage; (**g**) photograph of Anglas-Uzious vein mineralization; and (**h**) Schmidt stereographic projections (lower hemisphere) of poles to S_0-S_1 and S_2 foliations measured in Anglas-Uzious and Arre areas.

4.2.5.2 Arre-Anglas-Uzious District

Arre and Anglas-Uzious mines are hosted by Devonian schists and Lower Devonian limestone respectively (Figure 52E). S_2 cleavage is well-expressed even in Devonian limestone in the area and subvertical with a N090–100°E trend.

Arre mine is located in the western hinge of the Pierrefitte anticlinorium close to the contact of limestone and schistose rocks. The mineralization is composed of two ore bodies showing a trend of N040–090°E and a dip of 70°N to 90°N. Mineralization appears parallel to S_2 cleavage and discordant to S_0-S_1 (Figure 52F) which is typical of a vein mineralization. Anglas and Uzious mines are located in the northern part of the Pierrefitte anticlinorium. Mineralization consists in multiple pluri-centimeters to m vein orebodies, with several orientations from N060° to N100°E and subvertical dips. Uzious veins intersect magmatic aplite with a N050°E trend and have a pull-apart geometry (Figure 52G) linked to the presence of N090–100°E S_2 weak structures (Figure 52H). Many conjugate fractures N030–50°E with various dips are filled with mineralization close to the veins but their extension is limited to few dm.

4.2.6 Ore petrology and Microstructures

A synthetic paragenetic sequence of the three Pb-Zn mineralization geometries investigated in this study is presented in the Figure 53. Disseminated mineralization represents the primary layered ore that is essentially composed of sparsely disseminated pluri-µm to mm grains of sphalerite, pyrite, magnetite, and galena. In all the studied deposits this mineralization is minor and does not constitute the exploited ore. Sulfides may appear in graded-beds or have a typical framboidal appearance (Figure 54A).

Stratabound and vein mineralizations constitute the main sulfides mineralizations. Sphalerite is the more widespread sulfide in these two mineralizations. Pyrite, galena pyrrhotite, chalcopyrite, and arsenopyrite are present in minor amounts. Metamorphic muscovite, chlorite, or biotite are intimately associated to sulfide mineralization. In Victoria-Solitaria, metamorphic Zn-spinel or gahnite is present in the host rocks and in breccia clasts in stratabound sulfide mineralization. The presence of gahnite in Victoria was previously reported (*Alvarez-Perez et al. 1974*). In the host rock gahnite is elongated parallel to S_1 and is intersected by stratabound mineralization (Figure 54B).

Stratabound Pb-Zn mineralization is a post-disseminated mineralization. SEM images show a primary framboidal galena intersected by a secondary stratabound pull-apart mineralization in the Bentaillou mine (Figure 54A).

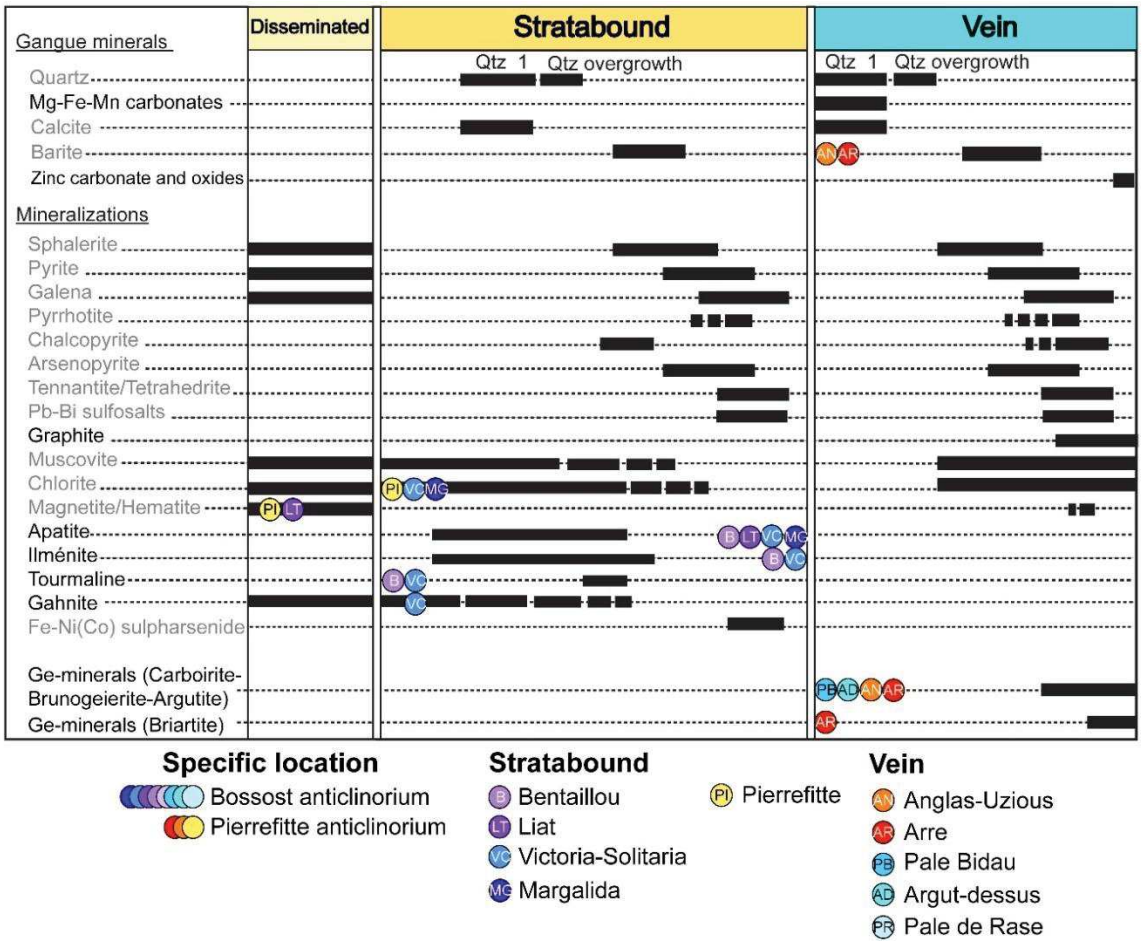

Figure 53. Paragenetic succession of ore and gangue minerals for all the eleven Pyrenean-studied Pb-Zn deposits. Minerals in grey are common to both stratabound and vein mineralizations and minerals in black are only present in stratabound or vein. Minerals only reported in a deposit are noted with the deposit circle. Several minerals like apatite, ilmenite, or tourmaline are only present in stratabound mineralization. Ge-minerals, graphite zinc carbonates or oxides, and Mg-Fe-Mn carbonates are only observed in vein mineralization (n = 110).

In the Pierrefitte anticlinorium stratabound magnetite is abundant, especially in the Pierrefitte mine. In the Pierrefitte mine syn-cinematic sphalerite crystallizes in asymmetric pressure shadows around a clast of magnetite (Figure 54C). It has crystallized prior to sphalerite. Sphalerite appears parallel to S_1 cleavage and intersects S_0 stratification in an isoclinal F_1 fold hinge (Figure 54D). In the Bossòst anticlinorium and especially in Liat mine, sphalerite and quartz mineralization intersect F_2 folded pelitic rocks (Figure 54E). The same quartz associated to sphalerite is present in crack and seal veins (Figure 54E). In Margalida a typical durchbewegung texture with quartz spheroids in a sphalerite matrix shows a deformational imprint on this mineralization.

Stratabound mineralization contain apatite, ilmenite, and tourmaline minerals that are only observed in this mineralization. In the Pierrefitte mineralization, the abundance of chlorite and muscovite associated to the mineralization is remarkable compared to other Pyrenean deposits.

Vein mineralization intersects S_0 at the micron scale (Figure 54F). In the Anglas deposit, vein mineralization is essentially composed of sphalerite, galena, quartz and calcite. The hanging wall of the vein is parallel to S_2 foliation and is marked by cordierite crystallization. Sphalerite in vein mineralization appears highly deformed and recrystallized with mm relictual grains and recrystallized μm-size crystals (like in Arre deposit, see Figure 54G). In Pale Bidau deposit, vein mineralization is only present in domains where the S_2 cleavage is well-marked. Note that Ge-minerals are exclusively present in the vein mineralization (Figure 53).

4.2.7 Discussion

4.2.7.1 Types of Pb-Zn Mineralizations in the PAZ

The presence of three major types of Pb-Zn mineralizations is demonstrated in this study: Disseminated but layered mineralization, which is now defined as Type 1, appears with graded-beds and framboidal appearance (Figure 54A). Stratabound mineralization (now defined as Type 2a) is a syn-D_1 mineralization concordant to the S_1 foliation. Vein mineralization (now defined as Type 2b) is a syn- to post-D_2 vein-type mineralization, parallel to the subvertical S_2 foliation. Type 2a and Type 2b are undoubtedly epigenetic and were formed as a consequence of Variscan tectonics.

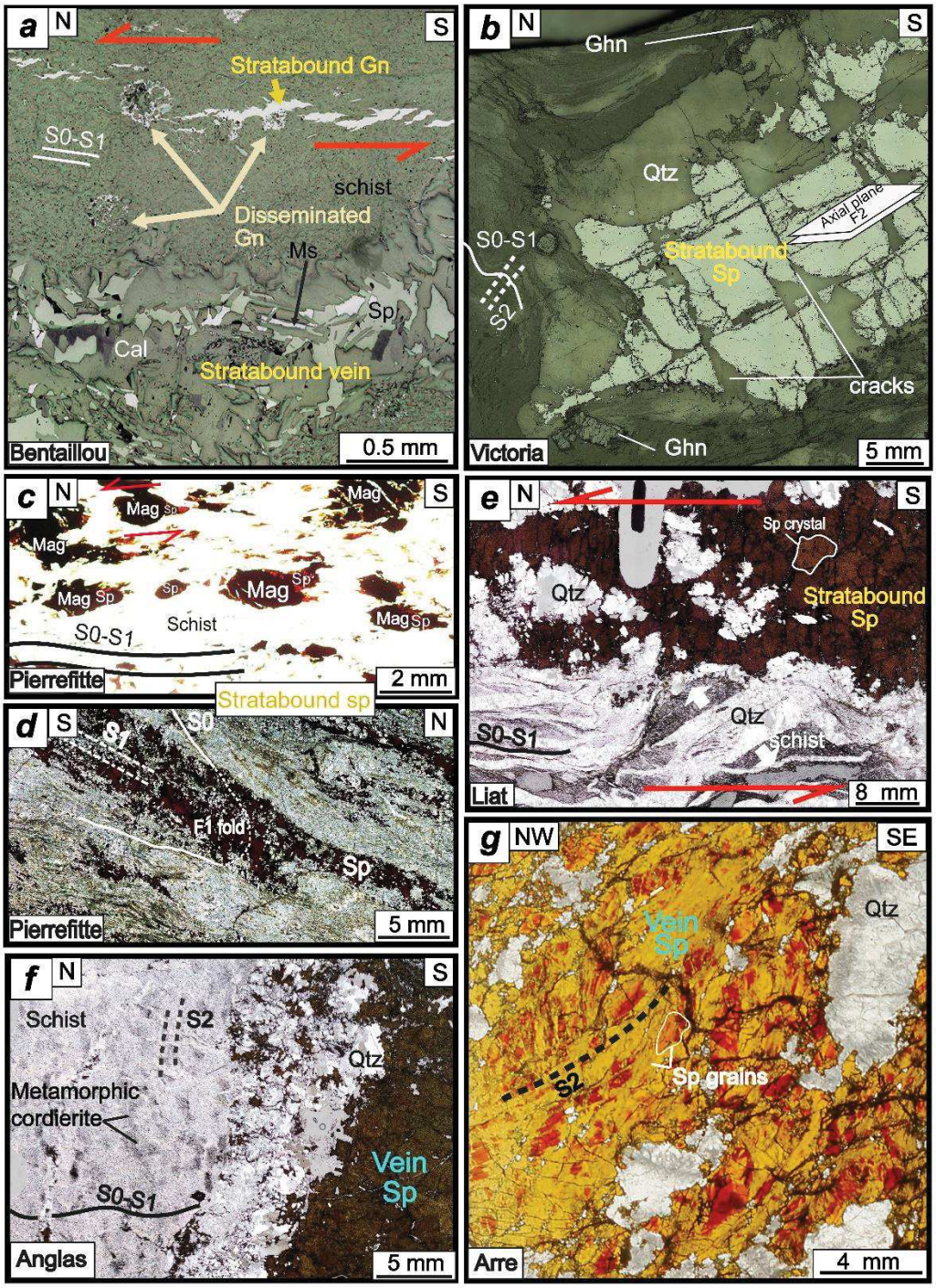

Figure 54. Microphotographs showing characteristics textures in the three mineralization types. (**a**) Bentaillou disseminated mineralization truncated by stratabound mineralizations (reflected light); (**b**) stratabound Victoria folded mineralization which intersects gahnite D_1 metamorphic mineral (reflected light); (**c**) syn-kinematic sphalerite which crystallizes in asymmetric pressure shadows around clasts of magnetite in Pierrefitte mine (transmitted light); (**d**) sphalerite mineralization from Pierrefitte mine parallel to S_1 and in F_1 isoclinal fold hinge. Mineralization intersects S0 stratification (transmitted light); and (**e**) stratabound sphalerite and quartz mineralizations which intersect pelitic host rock in Liat mine. Sphalerite is interpreted syn-kinematic D_1 (transmitted light); (**f**) vein mineralization in Anglas mine which intersect S_0-S_1 and parallel to S_2 cleavage marked by metamorphic cordierite (transmitted light); and (**g**) deformed and recrystallized vein sphalerite in Arre deposit. The two textures are identified with white line Recrystallization area in yellow marked S_2 cleavage (transmitted light). Mineral abbreviations: Cal—Calcite; Ghn—Gahnite; Gn—Galena; Mag—Magnetite; Ms—Muscovite; Qz—Quartz; Sp—Sphalerite.

The first and earlier Type 1 mineralization (Figure 55) is recognized in all the studied deposits in the Bossòst and Pierrefitte anticlinoriums, but it is not the main exploited resources. Its formation may be linked to the early volcanic Ordovician or Devonian events as proposed by *Pouit (1978)* and *Reyx (1973*). In Pierrefitte anticlinorium, *Nicol et al. (1997)* proposed a unique Devonian source for the Pb-Zn mineralizations. Syngenetic formation is preferred for the Type 1 mineralization as sulfides appear layered and with sedimentary affinities. Nevertheless, framboidal texture may as well form in a post-sedimentation environment like in hydrothermal veins (*Scott et al. 2009*).

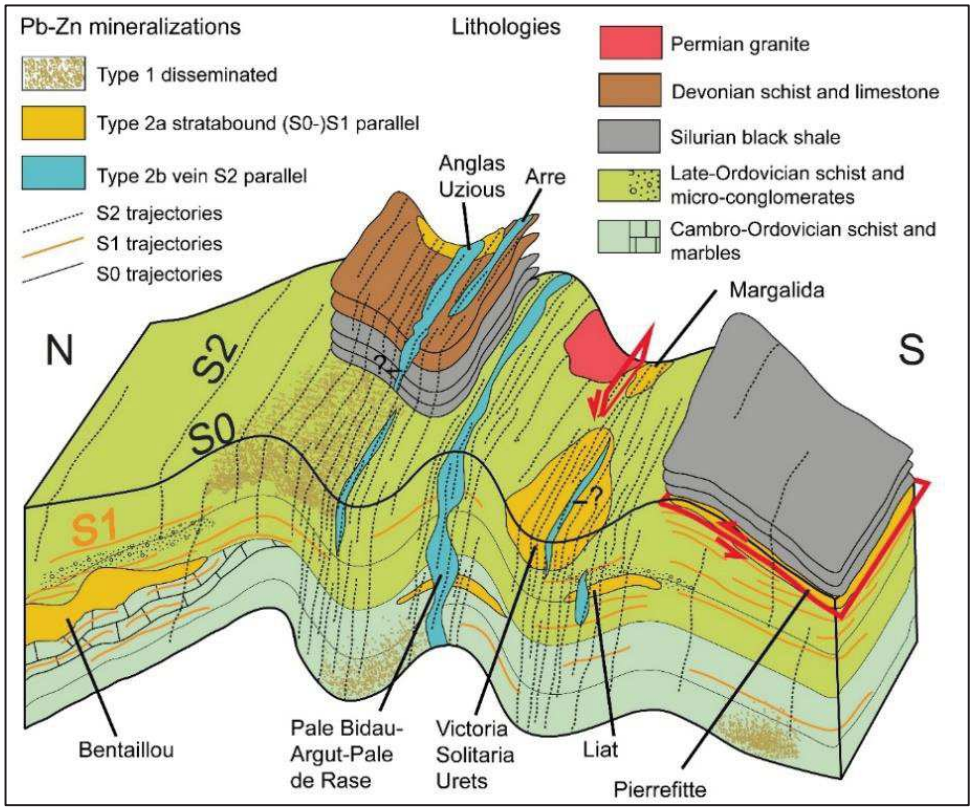

Figure 55. Schematic 3D sketch displaying the three main mineralization types which are typically observed in the studied area and related to each studied deposit. Note centimetric to pluri-metric pull apart geometries in Bentaillou Type 2a mineralizations and in Type 2b mineralizations. Type 2b vein mineralizations are located in intensely S2 deformed domains. Other structural traps like saddle-reef formation in fold hinge or rock competence interfaces are represented for Victoria-Solitaria, Urets, Pierrefitte, and Liat deposits respectively.

The second stratabound Type 2a mineralization (Figure 55) is deposited parallel to S0-S1. It corresponds to the main Pb-Zn mineralization episode in the PAZ (~95% of the total exploited ore volume). In the Bentaillou area, Type 2a mineralization intersects S0 stratification and is hosted by S1 cleavage (Figure 4e), which is axial planar to isoclinal F1 folds. *Fert (1976)* and *(Pouit 1978, 1986*) proposed a syngenetic model for the Bentaillou deposit and described a normal stratigraphic

succession that has been later folded by F2 folds. F1 isoclinal recumbent N090°E folds are absent in their model. Here we observe that Bentaillou Pb-Zn mineralization is localized essentially close to F1 fold hinges at the interface between marble and schist or microconglomerate (Figure 49C). The source for Type 2a sulfides may be related to layered and supposed syngenetic Type 1 sulfides that are disseminated in the Ordovician and Devonian neighboring metasediments, or to Late-Variscan granitic intrusions, probably at least temporally close to the Type 2a mineralizations. Opening of top to the north centimetric to pluri-metric pull-apart-type structures (Figure 49C) enables the formation of the large amount of mineralizations in Bentaillou. Pb-Zn ore is not observed at the base of Bentaillou marbles due to important karstification (Cigalere cave, Figure 48A), however it is deposed at Bularic (*Vernhet 1981*) both above and below this marble level. In the Liat area, *Pujals (1992)* described a syngenetic or diagenetic mineralization with apparent limited reworking. Our model shows that Type 2a stratabound mineralization is linked to the Variscan D1 deformation. In the Victoria-Solitaria area, Type 2a stratabound mineralization occurs where D2-related structures are present and can be locally remobilized in fold hinges. These thicker mineralizations in fold hinge may be linked to the saddle-reef process *(Windh 1995; Bull and Large 2015; Zeng et al. 2018*) associated with formation of the dilatation zone during folding. These deposits have been studied by *Pujals (1992)*, *Cardellach and Alvarez-Perez (1979), Cardellach et al. (1982)*, *Alvarez-Perez et al. (1977)*, and *(Ovejero Zappino 1987, 199*1). These authors argued for a SEDEX origin based on syngenetic mineralization associated to the presence of syn-sedimentary faults. These models differ from our hypothesis: here we report that S_1 cleavage is parallel to axial plane of recumbent km-size isoclinal folds and transposes the S_0 stratification. F_2 folded Type 2a stratabound mineralization is thicker in fold hinge and intersects metamorphic minerals as gahnite. Presence of this Zn-spinel may be linked to a primary minor sulfide mineralization (Type 1, Figure 55) or to a D_1 metamorphic fluid rich in Zn. Chemistry of gahnite was analyzed by (*Pujals 1992*) and its composition is typical to metamorphosed zinc deposits. This testifies that Type 2a Pb-Zn mineralization is syn- to post-M_1 metamorphism. *Alonso (1979)* demonstrated a predominant role of mechanical remobilization associated to deformation in the Bossòst anticlinorium and, especially, F_2 folds in Horcalh and fault in Liat. Our model is similar as we consider that the Variscan D_2 deformation locally remobilized Type 2a mineralization. The Margalida deposit records an additional deformational event compared to Victoria and Solitaria. Hosted in a ductile deformed marble and close to the Bossòst ductile fault, the Type 2a mineralization appears largely deformed with a typical durchbewegung texture. No sedimentary structure is recognized in the marble (*Alvarez-Perez et al. 1977*). This attests for a Late Hercynian and/or Pyrenean deformation associated to the fault on the mineralization. Comparison with the Pierrefitte anticlinorium shows

the same syn-D_1 Type 2a mineralization associated to regional thrust tectonics. The main exploited Pb-Zn mineralization in Pierrefitte mine was pluri-m scale levels parallel to S_0-S_1 and the regional thrust (Figure 55). Our work comforts the study of Nicol et al. (1997) which has shown an important remobilization of the mineralization in Ordovician and Devonian metasediments linked to D_1 deformation. On the contrary, *Bois et al. (1976)* proposed a syngenetic deposition related to the activity of Late-Ordovician syn-sedimentary faults and volcanism that may have induced these mineralizations. In this case, remobilization is weak and sulfides crystalize prior to Variscan metamorphism *Bois et al. (1976)*. But the presence of sphalerite parallel to S_1 cleavage and in pressure shadows around magnetite clast concordant to S_1 rather attests for a syn-D_1 mineralization event.

The third Type 2b vein mineralization (Figure 55) is parallel to S_2 cleavage. It intersects S_0-S_1 cleavage and former Type 2a stratabound mineralization. It has been recognized in the Pale Bidau-Argut-Pale de Rase districts (Cugerone et al. 2018a) and Arre-Uzious-Anglas districts. It appears in a limited number of deposits in the PAZ. Type 2b mineralization is present in pluri-dm veins with restricted extension and highly differs structurally and mineralogically. The presence of Ge-minerals and absence of apatite, tourmaline, or ilmenite are remarkable here. Nonetheless, possible Type 2a remobilization with external contribution is not excluded in the Type 2b vein formation. In the Uzious mine mineralization intersects magmatic aplite. Therefore it has probably emplaced syn- or post-Cauteret granite and is certainly late-Variscan in age (aplite from late-Variscan Cauteret granite) as supposed by *Reyx (1973)*. Deformation of sphalerite, which is supposed to be syn-D_2 and/or syn-D_3, and the unusual sulfide paragenesis are inconsistent with a Mesozoic age as described in Aulus-Les Argentieres undeformed sphalerite (Munoz et al. 2016). Other Pb-Zn deposits, like the La Gela deposit (*Militon 1987*) or Carboire deposit, could be attached to this third type as they are characterized by vertical Pb-Zn veins and presence of Ge-minerals. These late-Variscan Pb-Zn deposits have been recognized in Saint-Salvy (cf M_2 mineralization) even if the main Pb-Zn mineralization event is Mesozoic (*Munoz et al. 1994*).

4.2.7.2 Genetic Model of PAZ Pb-Zn Deposits Formation Linked to Regional Geology

The genetic model comprises four stages (Figure 56) based on the regional tectonic event model of *Mezger and Passchier (2003)* and *Garcia-Sansegundo and Alonso (1989)*.

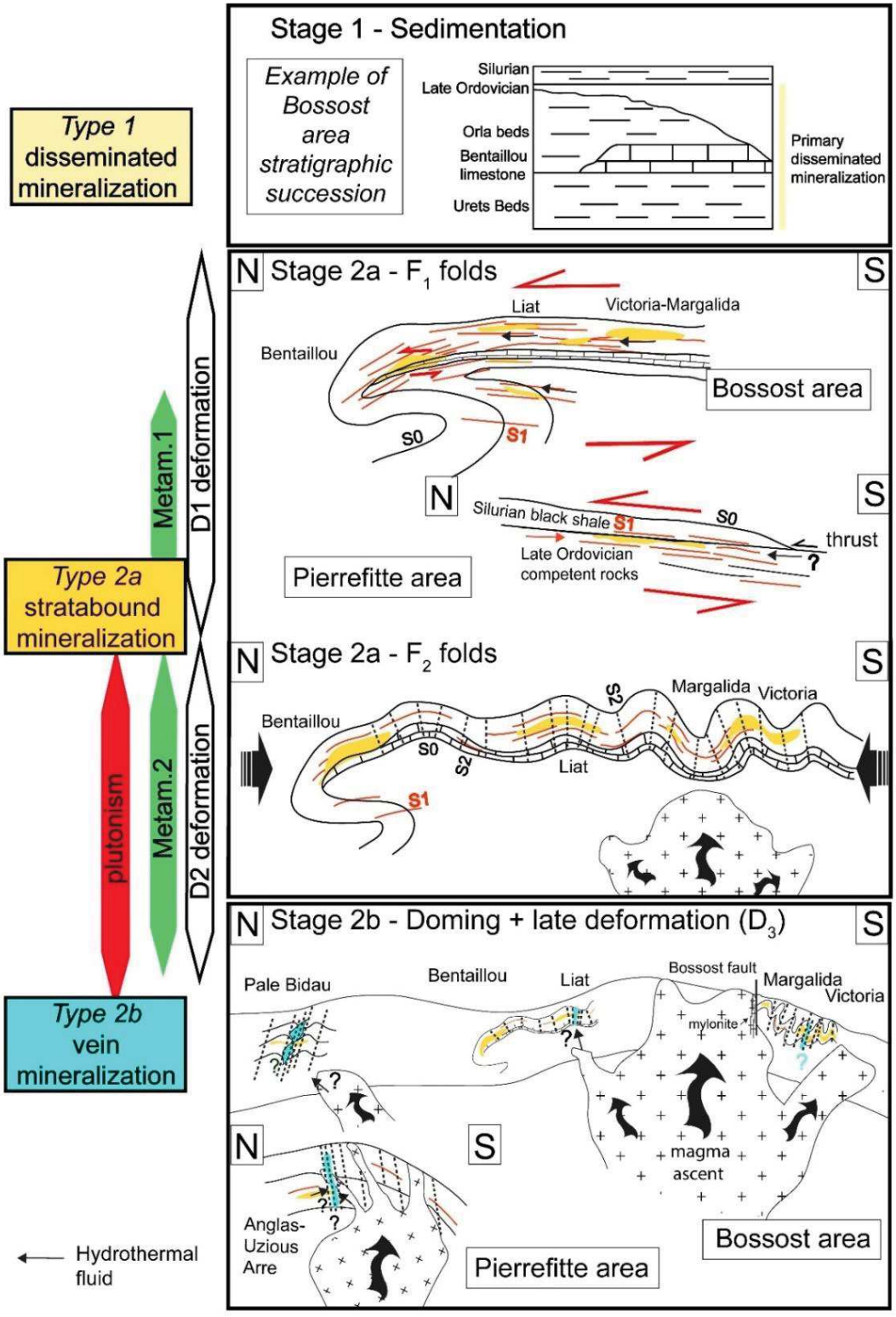

Figure 56. Genetic model for the formation of the three main Pb-Zn mineralization types. **Stage 1** is the disseminated Type 1 mineralization that is supposed to be syn-sedimentary. **Stage 2a** is the syn-D_1 Type 2a stratabound mineralization which is followed by the formation of F_2 folds and local remobilization of Pb-Zn mineralizations (saddle reef). **Stage 2b** represents the Type 2b late-Variscan vein mineralizations.

Stage 1 represents the syn-sedimentary layered mineralization (SEDEX deposit, Pb-Zn Type 1 disseminated mineralization). Primary sulfides were recognized in all pre-Silurian stratigraphic succession in the Bossòst area (Figure 56) and in Devonian rocks in Anglas-Uzious-Arre district. In the Pierrefitte area primary sphalerite is absent, which is probably linked to important hydrothermal low-grade alteration and D_1 overprint.

Stage 2a starts during the D_1 Variscan deformation and induces Type 2a stratabound mineralization. This mineralization occurs preferentially where a rheological contrast exists between two lithologies (e.g. marble-schist; schist-microconglomerates) and in highly D_1 deformed area (Figure 56). Stage 2a continues with D_2 Variscan deformation and the formation of N090–110°E F_2 upright folds. Granitic intrusions occur at that stage (Figure 56). This D_2 deformation locally reworked mineralization like in Victoria mines where the mineralization is remobilized in fold hinges. Horcalh mineralized fault (*Alonso 1979*) is interpreted as synchronous to D_2 deformation.

Stage 2b occurs during the doming phase and the late-Variscan Type 2b vein mineralizations (Figure 56). This mineralization type preferentially occurs parallel to the vertical S_2 cleavage and is mostly observed in the Pierrefitte and Bossòst anticlinoriums. Pull-apart-type structures are observed in Pale Bidau and Uzious mines. A late deformation D_3 corresponds to faults like the Bossòst mylonitic fault close to Margalida district.

We have shown that the Pb-Zn deposits in the PAZ were polyphased and closely linked to Variscan tectonics. There are at least three Pb-Zn mineralization-forming events, and two of them are evidently structurally controlled. Type 1 may be syngenetic, but little ore is present. The main exploited ores are Type 2a and Type 2b which have emplaced under a marked structurally control, either associated to S_1 and trapped in F_1 fold hinge, at lithology interface or in highly D_1 or D_2 deformed areas.

4.2.7.3 Is Pb-Zn Deposits Emplacement Sedimentary- or Structurally-Controlled?

SEDEX deposits are sedimentary controlled and syn- to diagenetic, and sulfides in them are laminated and included into the bedding (*Leach 2005*). In our study area, Pyrenean Pb-Zn mineralizations have been previously described as SEDEX by many authors *(Pouit 1974, 1986; Bois et al. 1976; Cardellach et al. 1982; Pouit and Bois 1986b)*. The origin of several world-class Pb-Zn deposits is debated as well. For example, the geneses of Broken Hill-type deposit (Lawrence 1973; Haydon and Mcconachy 1987; Bodon 1998a; Hobbs et al. 1998; Walters and Bailey 1998; Gibson

and Nutman 2004; Webster 2004) or Jinding deposit (*Shi et al. 1983; Wang et al. 1992; Kyle and Li 2002; Chi et al. 2005, 2012; Xue et al. 2007; Leach et al. 2017*) are still not understood and the authors have not yet decided between syngenetic or epigenetic models. In the Pyrenees, authors interpreted stratiform and lenses ore body shapes. The stratiform argument is not relevant because frequently S_0 stratification is parallel to the S_1 axial plane of isoclinal recumbent folds, typical of intensively deformed areas. Crystallization of sphalerite secant to isoclinal recumbent fold hinges attests that the main mineralization is parallel to S_1 and not to S_0. Structural observations are supported by the mineralogical study. The three PAZ Pb-Zn mineralization types contain the same constitutive minerals, like sphalerite, galena, and pyrite, but various trace minerals are present according to the type. These mineralogical differences are key parameters to distinguish between different Pb-Zn mineralization events in a single deposit.

In intensely deformed and metamorphosed terranes, the simple geometric link between mineralization and stratification is not relevant enough to distinguish between sedimentary or structural control. Structures are often parallelized due to pervasive tectonic events which makes the structural analysis difficult. Reworking of the ore-body during deformation can have obliterated geochemical tracers like isotopic data, especially Pb isotopes (*Marcoux and Moelo 1991; Kamona et al. 1999; Wagner and Schneider 2002)*. Consequently, a detailed structural study from regional to micro-scale focusing on the relationships between mineralization and cleavages is crucial. Pinpointing locations where structures like cleavage are secant (fold hinge), as well as deciphering textural relations between metamorphic minerals and mineralization, will lead to a better understanding of the ore-body genesis.

4.2.8 Conclusions

Three main types of Pb-Zn mineralizations have been distinguished in the Pyrenean Axial Zone. A minor type (Type 1*)* is a stratiform disseminated mineralization that presents syngenetic characteristics. The two other mineralization types, previously described as SEDEX, are in reality post-sedimentation and formed as a result of Variscan polyphased tectonics: Type 2a is a syn-D_1 stratabound mineralization that is parallel to S_1 foliation. Type 2b is a syn to post-D_2 vein-type mineralization that is parallel to subvertical S_2 cleavage. Structural control is thus a key parameter for the remobilization of Pb-Zn mineralizations in this area like in (D_1 and D_2) fold hinges (saddle reef), high (D_1) deformed zones, rock contrast interfaces, and S_2 cleavages. A multiscale detailed structural study is essential for unraveling the formation of Pb-Zn deposits, especially in deformed and/or metamorphosed terranes.

4.2.9 Acknowledgment

The authors gratefully acknowledge Kalin Kouzmanov and Stefano Salvi for their involvement in the project. We thank the ARSHAL association for Bentaillou mine access and Jean-Marc Poudevigne, Louis de Pazzis, and Bernard Lafage for their precious knowledge of the Pyrenean Pb-Zn mines. We acknowledge Christophe Nevado and Doriane Delmas for thin section preparation. The authors are thankful for the editorial handling of Jax Jiang and for the constructive comments of the three anonymous reviewers.

4.2.10 References

Aerden DGAM (1994) Kinematics of orogenic collapse in the Variscan Pyrenees deduced from microstructures in porphyroblastic rocks from the Lys-Caillaouas massif. Tectonophysics 238:139–160. doi: 10.1016/0040-1951(94)90053-1

Alonso JL (1979) Deformaciones sucesivas en el area comprendida entre Liat y el Puerto de Orla - Control estructural de los depositos de sulfuros (Valle de Aran, Pirineos Centrales). Tesis Licenciatura, Univ Oviedo 26p

Alvarez-Perez A, Campa-Vineta JA, Montoriol-Pous J (1974) Sobre la presencia de gahnita ferrífera en Bossost (Vall D'Aran, Lérida). Acta Geol Hisp 9:111–113

Alvarez-Perez A, Campa-Vineta JA, Montoriol-Pous J (1977) Mineralogénesis de los yacimientos del área de Bossost (Vall d'Aran, Lérida). Acta Geol Hisp 4–6:123–126

Bodon SB (1998) Paragenetic relationships and their implications for ore genesis at the Cannington Ag-Pb-Zn deposit, Mount Isa inlier, Queensland, Australia. Econ Geol 93:1463–1488. doi: 10.2113/gsecongeo.93.8.1463

Bois JP, Pouit G, Gros Y, B. G, Picot P (1976) Les minéralisations de Zn (Pb) de l'anticlinorium de Pierrefitte: un exemple de gisements hydrothermaux et sédimentaires associés au volcanisme dans le Paléozoïque des Pyrénées centrales. Bull du BRGM 6:543–567

BRGM (1984) Les gisements de Pb-Zn français (situation en 1977). BRGM Intern Rep 1–278

Cadarso A (2000) Minéralogie et géochimie des concentrations Zn-Pb exhalative-sédimentaires encaissées dans le Cambrien, l'Ordovicien et le Dévonien des Pyrénées Axiales. PhD Thesis, Univ Toulouse III 423p

Calvet P (1988) Etude structurale et métallogénique de l'anticlinorium de Pierrefitte : influence de la déformation sur les minéralisations stratiformes. Ph D Thesis Univ d'Orléans 283p

Cardellach E (1977) Estudio microscópico de las mineralizaciones de Pb-Zn de Liat, Baguergue y Montoliu. Acta Geol Hisp 12, 4–6, 1:3p

Cardellach E, Alvarez-Perez A (1979) Interpretación genética de las mineralizaciones de Pb-Zn del Ordovícico Sup. de la Vall de Aran. Acta Geol Hisp 14:117–120

Cardellach E, Phillips R, Ayora C (1982) Metamorphosed stratiform sulphides of the Liat area, Central Pyrenees, Spain. Inst Min Metall Trans Sect B Applied Ea:90–95

Carreras J, Capella I (1994) Tectonic levels in the Palaeozoic basement of the Pyrenees: a review and a new interpretation. J Struct Geol 16:1509–1524

Castroviejo Bolibar R, Serrano FM (1983) Estructura y metalogenia del campo filoniano de Cierco (Pb-Zn-Ag), en el Pirineo de Lérida. Boletín Geológio y Min 1983:291–320

Chi G, Qing H, Xue C (2005) An overpressured fluid system associated with the giant sandstone-hosted Jinding Zn-Pb deposit, western Yunnan, China Chapter. Mao J, Bierlein FP (eds), Miner Depos Res Meet Gobal challenge Springer-Verlag, Berlin 93–96. doi: 10.1007/3-540-27946-6

Chi G, Xue C, Qing H, Xue W, Zhang J, Sun Y (2012) Hydrodynamic analysis of clastic injection and hydraulic fracturing structures in the Jinding Zn-Pb deposit, Yunnan, China. Geosci Front 3:73–84. doi: 10.1016/j.gsf.2011.07.003

Cochelin B (2016) Champ de déformation du socle Paléozoïque des Pyrénées, PhD Thesis Université Toulouse 3 Paul Sabatier

Cugerone A, Cenki-Tok B, Chauvet A, Le Goff E, Bailly L, Alard O, Allard M (2018) Relationships between the occurrence of accessory Ge-minerals and sphalerite in Variscan Pb-Zn deposits of the Bossost anticlinorium, French Pyrenean Axial Zone: Chemistry, microstructures and ore-deposit setting. Ore Geol Rev 95:1–19. doi: 10.1016/j.oregeorev.2018.02.016

Denèle Y, Laumonier B, Paquette J-L, Olivier P, Gleizes G, Barbey P (2014) Timing of granite emplacement, crustal flow and gneiss dome formation in the Variscan segment of the Pyrenees. Geol Soc London, Spec Publ 405:265–287. doi: 10.1144/SP405.5

Dubois C (2015) Mangeuses d'homme. L'épopée des mines de Bentaillou et de Bulard en Ariège, Privat Edition, Privat

Fert D (1976) Un aspect de la métallogénie du zinc et du plomb dans l'Ordovicien des Pyrénées Centrales : le district de Sentein (Ariège, Haute-Garonne). PhD Thesis, Univ Pierre Marie Curie 149p

Garcia-Sansegundo J, Alonso JL (1989) Stratigraphy and structure of the southeastern Garona Dome. Geodin Acta 3:127–134. doi: 10.1080/09853111.1989.11105180

García-Sansegundo J, Martin-Izard A, Gavaldà J (2014) Structural control and geological significance of the Zn-Pb ores formed in the Benasque Pass area (Central Pyrenees) during the post-late Ordovician extensional event of the Gondwana margin. Ore Geol Rev 56:516–527. doi: 10.1016/j.oregeorev.2013.06.001

Gibson GM, Nutman AP (2004) Detachment faulting and bimodal magmatism in the Palaeoproterozoic Willyama Supergroup, south-central Australia; keys to recognition of a multiply deformed Precambrian metamorphic core complex. J Geol Soc London 161, Part:55–66. doi: 10.1144/0016-764903-060

Guerin P (1979) Les minéralisations zincifères de l'Ordovicien de la région de Liat (Val d'Aran, Province de Lérida, Espagne). Ph D Thesis, Univ Pierre Marie Curie 233p

Haydon RC, Mcconachy GW (1987) The Stratigraphic Setting of Pb-Zn-Ag Mineralization at Broken Hill. Econ Geol 82:826–856. doi: 10.2113/gsecongeo.82.4.826

Hazarika P, Upadhyay D, Mishra B (2013) Contrasting geochronological evolution of the Rajpura-Dariba and Rampura-Agucha metamorphosed Zn-Pb deposit, Aravalli-Delhi Belt, India. J Asian Earth Sci 73:429–439. doi: 10.1016/j.jseaes.2013.04.047

Hobbs BE, Walshe JL, Ord A, Zhang Y, Carr GC (1998) The Broken Hill orebody: A high temperature, high pressure scenario. Aust Geol Surv Organ Rec 1998 2:98–103

Kamona AF, Lévêque J, Friedrich G, Haack U (1999) Lead isotopes of the carbonate-hosted Kabwe, Tsumeb, and Kipushi Pb-Zn-Cu sulphide deposits in relation to Pan African orogenesis in the Damaran-Lufilian Fold Belt of Central Africa. Miner Depos 34:273–283. doi: 10.1007/s001260050203

Kelley KD, Jennings S (2004) A special issue devoted to barite and Zn-Pb-Ag deposits in the Red Dog district, Western Brooks Range, northern Alaska. Econ Geol 99:1267–1280. doi: 10.2113/gsecongeo.99.7.1267

Kleinsmiede WFJ (1960) Geology of the Valle de Aran (Central Pyrenees). Leidse Geol Meded 25:129–245

Kyle JR, Li N (2002) Jinding : A Giant Tertiary Sandstone-Hosted Zn-Pb deposit, Yunnan, China. SEG Newsl 50:1–9

Lawrence LJ (1973) Polymetamorphism of the sulphide ores of Broken Hill, NSW, Australia. Miner Depos 8:211–236

Leach DL (2005) Sediment-Hosted Lead-Zinc Deposits : A Global Perspective. Econ Geol 561–607. doi: 978-1-887483-01-8

Leach DL, Song YC, Hou ZQ (2017) The world-class Jinding Zn–Pb deposit: ore formation in an evaporite dome, Lanping Basin, Yunnan, China. Miner Depos 52:281–296. doi: 10.1007/s00126-016-0668-6

Marcoux E (1986) Isotope du plomb et paragénèses métalliques, traceurs de l'histoire des gites mineraux. Bur Rech Geol Minière 117:1–289

Marcoux E, Moelo Y (1991) Lead isotope geochemistry and paragenetic study of inheritance phenomena in metallogenesis: examples from base metal sulfide deposits in France. Econ Geol 86:106–120. doi: 10.2113/gsecongeo.86.1.106

Mezger JE (2005) Comparison of the western Aston-Hospitalet and the Bossòst domes: Evidence for polymetamorphism and its implications for the Variscan tectonic evolution of the Axial Zone of the Pyrenees. J Virtual Explor 19:1–19. doi: 10.3809/jvirtex.2005.00122

Mezger JE, Passchier CW (2003) Polymetamorphism and ductile deformation of staurolite–cordierite schist of the Bossòst dome: indication for Variscan extension in the Axial Zone of the central Pyrenees. Geol Mag 140:595–612. doi: 10.1017/S0016756803008112

Mezger JE, Schnapperelle S, Rölke C (2012) Evolution of the Central Pyrenean Mérens fault controlled by near collision of two gneiss domes. Hallesches Jahrb 34:11–29

Militon C (1987) Métallogénie polyphasée à Zn, Pb, Ba, F et Mg, Fe de ma région de Gèdre-Gavarnie- Barroude (Hautes-Pyrénées). Ph D Thesis Univ d'Orléans 413p

Moore DW, Young LE, Modene JS, Plahuta JT (1986) Geologic setting and genesis of the Red Dog zinc-lead-silver deposit, western Brooks Range, Alaska. Econ Geol 81:1696–1727. doi: 10.2113/gsecongeo.81.7.1696

Munoz M, Baron S, Boucher A, Béziat D, Salvi S (2015) Mesozoic vein-type Pb–Zn mineralization in the Pyrenees: Lead isotopic and fluid inclusion evidence from the Les Argentières and Lacore deposits. Comptes Rendus Geosci 348:322–332. doi: 10.1016/j.crte.2015.07.001

Munoz M, Boyce AJ, Courjault-Rade P, Fallick AE, Tollon F (1994) Multi-stage fluid incursion in the Palaeozoic basement-hosted Saint-Salvy ore deposit (NW Montagne Noire, southern France). Appl Geochemistry 9:609–626. doi: 10.1016/0883-2927(94)90022-1

Nicol N (1997) Etude structurale des minéralisations Zn-Pb du Paléozoïque du dôme de Pierrefitte (Hautes-Pyrénées). Goniométrie de texture appliquée aux minéraux transparents et opaques. PhD Thesis Univ Orléans 318p

Nicol N, Legendre O, Charvet J (1997) Les minéralisations Zn-Pb de la série paléozoïque de Pierrefitte (Hautes-Pyrénées) dans la succession des évènements tectoniques hercyniens. CR Acad Sci Paris 324:453–460

Ovejero Zappino G (1991) Mineralizaciones Zn-Pb ordovícicas del anticlinorio de Bossost. Yacimientos de Liat y Victoria. Valle de Arán. Pirineo (España). Boletín Geológico y Minero 102–3:356–377

Ovejero Zappino G (1987) Mineralizaciones Zn-Pb del Ordovicico Superior del Valle de Aran (Anticlinorio de Bossost). Pireneo de Lerida (Espana). Bol Soc Esp Mineral 10:35–37

Pouget P (1991) Hercynian Tectonometamorphic Evolution of the Bosost Dome (French Spanish Central Pyrenees). J Geol Soc London 148:299–314. doi: 10.1144/gsjgs.148.2.0299

Pouit G (1978) Différents Modeles de Mineralisations «Hydrothermale Sédimentaire », à Zn (Pb) du Paléozoïque des Pyrénees Centrales. Miner Depos 13:411–421

Pouit G (1974) Les minéralisations Zn-Pb dans l'Ordovicien des Pyrénées centrales-Etude préliminaire. Rapp BRGM 74 SGN 122:50

Pouit G (1986) Les minéralisations Zn-Pb exhalatives sédimentaires de Bentaillou et de l 'anticlinorium paléozoïque de Bosost (Pyrénées ariégeoises, France). Chron la Rech minière 485:3–16

Pouit G, Bois JP (1986) Arrens Zn (Pb), Ba Devonian deposit, Pyrénées, France: an exhalative-sedimentary-type deposit similar to Meggen. Miner Depos 21:181–189

Pouit G, Fortuné J-P (1980) Métallogénie comparée des Pyrénées et du Sud du Massif-central. In: 26ème congrès géologique international. p 61p

Pujals I (1992) Las mineralizaciones de sulfuros en el Cambro-Ordovicico de la Val d'Aran (Pirineo Central, Lérida). PhD Thesis, Univ Autónoma Barcelona 294p

Reyx J (1973) Relations entre tectonique, métamorphisme de contact et concentrations metalliques dans le secteur des anciennes mines d'Arre et Anglas (Hautes-Pyrénées - Pyrénées atlantiques). Ph D Thesis, Univ Paris VI 83p

Shi JX, Yi FH, Wen QD (1983) The rock-ore characteristics and mineralisation of Jinding lead–zinc deposit, Lanping. J Yunnan Geol 1983

Vernhet Y (1981) Les minéralisations zincifères de l'Ordovicien et du Dévonien du Val d'Orle (District de Sentein, Ariège) et de la région de Fourcaye (Val d'Aran, Espagne). Ph D Thesis, Univ Pierre Marie Curie 279p

Wagner T, Schneider J (2002) Lead isotope systematics of vein-type antimony mineralization, Rheinisches Schiefergebirge, Germany: A case history of complex reaction and remobilization processes. Miner Depos 37:185–197. doi: 10.1007/s00126-001-0211-1

Walters S, Bailey A (1998) Geology and Mineralization of the Cannington Ag-Pb-Zn Deposit: An Example of Broken Hill-Type Mineralization in the Eastern Succession, Mount Isa Inlier, Australia. Econ Geol 93:1307–1329. doi: 10.1016/j.precamres.2007.08.009

Wang JB, Li CY, Chen X (1992) Wang JB, Li CY, Chen X (1992) A new genetic model for the Jinding lead-zinc deposit, Geol Explor Non-Ferrous Metals 1:200–206 (in Chinese with English abstract). Geol Explor Non-Ferrous Met 1:200–206

Webster AE (2004) The Structural Evolution of the Broken Hill Pb-Zn-Ag Deposit , New South Wales, PhD Thesis University of Tasmania. PhD Thesis Univ Tasmania 1–430

Whitney DL, Evans BW (2010) Abbreviations for names of rock-forming minerals. Am Mineral 95:185–187. doi: 10.2138/am.2010.3371

Wilkinson JJ (2013) Sediment-Hosted Zinc-Lead Mineralization: Processes and Perspectives: Processes and Perspectives, Treatise on Geochemistry, Second Edition. Elsevier, H Holland, K Turekian (ed), Amsterdam, Netherlands 219–249. doi: 10.1016/B978-0-08-095975-7.01109-8

Xue C, Zeng R, Liu S, Chi G, Qing H, Chen Y, Yang J, Wang D (2007) Geologic, fluid inclusion and isotopic characteristics of the Jinding Zn-Pb deposit, western Yunnan, South China: A review. Ore Geol Rev 31:337–359. doi: 10.1016/j.oregeorev.2005.04.007

Yalikun Y, Xue C, Symons DTA (2018) Paleomagnetic age and tectonic constraints on the genesis of the giant Jinding Zn-Pb deposit, Yunnan, China. Miner Depos 53:245–259. doi: 10.1007/s00126-017-0733-9

Zwart HJ (1963) Metamorphic history of the Central Pyrenees, Part II, Valle de Aran. Leidse Geol Meded 28:321–376

Zwart HJ (1979) The Geology of the Central Pyrenees. Leidse Geol Meded 50:1–74

4.3 Additionnal fieldwork and mineralogical datas

This section is devoted to additional figures which complete the structural and mineralogical study of the previous paper with the structural field analyses of Pb-Zn deposits in the PAZ. The end of this section shows few QEMSCAN maps in order to improve the mineralogical section, especially in the detection of Ge-minerals.

4.3.1 Stratigraphic position of the Pb-Zn deposits in the Bossost dome

The position of eighteen studied deposits is located in the stratigraphic position (Figure 57). This figure clearly shows that the Pb-Zn deposits are nor related to a specific formation. Numerous deposits are located close or at the contact between two formations (Bentaillou, Liat,

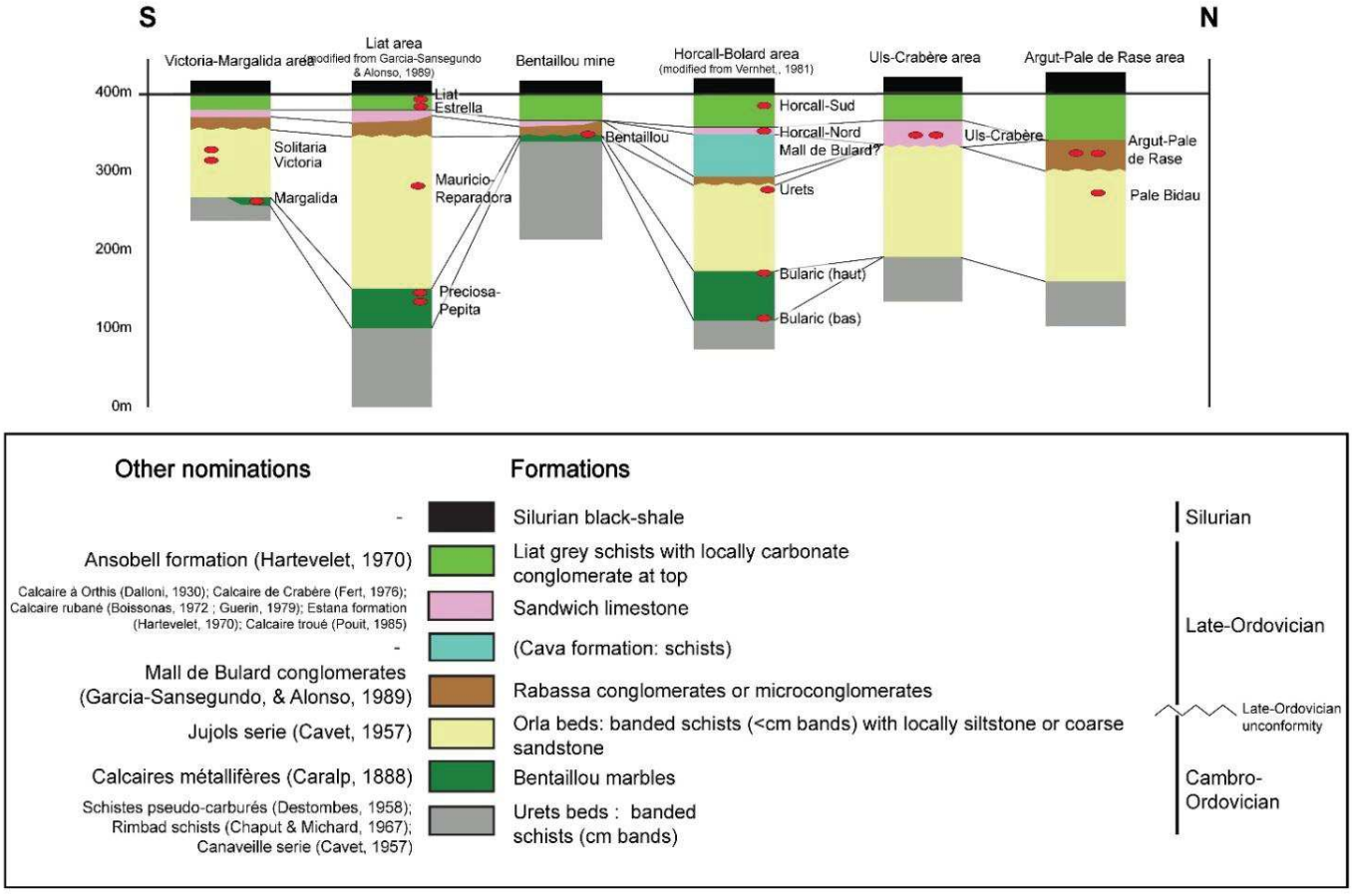

Figure 57. Stratigraphic position of the Pb-Zn deposits reported in the Bossost anticlinorium area.

Urets, etc.), which seem to confirm the importance of particular structures (herein competence contrast) in the apparition of Pb-Zn mineralization.

4.3.2 Bentaillou area

A schematic view of the Bentaillou area is represented in the Figure 58. The main Pb-Zn ore is associated to the N090–110°E kilometer-size F_1 recumbent fold. This large F_1 fold is folded by late F_2 N090°E with vertical deep and an associated axial plane S_2 cleavage. No vertical Pb-Zn mineralizations parallel to S_2 cleavage is observed in the area. Numerous other Pb-Zn stratabound ore bodies are observed but their extension is limited to several meters in length and thickness.

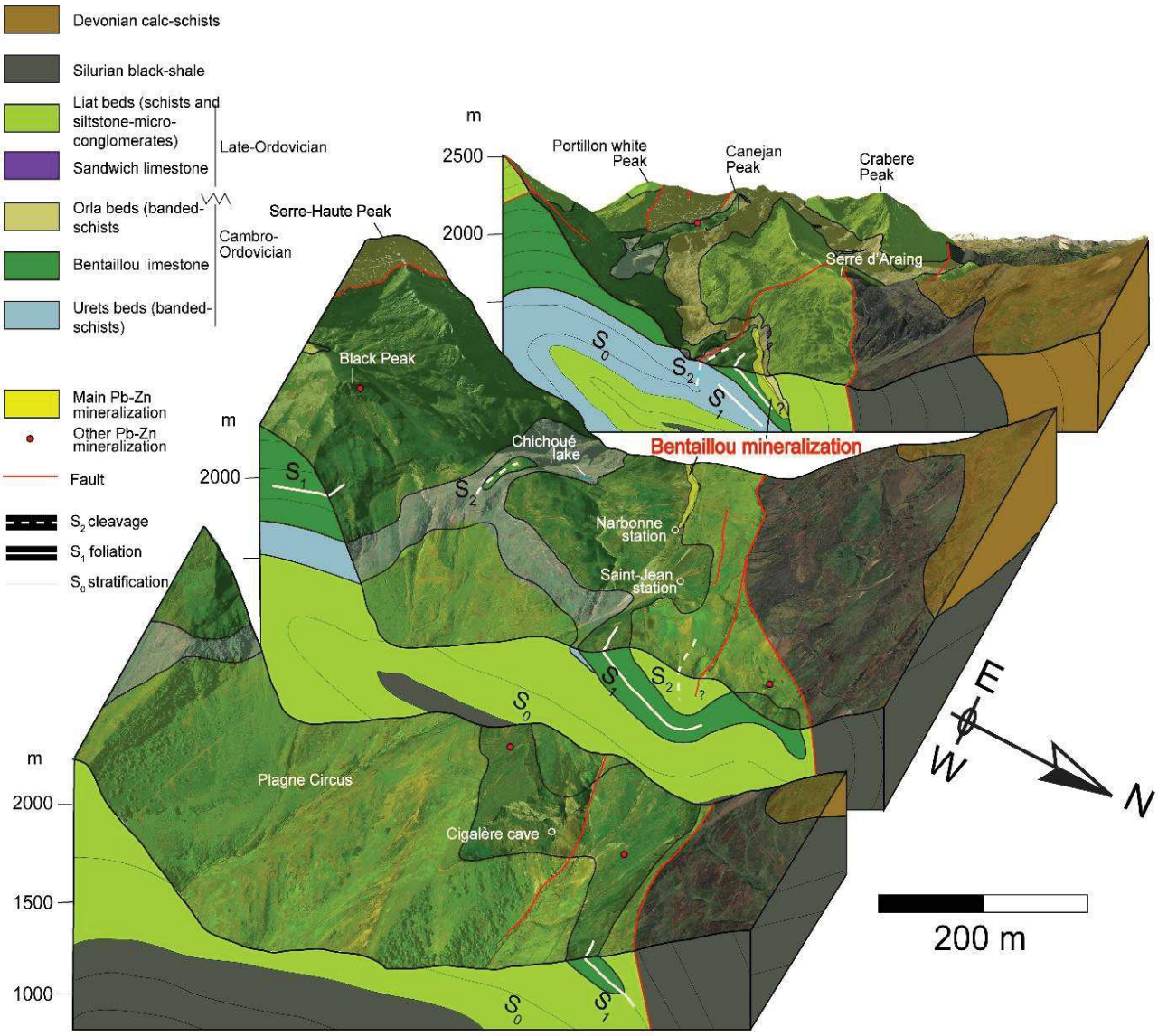

Figure 58: 3D structural bloc representing the geology of the Bentaillou area and the kilometric scale recumbent fold. Position of the Type 2a ore is represented.

4.3.3 Horcall (Fourcaye) area

This area is located at the East of the Bossost anticlinorium (Figure 45), and at the eastern part of the Bentaillou-Liat-Urets district. The Horcall area is well -deformed by D_1 deformation attested by hectometric north verging recumbent F_1 folds visible in a panoramic view between Orle

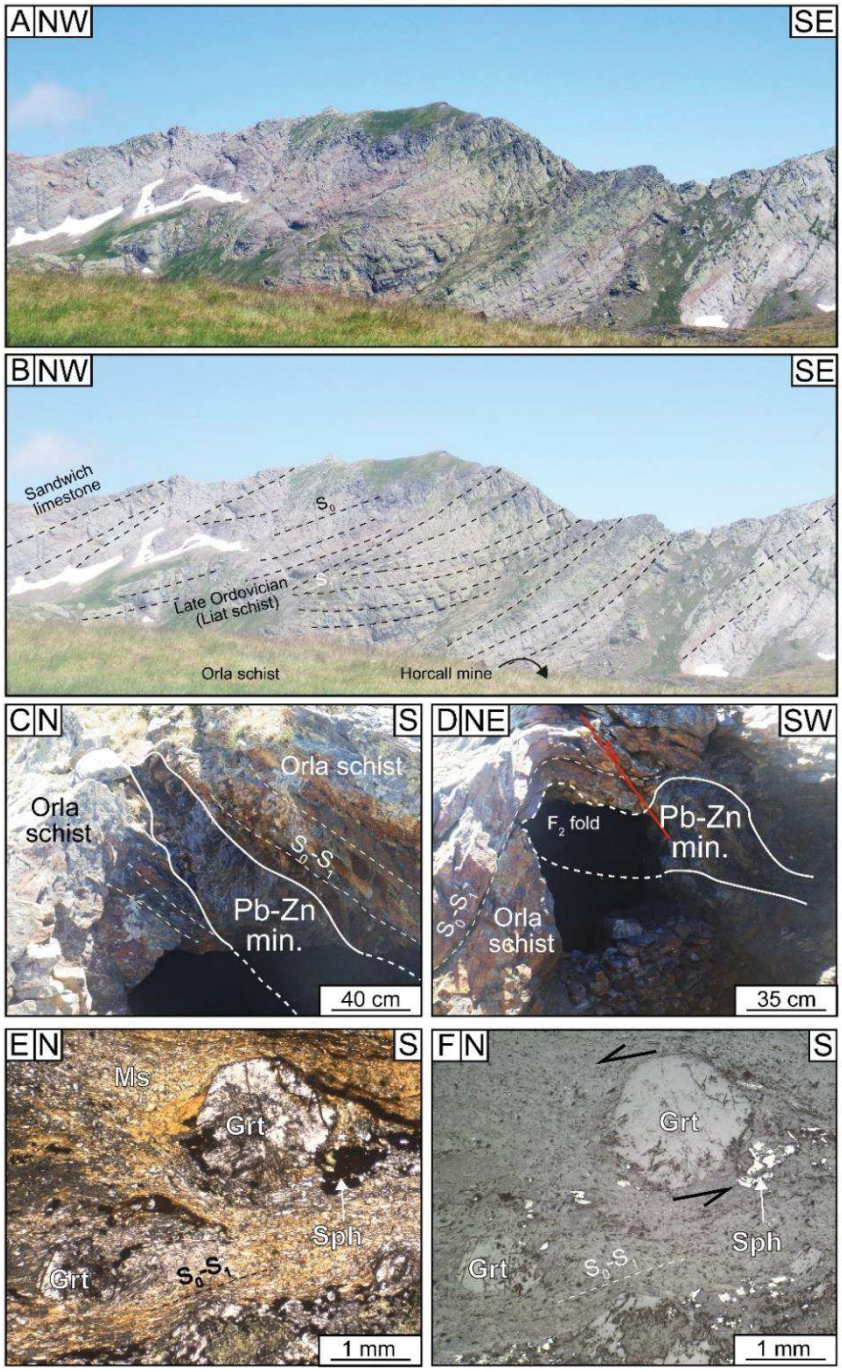

Figure 59. Horcall area. A and B represent panoramic view between Orle port and Malh de Bolard. F_1 recumbent fold are visible in the Liat beds. C. Stratabound Pb-Zn mineralization in Orla schists. D. Folded and faulted Pb-Zn mineralization in Orla schist. E and F are plane-polarized transmitted and reflected microphotographs respectively, of two garnet hosted in micaschist with occurrence of sphalerite in shadow-pressure.

Port and Malh de Bolard (Figure 59A and B). The ore mineralization is hosted in Cambro-Ordovician Orla schists oriented N110°E with various dips and is mainly stratabound (Figure 59C). Some remobilizations marked by F_2 folds (and related faults) are visible on the field (Figure 59D). The mineralization is reconcentrated in fold hinge (saddle reef), and these structures correspond to the main exploitation of the area.

At microscopic scale, metamorphic minerals like garnet are associated to the sphalerite coarse grain mineralization. Sphalerite crystals are observed in shadow-pressure of garnets which indicate a top to the north-kinematic and a sphalerite syn-kinematic (Figure 59E and Figure 59F).

4.3.4 Victoria-Margalida

Victoria-deposit exhibits an important D_2 deformation expressed in metamorphic Cambro-Ordovician to Late-Ordovician schists with apparition of mm to pluri-m N090–N120°E (Figure 60). Numerous galleries are located in fold axis where the ore mineralization is thicker and presence of mineralization parallel to S_2 is questioned even if no Type 2b vein mineralization was observed *in-situ*. Margalida area is different from Victoria deposit with presence of Pb-Zn mineralizations hosted in deformed marble (supposed Late-Ordovician) close to Bossost regional fault.

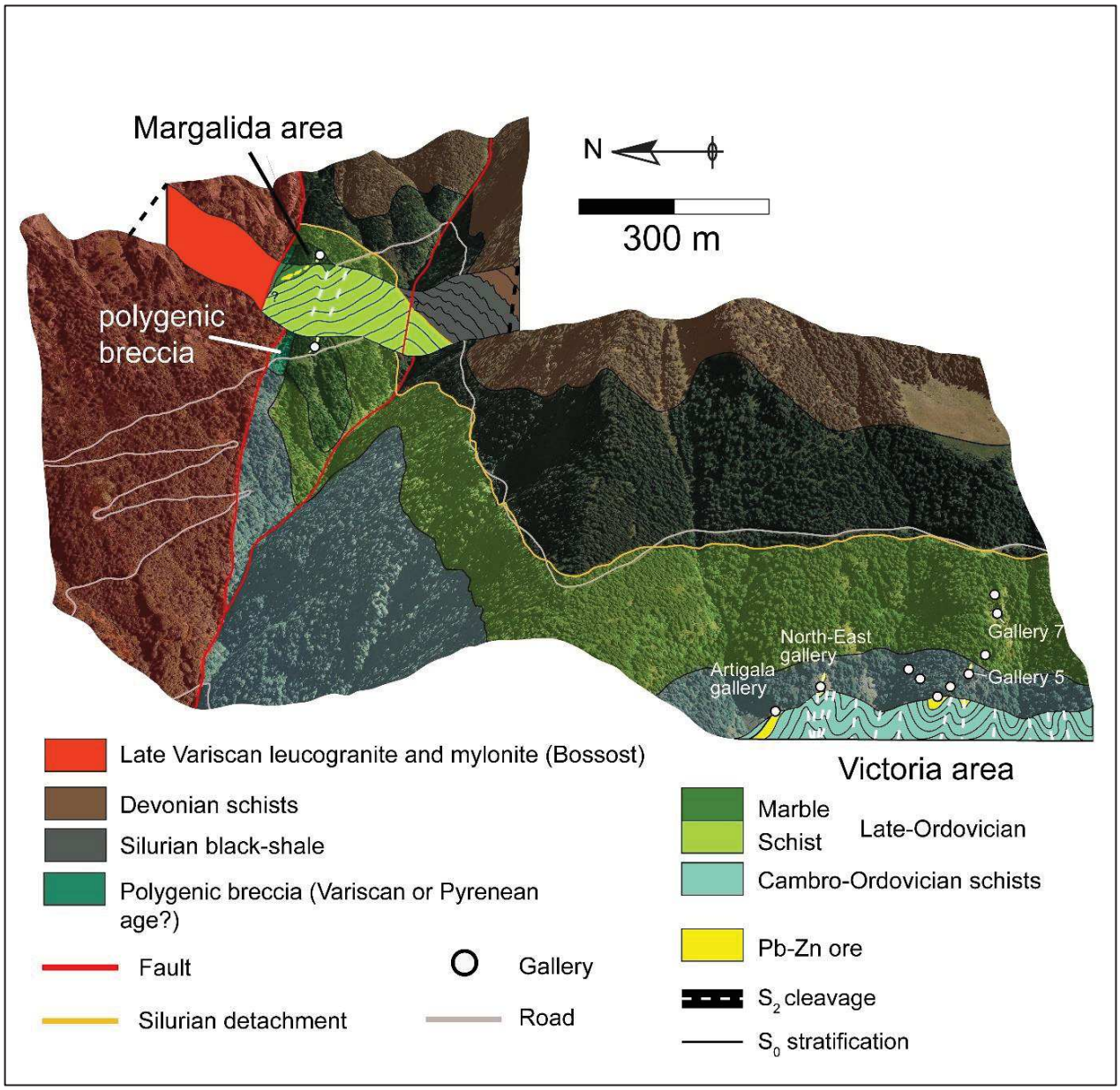

Figure 60 3D structural bloc representing the Victoria-Margalida area with position of the different galleries and Type 2a mineralizations.

4.3.5 Estaing-Arrouy (Pierrefitte anticlinorium)

Estaing-Arrouy deposit is situated at the west of the Pierrefitte mines (Figure 45) and produced 51 000t of Zn, and 46 000t of Pb (*Bois et al. 1976*). Ore mineralization is essentially

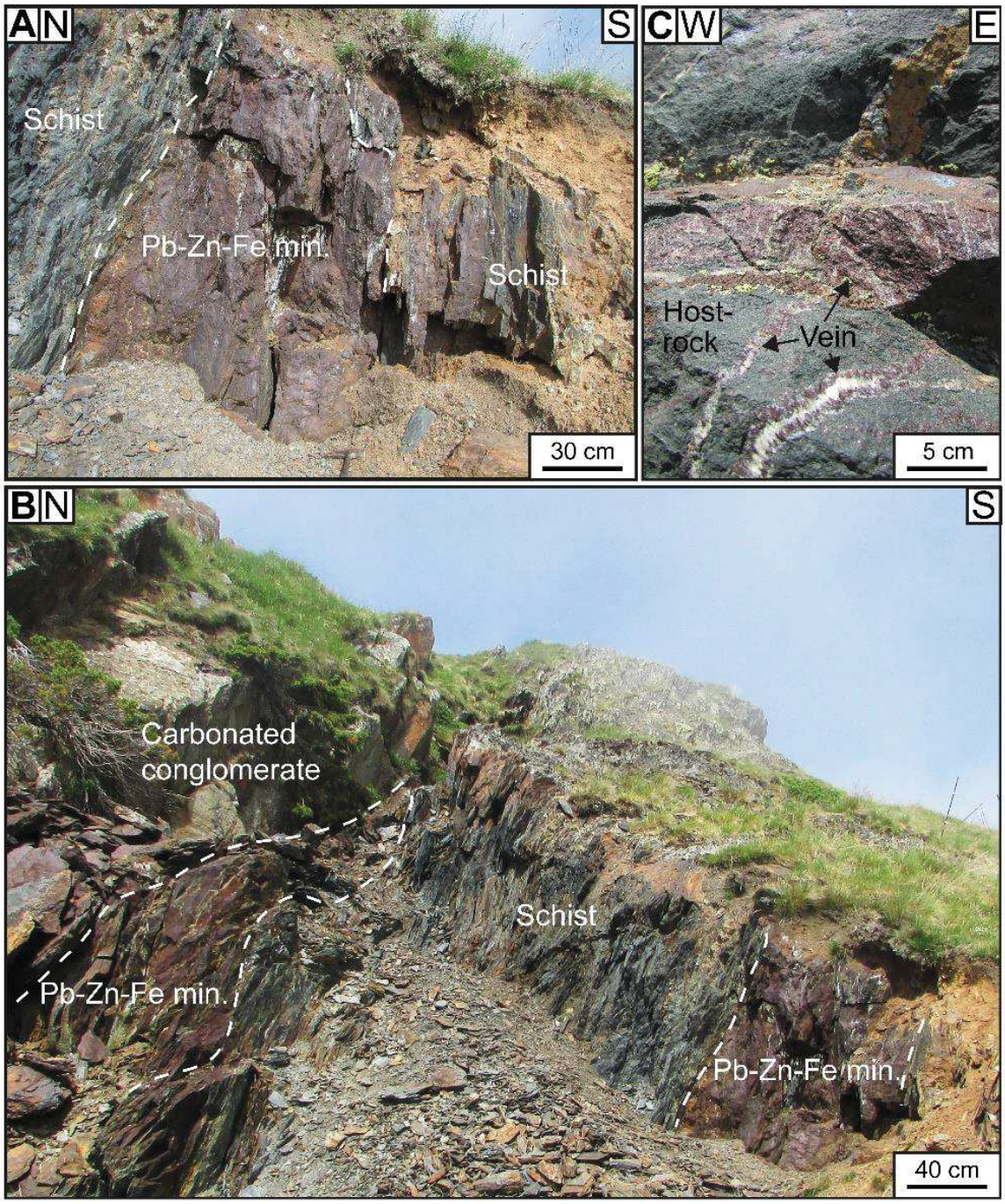

Figure 61. Estaing deposit (Type 2a and/or 2b mineralization). A. Pb-Zn mineralization hosted in Silurian schist. B. Ore mineralization at the contact between carbonated conglomerate and Silurian schist or only in the Silurian schist. C. Mineralization in veins with comb quartz and sphlaerite associated.

composed of sphalerite, magnetite and galena and is hosted at the contact between carbonated conglomerate with rounded clasts associated to rare fuchsite and Silurian low-grade schists (Figure 61A) or locally only in the Silurian schists (Figure 61B). The orientation of S_0-S_1 is N090-100°E with a dip varying between 70°N to vertical. S_2 is vertical in the area and is often parallel to S_0-S_1. Estaing may be Type 2a and/or Type 2b mineralizations. The presence of open-filling texture (Figure 61C) cross-cuting locally the stratification is typical of Type 2b vein. On the other hand, abundant magnetite associated to the Pb-Zn ore is characteristic of Type 2a mineralization.

4.3.6 Crabioulès

Crabioules deposit is situated in the central position of the PAZ, in the north of Lys-Caillaouas Late-Variscan granitoid (Figure 45). The host rock is composed of low-grade metamorphic schists with apparition of only rare biotite. Ore mineralization is composed of centimetric to pluri-decimetric lenticular bodies which are essentially parallel to N090-110°E S_0-S_1 foliations (Figure 62A). Some observations show that the Type 2a ore mineralization is not strictly parallel to S_0-S_1 with numerous evidences of injection of mineralization in a consolidated host-rock appear (Figure 62B and Figure 62C). Remobilization in fold hinge (saddle-reef) probably appear in Crabioulès like in Victoria area but D_2 deformation is largely less pronounced.

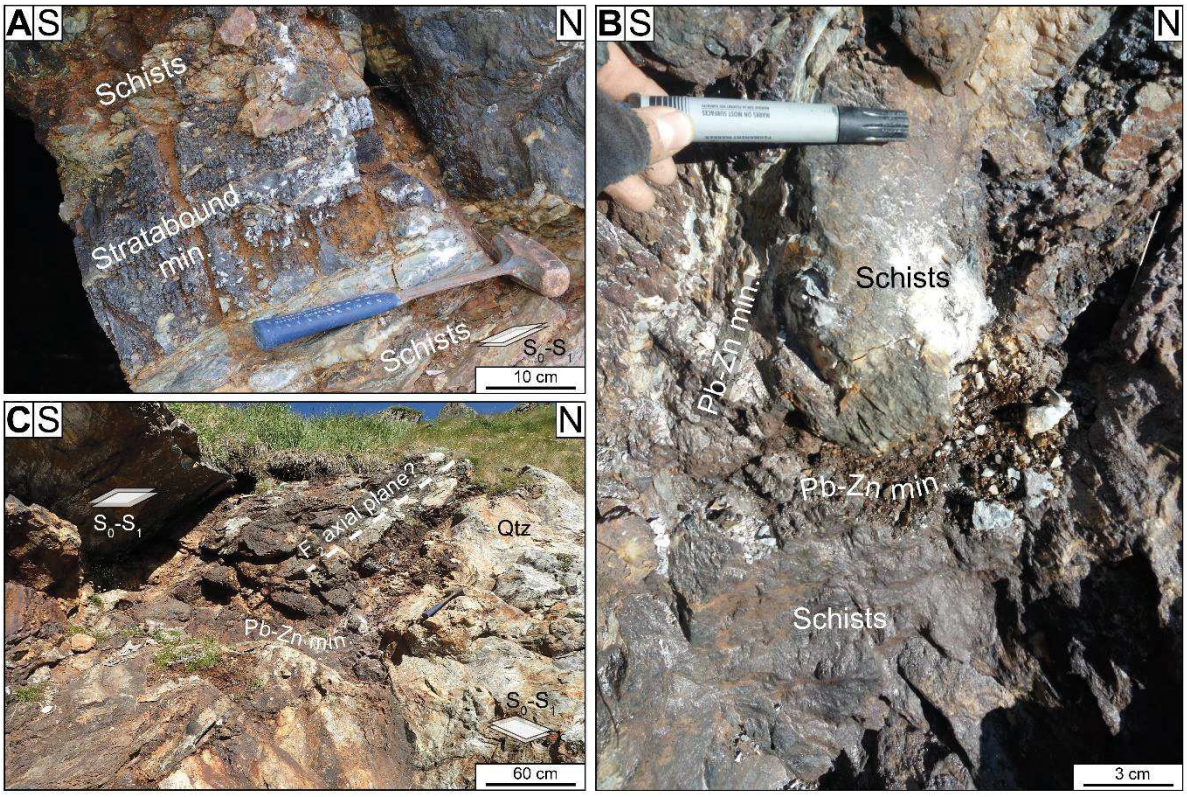

Figure 62. Crabioulès deposit (Type 2a). A. Typical view of the Crabioulès Pb-Zn stratabound mineralization hosted in low-grade metamorphic schists. B. Zoom on the relation between ore mineralization and the host-rock. With probable injection of Pb-Zn ore in the consolidated host-rock. C. Mineralization reconcentrated in a F_2 fold hinge.

4.3.7 *Arre-Anglas-Uzious area*

Arre-Anglas-Uzious deposits are structurally similar and contain Pb-Zn mineralizations in sub-vertical veins hosted in Devonian rocks with orientation varying from N040°E to N090°E. This trend is parallel to S_2 cleavage, axial plane of a km scale anticlinal (Figure 63). In Uzious, these mineralizations intersect an aplite, part of the Cauteret granite which is Late-Variscan in age. No relation with Cretaceous limestone was observed. Numerous deposits are hosted in granitoids in

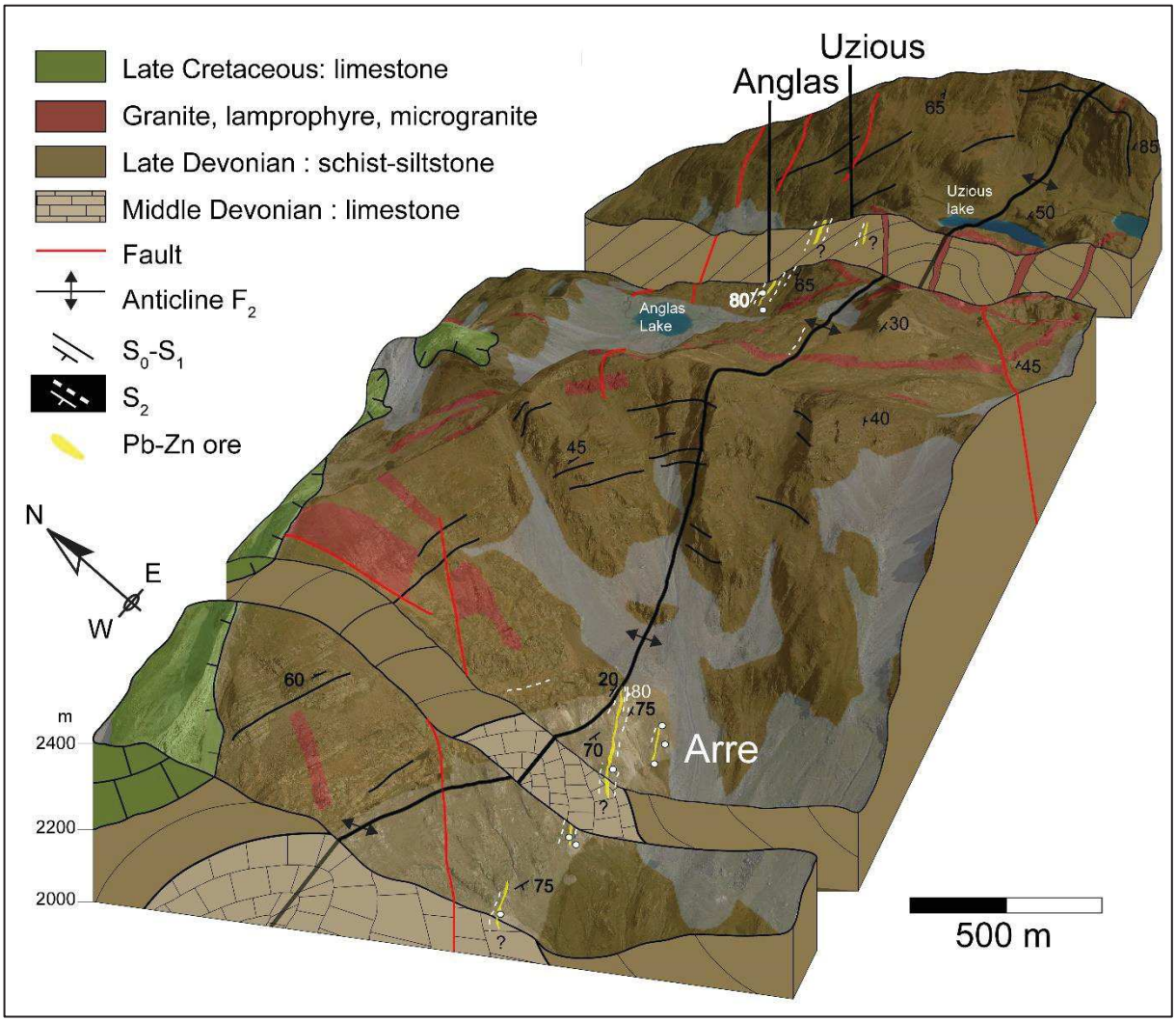

Figure 63 3D structural bloc representing the Arre-Anglas-Uzious area with position of the studied Type 2b mineralizations.

the Pyrenees like the Gavarnie, La Gela, Parzan or Cierco deposits and fewer in Mesozoic basement such as the Coume de Balour (West of the Arre-Anglas-Uzious area).

4.3.8 Cierco

Cierco deposit is situated in the Spanish part of the PAZ, in the south of the Maladeta Late-Variscan granitoids and produced until 1981, 1.4 Mt of ore with average grade of 4 % of Pb and 3 % of Zn (*Johnson et al. 1996*).

The mineralization is associated to north-south and east-west veins hosted in Devonian metasedimentary rocks or in the Bono granodiorite and is composed of sphalerite, galena, minor lead sulfosalt with gangue of quartz, calcite, barite and dolomite. Presence of Ge-minerals is attested in our sphalerite sample. *Johnson et al. (1996)* testify that the ore mineralization is also hosted in Triassic red beds, which is a key argument to attest for an ore genesis during Mesozoic extensional event in contrary to *Castroviejo Bolibar and Serrano (1983)* which postulate for a Late-Variscan origin. The difficulty of the field accessibility does not allow us to verify these field observations.

Cierco is certainly part of the Type 2b vein mineralization. This deposit is a key target to study the temporality of the Pb-Zn genesis for the PAZ vein-mineralization and question the validity of our genetic model. Type 2b veins may be formed during Mesozoic extension and not during Late Variscan times (D_2 deformation). Sphalerite deformation may be due to Alpine-Pyrenean cycle and do not correspond to our primary hypothesis of a Late Variscan deformation. Additional arguments are needed to confirm this late hypothesis due to lack of structural argument for the other Type 2b mineralizations (see section *8. Fluid inclusion analyses on the Pyrenean sphalerite*).

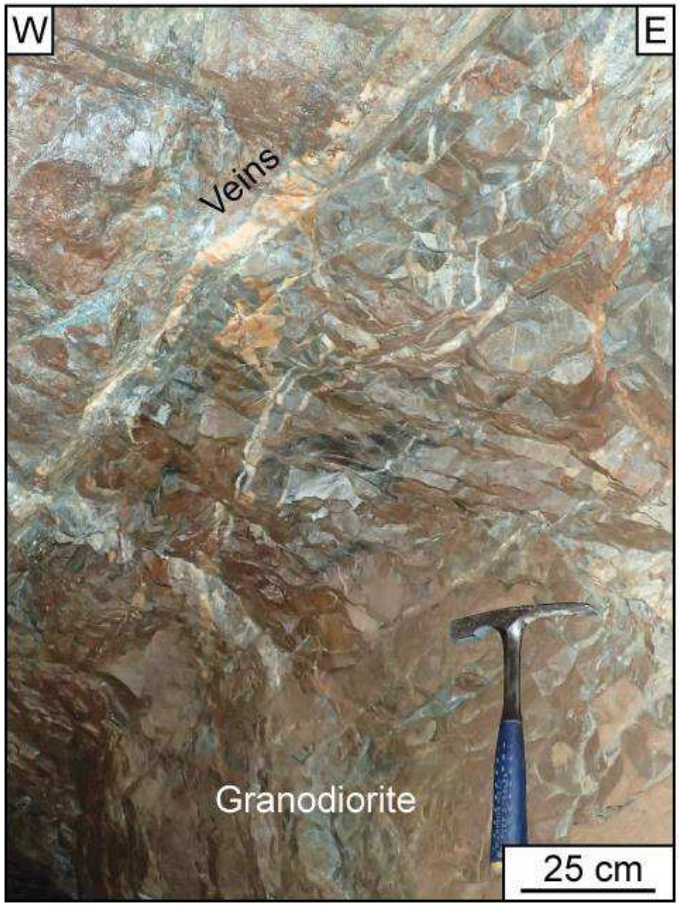

Figure 64. Cierco vein mineralization hosted in the Bono granodiorite

4.3.9 QEMSCAN (Quantitative Evaluation of Minerals by Scanning Electron Microscopy) datas

Mineralogical mapping (QEMSCAN) was performed in samples of Type 2b veins, Ge-minerals such as carboirite, brunogeierite, briartite and rare Ge-lepidomelane (only in Pale Bidau) were detected in QEMSCAN maps like in Pale Bidau, Argut-dessus (Figure 65), Arre and Anglas. Their quantification is estimated to 0.02 % on the entire map in Pale Bidau.

An ore sample from Bentaillou is shown with numerous stratabound vein in black schist in the Figure 66. Mineralogy is described and quantified and no Ge-mineral is reported in this sample. Additional maps in Type 2a stratabound mineralization from Liat, Margalida, Urets, Pierrefitte (Vieille mine) and Arrens were performed with no Ge-mineral detection.

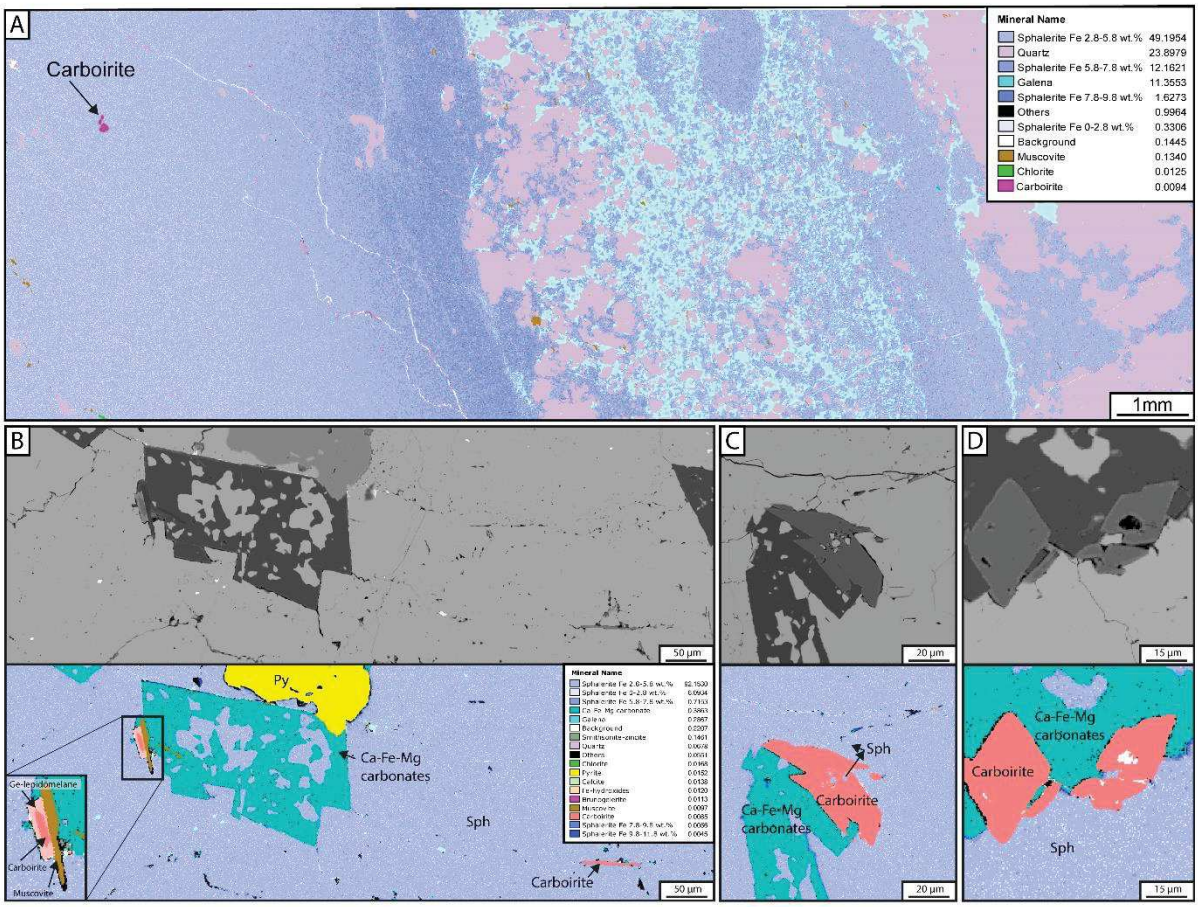

Figure 65. QEMSCAN maps from Argut-dessus and Pale Bidau ore samples. A. Sample from Argut-dessus (BO32) with two grains of carboirite (Ge-chloritoid) hosted in sphalerite. The main ore is composed of sphalerite (with various enrichment in Fe up to 10 wt.%), galena, quartz and muscovite. B-D. Sample from Pale Bidau (BO9) with three zoom on Ge-minerals composed of carboirite, brunogeieirite and rare Ge-lepidomelane hosted in sphlaerite and close to Ca-Fe-Mg carbonates. The legend and mineral quantification refer to the entire map.

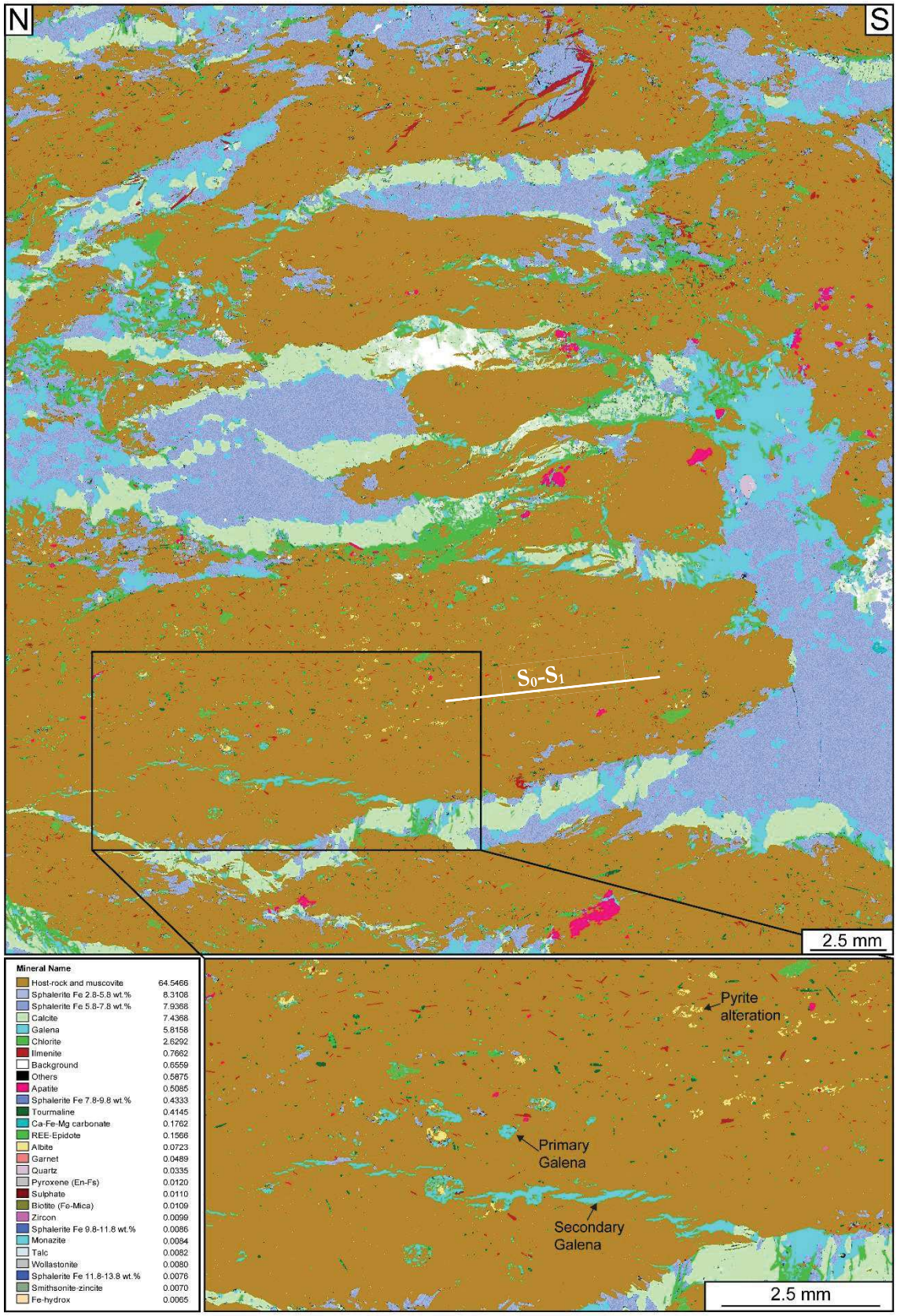

Figure 66. QEMSCAN mineralogical map of Bentaillou Pb-Zn associated to host-rock (indexed as muscovite). No Ge-mineral is reported. A zoom show the structural relation between two generations of galena also shown with an SEM picture in the previous article (see section 4.2.6. Ore petrology and Microstructures). S_0-S_1 is horizontal.

5 Germanium redistribution in sphalerite from the Pyrenean Axial Zone

In the following section, textural and chemical investigations on diverse sphalerite type from the Pyrenean Axial Zone (PAZ) are shown and exhibit the large heterogeneities especially in germanium. Textural (electron backscattered diffraction mapping – EBSD) and chemical analyses such as electron probe microanalyses (EPMA), laser ablation inductively coupled plasma mass spectrometry (LA-ICP-MS) and laser induced breakdown spectroscopy (LIBS) mapping analyses are coupled in numerous Pyrenean Pb-Zn deposits fully described in term of structural setting in "*4. Structural framework for the Pb-Zn deposits in the Pyrenean Axial Zone (PAZ)"*. Uses of these techniques are relevant to precisely define the important chemical and textural heterogeneity in sphalerite and the mechanisms responsible for the Ge-remobilization.

This section is divided in two parts, composed of one article published in Geology which exposed a first approach of the Ge-redistribution in sphalerite in one Pyrenean deposit (Arre) and a second article in revision in Mineralium Deposita fully describing the different sphalerite mineralization types in the Pyrenees, in term of texture and chemical contents.

5.1 ARTICLE – Redistribution of germanium during sphalerite dynamic recrystallization

This section is devoted to a short introduction of the Ge-redistribution in Pyrenean sphalerite with the published version of the article "Redistribution of germanium during dynamic recrystallization of sphalerite" which was accepted on November 2, 2019 in Geology.

In this study, we show that ductile deformation and subsequent dynamic recrystallization of sphalerite (zinc sulfide, ZnS) mineralization drives spatial redistribution of Germanium (Ge). Our investigation demonstrates that studying ore textures and microstructures at the thin-section scale is a major key to understand how trace elements (herein Ge) is redistributed in deformed ore deposit into accessory minerals. In this way, Electron Backscattered Diffraction (EBSD) and in-situ EPMA analyses have been coupled with innovative trace element chemical mapping (LIBS) as a first order approach to assess the physico-chemical processes leading to the internal redistribution of Ge through deformation and recrystallization of sphalerite.

GEOLOGY | THE GEOLOGICAL SOCIETY OF AMERICA®

Alexandre Cugerone[1], Bénédicte Cenki-Tok[1,2], Emilien Oliot[1], Manuel Munoz[1], Fabrice Barou[1], Vincent Motto-Ros[3], Elisabeth Le Goff[4]

[1]Géosciences Montpellier, Université de Montpellier, CNRS, 34095 Montpellier cedex 5, France ; alexandre.cugerone@umontpellier.fr; benedicte.cenki-tok@umontpellier.fr; emilien.oliot@umontpellier.fr; manuel.munoz@umontpellier.fr; fabrice.barou@umontpellier.fr

[2]Earthbyte Research Group, School of Geosciences, University of Sydney, NSW 2006, Sydney, Australia

[3]Institut Lumière Matière, Université Lyon 1, CNRS, 69622, Villeurbanne, France ; vincent.motto-ros@univ-lyon1.fr

[4]Bureau de Recherches Géologiques et Minières (BRGM), 34000 Montpellier, France ; e.legoff@brgm.fr

5.1.1 Abstract

Rare metals are essential to the development of the "green" technologies that are at the core of low-carbon societies. In nature, these metals are frequently present in trace amounts scattered in base metal ore deposits, but the physico-chemical processes that are responsible for their concentration into strategic minerals are still poorly understood. Based on laser-induced breakdown spectroscopy (LIBS), coupled with electron backscattered diffraction (EBSD) analysis, this study shows that plastic deformation and subsequent syntectonic recrystallization of sphalerite (zinc sulfide, ZnS) led to the spatial redistribution of germanium (Ge): from a background level of a few hundreds of parts per million in undeformed primary sphalerite to tens of weight-percent in neocrystallized Ge minerals. During dynamic recrystallization, Ge is likely released from the crystal lattice of parent sphalerite and subsequently concentrated in Ge minerals, leaving behind a Ge-depleted, recrystallized sphalerite matrix. Identifying how rare metals concentrate through deformation and syntectonic recrystallization at the mineral scale is essential to understand the spatial redistribution and localization at the deposit scale. This study highlights the importance of coupling in situ chemical mapping analysis with macro- and microstructural characterization when targeting rare metals in deformed ore.

5.1.2 Introduction

Many rare metals are critical to the sustained development of 21st century technologies. For example, germanium (Ge) is essential to optic fiber systems used in military and civil telecommunications. The production of rare metals remains challenging notably because only a few percent of the total rare metal content is recovered from base metal deposits *(Ruiz et al. 2018; U.S. Geological Survey 2019*). In this study, we focus on natural processes leading to the spatial redistribution of Ge, a rare metal whose background concentration level in the continental crust does not exceed 1.5 ppm (*Smith and Huyck 1999*). Redistribution of rare metals during metamorphism and deformation of base metal sulfides may be overlooked by the standard mineral exploration approach. Understanding the redistribution of rare metals forming their own high-grade minerals will lead to a better availability of these elements during ore processing as well as enhanced extraction and recovery efficiencies. In nature, Ge is associated with sphalerite (zinc sulfide, ZnS) deposits and coal seams at concentrations of a few thousand ppm (*Höll et al. 2007; Frenzel et al. 2014, 2016)*. Germanium is generally recovered through pyro- and hydro-metallurgical bulk ore processing (*Moskalyk 2004*). In some lead, zinc and copper deposits, small (< 100 μm) accessory Ge-minerals that can contain up to 70 wt. % Ge are locally described, testifying for Ge-

remobilization and/or concentration at the deposit scale *(Johan et al. 1983; Bernstein 1985; Melcher et al. 2006; Horn et al. 2018*). These Ge-minerals are found in a large variety of deposits like Kipushi-type (breccia-pipe), orogenic veins, volcanic-hosted massive sulfide (VHMS) or epithermal deposits *(Ottemann and Nuber 1972; Intiomale and Oosterbosch 1974; Wagner and Monecke 2005; Belissont et al. 2019*), and in host-rocks from Neoproterozoic to Variscan in age *(Johan et al. 1983; Melcher et al. 2006; Horn et al. 2018*). In addition, Ge-minerals typically occur in hydrothermal systems hosted in low-grade metamorphic rocks (*Cugerone et al. 2018a*). Nevertheless, the physico-chemical mechanisms that induce the remobilization of Ge in sulfide ores are not sufficiently understood and, consequently, the economic potential of this rare metal occurrence remains difficult to assess.

In the past two decades, numerous studies have shown that trace element distribution in deformed sulfides may be closely related to microstructures (*e.g.*, in pyrite, pyrrhotite, löllingite-arsenopyrite; *Tomkins and Mavrogenes 2001; Cook et al. 2009a; Vukmanovic et al. 2014*). Here, we propose an innovative approach combining (i) electron backscattered diffraction (EBSD), (ii) laser-induced breakdown spectroscopy (LIBS) and (iii) *in-situ* electron probe microanalyzer (EPMA) measurements to illustrate the relationships between Ge distribution and sphalerite microstructure. In naturally deformed sphalerite from the Arre Pb-Zn deposit in the Pyrenean Axial Zone (PAZ), Pyrenees, brunogeierite ($GeFe_2O_4$) and carboirite ($GeFeAl_2O_5(OH)_2$) have already been described *(Laforet et al. 1981; Oudin 1982; Johan et al. 1983; Johan and Oudin 1986*). Therefore, this ore deposit is a first-order target to decipher the links between sphalerite deformation and Ge remobilization.

5.1.3 Geological setting and samples

The study area is located in the Paleozoic basement of the Pyrenean Axial Zone (PAZ) where numerous Pb-Zn deposits have been exploited in the 20th century (Figure 67A). Following *Denèle et al. (2014)*, we documented three Variscan deformation stages (D_1 to D_3) have been documented. A poorly expressed S_1 foliation is associated with regional D_1 deformation and medium-pressure and low-temperature M_1 metamorphism. A well-expressed but local S_2 cleavage is subvertical and is related to a Late-Variscan D_2 deformation stage, characterized by a low-pressure and medium-temperature M_2 metamorphism (*Mezger and Passchier 2003)*. Finally, a very Late-Variscan or Pyrenean D_3 deformation occurs as localized shear zones and faults (Mezger et al. 2012; Carreras and Druguet 2014; Cochelin et al. 2017b).

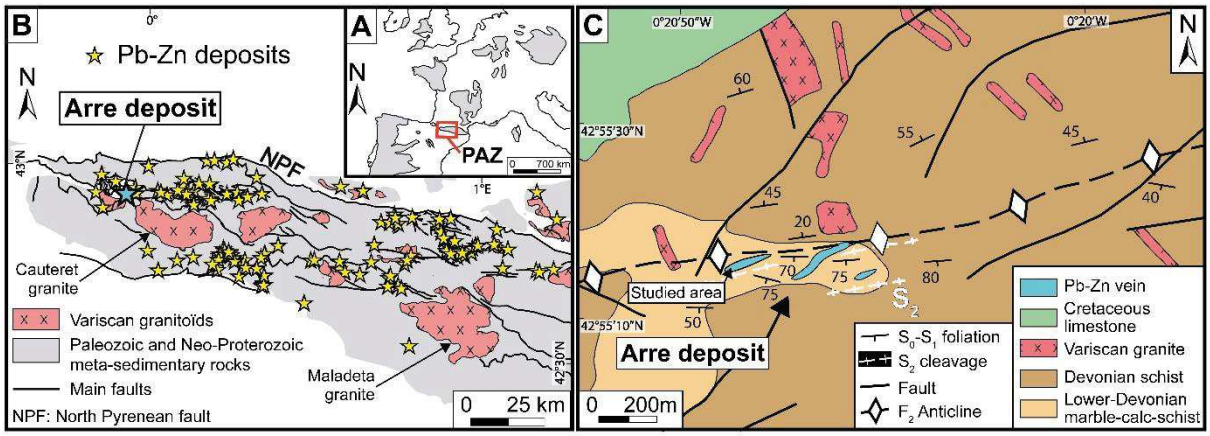

Figure 67. (A) Map of Variscan massifs in Western Europe, and location of B. (B) Simplified geological map of the Pyrenean Axial Zone (PAZ) and location of main Pb-Zn deposits (yellow stars, from *Pouit [1985]* and Bureau de Recherches Géologiques et Minières database *[http://infoterre.brgm.fr]* and Instituto Geológico y Minero de España database *[http://mapas.igme.es/Servicios/default.aspx]*). Study area is highlighted with blue star. (C) Geological and structural map of the Arre deposit area. Pb-Zn ore is hosted in N060°E–N080°E subvertical veins hosted in Lower Devonian marble calc-schist. Location of Figure 68A is indicated.

Three types of Pb-Zn occurrences are recognized by Cugerone et al. (2018b): type 1, type 2a and type 2b. This study focuses on the Arre locality (Figure 67B) where the existence of epigenetic Type 2b veins was reported (*Reyx 1973*). Three subvertical sphalerite veins, striking N060°E to N080°E, are embedded in Lower-Devonian host marble and calc-schist. These veins are structurally located in the hinge zone of a km-scale F_2 anticline and are parallel to the local S_2 cleavage (Figure 67C and Figure 68A).

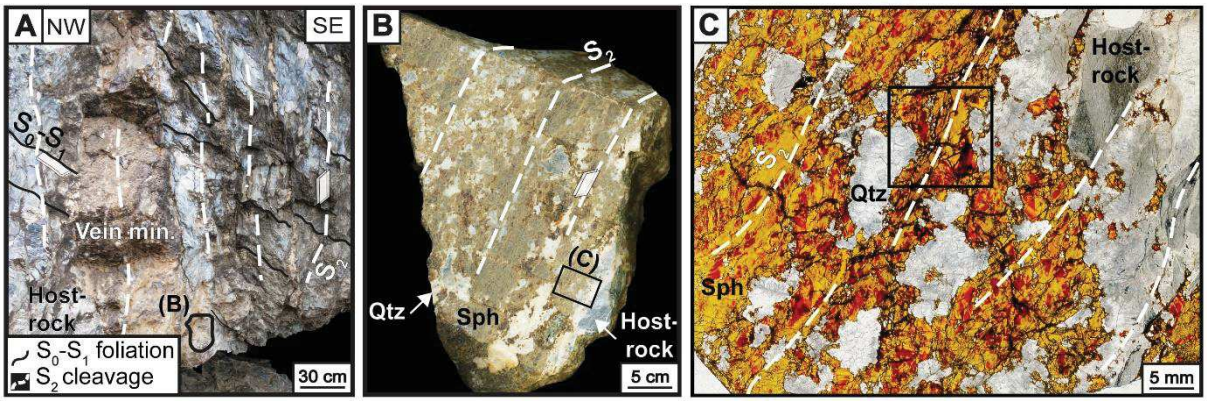

Figure 68. (A) Outcrop photograph of Arre (Pyrenean Axial Zone, Pyrenees) Pb-Zn vein type. Note S_2 cleavage in the host rock. Location of the studied sample (B) is indicated (modified from *Cugerone et al., 2018b*). (B) Photograph of ore. Sphalerite (Sph) appears light brown and is associated with quartz aggregate (Qtz) and schistose host rock. Location of the studied section (C) is indicated. (C) Plane-polarized (transmitted) light microphotograph of studied ore (150-µm-thick section). Sphalerite presents color zonations (dark and light brown) and is crosscut by S_2 cleavage. Location of Figure 70 is indicated. Sph—sphalerite, Qtz—quartz, S_2—S_2 regional cleavage plane.

The sphalerite occurrence was sampled in the westernmost part of Arre locality (Figure 67C). These decimetric veins cross-cut S_0-S_1 structures (Figure 68A) and are essentially composed of brownish sphalerite (ca. 80 vol.%; Figure 68B) with minor chalcopyrite, pyrite, galena, graphite and muscovite in a gangue of cockade quartz, carbonate and rare barite (Figure 68C).

5.1.4 Methods

EPMA was carried out using a Cameca SX100 at Géosciences Montpellier (Montpellier, France) following the methodology outlined in *Cugerone et al. (2018a)*. Ge and Cu were analyzed using two large lithiumfluoride (LLIF) monochromators. Detection limits calculated by internal Cameca procedures (PeakSight program (https://www.cameca.com/service/software/peaksight) in the SX100 software, using 1 sigma error) are 85 ppm and 123 ppm for Ge and Cu, respectively (Table 11).

Simultaneous energy-dispersive spectrometry (EDS) and EBSD mapping were acquired with a Camscan Crystal Probe X500FE scanning electron microscope at the University of Montpellier. Operating conditions were 20 kV and 5 nA with a working distance of 25 mm under 2 Pa low vacuum and a step size of 5 μm. Data were processed with the Oxford Instruments AZtec and Channel 5 software (https://nano.oxinst.com/products/ebsd/post-processing-software).

LIBS multi-elemental imaging was performed at the Institute Lumière Matière in University of Lyon 1 and is an all-optical analytical technique that was used to map the distribution of Ge in sphalerite (*Cáceres et al. 2017; Fabre et al. 2018*). The sample was analyzed using Nd:YAG laser with a pulse energy of 600 μJ operating at 100 Hz and a lateral resolution of 13 μm. The spectrometer was configured to detect an intense line of Ge located at 265.1 nm. The resulting detection limit was 10 ppm.

5.1.5 Results

5.1.5.1 Sphalerite microstructures and location of Ge-minerals

The vein is dominated by sphalerite associated with quartz (Figure 68B and Figure 68C). Sphalerite appears intensely zoned with brownish tints variations in transmitted light microscopy (Figure 68C, Figure 69A). The sphalerite grain size is highly heterogeneous (from < 10 μm to > 1 mm) and distributed in two distinct populations (Figure 69B and Figure 70C): the threshold

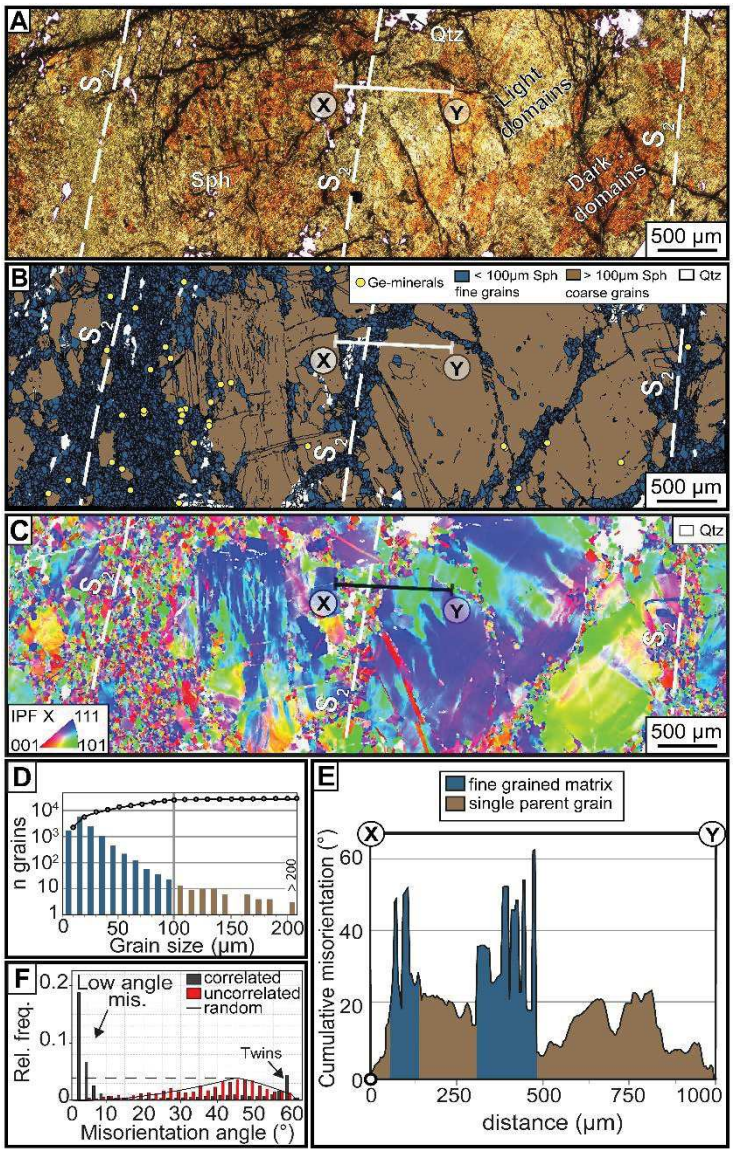

Figure 69. Sphalerite microstructures and locations of Ge minerals in Arre (Pyrenean Axial Zone, Pyrenees) sample. (A) Plane-polarized (transmitted) light microphotograph of mineralized sample (30 µm thin section). Sph—sphalerite, Qtz—quartz, S_2—S_2 cleavage plane. (B) Locations of Ge minerals superimposed on sphalerite electron backscattered diffraction (EBSD) grain-size map (misorientation threshold to define grains is fixed at 20°). Sphalerite grains are distinguished into two groups as a function of their grain size. Smaller grains (<100 µm) define aggregated bands parallel to S_2 cleavage. Note that Ge-minerals are mainly located in, or close to, these fine-grained bands. (C) Sphalerite EBSD inverse pole figure (IPF) map, plotted with respect to x-axis of projection sphere, showing internal plastic strain in coarse parent grains that are mantled by recrystallized smaller grains. S_2 cleavage is marked by fine-grained recrystallization bands that crosscut parent sphalerite. Location of cumulative misorientation profile (E) is specified. (D) Histogram distribution and cumulative frequency curve of sphalerite grain size displaying two grain-size populations: coarse (>100 µm, brown) parent grains and small (<100 µm, blue) recrystallized grains. Threshold is considered where cumulative frequency curve becomes subhorizontal. (E) Cumulative misorientation profile relative to start point acquired through single sphalerite parent grain, crosscut by fine-grained band of recrystallized grains. (F) Misorientation angle distribution histograms plotting neighbor-pair (correlated) and random-pair (uncorrelated) misorientations for sphalerite grains in studied area (>2°).

between coarse- and fine-grain size is fixed at 100 μm (Figure 69D). Combining the EBSD grain size map and optical observations, three grain types are distinguished: coarse millimeter-size grains with (i) dark or (ii) light brownish domains, and (iii) small (< 100 μm) light brownish grains. Microstructures in twinned primary sphalerite are mostly internal crystalline strain expressed through deformation bands and lamellae (Figure 69C and Figure 70A). In a single parent grain, the cumulative internal misorientation can reach a value of 22° (Figure 69E).

Small sphalerite grains form aggregates that pervasively mantle and/or cross-cut coarse primary sphalerite (Figure 69C, Figure 69E and Figure 70A). The misorientation angles distribution of the neighbor pairs reveals a dominance of low values (from 2° to 6°, Fig. Figure 69F), four time higher than the 45° peak of uncorrelated-pairs which follow the predicted random distribution. At thin section scale, fine-grained aggregates outline the S_2 cleavage (Figure 69and 4) and in coarse primary sphalerite, narrow bands composed of small grains are frequently parallel to twins (Figure 69C and Figure 70A).

The EDS chemical map acquired in this area (Figure 138-supp data) indicates that Ge is locally hyper-concentrated in micrometric Ge-minerals (reported as yellow dots in Figure 69B), located mostly in the fine-grained sphalerite aggregates.

5.1.5.2 Ge partitioning in sphalerite

Germanium concentration has been mapped in relation to sphalerite texture in a monomineralic layer of fine-grained sphalerite that cross-cuts an aggregate of large, twinned primary grains (Figure 70A-C). The distribution of Ge-cations in sphalerite at the thin section scale is highly heterogeneous (Fig. 4B) and mimics the patchy brownish domains visible in optical microscopy (Figure 138-supp data). The most Ge-depleted zones in sphalerite (i.e. blue areas in Figure 70B) correspond to both fine-grained population and random parts of light primary sphalerite (Figure 70A and Figure 70B). Intermediate Ge concentrations in sphalerite match the dark part of coarse grains (i.e. brown tints in Figure 70B). The limit between Ge-rich (dark) and Ge-depleted (light) sphalerite domains is generally progressive and diffuse (Figure 70B). Zones displaying higher Ge contents (i.e. > 15 wt. % Ge, yellow areas in Figure 70B) clearly indicate the presence of Ge-minerals (brunogeierite, see inset in Figure 70C). These are located in twinned, coarse primary grains, and in the fine-grained monomineralic layers that outline the S_2 cleavage (Figure 70A-C and Figure 138-supp data).

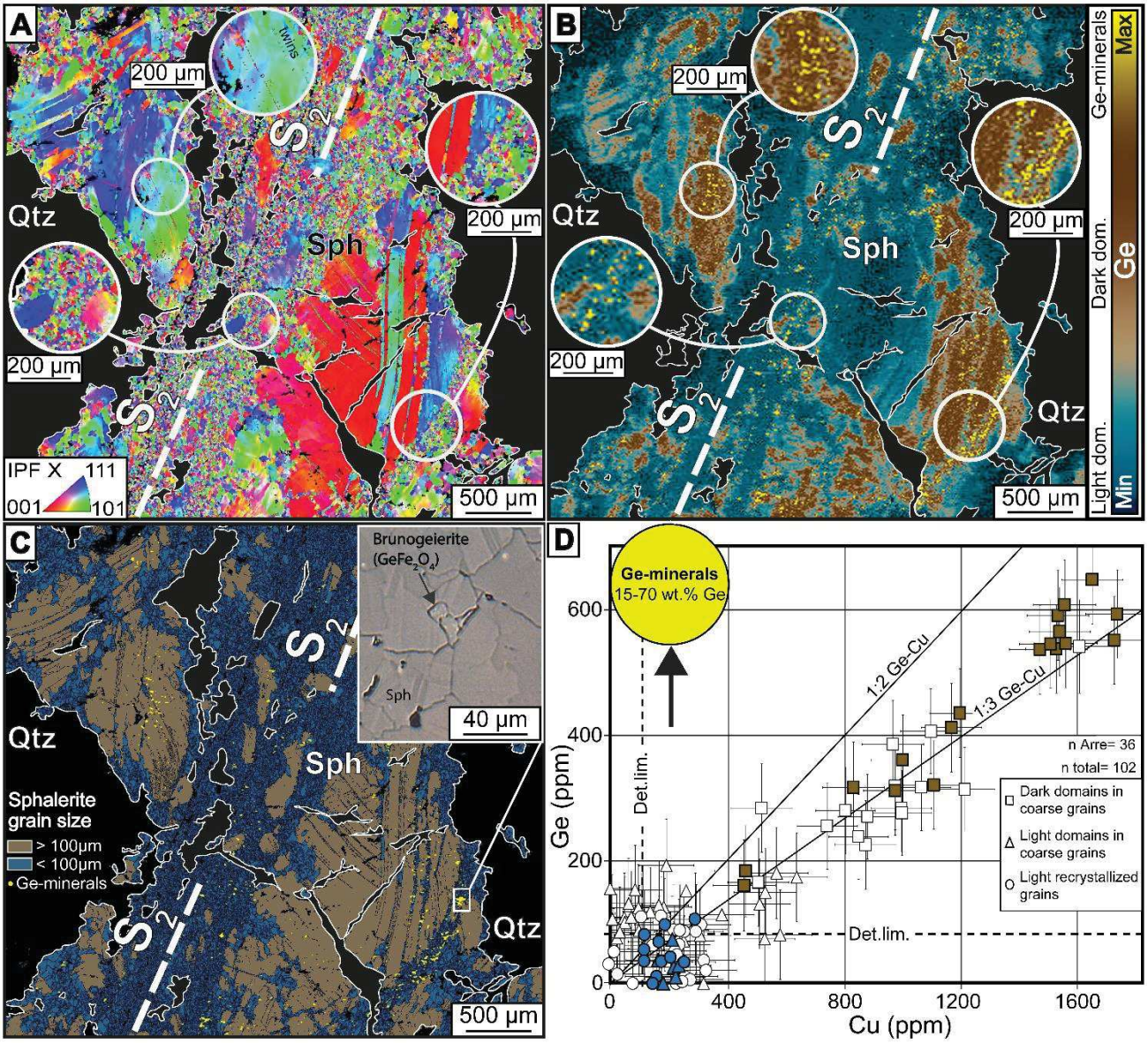

Figure 70. Ge concentration in sphalerite and locations of Ge minerals in Arre (Pyrenean Axial Zone, Pyrenees) sample. (A) Electron backscattered diffraction (EBSD) inverse pole figure (IPF) map, plotted with respect to x-axis of projection sphere. Note that S_2 cleavage is marked by fine-grained recrystallization bands that crosscut parent sphalerite. (B) Ge distribution map from laser-induced breakdown spectroscopy (LIBS). Ge-minerals are represented by higher Ge concentration (yellow areas). Patchy dark-brown domains correspond to higher Ge concentration (~600 ppm Ge) in parent sphalerite. Lighter domains (blue to light brown) indicate intermediate to low Ge concentrations (10–150 ppm Ge) in sphalerite. Recrystallized grains show lower Ge concentration (blue, <100 ppm Ge). Qtz—quartz. (C) Locations of Ge minerals superimposed on sphalerite EBSD grain-size map. Note the presence of Ge minerals in the finest sphalerite fraction (<100 µm) or in twin planes. Reflected plane-polarized light, close-up microphotograph shows brunogeierite ($GeFe_2O_4$) crystal. (D) Ge versus Cu concentrations (expressed in ppm) in sphalerites obtained from electron probe microanalyzer (EPMA) measurements, in dark, light, and recrystallized sphalerite from the Arre deposit (colored symbols) and other Pyrenean Axial Zone (PAZ) vein-type sphalerite (white symbols). Color code corresponds to that used in LIBS map in B.

Ge and Cu contents have been measured in the three sphalerite textures from several vein-type deposits in the PAZ (including the studied Arre deposit; Figure 70D and Table 12). The lowest Ge concentrations in sphalerite are below ~ 150 ppm Ge and found in light fine-grained

aggregates and light domains in coarse primary sphalerite. Dark domains in coarse primary grains display intermediate Ge concentrations from ~ 150 to ~ 650 ppm Ge.

5.1.6 Interpretation and discussion

5.1.7 Deformation and dynamic recrystallization of sphalerite

The Arre vein displays evidence of strain superimposition that is verified at the sample-scale by a subvertical S_2 cleavage. Strain in sphalerite is primarily accommodated by internal crystalline plasticity forming deformation bands and lamellae (Figure 69C and Figure 69E). This process indicated active dislocation creep mechanisms in the ZnS *(Kollenberg and Siemes 1983; Hirth and Tullis 1992*). By comparison with experimental deformation in sphalerite *(Siemes and Borges 1979)* and previously described deformation mechanisms in pyrite (*Barrie et al. 2011*), this process occurs at low- to medium-grade metamorphic conditions.

The textures show coarse sphalerite grains mantled by small grains (< 100 μm, Figure 69B and Figure 69D), or cut through by S_2-parallel zones of fine grained sphalerite. Twins in parent sphalerite often act as inherited structural heterogeneity during deformation *(Couderc et al. 1985)*, inducing the formation of narrow bands of small, aggregated grains (Figure 69C and Figure 70A). These observations point to syntectonic grain-size reduction, deriving from dynamic recrystallization. Indeed, small recrystallized grains develop at the expense of large parent grains (Figure 69C and Figure 70A). With the rising strain and the increase of internal misorientations within parent grains (beyond 20°, Figure 69E), the high-density of low misorientation angles between neighbor pairs (Figure 69F) suggests that strain-induced subgrain rotation recrystallization was the main deformation mechanism for sphalerite recrystallization *(e.g. Guillope and Poirier 1979)*.

5.1.8 Mechanisms for internal Ge remobilization

Sphalerite integrates tetravalent Ge involving monovalent Cu in a coupled substitution mechanism (*Belissont et al. 2016*). Germanium generally occurs in relative low concentration (up to few thousands of ppm) and often associated to coarse parent sphalerite grains that display Ge-rich (dark) and Ge-depleted (light) domains *(Cook et al. 2009b; Belissont et al. 2014; Bauer et al. 2018*). Here,

we show that deformation at low- to medium-grade (< 400°C) conditions leads to dynamic sphalerite recrystallization, inducing Ge partitioning between recrystallized Ge-depleted sphalerite and newly crystallized Ge-minerals. Although Ge is not homogeneously distributed in parent sphalerite (*i.e.* rich-dark vs. depleted-light domains), Ge displays higher pervasive concentration in dark coarse grains (up to ~ 650 ppm) compared to light recrystallized domains (< 100 ppm), in which Ge-minerals frequently occur (Figure 69B and Figure 70B-C). We propose that Ge-cations were internally remobilized from the parent sphalerite lattice during intracrystalline deformation, most likely via solid-state mechanical transfer (dislocation flow; *Marshall and Gilligan 1993*), as a result of increasing internal strain and subsequent recovery. During dynamic recrystallization and S_2 cleavage development, a probable fluid-assisted solution transfer (solution-precipitation creep) allowed Ge to be remobilized and promoted the neocrystallization of Ge-minerals (essentially oxides or chloritoids, Figure 70C; *Johan et al. 1983; Cugerone et al. 2018a*). Germanium from an external fluid source is not needed to crystallize the newly formed Ge-minerals.

5.1.9 Rare element redistribution in other world-class deposits

Germanium-minerals and Ge chemical heterogeneity are reported from other deformed sulfide occurrences. For example Kipushi-type deposits (*Melcher et al. 2006; Horn et al. 2018*), volcanic-hosted massive sulfide deposits (*Reiser et al. 2011*), and deformed carbonate-hosted deposits in China *(Ye et al. 2011*; ca. Huize, Niujiaotang deposits) and in Brazil *(Monteiro et al. 2006*) show recrystallized Ge-rich sphalerite ore. In other chemical systems, formation of the indium-bearing mineral (roquesite, $CuInS_2$) hosted in bornite (Cu_5FeS_4) may be attributed to indium remobilization and diffusion from In-rich sphalerite under metamorphic conditions *(Jonsson et al. 2013*). Coupling microstructural and in-situ chemistry in deformed sulfides is key to explore potential rare metal-rich deposits in orogens.

5.1.10 Conclusions

Multiscale textural and chemical observations show that the Arre vein-type zinc sulfide deposit has undergone deformation that promoted dynamic recrystallization of sphalerite, inducing Ge remobilization and subsequent concentration in Ge-minerals. This mechanism, assisted by hydrothermal fluids, led to the development of a fine-grained Ge-depleted sphalerite matrix, in which Ge-minerals crystallized. Numerous analogues to the Arre epigenetic sphalerite exist in world-class Pb-Zn deposits and coupling textural and microstructural observations with trace

element chemical mapping may be, in the future, a key improvement to understand the natural occurrence of rare metals.

5.1.11 Acknowledgments

This study was funded by the French national program "Référentiel Géologique de France" (RGF-Pyrénées) of the French Geological Survey (Bureau de Recherches Géologiques et Minières; BRGM), and through the INSU-CNRS Tellus CESSUR program. BCT acknowledges funding from the European Union's Horizon 2020 research and innovation program under grant agreement No 793978. The authors gratefully acknowledge C. Nevado and D. Delmas for the exceptional thin section preparation, B. Boyer for his involvement in EPMA and P. F. Rey and M. Alsaif for commenting on an earlier version of the manuscript. The authors are thankful to Mark Quigley for the editorial handling and to three anonymous reviewers for highly constructive comments.

5.1.12 References

Barrie, C.D., Pearce, M.A., and Boyle, A.P., 2011, Reconstructing the pyrite deformation mechanism map: Ore Geology Reviews, v. 39, p. 265–276, https://doi .org/10.1016/ j.oregeorev.2011.03.006.

Bauer, M.E., Burisch, M., Ostendorf, J., Krause, J., Frenzel, M., Seifert, T., and Gutzmer, J., 2018, Trace element geochemistry of sphalerite in contrasting hydrothermal fluid systems of the Freiberg district, Germany: Insights from LA-ICP-MS analysis, near-infrared light microthermometry of sphalerite-hosted fluid inclusions, and sulfur isotope geochemistry: Mineralium Deposita, v. 54, p. 237–262, https://doi .org/10.1007/s00126-018-0850-0.

Belissont, R., Boiron, M.C., Luais, B., and Cathelineau, M., 2014, LA-ICP-MS analyses of minor and trace elements and bulk Ge isotopes in zoned Ge-rich sphalerites from the Noailhac-Saint-Salvy deposit (France): Insights into incorporation mechanisms and ore deposition processes: Geochimica et Cosmochimica Acta, v. 126, p. 518–540, https://doi .org/10.1016/ j.gca.2013.10.052.

Belissont, R., Munoz, M., Boiron, M.C., Luais, B., and Mathon, O., 2016, Distribution and oxidation state of Ge, Cu and Fe in sphalerite by μ-XRF and K-edge μ-XANES: Insights into Ge incorporation, partitioning and isotopic fractionation: Geochimica et Cosmochimica Acta, v. 177, p. 298–314, https://doi .org/10.1016/ j.gca.2016.01.001.

Belissont, R., Munoz, M., Boiron, M., Luais, B., and Mathon, O., 2019, Germanium crystal chemistry in Cu-bearing sulfides from micro-XRF mapping and micro-Xanes spectroscopy: Minerals (Basel), v. 9, p. 1–12, https://doi .org/10.3390/min9040227.

Bernstein, L.R., 1985, Germanium geochemistry and mineralogy: Geochimica et Cosmochimica Acta, v. 49, p. 2409–2422, https://doi .org/10.1016/0016-7037(85)90241-8.

Cáceres, J.O., Pelascini, F., Motto-Ros, V., Moncayo, S., Trichard, F., Panczer, G., Marín-Roldán, A., Cruz, J.A., Coronado, I., and Martín-Chivelet, J., 2017, Megapixel multi-elemental imaging by laser-induced breakdown

spectroscopy: A technology with considerable potential for paleoclimate studies: Scientific Reports, v. 7, p. 1–11, https://doi .org/10.1038/s41598-017-05437-3.

Carreras, J., and Druguet, E., 2014, Framing the tectonic regime of the NE Iberian Variscan segment, in Schulmann, K., et al., eds., The Variscan Orogeny: Extent, Timescale and the Formation of the European Crust: Geological Society [London] Special Publication 405, p. 249–264, https://doi .org/10.1144/SP405.7.

Cochelin, B., Lemirre, B., Denèle, Y., De Saint Blanquat, M., Lahfid, A., and Duchêne, S., 2017, Structural inheritance in the Central Pyrenees: The Variscan to Alpine tectonometamorphic evolution of the Axial Zone: Journal of the Geological Society [London], v. 175, p. 336–351, https://doi .org/10.1144/jgs2017-066.

Cook, N.J., Ciobanu, C.L., and Mao, J., 2009a, Textural control on gold distribution in As-free pyrite from the Dongping, Huangtuliang and Hougou gold deposits, North China craton: Chemical Geology, v. 264, p. 101–121, https://doi .org/10.1016/ j.chemgeo.2009.02.020.

Cook, N.J., Ciobanu, C.L., Pring, A., Skinner, W., Shimizu, M., Danyushevsky, L., Saini-Eidukat, B., and Melcher, F., 2009b, Trace and minor elements in sphalerite: A LA-ICPMS study: Geochimica et Cosmochimica Acta, v. 73, p. 4761–4791, https://doi .org/10.1016/ j.gca.2009.05.045.

Couderc, J.J., Dudouit, I., Hennig-Michaeli, C., and Levade, C., 1985, The interaction between slip and twinning systems in natural sphalerite experimentally deformed: Physica Status Solidi, v. 90, p. 581–593, https://doi .org/10.1002/pssa.2210900222.

Cugerone, A., Cenki-Tok, B., Chauvet, A., Le Goff, E., Bailly, L., Alard, O., and Allard, M., 2018a, Relationships between the occurrence of accessory Ge-minerals and sphalerite in Variscan Pb-Zn deposits of the Bossost anticlinorium, French Pyrenean Axial Zone: Chemistry, microstructures and ore-deposit setting: Ore Geology Reviews, v. 95, p. 1–19, https://doi .org/10.1016/ j.oregeorev.2018.02.016.

Cugerone, A., Oliot, E., Chauvet, A., Gavalda, J., and Le Goff, E., 2018b, Structural control on the formation of Pb-Zn deposits: An example from the Pyrenean Axial Zone: Minerals (Basel), v. 8, p. 1–20, https://doi .org/10.3390/min8110489.

Denèle, Y., Laumonier, B., Paquette, J.-L., Olivier, P., Gleizes, G., and Barbey, P., 2014, Timing of granite emplacement, crustal flow and gneiss dome formation in the Variscan segment of the Pyrenees, in Schulmann, K., et al., eds., The Variscan Orogeny: Extent, Timescale and the Formation of the European Crust: Geological Society [London] Special Publication 405, p. 265–287, https://doi .org/10.1144/SP405.5.

Fabre, C., Devismes, D., Moncayo, S., Pelascini, F., Trichard, F., Lecomte, A., Bousquet, B., Cauzid, J., and Motto-Ros, V., 2018, Elemental imaging by laser-induced breakdown spectroscopy for the geological characterization of minerals: Journal of Analytical Atomic Spectrometry, p. 1–9, https://doi .org/10.1039/c8ja00048d.

Frenzel, M., Ketris, M.P., and Gutzmer, J., 2014, On the geological availability of germanium: Mineralium Deposita, v. 49, p. 471–486, https://doi .org/10.1007/s00126-013-0506-z.

Frenzel, M., Hirsch, T., and Gutzmer, J., 2016, Gallium, germanium, indium, and other trace and minor elements in sphalerite as a function of deposit type—A meta-analysis: Ore Geology Reviews, v. 76, p. 52–78, https://doi .org/10.1016/ j.oregeorev.2015.12.017.

Guillope, M., and Poirier, J.P., 1979, Dynamic recrystallization during creep of single-crystalline halite: An experimental study: Journal of Geophysical Research, v. 84, p. 5557–5567, https://doi .org/10.1029/JB084iB10p05557.

Hirth, G., and Tullis, J., 1992, Dislocation creep regimes in quartz aggregates: Journal of Structural Geology, v. 14, p. 145–159, https://doi .org/10.1016/0191-8141(92)90053-Y.

Höll, R., Kling, M., and Schroll, E., 2007, Metallogenesis of germanium—A review: Ore Geology Reviews, v. 30, p. 145–180, https://doi .org/10.1016/ j.oregeorev.2005.07.034.

Horn, S., Dziggel, A., Kolb, J., and Sindern, S., 2018, Textural characteristics and trace element distribution in carbonate-hosted Zn-Pb-Ag ores at the Paleoproterozoic Black Angel deposit, central West Greenland: Mineralium Deposita, v. 54, p. 507–524, https://doi .org/10.1007/s00126-018-0821-5.

Intiomale, M.M., and Oosterbosch, R., 1974, Géologie et géochimie du gisement de Kipushi, Zaïre, in Bartholomé P., ed., Gisements Stratiformes et Provinces Cuprifères: Liège, Centenaire Société Géologique de Belgique, p. 123–164, https://popups.uliege.be:443/0037-9395/index.php?id=3472.

Johan, Z., and Oudin, E., 1986, Présence de grenats, $Ca_3Ga(GeO_4)_3$, $Ca_3Al_2[(Ge,Si)O_4]_3$ et d'un équivalent ferrifere, germanifere et gallifere de la sapphirine, $Fe_4(Ga,Sn,Fe)_4$ $(Ga,Ge)_6O_{20}$, dans la blende des gisements de la zone axiale pyrénéenne. Conditions de formation des phases germanifères et gallifères: Comptes Rendus de l'Académie des Sciences Paris, v. 9, p. 811–816.

Johan, Z., Oudin, E., and Picot, P., 1983, Analogues germanifères et gallifères des silicates et oxydes dans les gisements de zinc des Pyrénées centrales, France: Argutite et carboirite, deux nouvelles espèces minérales: Tschermaks Mineralogische und Petrographische Mitteilungen, v. 31, p. 97–119, https://doi .org/10.1007/BF01084764.

Jonsson, E., Högdahl, K., Majka, J., and Lindeberg, T., 2013, Roquesite and associated indium-bearing sulfides from a Paleoproterozoic carbonate-hosted mineralization: Lindbom's prospect, Bergslagen, Sweden: Canadian Mineralogist, v. 51, p. 629–641, https://doi .org/10.3749/canmin.51.4.629.

Kollenberg, W., and Siemes, H., 1983, Experimental deformation of sphalerite-garnet ore under a confining pressure of 300 MPa and at temperatures between 250° C and 300° C, in Bilde-Sørensen, J.B., et al., eds., Deformation of Multi-Phase and Particle Containing Materials: Roskilde, Denmark, Risø National Laboratory, p. 351–356.

Laforet, C., Oudin, E., Picot, P., Pierrot, R., and Pillard, F., 1981, Métallogénie Régionale: Utilisation des Paragenèses Minéralogiques et des Minéraux Traceurs: Bureau de Recherches Geologiques et Minieres Rapport 80, SGN-175, 33 p., http://infoterre.brgm.fr/rapports/80-SGN-175-MGA.pdf.

Marshall, B., and Gilligan, L.B., 1993, Remobilization, syn-tectonic processes and massive sulphide deposits: Ore Geology Reviews, v. 8, p. 39–64, https://doi .org/10.1016/0169-1368(93)90027-V.

Melcher, F., Oberthür, T., and Rammlmair, D., 2006, Geochemical and mineralogical distribution of germanium in the Khusib Springs Cu-Zn-Pb-Ag sulfide deposit, Otavi Mountain Land, Namibia: Ore Geology Reviews, v. 28, p. 32–56, https://doi .org/10.1016/ j.oregeorev.2005.04.006.

Mezger, J.E., and Passchier, C.W., 2003, Polymetamorphism and ductile deformation of staurolite–cordierite schist of the Bossòst dome: Indication for Variscan extension in the Axial Zone of the central Pyrenees: Geological Magazine, v. 140, p. 595–612, https://doi .org/10.1017/S0016756803008112.

Mezger, J.E., Schnapperelle, S., and Rölke, C., 2012, Evolution of the Central Pyrenean Mérens fault controlled by near collision of two gneiss domes: Hallesches Jahrbuch für Geowissenschaften, v. 34, p. 11–30.

Monteiro, S.L.V., Bettencourt, S.J., Juliani, C., and de Oliveira, T.F., 2006, Geology, petrography, and mineral chemistry of the Vazante non-sulfide and Ambrosia and Fagundes sulfide-rich carbonate-hosted Zn-(Pb) deposits, Minas Gerais, Brazil: Ore Geology Reviews, v. 28, p. 201–234, https://doi .org/10.1016/ j.oregeorev.2005.03.005.

Moskalyk, R.R., 2004, Review of germanium processing worldwide: Minerals Engineering, v. 17, p. 393–402, https://doi .org/10.1016/ j.mineng.2003.11.014.

Ottemann, V.J., Nuber, B., 1972, Brunogeierit, ein Germanium-Ferritspinell: Neues Jahrbuch für Mineralogie, Monatshefte, p. 263–267.

Oudin, E., 1982, Minéralogie des Pyrénées Centrales: Bureau de Recherches Geologiques et Minieres Rapport 82, SGN-189 MGA, 38 p., http://infoterre.brgm.fr/rapports/82-SGN-189-MGA.pdf.

Pouit, G., 1985, Les minéralisations Zn (Pb) Ba du Paléozoïque des Pyrénées Centrales: Une Mise au Point et un Compte Rendu des Missions 1984: Bureau de Recherches Geologiques et Minieres Rapport 85, DAM-037 GMX, 72p.

Reiser, F.K.M., Rosa, D.R.N., Pinto, Ã.M.M., Carvalho, J.R.S., Matos, J.X., Guimaraes, F.M.G., Alves, L.C., and de Oliveira, D.P.S., 2011, Mineralogy and geochemistry of tin- and germanium-bearing copper ore, Barrigao re-mobilized vein deposit, Iberian Pyrite Belt, Portugal: International Geology Review, v. 53, p. 1212–1238, https://doi .org/10.1080/00206811003683168.

Reyx, J., 1973, Relations entre Tectonique, Métamorphisme de Contact et Concentrations Metalliques dans le Secteur des Anciennes Mines d'Arre et Anglas (Hautes-Pyrénées-Pyrénées Atlantiques) [Ph.D. thesis]: Paris, France, University of Paris VI, 83 p.

Ruiz, A.G., Sola, P.C., and Palmerola, N.M., 2018, Germanium: Current and novel recovery processes, in Lee, S., ed., Advanced Material and Device Applications with Germanium: London, IntechOpen Limited, p. 9–29. https://doi .org/10.5772/INTECHOPEN.77997.

Siemes, H., and Borges, B., 1979, Experimental deformation of sphalerite single crystals under confining pressures of 3000 and 5000 bars at temperatures between 25°C and 450°C: Neues Jahrbuch für Mineralogie, v. 134, p. 288–304.

Smith, K.S., and Huyck, H.L.O., 1999, An overview of the abundance, relative mobility, bioavailability, and human toxicity of metals, in Plumlee, G.S., and Logsdon, M.J., eds., The Environmental Geochemistry of Mineral Deposits: Reviews in Economic Geology, v. 6A, p. 29–70.

Tomkins, A.G., and Mavrogenes, J.A., 2001, Redistribution of gold within arsenopyrite and löllingite during pro- and retrograde metamorphism: Application to timing of mineralization: Economic Geology and the Bulletin of the Society of Economic Geologists, v. 96, p. 525–534, https://doi .org/10.2113/gsecongeo.96.3.525.

U.S. Geological Survey (2019) Mineral Commodity Summaries 2019: https://www.usgs.gov/centers/nmic/mineral-commodity-summaries (accessed).

Vukmanovic, Z., Reddy, S.M., Godel, B., Barnes, S.J., Fiorentini, M.L., Barnes, S.J., and Kilburn, M.R., 2014, Relationship between microstructures and grain-scale trace element distribution in komatiite-hosted magmatic sulphide ores: Lithos, v. 184–187, p. 42–61, https://doi .org/10.1016/ j.lithos.2013.10.037 (accessed 28 February 2019).

Wagner, T., and Monecke, T., 2005, Germanium-bearing colusite from the Waterloo volcanic-rock-hosted massive sulfide deposit, Australia: Crystal chemistry and formation of colusite-group minerals: Canadian Mineralogist, v. 43, p. 655–669, https://doi .org/10.2113/gscanmin.43.2.655.

Ye, L., Cook, N.J., Ciobanu, C.L., Yuping, L., Qian, Z., Tiegeng, L., Wei, G., Yulong, Y., and Danyushevskiy, L., 2011, Trace and minor elements in sphalerite from base metal deposits in South China: A LA-ICPMS study: Ore Geology Reviews, v. 39, p. 188–217, https://doi .org/10.1016/ j.oregeorev.2011.03.001.

5.2 ARTICLE – Behavior of germanium and associated critical elements in recrystallized Pb-Zn ore deposits: example from the Pyrenean Axial Zone

This section is devoted to the submitted version of the article "Behavior of germanium and associated critical elements in recrystallized Pb-Zn ore deposits: example from the Pyrenean Axial Zone". It was submitted on July 27, 2019 in Mineralium Deposita.

A detailed study of the chemical related to textural particularities of the Pyrenean sphalerite is shown in this section. Sphalerite ore is analysed with electron-back-scattered diffraction (EBSD) techniques to image its texture and grain boundaries. We couple EBSD on sphalerite with laser ablation inductively coupled plasma mass spectrometry (LA-ICPMS) in-situ analyses and innovative Laser induced breakdown spectroscopy (LIBS) mapping technique. These analyses are performed on the different mineralizations hosted in the Pyrenean Axial Zone such as Type 2b ore (Arre, Anglas and Pale Bidau sphalerite) but also the metamorphosed Type 2a stratabound mineralizations from Victoria, Bentaillou and Margalida deposits. Type 2b ore is the only host for Ge in the Pyrenees which may be present in sphalerite (up to 600 ppm Ge) or more commonly in Ge-minerals (carboirite, brunogeierite, briartite). This study allows us to clearly linked sphalerite recrystallization and mobility of elements such as Ge, Cu, or Ga. A comparison with other sphalerite rich in Ge in the world is performed to better emphasize the chemical control of Ge redistribution.

Alexandre Cugerone[1], Bénédicte Cenki-Tok[1], Manuel Muñoz[1], Kalin Kouzmanov[2], Emilien Oliot[1], Vincent Motto-Ros[3], Elisabeth Le Goff[4]

[1]Géosciences Montpellier, Université de Montpellier, France;
alexandre.cugerone@umontpellier.fr; benedicte.cenki-tok@umontpellier.fr ;
manuel.munoz@umontpellier.fr ; emilien.oliot@umontpellier.fr
[2]Department of Earth sciences, University of Geneva, Switzerland; Kalin.Kouzmanov@unige.ch
[3]Institut Lumière Matière Université Lyon 1, France; vincent.motto-ros@univ-lyon1.fr
[4]BRGM, Bureau de Recherches Géologiques et Minières, Montpellier, France ; e.legoff@brgm.fr

5.2.1 Abstract

Rare metals (Ge, Ga, In, Cd) are key resources for the development of the green technologies and are commonly found as traces in base-metal ore deposits (Pb-Zn-Cu). These deposits generally occur in orogens and the impact of recrystallization on rare metal content and distribution in sphalerite needs to be evaluated. Based on laser inductively coupled plasma mass spectrometry (LA-ICP-MS), laser-induced breakdown spectroscopy (LIBS)-based imaging and electron backscattered diffraction (EBSD) analyses, we investigate the minor and trace element chemistry related to sphalerite texture of three mineralization types from the Pyrenean Axial Zone (PAZ). Vein mineralization (Type 2b) is enriched in rare metals like Ge and Ga compared to disseminated and stratabound mineralization (Type 1 and Type 2a). In vein-type mineralization, deformation induced partial recrystallization led to the remobilization of Ge, Ga, and Cu from sphalerite lattices into accessory minerals. We propose that the interaction between intra-granular diffusion and fluid-assisted processes is responsible for the formation of patchy-striped zonations and the crystallization of accessory minerals. Chemical and textural heterogeneities are frequent in sphalerite from other world-class deposits and a coupled understanding of these heterogeneities is crucial to evaluate the rare metals potential of deformed base metal ores.

5.2.2 Introduction

Sphalerite (ZnS) is the major carrier of Zn in Pb-Zn deposits. It commonly contains important concentrations (up to a few 1000s of ppm) of rare metals such as germanium (Ge), indium (In), gallium (Ga) or cadmium (Cd) which are currently extracted from zinc concentrates as by-products *(Frenzel et al. 2014, 2016, 2017; Licht et al. 2015)* and considered critical by European Commission and U.S. Geological Survey (European Commission 2017a; U.S. Geological Survey 2019). These important concentrations are generally found related to non-deformed sphalerite in coarse crystals from open filling structures or colloform fine-grained banding (Cerny and Schroll 1995; Goffin et al. 2015; Henjes-Kunst et al. 2017b; Cugerone et al. 2018a). They occur mainly in undeformed MVT and polymetallic vein deposits (*Viets et al. 1992; Saini-Eidukat et al. 2009; Murakami and Ishihara 2013; Belissont et al. 2014; Bonnet 2014; Bauer et al. 2018*), preferentially mineralized at low-temperature even if some high-temperature veins may contain a sphalerite rich in rare metals mainly in In-rich systems (Shimizu and Morishita 2012; Sahlström et al. 2017a; Gallard-Esquivel et al. 2018). However, the largest amount of sphalerite ore on Earth is mainly found in orogenic domains (*Lawrence 1973; Moore et al. 1986; Kelley and Jennings 2004; Kampunzu et al. 2009; Wilkinson 2013; Gibson et al. 2017)*. Therefore, ores that have originally formed as Sediment-

Hosted Massive Sulfide (SHMS), Volcanic-Hosted Massive Sulfide (VHMS) or carbonate-hosted deposits (Kipushi-type, more rarely MVT) may have endured metamorphism and recrystallization (*Bernstein and Cox 1986; Hughes 1987; Murphy 2004; Wagner and Monecke 2005; Huston et al. 2006; Melcher et al. 2006; Monteiro et al. 2006; Kamona and Friedrich 2007; Reiser et al. 2011; Ye et al. 2011)*.

In metamorphic environments, remobilization of minor and trace elements related to recrystallization, annealing or brecciation has been studied for various sulfide minerals. The mobility of Au, As, Ni, Co, Pb, Bi, and Se has been examined in pyrite *(Cook et al. 2009a; Large et al. 2009; Reddy and Hough 2013; Velásquez et al. 2014; Dubosq et al. 2018; Kampmann et al. 2018*), arsenopyrite-löllingite (Tomkins and Mavrogenes 2001; Wagner et al. 2007; Fougerouse et al. 2016b) and pyrrhotite (*Vukmanovic et al. 2014)*. Dynamic recrystallization assisted by metamorphic fluids results in a release of invisible gold from the sulfide crystal lattice and subsequent crystallization of free gold (Fougerouse et al. 2016b; Dubosq et al. 2018). *Lockington et al. (2014)* reported sphalerite from diverse metamorphosed VHMS and SHMS deposits. Metamorphic recrystallization led to minor and trace element remobilization resulting in an absence of compositional zoning, and re-homogenization of Cu in the sphalerite lattice associated to a possible loss of Pb, Bi, Ag and an enrichment of Fe, Cd, Mn, In. These data were acquired in different deposits at different metamorphic grade and the role of the primary enrichment in these elements cannot be clearly established. In Neves Corvos (Iberian pyrite Belt, *Carvalho et al. 2018*), Indium is still contained in recrystallized sphalerite and chalcopyrite during late-remobilization but locally roquesite, an indium mineral ($CuInS_2$), occurs at sulfide grain boundaries. Nonetheless, Ge is essentially reported below ~100 ppm Ge in the sphalerite lattice (EPMA measurements). In another Iberian pyrite Belt deposit named Barrigão, *Reiser et al. (2011)* and *Belissont et al. (2019)* suggested a late-stage remobilization of Germanium in the Barrigão chalcopyrite associated with Germanium enrichment in fractures. Occurrence of rare metals such as Ge, Ga, In, and Cd within deformed/metamorphosed sphalerite ore is generally poorly documented and their behavior in such systems still needs to be evaluated even if some recent studies start to decipher their behavior during deformation in similar sulfide assemblages which may appear partly recrystallized in some cases (George et al. 2016; Carvalho et al. 2018; Cugerone et al. 2019; Frenzel et al. 2019). Even though sphalerite presents a ductile behavior at relatively low-temperature (< 400°C; in *Clark and Kelly, 1973; Siemes and Borges, 1979; Couderc et al., 1985; Cox, 1987*), no experimental study on the impact of deformation on trace elements behavior is available.

A recent study by *Cugerone et al. (2020)* describes the redistribution of Ge in a single partly recrystallized sphalerite observed in the Arre vein deposit (Pyrenean Axial Zone). Crystallographic lattices of recrystallized sphalerite are depleted in Ge but are the main host for the occurrence of

Ge-minerals compare to dark domain in coarse grains which still contains Ge in the sphalerite lattice (up to 600 ppm Ge). This study aims to decipher the behavior of rare metals (mainly Ge, Ga, In, Cd) in sphalerite from different Pb-Zn deposits and mineralizations of the Pyrenean Axial Zone (PAZ). The Pb-Zn deposits of the PAZ contain rare metal-rich sphalerite and accessory minerals hosted in sphalerite such as brunogeierite ($GeFe_2O_4$), briartite [$GeCu_2(Fe, Zn) S_4$], carboirite [$GeFeAl_2O_5(OH)_2$] or argutite (GeO_2) (Laforet et al. 1981; Johan et al. 1983; Bernstein 1985; Johan and Oudin 1986; Pouit and Bois 1986a; Julliot et al. 1987; Cugerone et al. 2018a). We have investigated the chemistry of diverse types of sphalerite mineralization in the Pyrenees based on an *in situ* quantitative analysis with LA-ICP-MS (laser ablation inductively coupled plasma mass spectrometry) and mapping of trace elements with LIBS (laser-induced breakdown spectroscopy). We present a detailed genetic model at vein and granular scales for the partitioning of Ge and associated trace elements between sphalerite and accessory minerals. Finally, we present a comparison with other Pb-Zn deposits in the world enriched in Ge.

5.2.3 Sampling and analytical methods

Oriented ore specimens were sampled *in situ* in underground mines or in surface outcrops. We have studied polished sections (either 30 or 150 μm-thick) from six Pb-Zn deposits with EBSD (electron backscattered diffraction), EPMA (electron probe micro-analysis) and LA-ICP-MS (laser inductively coupled plasma mass spectrometry). Their structural position in the regional tectonic framework is systematically documented (see below).

EBSD analysis was herein, essentially used to detect the texture and the grain size of the sphalerite. EBSD analysis of thin sections requires a well-polished surface. To remove surface defects, thin section polishing was first performed with diamond polisher at four different granulometric steps (6, 3, 1 and 0.25 μm). A last step of polishing was performed using a Vibromet polisher with 150 g of pressure on a polyurethane layer with colloidal silica. During this process, cleaning the frozen colloidal silica was necessary to avoid scratches on sphalerite. EBSD maps were performed with a Camscan Crystal Probe X500FE SEM-EBSD at Geosciences Montpellier (CNRS-University of Montpellier, France). Operating conditions were 20 kV and 5 nA, with a working distance of 25 mm under 2 Pa low vacuum. Samples surface were positioned horizontally at 20° to the incident electron beam to improve the collection of the backscattered electrons. Element distribution maps were simultaneously acquired by measuring X-ray fluorescence with an EDS (energy dispersive spectrometer) detector. The step size for 2D imaging was below 5 μm. In all studied samples, EBSD mapping was focused on sphalerite which was indexed as a cubic crystal

symmetry and Ge-minerals were located with EDS maps. Indexation of quartz, calcite, galena and pyrite was also performed. Match units used for sphalerite indexation were derived from published crystallographic data from *Villars and Calvert (1991)*. The lower limit of the misorientation grain boundary angle is fixed at 20° following careful investigation on misorientation boundary maps superimposed on orientation maps. Oxford Instruments softwares AZtec and Channel 5 were used to generate maps from the EDS (chemical maps) and EBSD (structural maps) detection systems.

Electron probe micro-analyses were carried out using a Cameca SX100 at the Service Inter-Régional Microsonde-Sud (Montpellier, France). Major, minor and trace elements were measured with a beam current of 100nA and accelerating voltage of 20 kV. The analytical procedure and detailed settings for each elemental analysis is detailed in *Cugerone et al. (2018a)*. Zinc concentrations of sphalerite crystals were used as an internal calibration for LA-ICP-MS analyses.

LA-ICP-MS was used to determine minor and trace elements concentrations in sphalerite. Analyses were carried out using an Excimer CompEx 102 coupled to a ThermoFinnigan Element XR at the OSU-OREME AETE platform (University of Montpellier, France). Laser ablation was performed using a constant 5 Hz pulse rate at 140 mJ. Each analysis comprises 180 s of background measurement and 60 s of sample ablation (signal measurement), followed by a 60 s retention time to ensure a proper cell washout. Data were processed using the Glitter 4.0 software package *(Van Achterbergh et al. 2001*). The following isotopes were measured: ^{29}Si, ^{34}S, ^{55}Mn, ^{57}Fe, ^{59}Co, ^{61}Ni, ^{63}Cu, ^{64}Zn, ^{69}Ga, ^{74}Ge, ^{75}As, ^{77}Se, ^{95}Mo, ^{105}Pd, ^{107}Ag, ^{111}Cd, ^{115}In, ^{118}Sn, ^{121}Sb, and ^{208}Pb. MASS-1 reference material (*Wilson et al. 2002)* was used as an external standard with a corrected 57 $\pm$ 1.75 ppm value for Ge (Dr. Stephen Wilson, personal communication). NIST SRM 610 *(Pearce et al. 1997)* was used as secondary external standard to identify possible instrumental drift. Concentrations for Ni, As, Mo, Se, Pd and Si were below detection limits in all measurements. Several time-integrated LA-ICP-MS spectra are reported in the supplementary material (Fig. SM1), illustrating the time intervals used for the measurements.

Laser-induced breakdown spectroscopy (LIBS)-based imaging was used to image the distribution of Ge, Cu, Ga, Zn, Si, Fe, Cd, Al, Mg, and Ti. It is an all-optical analytical technique, allowing the mapping of metallic elements in various type of solid matrices at a micrometric spatial resolution with a sensitivity at the ppm level *(Sancey et al. 2014; Cáceres et al. 2017; Fabre et al. 2018*). During the analysis, the sample surface is scanned, through single laser pulses, in a pixel-by-pixel manner to induce the breakdown of the material. The light radiation emitted by the plasma is then collected by an optical system and analyzed using a spectrometer. Among other elemental imaging approaches, LIBS offers several advantages such as table-top instrumentation, ease of use, speed

of operation, and detection of light elements (*Busser et al. 2018; Jolivet et al. 2019*). The sample was analyzed using Nd:YAG laser with a pulse energy of about 600 μJ operating at 100 Hz, and a lateral resolution (i.e. distance between two consecutive laser shots) of 13 μm. The surface analyzed is about 6 cm^2 (corresponding to an image size of 3.6 megapixels) and has been obtained in 6 h. The spectrometer was configured in the spectral range 250-330 nm to detect intense lines of Ge (265.1 nm), Cu (324.7 nm) and Ga (294.4 nm), among others. Due to an interference with an Al line, the Ge line at 269.1 nm was used in the aluminosilicate phases.

5.2.4 Geological setting

The studied Pb-Zn ore deposits are hosted in the Variscan Pyrenean Axial Zone (PAZ, Figure 71a), exhumed during the Paleogene collision between the Iberia and Eurasian plates *(Zwart 1979; Carreras and Druguet 2014)*. The PAZ is essentially composed of Paleozoic metasediments intruded by Ordovician and Late-Variscan granitoids (Figure 71b; *Kleinsmiede, 1960; Zwart, 1963; Denèle et al., 2014*). These Pb-Zn deposits are concentrated in pluri-kilometric anticlinoriums like the Bossost or Pierrefitte anticlinorium (Figure 71b).

The Pb-Zn district of the PAZ was exploited in 20th century. It has produced *ca.* 400 kt of Zn and 180 kt of Pb *(BRGM 1984; Ovejero Zappino 1991*). Three Pb-Zn mineralization types occur and fully described in *Cugerone et al. (2018b)*. Type 1 is a minor disseminated and laminated mineralization, probably associated to sedimentation during Cambro-Ordovician and Devonian times. Type 2a, colored in orange in Figure 71, is a stratabound mineralization parallel to S_0-S_1 (Figure 71c), epigenetic and synchronous to the Variscan D_1/M_1 regional deformation/metamorphism event. M_1 metamorphism is related to crustal thickening (Zwart 1963a, 1979; Mezger et al. 2004; Laumonier et al. 2010) and is characterized by medium pressure and low-temperature (MP/LT) conditions with a peak estimated at 580°C and 0.55 GPa in the Bossost dome (*Mezger et al., 2004*). In the field Type 2a mineralization appears in metric pull-apart type structures in Cambrian marble like in Bentaillou (BE) (Figure 71c) or folded by D_2 deformation in Late-Ordovician metamorphic schists in Victoria (VT) (Figure 71c). It can also be associated to fault damaged zones in Late-Ordovician marble in Margalida (MG) (Bossost fault, Figure 71b; *Cugerone et al., 2018b)*

Type 2b, colored blue in Figure 71, is an epigenetic vein-type mineralization probably late or post-dating the D_2/M_2 deformation event (*Cugerone et al. 2018b*). M_2 is described as contact

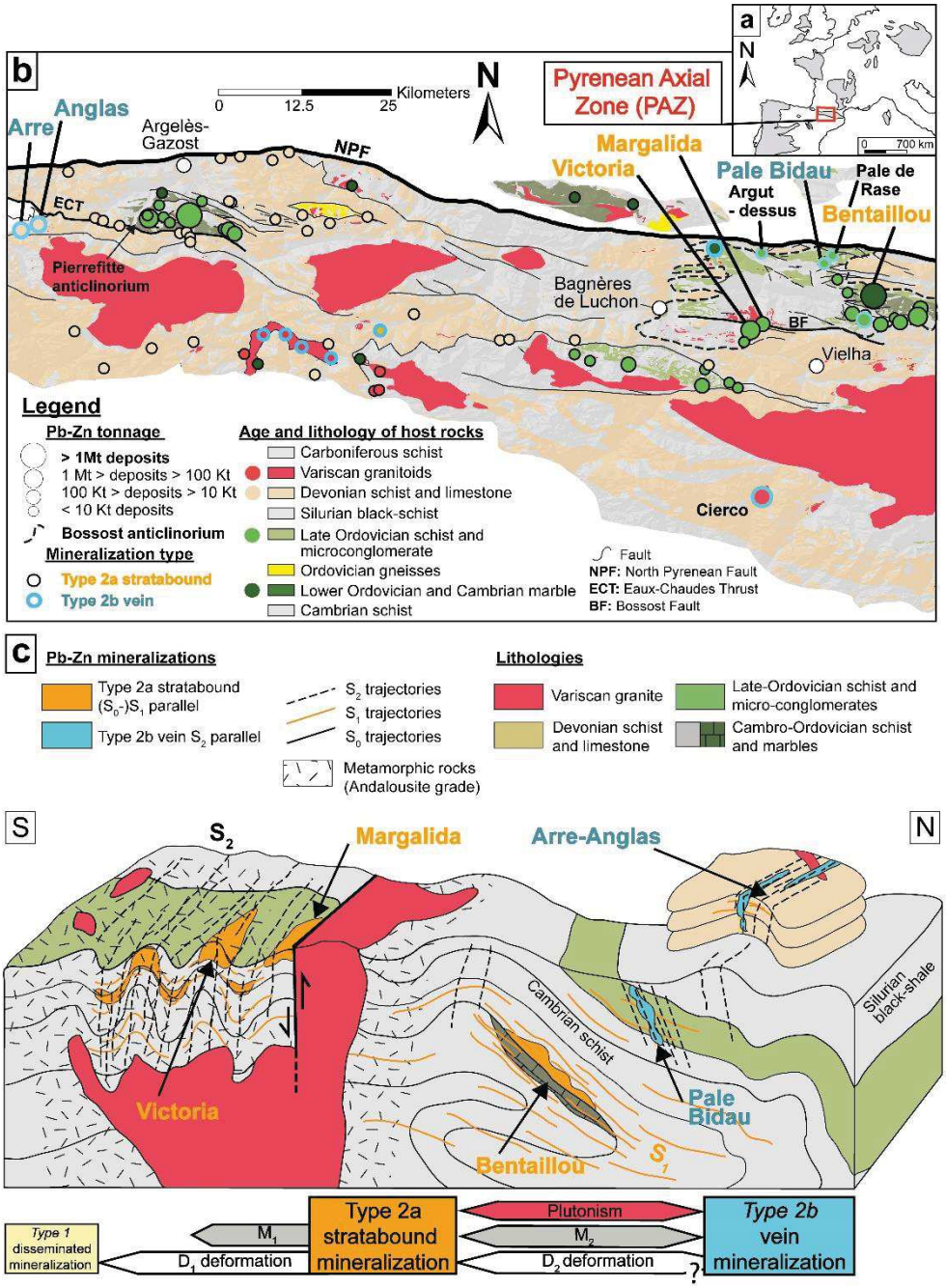

Figure 71. a Location of the Pyrenean Axial Zone in the Variscan belt of Western Europe. b Lithological and structural map of Central Pyrenean Axial Zone with location of Pb-Zn deposits (*BRGM and IGME databases*). The two main mineralization types are reported. Type 2b mineralization is newly differentiate from Type 2a in *Cugerone et al. (2018b)* and reported in investigated deposits. Numerous other non-explored Pb-Zn deposits may contain Type 2b mineralizations. c Structural 3D synthetic model with location of the studied Pb-Zn deposits and replaced according to lithologies, structures and metamorphic imprint. Chronological interpretation from *Cugerone et al. (2018b)* is reported below the model. Timing of mineralization for the Type 2b vein mineralizations is questioned but in this article, we consider deformation imprint as Late-Variscan (D_2).

metamorphism culminating at *ca.* 525°C and 0.2 GPa *(Mezger and Passchier 2003; Mezger et al. 2004; de Hoÿm de Marien et al. 2019)*. Pb-Zn mineralization occurs as vertical decimetric-sized veins parallel to S_2 cleavage which locally intersect Type 2a mineralization. No alteration halo has been observed along the contact with the host-rock. This mineralization which intersects Late-Variscan aplitic intrusions, is considered Late-Variscan in age because the zinc ore is impacted by a cleavage parallel to Late-Variscan S_2 cleavage in the host rock (*Cugerone et al. 2018b)* . We have studied samples from Type 2b Pale Bidau (PB) and Arre-Anglas (AR and AG) deposits hosted in calc-schists (Figure 72a). A late D_3 deformation is reported in the literature (Carreras and Druguet 2014; Cochelin et al. 2017b) and corresponds to faults like the Bossost mylonitic fault close to Type 2a MG deposit.

5.2.5 Results

5.2.5.1 Mineralization styles and textures

5.2.5.1.1 Macroscopic description

The three types of mineralization are essentially composed of sphalerite and galena, with minor pyrite, chalcopyrite, arsenopyrite and gangue of quartz-carbonate (Figure 72a). Type 1 mineralization comprises micrometric-sized disseminated crystals. Type 2a and Type 2b mineralization show distinct sulfide mineral textures. Type 2a sphalerite generally contains non-deformed-twinned crystals with a homogeneous millimetric-sized and polygonal shape that appear in dark-reddish color in transmitted light microscopy (Figure 72b). Ore textures is different at MG (Figure 72c), which present small μm-scale sphalerite grains with dark-brown color and constituting the matrix of a breccia composed of quartz and schist clasts. Sphalerite is folded in VT (Figure 72d) and may be associated with centimetric-size metamorphic minerals like gahnite (Figure 73; *Cugerone et al. 2018a*).

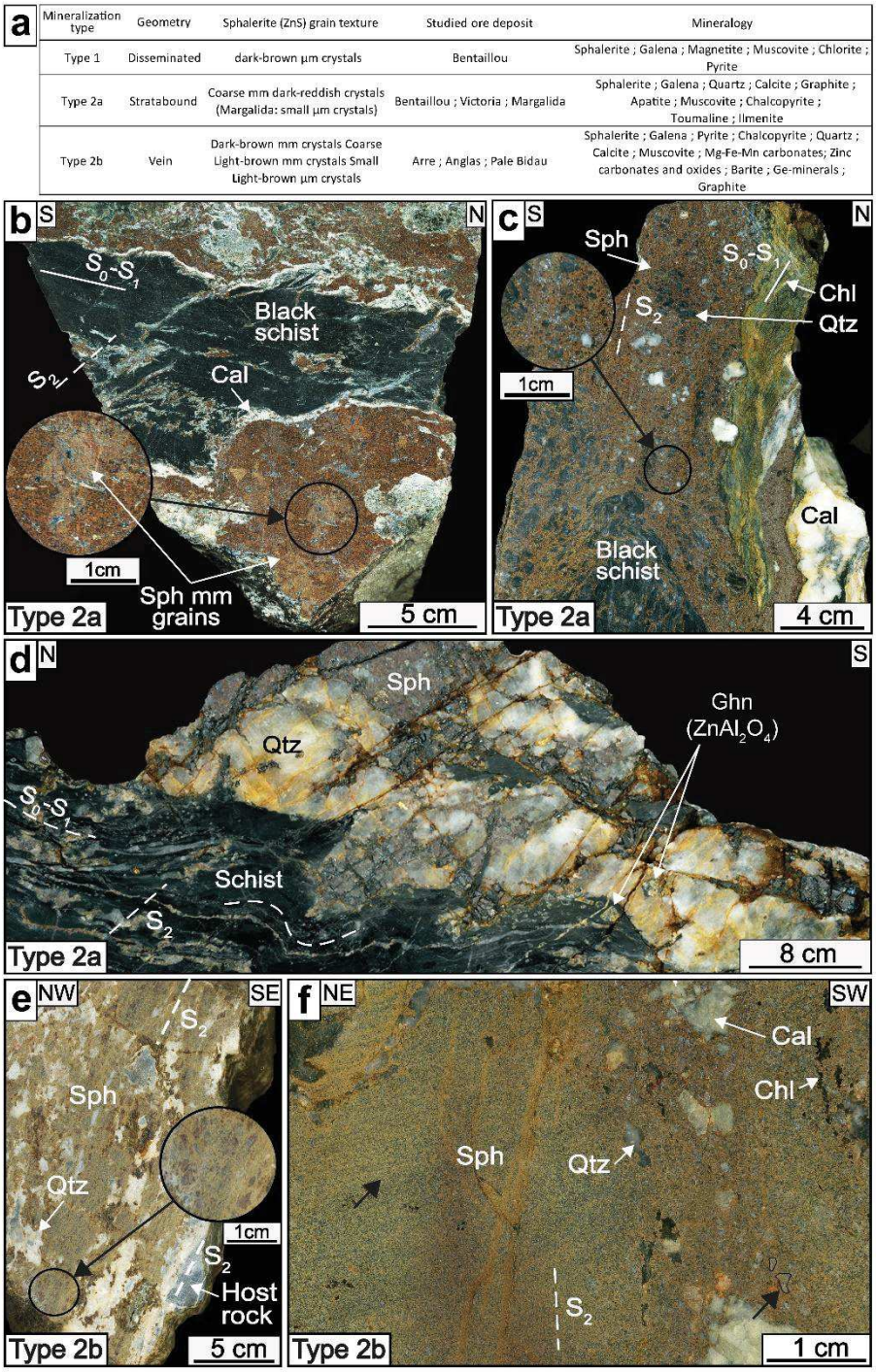

Figure 72. Sample photographs of the studied deposits. a Characteristics of the three mineralization types (Type 1, Type 2a, Type 2b) discussed in this study. b Bentaillou (BE) sample with millimetric coarse-grained sphalerite and dark-brown reddish colors associated to calcite and schist. A zoom on the sphalerite crystals is shown. c Margalida (MG) sample pluri-micrometric small-grained sphalerite with dark-brown reddish colors. A brecciated texture can be observed with clasts of quartz, calcite and black-schist. A zoom on the sphalerite crystals is presented. d Victoria (VT) sample with folded (F_2) coarse-grained sphalerite and quartz mineralization. Gahnite crystals are reported in schists and in the mineralization. e Arre (AR) sample with light to dark brown zonations in sphalerite crystals associated to quartz and calc-schist host rock. In the zoom, coalescence of coarse millimetric and small micrometric crystals appear. f Pale Bidau (PB) sample with light to dark brown sphalerite associated to quartz, calcite and chlorite. Dark brown vertical bands are visible on the sample. Sphalerite grains are locally visible as shown by the black arrow at bottom right.

Type 2b sphalerite shows a light to dark brown color in transmitted light and a heterogeneous grain-size resulting from a superimposed cleavage (considered to be S_2) parallel to the vein contact (Figure 72e and Figure 72f). In AR, AG and PB, sphalerite appears with different colors from dark-brown zonations in coarse grains and light-brown in coarse or fine grain fraction (Figure 72e and Figure 72f). Quartz and carbonate show comb textures with the occurrence of cockade breccia mainly in AR and AG Type 2b veins.

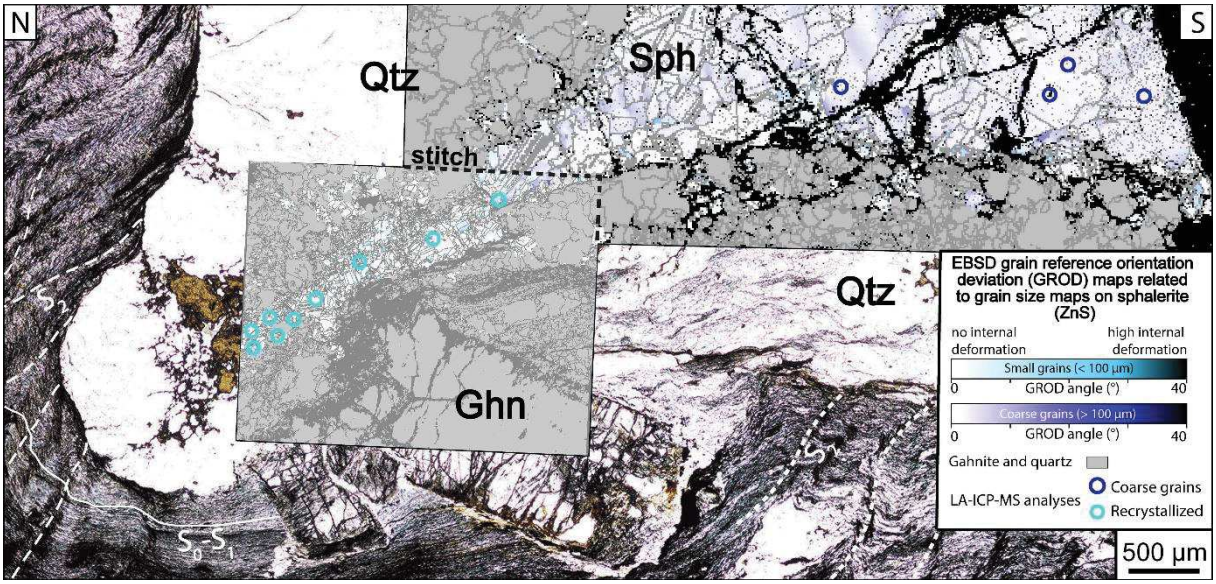

Figure 73. EBSD grains size map superposed onto a transmitted light microphotograph of sphalerite-quartz mineralization in F_2 fold hinge from VT deposit (Sph: sphalerite; Qtz: quartz; Ghn: gahnite). LA-ICP-MS spot analysis in Type 2a coarse and recrystallized sphalerite are indicated.

5.2.5.1.2 Microscopic description

Type 1 mineralization is crosscut by Type 2a veins (BT deposit, *Cugerone et al., 2018b*). It is composed of pluri-micrometric euhedral dark brown crystals. Type 2a mineralization is composed of millimetric sphalerite crystals with reddish-brown colors like in BT. In MG, pluri-micrometric sphalerite crystals constitute the matrix of a breccia (durchbewegung, *Cugerone et al., 2018b*) composed of millimetric-size black schist, calcite and quartz clast. In VT, sphalerite grains associated to quartz cross-cut centimetric metamorphic minerals such as gahnite (Figure 73; *Cugerone et al., 2018b*) and exhibit recrystallized textures in F_2 fold-hinges (Figure 73). The mineralogy of Types 2a and 2b veins (*Cugerone et al. 2018b*) is distinct with the presence of apatite, ilmenite, tourmaline in Type 2a and Ge-minerals, graphite, Mg-Fe-Mn-Zn carbonates in Type 2b. This sphalerite does not contain chalcopyrite inclusions.

Type 1 mineralization is cut by Type 2a veins (BT deposit, *Cugerone et al., 2018b*). It is composed of pluri-μm anhedral dark brown crystals. Type 2a mineralization is composed of reddish-brown sphalerite mm-size crystals like in BT. In MG pluri-μm-size sphalerite crystals constitute the matrix of a breccia (durchbewegung, *Cugerone et al., 2018b*) composed of mm-size black schist, calcite and quartz clast. In VT sphalerite grains can be associated to centimetric-size metamorphic minerals like gahnite (Figure 73; *Cugerone et al., 2018b*) and exhibit recrystallized textures in F_2 fold-hinges (Figure 73). The mineralogy of Types 2a and 2b veins (*Cugerone et al. 2018b*) is distinct with the presence of apatite, ilmenite, tourmaline in Type 2a and Ge-minerals, graphite, Mg-Fe-Mn-Zn carbonates in Type 2b. This sphalerite does not contain chalcopyrite inclusions.

Type 2b ore contains heterogeneous sphalerite textures and is the unique host for Ge-minerals and Ge-rich sphalerite in the PAZ. EBSD grain reference orientation deviation (GROD) maps and transmitted light thin section microphotographs are superimposed in Figure 74. Coarse grains (> 100 μm) and small recrystallized grains (< 100 μm) are colored in shaded of dark and light blue, respectively. Intensities of the distinct blue colors are as higher as the internal deformation is important. Three types of sphalerite textures appear in Type 2b mineralization: coarse grains with dark-brown domains, coarse grains with light-brown domains and recrystallized light-brown crystals. Sub-vertical fine recrystallized fraction domains appear mostly in white color in GROD maps (Figure 74a) which attests to poor internal deformation and commonly mark the cleavage, for example in PB (Figure 74a and Figure 74b). Coarse crystals (> 100 μm) with color zonations from light-brown to dark-brownish are reported in the AR-AG samples (Figure 74c-f) and commonly contain ductile deformation attested by intense dark-blue color mainly close to grain boundary (Figure 74e). In the EBSD GROD and the grain size maps, it is possible to discriminate between recrystallized and light coarse grains while these two fractions show the same light-orange color in transmitted light (Figure 74). Sphalerite from PB deposit exhibits blurred color domains with progressive variations from light to dark brownish tints and no intra-granular color zonations is observed. In this sphalerite, sphalerite crystals with coarse and recrystallized crystals with light color are dominant (Figure 74a).

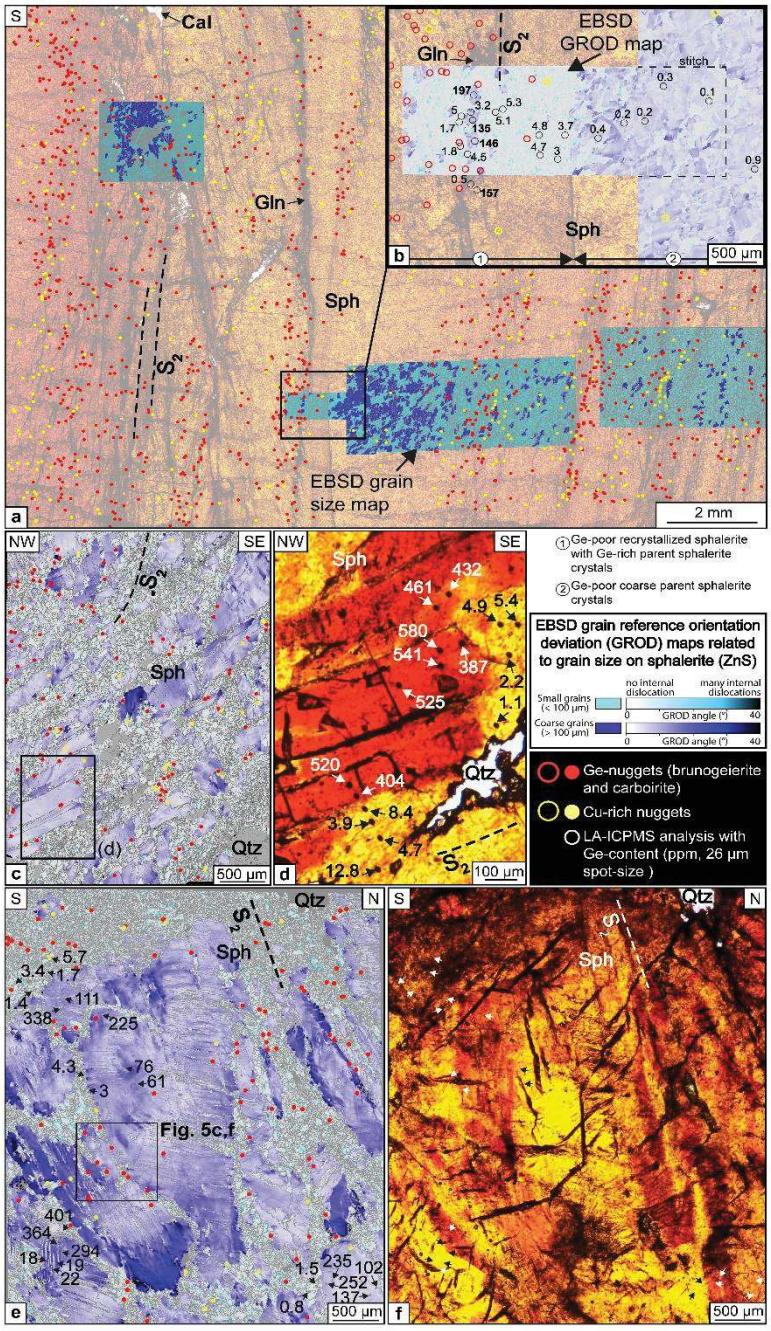

Figure 74. Microphotographs associated to EBSD grain size map with grain boundaries and chemical contents (Sph: sphalerite; Qtz: quartz; Gln: galena). a Scanned microphotograph of PB sample with superposition of fours EBSD grain size maps. Step of measurements is inferior to 4 µm for all maps. Ge and Cu minerals observed with EDS map are reported. Location of Figure 74B is noted b Zoom with location of LA-ICP-MS spot analyses associated to Ge-contents on EBSD grain size map. Presence of Ge and Cu rich inclusions are reported with empty yellow and blue circles to precisely discern the relations between Ge-Cu minerals and sphalerite. c AR sample EBSD grain size map with location of Ge and Cu rich phases. These minerals are preferentially located in the recrystallized sphalerite domains. Location of Figure 74D is represented. d Corresponding area in transmitted light with LA-ICP-MS spot analyses associated to Ge-contents. Note the color zonation which is corresponding to variations in Ge content. e AG sample EBSD grain size map with location of Ge and Cu rich minerals in recrystallized sphalerite. LA-ICP-MS spot analysis are located with their corresponding Ge-contents. Zoom in the Figure 75C and F is marked. f Corresponding area in transmitted light with important color zonations. LA-ICP-MS spots are indicated with black or white arrows.

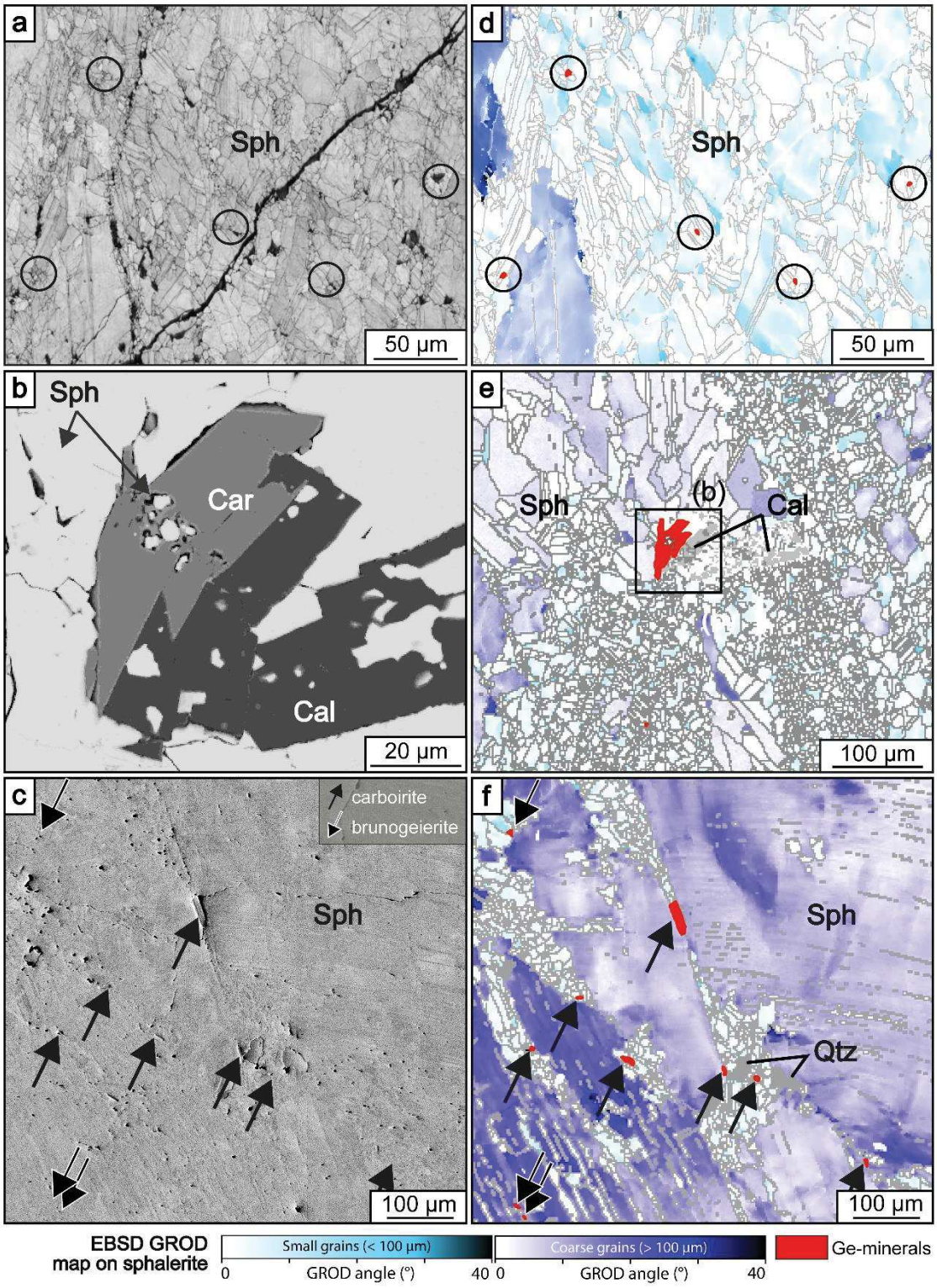

Figure 75. Images of Ge-minerals hosted in recrystallized sphalerite (Sph: sphalerite; Cal: calcite; Qtz: quartz). a Five brunogeierite (in the black circle) crystals in AR sample (Back scattered Electron image). b Carboirite crystals associated to sphalerite and calcite (SEM image from PB sample) c Nine Ge-minerals hosted in sphalerite. Carboirite grains are indicated with a white arrow and brunogeierite are shown with black arrows (Back scattered Electron image from AG sample). d-e-f EBSD grain size maps for Fig. 6a., b. and c., respectively.

Minerals in which Ge is a major element (further referenced as Ge-minerals in the text) have been identified as brunogeierite ($GeFe_2O_4$), carboirite [$FeA1_2GeO_5(OH)_2$], briartite [Cu_2(Fe, Zn) GeS_4] and argutite (GeO_2). Briartite is the main Ge-mineral in AR sphalerite but is rare in AG and PB sphalerite. Carboirite, brunogeierite and more rarely argutite minerals represent the essential occurrence of Ge-minerals in AG and PB deposits. These minerals are preferentially hosted in recrystallized sphalerite grains. In Figure 74 and Figure 75, Ge-minerals occur as small minerals (< 100 μm; see yellow dots in Figure 74) and are preferentially aligned in the S_2 cleavage. Similarly, Cu-rich micrometric minerals are preferentially aligned in the same recrystallized areas (blue dots in Figure 74). These inclusions are detected in all Type 2b studied samples (Figure 74c and Figure 74e). Carboirite crystals are coarser (from 10 to 100 μm) compared to brunogeierite, argutite, and briartite (size between 5 and 20 μm; Figure 75).

Figure 75a-c shows three representative examples of Ge-minerals occurrence (back-scattered electron, BSE images) characteristic of Type 2b mineralization. EBSD GROD maps performed on two sphalerite grain size (below and above 100 μm) are presented for the corresponding areas in Figure 75d-f. These maps show that Ge-minerals are only hosted in recrystallized sphalerite grains (< 100 μm, Figure 75d and Figure 75e) in areas with low GROD angle, at the contact or between coarse-grained sphalerite crystals or in twin boundaries (Figure 75f). Note that these Ge-minerals do not occur as inclusions inside the sphalerite grains.

5.2.5.2 In-situ LA-ICP-MS analysis of PAZ sphalerite

5.2.5.2.1 Vein sphalerite chemistry (Type 2b)

In Type 2b veins, the three textural varieties of sphalerite were observed in samples from AR (n=36), AG (n=40) and PB (n=30). The spots for LA-ICP-MS analyses were located based on the EBSD grain size maps to control the type of texture analyzed. Trace elements distribution for each analyzed element is plotted in Figure 76 (see complete data set in the supplementary material Table SM2). Iron content ranges from 1.3 to 3 wt.% Fe but no significant difference appears between deposits or textures (Figure 76). In PB, progressive color zonation results from variable Fe content (Figure 74a and Figure 74b). High Mn median values are reported for AG (151 ± 41 ppm), comparatively to PB and AR (24 ± 4 ppm and 18 ± 2 ppm, respectively). Conversely, low median Cd values are reported for AG (970 ± 38 ppm) and higher median values for PB and AR (1500 ± 75 ppm and 1110 ± 43 ppm, respectively). No correlation between grain-size or color and the chemical contents in Fe, Mn or Cd has been established. Cobalt content is

homogeneous between the three textures (Figure 76) with an average of 143 ± 11 ppm. Very low indium content is measured in these sphalerite types reaching a maximum of 6.2 ppm (Figure 76) and median value below 1 ppm. Indium content is slightly higher in PB light coarse grains with a median value of 4.1 ± 0.2 ppm.

Gallium content is generally below 100 ppm in the sphalerite lattice (Figure 76) but exhibit relative large dispersion in concentrations between 0.3 to 156 ppm Ga which is not clearly related to the type of grain or the deposit. Silver, Sn, Sb and Pb contents are relatively low and generally below 100 ppm. Some Pb-(Sb-Sn-Ag) pluri-micrometric inclusions are recognized in LA-ICP-MS spectra (Figure 139-supp data) preferentially in recrystallized domains with Pb values reaching up to 9420 ppm. Except for the presence of micro-inclusions, no clear difference between textures (Figure 76) and deposits can be defined.

Germanium and copper contents correlate with the type of texture (see Ge spot analyses in Figure 74). These contents show large variations from 102 to 580 ppm for Ge and from 209 to 1265 ppm for Cu.

- In the dark domains of the coarser grains, Ge and Cu are typically high in the three deposits with median value of 290 ± 19 ppm and 610 ± 61 ppm, respectively (Figure 76). In PB, only few dark domain relicts (n=4) are reported and analyzed with median values of 152 ± 20 ppm for Ge and 233 ± 45 ppm for Cu. AR samples show the highest Ge and Cu contents with median values of 433 ± 21 and 1012 ± 75 ppm, respectively.
- In light domains of the coarse grains, Ge and Cu contents are lower with median values of 20 ± 2 and 60 ± 8 ppm, respectively (Figure 76). PB shows the lowest median contents, with 0.7 ± 0.1 ppm for Ge and 29 ± 4.5 ppm for Cu compared to AR and AG which contain median contents of respectively 38 ± 1 and 61 ± 3 ppm for Ge, and 102 ± 7 and 191 ± 13 ppm for Cu.
- In recrystallized grains, Ge and Cu are systematically low, with median contents of 4.3 ± 1 ppm and 49 ± 10 ppm, respectively (Figure 76). In PB recrystallized grains may contain similar or larger enrichment in these two elements than in light domains of the coarse grains with Ge and Cu respective contents of 4.1 ± 0.5 ppm and 102 ± 19 ppm.

5.2.5.2.2 Stratabound and disseminated sphalerite chemistry (Type 2a)

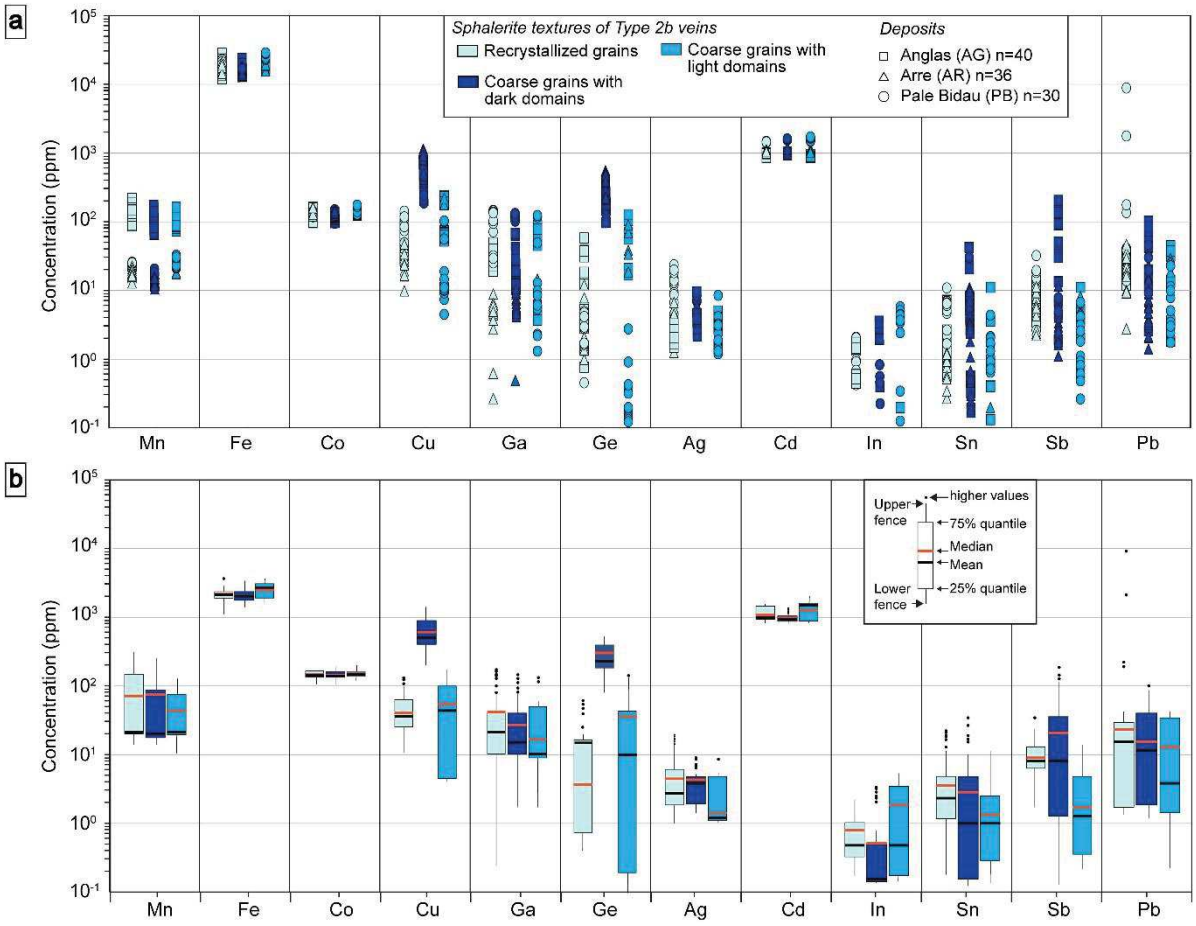

Figure 76. LA-ICP-MS data for Type 2b sphalerite, showing trace element concentration in three different textures and for three ore deposits (complete dataset available in Table 16-supp data). a. Display of all the analyses performed. b. Same data represented as box plot.

The main characteristic of Type 2a sphalerite mineralization is the absence of Ge (below 1 ppm, Figure 77). Copper and Ga contents are low with values below 70 and 30 ppm and median contents of 11 ± 13 ppm and 1.4 ± 6 ppm, respectively (Figure 77). Copper and Ga concentrations in disseminated Type 1 grains from BE have a greater dispersion with median values of 24 ± 22 ppm and 12 ± 1 ppm, respectively.

Recrystallized grains in VT show lower median contents in Mn, Fe, Co, Ga, and Cd but higher median values in Ag, Pb, Sb, Sn, compared to coarse grains in the same sample from VT (Figure 77; analyzed spot locations are reported in Figure 73). Recrystallized grains from VT and MG have similar Mn, Co, Cu contents (Figure 77). Iron and Cd median values are distinct with 2.6 ± 0.1 wt.% and 952 ± 20 ppm for VT recrystallized grains and 3.8 ± 0.4 wt.% and 1946 ± 42 ppm for MG recrystallized grains (Figure 77). Silver, Sn, Sb, and Pb concentrations are

similar between VT and BE coarse grains compared to Mn, Co, Cu, Ga and Cd contents that show large variations (Figure 77). For BE coarse grains median values are 282 ± 19 ppm for Mn, 3.8 ± 0.2 wt.% for Fe, 94 ± 7 ppm for Co, 1 ± 0.3 ppm for Ga and 2246 ± 35 ppm for Cd. In comparison to BE coarse grains, disseminated BE sphalerite shows large variations in Cu, Ga, Ag, Sn, Sb and Pb (Figure 77) but similar contents in Fe, Co with median values of 3.9 ± 0.4 wt.%, 88 ± 10 ppm and 7.6 ± 4 ppm respectively for Type 1 mineralization (Figure 77).

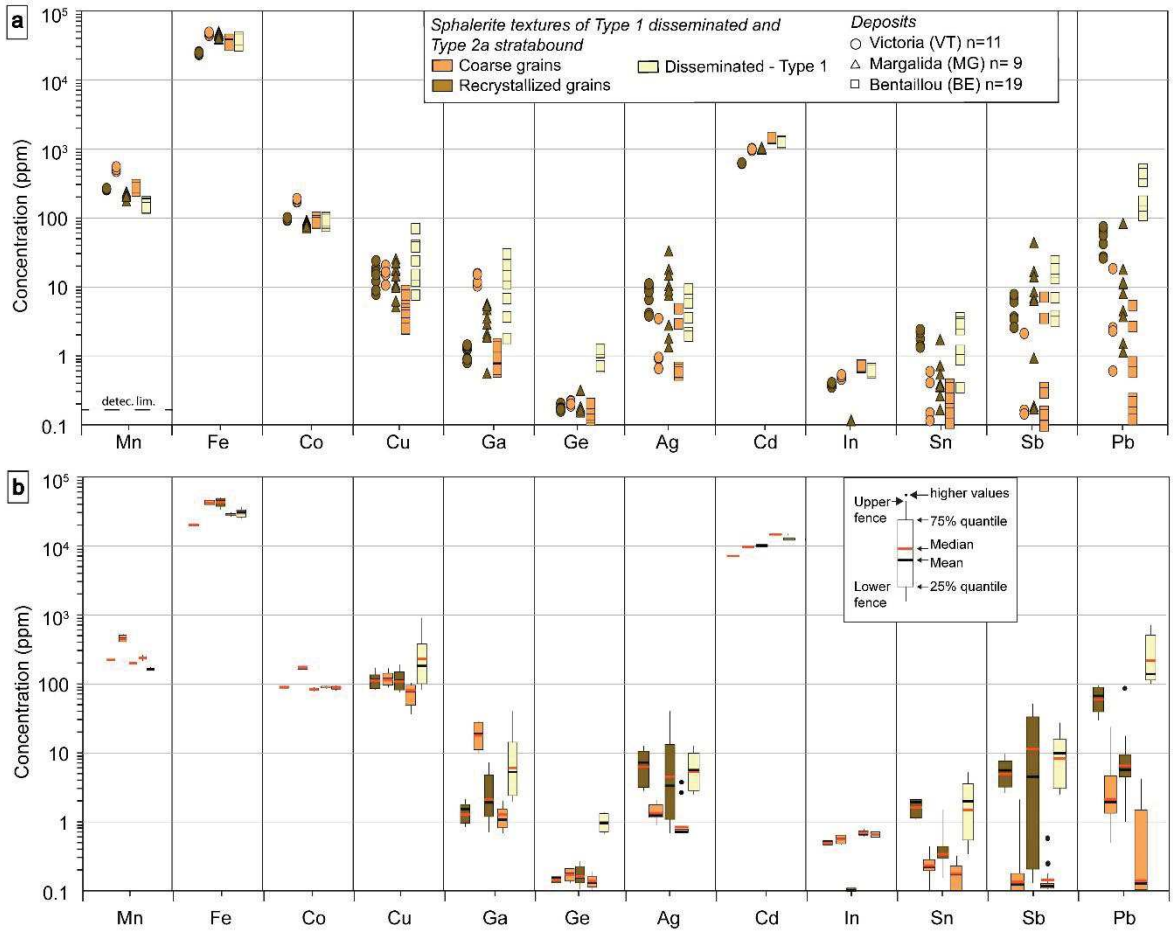

Figure 77. LA-ICP-MS data for Type 2a sphalerite, showing trace element concentration in three different textures and for three ore deposits (complete dataset available in Table 16-supp data). a. display of all the analyses performed. b. same data represented as box plot.

Manganese content is generally higher in coarse grains compared to Type 2b mineralization (Figure 76 and Figure 77) with median values of 289 ± 100 ppm for VT and BE coarse grains and 24.8 ± 66 ppm for Type 2b mineralization. Iron content in Type 1 and 2a is globally higher than in Type 2b with values between 2.5 ± 0.2 ppm and 5.4 ± 0.5 ppm. There is no similarity in the Fe content between MG and VT recrystallized grains with median value of 2.7 ± 0.2 ppm and 5.0 ± 0.5 ppm respectively. Cobalt content is high in VT coarse grains with median value of 172 ± 10

ppm compared to the grains analyzed in other textural position that present a median value of 89 ± 8 ppm.

Cadmium is highly variable according to deposit and texture. Recrystallized VT coarse grains show the lowest contents with a median value of 956 ± 20 ppm (Figure 77). VT coarse grains present higher Cd content with 1504 ± 28 ppm. MG recrystallized grains contain similar Cd values with median contents of 1557 ± 37 ppm. Indium content is generally below detection limit, when detected the median value is 0.8 ± 0.4 ppm.

Silver, Sn, Sb and Pb contents are globally higher in recrystallized grains and in disseminated crystals than in coarse grains (Figure 77). In addition, Ag contents are relatively low with total median value of 5 ± 8 ppm but locally, silver can reach 43 ± 13 ppm in MG sphalerite (Figure 77). The same range of concentrations is observed for Sb, with median value of 3.5 ± 9 ppm with contents up to 45 ± 15 ppm. Tin content is low with a median value of 0.4 ± 1 ppm. Lead is below 100 ppm for most of the studied sphalerite types except for Type 1 sphalerite which shows higher content with a median value of 172 ± 156 ppm.

5.2.5.3 Spatial distribution of trace elements in sphalerite

Figure 78 shows Ge, Cu and Ga spatial distribution in the AR Type 2b sample. Sphalerite color zoning in transmitted light (Figure 78a, see the left inset) correlates with these trace elements contents. Germanium and Cu contents are highly heterogeneous in sphalerite, with presence of patchy zonings, and sometimes stripe-like zoning (see white arrows in the right inset of the map in the Figure 78). Numerous Ge- and/or Cu-bearing mineral phases in Figure 78b and Figure 78c occur and are represented in yellow and cyan, respectively. Some of them correlate with Fe (see Figure 140 supp data) and correspond to briartite [$GeCu_2(Fe, Zn) S_4$]. These localized high Ge and/or Cu concentrations are preferentially hosted in Ge-Cu poor domains in sphalerite even if some of them occur in Ge and Cu-rich dark domains and are sub-parallel to S_2 cleavage (Figure 78b and Figure 78c).

After calculation based on LIBS mapping (see Table 17-supp data), Ge mass in Ge-rich grains is 4.72 wt.% Ge (considering an approximated content of 25 wt.% Ge). Light and dark domains present 0.1 and 2.07 wt.% Ge, respectively, considering a Ge-poor and Ge-rich sphalerite with 20 and 400 ppm Ge. Germanium mass fraction is two times higher in Ge-minerals than in sphalerite. The total Ge mass is equivalent to a sphalerite with 690 ppm Ge uniformly distributed in the structure without Ge-minerals.

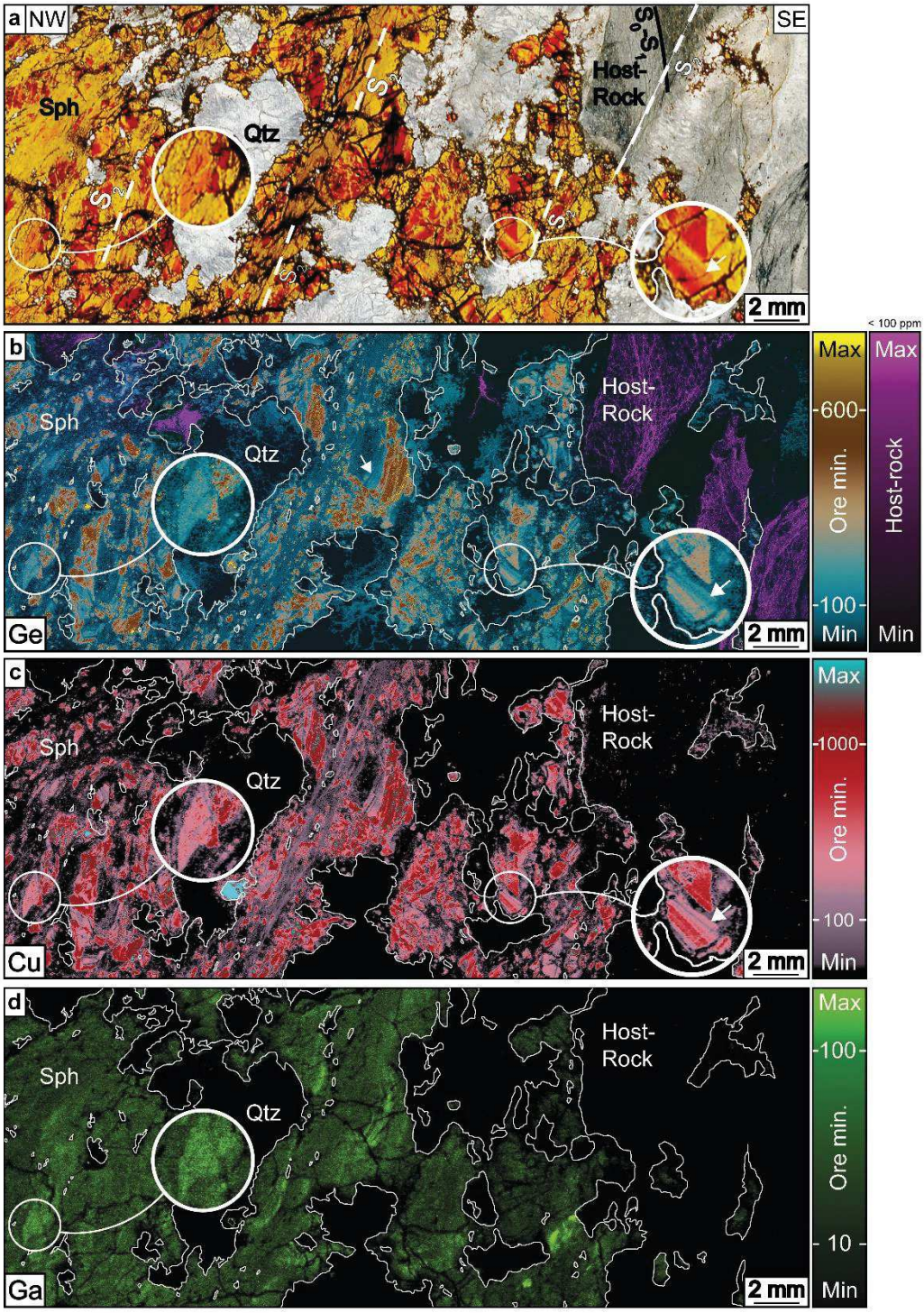

Figure 78. LIBS mapping on Arre Type 2b ore mineralization. Sph: sphalerite; Qtz: quartz; S_2: S_2 foliation. a Scan photograph (thick section, transmitted light) of Arre ore mineralization (sphalerite and quartz) and vein host-rock (calc-schist). b Ge map in ore mineralization and host-rock. Ge is shown in different color between these two phases because it is measured on different spectra due to Al interferences with Ge present in host-rock (schist). White arrows indicate specific Ge zonations. c Cu map in ore mineralization and host-rock. d Ga map in ore mineralization and host-rock.

Gallium in sphalerite shows zonal distribution on LIBS maps. Gallium-rich areas are located essentially in dark domains in transmitted light, correlating with relatively high Cu and Ge contents (Figure 78d, see the left inset). Gallium-bearing mineral phases have not been detected. Other elements like Fe and Cd show relatively homogeneous distribution in the studied sphalerite (see Figure 140-supp data).

Trace elements distribution in quartz spatially associated with sphalerite is reported in Figure 7. Several areas in quartz show enrichment in Ge (Figure 78b). Copper and Ga have not been detected in quartz (Figure 78c and Figure 78d). In the host rock, a few μm-large Cu-bearing grains were identified and Ge has been detected in structures parallel to S_0-S_1 or S_2 (Figure 78) and correlate with the higher Al contents (Figure 140-supp data), which correspond to muscovite mineral. Considering the signal intensity, concentrations in the host-rock can be estimated at 75 ppm maximum.

5.2.6 Discussion

5.2.6.1 Substitution mechanisms

The mechanism of Ge incorporation in sphalerite has been studied by different authors. *Cook et al. (2009b)* deduced from the apparent lack of correlation with other trace elements that Ge could be present in a divalent form and thus could substitute for Zn in the sphalerite structure ($Zn^{2+} \leftrightarrow Ge^{2+}$). Later *Cook et al. (2015)* reported a XANES study performed on Tres Maria Ge-Fe rich acicular sphalerite ores, demonstrating the exclusive occurrence of Ge^{4+} in this mineral. The proposed incorporation mechanism is the substitution of Zn^{2+} or Fe^{2+} by Ge^{4+} and a vacancy (i.e., $2Zn^{2+} \leftrightarrow Ge^{4+} + [\ ]$). In Central and East Tennessee, *Bonnet et al. (2017)* showed the presence of Ge^{2+} and Ge^{4+} in the same sphalerite crystals, which was interpreted as a difference of S_2 and O_2 fugacities. Recently, *Bauer et al. (2018)* have demonstrated a possible coupled substitution between Ge^{4+} and Ag^{+} in low-temperature (186 ± 36°C) Ge-rich sphalerite. *Johan (1988)* performed EPMA measurements on low-temperature Ge- and Cu-rich sphalerite from Saint-Salvy and shown a couple substitution between tetravalent Ge and monovalent combined with divalent Cu ($4Zn^{2+} \leftrightarrow 2Cu^{+} + Cu^{2+} + Ge^{4+}$). *Belissont et al. (2016)* performed a μ-XANES study on the same sphalerite and confirmed the exclusive occurrence of Ge^{4+} in sphalerite showing a clear correlation with only monovalent Cu^{+}, supporting the hypothesis of a coupled substitution mechanism. This substitution $3Zn^{2+} \leftrightarrow 2Cu^{+} + Ge^{4+}$ is illustrated in the PAZ sphalerite, by the 2Cu−Ge correlation line in Figure

79a. Coarse grains lay on the line and follow this substitution mechanism. Recrystallized and some coarse grains with light domains grains are not on the correlation line. In these two Ge-poor domains, it may be explained by the substantial importance of the incorporation of Cu with an

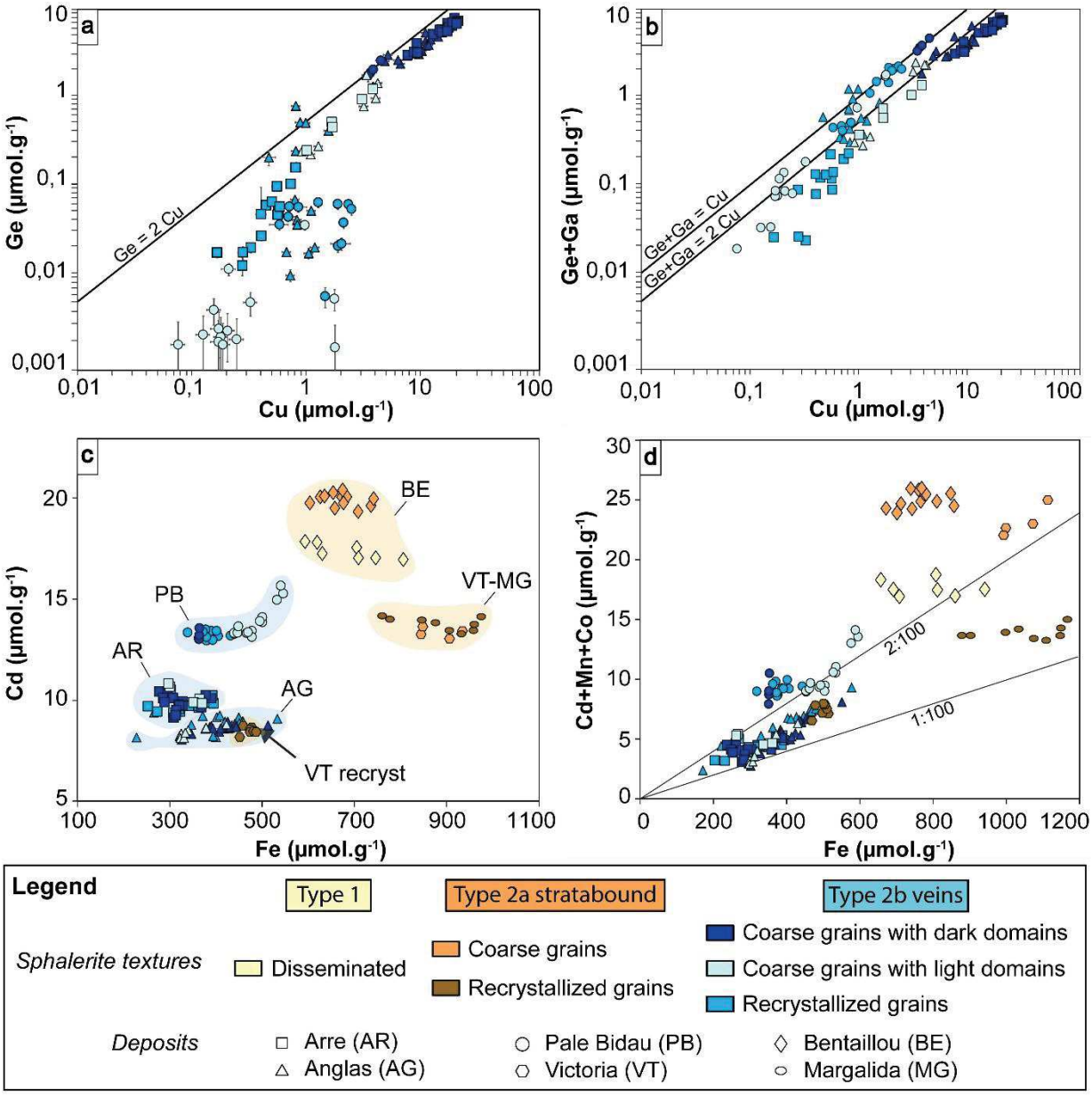

Figure 79. Compared content in representative elements for Type 2b sphalerite mineralizations in a et b and between Type 2a and Type 2b in c and d. a Ge vs Cu contents in sphalerite. In coarse grains within dark domains, analyses are close to the correlation line (Ge – 2Cu). Recrystallized domains with light blue tints do not lay on the correlation line. PB coarse grains within light domains present very low Ge contents. b Ga vs Cu content in sphalerite. Coarse grains within dark domains not lay on the correlation line. Recrystallized and coarse grains within light domains are close to the correlation line (Ga – Cu). c Cd vs Fe content in sphalerite. Note the cluster of compositions corresponding to each deposit. VT recrystallized grains contents are close to AG deposit compositions. d Cd+Mn+Co vs Fe content in sphalerite. Note the correlated enrichment between Cd+Mn+Co and Fe contents especially in Type 2b sphalerite. Higher Fe contents correspond to higher Cd+Mn+Co contents. VT recrystallized grains compositions are close to AG deposit.

additional coupled substitution involving Ga (Figure 79b). Gallium in sphalerite is considered to be trivalent (*Cook et al. 2009b; George et al. 2016; Wei et al. 2018*) and its incorporation occurs following the coupled substitution $2Zn^{2+} \leftrightarrow Cu^{+} + Ga^{3+}$. No correlation is observed between Ge and Ag or Fe in our dataset.

Divalent cations like Cd^{2+}, Mn^{2+}, Co^{2+} or Fe^{2+} are incorporated in direct substitution with Zn^{2+} ($X^{2+} \leftrightarrow Zn^{2+}$, *Cook et al., 2009b; George et al., 2016*). No correlation is present with Cd^{2+} and Fe^{2+} alone (Figure 79C), but a notable feature is the relation between Cd-Fe content and the deposit. In Figure 79D, lower Fe contents are correlated with lower Cd+Mn+Co values and attest for their coupled incorporation even if Fe contents are about two orders of magnitude higher than Cd+Mn+Co contents.

5.2.6.2 Relationship between texture, chemical composition and temperature of formation of sphalerite

Because the crystallization temperature of vein assemblages cannot be assessed directly, we use relative field chronology to place vein formation in the regional tectono-metamorphic framework. M_1 peak is estimated at 580°C and 0.55 GPa, and M_2 peak at 525°C and 0.2 GPa (*Mezger*

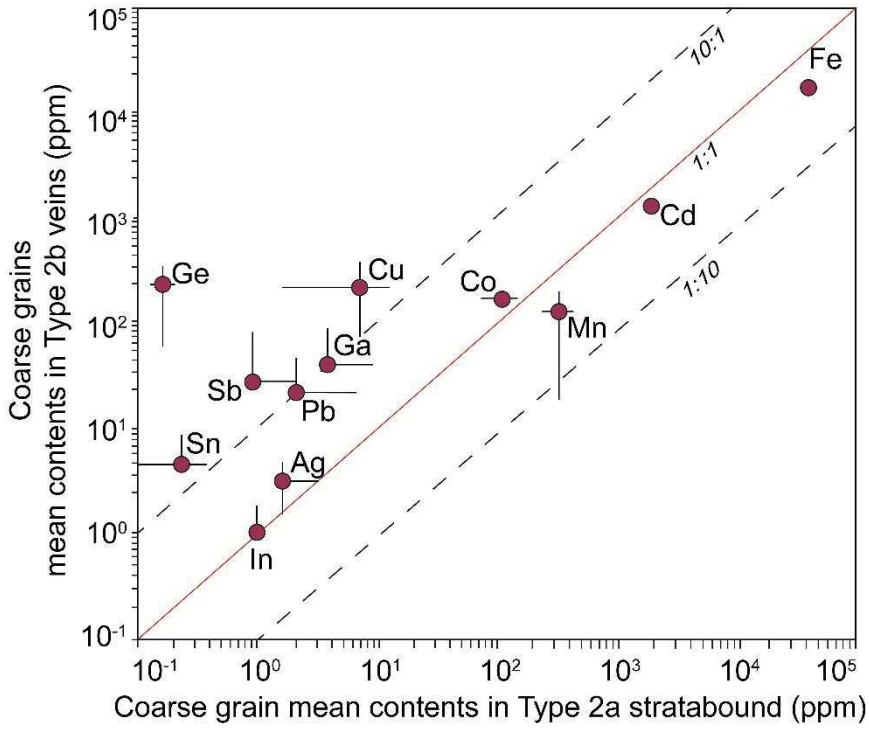

Figure 80. Trace element comparison between Type 2b coarse sphalerite grains and Type 2a coarse sphalerite crystals.

and Passchier 2003; Mezger et al. 2004). The three sphalerite mineralization types show significant differences in trace element signatures. Types 1 and 2a have very low Ge content (<0.5 ppm), as well as Cu, Ga, and Ag, Sb, Sn, Pb but higher Fe, Mn, and Cd contents (see comparison between Type 2a and Type 2b coarse grains in Figure 80). Type 1 disseminated mineralization from BE is considered pre-metamorphic and has endured Variscan M_1 regional and M_2 contact metamorphism (*Cugerone et al. 2018b*).

Type 2a sphalerite from BE, VT and MG is syn-M1 and prior to D_2 event associated to F_2 folds (Figure 73) and M_2 metamorphism. During metamorphism, sphalerite can incorporate Fe, Mn, and Cd and in a lesser extent Pb, Bi, Ag, Sn, and Sb (*Lockington et al. 2014*) associated to static recrystallization. Accordingly, Type 2a statically (coarse fraction) and dynamically recrystallized (small fraction) sphalerite in VT deposit shows respectively high and low Fe, Cd and Mn contents (Figure 76, Figure 77c, d). The GGIMFis geothermometer (*Frenzel et al., 2016*) based on Ge, Ga, In, Mn, and Fe contents in sphalerite lattice was applied (see values in supplementary material Table 18 supp data) for Type 1 and 2a sphalerite and yields temperatures below 150°C however, these data may not be valid because sphalerite has endured static recrystallization with temperature likely above 400°C and in some area subsequent dynamic recrystallization.

The chemistry of Type 2b sphalerite from AG, AR considered late to post-M_2 metamorphism is strongly heterogeneous with Ge, Cu and locally Ga enriched in coarse grains with dark domains (Figure 76) but lower contents in recrystallized and coarse grains with light domains as mentionned by *(Cugerone et al. 2019*). In PB, no chemical zonations in the sphalerite grains appear, but only color bands with differences in Fe-contents (Cugerone et al. 2018a). Ge-poor coarse crystals can be found (e.g., Figure 74b) and such Ge-poor grains are interpreted as inherited Ge-poor domains.

Type 2b mineralization has low Cd and Fe contents. Differences in Cd content between AR-AG and PB might be linked to differences in mineralized event or in the bulk host rock composition. The AR and AG deposits are situated in similar Devonian host rocks in the same mining district contrary to PB which is hosted in Late-Ordovician calc-schists (*Cugerone et al. 2018b*, Figure 71). Cadmium content in Type 2b mineralization is not affected by recrystallization contrary to Type 2a VT recrystallized sphalerite which has Fe, Mn, Co and Cd contents similar to the AG deposits. A potential hypothesis is that Type 2b mineralization may result from remobilization of early Type 2a mineralization in D_2 structures (like VT F_2 fold hinge, Figure 73). However, this hypothesis is limited by the absence of Ge-minerals in this recrystallized sphalerite and by the relatively low Ge, Cu or Ga contents in the entire Type 2a mineralization even if late Ge-Cu(-Ga)-

rich fluids circulating in S_2 cleavage during Type 2b mineralizing event may have been the main Ge-carrier.

The GGIMFis geothermometer (*Frenzel et al. 2016*) based on Ge, Ga, In, Mn and Fe contents in sphalerite lattice has been applied to the Type 2b dataset (see values in supplementary material Table 18-supp data). If Type 2b primary sphalerite had the same chemistry as coarse grains (dark and light domains), the estimated temperature is about 250°C but with large variations of more than ± 50°C due to large chemical heterogeneities. This geothermometer may be relevant in dark domains of the coarse grains if we supposed unchanged compositon since the primary mineralizing stage, however, in recrystallized grains (and even in light domain in coarse grains), the temperature recorded is certainly inconsistent due to the redistribution of elements in the sphalerite lattice associated to deformation and recrystallization, especially for Ge and Ga. Germanium-rich veins are commonly formed at lower temperature below 200-250 °C *(Munoz et al. 1994; Höll et al. 2007; Belissont et al. 2014; Frenzel et al. 2016; Bauer et al. 2018*). There is actually no fluid inclusion study yet available for the studied PAZ mineralizations to confirm these geothermometric results. Nonetheless, *Johnson et al. (1996)* has investigated fluid inclusions in the Cierco deposit which is similar to the PAZ Type 2b veins (Figure 71b). This deposit is considered Early Triassic to Early Cretaceous by *Johnson et al. (1996)* or Late Variscan by *Castroviejo Bolibar and Serrano (1983)*, but the complexity of these veins may be related to their polyphased origin. At Cierco some Ge-minerals have been identified in recrystallized sphalerite (from the Solana vein) hosted in Late-Variscan granodiorite. These indicate that at least a part of this mineralization belongs to Type 2b and that the analyzed temperature corresponds to deformation temperature (*Johnson et al.,1996*). Homogenization temperatures of fluid inclusions in quartz and sphalerite range between 150° and 200°C with salinities between 3 and 29 wt.% NaCl equivalent. Pressure is supposed negligible (*Johnson et al. 1996*).

In our samples, pressure-temperature conditions of the deformation events which are syn or post-mineralization are difficult to assess. Experimental studies on carboirite brackets its stability field between 340° and 600°C and 0.75 to 2 MPa. Brunogeierite appears above 510°C (H_20 pressure; *Julliot et al., 1987*) but these conditions are difficult to reconcile with petrographical observations. Quartz appears only slightly deformed, preserving original cockade textures and no alteration halo is observed along the vein contacts. Partial recrystallization of the Pyrenean sphalerite is localized in bands associated to a pronounced cleavage, parallel to the S_2 cleavage of the host-rock (Figure 74, Figure 78). Such a recrystallization might occur at temperatures below 400°C and low pressure in comparison with experimental studies on sphalerite that determine

deformation and recrystallization of sphalerite at low-grade *(Clark and Kelly 1973; Siemes and Borges 1979; Couderc et al. 1985; Cox 1987*).

5.2.6.3 Mechanisms of accessory minerals formation

As mentionned in *Cugerone et al. (2020)*, Ge-minerals are exclusively located in Type 2b veins which have been affected by subgrain rotation recrystallization or in close association with weak structures such as twin boundaries (Figure 78b). Figure 81a shows a genetic model for their formation. Stage 1 represents the primary Type 2b mineralization associated to a classical vein formation model and Ge appears in the sphalerite lattice. The ore mineralization has not endured recrystallization and deformation yet. Stage 2 is characterized by sphalerite dynamic recrystallization related to subgrain rotation mechanism (*Cugerone et al. 2020)* and the formation of Ge-minerals. Ge-minerals are not included in the sphalerite and appear often at sphalerite triple junctions (Figure 75d and f). They rim the grain boundaries of recrystallized zinc sulfide which attest of their late formation.

Occurence of intra-granular striped-like zonations may support diffusion mechanisms (inset in Figure 78 and Figure 141-141 supp data) within sphalerite coarse grains in dark to light domains. Intra-granular diffusion is composed of different mechanisms such as volume, high diffusivity pathway or dislocation–impurity pair diffusion (*Klinger and Rabkin 1999; Reddy et al. 2007; Plümper et al. 2012; Vukmanovic et al. 2014)*. In addition, hydrothermal fluids might have percolated and extract Ge, Cu and Ga from the sphalerite lattice along grain boundaries, and twin cleavage planes which constituted nucleation sites as Ge(-Cu) minerals are abundant in such locations (Figure 75). In hydrothermal fluids, Ge is transported as $Ge(OH)_4$ complex and its solubility increases with temperature (up to 400°C; *Pokrovski and Schott 1998; Pokrovski et al. 2005*). In Arre deposit, direct correlation between Ge and Cu in sphalerite lattice and in accessory minerals (briartite; Figure 78b and c, Figure 142 and Figure 143 supp data) may attest to similar behaviors for these two elements during remobilization. It could be linked to comparable ionic radius *(Shannon et al. 1976*) or specific conditions enhancing the extraction and coupled incorporation in accessory phases. In Pale Bidau and Anglas deposits (Figure 74a, b and Figure 74e, f) Ge-minerals such as carboirite and brunogeierite are detected and do not contain important Cu contents which may attest for possible differences in Ge and Cu behaviors. Gallium only appears in coarse grains, mostly correlated to Ge- and Cu-rich areas in the sphalerite lattice (inset in Figure 78) but no Ga enrichment occurs in specific Ga-bearing phases which may be due to loss of this metal or to poor primary content in the sphalerite (richest domains show content below ~ 100 μm, Figure 78). No

impact of recrystallization on Cd concentrations is detected in sphalerite (Figure 140d) which demonstrate poor mobility of this element.

Fields of stability of Ge in different minerals according to fO2 and fS2 is reported in Figure 11b (based on *Bernstein (1985)* from experimental data with additional informations from *Sahlström et al. (2017)*). The primary and secondary stages are represented according to the minerals reported in the PAZ and show potential increasing of fO_2 during formation of Ge-minerals (stage 2). Increasing of fO_2 may enhance the expulsion of Ge from the sphalerite lattice by circulating low-temperature fluids which significantly change and diversify the Ge-mineral paragenesis (silicates, oxides, hydroxides, sulfide). It is important to note that hydrothermal fluids responsible for Ge remobilization during deformation does not need to be rich in Ge if we consider a primary sphalerite with an uniform 700 ppm Ge content (Figure 81a and Table 17). These arguments allow to demonstrate that a primary Ge-rich sphalerite (and other sulfides) impacted by low-grade

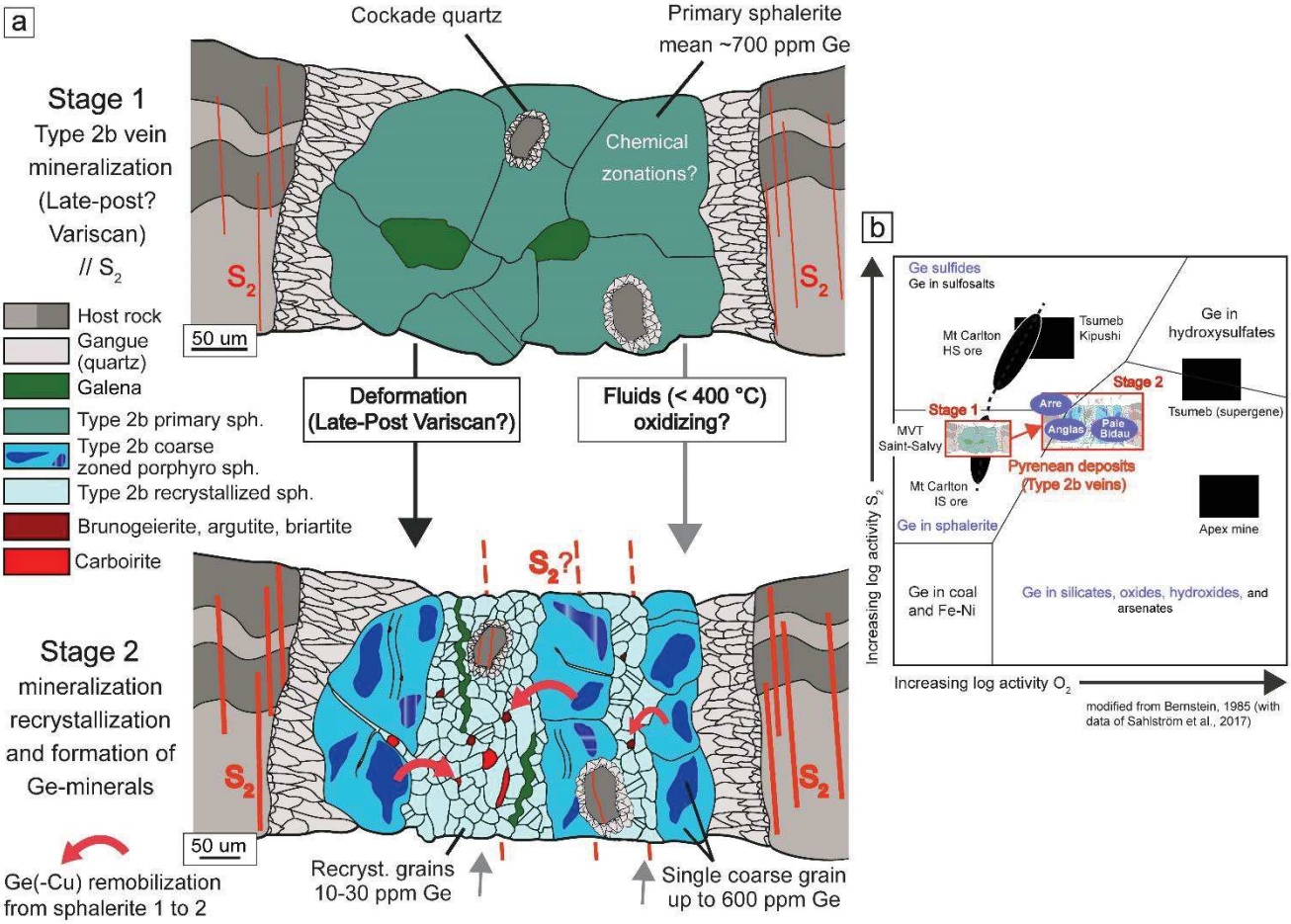

Figure 81. Two stage genesis model for the formation of Ge-minerals and sphalerite textures and chemistry in Type 2b Pb-Zn mineralization. Stage 1 represent the mineralzation before deformation. Stage 2 is the mineralization representation after deformation (supposed Variscan D_2).

deformation below 400 °C with significant increase in fO_2 conditions (Figure 81b) seem the best criteria to discover potential Ge-mineral rich deposit.

5.2.6.4 Comparison with other world-class Ge-rich deposits

Sphalerite from the PAZ, and especially Type 2b vein mineralization, contains chemical and textural similarities with other world-class districts. In a large amount of Pb-Zn(-Cu) deposits, metamorphism and deformation may have imprinted ore mineralization such as in SHMS or

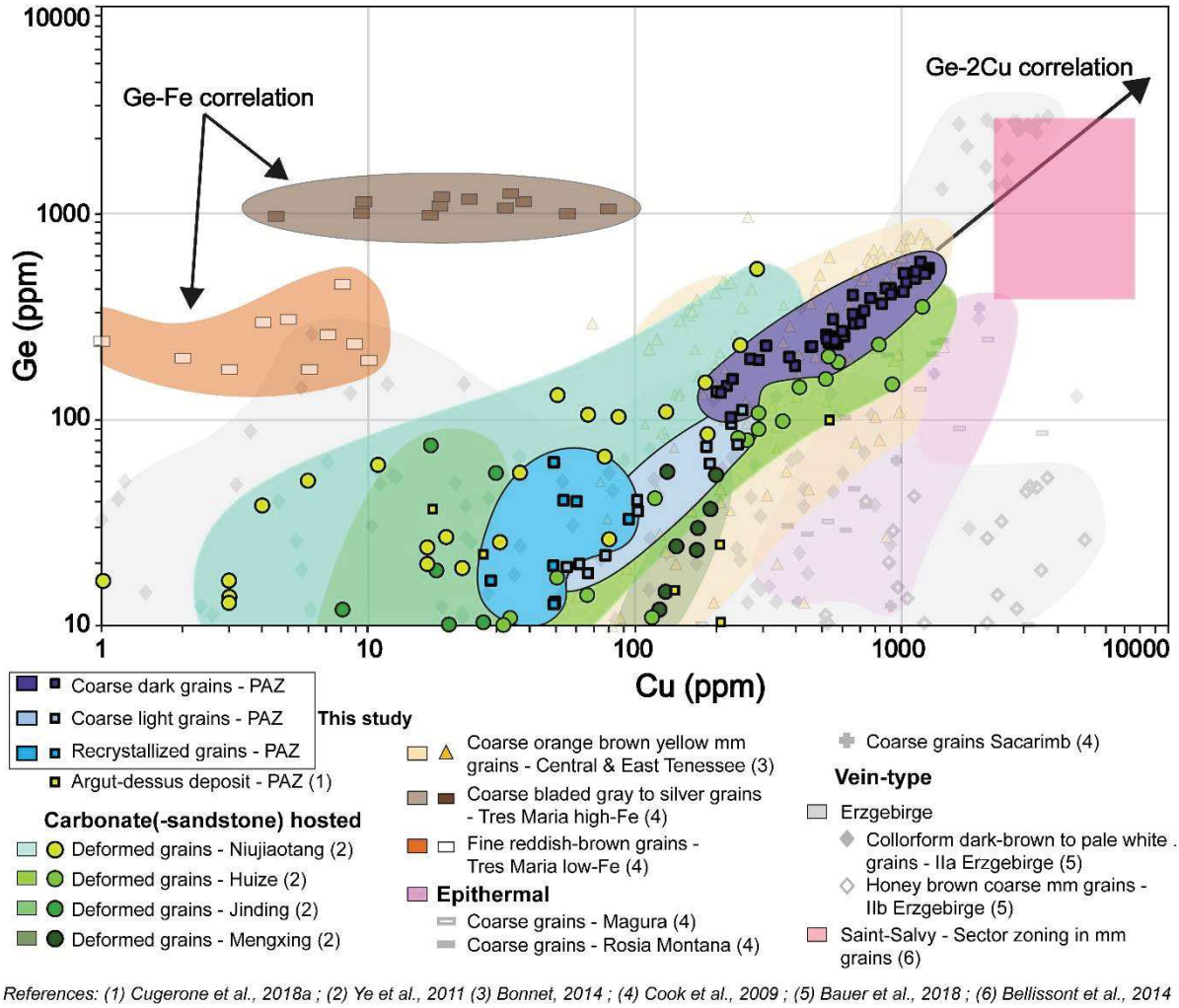

Figure 82. Ge vs Cu contents comparison between PAZ sphalerites (including Argut-dessus deposit; Cugerone et al., 2018a) and others sphalerite mineralizations in the world. A lower Ge limit of 10 ppm is present to only compare Ge-rich deposits. References: Niujiaotang, Huize, Jinding and Mengxing deposits: *Ye et al., 2011*; Central and East Tenessee deposits: *Bonnet, 2014*; Tres Maria, Magura, Rosia Montana, Sacarimb deposit: *Cook et al., 2009*; Erzgebirge deposits: *Bauer et al., 2018*; Saint-Salvy deposit (punctual data not available): *Belissont et al., 2014*.

VHMS (Bodon 1998b; Large et al. 2005; Huston et al. 2006; Wilkinson 2013; Vikentyev et al. 2016a)

as these may contain partly dynamically recrystallized sphalerite like in the world class George Fisher deposit (*Chapman 2004; Murphy 2004*) or in the Currawong deposit (*Bodon and Valenta 1995*), however, too few chemical analyzes on rare metals have been performed in these deposits. As an example, a compilation of Ge and Cu contents in sphalerite analyzed in a large panel of Pb-Zn(-Cu) deposits worldwide with Ge enrichments is shown in Figure 82. The legend points to the observed sphalerite textures as interpreted by the respective authors. These deposits are mostly related to low-temperature hydrothermal fluids (~100-250°C) with no or low-grade deformation imprint. Numerous studies on Pb-Zn(-Cu) deposits recording higher grade deformation/metamorphism (>400°C) do not document or report rare metals values in sphalerite or in accessory Ge-minerals. In some cases, the absence of description may be related to a lack of optical-textural or chemical measurements. Nonetheless, considering all deposits impacted by high grade metamorphism, it seems that Ge was lost during high-grade metamorphism (>400°C) if the bulk of initial sphalerite contained substantial enrichment in Ge before metamorphism and recrystallization. This assumption is probably relevant for example in the Broken Hill deposit impacted by granulite metamorphism (*Spry et al. 2008; George et al. 2016*) where no Ge is reported in the trace element analyses (LA-ICP-MS).

Distinctive examples of Ge-rich sphalerite are observed in the Saint-Salvy vein deposit in the Montagne Noire (France), in the Erzgebirge vein district (Germany), and in the MVT deposits from the Central and East Tennessee. The Ge-content is generally zoned in bands *(Bonnet 2014; Bauer et al. 2018*) or in sector zonings *(Belissont et al. 2014*) and may reach up to ~3000 ppm Ge (Figure 82) with no Ge-minerals reported. The same coupled substitution mechanisms between Ge^{4+}, Ga^{3+} and Cu^{+} are supposed, as reported in the Type 2b mineralization from the PAZ (Figure 82).

Despite relatively good correlation between Ge and Cu in Ge-rich sphalerite, Tres Maria zinc sulfide does not exhibit direct correlation between these two elements (Figure 82) due to general Ge-Fe correlation. Occurrence of würtzite, a non-cubic zinc sulfide, is inferred in the zinc ore (Type I mineralization; *Cook et al., 2009b, 2015; Saini-Eidukat et al., 2009*). Germanium-poor and Ge-rich sphalerite grains coexist with an acicular habit similar to the würtzite observed in the Kokanee range by *Beaudoin (2000)*. Recent geochronological and isotopic data by *Ostendorf et al. (2017)* suggest a possible link between magmatism and mineralization in Tres Maria.

Rare elements (Ge, Ga, In, Cd) are reported in deformed sulfide deposits such as Barrigão which is a Late-Variscan (354 Ma; *Oliveira et al., 2004*) remobilized Cu-rich VHMS deposit. Germanium-rich chalcopyrite with heterogeneous contents and Sn-Ge-rich phases can be found

(*Reiser et al. 2011*) probably resulting from Ge remobilisation during late-reworking *(Belissont et al. 2019)*. In China, Pb-Zn deposits considered to be deformed MVT deposits, contain abundant deformed sphalerite mineralization like at the Huize (*Han et al. 2006*), Niujiaotang *(Ye and Tiegeng 1999; Ye et al. 2012*), Mengxing (*Ye et al. 2011)*, Jinding (*Xue et al. 2007*) and Lehong *(Wei et al. 2019*) deposits. Germanium and Copper contents from these deposits are plotted in Figure 82. Their chemistry is similar to the PAZ deposits with a wider dispersion along the Ge-Cu correlation line especially in Huize and Niujiaotang. A recent study by *Wei et al. (2019)* describes in Lehong carbonate-hosted deposit, dark Ge-rich sphalerite and light Ge-poor sphalerite with Ge content similar to Pyrenean vein mineralization (up to 536 ppm and 118 ppm in dark and light domains respectively). No detail on the textural pattern of these sphalerite is provided but Ge-mineral are not reported. Another example of deformed sphalerite mineralization is reported by *Monteiro et al. (2006)* in Fagundes Pb-Zn deposit where large variations in Ge (up to 2390 ppm Ge) is measured. These heterogeneities may be related to differences in sphalerite texture like in the Type 2b sphalerite of the PAZ. A detailed textural work on sphalerite is essential to correlate in situ trace element analyses and texture and may reveal the location of Ge-minerals. The PAZ vein deposits may be integrated in a general recrystallized Pb-Zn deposit class as the Chinese deformed-MVT deposits.

Germanium minerals were generally reported in the Kipushi type deposits in which Ge contents are highly variable from 0.2 to 5930 ppm in possibly recrystallized sphalerite from the Kipushi mine (*Hughes 1987; Belissont 2016)*. In another recently studied Kipushi-type deposit (the Black Angel deposit; *Horn et al. 2018*), sphalerite is extremely depleted in Ge and Cu and briartite is observed. A recent LA-ICP-MS study in the Eastern-Alpine base metal sulfide ores *(Melcher and Onuk 2019*) indicates potential Ge-rich mineralizations associated to carbonate-hosted Pb-Zn deposits. Results show that Ge content in sphalerite is highly variable (from < 1 to 3700 ppm). Renierite [$(Cu,Zn)_{11}(Ge,As)_2Fe_4S_{16}$)] is reported as inclusions in bornite from one of these deposits but no textural work on sphalerite is available to document possible recrystallization and Ge remobilization.

5.2.7 Conclusions

Type 2a stratabound mineralizations has endured static recrystallization and locally dynamic recrystallization. This mineralization type is largely depleted in Ge, Cu, and Ga, but Cd is enriched in these sphalerite. However, Cd is highly variable according to deposit and texture with substantial depletion in dynamically recrystallized sphalerite.

Type 2b mineralization, interpreted as dynamically recrystallized Pb-Zn vein, contains major chemical heterogeneities in sphalerite especially in Ge and Cu which is related to deformation under relatively low-temperature (< 400°C) and probable increase in fO_2. Gallium is depleted in the recrystallized fraction and no impact of recrystallization on Cd concentrations is detected. The interplay between diffusion and dissolution processes in sphalerite may account for large variations in Ge and Cu contents in sphalerite and the precipitation of Ge-minerals.

Textural and chemical heterogeneities are frequent in Pb-Zn deposits around the world. Understanding the coupling between microstructures and chemistry has a major implication on evaluating rare element potential. Exploration methods for rare and critical metals (Ge, Ga, In, Cd) must integrate micro-textural and in situ chemical analysis of sulfides. LA-ICP-MS in situ analysis alone is not a good screening tool for critical metal deposit if, for example sphalerite is totally recrystallized for example. These elements will be enriched in discrete solid phases, that can generally be found only with chemical maps or luckily analyzed with LA-ICP-MS. Micro-inclusions may often be responsible for the high dispersion of chemical data as well. Recrystallized sphalerite may be more frequent than previously thought above all in orogenic domains: deformed MVTs like in China, and some Kipushi-type deposits must be further explored.

5.2.8 Acknowledgements

This study was funded through the French national program "Référentiel Géologique de France" (RGF-Pyrénées) of the French Geological Survey (Bureau de Recherches Géologiques et Minières; BRGM), and through the INSU-CNRS Tellus CESSUR program. Bénédicte Cenki-Tok acknowledges funding from the European Union's Horizon 2020 research and innovation program under grant agreement No 793978. The authors gratefully acknowledge Christophe Nevado and Doriane Delmas for the exceptional thin sections preparation, Olivier Bruguier for his involvement in LA-ICP-MS analyzes and Fabrice Barou for the acquisition of the EBSD analyzes. The authors are thankful for the editorial handling of Prof. Hans Albert Gilg and Prof. Georges Beaudoin and for the constructive comments of Prof. Steven Reddy and Dr Max Frenzel.

5.2.9 References

Bauer ME, Burisch M, Ostendorf J, Krause J, Frenzel M, Seifert T, Gutzmer J (2018) Trace element geochemistry of sphalerite in contrasting hydrothermal fluid systems of the Freiberg district, Germany: insights from LA-ICP-MS analysis, near-infrared light microthermometry of sphalerite-hosted fluid inclusions, and sulfur isotope geoc. Miner Depos 1–26

Beaudoin G (2000) Acicular sphalerite enriched in Ag, Sb, and Cu embedded within color-banded sphalerite from the Kokanee Range, British Columbia, Canada. Can Mineral 38:1387–1398. doi: 10.2113/gscanmin.38.6.1387

Belissont R, Boiron MC, Luais B, Cathelineau M (2014) LA-ICP-MS analyses of minor and trace elements and bulk Ge isotopes in zoned Ge-rich sphalerites from the Noailhac - Saint-Salvy deposit (France): Insights into incorporation mechanisms and ore deposition processes. Geochim Cosmochim Acta 126:518–540. doi: 10.1016/j.gca.2013.10.052

Belissont R, Munoz M, Boiron M, Luais B, Mathon O (2019) Germanium Crystal Chemistry in Cu-Bearing Sulfides from Micro-XRF Mapping and Micro-XANES Spectroscopy. Minerals 9:1–12. doi: doi.org/10.3390/min9040227

Belissont R, Munoz M, Boiron MC, Luais B, Mathon O (2016) Distribution and oxidation state of Ge, Cu and Fe in sphalerite by μ-XRF and K-edge μ-XANES: Insights into Ge incorporation, partitioning and isotopic fractionation. Geochim Cosmochim Acta 177:298–314. doi: 10.1016/j.gca.2016.01.001

Bernstein LR (1985) Germanium geochemistry and mineralogy. Geochim Cosmochim Acta 49:2409–2422. doi: 10.1016/0016-7037(85)90241-8

Bonnet J (2014) Distribution et contrôle cristallographique des éléments Ge , Ga et Cd dans les sphalérites des gisements de type Mississippi Valley dans les districts de Central et East Tennessee , USA. Ph D Thesis Univ Lorraine-Georessources 204

Bonnet J, Cauzid J, Testemale D, Kieffer I, Proux O, Lecomte A, Bailly L (2017) Characterization of Germanium Speciation in Sphalerite (ZnS) from Central and Eastern Tennessee, USA, by X-ray Absorption Spectroscopy. Minerals 7:1–16. doi: 10.3390/min7050079

BRGM (1984) Les gisements de Pb-Zn français (situation en 1977). BRGM Intern Rep 1–278

Busser B, Moncayo S, Coll J, Sancey L, Motto-ros V (2018) Elemental imaging using laser-induced breakdown spectroscopy : A new and promising approach for biological and medical applications. Coord Chem Rev 358:70–79. doi: 10.1016/j.ccr.2017.12.006

Cáceres JO, Pelascini F, Motto-Ros V, Moncayo S, Trichard F, Panczer G, Marín-Roldán A, Cruz JA, Coronado I, Martín-Chivelet J (2017) Megapixel multi-elemental imaging by Laser-Induced Breakdown Spectroscopy, a technology with considerable potential for paleoclimate studies. Sci Rep 7:1–11. doi: 10.1038/s41598-017-05437-3

Carreras J, Druguet E (2014) Framing the tectonic regime of the NE Iberian Variscan segment. Geol Soc London, Spec Publ 405:249–264. doi: 10.1144/SP405.7

Cassard D, Chabod JC, Marcoux E, Bourgine B, Castaing C, Gros Y, Kosakevitch A, Moisy M, Viallefond L (1993) Mise en place et origine des minéralisations du gisement filonien de Noailhac - Saint-Salvy Zn, Ge, Ag, (Pb, Cd) Tarn - France. BRGM BRGM R-376:82

Castroviejo Bolibar R, Serrano FM (1983) Estructura y metalogenia del campo filoniano de Cierco (Pb-Zn-Ag), en el Pirineo de Lérida. Boletín Geológio y Min 1983:291–320

Clark BR, Kelly WC (1973) Sulfide Deformation Studies; I, Experimental Deformation of Pyrrhotite and Sphalerite to 2,000 Bars and 500 degrees C. Econ Geol 68:332–352. doi: 10.2113/gsecongeo.68.3.332

Cochelin B, Lemirre B, Denèle Y, De Saint Blanquat M, Lahfid A, Duchêne S (2017) Structural inheritance in the Central Pyrenees : the Variscan to Alpine tectonometamorphic evolution of the Axial Zone. J Geol Soc London 16p

Cook N, Etschmann B, Ciobanu C, Geraki K, Howard D, Williams T, Rae N, Pring A, Chen G, Johannessen B, Brugger J (2015) Distribution and Substitution Mechanism of Ge in a Ge-(Fe)-Bearing Sphalerite. Minerals 5:117–132. doi: 10.3390/min5020117

Cook NJ, Ciobanu CL, Mao J (2009a) Textural control on gold distribution in As-free pyrite from the Dongping , Huangtuliang and Hougou gold deposits , North China Craton. Chem Geol 264:101–121. doi: 10.1016/j.chemgeo.2009.02.020

Cook NJ, Ciobanu CL, Pring A, Skinner W, Shimizu M, Danyushevsky L, Saini-Eidukat B, Melcher F (2009b) Trace and minor elements in sphalerite: A LA-ICPMS study. Geochim Cosmochim Acta 73:4761–4791. doi: 10.1016/j.gca.2009.05.045

Couderc JJ, Dudouit I, Hennig-Michaeli C, Levade C (1985) The interaction between slip and twinning systems in natural sphalerite experimentally deformed. Phys Status Solidi 90:581–593. doi: 10.1002/pssa.2210900222

Cox SF (1987) Flow mechanisms in sulphide minerals. Ore Geol Rev 2:133–171

Cugerone A, Cenki-Tok B, Chauvet A, Le Goff E, Bailly L, Alard O, Allard M (2018a) Relationships between the occurrence of accessory Ge-minerals and sphalerite in Variscan Pb-Zn deposits of the Bossost anticlinorium, French Pyrenean Axial Zone: Chemistry, microstructures and ore-deposit setting. Ore Geol Rev 95:1–19. doi: 10.1016/j.oregeorev.2018.02.016

Cugerone A, Oliot E, Chauvet A, Gavalda J, Le Goff E (2018b) Structural Control on the Formation of Pb-Zn Deposits: An Example from the Pyrenean Axial Zone. Minerals 8:1–20. doi: 10.3390/min8110489

de Hoÿm de Marien L, Le Bayon B, Pitra P, Van Den Driessche J, Poujol M, Cagnard F (2019) Two-stage Variscan metamorphism in the Canigou massif: Evidence for crustal thickening in the Pyrenees. J Metamorph Geol 1–26. doi: 10.1111/jmg.12487

Denèle Y, Laumonier B, Paquette J-L, Olivier P, Gleizes G, Barbey P (2014) Timing of granite emplacement, crustal flow and gneiss dome formation in the Variscan segment of the Pyrenees. Geol Soc London, Spec Publ 405:265–287. doi: 10.1144/SP405.5

Dubosq R, Lawley CJM, Rogowitz A, Schneider DA, Jackson S (2018) Pyrite deformation and connections to gold mobility : Insight from micro-structural analysis and trace element mapping. Lithos 310–311:86–104. doi: 10.1016/j.lithos.2018.03.024

Fabre C, Devismes D, Moncayo S, Pelascini F, Trichard F, Lecomte A, Bousquet B, Cauzid J, Motto-Ros V (2018) Elemental imaging by laser-induced breakdown spectroscopy for the geological characterization of minerals. J Anal At Spectrom R Soc Chem 1–9. doi: 10.1039/c8ja00048d

Fougerouse D, Micklethwaite S, Tomkins AG, Mei Y, Kilburn M, Guagliardo P, Fisher LA, Halfpenny A, Gee M, Paterson D, Howard DL (2016) Gold remobilisation and formation of high grade ore shoots driven by dissolution-

reprecipitation replacement and Ni substitution into auriferous arsenopyrite. Geochim Cosmochim Acta 178:143–159. doi: 10.1016/j.gca.2016.01.040

Frenzel M, Hirsch T, Gutzmer J (2016) Gallium, germanium, indium, and other trace and minor elements in sphalerite as a function of deposit type - A meta-analysis. Ore Geol Rev 76:52–78. doi: 10.1016/j.oregeorev.2015.12.017

George LL, Cook NJ, Ciobanu CL (2016) Partitioning of trace elements in co-crystallized sphalerite-galena-chalcopyrite hydrothermal ores. Ore Geol Rev 77:97–116. doi: 10.1016/j.oregeorev.2016.02.009

Gibson GM, Hutton LJ, Holzschuh J (2017) Basin inversion and supercontinent assembly as drivers of sediment-hosted Pb–Zn mineralization in the Mount Isa region, northern Australia. J Geol Soc London 174:jgs2016-105. doi: 10.1144/jgs2016-105

Han R-S, Liu C-Q, Huang Z-L, Chen J, Ma D-Y, Lei L, Ma G-S (2006) Geological features and origin of the Huize carbonate-hosted Zn–Pb–(Ag) District, Yunnan, South China. Ore Geol Rev 31:360–383. doi: 10.1016/j.oregeorev.2006.03.003

Höll R, Kling M, Schroll E (2007) Metallogenesis of germanium-A review. Ore Geol Rev 30:145–180. doi: 10.1016/j.oregeorev.2005.07.034

Horn S, Dziggel A, Kolb J, Sindern S (2018) Textural characteristics and trace element distribution in carbonate-hosted Zn-Pb-Ag ores at the Paleoproterozoic Black Angel deposit, central West Greenland. Miner Depos 1–18. doi: 10.1007/s00126-018-0821-5

Johan Z (1988) Indium and germanium in the structure of sphalerite: an example of coupled substitution with Copper. Mineral Petrol 39:211–229. doi: 10.1007/BF01163036

Johan Z, Oudin E (1986) Présence de grenats, Ca3 Ga (GeO4)3, Ca3 Al (sub 2) [(Ge,Si)O4]3 et d'un équivalent ferrifere, germanifere et gallifere de la sapphirine, Fe4 (Ga,Sn,Fe)4 (Ga,Ge)6 O20, dans la blende des gisements de la zone axiale pyrénéenne. Conditions de formation des. CR Acad Sc Paris 9:811–816

Johan Z, Oudin E, Picot P (1983) Analogues germanifères et gallifères des silicates et oxydes dans les gisements de zinc des Pyrénées centrales, France; argutite et carboirite, deux nouvelles espèces minérales. TMPM Tschermaks Mineral und Petrogr Mitteilungen 31:97–119. doi: 10.1007/BF01084764

Johnson CA, Cardellach E, Tritlla J, Hanan BB (1996) Cierco Pb-Zn-Ag Vein Deposits: Isotopic and Fluid Inclusion Evidence for Formation during the Mesozoic Extension in the Pyrenees of Spain. Econ Geol 91:497–506. doi: 10.5962/bhl.title.18736

Jolivet L, Leprince M, Moncayo S, Sorbier L, Lienemann C (2019) Spectrochimica Acta Part B Review of the recent advances and applications of LIBS-based imaging. Spectrochim Acta Part B 151:41–53. doi: 10.1016/j.sab.2018.11.008

Julliot JY, Volfinger M, Robert JL (1987) Mineralogy Petrology Experimental Study of Carboirite and Related Phases in the System GeO2-SiO2-AI203-FeO-H20 at P up to 2 kbar. Mineral Petrol 36:51–69

Kampmann TC, Jansson NF, Stephens MB, Olin PH, Gilbert S, Wanhainen C (2018) Syn-tectonic sulphide remobilization and trace element redistribution at the Falun pyritic Zn-Pb-Cu-(Au-Ag) sulphide deposit, Bergslagen, Sweden. Ore Geol Rev 96:48–71. doi: 10.1016/j.oregeorev.2018.04.010

Kelley KD, Jennings S (2004) A special issue devoted to barite and Zn-Pb-Ag deposits in the Red Dog district, Western Brooks Range, northern Alaska. Econ Geol 99:1267–1280. doi: 10.2113/gsecongeo.99.7.1267

Kleinsmiede WFJ (1960) Geology of the Valle de Aran (Central Pyrenees). Leidse Geol Meded 25:129–245

Klinger L, Rabkin E (1999) Beyond the fisher model of grain boundary diffusion: Effect of structural inhomogeneity in the bulk. Acta Mater 47:725–734. doi: 10.1016/S1359-6454(98)00420-0

Laforet C, Oudin E, Picot P, Pierrot R, Pillard F (1981) Métallogénie régionale Utilisation des paragenèses minéralogiques et des minéraux traceurs. Rapp BRGM 80 SGN175:33

Large RR, Danyushevsky L, Hollit C, Maslennikov V, Meffre S, Gilbert S, Bull S, Scott R, Emsbo P, Thomas H, Singh B, Foster J (2009) Gold and Trace Element Zonation in Pyrite Using a Laser Imaging Technique : Implications for the Timing of Gold in Orogenic and Carlin-Style Sediment-Hosted Deposits. Econ Geol 104:635–668

Laumonier B, Marignac C, Kister P (2010) Polymétamorphisme et évolution crustale dans les Pyrénées orientales pendant l'orogenèse varisque au Carbonifère supérieur. Bull la Société géologique Fr 181:411–428

Lawrence LJ (1973) Polymetamorphism of the sulphide ores of Broken Hill, NSW, Australia. Miner Depos 8:211–236

Lockington JA, Cook NJ, Ciobanu CL (2014) Trace and minor elements in sphalerite from metamorphosed sulphide deposits. Mineral Petrol 108:873–890. doi: 10.1007/s00710-014-0346-2

Melcher F, Onuk P (2019) Potential of Critical High-technology Metals in Eastern Alpine Base Metal Sulfide Ores. Berg- und Hüttenmännische Monatshefte 1–6. doi: 10.1007/s00501-018-0818-5

Mezger JE, Passchier CW (2003) Polymetamorphism and ductile deformation of staurolite–cordierite schist of the Bossòst dome: indication for Variscan extension in the Axial Zone of the central Pyrenees. Geol Mag 140:595–612. doi: 10.1017/S0016756803008112

Mezger JE, Passchier CW, Régnier J-L (2004) Metastable staurolite–cordierite assemblage of the Bossòst dome: Late Variscan decompression and polyphase metamorphism in the Axial Zone of the central Pyrenees. Comptes Rendus Geosci 336:827–837. doi: 10.1016/j.crte.2003.12.024

Monteiro SLV, Bettencourt SJ, Juliani C, Oliveira TF de (2006) Geology, petrography, and mineral chemistry of the Vazante non-sulfide and Ambrosia and Fagundes sulfide-rich carbonate-hosted Zn–(Pb) deposits, Minas Gerais, Brazil. Ore Geol Rev 28:201–234. doi: 10.1016/j.oregeorev.2005.03.005

Moore DW, Young LE, Modene JS, Plahuta JT (1986) Geologic setting and genesis of the Red Dog zinc-lead-silver deposit, western Brooks Range, Alaska. Econ Geol 81:1696–1727. doi: 10.2113/gsecongeo.81.7.1696

Munoz M, Boyce AJ, Courjault-Rade P, Fallick AE, Tollon F (1994) Multi-stage fluid incursion in the Palaeozoic basement-hosted Saint-Salvy ore deposit (NW Montagne Noire, southern France). Appl Geochemistry 9:609–626. doi: 10.1016/0883-2927(94)90022-1

Nance RD, Gutierrez-alonso G, Keppie JD, Linnemann U, Murphy JB, Quesada C, Strachan RA, Woodcock NH (2010) Evolution of the Rheic Ocean. Gondwana Res 17:194–222. doi: 10.1016/j.gr.2009.08.001

Oliveira JT, Pereira Z, Carvalho P, Pacheco N, Korn D (2004) Stratigraphy of the tectonically imbricated lithological succession of the Neves Corvo mine area , Iberian Pyrite Belt , Portugal. Miner Depos 39:422–436. doi: 10.1007/s00126-004-0415-2

Ostendorf J, Henjes-Kunst F, Schneider J, Melcher F, Gutzmer J (2017) Genesis of the carbonate-hosted tres marias Zn-Pb-(Ge) deposit, Mexico: Constraints from Rb-Sr sphalerite geochronology and Pb isotopes. Econ Geol 112:1075–1087. doi: 10.5382/econgeo.2017.4502

Ovejero Zappino G (1991) Mineralizaciones Zn-Pb ordovícicas del anticlinorio de Bossost. Yacimientos de Liat y Victoria. Valle de Arán. Pirineo (España). Boletín Geológico y Minero 102–3:356–377

Pearce NJG, Perkins WT, Westgate JA, Jackson SE, Neal CR, Chenery SP, Gorton MP (1997) A Compilation of New and Published Major and Trace Element Data for NIST SRM 610 and NIST SRM 612 Glass Reference Materials. Geostand Newsl 21:1–30

Plümper O, King HE, Vollmer C, Ramasse Q, Jung H, Austrheim H (2012) The legacy of crystal-plastic deformation in olivine: High-diffusivity pathways during serpentinization. Contrib to Mineral Petrol 163:701–724. doi: 10.1007/s00410-011-0695-3

Pokrovski GS, Roux J, Hazemann JL, Testemale D (2005) An X-ray absorption spectroscopy study of argutite solubility and aqueous Ge(IV) speciation in hydrothermal fluids to 500 °C and 400 bar. Chem Geol 217:127–145. doi: 10.1016/j.chemgeo.2005.01.006

Pokrovski GS, Schott J (1998) Thermodynamic properties of aqueous Ge(IV) hydroxide complexes from 25 to 350°C: Implications for the behavior of germanium and the Ge/Si ratio in hydrothermal fluids. Geochim Cosmochim Acta 62:1631–1642

Pouit G, Bois JP (1986) Arrens Zn (Pb), Ba Devonian deposit , Pyrénées , France : an exhalative-sedimentary-type deposit similar to Meggen. Miner Depos 21:181–189

Reddy SM, Hough RM (2013) Microstructural evolution and trace element mobility in Witwatersrand pyrite. Contrib to Mineral Petrol 166:1269–1284. doi: 10.1007/s00410-013-0925-y

Reddy SM, Timms NE, Pantleon W, Trimby P (2007) Quantitative characterization of plastic deformation of zircon and geological implications. Contrib to Mineral Petrol 153:625–645. doi: 10.1007/s00410-006-0174-4

Reiser FKM, Rosa DRN, Pinto ÃMM, Carvalho JRS, Matos JX, Guimaraes FMG, Alves LC, de Oliveira DPS (2011) Mineralogy and geochemistry of tin- and germanium-bearing copper ore, Barrigao re-mobilized vein deposit, Iberian Pyrite Belt, Portugal. Int Geol Rev 53:1212–1238. doi: 10.1080/00206811003683168

Sahlström F, Arribas A, Dirks P, Corral I, Chang Z (2017) Mineralogical Distribution of Germanium, Gallium and Indium at the Mt Carlton High-Sulfidation Epithermal Deposit, NE Australia, and Comparison with Similar Deposits Worldwide. Minerals 7:213. doi: 10.3390/min7110213

Saini-Eidukat B, Melcher F, Lodziak J (2009) Zinc-germanium ores of the Tres Marias Mine, Chihuahua, Mexico. Miner Depos 44:363–370. doi: 10.1007/s00126-008-0222-2

Sancey L, Motto-Ros V, Busser B, Kotb S, Benoit JM, Piednoir A, Lux F, Tillement O, Panczer G, Yu J (2014) Laser spectrometry for multi-elemental imaging of biological tissues. Sci Rep 4:1–8. doi: 10.1038/srep06065

Siemes H, Borges B (1979) Experimental deformation of sphalerite single crystals under confining pressures of 3000 and 5000 bars at temperatures between 25°C and 450°C. N Jb Miner Abb 134:288–304

Tomkins AG, Mavrogenes JA (2001) Redistribution of gold within arsenopyrite and löllingite during pro- and retrograde metamorphism: Application to timing of mineralization. Econ Geol 96:525–534. doi: 10.2113/gsecongeo.96.3.525

Van Achterbergh E, Ryan CG, Griffin WL (2001) Glitter! User's manual. On-line Interact Data Reduct LA-ICPMS Microprobe 1–72

Velásquez G, Béziat D, Salvi S, Siebenaller L, Borisova AY, Pokrovski GS, De Parseval P (2014) Formation and deformation of pyrite and implications for gold mineralization in the El Callao District, Venezuela. Econ Geol 109:457–486. doi: 10.2113/econgeo.109.2.457

Vukmanovic Z, Reddy SM, Godel B, Barnes SJ, Fiorentini ML, Barnes SJ, Kilburn MR (2014) Relationship between microstructures and grain-scale trace element distribution in komatiite-hosted magmatic sulphide ores. Lithos 184–187:42–61. doi: 10.1016/j.lithos.2013.10.037

Wagner T, Klemd R, Wenzel T, Mattsson B (2007) Gold upgrading in metamorphosed massive sulfide ore deposits: Direct evidence from laser-ablation-inductively coupled plasma-mass spectrometry analysis of invisible gold. Geology 35:775–778. doi: 10.1130/G23739A.1

Wei C, Huang Z, Yan Z, Hu Y, Ye L (2018) Trace Element Contents in Sphalerite from the Nayongzhi Zn-Pb Deposit, Northwestern Guizhou, China: Insights into Incorporation Mechanisms, Metallogenic Temperature and Ore Genesis. Minerals 8:490. doi: 10.3390/min8110490

Wilkinson JJ (2013) Sediment-Hosted Zinc-Lead Mineralization: Processes and Perspectives: Processes and Perspectives, Treatise on Geochemistry, Second Edition. Elsevier, H Holland, K Turekian (ed), Amsterdam, Netherlands 219–249. doi: 10.1016/B978-0-08-095975-7.01109-8

Wilson SA, Ridley WI, Koenig AE (2002) Development of sulfide calibration standards for the laser ablation inductively-coupled plasma mass spectrometry technique. J Anal At Spectrom 17:406–409. doi: 10.1039/b108787h

Xue C, Zeng R, Liu S, Chi G, Qing H, Chen Y, Yang J, Wang D (2007) Geologic, fluid inclusion and isotopic characteristics of the Jinding Zn-Pb deposit, western Yunnan, South China: A review. Ore Geol Rev 31:337–359. doi: 10.1016/j.oregeorev.2005.04.007

Ye L, Cook NJ, Ciobanu CL, Yuping L, Qian Z, Tiegeng L, Wei G, Yulong Y, Danyushevskiy L (2011) Trace and minor elements in sphalerite from base metal deposits in South China: A LA-ICPMS study. Ore Geol Rev 39:188–217. doi: 10.1016/j.oregeorev.2011.03.001

Ye L, Cook NJ, Liu T, Ciobanu CL, Gao W, Yang Y (2012) The Niujiaotang Cd-rich zinc deposit, Duyun, Guizhou province, southwest China: Ore genesis and mechanisms of cadmium concentration. Miner Depos 47:683–700. doi: 10.1007/s00126-011-0386-z

Ye L, Tiegeng L (1999) Sphalerite Chemistry, Niujiaotang Cd-Rich Zinc Deposit, Guizhou, Southwest China. Chinese J Geochemistry 18:62–68

Zwart HJ (1963) Metamorphic history of the Central Pyrenees, Part II, Valle de Aran. Leidse Geol Meded 28:321–376

Zwart HJ (1979) The Geology of the Central Pyrenees. Leidse Geol Meded 50:1–74

6 Geochronology of the Bossost granite, metamorphism and Pb-Zn mineralization

In order to constrain the relative and absolute timing of Pb-Zn-(Ge) mineralization events in the PAZ and relate them to the general geodynamical model, we have performed two types of geochronological analyses which were acquired recently: i) U-Th-Pb geochronology on zircons from the Bossost granite and monazite from metapelites; ii) $^{40}Ar/^{39}Ar$ analyzes on micas that crystallized synchronously to the Pb-Zn-(Ge) mineralizations.

The results show a probable magmatic emplacement of the Bossost granite in the range of most of the granite in the PAZ (~ 300 and 315 Ma). But such as previous studies in the Bossost massif *((Mezger and Gerdes 2016; Lopez-Sanchez et al. 2018*) an older Visean age (~330 Ma) appear in a single zircon. Monazite hosted in diverse textural position (parallel to S_0-S_1, S_2, included in metamorphic mineral or in foliation show an age of ~290 Ma. This age is probably linked to a late-Variscan thermal event, related to the end of the M_2 metamorphism. For the micas hosted in sphalerite, two ages appear: i) In the Type 2a stratabound mineralization from Bentaillou deposit, a pseudo-plateau age of 268.9 ± 2.8 Ma is observed which corresponds to a Late-Variscan thermal event, probably related to the M_2 metamorphism. Ii) In the Type 2b vein mineralization from the Anglas deposit, a relatively dispersed data between 96 and 144 Ma is obtained which is related to the Early-Cretaceous LP-HT metamorphism with contemporaneous Na(-Ca) metasomatism. This last age suggests an imprint of this metamorphism and metasomatism, slightly pre-dating the Pyrenean orogeny, on the sphalerite vein mineralization where abundant recrystallization is observed.

6.1 ARTICLE – Relation between magmatism, metamorphism and Pb-Zn-(Ge) mineralization events in the Pyrenean Axial Zone

Alexandre Cugerone[1], Françoise Roger[1], Bénédicte Cenki-Tok[1,2], Patrick Monié[1], Emilien Oliot[1], Jean-Louis Paquette[3].

[1]Géosciences Montpellier, University of Montpellier, Montpellier, France.

alexandre.cugerone@umontpellier.fr; francoise.roger@gm.univ-montp2.fr; benedicte.cenki-tok@umontpellier.fr; patrick.Monie@gm.univ-montp2.fr; emilien.oliot@umontpellier.fr

[2]Earthbyte Research Group, School of Geosciences, University of Sydney, NSW 2006, Sydney, Australia.

[3]Laboratoire Magmas et Volcans, Campus Universitaire des Cézeaux, Aubière, France; j.l.paquette@opgc.univ-bpclermont.fr

Keywords: Pyrenees; Variscan orogeny; Laser ablation U-Pb geochronology; $^{40}Ar/^{39}Ar$ geochronology; Pb-Zn mineralizations

6.1.1 Abstract

In the Pyrenean Axial Zone, the timing of Pb-Zn-(Ge) mineralizations and its relationships to tectono-metamorphic framework and the granites emplacement are complex. It is imperative to understand the chronology of events. A new interpretation of the geodynamical model of the Variscan basement is proposed based on U-Th-Pb ages of zircons and monazite analyzed with laser ablation inductively coupled plasma mass spectrometry (LA-ICP-MS) and obtained from two granitic sills (310.4 ± 2.7 Ma and 304 ± 6 Ma) and two metapelites (289.1 ± 5.9 Ma and 290.0 ± 3.8 Ma) which are closely related to the mineralized bodies of the Bossost dome. Muscovite hosted in sphalerite (ZnS) mineralizations are analyzed with $^{40}Ar/^{39}Ar$ on collected samples from the Bentaillou stratabound deposit (Bossost dome) and the Anglas vein deposit (western part of the Pyrenean Axial Zone). Our results suggest three main periods: (1) a single and long-lived period of magmatism and related metamorphism (M_2, HT/LP) between ca. 340 and 290 Ma in the Bossost dome. (2) Followed by a Lower Permian hydrothermal event (ca. 290-270) associated with probably the end of the Variscan M_2 metamorphism and the emplacement of the Bossost granitoids (3) And an Early-Cretaceous thermal event (ca. 120-90 Ma) which pre-dates Pyrenean orogeny is recorded in the Late or Post Variscan vein sphalerite mineralization from the Pyrenean Axial Zone. The Lower Permian and Early cretaceous events are responsible for the sphalerite recrystallization and subsequent Ge-redistribution.

6.1.2 Introduction

In orogens, determining the relative and absolute timing of mineral ore emplacement, granitic intrusion and metamorphism is generally challenging due to the superimposition of tectonic events. The Pyrenean Axial Zone (PAZ) is part of the western Variscan orogenic belt, exhumed during Pyrenean-Alpine orogeny and hosts numerous Pb-Zn-(Ge) deposits. Several authors described Pb-Zn mineralizations as syngenetic SEDEX-style *(Bois et al. 1976; Cardellach et al. 1982; Pouit 1985; Pouit and Bois 1986a*), remobilized or Variscan ore (*Alonso 1979; Nicol et al. 1997*) or vein mineralization probably Late-Variscan or Mesozoic in age (Reyx 1973; Johnson et al. 1996; Fanlo et al. 1998; Subias et al. 1999; Munoz et al. 2016). However, a recent structural study by *Cugerone et al. (2018b)* described three types of Pb-Zn mineralizations and has highlighted the major importance of structural control on their emplacement. Type 1 is a syngenetic and stratiform disseminated mineralization, pre-Variscan in age. Type 2a is an epigenetic and stratabound mineralization, probably Variscan in age based on field observations and pre-Varsican magmatic intrusive relationship with fold and foliation structures. Type 2b is an epigenetic deformed vein

mineralization which post-dates Variscan magmatism (*Cugerone et al. 2018b*). The two last epigenetic mineralizations are ubiquitous in the PAZ but their origin and age of emplacement are still unclear. The deformed Type 2b vein mineralizations have suffered dynamic recrystallization probably linked to Late-Variscan deformation but more recent events are not excluded during local HT/LP Pyrenean metamorphism (~110-85 Ma; *Golberg and Leyreloup 1990; Fallourd et al. 2014; Clerc et al. 2015*) or Pyrenean-Alpine orogeny (85-20 Ma; *Vergés et al., 2002)*. These late stage mineralizing fluids do contain rare metals (Ge, Ga…) hosted mainly in Ge-minerals (chloritoid, oxides, sulfides) that may become of economic importance *(Cugerone et al., 2018a; submitted*). Precisely deciphering the timing of magmatic bodies is of key importance for unravelling the timing of ore emplacement.

Emplacement of magmatic bodies is one of the most important indirect chronological markers to constrain the timing of Pb-Zn mineralizations and associated deformation. In the PAZ, a widespread magmatic (~315-300 Ma) event is documented *(Carreras and Druguet 2014; Denèle et al. 2014*) but an older Visean magmatism in the Bossost granite of the Central part of the PAZ (Figure 83) has been recently reported (~340 Ma*; Mezger and Gerdes, 2016; Lopez-Sanchez et al., 2018*). The duality of Variscan magmatism is described in other Variscan terranes such as the French Massif Central (*Roig et al. 1996; Laurent et al. 2017 and references therein*), northwest Iberia *(e.g. Gutiérrez-Alonso et al. 2018 and references therein*) or in Central Europe *(Schaltegger 1997; Oberc-Dziedzic et al. 2015; Jastrzębski et al. 2018*). It may be interpreted as continuous magmatic period or separated phases related to variable sources through time *(Schaltegger 1997; Bruguier et al. 2003; Gutiérrez-Alonso et al. 2018*). The presence of Visean magmatism also questions the timing of deformation, mostly dated indirectly using relative chronology and in considering the structural relations with dated magmatic bodies *(Denèle et al. 2014)*.

In order to decipher the timing of Pb-Zn mineralizations, their relation to the tectono-metamorphic framework and granites emplacement, we have performed U/Pb geochronology on zircon and on monazite in the host metapelites in the Bossost dome. In addition, direct dating of the two mineralized veins has been performed by $^{40}Ar/^{39}Ar$ analyses on micas associated to sphalerite mineralization.

6.1.3 Geological setting

The Pyrenean Axial Zone (PAZ; Figure 83A) is the basement of the E-W Pyrenean-Alpine mountain belt. The main deformation/metamorphism event is attributed to the convergence and subsequent subduction-collision of the Gondwana-Laurentia continents beneath Avalonia-

Armorica micro-continents during the Upper Paleozoic (*Matte 2001; Stampfli et al. 2013)*. The PAZ is composed of Neoproterozoic to Paleozoic metasedimentary rocks deformed during the Variscan orogeny, intruded by Ordovician granitoids which constitute the core of several metamorphic domes (Figure 83B). The metamorphic terranes preserving medium- to high-grade assemblages are commonly associated to the Infrastructure domain (*De Sitter and Zwart 1960; Zwart 1979*). It shows pervasive flat-lying foliations associated to recumbent fold and highly deformed domains appear locally with steep and penetrative crenulation foliations. The lower-grade metamorphic rocks belong to the Superstructure domain and contain generally moderate deformation associated to a slaty cleavage (*Carreras and Capella 1994; Carreras and Druguet 2014*).

6.1.3.1 Geologic overview of the Pyrenean Axial Zone and mineralization emplacement

The chronology of deformation events in the PAZ is debated according to the numerous geodynamic models that have been proposed in the past decades *(Soula et al., 1986; Van den Eeckhout and Zwart, 1988; Carreras and Capella, 1994; Matte, 2001; Mezger and Passchier, 2003; Martinez Catalan, 2011; Denèle et al., 2014; Mezger and Gerdes, 2016*). Nonetheless, recent structural studies focusing on the structural relationships between granites and metasedimentary rocks proposed a model where intrusion emplacement was coeval with crustal flow, dextral transpression and doming in an overall dextral strike-slip setting (*Martinez Catalan 2011; Denèle et al. 2014*). Deformation has been separated in three stages. The first stage is an early Variscan E-W D_1 deformation between ~323 and 308 Ma according to *Denèle et al. (2014*) related to crustal thickening and responsible for the formation of a flat-lying S_1 foliation in the Infrastructure and flat to step foliation in the Superstructure. This stage is synchronous to a regional M_1 MT/MP metamorphism (5.5 kbar and 580°C; staurolite-garnet assemblages; *Mezger and Passchier, 2003*). The second stage D_{2a} is considered late-Variscan and shows horizontal and lateral crustal flow (~ 306 Ma) synchronous to HT/LP peak of metamorphism (575-600°C at 3 kbar; andalusite-cordierite assemblages). It is mainly recorded in the Aston and Hospitalet orthogneisses *(Zwart 1979; Mezger and Passchier 2003; de Hoÿm de Marien et al. 2019*). This stage is directly followed by D_{2b} which corresponds to the formation of the gneiss domes around 304 Ma (*Denèle et al. 2014*). D_2 deformation is associated to the formation of a S_2 penetrative cleavage generally vertical in the two structural domains and axial planar to D_2 upright to isoclinal folds. The third event is late Variscan (~300 Ma) and is represented by metric E-W dextral shear-bands along regional faults, such as the Bossost (Mezger and Passchier 2003) or Merens faults (*Mezger et al. 2012; Ostkamp et al. 2019*).

The onset of Variscan deformation is commonly considered as Early-Namurian to Early-Westphalian (325-315 Ma) in age (Denèle et al. 2014), and related to the age of the flysch rocks regionally named Culm (*Delvolvé et al. 1993*). Another recent study by *Martín-Closas et al. (2018)* based on palaeobotanical data at the base of the flysch interval proposed the succession of two Variscan ductile deformations, pre- and syn- flysch deposition respectively. These are probably Visean and Namurian-Westphalian in ages respectively. The Late-Variscan granitoids are commonly considered Late-Carboniferous in age and may be contemporaneous to the dextral transpressif

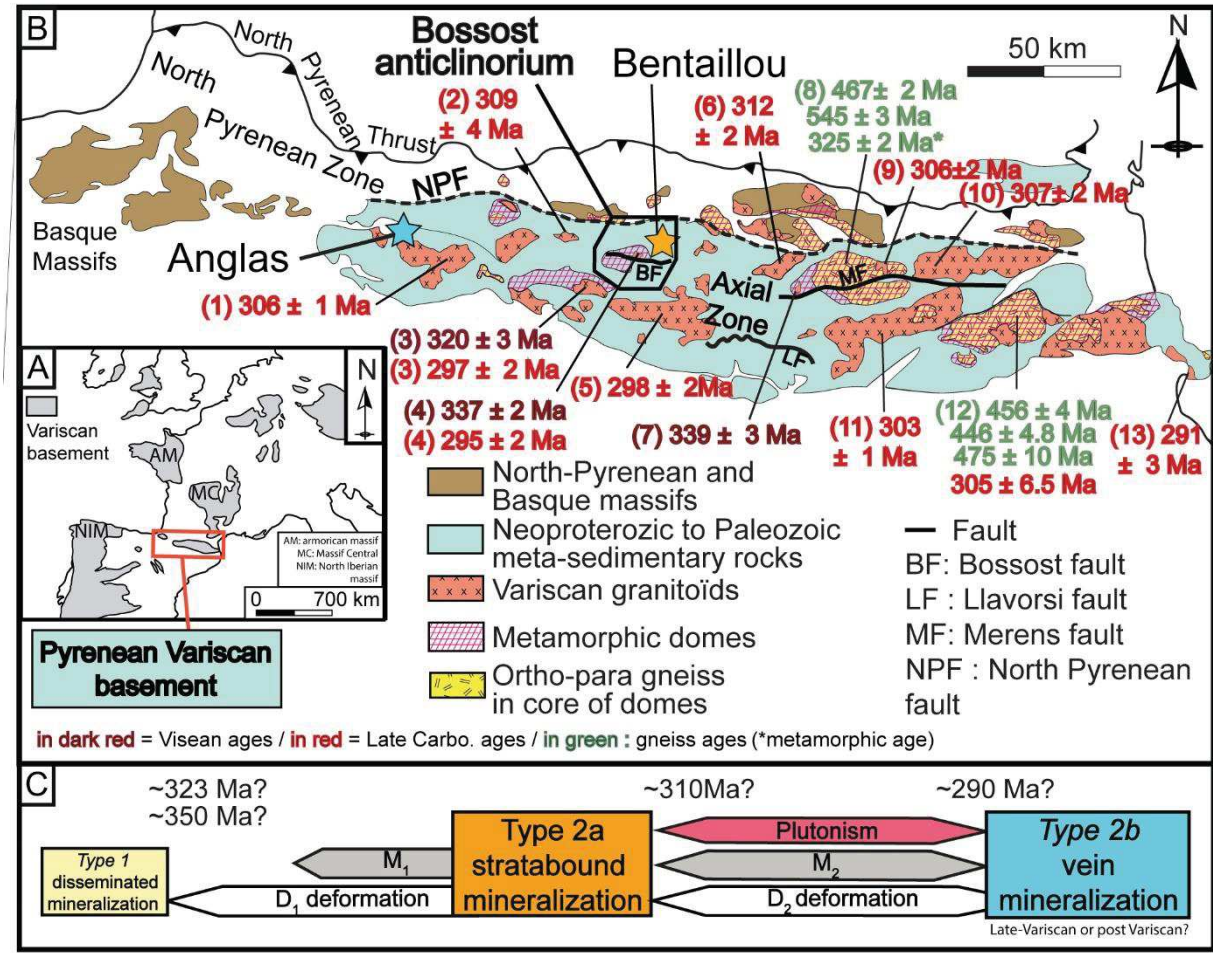

Figure 83. A. Location of the PAZ and other massifs in the Variscan belt of the Western Europe. B: Simplified geological map of the Pyrenean Axial Zone (PAZ) with location of the basement and metamorphic domes. The U/Pb data are in red for granites, and in green for gneiss (magmatic age except one with "*" which correspond to metamorphic age). References: 1-Cauteret (*Denèle et al. 2014*); 2-Bordères-Louron (*Gleizes et al. 2006*); 3-Lys-Caillaouas *(Lopez-Sanchez et al. 2018*); 4-Bossost (*Mezger and Gerdes 2016; Lopez-Sanchez et al. 2018)*; 5-Maladeta (*Evans et al. 1998*); 6-Bassiès (*Paquette et al. 1997*); 7-Soulcem (*Mezger and Gerdes 2016)*; 8-Aston (*Mezger and Gerdes 2016*)*;* 9-Ax-les-Thermes (*Denèle et al. 2014*); 10-Quérigut (Roberts et al. 2000b); 11-Mont-Louis (*Denèle et al. 2014*); 12-Canigou massif (*Alexandrov 2000; Cocherie et al. 2005; Casas et al. 2010*); 13-Roses (*Druguet et al. 2014*). C Chronological succession of the deformation, metamorphism and mineralization.

tectonic regime (~312-300 Ma; *Guitard et al. 1984; Paquette et al. 1997; Evans et al. 1998; Roberts et al. 2000; Carreras et al. 2004; Gleizes et al. 2006; Denèle et al. 2014*).

The chronology of mineralization with respect to the tectonic-metamorphic framework is highly debated in the PAZ and possible relations with tectonic events are presented in the Figure 83C. Type 2a stratabound mineralization stage was mainly considered Ordovician or Devonian in age (*Bois et al. 1976; Pouit 1978; Cardellach et al. 1982; Pouit and Bois 1986a; Pujals 1992*) even some studies have questioned this model (*Alonso 1979; Nicol 1997; Nicol et al. 1997)*. Recent regional study has demonstrated that mineralization emplacement occurred during the Variscan orogeny *(Cugerone et al. 2018b)*, especially in the Bentaillou stratabound deposit where mineralization appears in pull-apart structures close to F_1 km fold hinge. Type 2b vein mineralization is documented in Cierco and other marginal vein systems (Yenefrito, Parzan, etc.; *Johnson et al., 1996; Fanlo et al., 1998; Subias et al., 1999*). It could be related to Mesozoic extension and widespread hydrothermal event, even if some authors argued for a Late Variscan age *(Reyx 1973; Castroviejo Bolibar and Serrano 1983*). In Anglas vein deposit (Figure 83B), hosted in Devonian schists within the western part of the Pierrefitte anticlinorium, west of the PAZ *(Cugerone et al. 2018b)*, sphalerite (ZnS) ore appears deformed and is considered Late-Variscan *(Reyx 1973; Cugerone et al. 2018b*). Deformation could be more recent with a possible Pyrenean-Alpine deformation as supposed in Cierco and Yenefrito Pyrenean vein deposits (*Johnson et al. 1996; Subias et al. 1999)*.

6.1.3.2 Overview of the Bossost anticlinorium

The main studied area is the Bossost anticlinorium which is located in the central part of the PAZ, between the North Pyrenean Fault to the north and the Aran Valley synclinorium to the south (Figure 83 and Figure 84). The core of the metamorphic dome (Figure 84) is composed of a Late-Variscan plutonic complex which intrudes Cambro-Ordovician schists. This granitic complex is essentially composed of leucocratic muscovite-hornblende granites and minor two-micas granites (*Mezger and Passchier, 2003*). Recently, a geochronological study (U-Th-Pb LA-ICPMS zircon) performed on granitic samples situated at the core of the Bossost and Aston (Soulcem granite) domes yielded an age of ca. 339-336 Ma *(Mezger and Gerdes 2016*). North of the Bossost fault, ages for the Bossost granite and a granite sill are 338.2 ± 2.5 Ma and 336.8 ± 2 Ma respectively. These are interpreted by *Mezger and Gerdes (2016)* as the Visean emplacement ages of Bossost granitoids. For the first time a Visean magmatic episode that caused the HT/LP contact metamorphism M_2 in the PAZ has been proposed. Structurally, S_2 cleavage is already developed at depth during the formation of the Bossost granite and D_2 deformation may continue during the consolidation of

the granitic body *(Mezger and Gerdes 2016; Mezger and Régnier 2016*). However, the meaning of these ages is debated. For some authors (*Denèle et al. 2014; Cochelin 2016*), these ages have no geological significance and represent mixing ages between Carboniferous ages and an older inherited component (probably 450-480 Ma and/or ~620-640 Ma). More recently, an Early-Permian emplacement age of 295 ±2 Ma for an undeformed leucogranite of the Bossost massif (U-Pb LA-ICPMS zircon) was proposed by *Lopez-Sanchez et al., (2018)* who nonetheless consider an additional Visean event recorded in the core of the zircons. This study highlights the presence of inherited zircons which suggest the existence of an Early Carboniferous event probably (Lower intercept age: 326 ± 3 Ma) in the PAZ. The Bossost dome is truncated to the south by the E-W Bossost ductile fault. This mylonitic fault which separates the dome in two sub-domes (*Cochelin 2016*) is considered Variscan and/or Pyrenean-Alpine in age (*Carreras and Cirés 1986; Mezger 2005*). South of the fault, many localized granitic intrusions intruding the schists occur along an E-W trend (Figure 84). The HT/LP metamorphism (M_2) is well developed around the Bossost granitic intrusions. It is characterized by the absence of garnet and the abundance of cordierite and by a prograde zoning with biotite, staurolite-andalousite-cordierite and sillimanite-cordierite assembalges appearing towards the contact with the granite (*Mezgzer et Passchier, 2003; Lopez-Sanchez et al., 2018*).

6.1.4 Samples

In this study, we have performed zircon and monazite U-Pb dating on 4 samples (BOS32a, BOS32b, BOS18 and BOS17) in order to understand the relationships between deformation phases, metamorphic events and the emplacement of the Bossost granitoids and indirectly the different Pb-Zn mineralization stages. It is also essential to constrain indirectly the emplacement of the different Pb-Zn mineralization stages. Additional $^{40}Ar/^{39}Ar$ dating on muscovite from 2 samples (Bentaillou and Anglas) associated to sphalerite mineralization has been performed.

The two granite samples (BOS32a and BOS32b) were collected in the E-W trending granitic sills, in the southern part of the Bossost dome (Figure 84). These two-undeformed leucocratic granitic bodies intrude metapelitic rocks with a cordierite-sillimanite (M_2) assemblage. At microscopic scale, these samples are composed essentially of quartz, feldspar, and muscovite, with localized kink-bands in muscovite, recrystallized quartz with sub-grains indicating limited brittle-ductile deformation.

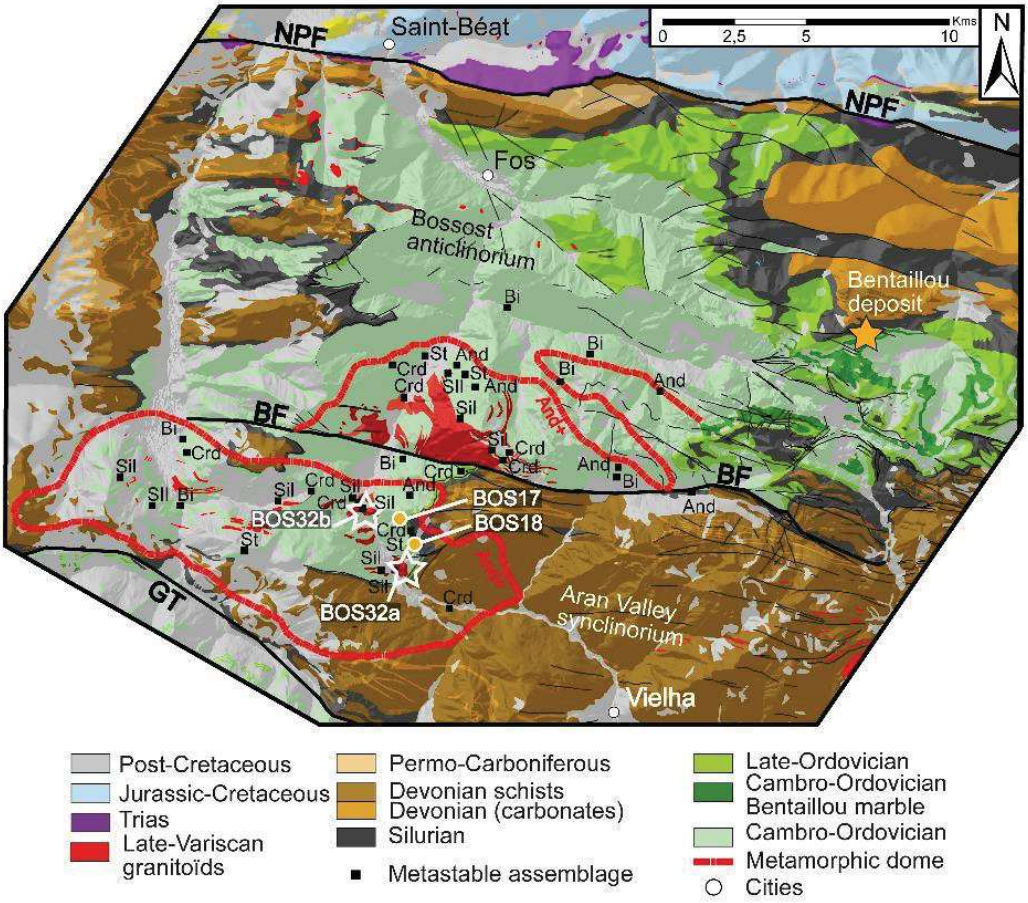

Figure 84. Geological map of the Bossost anticlinorium with the location of the collected sample for the U/Pb datations (BOS32a and BOS32b= granitic sill; BOS17 and BOS18=metapelites). Location of Bentaillou deposit (yellow star) is noted at the east of the Bossost anticlinorium ($^{40}Ar/^{39}Ar$ analyses). Abbreviations: NPF: North Pyrenean Fault; BF: Bossost fault; GT: Gavarnie thrust.

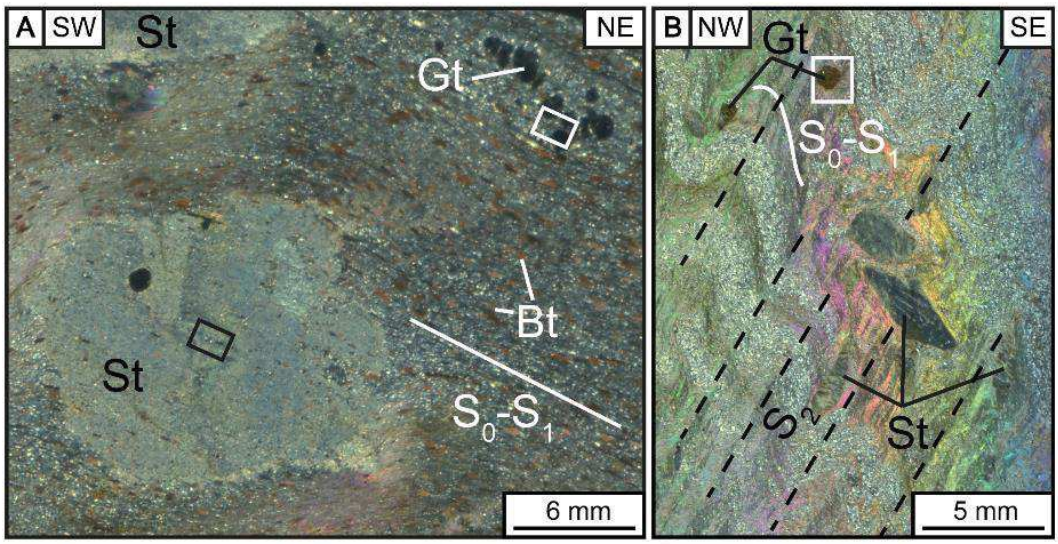

Figure 85. A. Metapelite (BOS17) with biotite (Bt), garnet (Gt) and staurolite (St) assemblages (plane polarized light). Location of the Figure 89F is noted with a white square. B. Metapelite (BOS18) with muscovite (Ms), garnet (Gt) and staurolite (St) assemblages (plane polarized light). Location of the Figure 89A is noted with a white square.

In the same zone, two metapelitic samples (BOS18 and BOS17) were collected (Figure 2). BOS17 sample exhibits a well-preserved D_1 foliation without pronounced D_2 overprint. The foliation is mainly marked by biotite and garnet related to M_1 (Figure 85A). Some centimetric-size staurolite porphyroblasts are parallel to S_1 foliation. BOS18 sample displays a well-preserved D_2 foliation marked by crenulation cleavage associated to F_2 folds. It is made of an assemblage of muscovite, garnet and staurolite (Figure 85B).

In order to date directly the mineralization from the PAZ with the $^{40}Ar/^{39}Ar$ method, we have investigated stratabound-type in the Bossost anticlinorium and vein-type mineralizations in the west of the PAZ. We have selected samples showing a clear association between muscovite and sphalerite mineralizations (Figure 86) in Bentaillou and Anglas localities (Figure 83 and Figure 84).

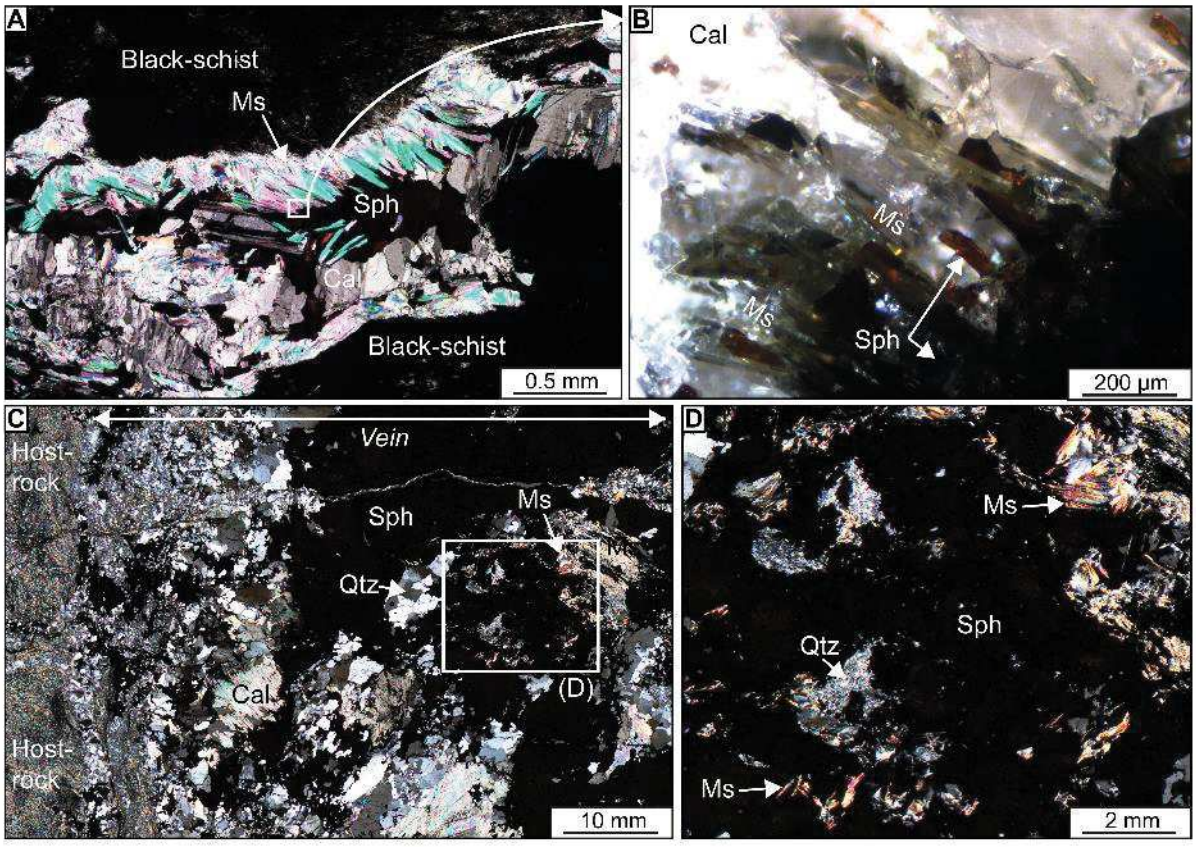

Figure 86. Microphotographs showing muscovite and sphalerite associations in: A, B – Bentaillou and C, D – Anglas deposits (plane polarized light except for B which is observed in reflected ligh with cross nicols).

The Bentaillou deposit is located in the eastern part of the Bossost anticlinorium, at the limit between Cambro-Ordovician marbles, Late-Ordovician schists and conglomerates. Mineralization is Type 2a, stratabound and parallel to the S_0-S_1 foliation (*Cugerone et al. 2018b)*. The host-rocks record a low-grade metamorphism M_1 that has impacted the sphalerite texture. It is present as polygonal grains or shows *foam* textures typical of annealing textures in sulfide.

Mineralization is essentially made of sphalerite and galena, with gangue minerals like calcite. Mm-size muscovite crystals are commonly associated to sphalerite and calcite and arranged orthogonal to the vein wall showing comb texture and intergrows with sphalerite and calcite (Figure 86A and B).

The Anglas deposit (Figure 83) is located in the western part of the PAZ, in the Pierrefitte anticlinorium (*Reyx 1973; Cugerone et al. 2018b*). The Type 2b vein-type mineralization clearly displays cross-cutting evidence with magmatic aplite associated to the Cauteret granite (Figure 83B) dated at 306 ± 1 Ma by (*Denèle et al. 2014)*. Ore mineralization is parallel to the S_2 cleavage, is hosted by Devonian calc-schists and is considered post-metamorphic. Sphalerite is the main ore associated to galena, calcite, and quartz. Muscovite crystals are smaller (few hundreds of μm) and thinner than in Bentaillou and have crystallized with sphalerite. They may be hosted directly by sphalerite or associated to gangue minerals like quartz or calcite (Figure 86C and D).

6.1.5 Instrumentation and analytical method

6.1.5.1 U-Th-Pb LA-ICPMS geochronology of zircon and monazite

The zircon minerals were separated from two granitic samples, in which 1-2 kg was processed at the mineral separation laboratory at Geosciences Montpellier (Montpellier University) following standard procedures of separation. The selected grains were mounted on 2.5 cm blocks with epoxy resin and polished. Before analysis, backscatter electron (BSE) and cathodoluminescence (CL) images were acquired for all grains using a FEI QUANTA 450w (at Bourgogne-Franche Comté University) in order to check spot positions with respect to the internal microstructures, inclusions, fractures and physical defects. The monazite grains were characterized by a FEI Quanta FEG 100 Scanning electron microscope (SEM) at Geosciences Montpellier.

In situ U-Th-Pb isotopic data were obtained by laser ablation inductively coupled plasma spectrometry (LA-ICPMS) at Laboratoire Magmas & Volcans (Clermont-Ferrand, France). The analyses involved the ablation of minerals with a Resonetics Resolution M-50 powered by an ultra-short-pulse (<4ns) ATL Atlex Excimer laser system operating at a wavelength of 193 nm. For monazite and zircon, spot diameters of 12μm and 33μm were used, associated with repetition rates of 1 Hz and 3 Hz and laser fluences of 9 /cm^2 and 4 J/cm^2, respectively. The ablated material was carried by helium and then mixed with nitrogen and argon before injection into the plasma source of an Agilent 7500 cs ICP-MS equipped with a dual pumping system to enhance sensitivity (*Paquette*

et al. 2014). The alignment of the instrument and mass calibration were performed before every analytical session using the NIST SRM 612 reference glass, by inspecting the signal of ^{238}U and by minimizing the ThO+/Th+ ratio (< 1%). The analytical method for isotope dating is similar to that developed and reported in *Paquette and Tiepolo (2007)* and detailed in *Hurai et al. (2010, 2012)* and *Gasquet et al. (2010)*. The signals of ^{204}(Pb+Hg), ^{206}Pb, ^{207}Pb, ^{208}Pb, ^{232}Th and ^{238}U masses were acquired. The occurrence of common Pb in the sample was monitored by the evolution of the ^{204}(Pb+Hg) signal intensity, but no common Pb correction was applied owing to the large isobaric interference from Hg. The ^{235}U signal was calculated from ^{238}U on the basis of the ratio $^{238}U/^{235}U$= 137.88. Single analyses consisted of 30 seconds of background integration with the laser off, followed by 60 seconds integration with the laser firing and a 20 second delay to wash out the previous sample and prepare for the next analysis. Complet U-Th-Pb dating methodology is given in Table 30.

Data were corrected for U-Pb fractionation occurring during laser sampling and for instrumental mass discrimination (mass bias) by standard bracketing with repeated measurements of the GJ-1 zircon (*Jackson et al. 2004*) and Trebilcock monazite (*Tomascak et al. 1996*) reference material. Repeated analyses of the zircon 91500 (*Wiedenbeck et al. 1995*) and the monazite Bananeira (*Gonçalves et al. 2016*) reference materials, treated as an unknown independently control the reproducibility and accuracy of the corrections. The detailed analytical procedures are described in *Paquette et al. (2014)* and detailed in *Hurai et al. (2010)* and in the supplementary material (Table SM1). Data reduction was carried out with the software package GLITTER® from Macquarie Research Ltd (*Van Achterbergh et al. 2001; Jackson et al. 2004*). For each analysis, the time resolved signals of single isotopes and isotope ratios were monitored and carefully inspected to verify the presence of perturbations related to inclusions, fractures, mixing of different age domains or common Pb. Calculated ratios were exported and ages and diagrams were generated using the Isoplot/Ex v. 2.49 software package of *Ludwig (2001)*. The concentrations of U-Th-Pb were calibrated relative to the values of the GJ-1 zircon (*Jackson et al. 2004*) and Trebilcock *(Tomascak et al. 1996)* reference materials. The decay constants used for the U-Pb system are those determined by *Jaffey et al. (1971)* and recommended by the IUGS (*Steiger and Jäger 1977*). In the text and figures, all uncertainties in ages are given at ± 2σ.

6.1.5.2 $^{40}Ar/^{39}Ar$ step-heating

During this study, both in situ and step-heating $^{40}Ar/^{39}Ar$ experiments were conducted selected samples. After preparation of the thick sections and single micas, the samples were

irradiated for 40 hours in the core of the Triga Mark II nuclear reactor of Pavia (Italy) with several aliquots of the Taylor Creek sanidine standard (28.34 ± 0.10 Ma, *Renne et al., 1998*) as flux monitor. Argon isotopic interferences on K and Ca were determined by irradiation of KF and CaF_2 pure salts from which the following correction factors were obtained: $(^{40}Ar/^{39}Ar)_K = 0.00969 \pm 0.00038$, $(^{38}Ar/^{39}Ar)_K = 0.01297 \pm 0.00045$, $(^{39}Ar/^{37}Ar)_{Ca} = 0.0007474 \pm 0.000021$ and $(^{36}Ar/^{37}Ar)_{Ca} = 0.000288 \pm 0.000016$.

Argon analyses were performed at Géosciences Montpellier (France) with an analytical system that consists of: (a) a UV laser for in situ experiments and a CO_2 laser for the step-heating experiments, (b) different lenses for laser beam focusing, (c) a steel sample chamber, maintained at 10^{-8} - 10^{-9} bar, with a drilled copper plate for individual grains, (d) an inlet line for purification of gases including two Zr-Al getters, (e) a multi-collector mass spectrometer (Argus VI from Thermo-Fisher). After loading in the sample chamber, the samples were baked at about 120 °C during 24 hours to remove atmospheric argon from the sample surface. For each in situ experiment, several laser pits with a spatial resolution of 20 μm were achieved a surface of about 200x200 μm. Step-heating experiments were conducted with a duration of heating of 30 seconds at each step.

A custom-made software was used to control the laser intensity, the timing of extraction/purification and the data acquisition. The ArArCalc software© v2.5.2 was used for data reduction and plotting. Atmospheric ^{40}Ar was estimated using a value of the initial $^{40}Ar/^{36}Ar$ ration of 295.5 (*Steiger and Jäger 1977*). Ages are reported with two sigma uncertainties.

6.1.6 Results

6.1.6.1 U-Th-Pb results

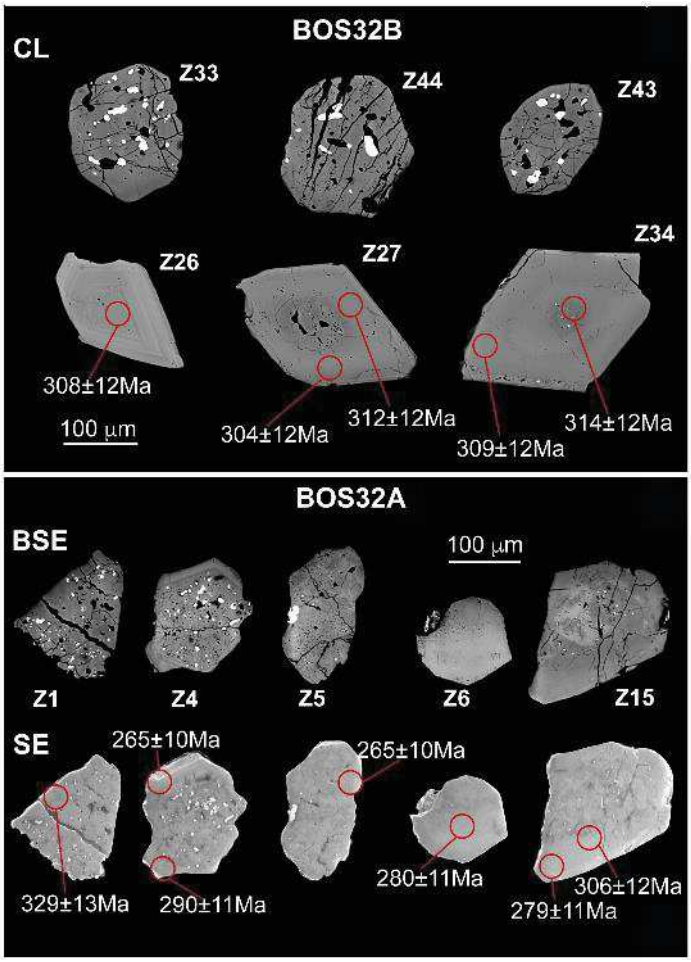

Figure 87. A. CL microphotographs of the zircons from the BOS32B sample. B. BSE and SE microphotographs of the zircons from the BOS32A sample. The red circle represents the spots analysis and the number corresponds to the $^{206}Pb/^{238}U$ age ($\pm 2\sigma$) obtained. Z number correspond to the grain number in the Table 3.

Zircons grains in the two Bossost granitic sill are rare, small (100-200 µm in size) and often metamicts. Their colors vary from opaque red to translucent slightly pink.

Sample BOS32b shows two zircon populations. One is opaque red with numerous inclusions of UO_2, biotite and quartz. The other is slightly more translucent showing euhedral crystal with bipyramidal shape and rare inclusions. Moreover, some grains have a thin inclusion-rich rim (~10 µm). Only the second population could be dated. Cathodoluminescence is low and displays a slight oscillatory zoning (Figure 87A). A total of 28 spots on 24 grains was performed

and plotted on the Concordia diagram (Table 3A; Figure 88A). These analyses have very low Th/U ratios (<<0.1) associated to low Th contents between 1.1 and 6.7 ppm, high to very high U concentration (3624-20918 ppm) and medium-high Pb concentration (165–930 ppm) (Table 3A). In the Concordia diagram, the 28 ellipses are concordant to sub-concordant between 230 to 330 Ma. Among these analyses, 18 form a cluster yielding a weighted average of $^{206}Pb/^{238}U$ ages of 310.4 ± 2.7 Ma (MSWD = 0.28). The other analyses which are represented by dotted ellipses are zircon rims presenting younger ages. These data are probably without significance and reflect Pb loss.

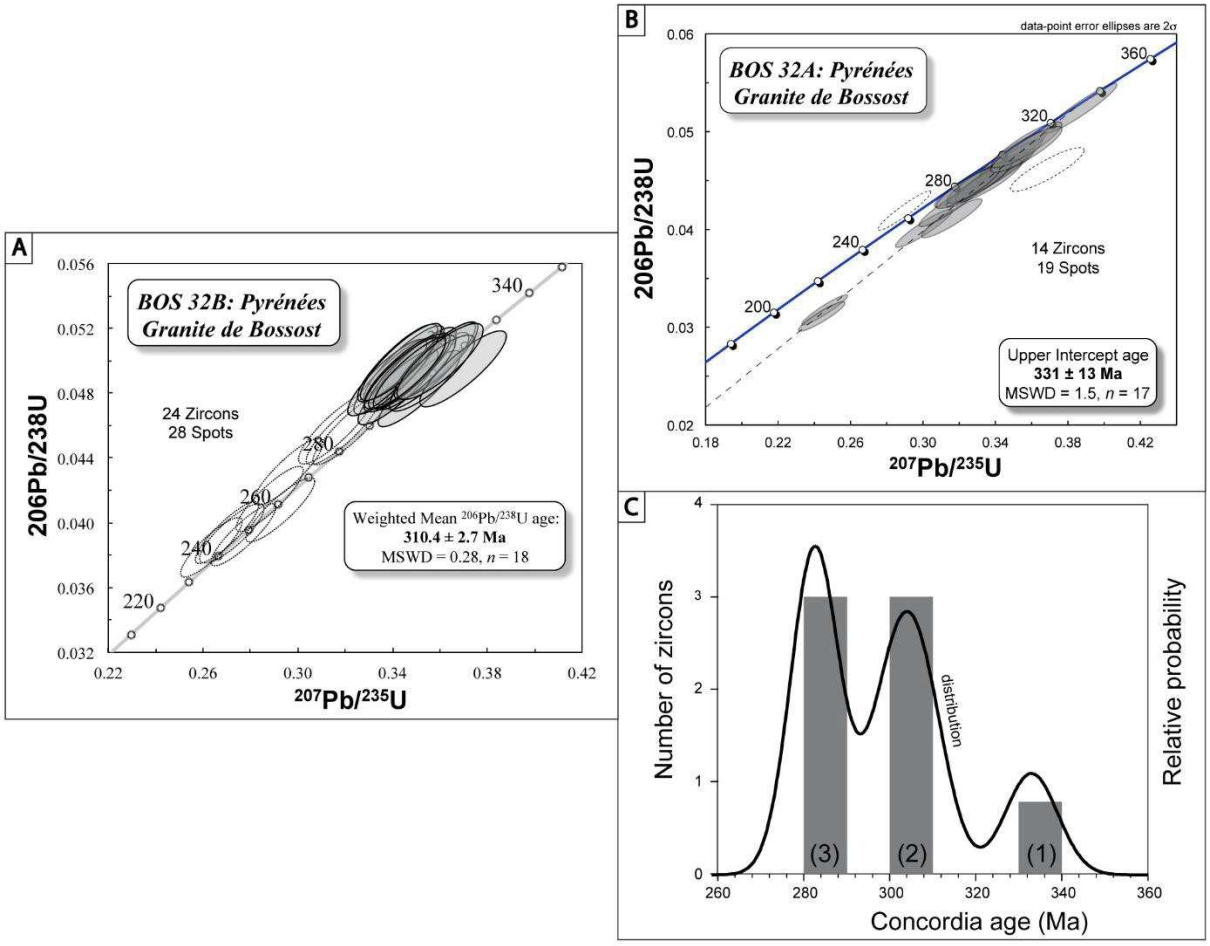

Figure 88. A. and B. Zircon U-Pb Concordia diagrams obtained on two granitic sills of the Bossost dome (BOS 32B and 32A, by LA-ICPMS. Error ellipses and uncertainties in ages are ± 2σ. The stippled ellipses are not taken into account for the age calculation. "n" corresponds to the number of data used to calculate the age. C. Histogram distribution diagrams for the sample BOS 32A. To avoid distorting the distribution of populations, only one date per grain is used

The majority of zircon grains of sample BOS32a are zircon fragments (Figure 87B). No internal structure has been identified. They contain many fractures and inclusions of UO_2 and

biotite. A total of 19 analyses, carried out on 14 crystals are listed in Table 3B and plotted in Figure 88B. Except for spots 1 and 5, the data show low Th concentration (1-7 ppm) and high U (3119-13398 ppm) and Pb (140-539 ppm) contents. Their Th/U ratios are very low (<<0.1) (Table 3B). The ellipses are concordant to discordant between 330 and 200 Ma (Figure 88B). A linear regression of 17 analyses (excepted spot 5 and 19) yields an upper intercept of 331 ± 13 Ma (MSWD = 1.5). Usually, the discordant data analyzed by LA-ICPMS are only considered if they can be reported on

A

BOS 32B		content				corrected ratios					Age (Ma)		Concordia	
Spot #	Name	Pb ppm	Th ppm	U ppm	Th/U	207Pb/235U	± 2 s	206Pb/238U	±2 s	Rho	206Pb/238U	± 2 s	age	± 2 s
1	Z4-c	372	1.8	8203	0.0002	0.357	0.014	0.0499	0.0020	0.88	313.8	12.2	310	11
2	Z5	356	1.2	8083	0.0001	0.351	0.014	0.0482	0.0019	0.88	303.6	11.8	305	11
3	Z6-c	368	1.1	8263	0.0001	0.354	0.014	0.0493	0.0020	0.87	310.3	12.1	308	11
4	Z7-b	571	3.2	13795	0.0002	0.322	0.013	0.0458	0.0018	0.89	288.4	11.2	283	10
5	Z8-b	458	2.3	12900	0.0002	0.277	0.011	0.0392	0.0016	0.88	248.0	9.7	248	9
6	Z10-b	511	3.7	13774	0.0003	0.292	0.012	0.0407	0.0016	0.88	257.4	10.0	260	10
7	Z11-b	586	4.2	14132	0.0003	0.316	0.013	0.0458	0.0018	0.87	288.4	11.2	/	
8	Z12-b	526	4.4	13959	0.0003	0.288	0.012	0.0414	0.0017	0.88	261.5	10.1	257	9
9	Z12-c	677	3.0	14979	0.0002	0.344	0.014	0.0497	0.0020	0.87	312.7	12.0	/	
10	Z13-b	499	2.8	14265	0.0002	0.263	0.011	0.0384	0.0015	0.87	243.0	9.4	238	9
11	Z13-c	468	1.9	13193	0.0001	0.270	0.011	0.0393	0.0016	0.88	248.6	9.6	243	9
12	Z14-b	614	4.1	14834	0.0003	0.319	0.013	0.0457	0.0018	0.88	288.2	11.1	281	10
13	Z27-b1	403	1.5	8983	0.0002	0.349	0.014	0.0496	0.0020	0.87	312.1	12.0	305	11
14	Z27-b2	425	1.7	9683	0.0002	0.342	0.014	0.0483	0.0019	0.87	304.2	11.7	299	10
15	Z26-c	930	6.7	20918	0.0003	0.340	0.014	0.0490	0.0019	0.87	308.3	11.8	/	
16	Z25-c	670	3.4	15081	0.0002	0.337	0.014	0.0489	0.0019	0.87	307.8	11.7	/	
17	Z24-c	538	2.2	13719	0.0002	0.296	0.012	0.0431	0.0017	0.87	271.9	10.4	/	
18	Z23-b	354	0.9	7769	0.0001	0.358	0.014	0.0500	0.0020	0.86	314.2	12.0	311	11
19	Z21-c	531	4.6	11845	0.0004	0.342	0.014	0.0498	0.0020	0.87	313.3	11.9	/	
20	Z20-b	325	1.8	7237	0.0002	0.369	0.015	0.0494	0.0019	0.86	311.1	11.8	317	11
21	Z19-b	416	1.4	9335	0.0002	0.347	0.014	0.0493	0.0019	0.86	310.3	11.8	/	
22	Z18-c	513	2.4	11391	0.0002	0.343	0.014	0.0499	0.0020	0.86	313.7	11.9	/	
23	Z17-b	271	1.1	6052	0.0002	0.356	0.015	0.0492	0.0019	0.85	309.6	11.7	309	11
24	Z28-b	418	1.7	9340	0.0002	0.349	0.014	0.0492	0.0019	0.84	309.8	11.7	305	11
25	Z34-b	431	2.1	9663	0.0002	0.345	0.014	0.0491	0.0019	0.84	308.9	11.7	302	11
26	Z34-c	165	0.4	3624	0.0001	0.360	0.015	0.0499	0.0019	0.83	313.9	11.9	313	11
27	Z48-c	443	1.8	9986	0.0002	0.345	0.014	0.0493	0.0019	0.84	309.9	11.7	303	11
28	Z48-b	509	4.8	14362	0.0003	0.272	0.011	0.0393	0.0015	0.84	248.4	9.4	246	9

B

BOS 32A		content				corrected ratios					Age (Ma)		Concordia	
Spot #	Name	Pb ppm	Th ppm	U ppm	Th/U	207Pb/235U	± 2 s	206Pb/238U	±2 s	Rho	206Pb/238U	± 2 s	age	± 2 s
1	Z1	590	29	12283	0.0024	0.387	0.016	0.0524	0.0021	0.95	329.2	12.7	333	12
2	Z2	221	7	7544	0.0010	0.246	0.010	0.0318	0.0013	0.94	201.7	7.9	/	
3	Z3-b	141	5	3834	0.0013	0.301	0.013	0.0401	0.0016	0.93	253.7	9.8	/	
4	Z4-b1	143	1	3414	0.0002	0.344	0.015	0.0460	0.0018	0.93	289.9	11.2	/	
5	Z4-b2	3443	135	90652	0.0015	0.290	0.012	0.0419	0.0017	0.95	264.8	10.2	/	
6	Z5-b	125	5	4358	0.0011	0.244	0.011	0.0311	0.0012	0.92	197.5	7.7	/	
7	Z6-c	498	2	12333	0.0002	0.323	0.014	0.0444	0.0017	0.93	280.1	10.8	283	10
8	Z7	158	1	4183	0.0003	0.316	0.014	0.0412	0.0016	0.91	260.0	10.1	/	
9	Z9	192	2	4606	0.0004	0.340	0.015	0.0457	0.0018	0.91	288.3	11.1	/	
10	Z10-1	306	1	7037	0.0002	0.350	0.015	0.0477	0.0019	0.92	300.5	11.6	303	11
11	Z10-2	296	1	6926	0.0001	0.348	0.015	0.0470	0.0019	0.92	295.9	11.4	300	11
12	Z12-1	518	3	13398	0.0002	0.314	0.014	0.0424	0.0017	0.93	267.5	10.4	/	
13	Z12-2	539	3	13301	0.0003	0.330	0.014	0.0445	0.0018	0.93	280.3	10.8	/	
14	Z13-1	129	2	3119	0.0006	0.336	0.015	0.0450	0.0018	0.89	283.6	11.0	/	
15	Z13-2	146	1	3555	0.0002	0.331	0.015	0.0449	0.0018	0.89	282.9	11.0	286	11
16	Z15-1	251	2	6206	0.0004	0.325	0.014	0.0443	0.0017	0.89	279.3	10.8	282	11
17	Z15-2	272	1	6145	0.0001	0.357	0.016	0.0487	0.0019	0.89	306.2	11.8	308	12
18	Z16	140	1	3194	0.0002	0.357	0.016	0.0482	0.0019	0.88	303.3	11.7	306	12
19	Z17	154	2	3605	0.0006	0.369	0.017	0.0461	0.0018	0.88	290.7	11.3	/	

Table 3. U-Th-Pb LA-ICP-MS data for the zircon grains in BOS32a and BOS32b samples

the Concordia diagrams; otherwise they are not taken into consideration because of doubtful interpretation. In LA-ICPMS analyses, several factors that cannot be easily detected from the inspection of the time-resolved signals might contribute to discordance (e.g. common Pb by way of low U content inclusions, mixing of different age domains, small cracks). If we consider the 7 concordant data (Table 3B), and if we avoid distorting the distribution of populations, only one date per grain is used, the age histogram (Figure 88C) shows the presence of three populations at

~330 Ma (group 1), ~305 Ma (group 2) and ~285 Ma (group 3). Group 1 is recorded by one zircon (Z1) with a concordia age of 333 ± 12 Ma. This analysis differs from the others by its Th content (29 ppm). Group 2 is determined from 3 grains. These data yield a mean age of 304 ± 6 Ma (MSWD = 0.37). The last group is composed of 3 grains, which yield a mean age of 284 ± 6 Ma (MSWD = 0.14).

6.1.6.2 Monazite U-Pb datation

Monazite grains from two metapelites (BOS18 and BOS 17) were analyzed *in situ* in thin section in order to preserve textural relationships between the accessory minerals, the rock-forming mineralogical assemblage and the fabrics.

Monazite is found as small tabular to rounded crystals (10 to 200 μm) either parallel to foliation-cleavage or not, or included in metamorphic minerals such as garnet, staurolite or muscovite in BOS18 (Figure 89A-C) and staurolite in BOS17 (Figure 89D-F). The crystals are homogeneous, without internal zoning. 19 and 11 spots were performed on 11 and 5 monazite crystals within BOS18 and BOS17 samples respectively (Table 4). Throughout, the analysed grains have a wide range of Th (~ 2000 -46500 ppm) and U contents (~100–3200 ppm) and Th/U (4.6–31). Concordia plots are presented on Figure 90. The ellipses of both samples plot between 280 and 330 Ma with a concordant cluster around 290 Ma and some discordant data. The discordance of these data is probably due to the presence of common Pb. The linear regression for the samples

A

BOS 18			content				corrected ratios				Age (Ma)			Concordia	
Textural position	Spot #	Name	Pb ppm	Th ppm	U ppm	Th/U	207Pb/235U	± 2 s	206Pb/238U	±2 s	Rho	206Pb/238U	± 2 s	age	± 2 s
in garnet //S2	1	Mz4-1	1262	43107	1708	25.2	0.353	0.020	0.0461	0.0018	0.69	290.6	11.2	291	11
in garnet //S2	2	Mz4-2	1380	46455	1930	24.1	0.376	0.025	0.0463	0.0019	0.62	291.7	11.5	/	
in matrix	3	Mz5	123	2693	423	6.4	0.408	0.041	0.0470	0.0020	0.43	295.8	12.3	/	
in matrix	4	Mz9	243	5808	714	8.1	0.381	0.050	0.0462	0.0022	0.36	291.1	13.5	291	13
in garnet //S2	5	Mz11-1	793	25426	1376	18.5	0.348	0.020	0.0464	0.0018	0.68	292.2	11.3	293	11
in matrix //S1	6	Mz11-2	811	24321	1719	14.1	0.361	0.020	0.0463	0.0018	0.72	291.8	11.3	/	
in matrix	7	Mz12	317	7635	1181	6.5	0.362	0.021	0.0466	0.0019	0.67	293.6	11.4	/	
in matrix	8	Mz13	739	16444	3158	5.2	0.340	0.019	0.0463	0.0018	0.73	291.5	11.3	292	11
in matrix	9	Mz15-1	923	28495	1915	14.9	0.355	0.021	0.0465	0.0019	0.67	293.0	11.4	294	11
in matrix	10	Mz15-2	1077	34462	1502	22.9	0.385	0.028	0.0470	0.0019	0.57	295.8	11.9	/	
in staurolite	11	Mz16'-1	48	824	162	5.1	0.731	0.096	0.0509	0.0026	0.39	320.2	15.8	/	
in matrix	12	Mz16'-2	684	18911	1605	11.8	0.398	0.024	0.0465	0.0019	0.67	293.2	11.5	/	
in matrix //S2	13	Mz16'-3	548	13644	1695	8.0	0.361	0.025	0.0470	0.0019	0.59	295.9	11.8	296	12
in staurolite	14	Mz16-1	651	19295	1250	15.4	0.454	0.038	0.0477	0.0020	0.52	300.3	12.6	/	
in matrix	15	Mz16-2	482	13200	779	16.9	0.470	0.033	0.0532	0.0022	0.59	333.9	13.3	/	
in matrix //S2	16	Mz14-1	779	25332	1002	25.3	0.591	0.038	0.0494	0.0020	0.65	310.5	12.6	/	
in matrix //S2	17	Mz14-2	664	22559	838	26.9	0.594	0.055	0.0495	0.0023	0.49	311.6	13.9	/	
in matrix	18	Mz18-1	176	4243	561	7.6	0.412	0.034	0.0466	0.0020	0.51	293.9	12.1	/	
in matrix	19	Mz18-2	437	13610	736	18.5	0.432	0.031	0.0469	0.0020	0.59	295.7	11.9	/	

B

BOS 17			content				corrected ratios				Age (Ma)			Concordia	
Textural position	Spot #	Name	Pb ppm	Th ppm	U ppm	Th/U	207Pb/235U	± 2 s	206Pb/238U	±2 s	Rho	206Pb/238U	± 2 s	age	± 2 s
in staurolite // S1	1	Mz2-1	185	4231	678	6.2	0.347	0.036	0.0464	0.0020	0.43	292.4	12.6	293	13
in staurolite // S1	2	Mz2-2	72	1898	158	12.0	0.785	0.170	0.0516	0.0039	0.35	324.5	23.9	/	
in staurolite // S1	3	Mz2-3	182	3632	796	4.6	0.349	0.027	0.0461	0.0019	0.54	290.6	11.9	291	12
in matrix //S1	4	Mz6-1	307	6194	1253	4.9	0.428	0.025	0.0468	0.0019	0.69	295.0	11.7	/	
in matrix //S1	5	Mz6-2	95	1950	304	6.4	0.805	0.081	0.0515	0.0025	0.49	323.8	15.4	/	
in matrix //S1	6	Mz6-3	858	26653	1671	16.0	0.392	0.021	0.0469	0.0019	0.74	295.2	11.6	/	
in matrix //S1	7	Mz6-4	463	11997	1270	9.4	0.643	0.041	0.0495	0.0021	0.66	311.1	12.8	/	
in matrix //S1	8	Mz5-1	181	4525	384	11.8	0.873	0.066	0.0532	0.0023	0.58	334.2	14.4	/	
in garnet //S1	9	Mz7-1	279	8418	276	30.5	0.394	0.050	0.0467	0.0021	0.36	294.5	13.1	294	13
in garnet //S1	10	Mz7-2	584	17723	567	31.2	0.435	0.040	0.0523	0.0023	0.48	328.7	14.0	329	14
in garnet //S1	11	Mz8-1	33	669	103	6.5	0.488	0.095	0.0476	0.0025	0.27	299.6	15.5	298	15

Table 4. U-Th-Pb LA-ICP-MS data for the monazite grains in BOS17 and BOS18 samples.

BOS17 and BOS18 yields a lower intercept of 289.1 ± 5.9 Ma (MSWD = 0.1; n= 10) and 290 ± 3.8 Ma (MSWD = 0.1; n= 18), respectively. There is no age difference between the included grains and the matrix monazite. These two ages are similar if all the data are grouped in a same diagram, the lower intercept age is 289.8 ± 3.0 Ma (MSWD = 0.1; n =28). Two ellipses near the

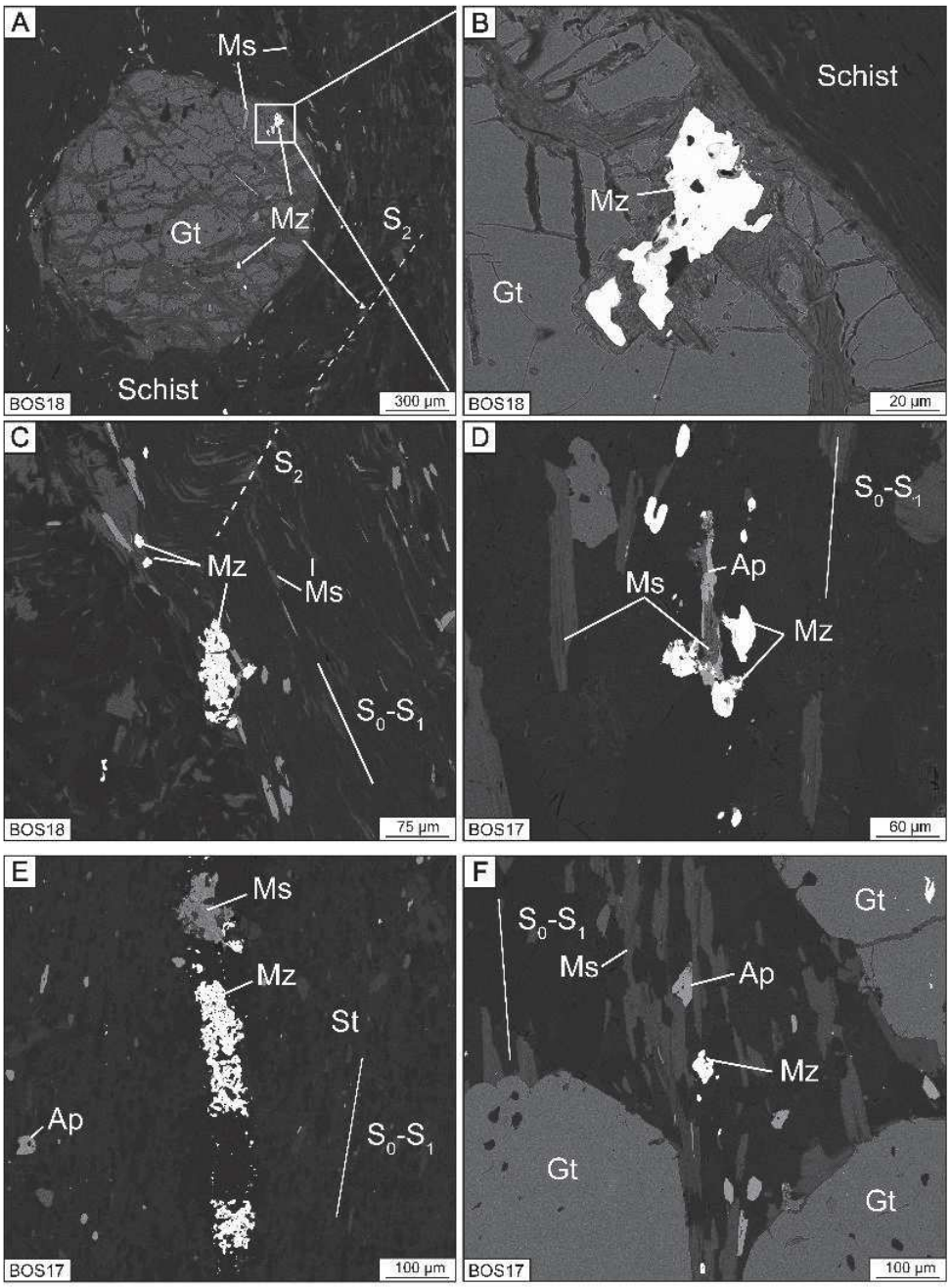

Figure 89. Back-scattered electron (BSE) images of the studied monazites (abbreviations: Mz: monazite, St: staurolite, Gt: garnet; Ms: muscovite; Ap: apatite). A. Monazites (Mz 4 & 5) include in garnet (BOS18). B. Zoom of the monazite Mz4 (BOS18). C. Monazite (Mz 2) in host rock aligned alon S_0-S_1 foliation (BOS18). D. Monazite (Mz 6) associated to muscovite and apatite grains (BO17). E. Monazite (Mz 2) included in staurolite centimetric crystal (BOS17). Monazite (Mz 5) in host-rock associated to muscovite and between garnet grains (BOS17).

Concordia were excluded to the calculation because they are older ages around 330 Ma (Table 4, Figure 90).

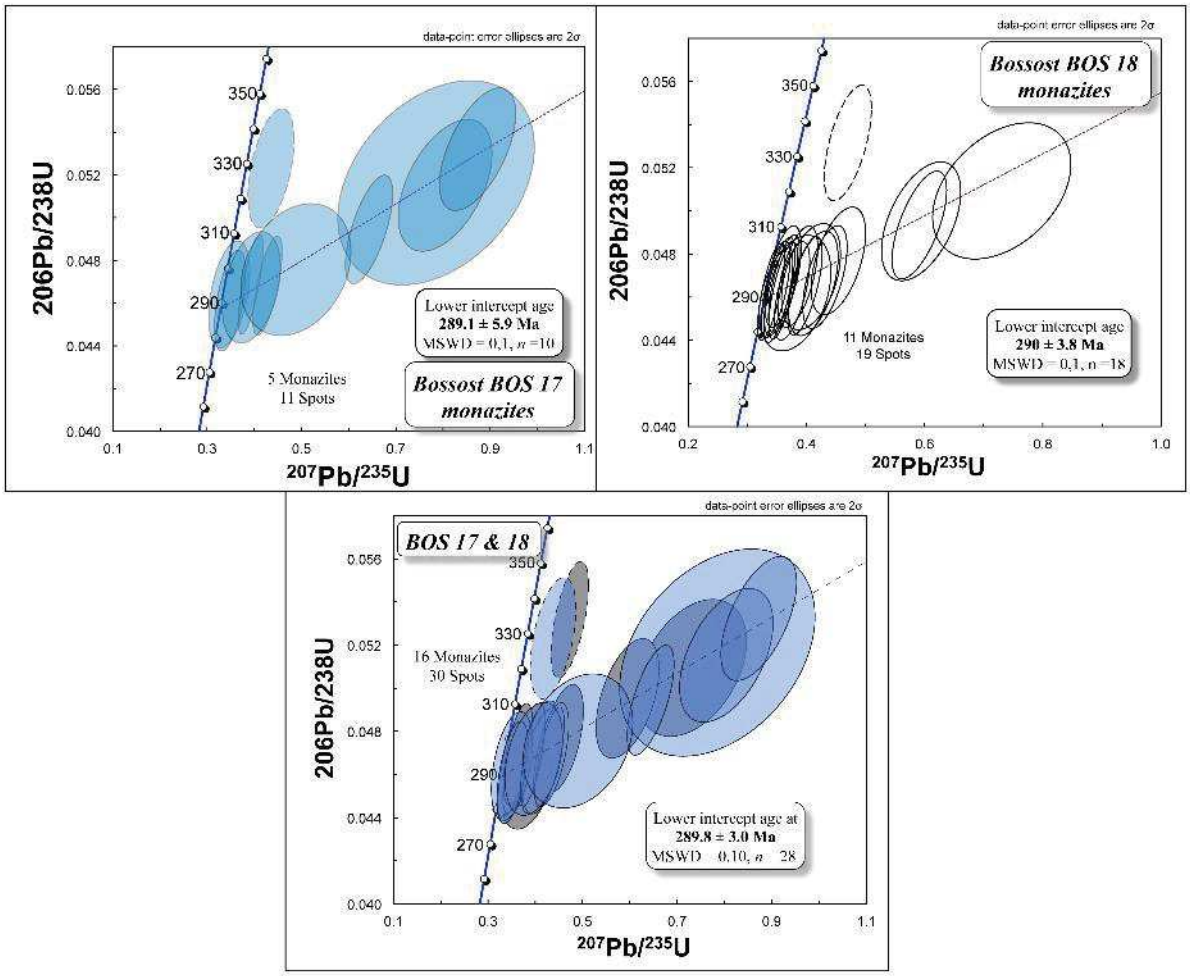

Figure 90. U-Th-Pb Concordia diagrams for the monazites analysed in the metapelites (BOS17, BOS18 and BOS17and BOS18). Error ellipses and uncertainties in ages are ± 2σ. The stippled ellipses are not taken into account for the age calculation.

6.1.6.3 Ar-Ar Data

In the Bentaillou sample, five muscovite grains were analyzed by progressive degassing on nineteen steps with a defocused laser beam (Figure 86; Table 6). The resulting age spectrum (Figure 91) shows discordant ages close to 150 Ma in the beginning of the degassing probably linked to grain surficial interference (Table 6A). It is followed by a population of ages comprised between 259 and 275 Ma which corresponds to a pseudo-plateau age of 268.9 ± 2.8 Ma obtained for 85 % of 39Ar released (Figure 91). The total gas age at 265 ± 0.9 Ma and the age obtained by an isochrone diagram at 266.9 ± 6.0 Ma are close to the previous age plateau. Additional eleven muscovite grains included in sphalerite were analyzed by in-situ laser ablation (Figure 92; Table 6) yielded ages

between 197 and 298 Ma (error between 0.8 and 2.3 %; Table 6B) without any clear maximum. This age scatter probably reflects the mixing of different argon reservoirs, both from the muscovite and adjacent minerals that were degassed during lasering.

A BENTAILLOU muscovite Step	36Ar (fA)	37Ar (fA)	38Ar(fA)	39Ar (fA)	40Ar(fA)	Age (Ma)	error	%40Ar rad.	%39Ar
1	0.0120	0.2070	0.0021	0.1852	6.17	**112.86**	**21.86**	63.25	0.20
2	0.0094	0.2800	0.0000	0.3957	18.10	**153.11**	**11.56**	86.59	0.43
3	0.0189	0.4071	0.0206	3.2246	237.69	**240.75**	**4.20**	97.67	3.51
4	0.0028	0.7044	0.0000	2.3675	187.27	**257.16**	**7.47**	99.54	2.58
5	0.0236	1.5760	0.0000	2.5250	195.47	**252.04**	**5.61**	96.51	2.75
6	0.0565	4.3409	0.0000	5.9183	472.16	**259.21**	**2.60**	96.54	6.44
7	0.0222	1.3250	0.0004	7.3789	602.85	**265.01**	**2.09**	98.90	8.03
8	0.0135	1.8268	0.0000	4.0795	326.03	**259.63**	**4.80**	98.76	4.44
9	0.0195	2.5424	0.0075	8.1768	671.00	**266.10**	**1.89**	99.13	8.90
10	0.0126	8.5892	0.0126	4.8709	401.68	**267.32**	**3.20**	99.06	5.30
11	0.0431	8.1833	0.0180	10.6015	901.08	**274.93**	**1.48**	98.58	11.54
12	0.0341	0.8248	0.0000	7.3328	595.87	**263.69**	**2.07**	98.31	7.98
13	0.0314	0.0000	0.0188	3.5633	292.02	**265.78**	**4.24**	96.88	3.88
14	0.0479	0.0000	0.0000	5.8703	494.17	**272.49**	**2.57**	97.18	6.39
15	0.0513	0.0903	0.0066	3.0254	248.57	**266.41**	**4.89**	94.18	3.29
16	0.0599	0.0000	0.0029	8.1010	683.14	**272.92**	**2.00**	97.44	8.82
17	0.0220	0.0000	0.0000	3.3389	270.68	**263.10**	**5.11**	97.62	3.63
18	0.0696	0.0000	0.0274	5.6827	478.83	**272.72**	**3.07**	95.83	6.18
19	0.0126	0.0674	0.0695	5.2568	425.15	**262.53**	**2.86**	99.11	5.72
					Total age	**265.0 ± 0.9 Ma**			
B BENTAILLOU section Analysis N°	36Ar (fA)	37Ar (fA)	38Ar(fA)	39Ar (fA)	40Ar(fA)	Age (Ma)	error	%40Ar rad.	%39Ar
1	0.1241	0.0117	0.0000	7.6352	478.64	**206.47**	**0.84**	92.80	12.60
2	0.1093	0.1410	0.0000	4.9681	297.65	**197.81**	**1.65**	90.11	8.20
3	0.1568	0.0476	0.0000	5.6401	389.25	**226.05**	**2.28**	89.26	9.30
4	0.0761	0.0000	0.0226	4.4788	359.08	**260.08**	**1.88**	94.04	7.39
5	0.1247	0.0207	0.0259	4.8792	358.75	**239.89**	**1.88**	90.59	8.05
6	0.2119	0.0079	0.0271	5.6524	525.71	**298.45**	**2.29**	89.25	9.32
7	0.3868	0.0914	0.0334	5.5566	372.86	**220.15**	**1.35**	76.34	9.17
8	0.0893	0.0000	0.0000	4.4369	264.70	**197.01**	**1.53**	90.83	7.32
9	0.2148	0.1074	0.0077	6.9908	623.29	**287.04**	**1.20**	90.66	11.53
10	0.1071	0.0114	0.0000	4.7210	397.15	**271.99**	**1.89**	92.54	7.79
11	0.1615	0.0231	0.0244	5.6605	406.63	**234.72**	**1.38**	89.39	9.34
					Mean age	**239.97**	**± 1.65**		

Table 6. $^{40}Ar/^{39}Ar$ data from A. Bentaillou separated muscovite crystals; B. Bentaillou muscovite analyzed in thick section.

ANG13 section Analysis N°	36Ar (fA)	37Ar (fA)	38Ar(fA)	39Ar (fA)	40Ar(fA)	Age (Ma)	error	%40Ar rad.	%39Ar
1	0.0161	0.0453	0.0000	3.0802	133.13	**144.24**	**6.07**	96.50	8.78
2	0.0725	0.0529	0.0085	4.6860	148.52	**106.89**	**3.72**	87.25	13.36
3	0.0449	0.0000	0.0000	4.9476	185.52	**125.79**	**3.56**	93.24	14.10
4	0.0301	0.1073	0.0000	4.8613	170.64	**118.00**	**3.62**	94.98	13.86
5	0.0330	0.0729	0.0163	4.2424	147.91	**117.24**	**4.11**	93.73	12.09
6	0.0297	0.0898	0.0000	4.5859	130.00	**95.89**	**3.77**	93.59	13.07
7	0.0106	0.0764	0.0000	3.0706	116.80	**127.54**	**5.70**	97.34	8.75
8	0.0113	0.0382	0.0000	3.6875	143.32	**130.22**	**4.91**	97.67	10.51

Table 5. $^{40}Ar/^{39}Ar$ data from Anglas muscovite associated to sphalerite mineralization and analyzed on thick section.

In the Anglas sample, the eight in-situ analyses on muscovite crystals (Figure 92) gave data which exhibit a relative large dispersion between 96 and 144 Ma (error between 3.6 and 6.1 %;Table 5) and a central age of 119 ± 3 Ma. It is very likely that this age dispersion is also due to the

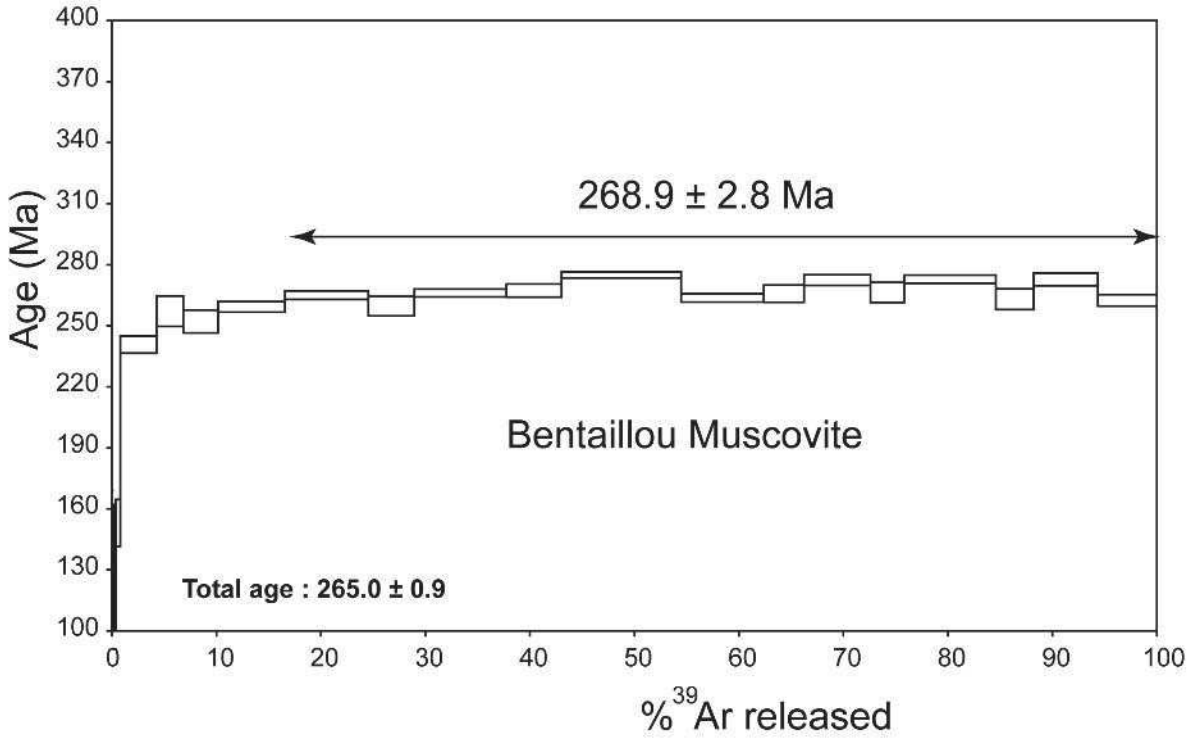

Figure 91. Step-heating $^{40}Ar/^{39}Ar$ results for Bentaillou muscovite.

simultaneous degassing of muscovite and adjacent minerals due to the low spatial resolution of in situ analyses (Figure 92). However, muscovite in Anglas appears to be significantly younger than in Bentaillou.

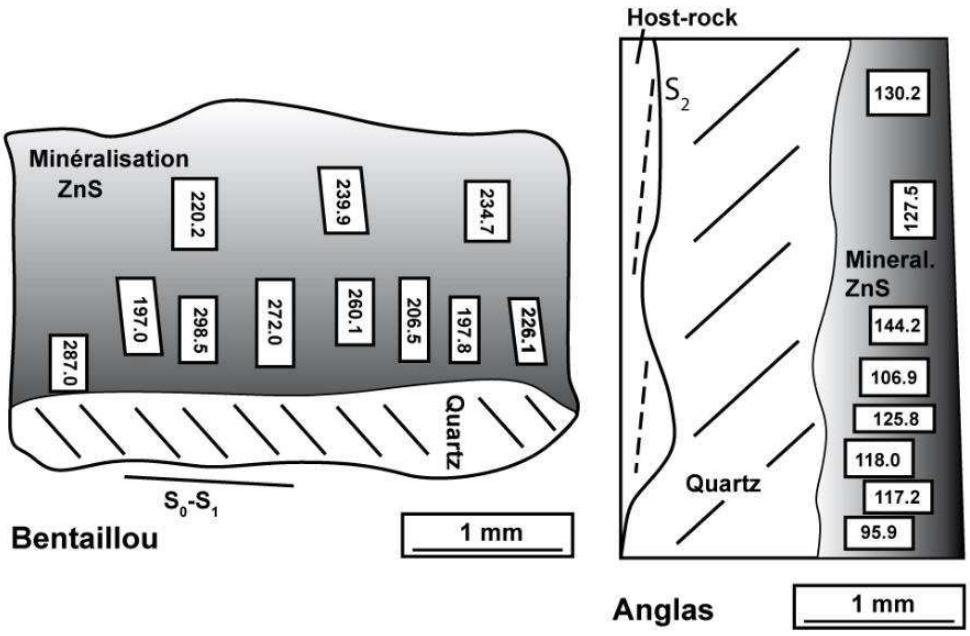

Figure 92. Two sketches representing the location and the age of the in-situ $^{40}Ar/^{39}Ar$ measurements on the Bentaillou and Anglas thick sections, composed essentially of sphalerite and quartz.

6.1.7 Interpretation and discussion

6.1.7.1 Interpretation of the geochronological data.

Even though the two granitic sills in the south of the Bossost dome present similar textural and petrogenetic patterns, the obtained U/Pb zircon ages are quite different. The first sample (BOS32b) shows a cluster of data with a weighted mean $^{206}Pb/^{238}U$ age of 310.4 ± 2.7 Ma. (MSWD = 0.28; n =18). The Th/U ratios are systematically very low (<0.0001) associated with high U contents above 3000 ppm which is common in the zircons from peraluminous granitoids *(Lopez-Sanchez et al. 2016, 2018*). This age can be interpreted as the emplacement age of this granitic sill. It is in agreement with the commonly reported ages for Variscan magmatism within the PAZ ranging between ~ 300 and 315 Ma (Figure 83; *Paquette et al., 1997; Denèle et al., 2014*).

The interpretation of results of the second sample (BOS32a) is more complex because the analytical points line up along or near the Concordia, and consequently two hypotheses can be proposed:

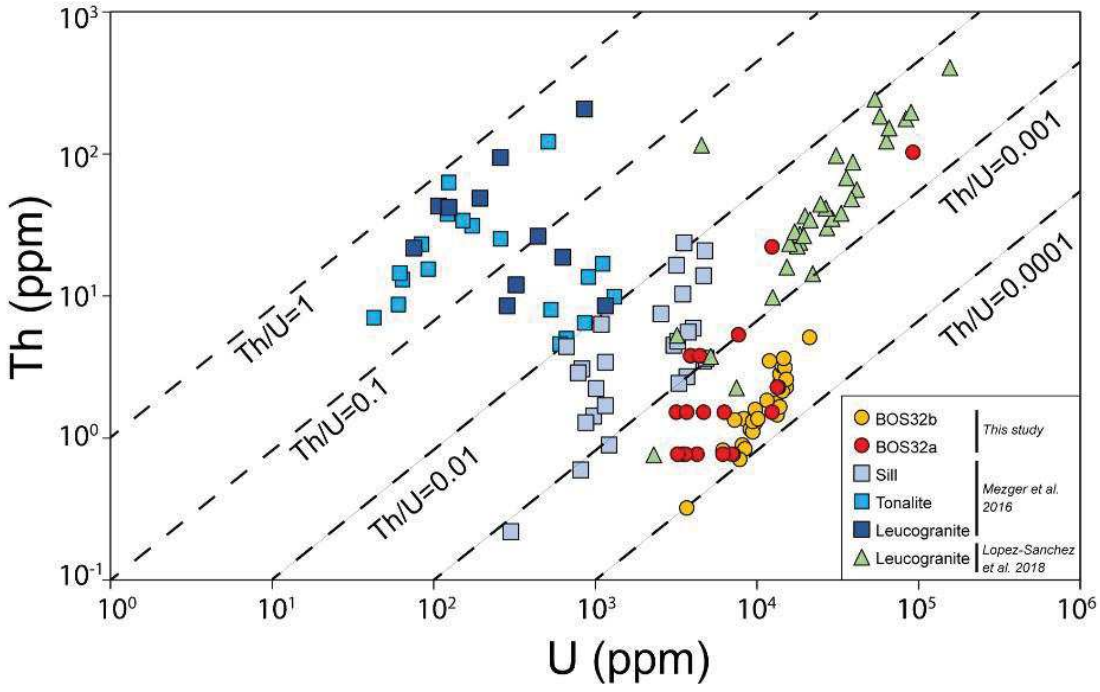

Figure 93. U vs Th contents comparison in Bossost zircon between our study and the zircon from *Mezger & Gerdes (2016)* and *Lopez-Sanchez et al. (2018).*

i) The lower intercept age of 331 ± 13 Ma (MSWD=1.5) obtained by a linear regression of 17 analyses can be considered as crystallization age (Figure 88C). The zircons of this sample

(BOS32A) have Th/U ratios similar to zircons from the previous sample (Figure 93) and the zircons reported in *Lopez-Sanchez et al. (2018)* which crystallized in the Early-Permian times. These ratios are clearly lower than values from zircons possibly crystallized during the Early Carboniferous in *Mezger and Gerdes (2016)*(Figure 93).

ii) If we consider only the concordant data, the age histogram shows the presence of three age populations in the Figure 88B. An older minor population consists of a single data with a concordant age of 333 ± 12 Ma (n=1). It may correspond to an older Variscan magmatism signature, Visean in age and reported in the Bossost granite recently by *Mezger and Gerdes (2016)* and *Lopez-Sanchez et al. (2018)* or in Soulcem granite by *Mezger and Gerdes (2016)*. These Visean ages are interpreted either as the emplacement age for all the granitic facies (*Mezger and Gerdes, 2016)* or as the existence of a widespread early Carboniferous magmatic event in the PAZ which is emphasized by the presence of an early Carboniferous inherited zircons, the crystallization age of these granitoids being early Permian (295-297 Ma) (*Lopez-Sanchez et al., 2018)*. The main population yields a mean age of 304 ± 6 Ma (MSWD = 0.37; n = 4) and is similar to the emplacement age of the sample BOS 32b (i.e. 310.4 ± 2.7 Ma) and the widespread magmatic event in the PAZ *(Paquette et al. 1997; Denèle et al. 2014*). The third major population yields a mean age of 284 ± 6 Ma (MSWD = 0.14; n=3) which is younger than the previous age for the Bossost granitic sill (BOS 32b) but ranges in the same age range than the crystallization age of the leucogranite facies (293-299 Ma) dated by *Lopez-Sanchez et al. (2018)*. This Late-Variscan age is similar to the monazite U-Th-Pb ages found in the metapelites BOS 17 and BOS 18 in the south of the Bossost dome, which are 289.1 ± 5.9 (MSWD = 0.1; n = 10) and 290 ± 3.8 Ma (MSWD = 0.1; n = 18) respectively. All data of both samples yield a lower intercept age of 289.8 ± 3.0 Ma (MSWD = 0.1; n = 28). Whether grains are parallel to S_1 or S_2 foliations, free in the S_1 foliation, S_2 cleavage, or directly included in metamorphic minerals such as garnet or staurolite, monazite grains exhibit similar ages. The reset of the monazite age is probably related to the recrystallization of the monazites during a late hydrothermal phase associated with the Variscan metamorphism M_2 stage and the related Late-magmatism (295-297 Ma). Fluid-assisted dissolution-precipitation mechanisms related to porosity, cracks in the monazite may modify the chemical and isotopic composition of monazite even at low temperature alteration (<300°C) *(Hawkins and Bowring 1997; Seydoux-Guillaume et al. 2002, 2012; Grand'Homme et al. 2016*). Similar monazite ages are reported in the Canigou massifs for monazite either included in metamorphic minerals or in the foliation (*de Hoÿm de Marien et al. 2019*). The $^{40}Ar/^{39}Ar$ age of 268.9 ± 2.8 Ma (Figure 91) recorded in the Bentaillou muscovite and associated to sphalerite mineralization is 20 Myrs younger than the monazite U-Th-Pb ages, and is probably related to the previous thermal event (M_2?), and not to the emplacement

of sphalerite mineralization. This stratabound mineralization cannot be related to a late Variscan stage (D_3, Figure 94) because it is folded by D_2 deformation.

The $^{40}Ar/^{39}Ar$ data recorded in the Anglas deformed vein sphalerite exhibit wide variations in age between 96 and 144 Ma (Figure 94), which suggest the presence of a partial or total rejuvenation of argon isotopic system during this period as has already been suggested in the PAZ by some authors (Boulvais et al. 2007; Boutin 2016; Boutin et al. 2016; Cochelin et al. 2017b) and is clearly not related to the mineralization crystallization. This period corresponds to important thermal events in the Pyrenees related to Na(-Ca) metasomatism (~550°C) recorded mainly in North Pyrenean Massif but also in the Eastern PAZ (*Golberg and Leyreloup 1990; Boulvais et al. 2007; Fallourd et al. 2014; Clerc et al. 2015*). It is probably related to the LP-HT (3-4 kbar and 500-600 °C close to North Pyrenean Zone) metamorphic event (Figure 94) developed during the Early-Cretaceous lithospheric extension and the final formation of talc-chlorite or albitite bodies (Fallourd et al. 2014). These different thermal events could be associated to the destabilization and dynamic recrystallization of sphalerite ore which is mainly responsible for the Ge-redistribution from the sphalerite lattice to accessory Ge-minerals (chloritoid, oxides, sulfides; *Cugerone et al., 2018a, 2018b*). This hypothesis is particularly relevant because sphalerite is considered as a ductile mineral and may recrystallize at temperatures as low as 300-400 °C *(Clark and Kelly 1973; Siemes and Borges 1979; Marshall and Gilligan 1987*) which correspond approximatively to the closure temperature of the micas *(Harrison et al. 2009*).

6.1.7.2 Variscan magmatism, metamorphism and mineralizing events in the PAZ

Variscan magmatism in the PAZ is commonly considered as Late-Variscan (~310-290 Ma) and establishes the onset of D_2 deformation (*Denèle et al. 2014*). However, the Visean age for the emplacement of Bossost and Soulcem peraluminous granite, the migmatization (HT metamorphism) on the Aston dome (Mezger and Gerdes 2016; Mezger and Régnier 2016) and the occurrence of Serpukhvian inherited zircon for Lys-Caillaouas granitoid (*Lopez-Sanchez et al., 2018*) question the geodynamic model of the PAZ, and the relationships between magmatic and metamorphic events that might be reconsidered (Figure 83). The Early and Late Carboniferous magmatic age reported in the PAZ may record a continuous magmatic period as evidenced by a large spread of magmatic ages recorded in the PAZ granites from 340 to 290 Ma (Figure 94) even if a large proportion of the recorded ages are more around ~ 300Ma, especially in the western and eastern part (Figure 94). Same spread of magmatic ages appear in the French Massif Central (*Laurent et al. 2017*) or in Corsica massif *(Faure et al. 2014*) which were paleogeographically close in Late-

Visean period (*Stampfli et al. 2007*). Thermal relaxation of the crust is supposed to explain Visean magmatism period (*Lopez-Sanchez et al. 2018*) following crustal thickening as proposed in other Variscan terranes where Visean magmatism is recognized *(Schaltegger 1997),* or related to intracontinental subduction zones (*Kroner and Romer 2013; Mezger and Gerdes 2016*). In Northwest Iberia, the occurrence of a short-lived Visean peraluminous magmatism (347-337 Ma) pre-dating

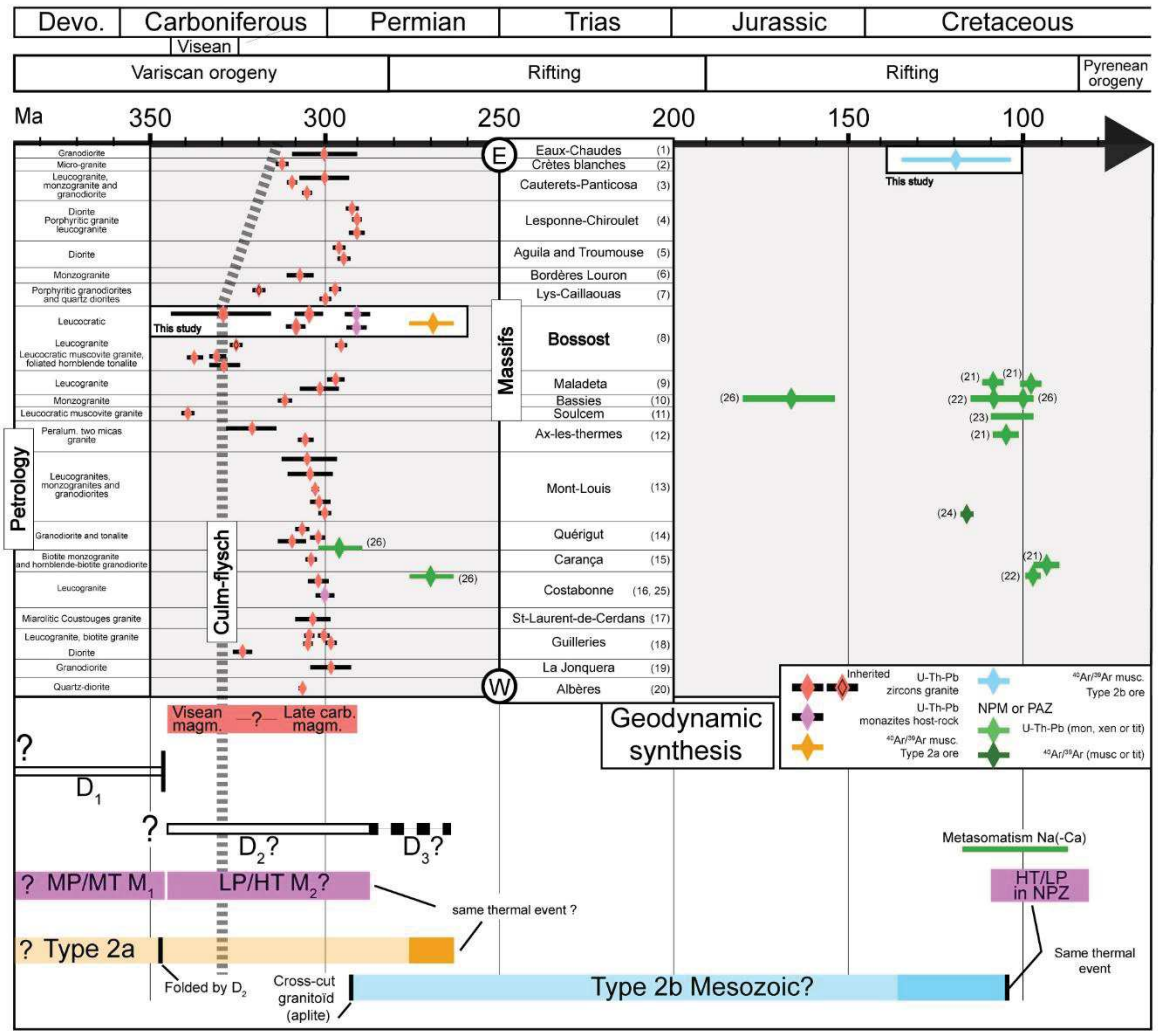

Figure 94. Chronological succession of the magmatic, metamorphic and Pb-Zn mineralizations events in the Pyrenean Axial Zone (PAZ) and in the North Pyrenean Massifs (NPM). The ages are disposed according to an E-W transect. Central column which names different massifs is reffered to the Variscan magmatic and metamorphic ages. References: *(1)*(Ternet et al. 2004) *; (2)*(Ternet et al. 2004) *; (3)* (Majesté-Menjoulàs et al. 1999; Denèle 2007) *; (4)* (Lemirre et al. 2019) *; (5)* (Kilzi et al. 2016) *; (6)* (Gleizes et al. 2006) *; (7)* (Esteban et al. 2015; Lopez-Sanchez et al. 2018) *; (8)* (Mezger and Gerdes 2016; Lopez-Sanchez et al. 2018) *; (9)* (Martínez et al. 2015) *; (10)* (Paquette et al. 1997) *; (11)* (Mezger and Gerdes 2016) *; (12)* (Denèle 2007; Denèle et al. 2014) *; (13)* (Alexandrov 2000; Maurel 2003; Denèle et al. 2014) *; (14)* (Roberts et al. 2000a; Baudin 2013) *; (15)* (Denèle et al. 2014) *; (16)* (Laumonier et al. 2015) *; (17)* (Baudin 2013) *; (18)* (Martínez et al. 2008) *; (19)* (Maurel 2003) *; (20)* (Guerrot 2001) *; (21)* (Fallourd et al. 2014) *(22)* (Poujol et al. 2010) *; (23)* (Schärer et al. 1999) *; (24)* (Boulvais et al. 2007) *; (25)* (de Hoÿm de Marien et al.

syn-orogenic (325-315 Ma) and post-orogenic (305-290 Ma, *Gutiérrez-Alonso et al., 2011*) magmatism is explained by rapid exhumation of the thickened crust and related melting *(Gutiérrez-Alonso et al. 2018*).

We propose that a regional-scale contact M_2 metamorphism LP/HT associated to magmatism began with the intrusion of Visean plutons as mentionned by *(Mezger and Gerdes 2016*) and persists probably until the end of the Carboniferous (D_3 deformation). This high thermal regime is recorded up to Permian times in monazite from metapelites and in micas hosted in stratabound Pb-Zn mineralization (Figure 94). Progression of the subduction of Gondwana beneath Armorica with probable north vergence and beginning during Late-Tournaisian (~350Ma; *Stampfli et al., 2013*) may lead to the steepening and roll-back of the slab with the final delamination of the lithospheric mantle which produce a widespread magmatism as proposed by *Lemirre et al., (2019)* for the Late-Variscan magmatic event in the PAZ and *Laurent et al. (2017)* for the Eastern French Massif-Central Variscan magmatism. The numerous dome formed due to the uplift of hot astenospheric mantle that triggered and maintained a widespread crustal melting.

Post-Variscan events are marked by a long-lasting extensional period in the PAZ during the Mesozoic (*Vergés et al. 2002; Martín-gonzález et al. 2019)* which allowed the circulation of hydrothermal fluid in the Variscan basement. Numerous Pb-Zn mineralizations are reported in Western European Variscan belt related to this extension *(Charef and Sheppard 1988; Munoz et al. 1994; Boiron et al. 2010; Cathelineau et al. 2012*) and is reported by *Boutin et al. (2016*) in the North Pyrenean Massifs in association with chlorite (Figure 94). The precipitation of epigenetic Pb-Zn ore in extensional veins parallel to the S_2 cleavage could be contemporaneous as recognized in Cierco or Yenefrito; (Figure 94). Around 120-90Ma, a main hydrothermal event is recorded in the North Pyrenean Massifs and circulation of fluids may occur as well in the PAZ in sub-vertical structures such as mineralized veins of Type2b which may impact the sphalerite ore with recrystallization and subsequent remobilization of the Ge present in the sulfide lattice *(Cugerone et al. 2018a*).

6.1.8 Conclusion

The relations between magmatism, metamorphism and Pb-Zn mineralization emplacement in the Pyrenean Axial Zone (PAZ) allow to propose a new interpretation and chronology of the geodynamical model of this Variscan basement. Based on new ages and synthetic analyses in the Bossost dome, a single period of magmatism and related regional contact metamorphism (M_2)

between ~340 and 290 Ma is proposed which began in the Central PAZ, progressively continue in the Western and Eastern part of the PAZ and finish during Early-Middle Permian age as recorded by monazite from metapelites and micas hosted in sphalerite stratabound mineralization. Vein sphalerite mineralization from the western part of the PAZ and parallel to S_2 cleavage could be post-Variscan in age and has probably endured an Early-Cretaceous thermal event which pre-date Pyrenean orogeny. These two last events are responsible of the sphalerite recrystallization and subsequent Ge-redistribution.

6.1.9 References

Van Achterbergh, E., Ryan, C.G., and Griffin, W.L., 2001, Glitter! User's manual: On-line Interactive Data Reduction for the LA-ICPMS Microprobe, p. 1–72.

Alexandrov, P., 2000, Géochronologie U/Pb et 40Ar/39Ar de deux segments de la chaîne Varisque: le haut Limousin et les Pyrénées orientales.: Unpublished Thesis, INPL, Nancy,.

Alonso, J.L., 1979, Deformaciones sucesivas en el area comprendida entre Liat y el Puerto de Orla - Control estructural de los depositos de sulfuros (Valle de Aran, Pirineos Centrales): Tesis Licenciatura, Univ. Oviedo, p. 26p.

Boiron, M.C., Cathelineau, M., and Richard, A., 2010, Fluid Flows and Metal Deposition near Basement/Cover Unconformity: Lessons and Analogies from Pb-Zn-F-Ba Systems for the Understanding of Proterozoic U Deposits: Frontiers in Geofluids, v. 10, p. 270–292, doi:10.1002/9781444394900.ch19.

Bois, J.P., Pouit, G., Gros, Y., B., G., and Picot, P., 1976, Les minéralisations de Zn (Pb) de l'anticlinorium de Pierrefitte: un exemple de gisements hydrothermaux et sédimentaires associés au volcanisme dans le Paléozoïque des Pyrénées centrales: Bulletin du BRGM, v. 6, p. 543–567.

Boulvais, P., Ruffet, G., Cornichet, J., and Mermet, M., 2007, Cretaceous albitization and dequartzification of Hercynian peraluminous granite in the Salvezines Massif (French Pyrénées): Lithos, v. 93, p. 89–106, doi:10.1016/j.lithos.2006.05.001.

Boutin, A., 2016, Etude des conditions de formations du gisement de talc-chlorite de Trimouns (Ariège, France): PhD thesis, Université de Toulouse 3 Paul Sabatier, p. 1–284, doi:10.1017/CBO9781107415324.004.

Boutin, A., de Saint Blanquat, M., Poujol, M., Boulvais, P., de Parseval, P., Rouleau, C., and Robert, J.F., 2016, Succession of Permian and Mesozoic metasomatic events in the eastern Pyrenees with emphasis on the Trimouns talc–chlorite deposit: International Journal of Earth Sciences, v. 105, p. 747–770, doi:10.1007/s00531-015-1223-x.

Bruguier, O., Becq-Giraudon, J.F., Clauer, N., and Maluski, H., 2003, From late Visean to Stephanian: Pinpointing a two-stage basinal evolution in the Variscan belt. A case study from the Bosmoreau basin (French Massif Central) and its geodynamic implications: International Journal of Earth Sciences, v. 92, p. 338–347, doi:10.1007/s00531-003-0321-3.

Cardellach, E., Phillips, R., and Ayora, C., 1982, Metamorphosed stratiform sulphides of the Liat area, Central Pyrenees, Spain: Institution of Mining and Metallurgy, Transactions, Section B, v. Applied Ea, p. 90–95.

Carreras, J., and Capella, I., 1994, Tectonic levels in the Palaeozoic basement of the Pyrenees: a review and a new interpretation: Journal of Structural Geology, v. 16, p. 1509–1524.

Carreras, J., and Cirés, J., 1986, The geological significance of the western termination of the Mérens Fault at Port Vell (central Pyrenees): Tectonophysics, v. 129, p. 99–114, doi:10.1016/0040-1951(86)90248-9.

Carreras, J., and Druguet, E., 2014, Framing the tectonic regime of the NE Iberian Variscan segment: Geological Society, London, Special Publications, v. 405, p. 249–264, doi:10.1144/SP405.7.

Carreras, J., Druguet, E., Griera, a., and Soldevila, J., 2004, Strain and deformation history in a syntectonic pluton. The case of the Roses granodiorite (Cap de Creus, Eastern Pyrenees): Geological Society, London, Special Publications, v. 224, p. 307–319, doi:10.1144/GSL.SP.2004.224.01.19.

Casas, J.M., Castiñeiras, P., Navidad, M., Liesa, M., and Carreras, J., 2010, New insights into the Late Ordovician magmatism in the Eastern Pyrenees: U-Pb SHRIMP zircon data from the Canigó massif: Gondwana Research, v. 17, p. 317–324, doi:10.1016/j.gr.2009.10.006.

Castroviejo Bolibar, R., and Serrano, F.M., 1983, Estructura y metalogenia del campo filoniano de Cierco (Pb-Zn-Ag), en el Pirineo de Lérida: Boletín Geológio y Minero, v. 1983, p. 291–320.

Cathelineau, M., Boiron, M.C., Fourcade, S., Ruffet, G., Clauer, N., Belcourt, O., Coulibaly, Y., Banks, D.A., and Guillocheau, F., 2012, A major Late Jurassic fluid event at the basin/basement unconformity in western France: 40Ar/39Ar and K-Ar dating, fluid chemistry, and related geodynamic context: Chemical Geology, v. 322–323, p. 99–120, doi:10.1016/j.chemgeo.2012.06.008.

Charef, A., and Sheppard, S.M.F., 1988, The Malines Cambrian carbonate-shale-hosted Pb-Zn deposit, France: Thermometric and isotopic (H, O) evidence for pulsating hydrothermal mineralization: Mineralium Deposita, v. 23, p. 86–95, doi:10.1007/BF00206655.

Clark, B.R., and Kelly, W.C., 1973, Sulfide Deformation Studies; I, Experimental Deformation of Pyrrhotite and Sphalerite to 2,000 Bars and 500 degrees C: Economic Geology, v. 68, p. 332–352, doi:10.2113/gsecongeo.68.3.332.

Cochelin, B., 2016, Champ de déformation du socle Paléozoïque des Pyrénées, PhD Thesis Université Toulouse 3 Paul Sabatier: 244 p.

Cochelin, B., Lemirre, B., Denèle, Y., De Saint Blanquat, M., Lahfid, A., and Duchêne, S., 2017, Structural inheritance in the Central Pyrenees : the Variscan to Alpine tectonometamorphic evolution of the Axial Zone: Journal of the Geological Society, p. 16p.

Cocherie, A., Baudin, T., Autran, A., Guerrot, C., Fanning, C.M., and Laumonier, B., 2005, U-Pb zircon (ID-TIMS and SHRIMP) evidence for the early ordovician intrusion of metagranites in the Late Proterozoic Canaveilles Group of the Pyrenees and the Montagne Noire (France): Bulletin de la Societe Geologique de France, v. 176, p. 269–282, doi:10.2113/176.3.269.

Cugerone, A., Cenki-Tok, B., Chauvet, A., Le Goff, E., Bailly, L., Alard, O., and Allard, M., 2018a, Relationships between the occurrence of accessory Ge-minerals and sphalerite in Variscan Pb-Zn deposits of the Bossost anticlinorium, French Pyrenean Axial Zone: Chemistry, microstructures and ore-deposit setting: Ore Geology Reviews, v. 95, p. 1–19, doi:10.1016/j.oregeorev.2018.02.016.

Cugerone, A., Oliot, E., Chauvet, A., Gavalda, J., and Le Goff, E., 2018b, Structural Control on the Formation of Pb-Zn Deposits: An Example from the Pyrenean Axial Zone: Minerals, v. 8, p. 1–20, doi:10.3390/min8110489.

Delvolvé, J.J., Souquet, P., Vachard, D., Perret, M.F., and Aguirre, P., 1993, Caractérisation d'un bassin d'avant-pays dans le Carbonifère des Pyrénées: faciès, chronologie de la tectonique synsédimentaire: Comptes Rendus Academie Science Paris, v. 316, p. 959–966.

Denèle, Y., Laumonier, B., Paquette, J.-L., Olivier, P., Gleizes, G., and Barbey, P., 2014, Timing of granite emplacement, crustal flow and gneiss dome formation in the Variscan segment of the Pyrenees: Geological Society, London, Special Publications, v. 405, p. 265–287, doi:10.1144/SP405.5.

Druguet, E., Castro, A., Chichorros, M., Pereira, M.F., and Fernandez, C., 2014, Zircon geochronology of intrusive rocks from Cap de Creus, Eastern Pyrenees: Geological Magazine, v. 151, p. 1095–1114, doi:10.1017/S0016756814000041.

Van den Eeckhout, B., and Zwart, H.J., 1988, Hercynian crustal-scale extensional shear zone in the Pyrenees: Geology, v. 16, p. 135–138, doi:10.1130/0091-7613(1988)016<0135:HCSESZ>2.3.CO;2.

Evans, N.G., Gleizes, G., Leblanc, D., and Bouchez, J.L., 1998, Syntectonic emplacement of the Maladeta granite (Pyrenees) deduced from relationships between Hercynian deformation and contact metamorphism: Journal of the Geological Society, v. 155, p. 209–216, doi:10.1144/gsjgs.155.1.0209.

Fallourd, S., Poujol, M., Boulvais, P., Paquette, J.L., de Saint Blanquat, M., and Rémy, P., 2014, In situ LA-ICP-MS U-Pb titanite dating of Na-Ca metasomatism in orogenic belts: The North Pyrenean example: International Journal of Earth Sciences, v. 103, p. 667–682, doi:10.1007/s00531-013-0978-1.

Fanlo, I., Touray, J.C., Subías, I., and Fernández-Nieto, C., 1998, Geochemical patterns of a sheared fluorite vein, Parzan, Spanish central Pyrenees: Mineralium Deposita, v. 33, p. 620–632, doi:10.1007/s001260050177.

Faure, M., Rossi, P., Gaché, J., Melleton, J., Frei, D., Li, X., and Lin, W., 2014, Variscan orogeny in Corsica: New structural and geochronological insights, and its place in the Variscan geodynamic framework: International Journal of Earth Sciences, v. 103, p. 1533–1551, doi:10.1007/s00531-014-1031-8.

Gasquet, D., Bertrand, J.M., Paquette, J.L., Lehmann, J., Ratzov, G., Ascenção De Guedes, R.A., Tiepolo, M., Boullier, A.M., Scaillet, S., and Nomade, S., 2010, Miocene to Messinian deformation and hydrothermal activity in a pre-Alpine basement massif of the French western Alps: New U-Th-Pb and argon ages from the Lauzière massif: Bulletin de la Societe Geologique de France, v. 181, p. 227–241, doi:10.2113/gssgfbull.181.3.227.

Gleizes, G., Crevon, G., Asrat, A., and Barbey, P., 2006, Structure, age and mode of emplacement of the Hercynian Bordères-Louron pluton (Central Pyrenees, France): International Journal of Earth Sciences, v. 95, p. 1039–1052, doi:10.1007/s00531-006-0088-4.

Golberg, J.M., and Leyreloup, A.F., 1990, High temperature-low pressure Cretaceous metamorphism related to crustal thinning (Eastern North Pyrenean Zone, France): Contributions to Mineralogy and Petrology, v. 104, p. 194–207, doi:10.1007/BF00306443.

Gonçalves, G.O. et al., 2016, An assessment of monazite from the Itambé pegmatite district for use as U-Pb isotope reference material for microanalysis and implications for the origin of the 'Moacyr' monazite: Chemical Geology, v. 424, p. 30–50, doi:10.1016/j.chemgeo.2015.12.019.

Grand'Homme, A., Janots, E., Seydoux-Guillaume, A.M., Guillaume, D., Bosse, V., and Magnin, V., 2016, Partial resetting of the U-Th-Pb systems in experimentally altered monazite: Nanoscale evidence of incomplete replacement: Geology, v. 44, p. 431–434, doi:10.1130/G37770.1.

Guitard, G., Geyssant, J., and Laumonier, B., 1984, Les plissements hercyniens tardifs dans le Paléozoïque inférieur du versant nord du Canigou. 1re partie: analyse géométrique et chronologie des phases superposees. Relations avec le granite de Mont-Louis et le métamorphisme régional: Géologie de la France, v. 4, p. 95–125.

Gutiérrez-Alonso, G., Fernández-Suárez, J., Jeffries, T.E., Johnston, S.T., Pastor-Galán, D., Murphy, J.B., Franco, M.P., and Gonzalo, J.C., 2011, Diachronous post-orogenic magmatism within a developing orocline in Iberia, European Variscides: Tectonics, v. 30, doi:10.1029/2010TC002845.

Gutiérrez-Alonso, G., Fernández-Suárez, J., López-Carmona, A., and Gärtner, A., 2018, Exhuming a cold case: The early granodiorites of the northwest Iberian Variscan belt-A Visean magmatic flare-up? Lithosphere, v. 10, p. 194–216, doi:10.1130/L706.1.

Harrison, T.M., Duncan, I., and McDougall, I., 1985, Diffusion of 40Ar in biotite: Temperature, pressure and compositional effects: Geochimica et Cosmochimica Acta, v. 49, p. 2461–2468, doi:10.1016/0016-7037(85)90246-7.

Hawkins, D.P., and Bowring, S.A., 1997, U-Pb systematics of monazite and xenotime: Case studies from the Paleoproterozoic of the Grand Canyon, Arizona: Contributions to Mineralogy and Petrology, v. 127, p. 87–103, doi:10.1007/s004100050267.

de Hoÿm de Marien, L., Le Bayon, B., Pitra, P., Van Den Driessche, J., Poujol, M., and Cagnard, F., 2019, Two-stage Variscan metamorphism in the Canigou massif: Evidence for crustal thickening in the Pyrenees: Journal of Metamorphic Geology, p. 1–26, doi:10.1111/jmg.12487.

Hurai, V., Paquette, J.-L., Huraiová, M., and Konečný, P., 2010, Age of deep crustal magmatic chambers in the intra-Carpathian back-arc basin inferred from LA-ICPMS U-Th-Pb dating of zircon and monazite from igneous xenoliths in alkali basalts: Journal of Volcanological and Geothermal Research, v. 198, p. 275–287.

Hurai, V., Paquette, J.L., Huraiová, M., and Sabol, M., 2012, U-Pb geochronology of zircons from fossiliferous sediments of the Hajnáčka i maar (Slovakia) type locality of the MN 16a biostratigraphic subzone: Geological Magazine, v. 149, p. 989–1000, doi:10.1017/S0016756812000106.

Jackson, S.E., Pearson, N.J., Griffin, W.L., and Belousova, E.A., 2004, The application of laser ablation-inductively coupled plasma-mass spectrometry to in situ U-Pb zircon geochronology: Chemical Geology, v. 211, p. 47–69, doi:10.1016/j.chemgeo.2004.06.017.

Jaffey, A.H., Flynn, K.F., Glendenin, L.E., Bentley, W.C., and Essling, A.M., 1971, Precision measurement of half-lives and specific activities of U235 and U238: Physical Review C, v. 4, p. 1889–1906, doi:10.1103/PhysRevC.4.1889.

Jastrzębski, M., Machowiak, K., Krzemińska, E., Lang Farmer, G., Larionov, A.N., Murtezi, M., Majka, J., Sergeev, S., Ripley, E.M., and Whitehouse, M., 2018, Geochronology, petrogenesis and geodynamic significance of the Visean igneous rocks in the Central Sudetes, northeastern Bohemian Massif: Lithos, v. 316–317, p. 385–405, doi:10.1016/j.lithos.2018.07.034.

Johnson, C.A., Cardellach, E., Tritlla, J., and Hanan, B.B., 1996a, Cierco Pb-Zn-Ag Vein Deposits: Isotopic and Fluid Inclusion Evidence for Formation during the Mesozoic Extension in the Pyrenees of Spain: Economic Geology, v. 91, p. 497–506, doi:10.5962/bhl.title.18736.

Johnson, C.A., Cardellach, E., Tritlla, J., and Hanan, B.B., 1996b, Cierco Pb-Zn-Ag Vein Deposits: Isotopic and Fluid Inclusion Evidence for Formation during the Mesozoic Extension in the Pyrenees of Spain: Economic Geology, v. 91, p. 497–506.

Kroner, U., and Romer, R.L., 2013, Two plates - Many subduction zones: The Variscan orogeny reconsidered: Gondwana Research, v. 24, p. 298–329, doi:10.1016/j.gr.2013.03.001.

Laurent, O., Couzinié, S., Zeh, A., Vanderhaeghe, O., Moyen, J.F., Villaros, A., Gardien, V., and Chelle-Michou, C., 2017, Protracted, coeval crust and mantle melting during Variscan late-orogenic evolution: U–Pb dating in the eastern French Massif Central: International Journal of Earth Sciences, v. 106, p. 421–451, doi:10.1007/s00531-016-1434-9.

Lemirre, B., Cochelin, B., Duchene, S., de Saint Blanquat, M., and Poujol, M., 2019, Origin and duration of late orogenic magmatism in the foreland of the Variscan belt (Lesponne — Chiroulet — Neouvielle area, French Pyrenees): Lithos, v. 336–337, p. 183–201, doi:10.1016/j.lithos.2019.03.037.

Lopez-Sanchez, M.A., Aleinikoff, J.N., Marcos, A., Martínez, F.J., and Llana-Fúnez, S., 2016, An example of low-Th/U zircon overgrowths of magmatic origin in a late orogenic variscan intrusion: The San Ciprián massif (NW Spain): Journal of the Geological Society, v. 173, p. 282–291, doi:10.1144/jgs2015-071.

Lopez-Sanchez, M.A., García-Sansegundo, J., and Martínez, F.J., 2018, The significance of early Permian and early Carboniferous U–Pb zircon ages in the Bossòst and Lys-Caillaouas granitoids (Pyrenean Axial Zone): Geological Journal, p. 1–16, doi:10.1002/gj.3283.

Ludwig, K.R., 2001, User's manual for Isoplot/Ex Version 2.49, a geochronological toolkit for Microsoft Excel: Berkeley Geochronological Center, Special Publication 1a, Berkeley, USA, p. 55p.

Marshall, B., and Gilligan, L.B., 1987, An introduction to remobilization: Information from ore-body geometry and experimental considerations: Ore Geology Reviews, v. 2, p. 87–131, doi:10.1016/0169-1368(87)90025-4.

Martín-Closas, C., Trias, S., and Casas, J.M., 2018, New palaeobotanical data from carboniferous culm deposits constrain the age of the variscan deformation in the eastern pyrenees: Geologica Acta, v. 16, p. 107–123, doi:10.1344/GeologicaActa2018.16.2.1.

Martín-gonzález, F. et al., 2019, Permian-Triassic Rifting Stage: In: The Geology of Iberia: A Geodynamic Approach, p. 29–112, doi:10.1007/978-3-030-11295-0.

Martinez Catalan, J.R., 2011, Are the oroclines of the Variscan belt related to late Variscan strike-slip tectonics? Terra Nova, v. 23, p. 241–247, doi:10.1111/j.1365-3121.2011.01005.x.

Matte, P., 2001, The Variscan collage and orogeny (480–290 Ma) and the tectonic definition of the Armorica microplate: a review - Matte - 2003 - Terra Nova - Wiley Online Library: Terra Nova, v. 13, p. 122–128, http://onlinelibrary.wiley.com/doi/10.1046/j.1365-3121.2001.00327.x/full%5Cnpapers2://publication/uuid/85445613-EAD8-49D7-AE4E-704E3D282C36.

Mezger, J.E., 2005, Comparison of the western Aston-Hospitalet and the Bossòst domes: Evidence for polymetamorphism and its implications for the Variscan tectonic evolution of the Axial Zone of the Pyrenees: Journal of the Virtual Explorer, v. 19, p. 1–19, doi:10.3809/jvirtex.2005.00122.

Mezger, J.E., and Gerdes, A., 2016, Early Variscan (Visean) granites in the core of central Pyrenean gneiss domes: Implications from laser ablation U-Pb and Th-Pb studies: Gondwana Research, v. 29, p. 181–198, doi:10.1016/j.gr.2014.11.010.

Mezger, J.E., and Passchier, C.W., 2003, Polymetamorphism and ductile deformation of staurolite–cordierite schist of the Bossòst dome: indication for Variscan extension in the Axial Zone of the central Pyrenees: Geological Magazine, v. 140, p. 595–612, doi:10.1017/S0016756803008112.

Mezger, J.E., and Régnier, J.L., 2016, Stable staurolite-cordierite assemblages in K-poor metapelitic schists in Aston and Hospitalet gneiss domes of the central Pyrenees (France, Andorra): Journal of Metamorphic Geology, v. 34, p. 167–190, doi:10.1111/jmg.12177.

Mezger, J.E., Schnapperelle, S., and Rölke, C., 2012, Evolution of the Central Pyrenean Mérens fault controlled by near collision of two gneiss domes: Hallesches Jahrbuch, v. 34, p. 11–29.

Munoz, M., Baron, S., Boucher, A., Béziat, D., and Salvi, S., 2015, Mesozoic vein-type Pb–Zn mineralization in the Pyrenees: Lead isotopic and fluid inclusion evidence from the Les Argentières and Lacore deposits: Comptes Rendus Geoscience, v. 348, p. 322–332, doi:10.1016/j.crte.2015.07.001.

Munoz, M., Boyce, A.J., Courjault-Rade, P., Fallick, A.E., and Tollon, F., 1994, Multi-stage fluid incursion in the Palaeozoic basement-hosted Saint-Salvy ore deposit (NW Montagne Noire, southern France): Applied Geochemistry, v. 9, p. 609–626, doi:10.1016/0883-2927(94)90022-1.

Nicol, N., 1997, Etude structurale des minéralisations Zn-Pb du Paléozoïque du dôme de Pierrefitte (Hautes-Pyrénées). Goniométrie de texture appliquée aux minéraux transparents et opaques: Ph.D Thesis Univ. Orléans, p. 318p.

Nicol, N., Legendre, O., and Charvet, J., 1997, Les minéralisations Zn-Pb de la série paléozoïque de Pierrefitte (Hautes-Pyrénées) dans la succession des évènements tectoniques hercyniens: C.R. Acad. Sci. Paris, v. 324, p. 453–460.

Oberc-Dziedzic, T., Kryza, R., and Pin, C., 2015, Variscan granitoids related to shear zones and faults: examples from the Central Sudetes (Bohemian Massif) and the Middle Odra Fault Zone: International Journal of Earth Sciences, v. 104, p. 1139–1166, doi:10.1007/s00531-015-1153-7.

Ostkamp, M., Schnapperelle, S., and Mertmann, D., 2019, Strukturgeologische Charakterisierung der Mérens Scher- und Störungszone bei Mérens-les-Vals (französische Pyrenäen): Hallesches Jahrbuch für Geowissenschaften, v. 42, p. 69–111.

Paquette, J.L., Gleizes, G., Leblanc, D., and Bouchez, J.L., 1997, Le granite de Bassies (Pyrénées): un pluton syntectonique d'âge westphalien. Géochronologie U– Pb sur zircons.: Compte Rendu Academie Science Paris, v. 324, p. 387–392.

Paquette, J.L., Piro, J.L., Devidal, J.L., Bosse, V., and Didier, A., 2014, Sensitivity enhancement in LA-ICP-MS by N2 addition to carrier gas: application to radiometric dating of U-Th- bearing minerals: Agilent ICP-MS Journal, v. 58, p. 4–5.

Paquette, J.L., and Tiepolo, M., 2007, High resolution (5 μm) U-Th-Pb isotope dating of monazite with excimer laser ablation (ELA)-ICPMS: Chemical Geology, v. 240, p. 222–237, doi:10.1016/j.chemgeo.2007.02.014.

Pouit, G., 1978, Différents Modeles de Mineralisations «Hydrothermale Sédimentaire », à Zn (Pb) du Paléozoïque des Pyrénees Centrales: Mineralium Deposita, v. 13, p. 411–421.

Pouit, G., 1985, Les minéralisations Zn (Pb) Ba du Paléozoïque des Pyrénées Centrales : Une mise au point et un compte rendu des missions 1984: Rapport BRGM, v. 85 DAM037, p. 72.

Pouit, G., and Bois, J.P., 1986, Arrens Zn (Pb), Ba Devonian deposit , Pyrénées , France : an exhalative-sedimentary-type deposit similar to Meggen: Mineralium deposita, v. 21, p. 181–189.

Poujol, M., Pitra, P., Van Den Driessche, J., Tartèse, R., Ruffet, G., Paquette, J.L., and Poilvet, J.C., 2017, Two-stage partial melting during the Variscan extensional tectonics (Montagne Noire, France): International Journal of Earth Sciences, v. 106, p. 477–500, doi:10.1007/s00531-016-1369-1.

Pujals, I., 1992, Las mineralizaciones de sulfuros en el Cambro-Ordovicico de la Val d'Aran (Pirineo Central, Lérida): Ph.D Thesis, Univ. Autónoma Barcelona, p. 294p.

Renne, P.R., Swisher, C.C., Deino, A.L., Karner, D.B., Owens, T.L., and DePaolo, D.J., 1998, Intercalibration of standards, absolute ages and uncertainties in 40Ar/39Ar dating': Chemical Geology, v. 145, p. 117–152, doi:10.1016/s0009-2541(98)00047-3.

Reyx, J., 1973a, Relations entre tectonique, métamorphisme de contact et concentrations metalliques dans le secteur des anciennes mines d'Arre et Anglas (Hautes-Pyrénées - Pyrénées atlantiques): Ph. D Thesis, Univ. Paris VI, p. 83p.

Reyx, J., 1973b, Relations entre tectonique, métamorphisme de contact et concentrations metalliques dans le secteur des anciennes mines d'Arre et Anglas (Hautes-Pyrénées - Pyrénées atlantiques): Ph. D Thesis, Univ. Paris VI, p. 83p.

Roberts, M.P., Pin, C., Clemens, J.D., and Paquette, J.L., 2000, Petrogenesis of Mafic to Felsic Plutonic Rock Associations: the Calc-alkaline Querigut Complex, French Pyrenees: Journal of Petrology, v. 41, p. 809–844, doi:10.1093/petrology/41.6.809.

Roig, J.Y., Faure, M., and Ledru, P., 1996, Polyphase wrench tectonics in the southern french Massif Central: Kinematic inferences from pre- And syntectonic granitoids: International Journal of Earth Sciences, v. 85, p. 138–153.

Schaltegger, U., 1997, Magma pulses in the central Variscan belt: episodic melt generation and emplacement during lithospheric thinning: Terra Nova, v. 9, p. 242–245, doi:10.1111/j.1365-3121.1997.tb00021.x.

Seydoux-Guillaume, A.M., Montel, J.M., Bingen, B., Bosse, V., de Parseval, P., Paquette, J.L., Janots, E., and Wirth, R., 2012, Low-temperature alteration of monazite: Fluid mediated coupled dissolution-precipitation, irradiation

damage, and disturbance of the U-Pb and Th-Pb chronometers: Chemical Geology, v. 330–331, p. 140–158, doi:10.1016/j.chemgeo.2012.07.031.

Seydoux-Guillaume, A.M., Paquette, J.L., Wiedenbeck, M., Montel, J.M., and Heinrich, W., 2002, Experimental resetting of the U-Th-Pb systems in monazite: Chemical Geology, v. 191, p. 165–181, doi:10.1016/S0009-2541(02)00155-9.

Siemes, H., and Borges, B., 1979, Experimental deformation of sphalerite single crystals under confining pressures of 3000 and 5000 bars at temperatures between 25°C and 450°C.: N. Jb. Miner. Abb., v. 134, p. 288–304.

De Sitter, L.U., and Zwart, H.J., 1960, Tectonic development in supra and infra-structures of a mountain chain: Proceedings 21st International Geological Congress, Copenhagen, v. 18, p. 248–256.

Soula, J.C., Debat, P., Deramond, J., and Pouget, P., 1986, The Geological Evolution of the Pyrenees A dynamic model of the structural evolution of the Hercynian Pyrenees: Tectonophysics, v. 129, p. 29–51, doi:10.1016/0040-1951(86)90244-1.

Stampfii, G.M., von Raumer, J.F., and Borel, G.D., 2007, Paleozoic evolution of pre-Variscan terranes: From Gondwana to the Variscan collision: Special Paper 364: Variscan-Appalachian dynamics: The building of the late Paleozoic basement, p. 263–280, doi:10.1130/0-8137-2364-7.263.

Stampfli, G.M., Hochard, C., Vérard, C., Wilhem, C., and vonRaumer, J., 2013, The formation of Pangea: Tectonophysics, v. 593, p. 1–19, doi:10.1016/j.tecto.2013.02.037.

Steiger, R.H., and Jäger, E., 1977, Submission on Geochronology: Convention on the use of decay constants in geo- and cosmochronology: Earth and Planetary Science Letters, v. 36, p. 359–362.

Subias, I., Fanlo, I., Yuste, A., and Fernandez-Nieto, C., 1999, The Yenefrito Pb-Zn mine (Spanish Central Pyrenees): an example of superimposed metallogenetic events: Mineralium Deposita, v. 34, p. 220–223.

Tomascak, P.B., Krogstad, E.J., and Walker, R.J., 1996, U-Pb Monazite Geochronology of Granitic Rocks from Maine: Implications for Late Paleozoic Tectonics in the Northern Appalachians: The Journal of Geology, v. 104, p. 185–195, doi:10.1086/629813.

Vergés, J., Fernàndez, M., and Martìnez, A., 2002, The Pyrenean orogen: Pre-, syn-, and post-collisional evolution: Journal of the Virtual Explorer, v. 8, p. 1–20, doi:10.3809/jvirtex.2002.00058.

Wiedenbeck, M., Allé, P., Corfu, F., Griffin, W.L., Meier, M., Oberli, F., Von Quadt, A., Roddick, J.C., and Spiegel, W., 1995, Three natural zircon standards for U-Th-Pb, Lu-Hf, trace element and REE analyses.: Geostandards Newsletters, v. 19, p. 1–23, doi:10.1111/j.1751-908X.1995.tb00147.x.

Zwart, H.J., 1979, The Geology of the Central Pyrenees: Leidse Geologische Mededelingen, v. 50, p. 1–74

7 Plastic deformation of naturally deformed sphalerite

This section is devoted to the article in preparation "Plastic deformation of naturally deformed sphalerite" planned to be submitted in American Mineralogy. This article is a preliminary and recent version that I have written. It presents an EBSD (electron backscaterred diffraction) analyses of the deformed and metamorphosed sphalerite textures occuring in the Pyrenean sphalerite in comparison with the macroscopically non-deformed sphalerite from Saint-Salvy, Montagne Noire. This article describes the deformation mechanisms linked to plastic deformation such as sub-grain rotation (SGR) responsible of the significant textural heterogeneity of the Pyrenean vein sphalerite (Type 2b). In addition, the study of the metamorphosed Type 2a sphalerite is presented with typical annealing textures and limited internal deformation, related to static recristallization. Trace element analyses with LIBS mapping (laser-induced breakdown spectroscopy) coupled to EBSD maps are performed on Pale Bidau sphalerite and at grain scale on Arre sphalerite to decipher the impact of recrystallization and dislocation on rare metals such as Ge.

7.1 ARTICLE – Plastic deformation of naturally deformed sphalerite

Alexandre Cugerone[1], Emilien Oliot[1], Bénédicte Cenki-Tok[1,2], Manuel Munoz[1], Fabrice Barou[1], Vincent Motto-Ros[3]

[1]Géosciences Montpellier, Université de Montpellier, France ; *alexandre.cugerone@umontpellier.fr*; *benedicte.cenki-tok@umontpellier.fr*; *emilien.oliot@umontpellier.fr; manuel.munoz@umontpellier.fr; fabrice.barou@umontpellier.fr.*

[2]Earthbyte Research Group, School of Geosciences, University of Sydney, Australia

[3]Institut Lumière Matière Université Lyon 1, France ; *vincent.motto-ros@univ-lyon1.fr*

Keywords: Sphalerite; EBSD; plastic deformation; trace element; remobilization

7.1.1 Abstract

Base metal sulfide such as sphalerite (ZnS) are widespread in numerous deposit-types which have endured deformation/metamorphism processes. But sphalerite deformation process is poorly studied in the literature even though it may have an impact on the global deformation of the deposit and on the spatial organization of rare metal, which are often hosted in sphalerite lattice. Herein, we studied the impact of natural deformation and metamorphism on sphalerite of Pb-Zn deposits from the Pyrenean Axial Zone in comparison with a non-deformed sphalerite from Saint-Salvy deposit (Montagne Noire). Pyrenean vein sphalerite deforms plastically by disclocation creep and dynamically recovers by subgrain rotation (SGR) in Arre (AR) and Anglas (AG) deposit. Pale Bidau (PB) sample is more complex with presence of SGR and bulging (BLG) recrystallization. Pyrenean metamorphosed sphalerite from Bentaillou (BT) deposit exhibits annealing texture which is clean of internal dislocations unlike macroscopically non-deformed sphalerite grains from Saint-Salvy which preserve some internal dislocations. The presence of internal dislocations in sphalerite can induce a loss of trace elements (Ge, Cu, Ga) from the sphalerite lattice and seem to be a key process for the neoformation of accessory minerals. Furthermore, sphalerite dynamic recrystallization preferentially occurs in trace-element-rich banded sphalerite.

7.1.2 Introduction

Sphalerite (ZnS) is a common base metal sulfide and is often associated with sulfides like galena (PbS) or pyrite (FeS). It exhibits frequent metamorphosed and/or deformed textures associated to sulfide ore remobilization (Gilligan and Marshall 1987; Plimer 1987; McClay 1991; Craig and Vokes 1992; Pesquera and Velasco 1993; Bodon 1998b; Wagner and Cook 1998; Craig 2001). But plastic deformation mechanisms of sphalerite is poorly documented *(Siemes et al. 1991)* and observation of the precise texture is often difficult without etching, especially in pure sphalerite.

Some old experimental studies are present in the literature such as *Siemes et al., (1973)* who shows the operation of translation gliding and twin gliding parallel to {111}. *Couderc et al. (1985)* describe the development of significant slip bands along {111} planes and the appearancen of deformation twinning during axial compression between 450 to 600°C. Some other experimental studies exist in the literature *(Stanton and Gorman 1968; Gill 1969; Clark and Kelly 1973; Siemes and Borges 1979; Siemes and Hennig-Michaeli 1985)* which determine relative low temperature (<400°C) conditions to anneal this material, demonstrating the relative softness of this mineral.

Deciphering the precise type of texture and the mode of deformation and recrystallization in sphalerite is notably relevant due to numerous chemical elements of interest being hosted in the crystal lattice (Ge, Ga, In, Cd) in substitution with zinc cations *(Viets et al. 1992; Cook et al. 2009b; Belissont et al. 2014; Frenzel et al. 2016; Bauer et al. 2018; Cugerone et al. 2018a)*.

Impact of recrystallization on trace element content in sulfide is described in gold systems with host-minerals like pyrite or arsenopyrite *(Wagner et al. 2007; Cook et al. 2009a; Dubosq et al. 2018)* but only few investigations exist for trace-element hosted in deformed sphalerite *(Lockington et al. 2014; George et al. 2016)*. These elements may be redistributed associated to recristallization (e.g. Ge; *Cugerone et al. 2019*).

In this study, we present a detailed microstructural study of several sphalerite samples hosted in Variscan basements from Montagne-Noire and Pyrenees. The study will display sphalerite with different deformational/metamorphic imprints, from non-deformed to completely annealed. An additional chemical study is performed to investigate the relation between microstructures and trace element chemistry in sphalerite lattice. Microstructural study is performed with EBSD (electron back-scattered diffraction) coupled to chemical mapping (LIBS mapping).

7.1.3 Tectonometamorphic setting

Variscan-deformed basement from the French Massif-Central – Les Cevennes and the Pyrenees (Figure 95A) host numerous Pb-Zn deposits with different origins, textures and chemistries.

Five samples from three mineralization types are examined in this study. The first was collected in Saint-Salvy (SA), Montagne Noire (Figure 95B) and the others were taken within the Pyrenean Axial zone (PAZ), in Bentaillou (BT), Arre (AR), Pale Bidau (PB) and Anglas (AG) deposits (Figure 95B).

The SA deposit is hosted in Cambrian black schist and is composed of several mineralization types described from syngenetic primary mineralization to skarn and vein epigenetic mineralizations *(Cassard et al. 1993; Munoz et al. 1994)*. The discussed sample was collected in the mine and belongs to the M4 economic decametric vein mineralization type *(Barbanson and Geldron 1983; Cassard et al. 1993; Munoz et al. 1994)* which exhibits cockade breccia with clasts of schist filled with siderite, quartz and sphalerite essentially. This mineralization event is probably associated to the Lias-Dogger transition during an extensive strike-slip regime (*Munoz et al., 1994*) and has not endured any further deformation event syn or post-mineralization.

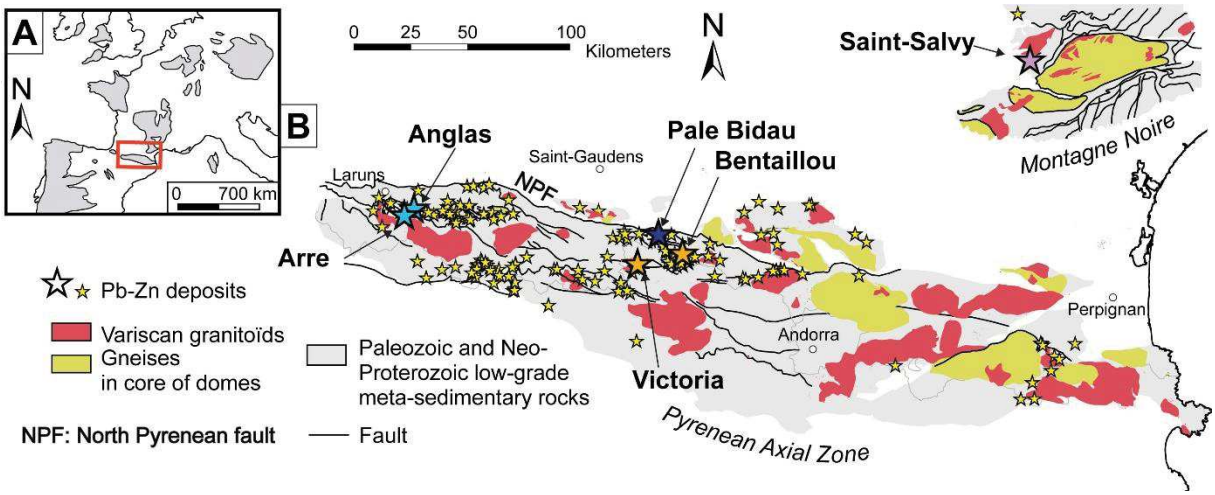

Figure 95. A Location of the Pyrenean Axial Zone and Montagne Noire in the Variscan belt of Western Europe. B Lithological and structural map of the Pyrenean Axial Zone and Montagne Noire with location of Pb-Zn deposits (BRGM and IGME databases). The five studied deposits are reported in bold.

Pyrenean deposits are hosted in the Pyrenean Axial Zone (PAZ) basement intensly deformed during Variscan orogeny *(Zwart 1963b; Denèle et al. 2014; Mezger and Gerdes 2016; Cochelin et al. 2017a)* and exhumed during Pyrenean-Alpine orogeny during the Paleogene. Three major deformation events are documented in the PAZ (D_1 to D_3) associated to two metamorphism events (regional M_1 and contact M_2 metamorphisms). Bentaillou (BT) and Pale Bidau (PB) deposits belong to the Bosssot Cambro-Devonian anticlinorium, which host a large number of Pb-Zn deposits in the PAZ (*Cugerone et al., 2018b*). Arre (AR) and Anglas (AG) deposits are located at the west of the Pyrenean Axial Zone, close to the Pierrefitte anticlinorium. The four studied deposits are hosted in various rocks (*Cugerone et al. 2018b*) from Cambrian marble (BT) to Late-Ordovician calc-schist (PB), and Devonian schist (AG) or calc-schist (AR). Two main mineralization types exist in the PAZ:

- Variscan stratabound epigenetic mineralization, named Type 2a in the Pyrenees *(Cugerone et al. 2018b)* appear in BT deposit. The mineralization is mostly parallel to S_0-S_1 and is hosted in pluri metric pull-apart structures. The sphalerite ore has endured green-schist regional M_1 metamorphism (<400°C) with muscovite intimately associated to sphalerite.
- Vein mineralization, named Type 2b in the Pyrenees is found in Arre (AR), Anglas (AG) and Pale Bidau (PB) deposits (Figure 95). The AR and AG deposits are at the westernmost part of the PAZ, close to Pierrefitte anticlinorium These dm to m vein mineralizations appear vertical and parallel to the N090-110°E S_2 Variscan cleavage. They have endured plastic deformation at low grade (<400°C) and recrystallization parallel to a cleavage parallel to S_2 (*Cugerone et al. 2019*). Sphalerite lattice is enriched in diverse elements such as Ge, Cu, and Ga with highly heterogeneous content due to remobilization by the sphalerite recrystallization and probable fluid circulation.

7.1.4 Sampling and methods

Ore samples from the Pyrenees were collected *in situ* in underground galleries, or in outcrop. Sample from the SA deposit was taken in the main mineralization zone (M4 veins) and is part of M. Munoz collection (*Munoz et al. 1994*).

Sample preparation for Electron-BackScattered Diffraction (EBSD) analyses requires an accurate polishing so that sphalerite structure can be efficiently indexed. To remove surface defects, thin section polishing was first performed with diamond polisher at four different granulometric steps (6, 3, 1 and 0.25 μm). A last step of polishing was performed using a Vibromet polisher with 150 grams of pressure on a polyurethane layer with colloidal silica. During this process, cleaning with frozen colloidal silica was necessary to avoid scratches on sphalerite.

Electron-BackScattered Diffraction (EBSD) maps were performed with a Camscan Crystal Probe X500FE SEM-EBSD at Geosciences Montpellier (CNRS-University of Montpellier, France). Condition of acquisition were 20 keV for the voltage and 5 nA for the probe current with a working distance of 25 mm under 2 Pa low vacuum. Samples surface were positioned horizontally at 20° to the incident electron beam to improve the collection of the backscattered electrons. EDS maps were acquired simultaneously with electron backscatter pattern data. The measurement steps were systematically below 5 μm, with 0.5 μm for the lowest measurement step. Oxford Instruments Aztec and Channel 5 softwares were used to generate EDS and EBSD grain size maps.

Laser-induced breakdown spectroscopy (LIBS)-based imaging was used to map the distribution of Ge, Cu, Ga. It is an all-optical analytical technique, allowing the mapping of metallic elements in various type of minerals at a micrometric spatial resolution with a sensitivity at the ppm level (Sancey et al. 2014; Cáceres et al. 2017; Fabre et al. 2018). During the analysis, the sample surface is scanned, in a pixel-by-pixel manner to induce the breakdown and sparks of the material. The light radiation emitted by the plasma is then collected by an optical system and analyzed using a spectrometer. The sample was analyzed using Nd:YAG laser with a pulse energy of about 600 μJ operating at 100 Hz, and a lateral resolution (i.e. distance between two consecutive laser shots) of 13 μm. The spectrometer was configured in the spectral range 250-330 nm in order to detect intense lines of Ge (265.1 nm), Cu (324.7 nm) and Ga (294.4 nm), among others.

7.1.5 Macroscopic sample study

Important textural differences appear in the three sphalerite mineralizations even at microscopic scale. Saint Salvy sphalerite seals typical cockade breccia formed by siderite and quartz around clast of schist. This sphalerite exhibits mm grain size with apparition of rhythmic bands and local sector zonings (Figure 96A) previously described by *Belissont et al. (2014)* and no apparent deformation. Sphalerite represents 70 vol.% of the total sample.

Pyrenean Pb-Zn vein mineralization is composed essentially of sphalerite with proportions varying from 60-70 vol.% in AR and AG (Figure 96B and C) to 90 vol.% in PB (Figure 96D). Zinc sulfide hosted in a brecciated schist can be associated to galena, pyrite, chalcopyrite for sulfide, and quartz, calcite or rarely baryte for the gangue minerals (Figure 96B). Light to dark sphalerite mineralizations (Figure 96B and C) shows a well-preserved deformation imprint with observed textural heterogeneities aligned with S_2 Variscan cleavage. Coarse sphalerite crystals with a dark-brown color are surrounded by a matrix of pluri-μm light brownish grains.

Pyrenean stratabound mineralization is largely dominated by sphalerite with a dark brown color. Sphalerite crystals shows a different macroscopic texture with coarse millimetric to centimetric xenomorph crystals (Figure 96E), homogeneously distributed and associated to a gangue of calcite, ilmenite and rarely quartz.

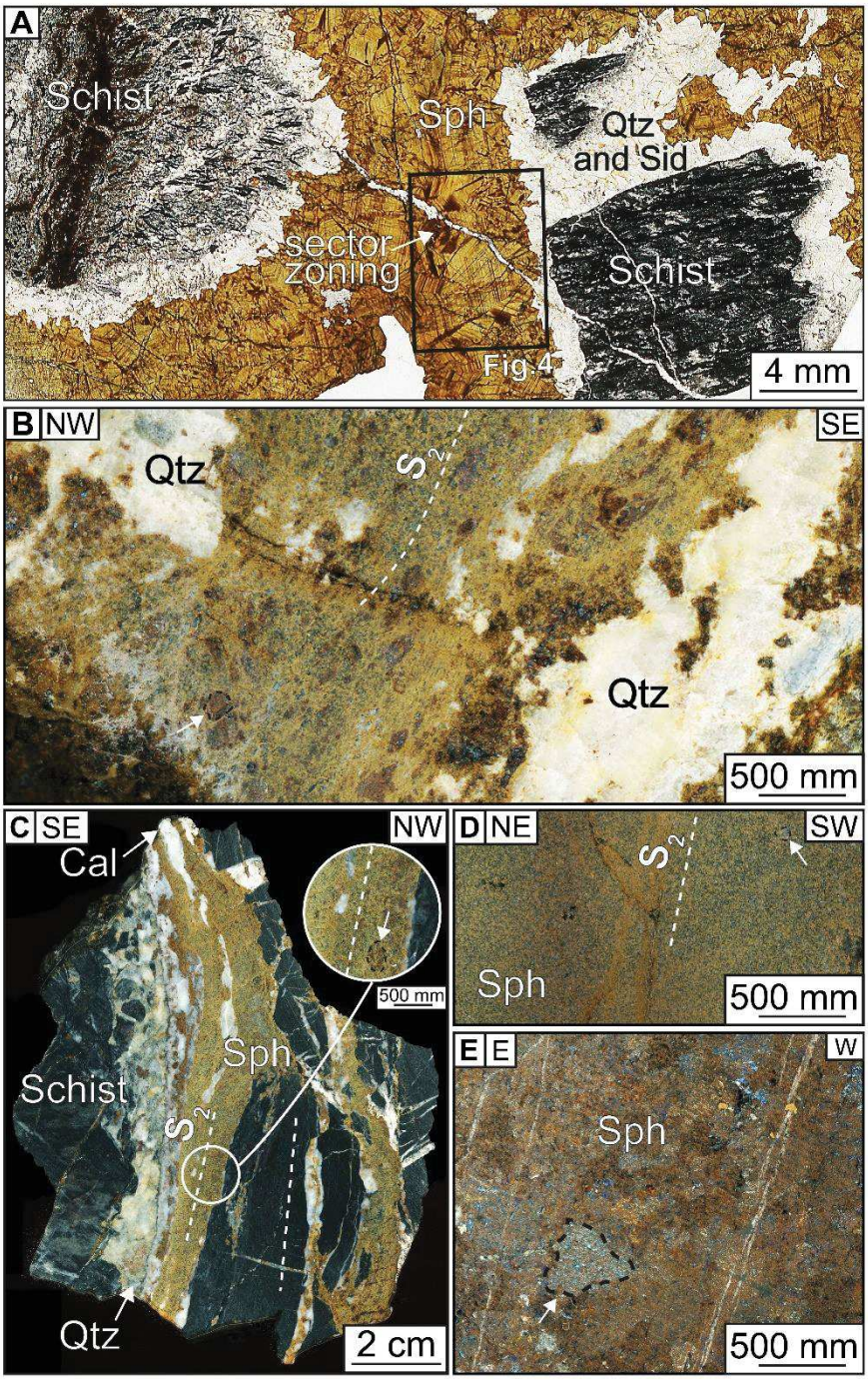

Figure 96. Samples photographs and scan of the studied deposits. A Saint Salvy (SA) mineralization (thin section scan). B Arre (AR) sample with presence of superimposed S_2 cleavage in sphalerite mineralization. Dark brown coarse mm grains are visible and noted with a white arrow. C Anglas (AG) sample with a brecciated schist which host sphalerite mineralization associated to calcite and quartz. Note the presence of dark brown color in the mainly light brown sphalerite (white arrow) and represents coarse mm grains. D Pale Bidau (PB) quasi pure sphalerite sample. E Bentaillou (BT) sample with presence of dark reddish coarse mm grains.

7.1.6 Microstructural study

Grain size and quantitative deformation analysis of all the analyzed samples is present in Figure 97A and B. Grain orientation spread (GOS) is a measure of the intragranular lattice distortion *(Cross et al. 2017)* and is represented in the Figure 97B. It is a good indication of the deformation level between the different sphalerite samples and a way to discrimine recrystallized and ductily deformed parent crystals (*Allain-Bonasso et al. 2012; Hadadzadeh et al. 2018*). A threshold is positioned at 5° (knee of the three curves in the Figure 97B). A sphalerite crystal with a weak GOS (<5°) is assumed to be recrystallized whereas a crystal with a stronger GOS (>5°) is considered parent. This measurement is highly dependent of parameter like grain boundary limit which is fixed at 20° of misorientation after careful observation of grain and sub-grain boundaries.

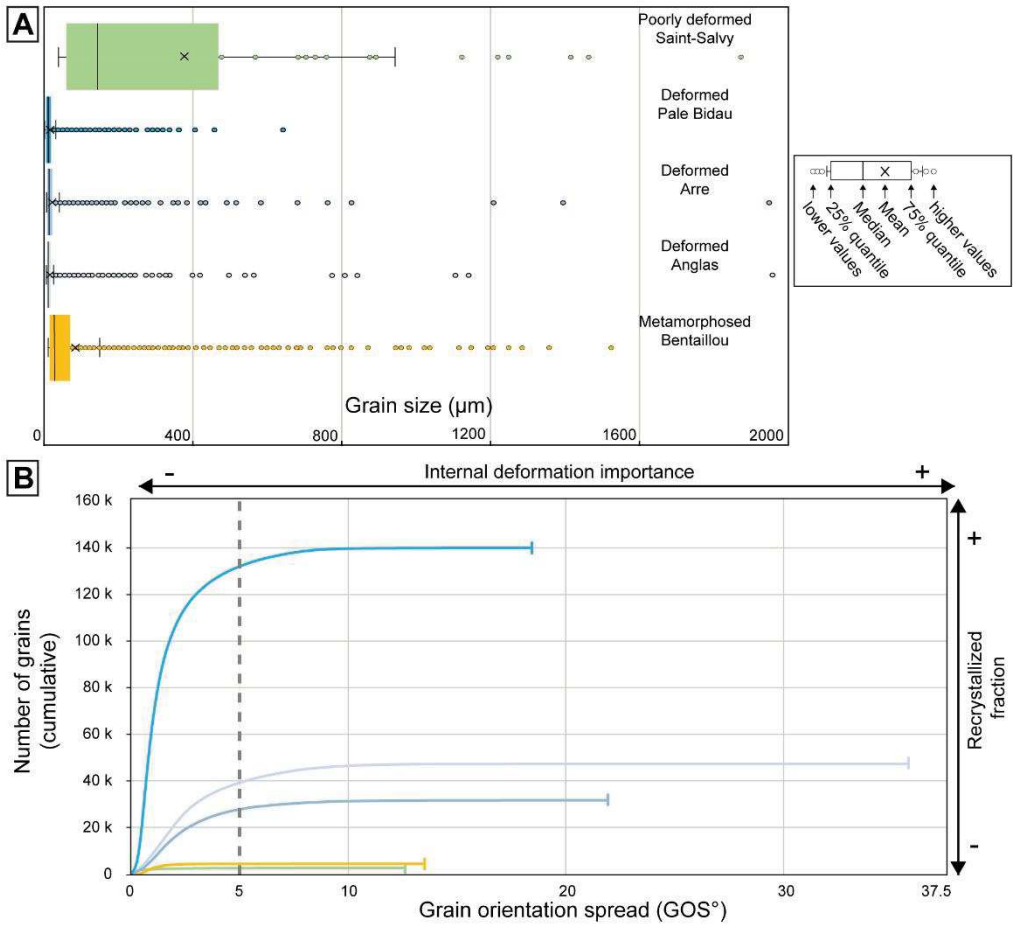

Figure 97. A Box plot of grain size for all sphalerite samples (grain > 20° misorientation angle with consideration of twin boundaries (55-60°). B Cumulative plot of the number of grain compared to the grain orientation spread (GOS).

The results are presented in order of increasing deformation, from poorly to highly deformed, and finally metamorphosed. The following figures present zoom in several areas and complete map data can be found in supplementary data (section 11.11).

7.1.6.1 Non-deformed sphalerite vein (Saint-Salvy deposit)

Figure 98A shows a sphalerite thin section observed in transmitted light with a superimposed grain boundary map. Chemical zonations like sector zoning or rhythmic bands are visible and limited by grain boundaries. Saint-Salvy sphalerite crystals averages 375 μm with a presence of coarse grains up to 3.2 mm. No grain is below 25 μm, and the relative frequency of grain superior to 100 μm reaches 64 % (Figure 97A). Grain boundaries are often straight or slightly curved, and cross-cut rhythmic banding. Sector zoning is restricted to the boundary of some crystals, and no preferential orientation is reported in these specific grains. Low angle (2-5°) misorientations are generally rare and restricted to grain boundary or close to the numerous {111} twins (Figure 98B and C). Two types of twin shapes with misorientations between 55° and 60° are observed. The first type has a straight shape with regular gap between them. A second type is commonly twisting, with numerous twin intersections. The thickness of the twins is variable, from few μm to hundreds μm. An Euler map combined with grain boundaries (Figure 98D) and exhibits poor color variation inside each grain., coherent with the low GOS value (i.e. 12.6°; Figure 97B) even if some lattice distortion is present in the pole figures performed in one grain (Figure 98E). Figure 98F represents scatter and contoured one point per grain pole figures. It shows CPO developments on <110> and on <111>.

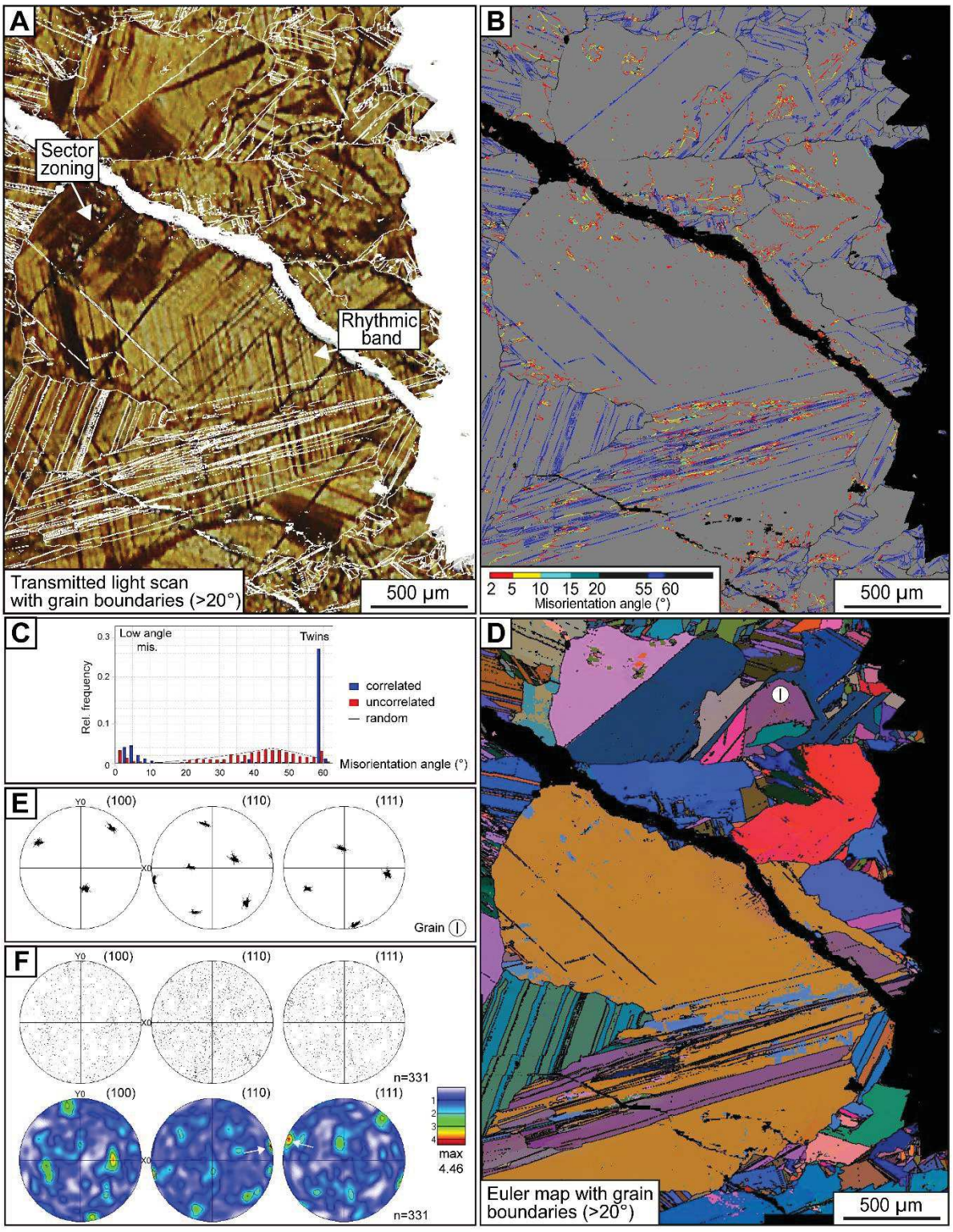

Figure 98 Saint-Salvy (SA, M4 type) sample (step of measurement: 5.7 µm). A Sphalerite observed in transmitted plane polarized light with a superimposed EBSD grain boundary map (> 20° misorientation map). B EBSD misorientation boundary map in sphalerite C Misorientation angle distribution in sphalerite grains (>2°misorientation boundary). D. EBSD Euler map with grain boundaries (>20°) superimposed. E. Pole figure for the grain I (represented in D). F Pole figure plots for one point per sphalerite grain for the entire map (upper hemisphere).

7.1.6.2 Deformed sphalerite veins (Pyrenean deposit)

7.1.6.2.1 Deformed pure sphalerite

Figure 99A exhibits sphalerite deformed in three different domains (a), (b) and (c) vertically organized. Domain (a) is composed of coarse grains (>100 μm) with frequent curved or lobate grain boundaries (Figure 99B) and few small grains (<10 μm). Low misorientations (2° to 15°) are poorly expressed (Figure 99C) but more developed in coarser grains (Figure 99B, see inset below). Long axis slope represents the preferential direction of elongation of the crystal shape according to the horizontal direction and is shown in a rose diagram in Figure 99D. Most of the sphalerite grain shapes are oriented vertically (90° from the horizontal direction), parallel to S_2 cleavage.

In the domain (a), twins appear slightly ondulated but regularly spaced in the whole grain. Some twins are larger close to grain boundary and disappear in the center of the crystal, which correspond to "deformation twins" (Figure 99B) Small variations in intra-grain orientation are observed in the Figure 99A. Misorientation profile in Figure 99E located in a coarse grain shows a maximum cumulative misorientation variation of about 8°. Pole figure in two different grains (I and II) display a rotation of the crystal lattice on (111) direction with cumulative orientation of about 10-15° (Figure 99F).

Domain (b) is essentially composed of small grains (<25 μm) with rounded habit. Twins are broadly present and are essentially straight and cross the entire crystal. Very few amounts of low misorientation (2-5°) appear compared to domain (a) (Figure 99B inset). Presence of rare low misorientations (2-5°) in the few coarse grains (>100 μm) are also noted in the domain (c), which represent a domain less deformed than domain (b).

Figure 99G presents scatter and contoured one point per grain pole figures comparing between grains superior and inferior to 50 μm in all the map. No preferential crystallographic orientation appears in the grain inferior to 50 μm. Coarse grains superior to 50 μm are fewer but a small crystallographic orientation is present in (110) and probably in (100).

7.1.6.2.2 Deformed sphalerite associated to quartz

Sphalerite from AR deposit (80 vol.%) is essentially composed of recrystallized pluri-μm grains which mantled parent mm crystals. Parent grains are elongated along S_2 cleavage (Figure 100A) and are poorly twinned even if some curved deformation twins are confined at some grain boundaries (Figure 100B). Regular and straight twins are numerous and are more abundant in

relative frequency than low angle misorientation boundaries (Figure 100C). Low misorientation boundaries from 2° to 10° is relatively frequent (Figure 100C) but less abundant than twin boundaries.

To better visualize the deformational imprint in the parent grains, a texture component map is shown on two grains in the Figure 100D. Expression of the crystallographic deformation appear with the formation of numerous deformation lamellae associated to low angle boundaries (<20°), essentially perpendicular and rarely parallel to S_2 cleavage (Figure 100D). Deformation lamellae are not present in the entire grain and are organized in deformation bands Cumulative misorientation of the deformation lamellae is variable and can reach locally 26° (Figure 100E).

A zoom on two areas and at grain scale acquired with a high resolution EBSD map is shown in Figure 101. Textural component and misorientation boundary maps illustrate the deformed textures. Grain 1 shows variation of crystallographic orientation represented by changes of color in the textural component map Figure 101A. Misorientation boundary map shows the presence of numerous low angle boundaries (2-5°) arranged in multiple polygonal shapes or chessboard texture in the external part of the grain 1 Figure 101B. Some 5-15° misorientation boundaries appear and are associated to the low angle boundaries (2-5°).

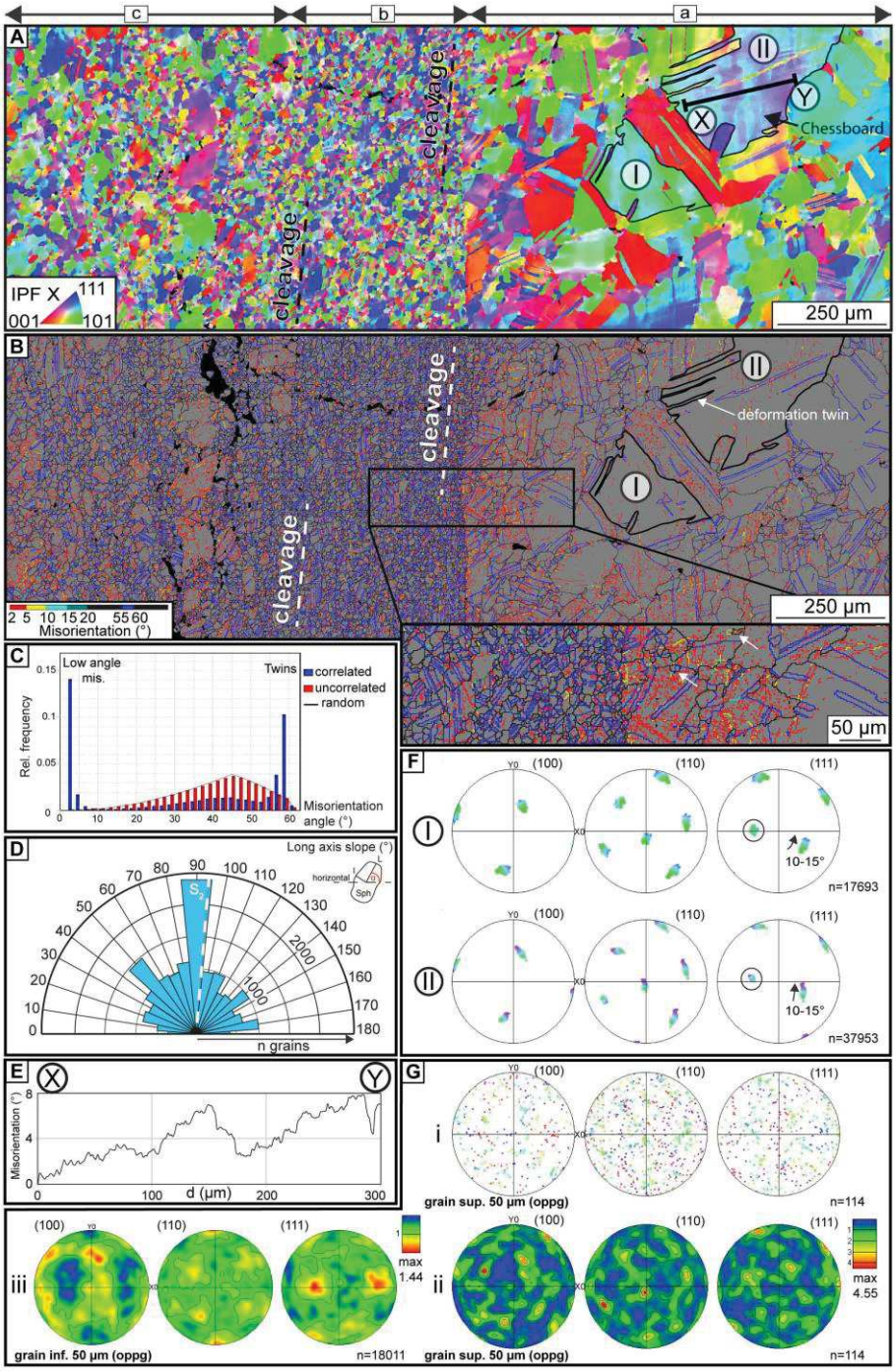

Figure 99. Pale Bidau (PB) sample (step of measurement: 1.5 µm). A EBSD inverse pole figure map plotted according to the X axis. B EBSD misorientation boundary map. Note the small inset below which is a zoom of a selected area. C Misorientation angle distribution in sphalerite grains (>2°misorientation boundary). D Rose diagram which represent direction for all the sphalerite grains, the angle between the grain long axis and the horizontal (long axis slope). E Misorientation profile relative to the first point. The position of the profile is noted in the Figure 5A. F Pole figure plots for two selected grains I and II. Their position is represented in the A and B. Color variation are the same as in Figure 5A. G Pole figures plots for one point per sphalerite grains. Grains inferior to 50 µm are selected for the pole figure at the left with contours, and grains superior to 50 µm are represented in the two pole figures at the right, with points and contours.

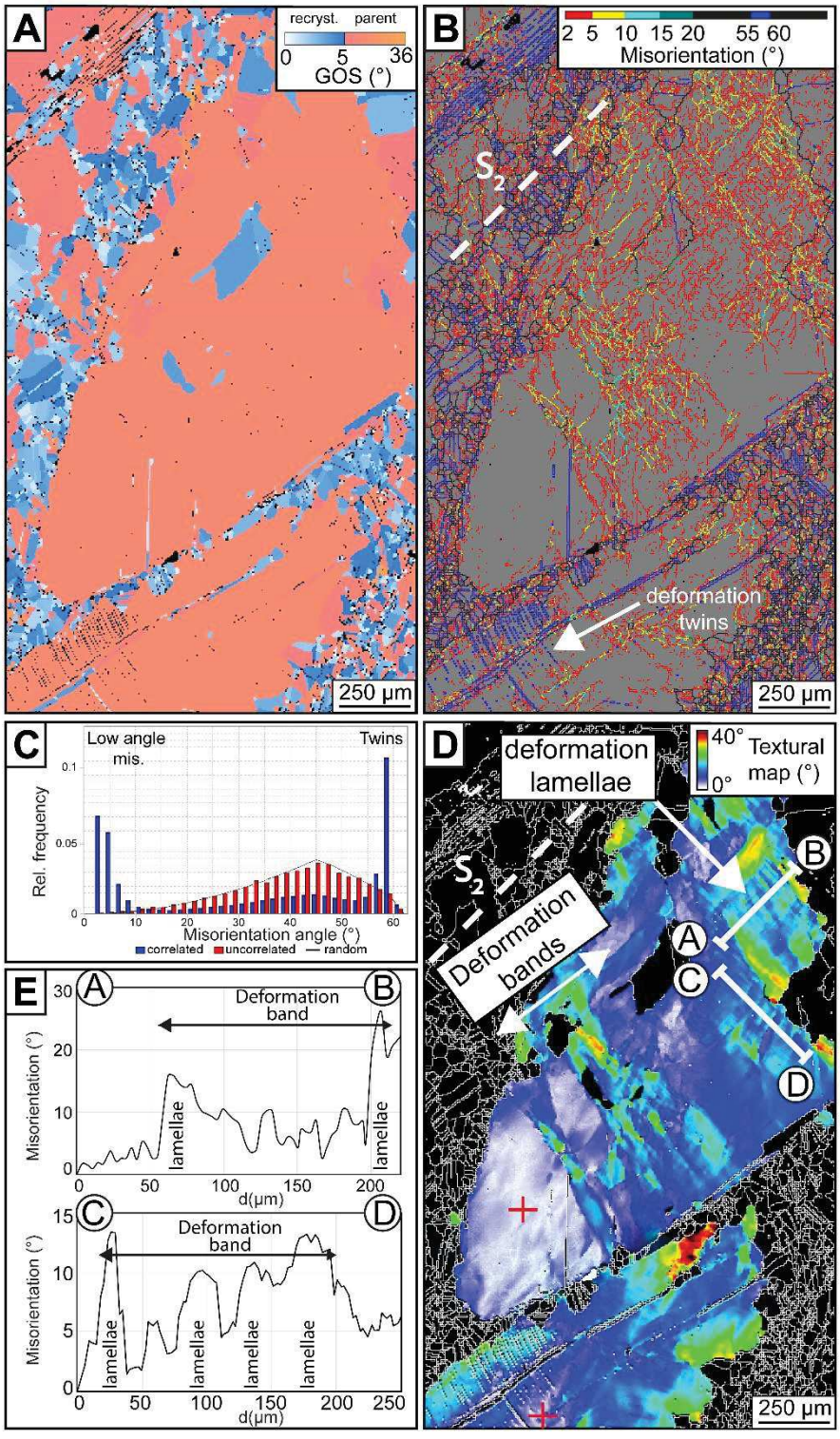

Figure 100. Arre (AR) sample (step of measurement: 2.5 µm). A EBSD GOS separated recrystallized and parent grains map. The threshold is fixed at 5° according to Figure 97. B EBSD misorientation boundary map C Misorientation angle distribution in the sphalerite grains (>2° misorientation boundary). D EBSD textural component map for two selected sphalerite parent crystals. The variation in crystal lattice orientation from the red cross is fixed between 0 and 40°. E Misorientation profiles relative to the first point. The positions of the profile are noted in D.

Grain 2 exhibits an advanced stage of deformation. Low angle boundaries are everywhere in the grain and show a well-formed chessboard texture (Figure 101C and D)., Some 5° to 20°angle boundaries are situated close to grain boundary, especially on the right of the grain where a higher strain area is observed.

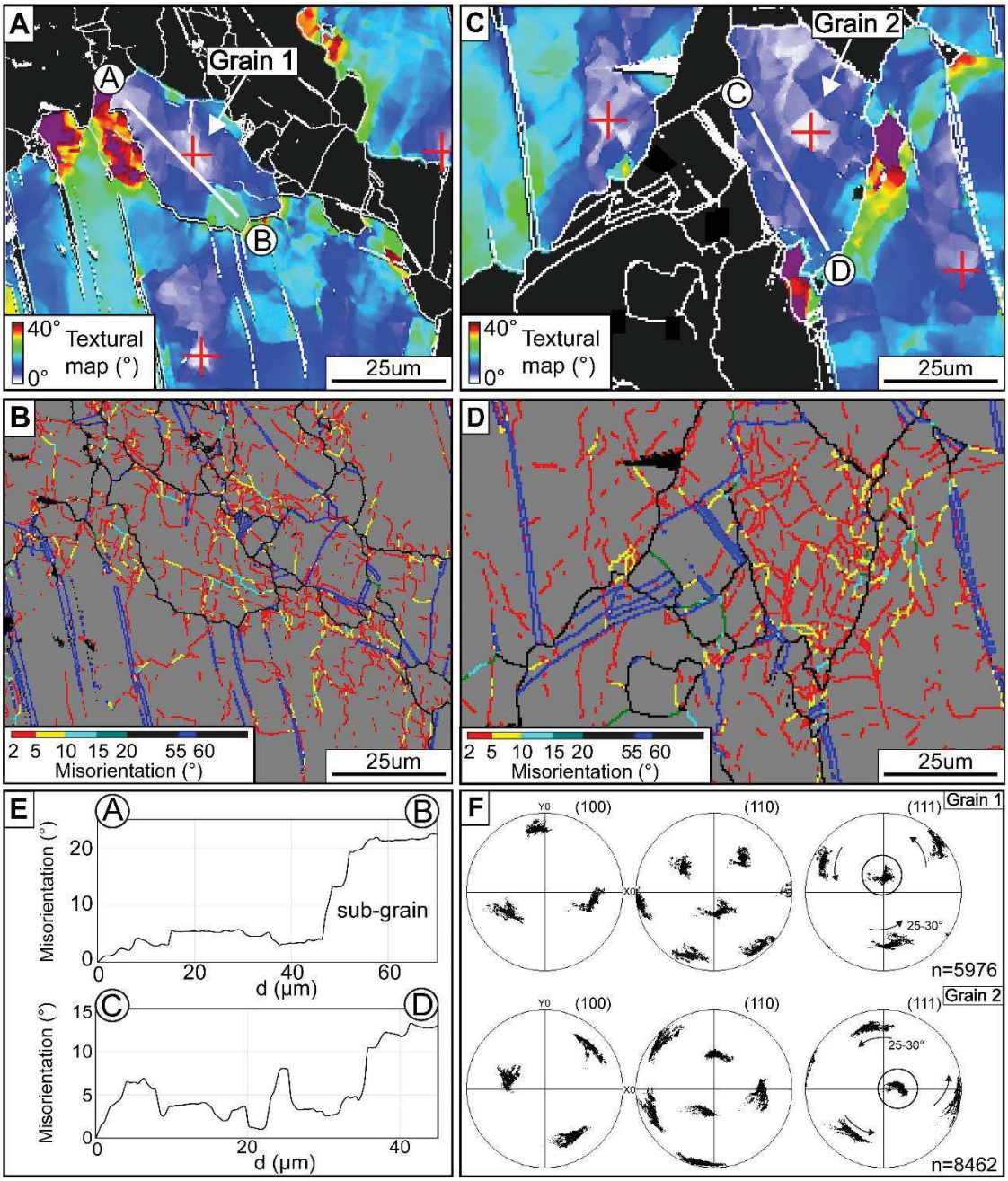

Figure 101. Zoom in Arre (AR) sphalerite crystals (step of measurement: 0.5 µm). A EBSD textural component map for selected sphalerite parent crystals. The variation in crystal lattice orientation from the red cross is fixed between 0 and 40°. B EBSD misorientation boundary map. C EBSD textural component map for selected sphalerite parent crystals. The variation in crystal lattice orientation from the red cross is fixed between 0 and 40°. D EBSD misorientation boundary map. E Two misorientation profiles relative to the first point. Their positions are represented in the Figure 7A and 7C. F Pole figure plots for two selected grains (1 and 2).

Misorientation profile in the two grains (Figure 101E) shows abrupt changes in misorientation which can reach locally up to 20° and define sub-grain formation. Lattice rotation of grains occurs according to (111) plane in grain 1 and 2 with cumulative orientation of about 25-30° (Figure 101F).

7.1.6.2.3 Highly deformed sphalerite associated to quartz

Figure 102A displays a deformed sphalerite from AG deposit (85 vol.%) with large grain size variations from 5 μm to 2.4 mm. Nonetheless, the grain size spread is mainly below 25 μm (Figure 97A). The coarser grains (> 100 μm) exhibit irregular shapes with sharp boundaries and occupy most of the analyzed area (Figure 102A). They are mantled by numerous small crystals (<100 μm) which are also found in [111] twin planes. These <111> twins, perpendicular to S_2 cleavage in grain 1, are often wider close to the crystal boundaries and thinner in the core of the grain (Figure 102A) which suggest they are "deformation twins". Low misorientations (2-15°) are more frequent than twins boundaries (Figure 102C) and appear in domains where these twins are absent (Figure 102A) preferentially close to the grain boundary (grain2, Figure 102C). But some low misorientations are localized and aligned perpendicular to twins in grains 1 and 2. Changes in crystal orientation in two coarse grains from 0 to 40° are shown in a textural component map (Figure 102B). Two misorientation profiles are plotted. Profile A-B (Figure 102E) is perpendicular to twin cleavages and exhibits deformation bands associated to < 10° misorientation variations. Profile C-D (Figure 102) is perpendicular to Profile A and parallel to twins. It shows same deformation bands with < 10° misorientations but also some localized and more pronounced deformation bands with ~ 15°misorientations.

Two areas are selected in grain 1 and 2 to observe variation in crystal orientation for each pixel analyzed and plotted in pole figures in Figure 102F. Colors of pixels correspond to the textural map in Figure 102B. Lattice rotation of grains occurs according to <100> plane in grain 1 and probably <110> plane in grain 2.

Investigation of possible CPO differences between coarse and small grains are shown in Figure 102G. A small area with presence of a restricted small grains band between grain 1 and grain 2 is chosen. For the two textures, a set of inverse pole figures according to the three direction X, Y and Z is present in Figure 102G. Coarse grain exhibit relative homogeneous orientation shown by small change in misorientation (Figure 102G). Small grains present a total uniform orientation (Figure 102G).

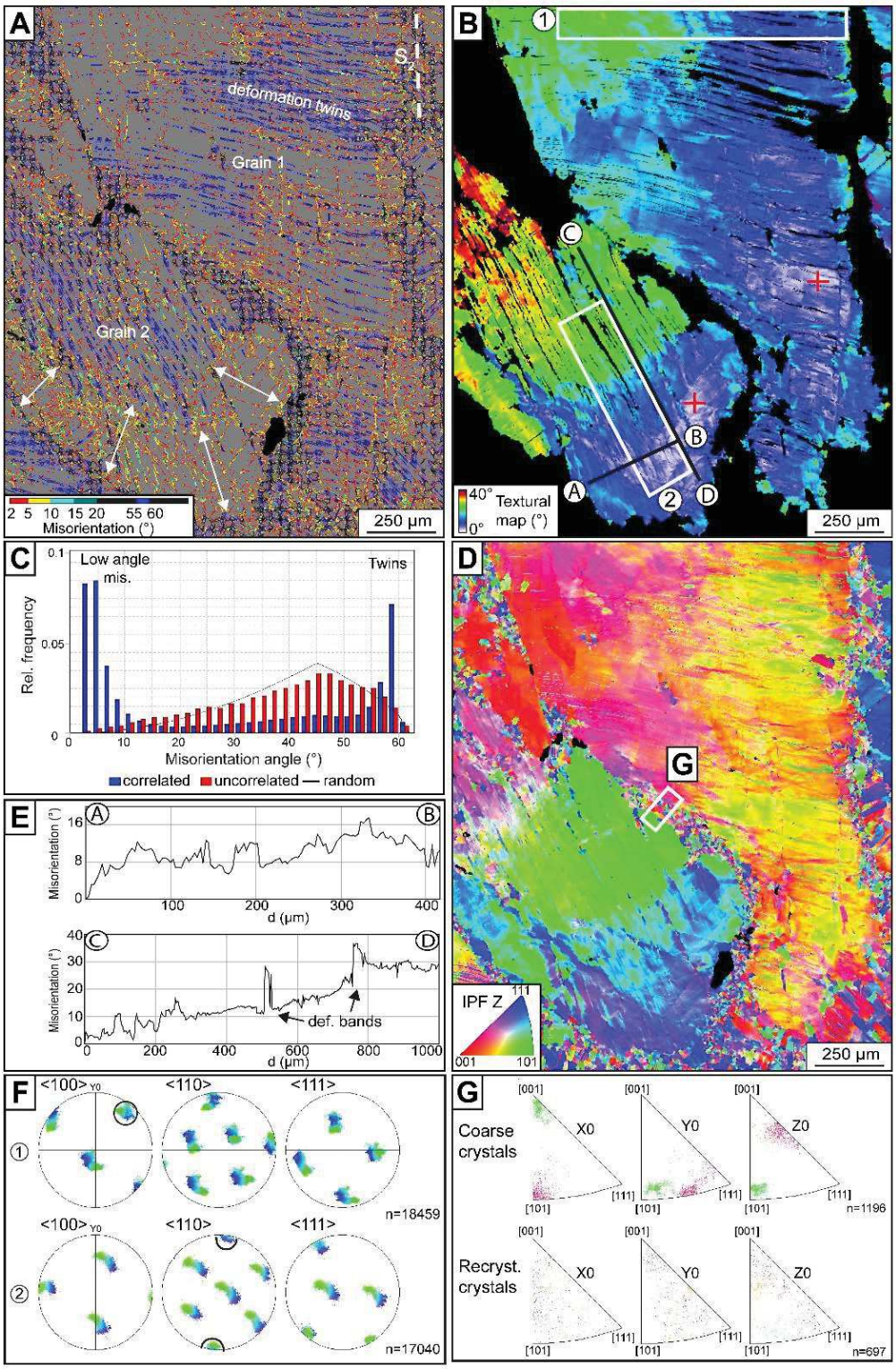

Figure 102. Anglas (AG) sample (step of measurement: 3 µm). A EBSD Misorientation boundary map. B EBSD Textural map for selected sphalerite parent crystals. The variation in crystal lattice orientation is fixed between 0 and 40°. C Misorientation angle distribution in the sphalerite grains (>2° misorientation boundary). D EBSD inverse pole figure map plotted according to the Z axis. E Two misorientation profile relative to the first point. The position of the two profiles is noted in the Figure 8B. F Pole figure plots for two selected areas In the parent grains (position noted in Fig. 8B). G Recrystallized and parent selected inverse pole figures plots. The corresponding area and color variations are represented in D.

7.1.6.3 Metamorphosed sphalerite textures (Pyrenean deposit)

Sphalerite from BT exhibits coarse grains with polygonal shape (Figure 103A and B). Misorientation boundaries are essentially constituted of twins and boundaries above 20° (Figure 103B and C). Very low content of low angle boundary is present (Figure 103C) associated to a poor internal lattice deformation, attested by the concentrated points of the pole figure (Figure 103D,

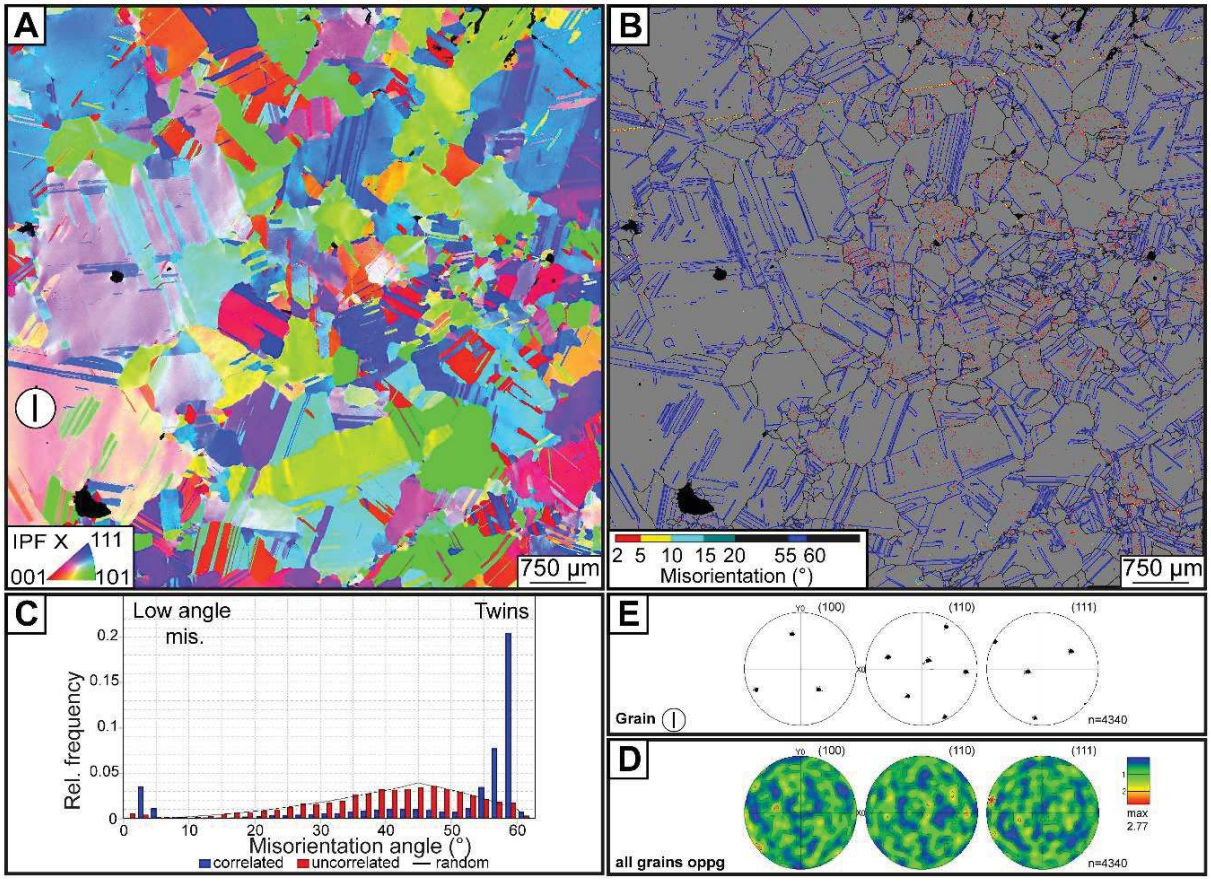

Figure 103. Bentaillou (BT) sample (step of measurement: 5.7 µm). A EBSD inverse pole figure map plotted according to the X axis. EBSD Misorientation boundary map. B. EBSD misorientation boundary map. C Misorientation angle distribution in the sphalerite grains (>2° misorientation boundary). The low values are overestimated due to polishing scratch. D Pole figure plot for a selected sphalerite crystal (position represented in A). E Pole figure plot for one point per grain, with contours.

referred to grain 1). Abundant twins are straight and not deformed, often regularly spaced with tabular aspect. Numerous twins are limited in extent and do not cross the entire grain but keep the same width (Figure 103B). Figure 103D represents scatter and contoured one point per grain pole figures and no real crystal preferred orientation appears.

7.1.7 Chemical mapping in deformed sphalerite

Combined misorientation boundary and chemical LIBS maps are presented in the following paragraph to evaluate the impact of crystal plastic deformation on the trace element content in sphalerite.

7.1.7.1 Chemical distribution in banded sphalerite

A large sphalerite area (16 x 2.5 mm) is analyzed with LIBS mapping (Ge, Cu, Ga) and is partly mapped with EBSD (Figure 104A). Area in Figure 99 is reported in the centre of the Figure 104A. Copper contents are highly heterogeneous in the PB sphalerite and are arranged in chemical bands, parallel to S_2 cleavage. (Figure 104B). Copper poor bands appear in a coarse sphalerite crystals domain (named (1) in the Figure 104B). Grain shape in the Cu-map are visible in this Cu-poor domain with presence of some small Cu-rich domains in the grain boundary (see Figure 104A and B for comparison). Other smaller Cu-poor bands appear in smaller sphalerite grain size.

Copper-rich bands are constituted to medium diffuse content in light to dark red (up to ~ 1500 ppm) and locally of high content in cyan color (Figure 104B) which correspond to chalcopyrite minerals. The medium Cu-rich contents are localized in small to medium grain size sphalerite but not in the coarse sphalerite crystals. Nevertheless, in the finest sphalerite fraction (domain-b in the Figure 99), Cu-rich content appear lower than in the closer medium grain size area (domain-c; Figure 104B).

Gallium contents (up to ~ 200 ppm) are positively correlated to Cu concentrations in the sphalerite (Figure 104C) but no Ga-rich phases are present. Germanium contents are comparatively poor in the sphalerite (< 100 ppm) and small dark brown areas which correspond to Ge-rich sphalerite are only observed close to yellow dots correlated to Ge-minerals. Ge minerals are only present the Cu-Ga rich areas and in the small grains area (<100 μm).

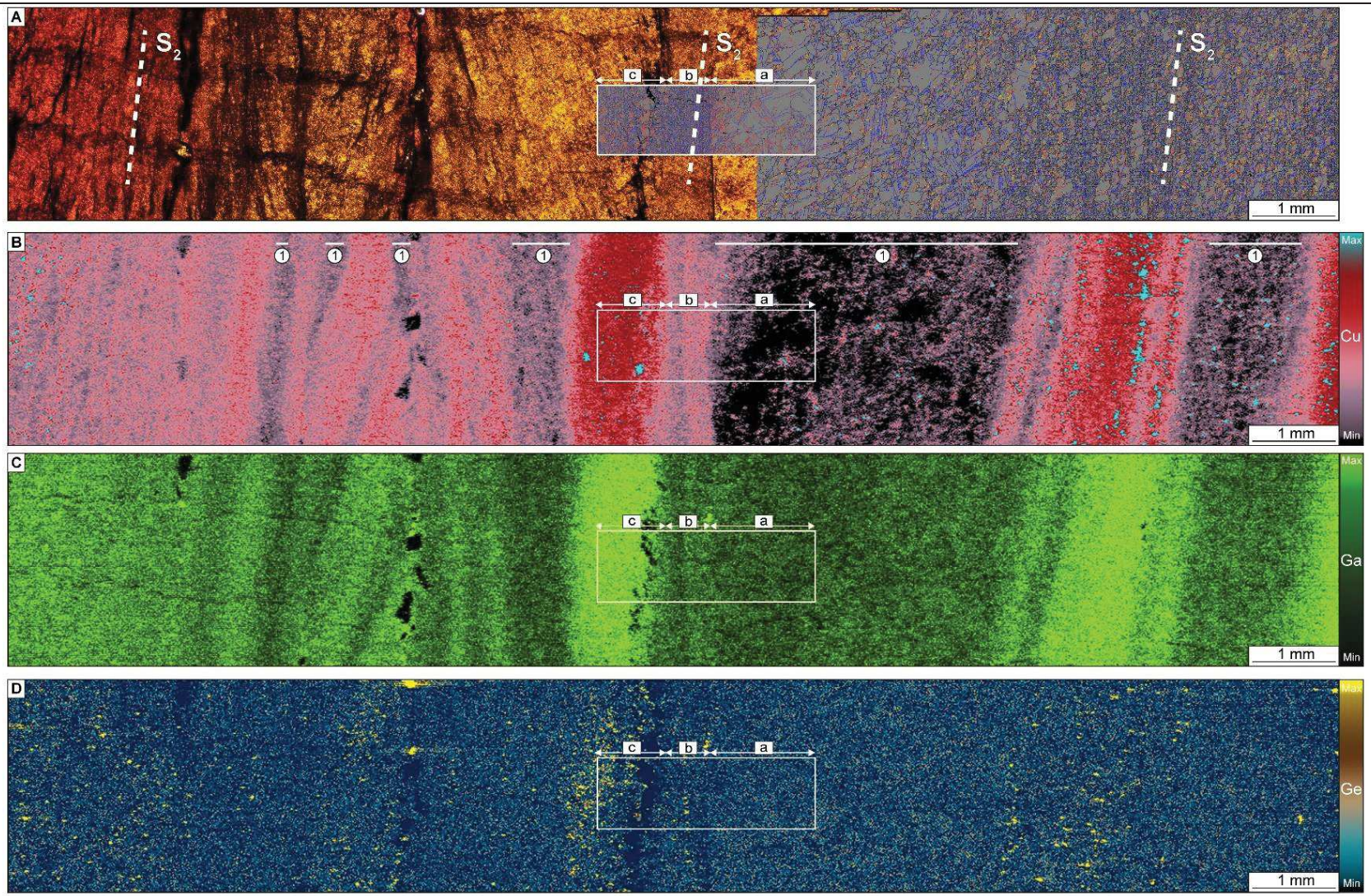

Figure 104. LIBS coupled to EBSD misorientation boundary maps on PB sphalerite sample. Position of Figure 99 is represented in all the map. A EBSD misorientation map superimposed to a transmitted plane polarized light sphalerite scan (step of measurement: 1.5 and 4 μm for the left and right maps respectively). B Copper LIBS map with indication of the coarse grain domains noted with the number 1. C Gallium LIBS map with contents highly correlated to Cu in sphalerite. D Germanium map with small yellow dots which represent Ge-minerals hosted in sphalerite. Areas where they are concentrated correspond to the high Cu-Ga contents in sphalerite.

7.1.7.2 Chemical distribution in Ge and Cu rich-coarse grains

Sphalerite crystals studied in the Figure 100 are analyzed with LIBS mapping (Figure 105). Only the highest Ge and Cu contents in the sphalerite are shown and superimposed to misorientation grain boundary map to better visualize the link between microstructures and chemistry.

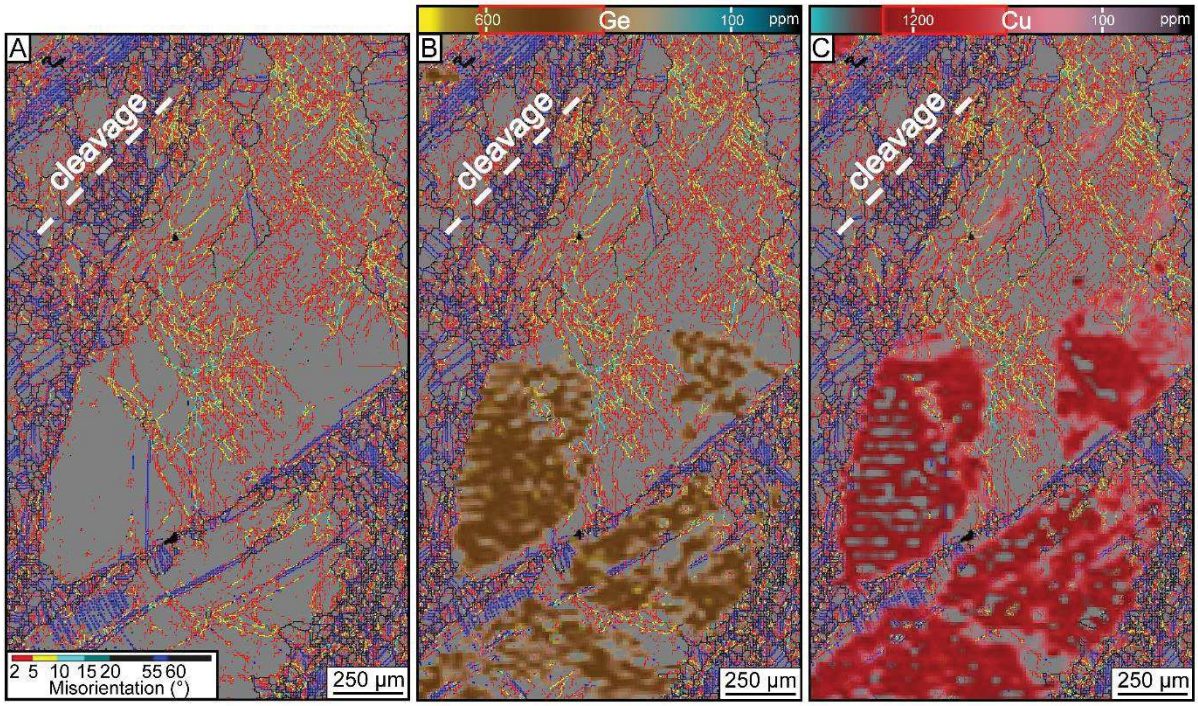

Figure 105. LIBS coupled to EBSD maps on AR sphalerite sample (same area as the Figure 100, step of measurement: 2.5 µm). The highest Ge and Cu contents in sphalerite lattice are selected for the LIBS maps. A Germanium LIBS map superimposed on a EBSD misorientation boundary map. Note that the highest contents are present in the domains free of low-angle boundaries. B Copper LIBS map superimposed on a EBSD misorientation boundary map. Correlation between Ge and Cu is globally present in the sphalerite lattice.

The higher Ge and Cu contents in the sphalerite are located only in the coarse grains (> 1 mm) and are particularly well positively correlated but heterogeneously distributed (Figure 105A and B). In the sphalerite crystals, where low angle misorientation boundaries are present, no Ge or Cu content appear comparatively to sphalerite with no apparent ductile deformation which preserve Ge and Cu contents (Figure 105).

7.1.8 Discussion

7.1.8.1 Summary of the observations

The synthesis of the observations is present in the Figure 106 and describes the micro-textures and structures of the different type of studied sphalerite. Mean grain size is largely higher in non-deformed sphalerite than in deformed sphalerite and slightly higher than in metamorphosed sphalerite (Figure 97A). A strong SPO (shape preferred orientation) is exclusively observed in the deformed sphalerite (Figure 99D).

Internal lattice distortion is absent in metamorphosed sphalerite and low in non-deformed sphalerite comparatively to deformed sphalerite in which globally exhibits numerous low-angle-boundaries (2-10°). In deformed sphalerite, these low angle boundaries can form deformation bands or lamellae (Figure 100E and Figure 102E) in coarse parent grains but, in recrystallized daughter grains, little or no low-angle misorientation boundary appear (Figure 99B). Growth twins are numerous in non-deformed but less frequent and dominated by deformation twins in deformed sphalerite. Numerous annealing twins are observed in recrystallized or annealing sphalerite. Lattice rotation appears in coarse parent grains with cumulative rotation from 10° to 30° (Figure 99F and Figure 101F) comparatively to non-deformed or metamorphosed sphalerite which exhibit little or no lattice rotation.

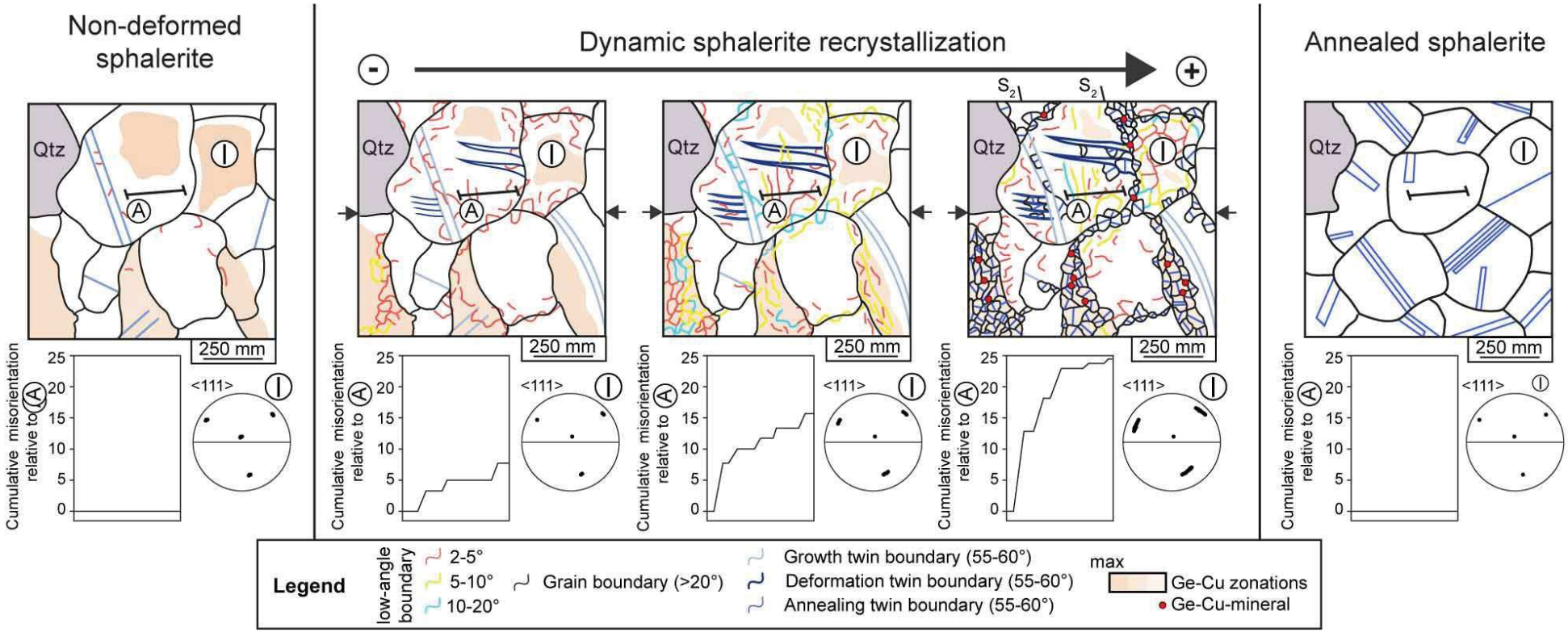

Figure 106. Synthetic sketches representing the deformational features related to chemical heterogeneities in sphalerite, from non-deformed, and deformed/recrystallized to metamorphosed crystals.

7.1.8.2 Deformation mechanisms in Pyrenean sphalerite

The first visual evidence of deformation in the sphalerite veins appear in a hand-specimen with presence of dark and light brown areas parallel to S_2 Pyrenean cleavage (Figure 96). Determining the precise mechanism of deformation in sphalerite is important to decipher the link between deformation and chemical heterogeneities existing in this material (Cugerone et al. 2019).

In the sphalerite Pyrenean veins, a common texture is the apparition of coarse porphyroclastic grains mantled by small daughter crystals. Porphyroclasts present numerous low-angle sub-grain boundaries, testifying of important internal dislocations. These boundaries or dislocation walls are often organized in deformation lamellae and bands, or chessboard structures attesting for dislocation creep mechanisms *(Cox 1987; Hirth and Tullis 1992; Fliervoet et al. 1999; Barrie et al. 2007*). No real bulk CPO or CPO recorded in small (<50 μm) or coarse (>50 μm) grains appear and may be due to large slip systems on <111> reported by *Siemes et al. (1973; 1979*) and *Couderc et al. (1985)* or grain boundary sliding during deformation (*Barrie et al. 2007*).

In the Figure 101, the low-angle boundaries (<20°) form pluri-μm sub-grains in porphyroclastic sphalerite and are numerically more abundant closer to the grain boundary (>20°). Important cumulative lattice rotations appear and can reach up to 30° (Figure 101F). Recrystallized sphalerite shows little or no low-angle misorientation (Figure 99B) which evidences the presence of sub-grain rotation (SGR) recrystallization during recovery *(Drury and Urai 1990; Hirth and Tullis 1992*) and forms small grains systematically twinned in sphalerite (Figure 99B and Figure 100B).

Sphalerite from the PB deposit exhibits a pronounced change in texture with presence of recrystallized grains vertically aligned close to a coarse grain (>100 μm) area (Figure 99). No abrupt change of this type appears in the other sphalerite veins. In the poorly recrystallized domain (a) (Figure 99), there are only few small sub-grains (<10 μm) that often appear in lobate coarse grain boundaries, showing the presence of bulging recrystallization (BLG; *Cox, 1987; Hirth and Tullis, 1992; Stünitz and Fitz Gerald, 1993; Rosenberg and Stünitz, 2003)*. In the domain (b) and (c), recrystallization is largely dominant even if some coarse parent crystals are still present. These domains have endured sub-grain rotation recrystallization (SGR). Bulging is a recrystallization mechanism which is often linked to sub-grain rotation mechanisms but appears at lower temperature in some minerals such as quartz, calcite or pyrite (*Cox et al. 1981; Drury and Urai 1990; Hirth and Tullis 1992; Barrie et al. 2007; Valcke et al. 2014*) and is supported by geothermometer calculation (Frenzel et al. 2016) applied to trace element composition of sphalerite in *Cugerone et al. submitted*. In the domain a, mean temperature is 159 ± 3 °C compare to domain b and c which

exhibit mean temperature up to 283 ± 20°C. Localization of the deformation and recrystallization in PB sphalerite is certainly linked to a difference of mineralogical association. Sphalerite from the PB deposit occupy about 95 vol.% of the ore, compared to the sphalerite from AR and AG deposit which contains more quartz and other gangue minerals (calcite or barite with about 20-30 vol.%).

In metamorphosed sphalerite, deformation relic are still present but were largely erased by a typical "annealing" texture, with polygonal grains without internal dislocation and straight and tabular annealing twins. Presence of annealing may be confused with non-deformed textures which also exhibit polygonal shape in coarse grains. Non-deformed sphalerite (Figure 98) exhibit no tabular twin, and some internal dislocation, especially close to twins or grain boundaries. Sphalerite is a relatively "soft" mineral (*Stanton and Gorman 1968; Clark and Kelly 1973; Siemes and Borges 1979)* and even if sphalerite has not endured a major deformational event, lattice distortion may appear. Annealed sphalerite has no remaining internal dislocation and consequently is in total equilibrium with the host-rock and more resistant to minor tectonic event.

7.1.8.3 Relation between trace element chemistry and microstructures

Saint-Salvy non-deformed sphalerite exhibit chemical zonations (*Belissont et al. 2014*). Sector zonings (enriched in Ge and Cu) and rhythmic bands are limited to crystal boundaries (Figure 98A) without preferential orientation or remobilization close to grain boundaries.

In deformed Pyrenean sphalerite crystals, clear evidence of a link between microstructures and chemistry appear in sphalerite porphyroclasts (Figure 105). Germanium and copper which are positively correlated in sphalerite lattice (*Cugerone et al., submitted*), appear in the areas where fewer misorientations exist. Two hypotheses exist for these studied sphalerite: trace elements like Ge or Cu may be (i) redistributed to clean dislocation areas in the sphalerite lattice or (ii) dislocations facilitate faster diffusion and so Ge and Cu are lost from domains with high dislocation density. Several studies show that the presence of internal dislocations which can act as a trap for trace elements associated or not to a fluid circulating in the deformed mineral lattice. For example in EBSD studies, *Piazolo et al. (2016)* describe the accumulation of uranium atoms in dislocation areas in zircons. In pyrite, *Fougerouse et al. (2018)* observe a redistribution of diverse elements like Pb, Ni, Sb, Bi in dislocations or high-angle boundaries, associated to plastic deformation or metamorphism. These examples are in contradiction to our example, where a depletion in trace element is observed close to crystal internal dislocations. Recrystallization and subsequent fracturing of Au-rich arsenopyrite (*Fougerouse et al. 2016a*) induced the possibility for circulating fluid to penetrate in the low and high angle boundaries, and remobilize Au. *Cugerone et al., submitted*,

shows in AR sphalerite the presence of recrystallized grains depleted in Ge-Cu-Ga which mantled Ge-Cu-Ga poor to rich coarse crystals. This remobilization is probably linked to diffusional and fluid-assisted processes (Cugerone et al., submitted).

In the PB deposit, repartition of these elements is relatively different. The sphalerite is vertically and chemically banded in Cu and Ga. Some Ge-minerals hosted in sphalerite grain boundaries, appear in Cu and Ga rich areas. The coarser sphalerite crystals (such as domain (a) in Figure 99) are highly depleted in Cu, Ge and Ga but the small sphalerite crystals area (such as domain (b) and (c) in Figure 99) preserve higher Cu and Ga contents. The smallest and permeable fraction in domain (b) is less rich in Cu and Ga which is not in agreement with a possible later Cu and Ga input. Therefore, these differences are rather interpreted to be primary chemistry differences. PB sphalerite was probably chemically banded in Ge, Cu, Ga before deformation and recrystallization preferentially appear in the trace element-rich bands. An hypothesis may be these trace elements weaken the ZnS structure, which entered in the ZnS lattice by coupled substitution with Zn ($Ge^{4+}+2Cu^{+}\leftrightarrow 2Zn^{2+}$ or $Ga^{3+}+Cu^{+}\leftrightarrow 2Zn^{2+}$; *Belissont et al., 2016*). Quasi integral remobilization in accessory Ge-minerals appears for Ge but is probably not complete for Cu and Ga which are retained as trace contents in sphalerite, and in accessory minerals (chalcopyrite, Figure 104). In garnet, dynamically recrystallized zones show the presence of newly formed kyanite, apatite, xenotime and rutile and enrichment in Ca which is related to diffusion processes *(Bestmann et al. 2008*).

7.1.9 Conclusion

Pyrenean sphalerite samples were compared to a non-deformed sphalerite from Saint-Salvy deposit and analyzed with EBSD in order to highlight the deformation and recrystallization mechanisms in zinc sulfide.

-Pyrenean vein sphalerite can deform plastically by disclocation creep and dynamically recover by sub-grain rotation (SGR) in AR and AG samples. PB sample is more complex with presence of SGR and bulging (BLG) recrystallization.

-Pyrenean statically recrystallized sphalerite exhibits annealing texture which is clean of internal dislocations unlike non-deformed sphalerite grains which preserve some internal dislocations.

-Propagation of the internal dislocations in sphalerite induces a loss of trace elements (Ge, Cu, Ga) from the sphalerite lattice and is a key process for the neoformation of accessory minerals enriched in these elements.

-Sphalerite dynamic recrystallization may preferentially occur in trace-element-rich banded sphalerite.

7.1.10 Acknowledgment

This study was funded through the French national program "Référentiel Géologique de France" (RGF-Pyrénées) of the French Geological Survey (Bureau de Recherches Géologiques et Minières; BRGM), and through the INSU-CNRS Tellus CESSUR program. Bénédicte Cenki-Tok acknowledges funding from the European Union's Horizon 2020 research and innovation programme under grant agreement No 793978. The authors gratefully acknowledge Christophe Nevado and Doriane Delmas for the exceptional thin sections preparation.

7.1.11 References

Allain-Bonasso N, Wagner F, Berbenni S, Field DP (2012) A study of the heterogeneity of plastic deformation in IF steel by EBSD. Mater Sci Eng A 548:56–63. doi: 10.1016/j.msea.2012.03.068

Barbanson L, Geldron A (1983) Distribution du germanium, de l 'argent et du cadmium entre les schistes et les mineralisations stratiformes et filoniennes a blende- siderite de la region de Saint-Salvy (Tarn). Chron la Rech minière 470:33–42

Barrie CD, Boyle AP, Prior DJ (2007) An analysis of the microstructures developed in experimentally deformed polycrystalline pyrite and minor sulphide phases using electron backscatter diffraction. J Struct Geol 29:1494–1511. doi: 10.1016/j.jsg.2007.05.005

Bauer ME, Burisch M, Ostendorf J, Krause J, Frenzel M, Seifert T, Gutzmer J (2018) Trace element geochemistry of sphalerite in contrasting hydrothermal fluid systems of the Freiberg district, Germany: insights from LA-ICP-MS analysis, near-infrared light microthermometry of sphalerite-hosted fluid inclusions, and sulfur isotope geochemi. Miner Depos 1–26

Belissont R, Boiron MC, Luais B, Cathelineau M (2014) LA-ICP-MS analyses of minor and trace elements and bulk Ge isotopes in zoned Ge-rich sphalerites from the Noailhac - Saint-Salvy deposit (France): Insights into incorporation mechanisms and ore deposition processes. Geochim Cosmochim Acta 126:518–540. doi: 10.1016/j.gca.2013.10.052

Belissont R, Munoz M, Boiron MC, Luais B, Mathon O (2016) Distribution and oxidation state of Ge, Cu and Fe in sphalerite by μ-XRF and K-edge μ-XANES: Insights into Ge incorporation, partitioning and isotopic fractionation. Geochim Cosmochim Acta 177:298–314. doi: 10.1016/j.gca.2016.01.001

Bestmann M, Habler G, Heidelbach F, Thöni M (2008) Dynamic recrystallization of garnet and related diffusion processes. J Struct Geol 30:777–790. doi: 10.1016/j.jsg.2008.02.007

Bodon SB (1998) Paragenetic Relationships and Their Implications for Ore Genesis at the Cannington. Econ Geol 93:1463–1488

Cáceres JO, Pelascini F, Motto-Ros V, Moncayo S, Trichard F, Panczer G, Marín-Roldán A, Cruz JA, Coronado I, Martín-Chivelet J (2017) Megapixel multi-elemental imaging by Laser-Induced Breakdown Spectroscopy, a technology with considerable potential for paleoclimate studies. Sci Rep 7:1–11. doi: 10.1038/s41598-017-05437-3

Cassard D, Chabod JC, Marcoux E, Bourgine B, Castaing C, Gros Y, Kosakevitch A, Moisy M, Viallefond L (1993) Mise en place et origine des minéralisations du gisement filonien de Noailhac - Saint-Salvy Zn, Ge, Ag, (Pb, Cd) Tarn - France. BRGM BRGM R-376:82

Clark BR, Kelly WC (1973) Sulfide Deformation Studies; I, Experimental Deformation of Pyrrhotite and Sphalerite to 2,000 Bars and 500 degrees C. Econ Geol 68:332–352. doi: 10.2113/gsecongeo.68.3.332

Cochelin B, Chardon D, Denèle Y, Gumiaux C, Le Bayon B (2017) Vertical strain partitioning in hot Variscan crust: Syn-convergence escape of the Pyrenees in the Iberian-Armorican syntax. Bull la Société géologique Fr 188:39. doi: 10.1051/bsgf/2017206

Cook NJ, Ciobanu CL, Mao J (2009a) Textural control on gold distribution in As-free pyrite from the Dongping , Huangtuliang and Hougou gold deposits , North China Craton. Chem Geol 264:101–121. doi: 10.1016/j.chemgeo.2009.02.020

Cook NJ, Ciobanu CL, Pring A, Skinner W, Shimizu M, Danyushevsky L, Saini-Eidukat B, Melcher F (2009b) Trace and minor elements in sphalerite: A LA-ICPMS study. Geochim Cosmochim Acta 73:4761–4791. doi: 10.1016/j.gca.2009.05.045

Couderc JJ, Dudouit I, Hennig-Michaeli C, Levade C (1985) The interaction between slip and twinning systems in natural sphalerite experimentally deformed. Phys Status Solidi 90:581–593. doi: 10.1002/pssa.2210900222

Cox SF (1987) Flow mechanisms in sulphide minerals. Ore Geol Rev 2:133–171

Cox SF, Etheridge MA, Hobbs BE (1981) The experimental ductile deformation of polycrystalline and single crystal pyrite. Econ Geol 76:2105–2117. doi: 10.2113/gsecongeo.76.8.2105

Craig JR (2001) Ore-mineral textures and the tales they tell. Can Mineral 39:937–956. doi: 10.2113/gscanmin.39.4.937

Craig JR, Vokes FM (1992) Ore mineralogy of the Appalachian-Caledonian stratabound sulfide deposits. Ore Geol Rev 7:77–123. doi: 10.1016/0169-1368(92)90007-8

Cross AJ, Prior DJ, Stipp M, Kidder S (2017) The recrystallized grain size piezometer for quartz: An EBSD-based calibration. Geophys Res Lett 44:6667–6674. doi: 10.1002/2017GL073836

Cugerone A, Cenki-Tok B, Chauvet A, Le Goff E, Bailly L, Alard O, Allard M (2018a) Relationships between the occurrence of accessory Ge-minerals and sphalerite in Variscan Pb-Zn deposits of the Bossost anticlinorium, French Pyrenean Axial Zone: Chemistry, microstructures and ore-deposit setting. Ore Geol Rev 95:1–19. doi: 10.1016/j.oregeorev.2018.02.016

Cugerone A, Oliot E, Chauvet A, Gavalda J, Le Goff E (2018b) Structural Control on the Formation of Pb-Zn Deposits: An Example from the Pyrenean Axial Zone. Minerals 8:1–20. doi: 10.3390/min8110489

Denèle Y, Laumonier B, Paquette J-L, Olivier P, Gleizes G, Barbey P (2014) Timing of granite emplacement, crustal flow and gneiss dome formation in the Variscan segment of the Pyrenees. Geol Soc London, Spec Publ 405:265–287. doi: 10.1144/SP405.5

Drury MR, Urai JL (1990) Deformation-related recrystallization processes. Tectonophysics 172:235–253. doi: 10.1109/IMFEDK.2013.6602261

Dubosq R, Lawley CJM, Rogowitz A, Schneider DA, Jackson S (2018) Pyrite deformation and connections to gold mobility : Insight from micro-structural analysis and trace element mapping. Lithos 310–311:86–104. doi: 10.1016/j.lithos.2018.03.024

Fabre C, Devismes D, Moncayo S, Pelascini F, Trichard F, Lecomte A, Bousquet B, Cauzid J, Motto-Ros V (2018) Elemental imaging by laser-induced breakdown spectroscopy for the geological characterization of minerals. J Anal At Spectrom R Soc Chem 1–9. doi: 10.1039/c8ja00048d

Fliervoet TF, Drury MR, Chopra PN (1999) Crystallographic preferred orientations and misorientations in some olivine rocks deformed by diffusion or dislocation creep. Tectonophysics 303:1–27. doi: 10.1016/S0040-1951(98)00250-9

Fougerouse D, Micklethwaite S, Halfpenny A, Reddy SM, Cliff JB, Martin LAJ, Kilburn M, Guagliardo P, Ulrich S (2016) The golden ark: Arsenopyrite crystal plasticity and the retention of gold through high strain and metamorphism. Terra Nov 28:181–187. doi: 10.1111/ter.12206

Fougerouse D, Reddy SM, Kirkland CL, Saxey DW, Rickard WD, Hough RM (2019) Time-resolved, defect-hosted, trace element mobility in deformed Witwatersrand pyrite. Geosci Front 10:55–63. doi: 10.1016/j.gsf.2018.03.010

Frenzel M, Hirsch T, Gutzmer J (2016) Gallium, germanium, indium, and other trace and minor elements in sphalerite as a function of deposit type - A meta-analysis. Ore Geol Rev 76:52–78. doi: 10.1016/j.oregeorev.2015.12.017

George LL, Cook NJ, Ciobanu CL (2016) Partitioning of trace elements in co-crystallized sphalerite-galena-chalcopyrite hydrothermal ores. Ore Geol Rev 77:97–116. doi: 10.1016/j.oregeorev.2016.02.009

Gill JE (1969) Experimental deformation and annealing of sulfides and interpretation of ore textures. Econ Geol 64:500–508. doi: 10.2113/gsecongeo.64.5.500

Gilligan LB, Marshall B (1987) Textural evidence for remobilization in metamorphic environments. Ore Geol Rev 2:205–229. doi: 10.1016/0169-1368(87)90029-1

Hadadzadeh A, Mokdad F, Wells MA, Chen DL (2018) A new grain orientation spread approach to analyze the dynamic recrystallization behavior of a cast-homogenized Mg-Zn-Zr alloy using electron backscattered diffraction. Mater Sci Eng A 709:285–289. doi: 10.1016/j.msea.2017.10.062

Hirth G, Tullis J (1992) Dislocation creep regimes in quartz aggregates. J Struct Geol 14:145–159. doi: 10.1016/0191-8141(92)90053-Y

Lockington JA, Cook NJ, Ciobanu CL (2014) Trace and minor elements in sphalerite from metamorphosed sulphide deposits. Mineral Petrol 108:873–890. doi: 10.1007/s00710-014-0346-2

McClay KR (1991) Deformation of stratiform ZnPb(-barite) deposits in the northern Canadian Cordillera. Ore Geol Rev 6:435–462. doi: 10.1016/0169-1368(91)90040-E

Mezger JE, Gerdes A (2016) Early Variscan (Visean) granites in the core of central Pyrenean gneiss domes: Implications from laser ablation U-Pb and Th-Pb studies. Gondwana Res 29:181–198. doi: 10.1016/j.gr.2014.11.010

Munoz M, Boyce AJ, Courjault-Rade P, Fallick AE, Tollon F (1994) Multi-stage fluid incursion in the Palaeozoic basement-hosted Saint-Salvy ore deposit (NW Montagne Noire, southern France). Appl Geochemistry 9:609–626. doi: 10.1016/0883-2927(94)90022-1

Pesquera A, Velasco F (1993) Ore Metamorphism in Sulfide Mineralizations from the Cinco Villas Massif (Western Pyrenees, Spain). Econ Geol 88:266–282

Piazolo S, La Fontaine A, Trimby P, Harley S, Yang L, Armstrong R, Cairney JM (2016) Deformation-induced trace element redistribution in zircon revealed using atom probe tomography. Nat Commun 7:10490. doi: 10.1038/ncomms10490

Plimer IR (1987) Remobilization in high-grade-metamorphic environments. Ore Geol Rev 2:231–245

Rosenberg CL, Stünitz H (2003) Deformation and recrystallization of plagioclase along a temperature gradient: An example from the Bergell tonalite. J Struct Geol 25:389–408. doi: 10.1016/S0191-8141(02)00036-6

Sancey L, Motto-Ros V, Busser B, Kotb S, Benoit JM, Piednoir A, Lux F, Tillement O, Panczer G, Yu J (2014) Laser spectrometry for multi-elemental imaging of biological tissues. Sci Rep 4:1–8. doi: 10.1038/srep06065

Siemes H, Borges B (1979) Experimental deformation of sphalerite single crystals under confining pressures of 3000 and 5000 bars at temperatures between 25°C and 450°C. N Jb Miner Abb 134:288–304

Siemes H, Hennig-Michaeli C (1985) Ore Minerais. Prefer Orientat Deform Met rocks, an Introd to Mod texture Anal (Ed HR Wenk Acad Press Orlando 335–360

Siemes H, Hennig-Michaeli C, Martens L (1991) The importance of deformation experiments on minerals for the interpretation of metamorphic ore textures. Ore Geol Rev 6:475–483. doi: 10.1016/0169-1368(91)90042-6

Siemes H, Saynisch HJ, Borges B (1973) Experimentelle Verformung von Zinkblendeeinkristallen bei Raumtemperatur und 5000 bar Manteldruck. N Jb Miner Abb 119:65–82

Stanton RL, Gorman H (1968) A phenomenological study of grain boundary migration in some common sulfides. Econ Geol 63:907–923. doi: 10.2113/gsecongeo.63.8.907

Stünitz H, Fitz Gerald JD (1993) Deformation of granitoids at low metamorphic grade. I: Reactions and grain size reduction. Tectonophysics 221:299–324. doi: 10.1016/0040-1951(93)90164-F

Valcke SLA, de Bresser JHP, Pennock GM, Drury MR (2014) Influence of deformation conditions on the development of heterogeneous recrystallization microstructures in experimentally deformed Carrara marble. Geol Soc London, Spec Publ 409:175–200. doi: 10.1144/sp409.4

Viets J, Hopkins R, Miller B (1992) Variations in minor and trace metals in sphalerite from Mississipi Valley-type deposits of the Ozark Region: Genetic implications. Econ Geol 87:1897–1905

Wagner T, Cook NJ (1998) Sphalerite remobilization during multistage hydrothermal mineralization events — examples from siderite-Pb-Zn-Cu-Sb veins, Rheinisches Schiefergebirge, Germany. Mineral Petrol 63:223–241. doi: 10.1007/BF01164152

Wagner T, Klemd R, Wenzel T, Mattsson B (2007) Gold upgrading in metamorphosed massive sulfide ore deposits: Direct evidence from laser-ablation-inductively coupled plasma-mass spectrometry analysis of invisible gold. Geology 35:775–778. doi: 10.1130/G23739A.1

Zwart HJ (1963) The Structural Evolution of the Paleozoïc of the Pyrenees. Geol Rundschau 53:170–205

8 Fluid inclusion analyses on the Pyrenean sphalerite

This section is devoted to the article in preparation for Lithos "Geochemical signatures of mineralizing fluids in metamorphosed Pb-Zn ore bodies in the Pyrenean Axial Zone: Constraints from fluid inclusion microthermometry and LA-ICP-MS analysis". We performed fluid inclusion analyses on ore samples from Type 2a (Crabioules, Victoria, Margalida) and Type 2b (Arre, Pale Bidau, Argut-dessus and Pale de Rase) mineralizations. Structural analyses of these deposits is referred to the sections *4. Structural framework for the Pb-Zn deposits in the Pyrenean Axial Zone (PAZ).*

Four types of fluid inclusions were observed in quartz associated to sphalerite assisted by optical microscopy and cathodoluminescence (hot) on quartz: brines (i); aqueous-carbonic (ii), aqueous (iii) and vapor-rich (iv) inclusions. Microthermometry results show two main types of fluid signature in all samples:

I) A low- to medium-salinity (<20 wt.% NaCl eq.) and high-temperatures (200-350 °C) fluid is hosted in primary to pseudo-secondary (ii) and (iii) inclusions within quartz from Pale Bidau (PB), Argut-dessus (AD), or Pale de Rase (PR). This fluid is recorded in secondary inclusions from the Type 2a Margalida (MG) deposit hosted in the damaged zone of the regional Bossost fault. II) A highly-saline (15-35 wt.% NaCl eq.) low- temperature (< 200 °C) signature hosted in primary and secondary (iii) inclusions from Arre (AR) quartz and in secondary (i) and (ii) inclusions from Type 2a Victoria (VT) and Crabioules (CR). Laser ablation inductively coupled plasma mass spectrometric (LA-ICP-MS) study show a salinity derived essentially from seawater evaporation for the two types of mineralizations and relative enrichments in Ca (~5 wt.%) and K (~1-2 wt.%) for the Mesozoic mineralization.

These two types of fluids are probably related to two mineralizing stages of Late-Variscan and Mesozoic ages after comparison with other Pb-Zn deposits in the Pyrenees (Cierco, Parzan, etc.) and the Montagne Noire (Saint-Salvy, Peyrebrune). Due to this new genesis model which imply two different mineralization stages for Type 2b veins, this study highlights the probable Pyrenean-Alpine deformation associated to precoce LP-HT metamorphism which is superimposed on the sphalerite mineralization and responsible of the Ge-redistribution.

8.1 ARTICLE – Geochemical signatures of mineralizing fluids in metamorphosed Pb-Zn ore bodies in the Pyrenean Axial Zone: Constraints from fluid inclusion microthermometry and LA-ICP-MS analysis

Alexandre Cugerone[1], Kalin Kouzmanov[2], Stefano Salvi[3], Oscar Laurent[4], Elisabeth Le Goff[5], Bénédicte Cenki-Tok[1,6]

[1]*Géosciences Montpellier, Université de Montpellier, France; alexandre.cugerone@umontpellier.fr; benedicte.cenki-tok@umontpellier.fr;*

[2]*Department of Earth sciences, University of Geneva, Switzerland; Kalin.Kouzmanov@unige.ch;*

[3] *Géosciences Environnement Toulouse, Université de Toulouse, CNRS, IRD, OMP : stefano.salvi@get.omp.eu;*

[4]*Institute of Geochemistry and Petrology, ETH Zurich, Switzerland*

oscar.laurent@erdw.ethz.ch

[5]*Bureau de Recherches Géologiques et Minières (BRGM), 34000 Montpellier, France ; e.legoff@brgm.fr*

[6]*Earthbyte Research Group, School of Geosciences, University of Sydney, NSW 2006, Sydney, Australia*

Keywords: Fluid inclusions; microthermometry; LA-ICP-MS on fluid inclusions; Pyrenees; Pb-Zn deposits

8.1.1 Abstract

Unravelling the origin of ore-forming fluid in poly-metamorphic terranes is often challenging due to loss or modification of primary fluid systems. In this study, we test this assumption in Pb-Zn ore of the Pyrenees to elucidate the physico-chemical conditions of ore formation and the timing of mineralization. These microthermometric and laser ablation inductively coupled plasma mass spectrometric (LA-ICP-MS) studies evidence two major hydrothermal Pb-Zn vein mineralizing events related to four types of fluid inclusions. I) A hydrothermal fluid shows low- to medium-salinity (<20 wt.% NaCl eq.) and medium temperatures (200-350 °C) probably related to the circulation of Late-Variscan fluids. This mineralization stage appears in the Pale Bidau (PB), Argut-dessus (AD), or Pale de Rase (PR) sphalerite hosted in the low-grade domains of the Pyrenean Axial Zone; II) A hydrothermal highly saline (15-35 wt.% NaCl eq.) low temperature (< 200 °C) fluid rich in Ca and K that is recorded in the Arre (AR) deposits but also in Victoria (VT) and Crabioules (CR). This fluid signature is similar to many other vein-type mineralizations interpreted as Mesozoic in age in the Pyrenees (Cierco, Parzan, etc.) or in the Montagne Noire (Saint-Salvy, Peyrebrune). Both hydrothermal events are certainly derivate from seawater evaporation and regularly recorded in stratabound mineralization as secondary fluid inclusion assemblages. Both sphalerite vein-type mineralizations are deformed at low-grade (<250 °C) and imply an imprint of Pyrenean-Alpine deformation on the ore and not Variscan tectonics as previously inferred.

8.1.2 Introduction

Many Pb-Zn deposits in the world are located in orogens, and the question of their timing is often difficult to assess, due to lack of field or textural arguments. Establishing direct relationships between their genesis and their tectonic environment is therefore challenging especially for epigenetic mineralizations which do not exhibit contemporaneous relations with the host-rock. Numerous Pb-Zn ore bodies are imprinted by deformation, recrystallization and metamorphism (*Prokin and Buslaev 1999; Murphy 2004; Bailie and Reid 2005; Heijlen et al. 2008; Cugerone et al. 2019*) and question of representativity of the fluid assemblages may be difficult to reconcile with geodynamic evolution. In Western Europe, numerous Pb-Zn vein systems are reported, and Mesozoic emplacement is widely inferred, associated to the Triassic-Jurassic extension event and to the opening of the Atlantic Ocean, before the Pyrenean-Alpine orogeny (Late Cretaceous-Miocene). Examples of such Pb-Zn vein systems include the Cevennes-

Montagne Noire deposits in France *(Charef and Sheppard 1988; Munoz et al. 1994, 1997; Leach et al. 2006)*, the Freiberg and Schwarzwald districts in Germany *(Seifert and Sandmann 2006; Baatartsogt et al. 2007; Fusswinkel et al. 2013; Bauer et al. 2018)* and the Catalonian coastal range district *(Canals et al. 1992*).

In the Pyrenees, more than a hundred Pb-Zn mineral deposits occur in the deformed Variscan basement. Some authors have proposed an Ordovician-Devonian SEDEX style mineralization for the main economic occurrences of the Pierrefitte and Bentaillou deposits supported by ore body description on the field *(Bois et al. 1976; Pouit 1978, 1986)*. Other authors suggest a Variscan remobilization event in Liat-Urets and Pierrefitte deposits (*Alonso 1979; Nicol et al. 1997*) or a Late-Variscan stage for the Arre and Anglas deposits (Reyx 1973; Cugerone et al. 2018b) attested by observations of numerous deformation features on the Pb-Zn ore, located in lithological or structural weakness structures. Some post-Variscan or Mesozoic Pb-Zn mineralizations is additionally reported for example in the Cierco, Parzan and Aulus-Les Argentieres deposits *(Johnson et al. 1996; Fanlo et al. 1998; Munoz et al. 2016)*. This late stage is supported by field cross-cutting evidences with ore bodies hosted in Late-Variscan granitoids and in Triassic sedimentary rocks (*Johnson et al. 1996)*, and is characterized by the circulation of *h*ighly saline and low-temperature Pb-Zn mineralized fluids.

A recent study, integrating data from several deposits across the Pyrenean range, proposed a three-stage mineralization model. It consists of a minor syngenetic-stratiform Pb-Zn mineralization followed by two epigenetic stages, including Variscan stratabound ore and recrystallized Pb-Zn vein systems (*Cugerone et al., 2018b;* Figure 107C). Noteworthy, the latest mineralization is the only one that consistently hosts important Germanium mineralization, which is intimely related to deformation and recrystallization of sphalerite during probable Late-Variscan deformation.

Although fluid inclusion systematics of a few Pb-Zn occurrences in the Pyrenees have been investigated *(Johnson et al. 1996; Fanlo et al. 1998; Subias et al. 1999)*, these studies are restricted to individual deposits and as such remain inadequate for understanding large-scale fluid migration patterns and regional timing of emplacement. In this study, we present petrographic, microthermometric and LA-ICPMS analyses of fluid inclusions from two stratabound and four vein-type Pb-Zn mineralized systems from the central and western part of the Pyrenean Axial Zone (PAZ). By integrating our new fluid inclusion data with existing fluid inclusion studies, we propose a new genetic model for Pb-Zn-(Ge) mineralization in the Pyrenees.

8.1.3 Regional geology and Pb-Zn ore setting

The Pyrenean Axial Zone (PAZ) constitutes the Paleozoic core of the Pyrenean mountain range which is essentially composed of metasediments intruded by Ordovician and Late-Variscan granitoids (Figure 107B; *Kleinsmiede, 1960; Zwart, 1963; Denèle et al., 2014)*.

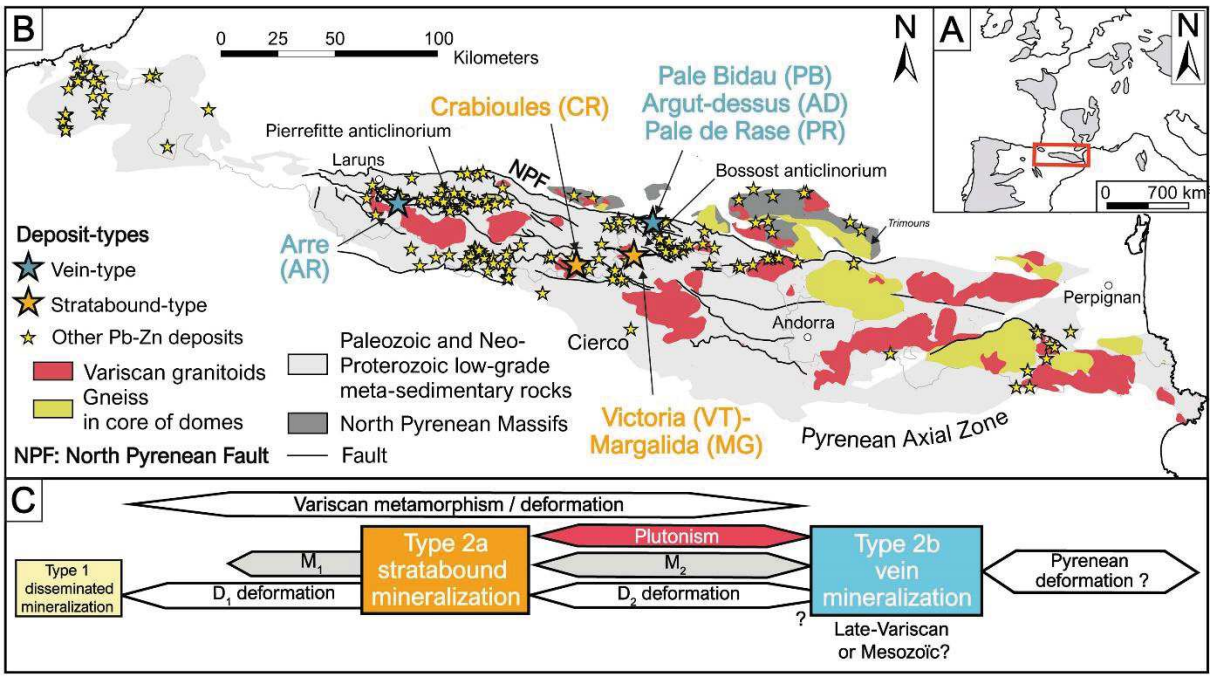

Figure 107. A. Location of the Pyrenean Axial Zone in the Variscan belt of Western Europe. B Lithological and structural map of Pyrenean Axial Zone with location of Pb-Zn deposits (BRGM and IGME databases). The studied deposits are reported (modified from *Cugerone et al., 2018b)*. C Provisional chronological position of the mineralization events related to Variscan metamorphism/deformation (modified from *Cugerone et al., 2018b)*. Numerous uncertainties remain on the impact and timing of deformation impacting Type 2b vein mineralization.

Three Variscan deformation and/or metamorphic stages are commonly described in the PAZ in the literature which may impact fluid circulation in upper crust: D_1 deformation is related to crustal thickening (Zwart 1963a, 1979; Mezger and Passchier 2003; Mezger et al. 2004; de Hoÿm de Marien et al. 2019) which lead to regional metamorphism M_1 characterized by Medium Pressure and Low-Temperature (MP/LT) conditions and the formation of a S_1 flat-lying foliation. The peak of M_1 metamorphism is estimated at ca. 580°C and 550 MPa in the Bossost dome (Mezger et al. 2004). D_2 deformation is related to the formation of metamorphic dome and presence of magmatism and contact M_2 metamorphism Low-Pressure and High-Temperature (LP/HT) culminating at *ca.* 525°C and 200 MPa (*Mezger et al. 2004*). D_3 deformation is localized in regional mylonitic shear bands such as the Merens fault (*Denèle et al. 2008; Mezger et al. 2012; Ostkamp et al. 2019*) and possibly the Bossost fault (Mezger and Passchier 2003; Cugerone et al. 2018b).

Successive periods of extension and rifting during Mesozoic times are documented as well *(Vergés et al. 2002; Martín-gonzález et al. 2019)*. A dominant Low-Pressure High-Temperature (LP/HT) metamorphism (~120-85 Ma; ca. >600°C) is recorded mainly in the North Pyrenean Massif (north of North Pyrenean fault; Figure 107B) but also in the PAZ *(Fallourd et al. 2014)*. During this period, widespread Na-Ca metasomatism is evidenced by the formation of numerous albitite, serpentinite and talc-chlorite bodies that related to mantle exhumation *(Boulvais et al. 2007; Fallourd et al. 2014; Boutin et al. 2016; de Saint Blanquat et al. 2016)*. The Pyrenean-Alpine deformation (85-20 Ma) in the PAZ is poorly described or only associated to reactivations in narrow corridors or thrusts such as Merens or Bossost faults (*McCaig and Miller 1986; García-Sansegundo 1992; Mezger and Passchier 2003; Cochelin et al. 2017b*).

The main Pb-Zn mineralizations in the Pyrenees are hosted by pluri-kilometric anticlinoriums like the Bossost or Pierrefitte anticlinorium (Figure 107B). The PAZ Pb-Zn district was exploited in 20th century and produced about 750 000 t Pb+Zn *(BRGM 1984; Ovejero Zappino 1991*).

Two major Pb-Zn mineralization types occur in the area and their characteristics have been recently summarized by *Cugerone et al. (2018b)*. Type 2a veins cross-cut Type 1 and are epigenetic stratabound mineralizations, probably synchronous to the Variscan D_1/M_1 deformation metamorphism event. In the field, Type 2a stratabound mineralization appears intensely folded by Variscan D_2 deformation in Late-Ordovician metamorphic schists in Victoria (VT) or in Crabioules deposits (CR; Figure 107C), or hosted in Late-Ordovician marble in Margalida (MG) deposit impacted by the Bossost regional fault, probably related to Late-Variscan D_3 or Alpine deformation (MG close to Bossost fault, Figure 107B, *Cugerone et al., 2018b*). iii) Type 2b is an epigenetic vein-type mineralization, probably synchronous to or post-dating the D_2/M_2 deformation event (Cugerone et al. 2018b). Here, Pb-Zn mineralization occurs as vertical dm-sized veins parallel to S_2 cleavage which locally intersect Type 2a mineralization. No alteration halo has been observed along the contact with the host-rock. This mineralization is considered Late-Variscan in age due to geometrical relation with the S_2 cleavage and local recrystallization of sphalerite. Four vein deposits were sampled: Arre (AR) deposit (Figure 107B) is hosted in Devonian calc-schists and Pale Bidau (PB), Argut-dessus (AD) and Pale de Rase (PR) are hosted in Late-Ordovician calcschist or micro-conglomerates(Figure 107B).

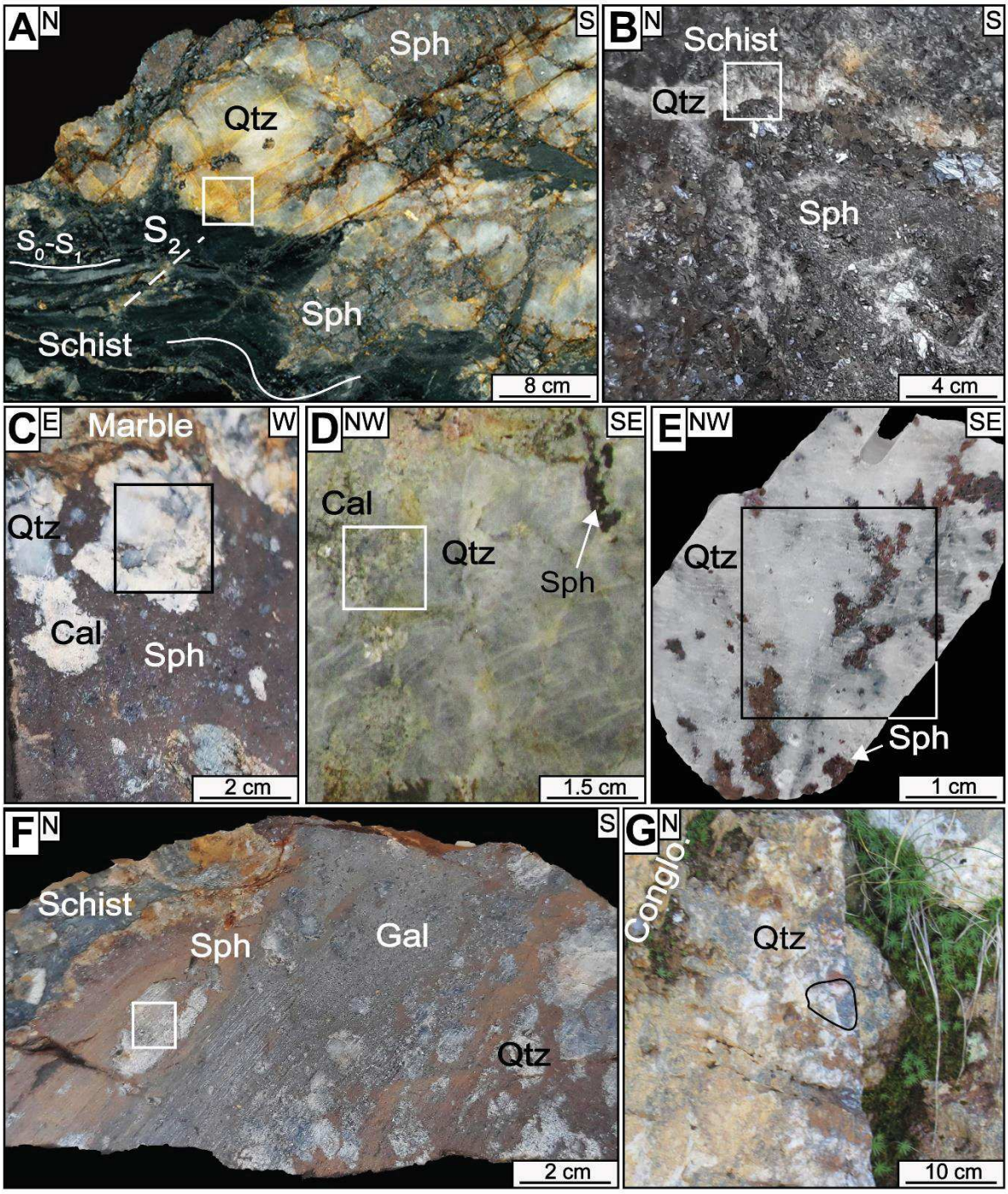

Figure 108. Ore samples photographs and scan of the studied deposits (Qtz: quartz; Sph: sphalerite; Gal: galena; Cal: calcite; conglo: conglomerate). Position of the sample collected is noted. A. Victoria (VT) ore sample and location of the sample mainly in quartz gangue (sample scan). B. Crabioules (CR) ore sample mainly composed of sphalerite associated to minor quartz (photograph). C. Margalida (MG) ore sample with sphalerite associated to quartz and calcite (sample scan). D. Pale Bidau (PB) ore sample mainly constituted of quartz associated to minor calcite (PB10 sample scan). E. Arre (AR) ore sample composed of quartz and sphalerite (sample scan). F. Argut-dessus (AD) ore sample constituted of sphalerite, galena and quartz in schist host (sample scan). G. Pale de Rase (PR) ore photograph showing typical opening textures related to comb quartz.

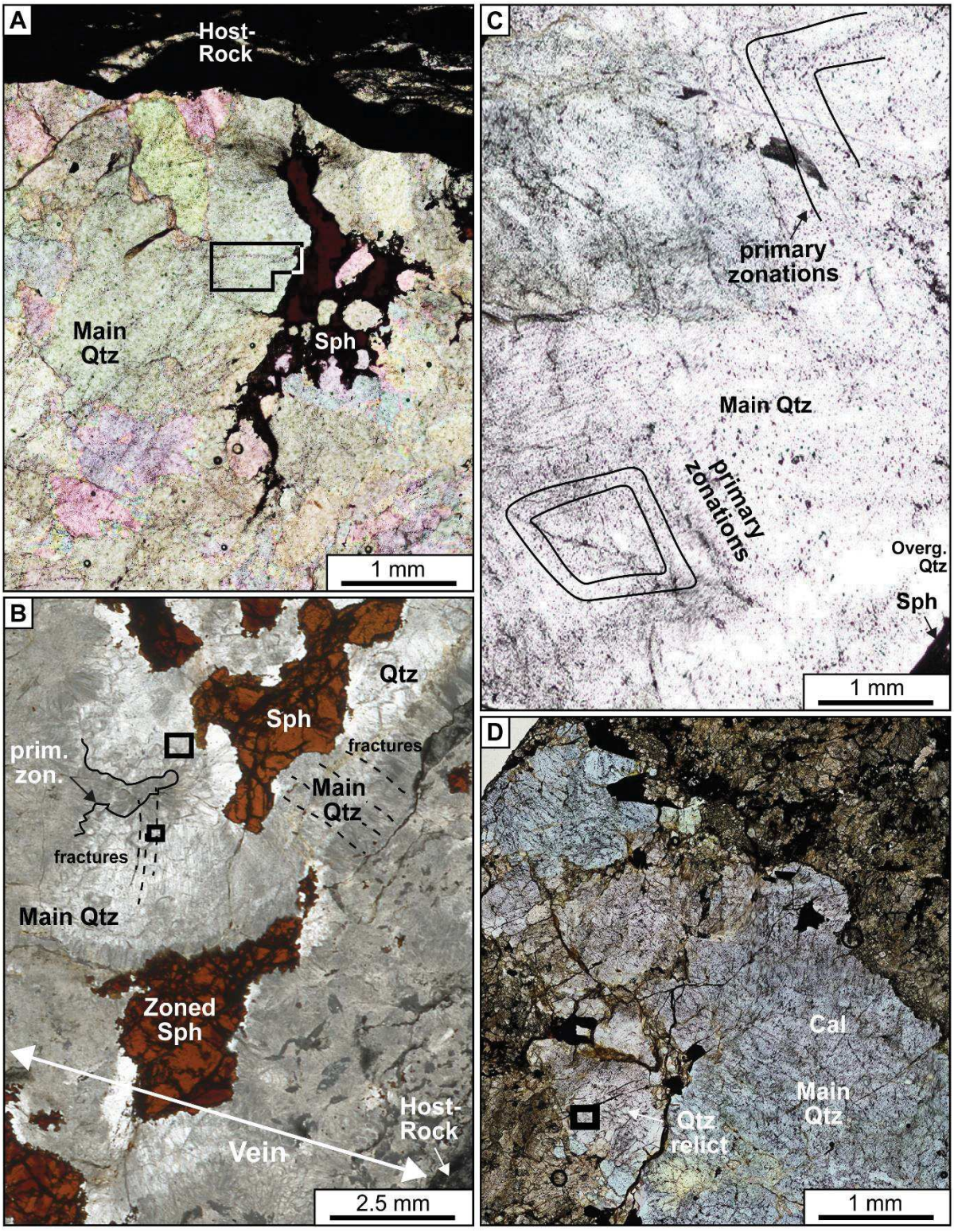

Figure 109. Sample description observed in transmitted plane polarized light (Qtz: quartz; Sph: sphalerite; Cal: calcite). A. Quartz associated to late-sphalerite in stratabound mineralization from Victoria (VT) Position of the Figure 111A . B. Sphalerite and quartz vein mineralization from Arre (AR). Note the presence of zonations in quartz. Position of the Figure 113Figure 113 and E are represented by two black rectangle. C. Primary zonation in quartz from Argut-dessus vein mineralization (AD). D. Deformed quartz associated to calcite in Pale Bidau (PB12). Position of Figure 111D is noted by a black rectangle.

8.1.4 Samples

All the samples were collected *in-situ,* from underground galleries of old mine or in outcrop. Ore samples with large gangue of quartz associated to sphalerite were preferentially selected. Three representative samples of Type 2a stratabound mineralization have been selected in the main exploited stratabound ore bodies, hosted in the core of fold hinge in Victoria (VT; Figure 107B) in Crabioules (CR), and in Margalida (MG) (Figure 108A-C; Figure 109A).

Five samples from Type 2b vein mineralization have been selected from Arre (AR), Pale Bidau (PB), Argut-dessus (AD) and Pale de Rase (PR) in the main exploited ore bodies (Figure 108D-G). Samples from AR, AD and PR exhibit well-preserved comb-quartz texture (Figure 109B, C). Close to sphalerite, quartz becomes more translucent. Two different samples were chosen at PB in two similar decimetric veins (Figure 109D).

8.1.5 Analytical methods

Cathodoluminescence (CL) images were obtained using a HC6-LM hot cathode system by Lumic Special Microscopes at Geosciences Environment Toulouse (GET). It was operated with a voltage of 14 kV and a current density of ca. 10 μA mm^2 *(Neuser 1995)*. CL images were captured with a very-high sensitivity Olympus XC10 camera.

We have performed a detailed petrographic study to identify fluid inclusion assemblages (FIA, *Goldstein and Reynolds, 1994*) in eight 150 μm thick doubly polished sections, one representative for each studied deposit except for PB where two samples were selected in two vein systems. Primary and secondary fluid inclusions were identified using the criteria of *Roedder (1984)*.

Microthermometric measurements were performed at Geosciences Environment Toulouse (GET), following the procedures outlined by *Roedder (1984)* using a Linkam THMGS 600 heating–freezing stage mounted on a BX-51 Olympus microscope. The stage was calibrated against synthetic pure H_2O inclusions (0° and 374.1°C) supplied by SynFlinc and with natural pure CO_2 inclusions (−56.6°C) from Camperio (Ticino, Switzerland). The accuracy of measurements is ±0.2 °C below ~0 °C and ±2 °C above ~0 °C. Homogenization temperatures were observed at 1 to 5 °C/min heating rates, depending on the inclusion size. Cryogenic experiments were carried out before heating to reduce the risk of decrepitating the inclusions. Fluid salinity (expressed as wt.% NaCl eq. or wt.% NaCl+$CaCl_2$ eq.) data was calculated for aqueous fluid inclusions using the HokieFlincs_H_2O-NaCl spreadsheets of *Steele-MacInnis et al. (2011)* and *Steele-MacInnis et al. (2012)*

for aqueous fluid inclusions and using the H_2O-NaCl-CO_2 spreadsheet of *Steele-MacInnis (2018)* for CO_2-bearing fluid inclusions.

Laser inductively coupled plasma mass spectrometric (LA-ICP-MS) analyses were carried out to quantify major, minor and trace element content of individual fluid inclusions. These analyses were performed at ETH Zurich using the ETH-prototype GeoLas system equipped with a 193- nm ArF-Excimer Compex 102F laser ablation system (Lamba Physik-Coherent, Germany) coupled to a Nexion2000 (PerkinElmer, USA/Canada) fast-scanning quadrupole ICP mass spectrometer for multi-element analysis. Five samples were analyzed in a ca. 5-cm^3 round glass cell. Gas blanks and system contamination were minimized following the cleaning and setup procedures described in (*Schlöglova et al. 2017*). The cell was fluxed with carrier gas consisting of high- purity (5.0 grade) He (1.1 L min−1), to which H2 was added (5 mL min−1) to enhance sensitivity for heavy elements (*Guillong and Heinrich 2007*). Sample gas consisting of 6.0 grade Ar (ca. 1 $L.min^{-1}$) was admixed downstream of the ablation cell prior to injection in the plasma. The ICP-MS was optimized for maximum sensitivity on the entire mass range and low oxide rate formation ($^{248}ThO+/^{232}Th+$ <0.5%). The glass standard NIST SRM 610 *(Jochum et al. 2011)* was used as a primary reference material except for Br, Cl, and S for which we used the Sca-17 scapolite standard (*Seo et al. 2011*). Both standards were analyzed with 40 µm pit size, repetition rates of 10 Hz and ca. 1 min measurement consisting of 30 s gas blank + 30 s ablation. Fluid inclusions in quartz were analyzed by slowly incrementing the spot size using an opening aperture ("iris diaphragm") to prevent cracking *(Guillong and Heinrich 2007*). Repetition rates of 10 Hz with laser output energies around 50 mJ (corresponding to energy densities on sample of ca. 10 $J.cm^{-2}$) were applied. Sphalerite was analyzed with a repetition rate of 10 Hz and output energies of 105 mJ (energy densities of ca. 9 $J.cm^{-2}$). In total, 35 elements were measured with a dwell time of 5 ms for ^{7}Li, ^{11}B, ^{23}Na, ^{25}Mg, ^{29}Si, ^{39}K, ^{55}Mn, ^{85}Rb, ^{88}Sr, ^{93}Nb, ^{133}Cs, ^{138}Ba, ^{140}Ce, ^{203}Tl, ^{208}Pb, ^{74}Ge, ^{232}Th, ^{238}U, 10 ms for ^{34}S, ^{35}Cl, ^{43}Ca, ^{57}Fe, ^{63}Cu, ^{66}Zn, ^{75}As, ^{107}Ag, ^{111}Cd, ^{115}In, ^{121}Sb and 20 ms for ^{78}Br. The elements Mg, Ce, Tl, Ge, Th, U, S, Fe, Cu, As, Ag, In and Sb were not detected in our samples. The total sweep time was 60 ms. The data were reduced using the SILLS software (*Guillong et al. 2008*), using the salinity determined by microthermometry as internal standard for the FI and stoichiometric contents of major elements as internal standard to correct the contribution of the host mineral (Si for quartz and Zn for sphalerite).

8.1.6 Results

8.1.6.1 Mineralogical and petrographical observations

In Type 2a stratabound mineralizations, quartz is deformed with numerous cracks at VT or CR (Figure 109A) or in durchbewegung breccia with sphalerite matrix at MG. Sphalerite fills the porosity in the gangue and clearly postdates quartz precipitation (Figure 109A).

In Type 2b vein mineralizations, quartz endured some fracking however some areas without deformation imprint may appear, for example close to carbonate in PB quartz (Figure 109D). Quartz in the PR sample occurs as very poorly deformed with large pluri-millimetric crystals and is associated with chlorite. Deformation and recrystallization has largely imprinted the sphalerite grain texture in Type 2b vein mineralizations. In the AR sample, numerous cracks sub-parallel to the vein contact appear and intersect quartz primary zonations in some areas (Figure 109B). In the same sample, sphalerite slightly post-quartz mineralization (Figure 109B) present a highly heterogeneous texture with apparition of coarse grains in dark to light-brownish colors (in plane polarized transmitted light; *Cugerone et al. 2020*) and recrystallized grains with light-brownish color.

8.1.6.2 Fluid inclusion petrography in quartz and sphalerite

Two generations of quartz occur in transmitted light in all the samples studied. The main quartz is often smoky and contain abundant FI in growth zones or in cracks. A second type of quartz appears in overgrowth of sulfide mineralization but FI were too small to be analyzed. Some fluid inclusion with evidences of stretching, necking down and leaching were observed but were not considered. Based on the phase volume proportions observed at room temperature, four types of fluid inclusions hosted in quartz can be distinguished in all samples: (i) brine inclusion type; (ii) aqueous-carbonic inclusion type; (iii) aqueous inclusion type, (iv) vapor-rich inclusion type (Figure 110).

Brine inclusions (i) only occur in stratabound mineralizations (CR and VT; Figure 110) except for the MG deposit where these FI do not appear at all. They typically form trails along secondary cracks in main quartz (Figure 111A). Their size ranges between 10 and 40 μm and can locally reach 60 μm. These consist of 60-70 vol.% liquid, 10-20 vol.% vapor and up to 20 vol.% of transparent daughter mineral with cubic habit, which probably correspond to halite.

In quartz from stratabound mineralization (Figure 110), aqueous-carbonic FI (ii) are frequently observed with CO_2 volume proportion varying from 50 to 90 vol.%. These inclusions may form large clusters located within a few hundred μm from type (i) assemblages (Figure 111A) or may be locally associated with type (i) FI and rare vapor inclusions (iv) in cracks (Figure 111B). In PB and AD vein quartz, type (ii) inclusions are associated to aqueous inclusion type (iii)(Figure

Fluid inclusion type	Microphotograph	Phases at room T°	Microthermometric measurements (mean with 1σ value)	Petrographical position	Type of quartz-host	Deposit name
i - brine inclusions	25 µm 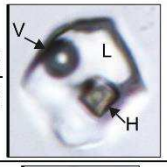	H_2O Liquid (L) Vapor (V) Halite (H)	Te = -48.4 ± 8 °C Tm = -30.7 ± 8 °C Th = 214 ± 13 °C Tmh = 194 ± 2 °C	Fracture filling - secondary	Type 2a stratabound	Victoria (VT) - Crabioules (CR)
ii - aqueous-carbonic inclusions	13 µm 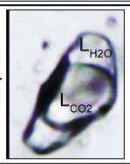	H_2O Liquid (L) CO_2 Liquid (L)	Fracture $TmCO_2$ = -59 ± 3 °C Tmclath = 4 ± 3 °C $ThCO_2$ = 8 ± 7 °C Th total = 301 ± 7 °C Cluster $TmCO_2$ = -63 ± 3 °C Tmclath = 1.5 ± 2 °C $ThCO_2$ = -32 ± 4 °C Th total = 317 ± 8 °C	Primary zonations - primary / fracture filling - (pseudo) secondary	Type 2b vein	Argut-dessus (AD) - Arre (AR) - Pale Bidau (PB)
					Type 2a stratabound	Crabioules (CR) - Margalida (MG) - Victoria (VT)
iii - aqueous inclusions	10 µm 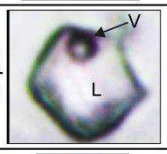	H_2O Liquid (L) Vapor (V)	Blue field Te = -47.9 ± 6 °C Tm = -24.2 ± 5 °C Thh = -26.1 ± 2 °C Th = 174 ± 9 °C Green field Te = -24.2 ± 4 °C Tm = -16.4 ± 1 °C Thh = -6.3 ± 1 °C Th = 259 ± 12 °C	Primary zonations - primary / fracture filling - secondary	Type 2b vein	Argut-dessus (AD) - Arre (AR) - Pale Bidau (PB) - Pale de Rase (PR)
					Type 2a stratabound	Margalida (MG)
iv - vapor-rich inclusions	5 µm 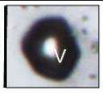	Vapor (V)	-	Primary zonations - primary Fracture filling - secondary	Type 2b vein	Arre (AR)
					Type 2a stratabound	Victoria (VT) Crabioules (CR)

Figure 110. Synthesis of the four types of fluid inclusions analysed in quartz from the studied deposits. Mean contents of microthermometric analyses are given (Abbreviations: Te: eutectic temperature; Tm: last melting temperature; Th: homogenization temperature to liquid phase; Tmh: last melting temperature of halite. $TmCO_2$: CO_2 melting temperature; $ThCO_2$: CO_2 homogenization temperature to liquid phase; Thh: hydrohalite melting temperature.

111C and D) and consist of 20-80 vol.% liquid CO_2. In the AD sample, type (ii) FI are aligned along primary growth zones in quartz and in PB samples, these FI form pseudo-secondary trails.

Aqueous FI (iii) occur exclusively in vein-type mineralization. They are the only FI type present in the PR deposit, where they are aligned along growth zones in quartz (Figure 111E). They consist of 10-15 vol.% vapor and 85-90 vol.% liquid and range from 10 to 60 μm in size. At PB (samples 10 and 12), type (iii) occurs as pseudo-secondary and secondary inclusions ranging in size from 5 to 20 μm and showing a vapor volume of about 10 vol. % (Figure 111C and D).

In the AR sample, CL observations reveal the presence of primary growth banding in quartz (Figure 112A and B) and the existence of three sub-generations of quartz annoted in the Figure 112A. Comb texture is common and quartz crystals are often intersected by late-cracks. The quartz contains type (iii) FI ranging from 5 to 40 μm in size and containing a vapor bubble of 10-15 vol.%.

They are locally associated to low-density vapor inclusions with a size varying from 5 to 15 µm (Figure 112C and D). Only type (iii) is associated with cracks (Figure 112E).

In sphalerite, FI assemblages are located in dark domains of the coarse grains with no preferential orientation (Figure 113A and B). The light domains present in coarse grains but also in recrystallized grains are systematically devoid of FI. Microscopic observations in visible or near

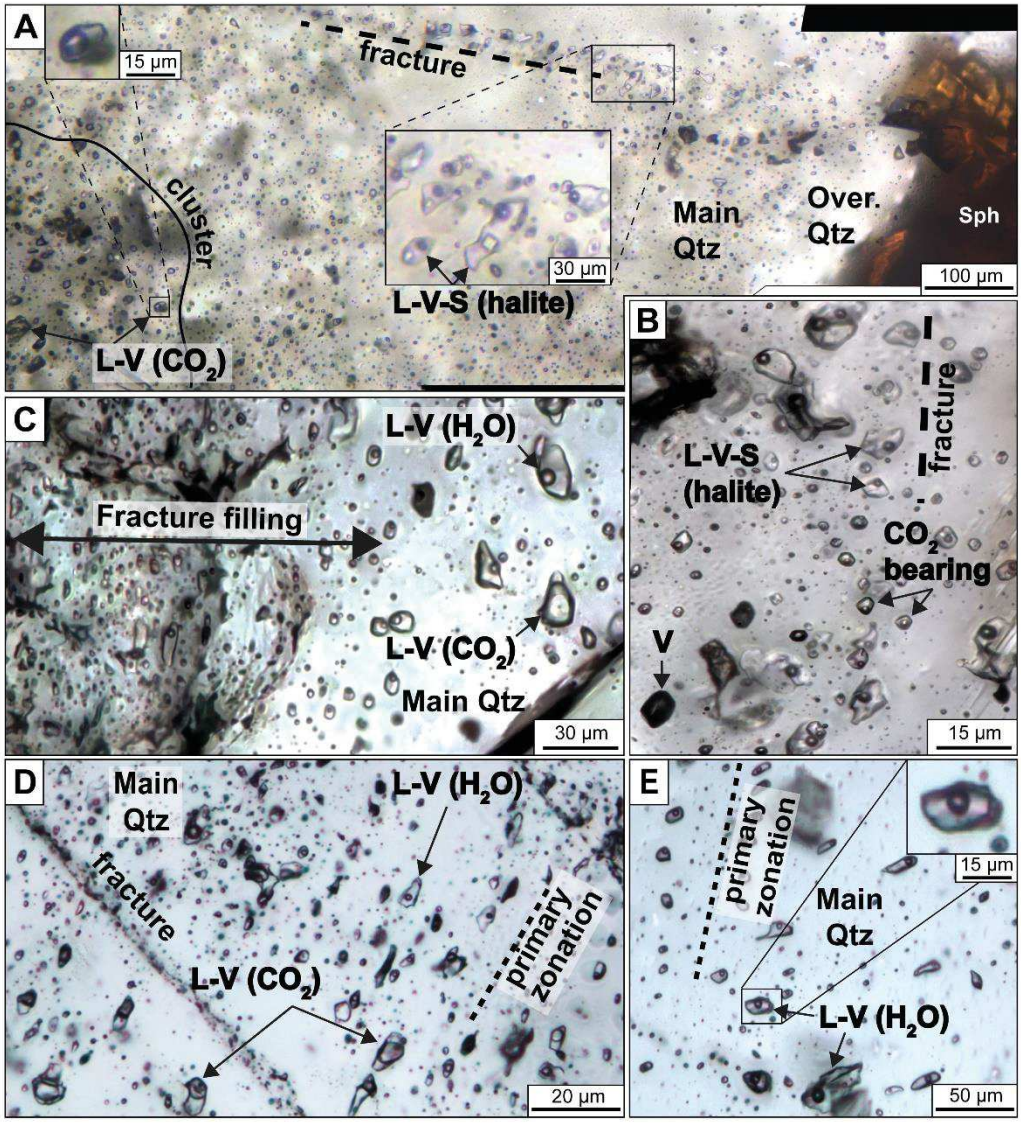

Figure 111. Fluid inclusions in quartz (Qtz). A. Secondary liquid-vapor aqueous fluid inclusions with presence of salt in cracks (brines) and CO_2-bearing fluid inclusions in "cluster" (Victoria, VT; stacked picture). B. Secondary brines associated to CO_2-bearing and vapor-rich fluid inclusions in cracks. (Crabioules, CR; stacked picture). C. Two-phase aqueous fluid inclusions filling fracture or occuring as pseudosecondary aqueous inclusions associated to CO_2-bearing fluid inclusions (Pale Bidau, PB12, stacked picture). D. Primary two-phase aqueous associated to CO_2-bearing fluid inclusions in primary zonation (Argut-dessus-AD; stacked picture). E. Primary liquid-vapor aqueous fluid inclusions (Pale de Rase, PR; stacked picture).

infrared light did not allow us to visualize the phases present in the FI trapped in sphalerite. This may be due to negative crystal shape of the inclusion vacuoles (Bonev and Kouzmanov 2002).

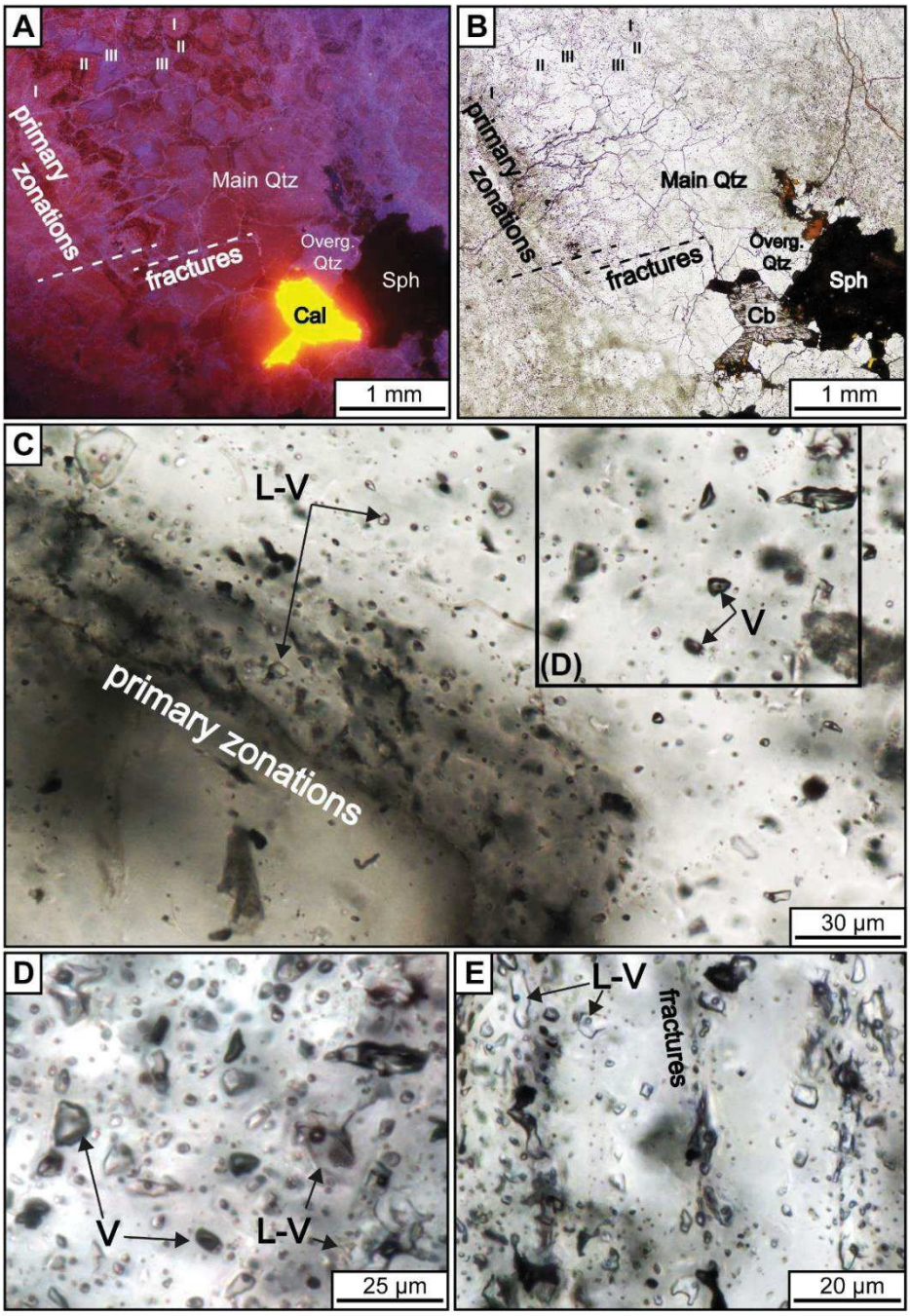

Figure 112. Fluid inclusions in quartz (Qtz) of the vein mineralization from Arre (AR). A. Ore mineralization observed with cathodoluminescence. Note the presence of primary zonation in quartz which can be intersected by secondary cracks (Sph: sphalerite; Cal: calcite). The three sub-generations of quartz (I, II, III) are noted at the upper-left part of the microphotograph. B: Corresponding area in transmitted plane polarized light. C. Two-phase aqueous fluid inclusions associated to vapor-rich inclusions and aligned along quartz primary zonations. D. Zoom with association of primary vapor-rich inclusions and two-phase aqueous fluid inclusions (stacked picture). E. Secondary two-phase aqueous fluid inclusions in cracks (stacked picture).

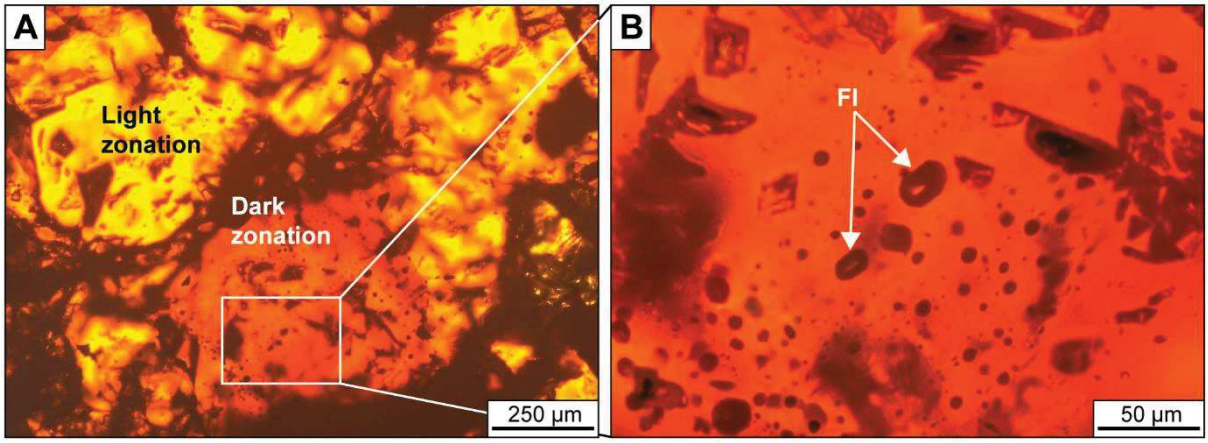

Figure 113. Fluid inclusions in sphalerite (transmitted plane polarized light). A. Sphalerite with dark and light domains. Dark domains are only present in coarse porphyroclastic sphalerite. B. Zoom on dark domain in sphalerite showing multiple fluid inclusions.

8.1.6.3 Microthermometry

A total of 383 individual fluid inclusions grouped in 65 FI assemblages from two types of mineralizations (stratabound and vein-type) in seven deposits were investigated by microthermometry in quartz at low temperature (< 0°C) to determine melting of the FI and related salinity and at high temperature (generally > 0°C) to determine homogenization temperature.

In type (i) brines inclusions, Tm is low (mean of ~ -30 °C) which is consistent with the presence of $CaCl_2$ in relative high quantity. Fluid inclusions from CR and VT show high salinities (mean values of 22 wt.% NaCl eq. with 12 wt.% $CaCl_2$ eq.) and moderate Th (175 to 240 °C).

In type (ii) FI, CO_2 melting ($TmCO_2$) is below -56.6 °C (Figure 110). Homogenization to the liquid phase ($ThCO_2$ = LCO_2-V→LCO_2) and total homogenization (Thtot = LCO_2-Laq→L) are plotted for type (ii) FI in the Figure 114A. Two groups of data appear: Type (ii) inclusions form large clusters (Figure 111A) and exhibit lower $ThCO_2$ (<-10 °C; Figure 114A) compared to type (ii) FI contained in isolated cracks with higher $ThCO_2$ (>-10 °C). Fluid inclusions in cracks from the stratabound mineralization show similar values for $ThCO_2$ (~– 5 to 20 °C) and Thtot (~287 to

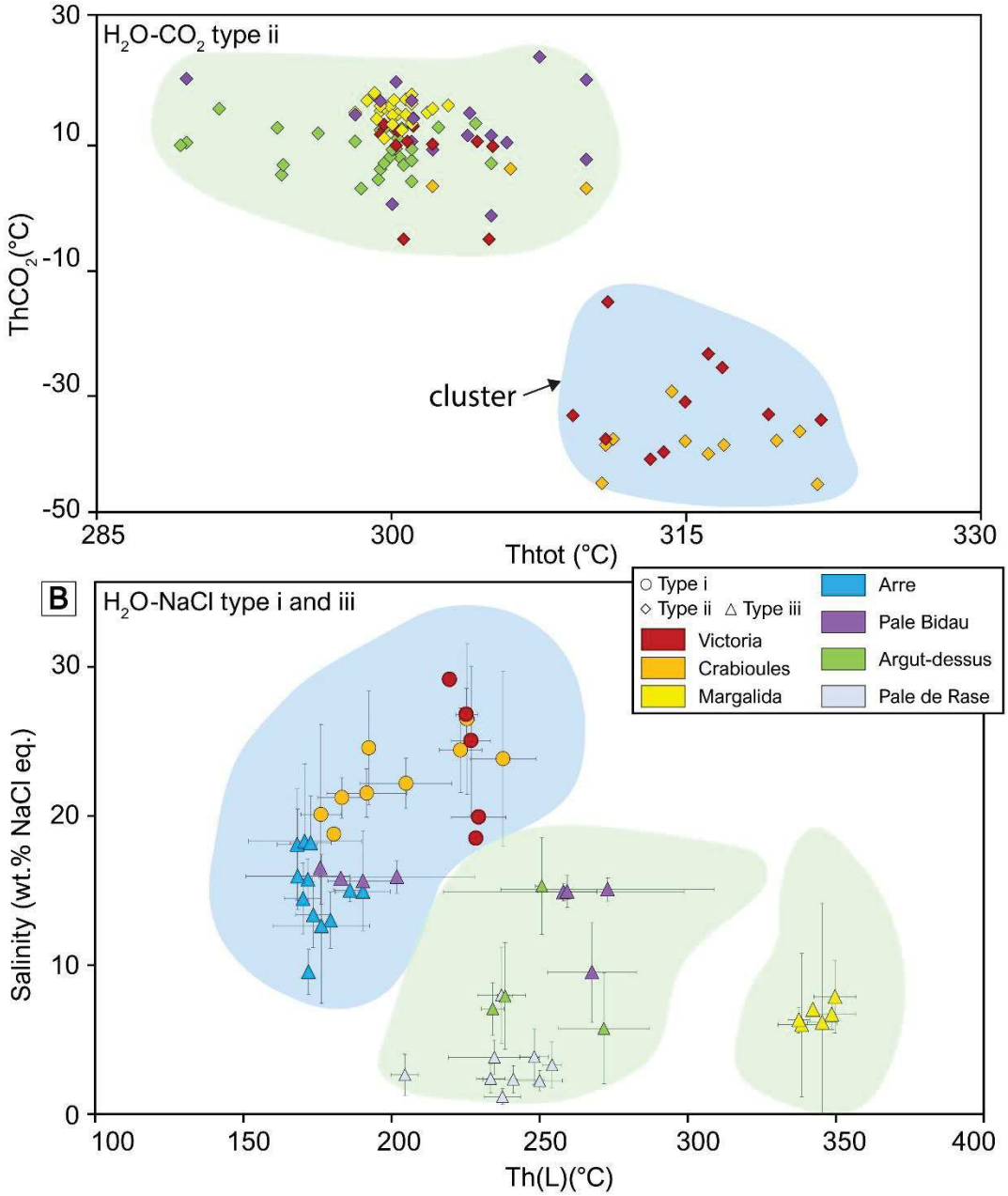

Figure 114. Results of microthermometric analyses on fluid inclusions. A. CO_2 homogenization temperature (°C) vs total homogenization (°C) in CO_2-bearing fluid inclusions. Note the apparition of VT and CR fluid inclusions in cracks close to PB, AD, and MG fields and the difference between VT and CR fluid inclusions in clusters, which present lower Th_{CO2}. B. Salinity (wt.% NaCl eq.) vs aqueous homogenization temperature (°C) in two phase fluid inclusions assemblages. Related full fluid inclusions analyses are in transparence. Note the presence of four different fields not always related to the deposit. Complete dataset can be found in Table 19-26-supp data.

310 °C) that primary FI from the vein-type with type (ii) and (iii) FI (PB and AD deposits) and secondary inclusions from stratabound MG quartz with type (ii) FI.

In type (iii) FI, salinity and homogenization temperatures (Th) are not homogeneous. Type (iii) FI from the AR vein deposit have low melting temperature (mean Tm of -24 ± 2 °C) and contain relative high amount of $CaCl_2$. Salinities and homogenization temperatures (Th) are close to those measured from type (i) FI of the CR and VT deposits hosted in cracks (mean values of 16 wt.% NaCl eq. with 9 wt.% $CaCl_2$ eq.) (Figure 114B). Similar salinities and Th are recorded in secondary type (iii) FI with 172 ± 3.4 °C and 24 ± 1.1 wt.% NaCl eq. compared to primary type (iii) FI with 176 ± 7.2 °C and 26 ± 1.3 wt.% NaCl eq. Coexisting aqueous FI with vapor-phase inclusions are commonly observed. In some fluid inclusions from one sample in PB (sample PB10), FI considered as pseudosecondary due to petrographic evidences lie on the equivalent salinity and Th field to AR type (iii) FI; (Figure 8B).

Pale Bidau, AD, and PR deposits show substantial salinity and Th variations for type (iii) inclusions (Figure 114B). Melting temperatures (Tm) vary between -9.6 ± 5°C and -2 ± 2°C for PB and PR samples respectively which show relative low amount of $CaCl_2$ comparatively to NaCl. Primary FI (iii) from PB (sample 12), AD and PR samples exhibit similar Th in the range of ~240-260 °C. Salinities in these samples vary between 1 and 13 wt.% NaCl eq. with PR presenting the lowest values (< 5 wt.% NaCl), AD the median values (5-15 wt.% NaCl) and PB samples (10-15 wt.% NaCl) the higher salinity. In PB (sample 12), some FI are described as secondary and appear with the same salinity (~15 wt.% NaCl) but lower Th (~200 °C) than primary FI. The higher Th (344 ± 5.1 °C) are recorded in MG type (iii) FI which show relative low salinities (mean values of 8 ± 1.5 wt.% NaCl eq.)(Figure 114B).

Microthermometric analyses and petrographic observations can be summarized as follow:

-No distinction between FI from Type 2a and 2b mineralization exist in our dataset.

-Two types of fluid are observed in fluid inclusion in this dataset:

- High-salinity (10-30 wt.% NaCl) and low homogenization temperatures (Th < 250 °C) fluid, with high amounts of $CaCl_2$ ~ 10 wt.% $CaCl_2$ eq.) appears in secondary type (i) and (ii) from VT-CR and primary-secondary type (iii) inclusions from AR. In (ii) FI, temperature of CO_2 melting ($TmCO_2$) is systematically below -56.6 °C, indicating presence of minor CH_4 or N_2 associated to CO_2 especially in the stratabound mineralization (CR and VT). In PB, this fluid is reported in numerous pseudosecondary FI from type (ii) and (iii) that present homogenization temperature between 150 to 200 °C.
- Low-salinity (1-15 wt.% NaCl) and high homogenization temperature (>200 °C) fluid appears in AD-PR primary and most of the PB pseudosecondary FI of types (ii) and (iii).

The higher homogenization temperatures reach ~ 350 °C in MG secondary fluid inclusions.

-Homogenization temperatures ($ThCO_2$) of type (ii) pseudosecondary and primary FI from PB and AD are similar to those of type (ii) secondary inclusions from MG, VT and CR ($ThCO_2$(L) between -10 to +20 °C). Fluid inclusions clusters in VT and CR show higher Thtot and lower $ThCO_2$.

8.1.6.4 LA-ICP-MS results

A total of 246 individual FI were analyzed in quartz from stratabound (CR and VT) and vein-type (PB and AR) mineralizations as well as in sphalerite (AR vein mineralization). Trace element contents are indicated in Figure 115 sorted by mineralization-type and FI type and their Th°/salinity from microthermometric data are reported (Figure 115A).

Systematic high contents in Pb, Zn and Mn are present in brines (i) from VT inclusions with mean contents of 7 300, 6 800 and 5 960 ppm respectively (Figure 115B). In this sample type (ii) FI show similar patterns. Zinc, Pb and Mn contents appear equivalent in CR compare to VT inclusions (Figure 115B) even if FI from CR contain substantial lower values especially in Pb. Compare to type (i) inclusions, Pb and Mn contents appear lower in type (iii) FI (from PB and AR) with values mostly below few thousands of ppm (Figure 115B).

Strontium, Rb and Cs contents are relatively similar between the three types of FI with values between 1 000 and 10 000 ppm for Sr and between 10 and 1 000 ppm for Rb and Cs. Nonetheless, type (ii) and (iii) FI from PB present lower Sr essentially close or below 1 000 ppm Sr. Relatively higher values in Sr and Cs are reported in AR from secondary FI compared to primary inclusions with mean contents of 9 400 and 5 600 ppm respectively. In PB inclusions, Sr contents are lower and mostly close to 1 000 ppm (Figure 115C). In PB (from PB10 sample), all type (ii) FI exhibit low Cs concentrations, between ~10 and 100 ppm.

Contents of Li, B and Br are homogeneous within localities and FI types (Figure 115D) with average contents of 1 430, 2 000 and 7960 ppm respectively, even if Br from VT type (i) inclusions may reach up to few tens of thousands of ppm (Figure 115D).

Potassium and Ca present average concentrations in all the analysed FI of 1.5 and 4.9 wt.% respectively (Figure 115E). Their ratio (K/Ca) reaches 0.87 in the entire dataset and 0.7 in the type (iii) inclusions from AR hosted in quartz and sphalerite, but Na remains the main alkali component

of the studied FI with content up to 13 wt.% Na (Figure 115D and E; Figure 116). Higher concentrations for K and Ca elements are observed in type (iii) FI from AR with 2.15 and 5.58 wt.% for K and Ca respectively which is similar to the VT and CR inclusions (Figure 116A and B). Lower concentrations in K and Ca appear in PB inclusions with mean contents of 6 500 and 13 900 ppm respectively. Barium values are constant with average values of ca. 1 600 ppm in all the FI.

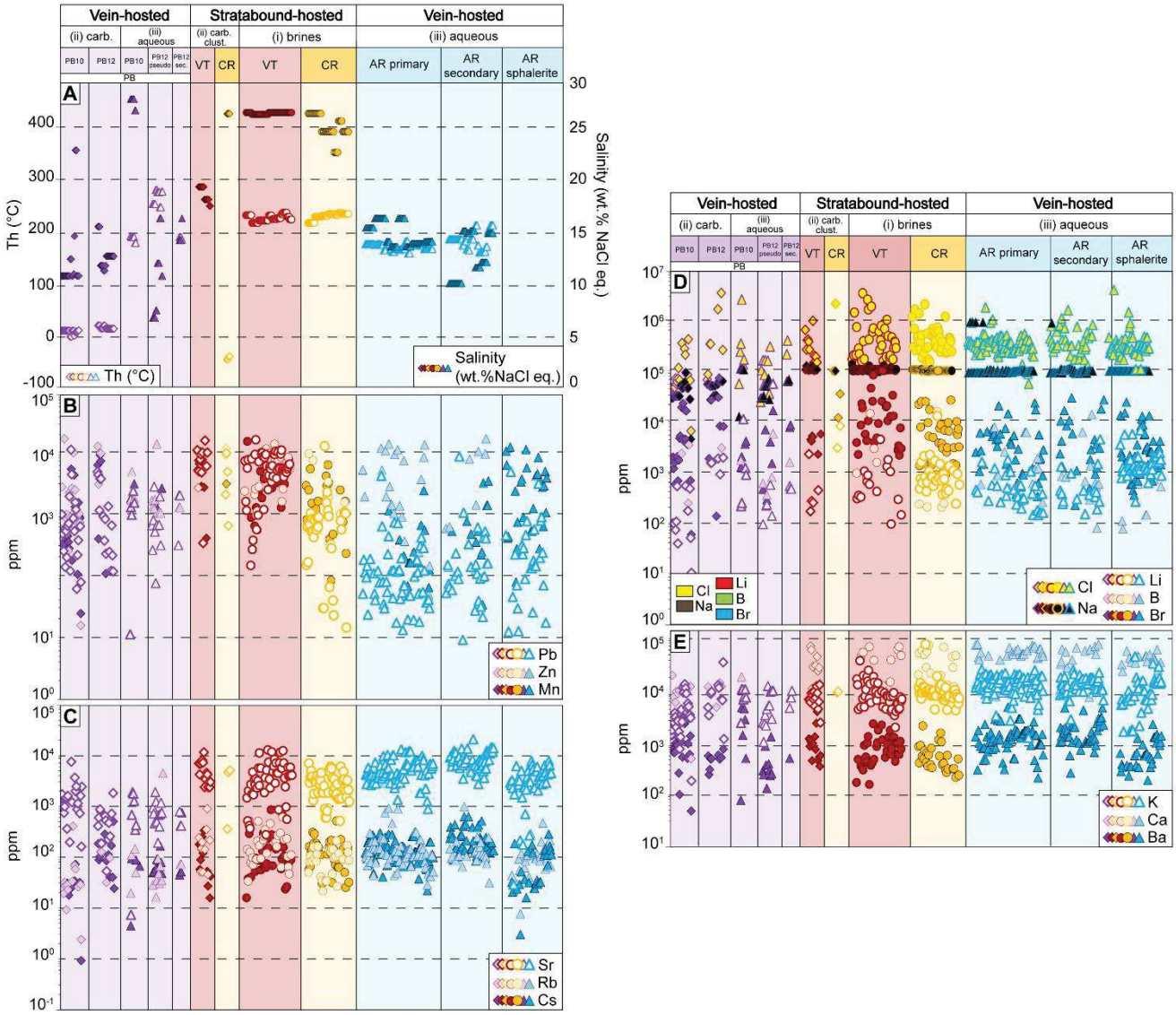

Figure 115. LA-ICP-MS results related to microthermometric datas for all the fluid inclusions analyses, performed on quartz and sphalerite, in Pale Bidau (PB10 and 12; upward triangle), Victoria (VT; circle), Crabioules (CR; circle) and Arre (AR; square). A. Homogenization temperature (Th= aqueous or Thtot= CO_2) vs salinity (wt.% NaCl eq.). B-E. Element contents (LA-ICP-MS analyses) in fluid inclusions. Complete dataset can be found in Table 26and Table 28-supp data with detection limit for each analyses (from SILLS software).

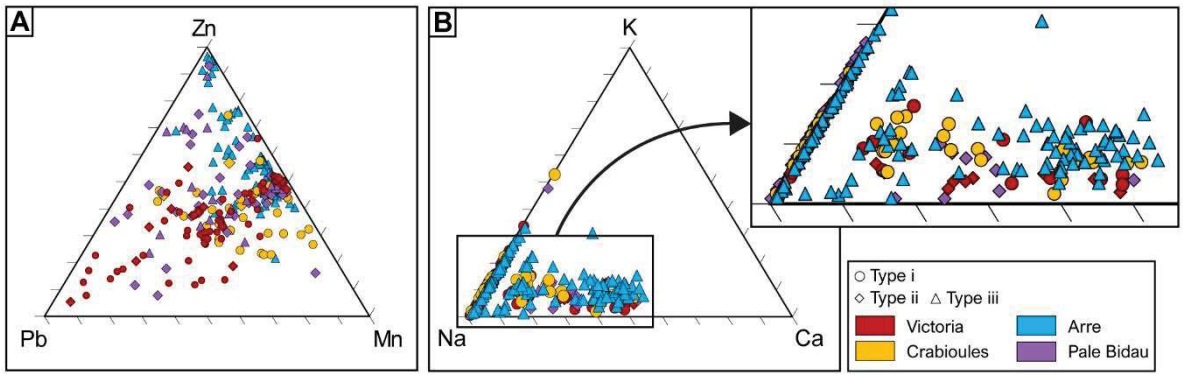

Figure 116. A. Zn-Pb-Mn diagram of the LA-ICPMS fluid inclusion dataset showing large enrichment in Zn comparatively to low Pb and Mn content for AR fluid inclusions. In VT and CR fluid inclusions, equivalent enrichment in Zn, Pb and Mn is present. B. Na-K-Ca diagram of the LA-ICPMS dataset.

8.1.7 Discussion

8.1.7.1 P-T-X characteristics of the mineralizing fluids

After careful petrographical observations to avoid measurements on FI assemblages impacted by post-entrapment modifications (necked or leached), microthermometric analyses performed on eight samples from two mineralization types in seven Pyrenean Pb-Zn deposits evidences two distinct fluid signatures which are not related to the mineralization-type or locality: 1) a low-salinity (1-15 wt.% NaCl eq.)-high-temperature (200-360 °C) fluid hosted in primary FI at AD, PR, PB veins and (pseudo)secondary FI at MG stratabound ore and PB veins. 2) a high-salinity (~ 15-30 wt.% NaCl eq.)-low temperature (< 230 °C) fluid rich in Ca and K-hosted in primary or secondary aqueous FI at AR and in secondary CO_2-bearing inclusions in clusters at VT and CR stratabound ore.

The coexistence of vapor-rich and aqueous FI (Fig. 4C) may evidence boiling conditions *(Ramboz et al. 1982; Hedenquist 1991*) even if variations in Th and salinity especially in AR remain relatively poor *(Canet et al. 2011)*. Using of the minimum Th measured (Th~140°C; Figure 114B) in the H_2O-NaCl system *(Steele-MacInnis et al. 2011)*, the minimum formation pressure for this mineralization is below 20 bars corresponding to a depth of less than ~100 m with direct estimation of the fluid pressure from the boiling curve (*Diamond 2003*). This is a minimum pressure as indicated by *Bauer et al., (2018)* which shows an important influence of the CO_2 content, even in small quantity, on the obtained pressure. The low-salinity fluid was trapped at relatively higher

pressure compared to the highly-saline fluid stage. Considering Th between 200 and 300 °C, pressure related to low-salinity fluid is spread between 15 to 100 bars with a mean pressure around 30 bars for PB and PR inclusions.

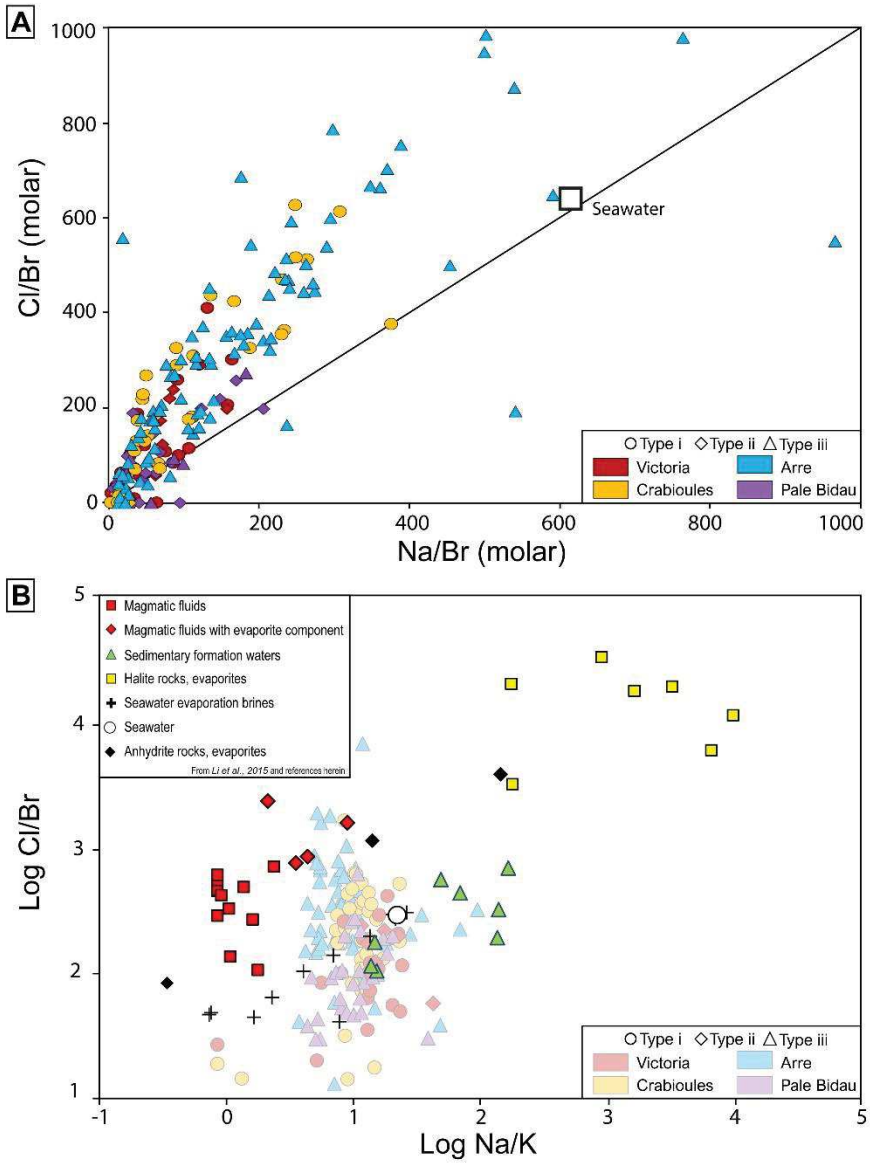

Figure 117. A. Na-Cl-Br systematics of measures inclusion fluids composition from CR, VT, AR and PB deposits. B. Comparison based on ratio Cl/Br vs Na/K of FI analysed in this study with the compositon of seawater, representative analyses of magmatic fluids, magmatic fluids involving an evaporite component, sedimentary formation waters, residual brines after various degrees of seawater evaporation, and halite-dominated versus anhydrite-dominated evaporite rocks (data synthetized by Li et al., 2005). Legend is referred to (A) for the FI analysed in this study.

8.1.7.2 Fluid composition and origin

The ratio between several dissolved salts (Cl, Br, Na) in fluid inclusions is used to understand the possible source and evolution of fluids circulating in the crust (*Walter et al. 1990; Kesler et al. 1995; Banks et al. 2000; McCaig et al. 2000; Fusswinkel et al. 2013*). In the studied FI from Pyrenean Pb-Zn deposits, this ratio exhibits no important difference between FI types or stratabound and vein mineralization (Figure 117A). Most of the data are below the seawater value (from *McCaffrey et al. 1987*), indicating a predominant seawater evaporation origin for the brines *(Walter et al. 1990; Stoffell et al. 2008*). The data do not lie exactly on the 1:1 line, especially for the higher values, indicating additional Na-Ca exchange *(Walter et al. 1990; Kesler et al. 1995)*. The ratio of Cl/Br and Na/K do not discriminate between mineralization type of FI types (Figure 117B; values from *Li et al., 2015* and referenced herein). They essentially plot into the field of seawater evaporation trajectory and sedimentary formation waters (Figure 117B) which is consistent with a predominant evaporation process as source for the brines.

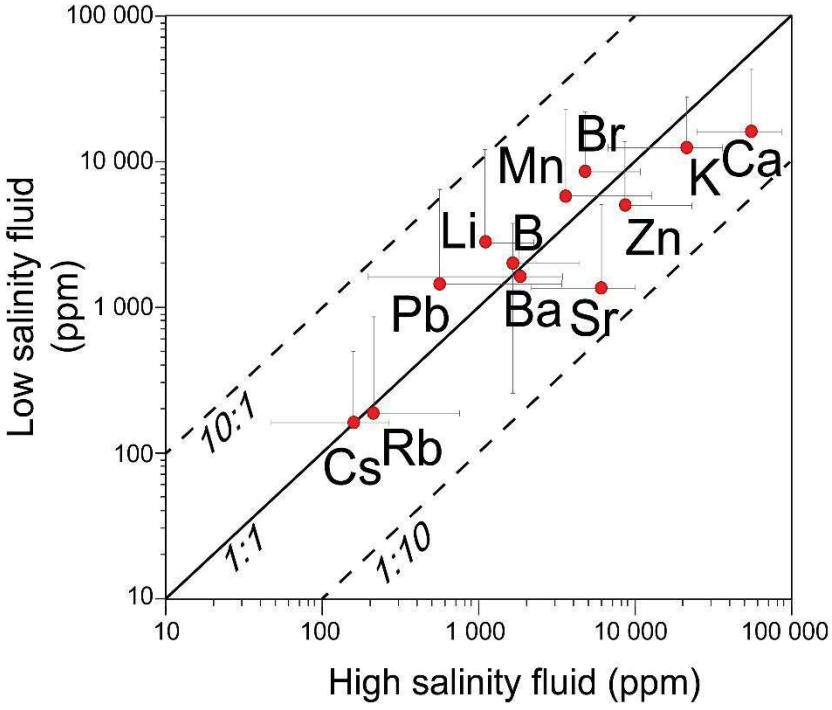

Figure 118. Comparison of trace element data from fluid inclusions in low and high salinity fluid. Low salinity fluid is only considered in Pale Bidau (PB) and high salinity fluid appear in Arre (AR), Victoria (VT) and Crabioules (CR). High salinity fluid is subsequently interpreted as Mesozoic in age and low salinity fluid as Late-Variscan.

Compositions of the two types of fluids (high and low salinity) in different cations is compared to precise if some differences appear. Calcium is generally high (mean value of ~ 5.4 wt.% Ca) in the high salinity fluid (Figure 116), K is low (<1-2 wt.%) and Mg not detected which

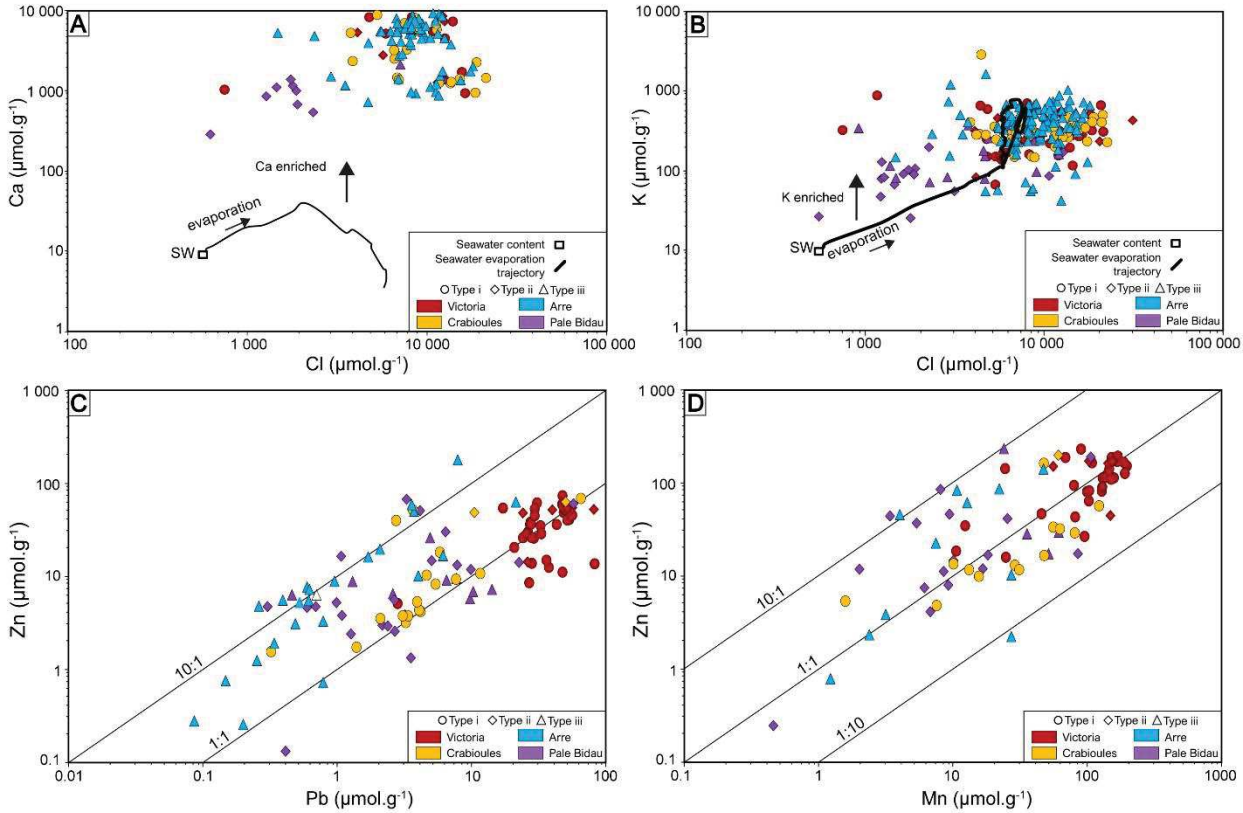

Figure 119. A-B. Ca and K vs Cl plots for fluid inclusions in all deposits. Also shown are seawater composition and the seawater evaporation trajectory, from Mc Caffrey et al. (1987). C-D Zn vs Pb and Mn correlation plots.

correlate to other Pyrenean vein deposit like in Cierco (4.4 to 4.8 wt.% Ca, *Johnson et al., 1996*). Low salinity fluid from PB (sample 12) is lower in Ca and K with mean contents of 1.5 and 1.2 wt.% respectively (Figure 119). Calcium or K enrichment (Figure 119A and B) and Mg depletion according to seawater composition are interpreted as presence of dissolution or precipitation of Ca-, K- or Mg- enriched phases respectively such as calcite or dolomite (*Stoffell et al. 2008*).

Type (i) and (ii) inclusions from VT and CR are enriched in metals (Pb, Zn, Mn) compare to AR and PB inclusions (type (ii) and (iii); Figure 119C). Zinc and Lead concentrations are usually correlated in quartz-hosted fluid inclusions as the results of similar geochemical behavior *(Yardley 2005; Wilkinson et al. 2009; Fusswinkel et al. 2013*). This ratio typically plots between 1:1 and 10:1 (Figure 119C) which probably correspond to a saturation limit (*Yardley 2005*) beyond which trace metals precipitate as sphalerite or galena. Type (i) and (ii) inclusions from VT and CR have a lower Zn-Pb ratio than AR and PB inclusions. This fluid is assumed to be related to formation of Pyrenean vein mineralization and this lower ratio in VT and CR is certainly responsible for absence of vein sphalerite in these deposits (Ovejero Zappino 1991; Pujals 1992; Cugerone et al. 2018b) whereas in PB and AR deposits, abundant Zn mineralization is described which correlates with

higher Zn-Pb ratio. Same trend exists between Zn and another metal Mn with most of the VT and CR points close to the 1:1 line (Figure 119D).

8.1.7.3 Comparison with similar Pb-Zn ore and implications on the timing of vein mineralization/deformation

No datation analysis is shown in this study but comparison with other mineralizing systems in term of fluid data supported by field evidences may bring closer studied Pyrenean mineralizing stages with other regional fluid systems and indirectly may evidence Pb-Zn mineralization stages.

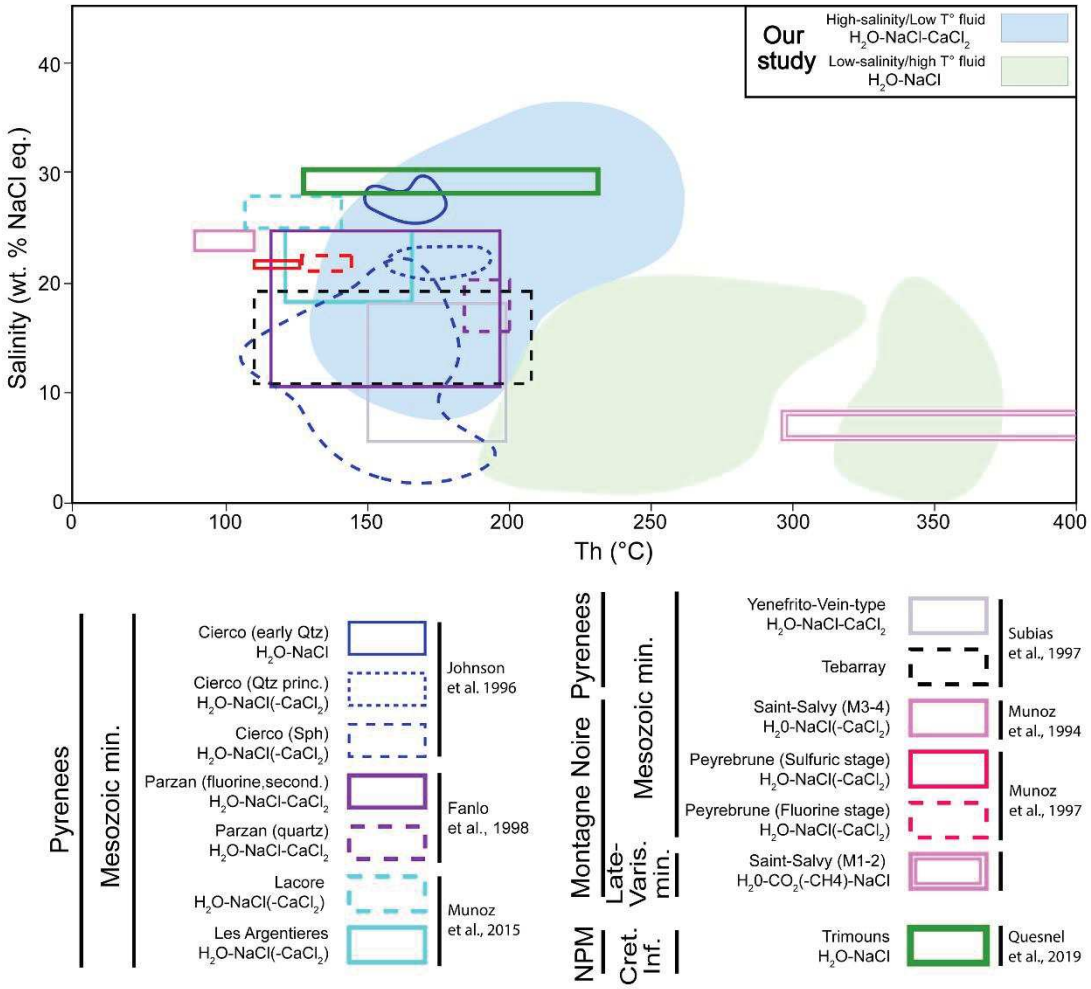

Figure 120. Plot of salinity (wt.% NaCl eq.) vs homogenization temperature (Th) for the aqueous fluid inclusions from this study and between the studied Pb-Zn mineralizations and other studied deposits in the Pyrenees or the Montagne Noire.

Hydrothermal fluids with high-salinity and low-temperature characteristics are documented in Pyrenees as well as in other Variscan terranes. *Johnson et al. (1996)* studied fluid inclusions in the

Pyrenean vein deposit of Cierco (location in Figure 107B) describing two-phase aqueous FI with Th between 150 and 200 °C and salinity between 20 and 30 wt.% NaCl eq. in quartz and below 20 wt.% NaCl eq. in sphalerite. These measurements totally overlap with the field of our high-salinity and-low-temperature FI (blue field; Figure 120). Other fluid inclusion studies were performed in Les Argentieres-Lacore (Aulus), Yenefrito and Parzan vein-deposits (*Subias et al. 1997; Fanlo et al. 1998; Munoz et al. 2016)* and they all describe high-salinity and low-temperature fluids which correlate with our dataset (Figure 120). According to these authors, these Pb-Zn vein mineralizations are Mesozoic (Triassic to Jurassic? in age) which is validated by numerous studies of Alpine fluids in the Pyrenean thrust *(Grant et al. 1990; Banks et al. 1991; Henderson and McCaig 1996)* and thus demonstrating a similar mineralization age for AR and part of the PB veins. The signature of these highly-saline and low-temperature fluids is closer to the Mesozoic Saint-Salvy (i.e. M4 Zn-Ag(-Ge)) and Peyrebrune ore mineralizations in the Variscan Montagne Noire *(Munoz et al., 1994, 1997;* Figure 120) even if Th appear to be slightly lower (80-150 °C). This is also coherent with other Mesozoic hydrothermal Pb-Zn(-F) systems in Central-Eastern Europe (*Macquar and Lagny 1981; Charef and Sheppard 1988; Munoz et al. 1999; Seifert and Sandmann 2006; Boiron et al. 2010*) where fluids have interacted with evaporites in basin during the pre-Pyrenean-Alpine orogeny.

Recent fluid inclusion study on Trimouns talc-chlorite deposit (North Pyrenean Massif) describe the circulation of brines and Mg metasomatism during Cretaceous times *(Schärer et al. 1999; Boutin et al. 2016)* related to high-salinity and low-temperature fluids (28.6-30.5 wt.% NaCl eq. and 130 to 230 °C) (*Quesnel et al. 2019*) which correlate with our dataset.

Low-salinity and high-temperature fluids are not well-documented in the Pyrenees but seem typical of Late-Variscan fluids in other Variscan terranes like in the Montagne Noire *(Munoz et al. 1994*). Microthermometry on FI from MG shows a similar fluid signature as the Late-Variscan M3 mineralization from the Saint-Salvy deposit (green field; Figure 120). Margalida deposit is located in the damaged zone of the pluri-km Bossost fault (Cugerone et al. 2018b) supposed to be Late-Variscan and/or Alpine in age *(García-Sansegundo 1992; Mezger and Passchier 2003; Mezger 2009; Lopez-Sanchez et al. 2018*). Fluid inclusions in MG quartz do not record an Alpine event and Bossost fault is only Late-Variscan according to our results.

The AD and PR fluid inclusions with low-salinity and high-temperature characteristics are not in the field of AR fluid and are probably related to another mineralizing event, certainly to a Late-Variscan stage (Figure 120) even if their homogenization can be as lower as 200 °C. In PB samples, the data are close to AR or AD-PR fields (Figure 114). The PB deposit is certainly linked to a Late-

Variscan mineralizing event and was overprinted by important hydrothermal fluid circulation during the Mesozoic.

Previously only interpreted as Late-Variscan in age (Cugerone et al. 2018b), this study questions indirectly this timing with fluid inclusion analysis and regional comparison with other Pb-Zn mineralizations. Microthermometric and chemical data on fluid inclusions show two signatures for the epigenetic vein systems which question the probable presence of two types of fluids, Late and Post Variscan. The latter (Arre and Anglas deposits) may be related to the widespread hydrothermal event occuring with the opening of the Atlantic Ocean during Trias-Jurassic ages *(Vergés et al. 2002; Boiron et al. 2010; Cathelineau et al. 2012; Burisch et al. 2017*). The understanding of the timing of mineralization have important implications on the deformation age for these vein mineralizations (Cugerone et al. 2018b, 2019). This new constraint on AR vein formation probably related to Mesozoic mineralizing event discredits a Variscan (Carboniferous-Permian) deformation overprint. Variscan and Pyrenean structures exhibit similar orientations in the PAZ which make difficult the identification of a precise deformation event on the field. A pronounced E-W cleavage in sphalerite is parallel to D_2 Late-Variscan deformation in calc-schist (Cugerone et al. 2018b, 2019). Following this fluid inclusion study, the deformation in Arre-Anglas sphalerite like in other deposits (Anglas, Cierco, Parzan, Yenefrito) may be linked to the subsequent orogenic event, the Pyrenean orogeny (85-20Ma). Precoce and local LP/HT metamorphism (~120-85 Ma) and related Na-Ca metasomatism (*Fallourd et al. 2014)* may have imprinted the ore mineralization due to similar fluid signature *(Quesnel et al. 2019)*. Pyrenean deformation is supposed to be poorly developed in the PAZ *(Denèle et al. 2014; Cochelin et al. 2017a)* and to reactive only some shear zones (Merens fault, *Carreras and Cirés, 1986; Mezger et al., 2012*).

8.1.8 Conclusion

This study demonstrates the importance of fluid inclusion in deformed/metamorphosed ore mineralization to unravel polyphased mineralizations and replace them in geodynamic setting. Two distinct fluid types at the origin of Pb-Zn vein mineralizations are shown in this study: i) low- to medium-salinity (<20 wt.% NaCl eq.) and high temperatures (200-350 °C) fluid which is the more probable mineralization stage for the Pale Bidau (PB), Argut-dessus (AD), or Pale de Rase (PR) sphalerite; ii) highly-saline (15-35 wt.% NaCl eq.) -low temperature (< 200 °C) fluid with some enrichments in Ca, K appears in the Arre (AR) and locally in Pale Bidau (PB) deposits, and also observed in secondary fluid inclusions in Victoria (VT) and Crabioules (CR). This fluid shares some similarities with numerous other mineralized veins mineralizations reported as Mesozoic in age

described in the Pyrenees (Cierco, Parzan, etc.) or in the Montagne Noire (Saint-Salvy, Peyrebrune). Considering Arre as Mesozoic mineralization has important implications in the period of deformation and recrystallization of sphalerite vein because this deformation stage cannot be Variscan but probably associated to subsequent Pyrenean-Alpine orogeny.

These two fluids are recorded in stratabound mineralization as secondary type (i) or (ii) FI. In these inclusions from VT and CR, Pb, Zn, and Mn are globally higher than in FI hosted in vein mineralization but the ratio between these elements (Zn vs Pb and Zn vs Mn) is between 1:1 and 10:1 lines. In the Margalida (MG) deposit, only low-salinity fluids is reported in secondary FI probably associated to the circulation of hydrothermal fluid during Late-Variscan activation of the Bossost fault in Margalida. This study evidences that fluid inclusion analyses in deformed environment completed at regional scale may be relevant to understand genesis of ore mineralization.

8.1.9 Acknowledgment

This study was funded through the French national program "Référentiel Géologique de France" (RGF-Pyrénées) of the French Geological Survey (Bureau de Recherches Géologiques et Minières; BRGM). Bénédicte Cenki-Tok acknowledges funding from the European Union's Horizon 2020 research and innovation program under grant agreement No 793978. The authors also acknowledge the PHC Germaine de Stael funding and the handling of Alain Chauvet. The authors gratefully acknowledge Christophe Nevado and Doriane Delmas for the exceptional thin sections preparation.

8.1.10 References

Alonso JL (1979) Deformaciones sucesivas en el area comprendida entre Liat y el Puerto de Orla - Control estructural de los depositos de sulfuros (Valle de Aran, Pirineos Centrales). Tesis Licenciatura, Univ Oviedo 26p

Baatartsogt B, Schwinn G, Wagner T, Taubald H, Beitter T, Markl G (2007) Contrasting paleofluid systems in the continental basement: A fluid inclusion and stable isotope study of hydrothermal vein mineralization, Schwarzwald district, Germany. Geofluids 7:123–147. doi: 10.1111/j.1468-8123.2007.00169.x

Bailie RH, Reid DL (2005) Ore textures and possible sulphide partial melting at Broken Hill, Aggeneys, South Africa I: Petrography. South African J Geol 108:51–70. doi: 10.2113/108.1.51

Banks DA, Da Vies GR, Yardley BWD, McCaig AM, Grant NT (1991) The chemistry of brines from an Alpine thrust system in the Central Pyrenees: An application of fluid inclusion analysis to the study of fluid behaviour in orogenesis. Geochim Cosmochim Acta 55:1021–1030. doi: 10.1016/0016-7037(91)90160-7

Banks DA, Green R, Cliff RA, Yardley BWD (2000) Chlorine isotopes in fluid inclusions: Determination of the origins of salinity in magmatic fluids. Geochim Cosmochim Acta 64:1785–1789. doi: 10.1016/S0016-7037(99)00407-X

Bauer ME, Burisch M, Ostendorf J, Krause J, Frenzel M, Seifert T, Gutzmer J (2018) Trace element geochemistry of sphalerite in contrasting hydrothermal fluid systems of the Freiberg district, Germany: insights from LA-ICP-MS analysis, near-infrared light microthermometry of sphalerite-hosted fluid inclusions, and sulfur isotope geochemi. Miner Depos 54:237–262

Boiron MC, Cathelineau M, Richard A (2010) Fluid Flows and Metal Deposition near Basement/Cover Unconformity: Lessons and Analogies from Pb-Zn-F-Ba Systems for the Understanding of Proterozoic U Deposits. Front Geofluids 10:270–292. doi: 10.1002/9781444394900.ch19

Bois JP, Pouit G, Gros Y, B. G, Picot P (1976) Les minéralisations de Zn (Pb) de l'anticlinorium de Pierrefitte: un exemple de gisements hydrothermaux et sédimentaires associés au volcanisme dans le Paléozoïque des Pyrénées centrales. Bull du BRGM 6:543–567

Bonev IK, Kouzmanov K (2002) Fluid inclusions in sphalerite as negative crystals: A case study. Eur J Mineral 14:607–620. doi: 10.1127/0935-1221/2002/0014-0607

Boulvais P, Ruffet G, Cornichet J, Mermet M (2007) Cretaceous albitization and dequartzification of Hercynian peraluminous granite in the Salvezines Massif (French Pyrénées). Lithos 93:89–106. doi: 10.1016/j.lithos.2006.05.001

Boutin A, de Saint Blanquat M, Poujol M, Boulvais P, de Parseval P, Rouleau C, Robert JF (2016) Succession of Permian and Mesozoic metasomatic events in the eastern Pyrenees with emphasis on the Trimouns talc–chlorite deposit. Int J Earth Sci 105:747–770. doi: 10.1007/s00531-015-1223-x

BRGM (1984) Les gisements de Pb-Zn français (situation en 1977). BRGM Intern Rep 1–278

Burisch M, Walter BF, Markl G (2017) Silicification of hydrothermal gangue minerals in Pb-Zn-Cu-fluorite-quartz-baryte veins. Can Mineral 55:501–514. doi: 10.3749/canmin.1700005

Canals A, Cardellach E, Rye DM, Ayora C (1992) Origin of the Atrevida vein (Catalonian Coastal Ranges, Spain): mineralogic, fluid inclusion, and stable isotope study. Econ Geol 87:142–153. doi: 10.2113/gsecongeo.87.1.142

Canet C, Franco SI, Prol-Ledesma RM, González-Partida E, Villanueva-Estrada RE (2011) A model of boiling for fluid inclusion studies: Application to the Bolaños Ag-Au-Pb-Zn epithermal deposit, Western Mexico. J Geochemical Explor 110:118–125. doi: 10.1016/j.gexplo.2011.04.005

Carreras J, Cirés J (1986) The geological significance of the western termination of the Mérens Fault at Port Vell (central Pyrenees). Tectonophysics 129:99–114. doi: 10.1016/0040-1951(86)90248-9

Cathelineau M, Boiron MC, Fourcade S, Ruffet G, Clauer N, Belcourt O, Coulibaly Y, Banks DA, Guillocheau F (2012) A major Late Jurassic fluid event at the basin/basement unconformity in western France: 40Ar/ 39Ar and K-

Ar dating, fluid chemistry, and related geodynamic context. Chem Geol 322–323:99–120. doi: 10.1016/j.chemgeo.2012.06.008

Charef A, Sheppard SMF (1988) The Malines Cambrian carbonate-shale-hosted Pb-Zn deposit, France: Thermometric and isotopic (H, O) evidence for pulsating hydrothermal mineralization. Miner Depos 23:86–95. doi: 10.1007/BF00206655

Cochelin B, Chardon D, Denèle Y, Gumiaux C, Le Bayon B (2017a) Vertical strain partitioning in hot Variscan crust: Syn-convergence escape of the Pyrenees in the Iberian-Armorican syntax. Bull la Société géologique Fr 188:39. doi: 10.1051/bsgf/2017206

Cochelin B, Lemirre B, Denèle Y, De Saint Blanquat M, Lahfid A, Duchêne S (2017b) Structural inheritance in the Central Pyrenees : the Variscan to Alpine tectonometamorphic evolution of the Axial Zone. J Geol Soc London 175:336–351. doi: https://doi.org/10.1144/jgs2017-066

Cugerone A, Cenki-tok B, Oliot E, Muñoz M, Barou F, Motto-Ros V, Le Goff E (2019) Redistribution of germanium during dynamic recrystallization of sphalerite. Geology 48:. doi: 10.1130/G46791.1

Cugerone A, Oliot E, Chauvet A, Gavalda J, Le Goff E (2018) Structural Control on the Formation of Pb-Zn Deposits: An Example from the Pyrenean Axial Zone. Minerals 8:1–20. doi: 10.3390/min8110489

de Hoÿm de Marien L, Le Bayon B, Pitra P, Van Den Driessche J, Poujol M, Cagnard F (2019) Two-stage Variscan metamorphism in the Canigou massif: Evidence for crustal thickening in the Pyrenees. J Metamorph Geol 1–26. doi: 10.1111/jmg.12487

de Saint Blanquat M, Bajolet F, Grand'Homme A, Proietti A, Zanti M, Boutin A, Clerc C, Lagabrielle Y, Labaume P (2016) Cretaceous mantle exhumation in the central Pyrenees: New constraints from the peridotites in eastern Ariège (North Pyrenean zone, France). Comptes Rendus - Geosci 348:268–278. doi: 10.1016/j.crte.2015.12.003

Denèle Y, Laumonier B, Paquette J-L, Olivier P, Gleizes G, Barbey P (2014) Timing of granite emplacement, crustal flow and gneiss dome formation in the Variscan segment of the Pyrenees. Schulmann, K, al, eds, Variscan Orogeny Extent, Timescale Form Eur Crust Geol Soc London, Spec Publ 405:265–287. doi: 10.1144/SP405.5

Denèle Y, Olivier P, Gleizes G (2008) Progressive deformation of a zone of magma transfer in a transpressional regime: The Variscan Mérens shear zone (Pyrenees, France). J Struct Geol 30:1138–1149. doi: 10.1016/j.jsg.2008.05.006

Diamond LW (2003) Chapter 3. Systematics of H2O inclusions. Samson I, Anderson A, Marshall D Fluid inclusions Anal Interpret Mineral Assoc Canada, Short Course, 32:55–78

Fallourd S, Poujol M, Boulvais P, Paquette JL, de Saint Blanquat M, Rémy P (2014) In situ LA-ICP-MS U-Pb titanite dating of Na-Ca metasomatism in orogenic belts: The North Pyrenean example. Int J Earth Sci 103:667–682. doi: 10.1007/s00531-013-0978-1

Fanlo I, Touray JC, Subías I, Fernández-Nieto C (1998) Geochemical patterns of a sheared fluorite vein, Parzan, Spanish central Pyrenees. Miner Depos 33:620–632. doi: 10.1007/s001260050177

Fusswinkel T, Wagner T, Wälle M, Wenzel T, Heinrich CA, Markl G (2013) Fluid mixing forms basement-hosted Pb-Zn deposits: Insight from metal and halogen geochemistry of individual fluid inclusions. Geology 41:679–682. doi: 10.1130/G34092.1

García-Sansegundo J (1992) Estratigrafia y estructura de la Zona Axial Pirenaica en la Transversal del Valle de Aran y de la Alta Ribagorça. Publicación Espec del Boletín Geológico y Min España 102–103:1–290

Goldstein RH, Reynolds TJ (1994) Systematics of Fluid Inclusions in Diagenetic Minerals. SEPM Short Course 31 1–213

Grant NT, Banks DA, McCaig AM, Yardley BWD (1990) Chemistry, source and behavior of fluids involved in alpine thrusting of the central Pyrenees. J Geophys Res 95:9123–9131. doi: 10.1029/JB095iB06p09123

Guillong M, Heinrich CA (2007) Sensitivity enhancement in laser ablation ICP-MS using small amounts of hydrogen in the carrier gas. J Anal At Spectrom 22:1488–1494. doi: 10.1039/b709489b

Guillong M, Meier DL, Allan MM, Heinrich CA, Yardley BWD (2008) SILLS: A Matlab-Based program for the reduction of Laser Ablation ICP-MS data of homogeneous materials and inclusions. Mineral Assoc Canada Short Course 40:328–333

Hedenquist JW (1991) Boiling and dilution in the shallow portion of the Waiotapu geothermal system, New Zealand. Geochim Cosmochim Acta 55:2753–2765. doi: 10.1016/0016-7037(91)90442-8

Heijlen W, Banks DA, Muchez P, Stensgard BM, Yardley BWD (2008) The nature of mineralizing fluids of the Kipushi Zn-Cu deposit, Katanga, Democratic Repubic of Congo: Quantitative fluid inclusion analysis using laser ablation ICP-MS and bulk crush-leach methods. Econ Geol 103:1459–1482. doi: 10.2113/gsecongeo.103.7.1459

Henderson IHC, McCaig AM (1996) Fluid pressure and salinity variations in shear zone-related veins, central Pyrenees, France: Implications for the fault-valve model. Tectonophysics 262:321–348. doi: 10.1016/0040-1951(96)00018-2

Jochum KP, Weis U, Stoll B, Kuzmin D, Yang Q, Raczek I, Jacob DE, Stracke A, Birbaum K, Frick DA, Günther D, Enzweiler J (2011) Determination of reference values for NIST SRM 610-617 glasses following ISO guidelines. Geostand Geoanalytical Res 35:397–429. doi: 10.1111/j.1751-908X.2011.00120.x

Johnson CA, Cardellach E, Tritlla J, Hanan BB (1996) Cierco Pb-Zn-Ag Vein Deposits: Isotopic and Fluid Inclusion Evidence for Formation during the Mesozoic Extension in the Pyrenees of Spain. Econ Geol 91:497–506. doi: 10.5962/bhl.title.18736

Kesler SE, Richard Kyle J, Appold MS, Huston TJ, Walter LM, Martini AM (1995) Na-Cl-Br systematics of mineralizing brines in Mississippi Valley–type deposits. Geology 23:641–644. doi: 10.1130/0091-7613(1995)023<0641:ncbsom>2.3.co;2

Kleinsmiede WFJ (1960) Geology of the Valle de Aran (Central Pyrenees). Leidse Geol Meded 25:129–245

Leach DL, Macquar JC, Lagneau V, Leventhal JS, Emsbo P, Premo W (2006) Precipitation of lead-zinc ores in the Mississippi Valley type deposit at Treves, cevennes region of southern France. Geofluids 6:24–44. doi: 10.1111/j.1468-8123.2006.00126.x

Li W, Audétat A, Zhang J (2015) The role of evaporites in the formation of magnetite-apatite deposits along the Middle and Lower Yangtze River, China: Evidence from LA-ICP-MS analysis of fluid inclusions. Ore Geol Rev 67:264–278. doi: 10.1016/j.oregeorev.2014.12.003

Lopez-Sanchez MA, García-Sansegundo J, Martínez FJ (2018) The significance of early Permian and early Carboniferous U–Pb zircon ages in the Bossòst and Lys-Caillaouas granitoids (Pyrenean Axial Zone). Geol J 1–16. doi: 10.1002/gj.3283

Macquar JC, Lagny P (1981) Minéralisations Pb-Zn 'Sous Inconformité' des Series de Plates-Formes Carbonatées. Exemple du Gisement de Trèves (Gard, France). Relations entre Dolomitisations, Dissolutions et Minéralisations. Miner Depos 16:283–307. doi: 10.1007/BF00202741

Martín-gonzález F, Marzo M, Mercedes-martín R, Ortí F, Pérez-lópez A, Pérez-valera F, Pérez-valera JA, Plasencia P, Ramos E, Rodríguez-méndez L, Ronchi A, Salas R, Suárez-rodríguez Á, Tubía JM, Ubide T (2019) Permian-Triassic Rifting Stage. Geol Iberia A Geodyn Approach 29–112. doi: 10.1007/978-3-030-11295-0

McCaffrey MA, Lazar B, Holland HD (1987) The Evaporation Path of Seawater and the Coprecipitation of Br- and K+ with Halite. J Sediment Res Vol. 57:928–937. doi: 10.1306/212f8cab-2b24-11d7-8648000102c1865d

McCaig AM, Miller JA (1986) 40Ar-39Ar age of Mylonites along the Merens fault, Central Pyrenees. Tectonophysics 129:149–172

McCaig AM, Tritlla J, Banks DA (2000) Fluid flow patterns during Pyrenean thrusting. J Geochemical Explor 70:539–543

Mezger JE (2009) Transpressional tectonic setting during the main Variscan deformation: Evidence from four structural levels in the Bossòst and Aston-Hospitalet mantled gneiss domes, central Axial Zone, Pvrenees. Bull la Soc Geol Fr 180:199–207. doi: 10.2113/gssgfbull.180.3.199

Mezger JE, Passchier CW (2003) Polymetamorphism and ductile deformation of staurolite–cordierite schist of the Bossòst dome: indication for Variscan extension in the Axial Zone of the central Pyrenees. Geol Mag 140:595–612. doi: 10.1017/S0016756803008112

Mezger JE, Passchier CW, Régnier J-L (2004) Metastable staurolite–cordierite assemblage of the Bossòst dome: Late Variscan decompression and polyphase metamorphism in the Axial Zone of the central Pyrenees. Comptes Rendus Geosci 336:827–837. doi: 10.1016/j.crte.2003.12.024

Mezger JE, Schnapperelle S, Rölke C (2012) Evolution of the Central Pyrenean Mérens fault controlled by near collision of two gneiss domes. Jahrb für Geowissenschaften 34:11–29

Munoz M, Baron S, Boucher A, Béziat D, Salvi S (2016) Mesozoic vein-type Pb–Zn mineralization in the Pyrenees: Lead isotopic and fluid inclusion evidence from the Les Argentières and Lacore deposits. Comptes Rendus Geosci 348:322–332. doi: 10.1016/j.crte.2015.07.001

Munoz M, Boyce A, Courjault-Rade P, Fallick A, Tollon F (1997) Le filon (Zn, F) de Peyrebrune (SW Massif central, France): caractérisation géochimique des fluides au cours du Mésozoïque à la bordure orientale du bassin d'Aquitaine. Compte Rendu Acad Sci Paris t. 324:899–906

Munoz M, Boyce AJ, Courjault-Rade P, Fallick AE, Tollon F (1994) Multi-stage fluid incursion in the Palaeozoic basement-hosted Saint-Salvy ore deposit (NW Montagne Noire, southern France). Appl Geochemistry 9:609–626. doi: 10.1016/0883-2927(94)90022-1

Munoz M, Boyce AJ, Courjault-Rade P, Fallick AE, Tollon F (1999) Continental basinal origin of ore fluids from southwestern Massif central fluorite veins (Albigeois, France): Evidence from fluid inclusion and stable isotope analyses. Appl Geochemistry 14:447–458. doi: 10.1016/S0883-2927(98)00070-5

Murphy TE (2004) Structural and stratigraphic controls on mineralization at the George Fisher Zn-Pb-Ag Deposit, northwest Queensland, Australia. Ph D Thesis, James Cook Univ 1–423

Neuser RD (1995) A new high-intensity cathodoluminescence microscope and its application to weakly luminescing minerals. Bochumer Geol und Geotech Arb 44:116–118

Nicol N, Legendre O, Charvet J (1997) Les minéralisations Zn-Pb de la série paléozoïque de Pierrefitte (Hautes-Pyrénées) dans la succession des évènements tectoniques hercyniens. CR Acad Sci Paris 324:453–460

Ostkamp M, Schnapperelle S, Mertmann D (2019) Strukturgeologische Charakterisierung der Mérens Scher-und Störungszone bei Mérens-les-Vals (französische Pyrenäen). Hallesches Jahrb für Geowissenschaften 42:69–111

Ovejero Zappino G (1991) Mineralizaciones Zn-Pb ordovícicas del anticlinorio de Bossost. Yacimientos de Liat y Victoria. Valle de Arán. Pirineo (España). Boletín Geológico y Minero 102–3:356–377

Pouit G (1978) Différents Modeles de Mineralisations «Hydrothermale Sédimentaire », à Zn (Pb) du Paléozoïque des Pyrénees Centrales. Miner Depos 13:411–421

Pouit G (1986) Les minéralisations Zn-Pb exhalatives sédimentaires de Bentaillou et de l 'anticlinorium paléozoïque de Bosost (Pyrénées ariégeoises, France). Chron la Rech minière 485:3–16

Prokin VA, Buslaev FP (1999) Massive copper–zinc sulphide deposits in the Urals. Ore Geol Rev 14:1–69. doi: http://dx.doi.org/10.1016/S0169-1368(98)00014-6

Pujals I (1992) Las mineralizaciones de sulfuros en el Cambro-Ordovicico de la Val d'Aran (Pirineo Central, Lérida). PhD Thesis, Univ Autónoma Barcelona 294p

Quesnel B, Boiron M-C, Cathelineau M, Truche L, Rigaudier T, Bardoux G, Agrinier P, de Saint Blanquat M, Masini E, Gaucher EC (2019) Nature and Origin of Mineralizing Fluids in Hyperextensional Systems: The Case of Cretaceous Mg Metasomatism in the Pyrenees. Geofluids 2019:1–18. doi: 10.1155/2019/7213050

Ramboz C, Pichavant M, Weisbrod A (1982) Fluid immiscibility in natural processes: Use and misuse of fluid inclusion data. II. Interpretation of fluid inclusion data in terms of immiscibility. Chem Geol 37:29–48. doi: 10.1016/0009-2541(82)90065-1

Reyx J (1973) Relations entre tectonique, métamorphisme de contact et concentrations metalliques dans le secteur des anciennes mines d'Arre et Anglas (Hautes-Pyrénées - Pyrénées atlantiques). Ph D Thesis, Univ Paris VI 83p

Roedder E (1984) Fluid inclusions. Mineral Soc Am 646p

Schärer U, De Parseval P, Polvé M, De Saint Blanquat M (1999) Formation of the Trimouns talc-chlorite deposit (Pyrenees) from persistent hydrothermal activity between 112 and 97 Ma. Terra Nov 11:30–37. doi: 10.1046/j.1365-3121.1999.00224.x

Schlöglova K, Wälle M, Heinrich CA (2017) LA-ICP-MS analysis of fluid inclusions: Contamination effects challenging micro-analysis of elements close to their detection limit. J Anal At Spectrom 32:1052–1063. doi: 10.1039/c7ja00022g

Seifert T, Sandmann D (2006) Mineralogy and geochemistry of indium-bearing polymetallic vein-type deposits: Implications for host minerals from the Freiberg district Eastern Erzgebirge, Germany. Ore Geol Rev 28:1–31. doi: 10.1016/j.oregeorev.2005.04.005

Seo JH, Guillong M, Aerts M, Zajacz Z, Heinrich CA (2011) Microanalysis of S, Cl, and Br in fluid inclusions by LA-ICP-MS. Chem Geol 284:35–44. doi: 10.1016/j.chemgeo.2011.02.003

Steele-MacInnis M (2018) Fluid inclusions in the system H2O-NaCl-CO2: An algorithm to determine composition, density and isochore. Chem Geol 498:31–44. doi: 10.1016/j.chemgeo.2018.08.022

Steele-MacInnis M, Bodnar RJ, Naden J (2011) Numerical model to determine the composition of H2O – NaCl – CaCl2 fluid inclusions based on microthermometric and microanalytical data. Geochemica Cosmochim Acta 75:21–40. doi: 10.1016/j.gca.2010.10.002

Steele-MacInnis M, Lecumberri-Sanchez P, Bodnar RJ (2012) HokieFlincs_H2O-NaCl: A Microsoft Excel spreadsheet for interpreting microthermometric data from fluid inclusions based on the PVTX properties of H2O-NaCl. Comput Geosci 49:334–337. doi: 10.1016/j.cageo.2012.01.022

Stoffell B, Appold MS, Wilkinson JJ, Mcclean NA, Jeffries TE (2008) Geochemistry and evolution of mississippi valley-type mineralizing brines from the Tri-State and Northern Arkansas districts determined by LA-ICP-MS microanalysis of fluid inclusions. Econ Geol 103:1411–1435. doi: 10.2113/gsecongeo.103.7.1411

Subias I, Fanlo I, Yuste A, Fernandez-Nieto C (1999) The Yenefrito Pb-Zn mine (Spanish Central Pyrenees): an example of superimposed metallogenetic events. Miner Depos 34:220–223

Subias I, Recio C, Fanlo I, Fernandez-Nieto C (1997) Stable isotope composition of F-Pb-Zn mineralization in the Valle de Tena (Spanish Central Pyrenees). Miner Depos 32:180–188

Vergés J, Fernàndez M, Martìnez A (2002) The Pyrenean orogen: Pre-, syn-, and post-collisional evolution. J Virtual Explor 8:1–20. doi: 10.3809/jvirtex.2002.00058

Walter LM, Stueber AM, Huston TJ (1990) Br-Cl-Na systematics in Illinois basin fluids: Constraints on fluid origin and evolution. Geology 18:315–318. doi: 10.1130/0091-7613(1990)018<0315:BCNSII>2.3.CO;2

Wilkinson JJ, Stoffell B, Wilkinson CC, Jeffries TE, Appold MS (2009) Anomalously metal-rich fluids form hydrothermal ore deposits. Science (80-) 323:764–767. doi: 10.1126/science.1164436

Yardley BWD (2005) Metal Concentrations in Crustal Fluids and Their Relationship to Ore Formation. Econ Geol 100:613–632

Zwart HJ (1963) Metamorphic history of the Central Pyrenees, Part II, Valle de Aran. Leidse Geol Meded 28:321–376

Zwart HJ (1979) The Geology of the Central Pyrenees. Leidse Geol Meded 50:1–74

9 Discussion and conclusion

The distribution of Ge in metamorphosed Pb-Zn deposits from the Pyrenean Axial Zone (PAZ) is highly heterogeneous. In this PhD thesis, I have highlighted the role of recrystallization in redistributing this rare metal from the sphalerite lattice into accessory minerals. I have performed a detailed multi-scale investigation from the field to the electronic microscope, focusing on textural and chemical analyses, in order to decipher timing, specific processes and conditions of formation of Ge-minerals.

9.1 New genesis model of Pb-Zn(-Ge) mineralization

Unravelling the succession of tectonic events related to mineralization stages is often difficult, not only in the Pyrenees but in all Pb-Zn deposits located in deformed/metamorphosed terranes (*De Vera et al. 2004; Gibson and Nutman 2004; Wilkinson 2013)*. Understanding the structural relationships between mineralizations and their host rock is essential in order to characterize ore forming processe as an aid to exploration and exploitation. Therefore, deciphering whether an ore is syngenetic or epigenetic necessitates a detailed structural study.

In the PAZ this question has remained unresolved for the past decades. Coupling structural field measurements with modern textural, chemical and fluid inclusions studies is especially relevant in this context. For example, Type 2a stratabound ore was considered SEDEX (Ordovician and/or Devonian in age; *Bois et al. 1976; Marcoux 1986b; Pouit 1986; Pouit and Bois 1986a)*. In this study, Type 2a is interpreted as synchronous to the Variscan tectonic event and Type 2b veins are Late-Variscan or Mesozoic, depending their location (Figure 121). A detailed structural regional study was the key for unravelling the structural setting of mineralization, especially for distinguishing between stratabound and vein-type mineralizations. In the field, sphalerite from stratabound mineralization exhibits centimetric to millimetric coarse grains compared to vein mineralizations which contain heterogeneous grain size from micrometric to millimetric grains related to a late cleavage (Figure 121). In addition, fluid inclusions that record vein mineralization hydrothermal events in primary and secondary assemblages show a clear difference in fluid composition. Type 2b vein mineralization is associated to two distinct episodes of mineralization. The first one shows a low salinity (<20 wt.% NaCl eq.) and high temperature (>200°C) and is associated to Late-

Variscan extension. The second shows high salinity (15-35 wt.% NaCl eq.) and low temperature (~160°C) and corresponds to a Mesozoic (Triassic-Jurassic) fluid signature. The latter is deformed and impacted by Pyrenean-Alpine deformation (D_p) opposed to the Late-Variscan cleavage as previously supposed. This Pyrenean event is responsible for the main Ge redistribution event (Figure 121).

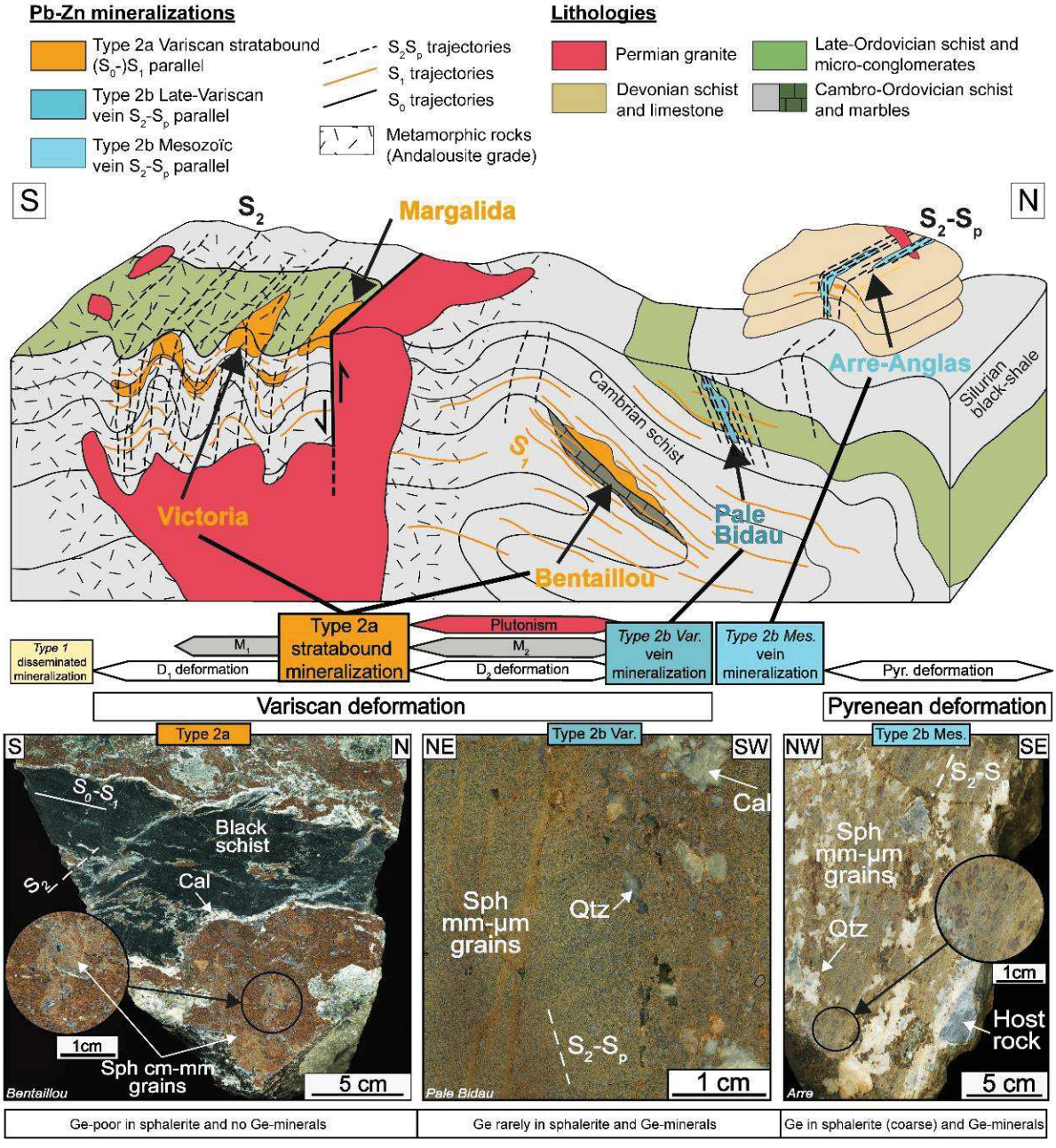

Figure 121. Revised model with structural position, chronology, textures and Ge-contents of the four main Pb-Zn mineralizations in the Pyrenean Axial Zone (PAZ). The two Type 2b mineralizations are the only host for Ge. Note the difference in sphalerite texture between Type 2a and Type 2b sphalerite.

9.2 Mode of concentration of Ge and other related rare metals in sulphide environment

This study couples textural and chemical (*in-situ* and mapping) techniques to decipher the formation mechanisms of Ge-minerals in the PAZ. Sphalerite from Type 2b mineralization shows large heterogeneities in texture from small recrystallized grains to coarse porphyroclastic crystals related to a probable Pyrenean cleavage (Figure 121). In vein-type sphalerite, Ge-minerals occur mainly in recrystallized domains (revised genetic model in Figure 122). Dynamic recrystallization of sphalerite plays a major role in remobilizing trace Ge contents from the sphalerite lattice into Ge-minerals. The lattice is distorted, sub-grain boundaries form and allow the circulation of a hydrothermal-metamorphic fluid (probably with low-temperature below 450°C) that dissolves sphalerite lattice impurities such as Ge. These impurities reprecipitate preferentially in recrystallized sphalerite grain boundaries and form accessory minerals enriched in Ge (>wt. % Ge). This key process that concentrates rare metals seems to be frequent in numerous other rare metal deposits (Ge, Ga, In) such as in deformed MVT or veins deposits (*Monteiro et al. 2006; Reiser et al. 2011; Ye et al. 2011; Belissont et al. 2019)* where deformation, probably dynamic recrystallization of Ge-rich sulfide is described. To form Ge-minerals, a primary Ge enrichment is necessary (> 100 ppm Ge) in the sulfide lattice (sphalerite, chalcopyrite, bornite, etc.). In vein-type sphalerite from the PAZ, deformation was not intense enough to affect quartz whereas sphalerite appears locally totally recristallized. Sphalerite is one of the more ductile sulfide *(Clark and Kelly 1973; Marshall and Gilligan 1993*) and may recrystallized at temperature as low as 300-400°C, and probable low pressure. Increase in fO_2 conditions is also supposed during deformation and possible hydrothermal fluid circulation (Figure 122) with apparition of Ge-oxides in Late-Variscan and Mesozoic veins, even if some briartite (Ge sulfide) is reported, like in Arre Mesozoic vein deposit. The circulation of a hydrothermal fluid is only supposed, and Ge isotopic analyses may be a future interesting benefit to understand the possible fractionation between Ge in recrystallized and coarse sphalerite crystals. Absence of Ge in Type 2a stratabound ore does not imply that Ge is absent in metamorphosed sphalerite as it may be an effect of the effective primary bulk composition.

The redistribution of Ge from the sphalerite lattice into Ge-minerals can be well-assessed in the PAZ because recrystallization is localized in discrete domains, and evidence of the presence of initial Ge is preserved locally in parent sphalerite dark zonations. Nonetheless, in numerous other deposits in deformed environments, Ge only appears in Ge-minerals and the sulfide lattice is depleted. This study focusses on Ge-rich sphalerite but similar processes are likely to occur for

other rare metals (In, Ga) hosted in various sulfides such as Barrigão chalcopyrite *(Reiser et al. 2011; Belissont et al. 2019)* or in bornite (*Bernstein and Cox 1986*). Furthermore, other chemical systems report substantial accessory minerals exploitation linked to redistribution processes or magmatic differentiation such as scandium (*Bernhard 2001*) or REE systems *(MacDonald et al. 2013; Goodenough et al. 2016; Dostal 2017; Kontonikas-Charos et al. 2018*).

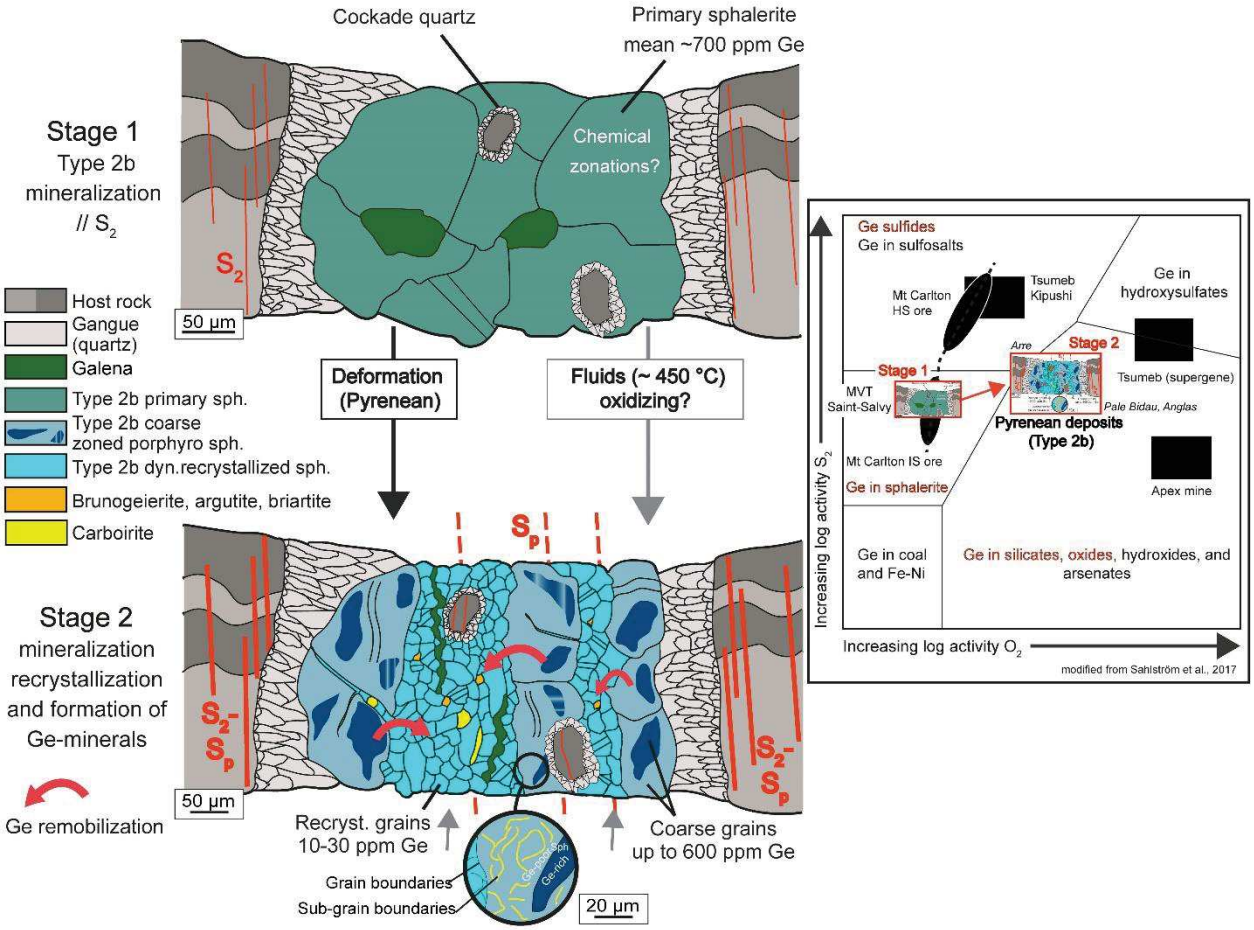

Figure 122. Revised model of formation of Ge-minerals in the PAZ Type2b veins (Late-Variscan and Mesozoïc). The figure on the right is from *Sahlström et al., 2017* (modified version of *Bernstein, 1985*) and represents the relation between fO_2 and fS_2 activities. Position of the different Pyrenean Vein sphalerite is shown. In Arre, dominance of Ge-sulfide (briartite) appear compare to Pale Bidau and Anglas where Ge-oxides and chloritoid appear.

Source of the Ge is still an unresolved issue in the Pyrenean sphalerite. Germanium seems clearly associated to an epigenetic input related to vein mineralization. These veins are related to widespread hydrothermal circulation in the Variscan basement during Late-Variscan and Mesozoic ages. The most probable Ge-source may reside in black schist series due to organophile Ge affinity, probably in the Silurian series which are abundant in the Pyrenean Axial Zone. Germanium content was mapped and detected in the calc-schist rocks of Arre deposit but was structurally interpreted

as epigenetic input related to vein mineralization (Figure 78). Another common source present in the literature is associated the hydrothermal alteration of late-igneous intrusions, and may also be considered (*Belissont 2016*).

Exploration for Ge currently focusses on targeting high contents in sphalerite lattice, even if Ge extraction is poorly efficient with only 2-3% of the total Ge recovered from zinc ores *(Licht et al. 2015; Ruiz et al. 2018*). Higher contents (thousands of ppm Ge) appear exclusively in non-deformed deposits such as Tennessee MVT or Saint-Salvy sphalerite *(Belissont et al. 2014; Bonnet 2014*).

Ge-minerals with content up to 70 wt.% Ge are described in deformed and metamorphosed environment such as the Pyrenean deposits and in a large number of Kipushi-type deposits. Deformed and metamorphosed Pb-Zn deposits constitute the largest base metal ressources in the world. Their economic potential may be investigated. These Ge resources hosted in Ge-minerals may be processed better during Ge extraction (mechanical separation?) and may represent a more valuable product if the tonnage of the main resource (sphalerite – Zn, chalcopyrite – Cu) is sufficient. Germanium and associated rare metals are currently economically linked to these base metals.

Ge-minerals are not easy to find by optical means only, which may explain their rare description in Pb-Zn(-Cu) deposits. Electron beam imaging and mapping techniques or high resolution optical instruments (e.g. SEM-EBSD and LIBS mapping) are necessary to identify these potential valuable rare metal resources. In order to detect these localized high Ge concentrations in ore or tailings of deformed/metamorphosed Pb-Zn deposits, a textural study is essential to identify recrystallized domains which should be the target of chemical mapping or bulk analyses (without Ge-loss during acidic digestion). In addition, the presence of strong variations in Ge contents in the deformed sphalerite lattice may be a good evidence for Ge redistribution in sphalerite and the presence of Ge-minerals.

10 Bibliography

Aerden DGAM (1994) Kinematics of orogenic collapse in the Variscan Pyrenees deduced from microstructures in porphyroblastic rocks from the Lys-Caillaouas massif. Tectonophysics 238:139–160. doi: 10.1016/0040-1951(94)90053-1

Akinfiev NN, Tagirov BR (2014) Zn in hydrothermal systems: Thermodynamic description of hydroxide, chloride, and hydrosulfide complexes. Geochemistry Int 52:197–214. doi: 10.1134/S0016702914030021

Albarède F, Michard-Vitrac A (1978) Age and significance of the North Pyrenean metamorphism. Earth Planet Sci Lett 40:327–332. doi: 10.1016/0012-821X(78)90157-7

Alexandrov P (2000) Géochronologie U/Pb et 40Ar/39Ar de deux segments de la chaîne Varisque: le haut Limousin et les Pyrénées orientales. Unpubl Thesis, INPL, Nancy

Allain-Bonasso N, Wagner F, Berbenni S, Field DP (2012) A study of the heterogeneity of plastic deformation in IF steel by EBSD. Mater Sci Eng A 548:56–63. doi: 10.1016/j.msea.2012.03.068

Alonso JL (1979) Deformaciones sucesivas en el area comprendida entre Liat y el Puerto de Orla - Control estructural de los depositos de sulfuros (Valle de Aran, Pirineos Centrales). Tesis Licenciatura, Univ Oviedo 26p

Alvarez-Perez A, Campa-Vineta JA, Montoriol-Pous J (1974) Sobre la presencia de gahnita ferrífera en Bossost (Vall D'Aran, Lérida). Acta Geol Hisp 9:111–113

Alvarez-Perez A, Campa-Vineta JA, Montoriol-Pous J (1977) Mineralogénesis de los yacimientos del área de Bossost (Vall d'Aran, Lérida). Acta Geol Hisp 4–6:123–126

Arne DC, Curtis LW, Kissin SA (1991) Internal Zonation in a Carbonate-Hosted Zn-Pb-Ag Deposit. Nanisivik, Barfin Island, Canada. Econ Geol 86:699–717

Atkinson BK (1976) Deformation mechanism maps for polycrystalline galena. Earth Planet Sci Lett 29:210–218. doi: 10.1016/0012-821X(76)90041-8

Atkinson BK (1975) Experimental deformation of polycrystalline pyrite; effects of temperature, confining pressure, strain rate, and porosity. Econ Geol 70:473–487. doi: 10.2113/gsecongeo.70.3.473

Auréjac JB, Gleizes G, Diot H, Bouchez JL (2004) Le complexe granitique de Quérigut (Pyrénées, France) ré-examiné par la technique de l'ASM: Un pluton syntectonique de la transpression dextre hercynienne. Bull la Soc Geol Fr 175:157–174. doi: 10.2113/175.2.157

Aye F, Bouladon J, Picot P, Pouit G (1978) Quelques exemples d'apports de la minéralogie à la connaissance et la recherche des gîtes minéraux. Bull minéralogique 101:139–147

Baatartsogt B, Schwinn G, Wagner T, Taubald H, Beitter T, Markl G (2007) Contrasting paleofluid systems in the continental basement: A fluid inclusion and stable isotope study of hydrothermal vein mineralization, Schwarzwald district, Germany. Geofluids 7:123–147. doi: 10.1111/j.1468-8123.2007.00169.x

Bailie RH, Reid DL (2005) Ore textures and possible sulphide partial melting at Broken Hill, Aggeneys, South Africa I: Petrography. South African J Geol 108:51–70. doi: 10.2113/108.1.51

Bailly L, Tamas C-G, Minut A (2005) Te-Rich argyrodite occurrence in Rosia Montana ore deposit, Apuseni Mountains, Romani.

C R Geosci Geomaterials (Ore Depos 337:755–762. doi: 10.1016/j.crte.2005.03.011

Banks DA, Da Vies GR, Yardley BWD, McCaig AM, Grant NT (1991) The chemistry of brines from an Alpine thrust system in the Central Pyrenees: An application of fluid inclusion analysis to the study of fluid behaviour in orogenesis. Geochim Cosmochim Acta 55:1021–1030. doi: 10.1016/0016-7037(91)90160-7

Banks DA, Green R, Cliff RA, Yardley BWD (2000) Chlorine isotopes in fluid inclusions: Determination of the origins of salinity in magmatic fluids. Geochim Cosmochim Acta 64:1785–1789. doi: 10.1016/S0016-7037(99)00407-X

Barbanson L, Geldron A (1983) Distribution du germanium , de l 'argent et du cadmium entre les schistes et les mineralisations stratiformes et filoniennes a blende- siderite de la region de Saint-Salvy (Tarn). Chron la Rech minière 470:33–42

Barrère P, Bouquet C, Debroas EJ, Pelissonnier H, Peybernes B, Soulé JC, Souquet P, Ternet Y (1984) Arreau. BRGM Geol map 1/50 000 with note 60p

Barrie CD, Boyle AP, Cox SF, Prior DJ (2008) Slip systems and critical resolved shear stress in pyrite: an electron backscatter diffraction (EBSD) investigation. Mineral Mag 72:1181–1199. doi: 10.1180/minmag.2008.072.6.1181

Barrie CD, Boyle AP, Prior DJ (2007) An analysis of the microstructures developed in experimentally deformed polycrystalline pyrite and minor sulphide phases using electron backscatter diffraction. J Struct Geol 29:1494–1511. doi: 10.1016/j.jsg.2007.05.005

Barrie CD, Boyle AP, Salter M (2009) How low can you go? - Extending downwards the limits of plastic deformation in pyrite. Mineral Mag 73:895–913. doi: 10.1180/minmag.2009.073.6.895

Barrie CD, Pearce MA, Boyle AP (2011) Reconstructing the pyrite deformation mechanism map. Ore Geol Rev 39:265–276. doi: 10.1016/j.oregeorev.2011.03.006

Baudin T (2013) Notice explicative, Carte géologique de France (1/50 000), feuille Ax-les- Thermes (1088). Cart géologique BRMG, Orléans. doi: 10.1016/j.jns.2003.09.014

Bauer ME, Burisch M, Ostendorf J, Krause J, Frenzel M, Seifert T, Gutzmer J (2018) Trace element geochemistry of sphalerite in contrasting hydrothermal fluid systems of the Freiberg district, Germany: insights from LA-ICP-MS analysis, near-infrared light microthermometry of sphalerite-hosted fluid inclusions, and sulfur isotope geochemi. Miner Depos 54:237–262

Beaudoin G (2000) Acicular sphalerite enriched in Ag, Sb, and Cu embedded within color-banded sphalerite from the Kokanee Range, British Columbia, Canada. Can Mineral 38:1387–1398. doi: 10.2113/gscanmin.38.6.1387

Belissont R (2016) Germanium and related elements in sulphide minerals: crystal chemistry, incorporation and isotope fractionation. Ph D Thesis Univ Lorraine-Georessources-CRPG p210

Belissont R, Boiron M-C, Luais B, Cathelineau M (2014) LA-ICP-MS analyses of minor and trace elements and bulk Ge isotopes in zoned Ge-rich sphalerites from the Noailhac - Saint-Salvy deposit (France): Insights into incorporation mechanisms and ore deposition processes. Geochim Cosmochim Acta 126:518–540. doi: 10.1016/j.gca.2013.10.052

Belissont R, Munoz M, Boiron M-C, Luais B, Mathon O (2016) Distribution and oxidation state of Ge, Cu and Fe in sphalerite by μ-XRF and K-edge μ-XANES: Insights into Ge incorporation, partitioning and isotopic fractionation. Geochim Cosmochim Acta 177:298–314. doi: 10.1016/j.gca.2016.01.001

Belissont R, Munoz M, Boiron M-C, Luais B, Mathon O (2019) Germanium Crystal Chemistry in Cu-Bearing Sulfides from Micro-XRF Mapping and Micro-XANES Spectroscopy. Minerals 9:1–12. doi: doi.org/10.3390/min9040227

Bernadini GP, Borgheresi M, Cipriani C, Benedetto F Di, Romanelli M (2004) Mn distribution in sphalerite : an EPR study. Phys

Chem Miner 31:80–84. doi: 10.1007/s00269-003-0374-7

Bernhard F (2001) Scandium mineralization associated with hydrothermal lazulite-quartz veins in the Lower Austroalpine Grobgneis complex , Eastern Alps , Austria. Miner Depos Begin 21st Century Proc Jt sixth Bienn SGA-SEG Meet Kraków, Poland AABalkema Publ 935–938

Bernstein LR (1986a) Renierite, Cu10ZnGe2Fe4S16- Cu11GeAsFe4S16: A coupled solid solution series. Am Mineral 71:210

Bernstein LR (1985) Germanium geochemistry and mineralogy. Geochim Cosmochim Acta 49:2409–2422. doi: 10.1016/0016-7037(85)90241-8

Bernstein LR (1986b) Geology and mineralogy of the Apex germanium-gallium mine, Washington County, Utah. USGS Bull 1577:20

Bernstein LR, Cox DP (1986) Geology and Sulfide Mineralogy of the Number One Orebody, Ruby Creek Copper Deposit, Alaska. Geology 81:1675–1689

Bernstein LR, Waychunas GA (1987) Germanium crystal chemistry in hematite and goethite from the Apex Mine, Utah, and some new data on germanium in aqueous solution and in stottite. Geochim Cosmochim Acta 51:623–630. doi: 10.1016/0016-7037(87)90074-3

Bestmann M, Habler G, Heidelbach F, Thöni M (2008) Dynamic recrystallization of garnet and related diffusion processes. J Struct Geol 30:777–790. doi: 10.1016/j.jsg.2008.02.007

Bindi L, Putz H, Paar WH, Stanley CJ (2017) Omariniite, Cu8Fe2ZnGe2S12, the germanium analogue of stannoidite, a new mineral species from Capillitas, Argentina. Mineral Mag 81:1151–1159. doi: 10.1180/minmag.2016.080.164

Bodnar RJ, Lecumberri-Sanchez P, Moncada D, Steele-MacInnis M (2013) Fluid Inclusions in Hydrothermal Ore Deposits. Treatise Geochemistry Second Ed. doi: 10.1016/B978-0-08-095975-7.01105-0

Bodon SB (1998a) Paragenetic relationships and their implications for ore genesis at the Cannington Ag-Pb-Zn deposit, Mount Isa inlier, Queensland, Australia. Econ Geol 93:1463–1488. doi: 10.2113/gsecongeo.93.8.1463

Bodon SB (1998b) Paragenetic Relationships and Their Implications for Ore Genesis at the Cannington. Econ Geol 93:1463–1488

Bodon SB, Valenta RK (1995) Primary and Tectonic Features of the Currawong Zn-Cu-Pb(-Au) Massive Sulfide Deposit, Benambra, Victoria: Implications for Ore Genesis. Econ Geol 90:1694–1721

Boiron MC, Cathelineau M, Richard A (2010) Fluid Flows and Metal Deposition near Basement/Cover Unconformity: Lessons and Analogies from Pb-Zn-F-Ba Systems for the Understanding of Proterozoic U Deposits. Front Geofluids 10:270–292. doi: 10.1002/9781444394900.ch19

Bois JP (1981) Minéralisations Zn-Pb (Barytine) du secteur d'Arrens. Rapp BRGM 81 RDM 033 FE 1–61

Bois JP, Pouit G, Gros Y, B. G, Picot P (1976) Les minéralisations de Zn (Pb) de l'anticlinorium de Pierrefitte: un exemple de gisements hydrothermaux et sédimentaires associés au volcanisme dans le Paléozoïque des Pyrénées centrales. Bull du BRGM 6:543–567

Bonev IK, Kouzmanov K (2002) Fluid inclusions in sphalerite as negative crystals: A case study. Eur J Mineral 14:607–620. doi: 10.1127/0935-1221/2002/0014-0607

Bonnet J (2014) Distribution et contrôle cristallographique des éléments Ge , Ga et Cd dans les sphalérites des gisements de type Mississippi Valley dans les districts de Central et East Tennessee , USA. Ph D Thesis Univ Lorraine-Georessources 204

Bonnet J, Cauzid J, Testemale D, Kieffer I, Proux O, Lecomte A, Bailly L (2017) Characterization of Germanium Speciation in Sphalerite (ZnS) from Central and Eastern Tennessee, USA, by X-ray Absorption Spectroscopy. Minerals 7:1–16. doi: 10.3390/min7050079

Boulvais P, Ruffet G, Cornichet J, Mermet M (2007) Cretaceous albitization and dequartzification of Hercynian peraluminous granite in the Salvezines Massif (French Pyrénées). Lithos 93:89–106. doi: 10.1016/j.lithos.2006.05.001

Boutin A (2016) Etude des conditions de formations du gisement de talc-chlorite de Trimouns (Ariège, France). PhD thesis, Univ Toulouse 3 Paul Sabatier 1–284. doi: 10.1017/CBO9781107415324.004

Boutin A, de Saint Blanquat M, Poujol M, Boulvais P, de Parseval P, Rouleau C, Robert JF (2016) Succession of Permian and Mesozoic metasomatic events in the eastern Pyrenees with emphasis on the Trimouns talc–chlorite deposit. Int J Earth Sci 105:747–770. doi: 10.1007/s00531-015-1223-x

Brebrick RF, Scanlon WW (1957) Chemical Etches and Etch Pit Patterns on PbS Crystals. J Chem Phys 27:607. doi: 10.1063/1.1743796

Breiter K, Gardenova N, Kanicky V, Vaculovic T (2013) Gallium and germanium geochemistry during magmatic fractionation and post-magmatic alteration in different types of granitoids: a case study from the Bohemian Massif (Czech Republic). Geol Carpathica 64:171+. doi: 10.2478/geoca-2013-0018

BRGM (1972) Pic de Mauberme. BRGM Geol map 1/50 000 with note 24p

BRGM (1984) Les gisements de Pb-Zn français (situation en 1977). BRGM Intern Rep 1–278

Brugger J, Giere R (2000) Origin and distribution of some trace elements in metamorphosed Fe-Mn deposits, Val Ferrara, Eastern Swiss Alps. Can Mineral 38:1075–1101. doi: 10.2113/gscanmin.38.5.1075

Bruguier O, Becq-Giraudon JF, Clauer N, Maluski H (2003) From late Visean to Stephanian: Pinpointing a two-stage basinal evolution in the Variscan belt. A case study from the Bosmoreau basin (French Massif Central) and its geodynamic implications. Int J Earth Sci 92:338–347. doi: 10.1007/s00531-003-0321-3

Bull SW, Large RR (2015) Setting the stage for the genesis of the giant Bendigo ore system. Geol Soc London, Spec Publ 393:161–187. doi: 10.1144/SP393.10

Burisch M, Walter BF, Markl G (2017) Silicification of hydrothermal gangue minerals in Pb-Zn-Cu-fluorite-quartz-baryte veins. Can Mineral 55:501–514. doi: 10.3749/canmin.1700005

Burkhard M (1993) Calcite twins, their geometry, appearance and significance as stress-strain markers and indicators of tectonic regime: a review. J Struct Geol 15:351–368. doi: 10.1016/0191-8141(93)90132-T

Burton J., Culkin F, Riley J. (1958) The abundances of gallium and germanium in terrestrial materials. Geochim Cosmochim Acta 16:151–180. doi: 10.1016/0016-7037(59)90052-3

Busser B, Moncayo S, Coll J, Sancey L, Motto-ros V (2018) Elemental imaging using laser-induced breakdown spectroscopy : A new and promising approach for biological and medical applications. Coord Chem Rev 358:70–79. doi: 10.1016/j.ccr.2017.12.006

Butterman BWC, Jorgenson JD (2005) Germanium. Miner Commod profiles 19

Cáceres JO, Pelascini F, Motto-Ros V, Moncayo S, Trichard F, Panczer G, Marín-Roldán A, Cruz JA, Coronado I, Martín-Chivelet J (2017) Megapixel multi-elemental imaging by Laser-Induced Breakdown Spectroscopy, a technology with considerable potential for paleoclimate studies. Sci Rep 7:1–11. doi: 10.1038/s41598-017-05437-3

Calvet P (1988) Etude structurale et métallogénique de l'anticlinorium de Pierrefitte : influence de la déformation sur les minéralisations stratiformes. Ph D Thesis Univ d'Orléans 283p

Canals A, Cardellach E, Rye DM, Ayora C (1992) Origin of the Atrevida vein (Catalonian Coastal Ranges, Spain): mineralogic, fluid inclusion, and stable isotope study. Econ Geol 87:142–153. doi: 10.2113/gsecongeo.87.1.142

Canet C, Franco SI, Prol-Ledesma RM, González-Partida E, Villanueva-Estrada RE (2011) A model of boiling for fluid inclusion studies: Application to the Bolaños Ag-Au-Pb-Zn epithermal deposit, Western Mexico. J Geochemical Explor 110:118–125. doi: 10.1016/j.gexplo.2011.04.005

Cardellach E (1977) Estudio microscópico de las mineralizaciones de Pb-Zn de Liat, Baguergue y Montoliu. Acta Geol Hisp 12, 4–6, 1:3p

Cardellach E, Alvarez-Perez A (1979) Interpretación genética de las mineralizaciones de Pb-Zn del Ordovícico Sup. de la Vall de Aran. Acta Geol Hisp 14:117–120

Cardellach E, Canals A, Pujals I (1996) La composicion isotopica del azufre y del plomo en las mineralizaciones de Zn-Pb del Valle de Aran (Pirineo Central) y su significado metalogenetico. Estud Geol 52:189–195

Cardellach E, Phillips R, Ayora C (1982) Metamorphosed stratiform sulphides of the Liat area, Central Pyrenees, Spain. Inst Min Metall Trans Sect B Applied Ea:90–95

Carreras J (2001) Zooming on Northern Cap de Creus shear zones. J Struct Geol 23:1457–1486. doi: 10.1016/S0191-8141(01)00011-6

Carreras J, Capella I (1994) Tectonic levels in the Palaeozoic basement of the Pyrenees: a review and a new interpretation. J Struct Geol 16:1509–1524

Carreras J, Cirés J (1986) The geological significance of the western termination of the Mérens Fault at Port Vell (central Pyrenees). Tectonophysics 129:99–114. doi: 10.1016/0040-1951(86)90248-9

Carreras J, Druguet E (2014) Framing the tectonic regime of the NE Iberian Variscan segment. Schulmann, K, al, eds, Variscan Orogeny Extent, Timescale Form Eur Crust Geol Soc London, Spec Publ 405:249–264. doi: 10.1144/SP405.7

Carreras J, Druguet E, Griera a., Soldevila J (2004) Strain and deformation history in a syntectonic pluton. The case of the Roses granodiorite (Cap de Creus, Eastern Pyrenees). Geol Soc London, Spec Publ 224:307–319. doi: 10.1144/GSL.SP.2004.224.01.19

Carvalho JRS, Relvas JMRS, Pinto AMM, Frenzel M, Krause J, Gutzmer J, Pacheco N, Fonseca R, Santos S, Caetano P, Reis T, Gonçalves M (2018) Indium and selenium distribution in the Neves-Corvo deposit, Iberian Pyrite Belt, Portugal. Mineral Mag 82:S5–S41. doi: 10.1180/minmag.2017.081.079

Casas JM (2010) Ordovician deformations in the Pyrenees: new insights into the significance of pre-Variscan ('sardic') tectonics. Geol Mag 147:674–689. doi: 10.1017/S0016756809990756

Casas JM, Castiñeiras P, Navidad M, Liesa M, Carreras J (2010) New insights into the Late Ordovician magmatism in the Eastern Pyrenees: U-Pb SHRIMP zircon data from the Canigó massif. Gondwana Res 17:317–324. doi: 10.1016/j.gr.2009.10.006

Casas JM, Fernández O (2007) On the Upper Ordovician unconformity in the Pyrenees: New evidence from the La Cerdanya area. Geol Acta 5:193–198

Cassard D, Chabod JC, Marcoux E, Bourgine B, Castaing C, Gros Y, Kosakevitch A, Moisy M, Viallefond L (1993) Mise en place et origine des minéralisations du gisement filonien de Noailhac - Saint-Salvy Zn, Ge, Ag, (Pb, Cd) Tarn - France. BRGM

BRGM R-376:82

Castiñeiras P, Navidad M, Liesa M, Carreras J, Casas JM (2008) U-Pb zircon ages (SHRIMP) for Cadomian and Early Ordovician magmatism in the Eastern Pyrenees: New insights into the pre-Variscan evolution of the northern Gondwana margin. Tectonophysics 461:228–239. doi: 10.1016/j.tecto.2008.04.005

Castroviejo Bolibar R, Serrano FM (1983) Estructura y metalogenia del campo filoniano de Cierco (Pb-Zn-Ag), en el Pirineo de Lérida. Boletín Geológio y Min 1983:291–320

Cathelineau M, Boiron MC, Fourcade S, Ruffet G, Clauer N, Belcourt O, Coulibaly Y, Banks DA, Guillocheau F (2012) A major Late Jurassic fluid event at the basin/basement unconformity in western France: 40Ar/ 39Ar and K-Ar dating, fluid chemistry, and related geodynamic context. Chem Geol 322–323:99–120. doi: 10.1016/j.chemgeo.2012.06.008

Cavet P (1957) Le Paléozoique de la zone axiale des Pyrénées Orientales françaises entre le Rousillon et l'Andorre. Bull Serv Cart Géol Fr 55:303–518

Cempírek J, Groat LA (2013) Note on the formula of brunogeierite and the first bond-valence parameters for Ge2+. J Geosci (Czech Republic) 58:71–74. doi: 10.3190/jgeosci.130

Cerny I, Schroll E (1995) Heimische Vorräte an Spezialmetallen (Ga, In, Tl, Ge, Se, Te und Cd) in Blei-Zink- und anderen Erzen. Arch Für Lagerstättenforsch der Geol Bundesanstalt 18:5–33

Chabu M (1989) Metamorphism of the Kipushi carbonate hosted Zn-Pb-Cu deposit (Shaba, Zaire), Regional metamorphism of Ore deposits and genetic implications. Proc 28th Int Geol Congr 9–19 July, Utrecht, Netherlands 27–47

Chapman LH (2004) Geology and Mineralization Styles of the George Fisher Zn-Pb-Ag Deposit, Mount Isa, Australia. Econ Geol 99:233–255. doi: 10.2113/gsecongeo.40.7.431

Chaput M., Michard A. (1967) L'Ordovicien supérieur d'Argut et ses minéralisations Pb-Zn. BRGM Rep DRMM67 A-9:38

Charef A, Sheppard SMF (1988) The Malines Cambrian carbonate-shale-hosted Pb-Zn deposit, France: Thermometric and isotopic (H, O) evidence for pulsating hydrothermal mineralization. Miner Depos 23:86–95. doi: 10.1007/BF00206655

Chen J, Liu G, Li H, Wu B (2014) Mineralogical and geochemical responses of coal to igneous intrusion in the Pansan Coal Mine of the Huainan coalfield, Anhui, China. Int J Coal Geol 124:11–35. doi: 10.1016/j.coal.2013.12.018

Chi G, Qing H, Xue C (2005) An overpressured fluid system associated with the giant sandstone-hosted Jinding Zn-Pb deposit, western Yunnan, China Chapter. Mao J, Bierlein FP (eds), Miner Depos Res Meet Gobal challenge Springer-Verlag, Berlin 93–96. doi: 10.1007/3-540-27946-6

Chi G, Xue C, Qing H, Xue W, Zhang J, Sun Y (2012) Hydrodynamic analysis of clastic injection and hydraulic fracturing structures in the Jinding Zn-Pb deposit, Yunnan, China. Geosci Front 3:73–84. doi: 10.1016/j.gsf.2011.07.003

Choukroune P (1992) Tectonic evolution of the Pyrenees. Annu Rev Earth Planet Sci 20:143–158

Ciobanu CL, Cook NJ, Damian F, Damian G (2006) Gold scavenged by bismuth melts: An example from Alpine shear-remobilizates in the Highiş Massif, Romania. Mineral Petrol 87:351–384. doi: 10.1007/s00710-006-0125-9

Clark BR, Kelly WC (1973) Sulfide Deformation Studies; I, Experimental Deformation of Pyrrhotite and Sphalerite to 2,000 Bars and 500 degrees C. Econ Geol 68:332–352. doi: 10.2113/gsecongeo.68.3.332

Clerc C, Lahfid A, Monié P, Lagabrielle Y, Chopin C, Poujol M, Boulvais P, Ringenbach JC, Masini E, De St Blanquat M (2015) High-temperature metamorphism during extreme thinning of the continental crust: A reappraisal of the North Pyrenean passive paleomargin. Solid Earth 6:643–668. doi: 10.5194/se-6-643-2015

Clin M, Taillefer F, Pouchan P, Muller A (1989) Bagnères de Luchon. BRGM Geol map 1/50 000 with note 78p

Cochelin B (2016) Champ de déformation du socle Paléozoïque des Pyrénées, PhD Thesis Université Toulouse 3 Paul Sabatier

Cochelin B, Chardon D, Denèle Y, Gumiaux C, Le Bayon B (2017a) Vertical strain partitioning in hot Variscan crust: Syn-convergence escape of the Pyrenees in the Iberian-Armorican syntax. Bull la Société géologique Fr 188:39. doi: 10.1051/bsgf/2017206

Cochelin B, Lemirre B, Denèle Y, De Saint Blanquat M, Lahfid A, Duchêne S (2017b) Structural inheritance in the Central Pyrenees : the Variscan to Alpine tectonometamorphic evolution of the Axial Zone. J Geol Soc London 175:336–351. doi: https://doi.org/10.1144/jgs2017-066

Cocherie A, Baudin T, Autran A, Guerrot C, Fanning CM, Laumonier B (2005) U-Pb zircon (ID-TIMS and SHRIMP) evidence for the early ordovician intrusion of metagranites in the Late Proterozoic Canaveilles Group of the Pyrenees and the Montagne Noire (France). Bull la Soc Geol Fr 176:269–282. doi: 10.2113/176.3.269

Cook N, Etschmann B, Ciobanu C, Geraki K, Howard D, Williams T, Rae N, Pring A, Chen G, Johannessen B, Brugger J (2015) Distribution and Substitution Mechanism of Ge in a Ge-(Fe)-Bearing Sphalerite. Minerals 5:117–132. doi: 10.3390/min5020117

Cook NJ (1996) Mineralogy of the sulphide deposits at Sulitjelma, northern Norway

Cook NJ, Ciobanu CL, Brugger J, Etschmann B, Howard DL, De Jonge MD, Ryan C, Paterson D (2012) Determination of the oxidation state of Cu in substituted Cu-In-Fe-bearing sphalerite via μ-XANES spectroscopy. Am Mineral 97:476–479. doi: 10.2138/am.2012.4042

Cook NJ, Ciobanu CL, Mao J (2009a) Textural control on gold distribution in As-free pyrite from the Dongping , Huangtuliang and Hougou gold deposits , North China Craton. Chem Geol 264:101–121. doi: 10.1016/j.chemgeo.2009.02.020

Cook NJ, Ciobanu CL, Pring A, Skinner W, Shimizu M, Danyushevsky L, Saini-Eidukat B, Melcher F (2009b) Trace and minor elements in sphalerite: A LA-ICPMS study. Geochim Cosmochim Acta 73:4761–4791. doi: 10.1016/j.gca.2009.05.045

Cook NJ, Spry PG, Vokes FM (1998) Mineralogy and textural relationships among sulphosalts and related minerals in the Bleikvassli Zn-Pb-(Cu) deposit, Nordland, Norway. Miner Depos 34:35–56. doi: 10.1007/s001260050184

Cotton FA, Wilkinson G (1980) Advanced Inorganic Chemistry. Adv. Inorg. Chem. 981–994

Couderc JJ, Dudouit I, Bras J, Fagot M (1983) Observation par microscopie electronique en transmission d'echantillons de blende de diverses provenances. Bull Mineral 106:369–381

Couderc JJ, Dudouit I, Hennig-Michaeli C, Levade C (1985) The interaction between slip and twinning systems in natural sphalerite experimentally deformed. Phys Status Solidi 90:581–593. doi: 10.1002/pssa.2210900222

Coullaut Sáenz de Sicilia J-L (2013) Going for growth: Spain's mining sector presents strong growth prospects. Min J 16–20

Cox SF (1987) Flow mechanisms in sulphide minerals. Ore Geol Rev 2:133–171

Cox SF, Etheridge MA, Hobbs BE (1981) The experimental ductile deformation of polycrystalline and single crystal pyrite. Econ Geol 76:2105–2117. doi: 10.2113/gsecongeo.76.8.2105

Craig JR (2001) Ore-mineral textures and the tales they tell. Can Mineral 39:937–956. doi: 10.2113/gscanmin.39.4.937

Craig JR, Vokes FM (1992) Ore mineralogy of the Appalachian-Caledonian stratabound sulfide deposits. Ore Geol Rev 7:77–123. doi: 10.1016/0169-1368(92)90007-8

Cross AJ, Prior DJ, Stipp M, Kidder S (2017) The recrystallized grain size piezometer for quartz: An EBSD-based calibration. Geophys Res Lett 44:6667–6674. doi: 10.1002/2017GL073836

Cugerone A, Cenki-Tok B, Chauvet A, Le Goff E, Bailly L, Alard O, Allard M (2018a) Relationships between the occurrence of accessory Ge-minerals and sphalerite in Variscan Pb-Zn deposits of the Bossost anticlinorium, French Pyrenean Axial Zone: Chemistry, microstructures and ore-deposit setting. Ore Geol Rev 95:1–19. doi: 10.1016/j.oregeorev.2018.02.016

Cugerone A, Cenki-tok B, Oliot E, Muñoz M, Barou F, Motto-Ros V, Le Goff E (2019) Redistribution of germanium during dynamic recrystallization of sphalerite. Geology 48:. doi: 10.1130/G46791.1

Cugerone A, Oliot E, Chauvet A, Gavalda J, Le Goff E (2018b) Structural Control on the Formation of Pb-Zn Deposits: An Example from the Pyrenean Axial Zone. Minerals 8:1–20. doi: 10.3390/min8110489

Dai S, Ren D, Chou CL, Li S, Jiang Y (2006a) Mineralogy and geochemistry of the No. 6 Coal (Pennsylvanian) in the Junger Coalfield, Ordos Basin, China. Int J Coal Geol 66:253–270. doi: 10.1016/j.coal.2005.08.003

Dai S, Ren D, Li S (2006b) Discovery of the superlarge gallium ore deposit in Jungar, Inner Mongolia, North China. Chinese Sci Bull 51:2243–2252. doi: 10.1007/s11434-006-2113-1

de Hoÿm de Marien L, Le Bayon B, Pitra P, Van Den Driessche J, Poujol M, Cagnard F (2019) Two-stage Variscan metamorphism in the Canigou massif: Evidence for crustal thickening in the Pyrenees. J Metamorph Geol 1–26. doi: 10.1111/jmg.12487

de Saint Blanquat M, Bajolet F, Grand'Homme A, Proietti A, Zanti M, Boutin A, Clerc C, Lagabrielle Y, Labaume P (2016) Cretaceous mantle exhumation in the central Pyrenees: New constraints from the peridotites in eastern Ariège (North Pyrenean zone, France). Comptes Rendus - Geosci 348:268–278. doi: 10.1016/j.crte.2015.12.003

De Sitter LU, Zwart HJ (1960) Tectonic development in supra and infra-structures of a mountain chain. Proc 21st Int Geol Congr Copenhagen, 18:248–256

De Vera J, McClay KR, King AR (2004) Structure of the Red Dog District , Western Brooks Range , Alaska. Econ Geol 99:1415–1434

De Vos W, Viaene W, Moreau J, Wautier J (1974) Minéralogie du gisement de Kipushi Shaba, Zaïre. Ann. la Société géologique Belgique [En ligne], Publ. spéciales Gisements Stratif. Prov. cuprifères - Centen. la Société Géologique Belgique 20

Deane JG (1995) The structural evolution of the Kombat deposits, Otavi Mountainland, Namibia. Commun Geol Surv Namib 10:99–107

Deloule E, Alexandrov P, Cheilletz A, Laumonier B, Barbey P (2002) In-situ U-Pb zircon ages for Early Ordovician magmatism in the eastern Pyrenees, France: The Canigou orthogneisses. Int J Earth Sci 91:398–405. doi: 10.1007/s00531-001-0232-0

Delvolvé JJ, Souquet P, Vachard D, Perret MF, Aguirre P (1993) Caractérisation d'un bassin d'avant-pays dans le Carbonifère des Pyrénées: faciès, chronologie de la tectonique synsédimentaire. Comptes Rendus Acad Sci Paris 316:959–966

Denèle Y (2007) Formation des dômes gneissiques hercyniens dans les Pyrénées : exemple du massif de l ' Aston-Hospitalet Formation des dômes gneissiques hercyniens dans les Pyrénées : exemple du massif de l 'Aston-Hospitalet, PhD Thesis Université Toulouse 3 Paul Sabatie

Denèle Y, Barbey P, Deloule E, Pelletier E, Olivier P, Gleizes G (2009) Middle Ordovician U-Pb age of the Aston and Hospitalet orthogneissic laccoliths : Their role in the Variscan evolution of the Pyrenees. Bull la Société Géologique Fr 3:209–216. doi: 10.2113/gssgfbull.180.3.209

Denèle Y, Laumonier B, Paquette J-L, Olivier P, Gleizes G, Barbey P (2014) Timing of granite emplacement, crustal flow and gneiss

dome formation in the Variscan segment of the Pyrenees. Schulmann, K, al, eds, Variscan Orogeny Extent, Timescale Form Eur Crust Geol Soc London, Spec Publ 405:265–287. doi: 10.1144/SP405.5

Denèle Y, Olivier P, Gleizes G (2008) Progressive deformation of a zone of magma transfer in a transpressional regime: The Variscan Mérens shear zone (Pyrenees, France). J Struct Geol 30:1138–1149. doi: 10.1016/j.jsg.2008.05.006

Denèle Y, Paquette JL, Olivier P, Barbey P (2012) Permian granites in the Pyrenees: The Aya pluton (Basque Country). Terra Nov 24:105–113. doi: 10.1111/j.1365-3121.2011.01043.x

Di Benedetto F, Bernardini GP, Costagliola P, Plant D, Vaughan DJ (2005) Compositional zoning in sphalerite crystals. Am Mineral 90:1384–1392. doi: 10.2138/am.2005.1754

Diamond LW (2003) Chapter 3. Systematics of H2O inclusions. Samson I, Anderson A, Marshall D Fluid inclusions Anal Interpret Mineral Assoc Canada, Short Course, 32:55–78

Dostal J (2017) Rare earth element deposits of alkaline igneous rocks. Resources 6:. doi: 10.3390/resources6030034

Druguet E, Castro A, Chichorros M, Pereira MF, Fernandez C (2014) Zircon geochronology of intrusive rocks from Cap de Creus, Eastern Pyrenees. Geol Mag 151:1095–1114. doi: 10.1017/S0016756814000041

Drury MR, Urai JL (1990) Deformation-related recrystallization processes. Tectonophysics 172:235–253. doi: 10.1109/IMFEDK.2013.6602261

Du G, Zhuang X, Querol X, Izquierdo M, Alastuey A, Moreno T, Font O (2009) Ge distribution in the Wulantuga high-germanium coal deposit in the Shengli coalfield, Inner Mongolia, northeastern China. Int J Coal Geol 78:16–26. doi: 10.1016/j.coal.2008.10.004

Dubois C (2015) Mangeuses d'homme. L'épopée des mines de Bentaillou et de Bulard en Ariège, Privat Edition, Privat

Dubois P, Seguin J-C (1978) Les flyschs crétacé et éocène de la zone commingeoise et leur environnement. Bull la Soc Geol Fr 7:657–671

Dubosq R, Lawley CJM, Rogowitz A, Schneider DA, Jackson S (2018) Pyrite deformation and connections to gold mobility : Insight from micro-structural analysis and trace element mapping. Lithos 310–311:86–104. doi: 10.1016/j.lithos.2018.03.024

Dutrizac JE, Jambor JL, Chen TT (1986) Host minerals for the gallium-germanium ores of the Apex Mine, Utah. Econ Geol 81:946–950

Emslie DP (1960) The Mineralogy and Geochemistry of the copper, lead, and zinc sulphides of the Otavi Mountainland. Rep Natl Inst Metall 1–52

Eremin NI, Sergeeva NE, Dergachev a. L (2007) Rare minerals from massive sulfide ores: Typomorphic features and geochemical trend. Moscow Univ Geol Bull 62:98–106. doi: 10.3103/S0145875207020044

Eskenazy GM (2006) Geochemistry of beryllium in Bulgarian coals. Int J Coal Geol 66:305–315. doi: 10.1016/j.coal.2005.07.005

Essaifi A, Goodenough K, Tornos F, Outigua A, Ouadjou A, Maacha L (2019) The Moroccan Massive Sulphide Deposits : Evidence for a Polyphase Mineralization. Minerals 9:1–31. doi: 10.3390/min9030156

Esteban JJ, Aranguren a., Cuevas J, Hilario a., Tubía JM, Larionov a., Sergeev S (2015) Is there a time lag between the metamorphism and emplacement of plutons in the Axial Zone of the Pyrenees? Geol Mag 1–7. doi: 10.1017/S001675681500014X

Etschmann B, Liu W, Li K, Dai S, Reith F, Falconer D (2017) Enrichment of germanium and associated arsenic and tungsten in

coal and roll-front U deposits Enrichment of germanium and associated arsenic and tungsten in coal and roll-front uranium deposits. Chem Geol 463:29–49. doi: 10.1016/j.chemgeo.2017.05.006

Etschmann BE, Liu W, Testemale D, Müller H, Rae NA, Proux O, Hazemann JL, Brugger J (2010) An in situ XAS study of copper(I) transport as hydrosulfide complexes in hydrothermal solutions (25-592°C, 180-600bar): Speciation and solubility in vapor and liquid phases. Geochim Cosmochim Acta 74:4723–4739. doi: 10.1016/j.gca.2010.05.013

European Commission (2017a) Study on the review of the list of Critical Raw Materials Criticality Assessments. Eur Comm - Final Rep 1–93

European Commission (2017b) Communication from the Commission to the European Parliament, the Council, the Eurpean Economic and Social Committee and the Committee of the Regions: on the 2017 list of Critical Raw Materials for the EU. Off J Eur Union 8

Evans NG, Gleizes G, Leblanc D, Bouchez JL (1998) Syntectonic emplacement of the Maladeta granite (Pyrenees) deduced from relationships between Hercynian deformation and contact metamorphism. J Geol Soc London 155:209–216. doi: 10.1144/gsjgs.155.1.0209

Fabre C, Devismes D, Moncayo S, Pelascini F, Trichard F, Lecomte A, Bousquet B, Cauzid J, Motto-Ros V (2018) Elemental imaging by laser-induced breakdown spectroscopy for the geological characterization of minerals. J Anal At Spectrom R Soc Chem 1–9. doi: 10.1039/c8ja00048d

Fallourd S, Poujol M, Boulvais P, Paquette JL, de Saint Blanquat M, Rémy P (2014) In situ LA-ICP-MS U-Pb titanite dating of Na-Ca metasomatism in orogenic belts: The North Pyrenean example. Int J Earth Sci 103:667–682. doi: 10.1007/s00531-013-0978-1

Fanlo I, Touray JC, Subías I, Fernández-Nieto C (1998) Geochemical patterns of a sheared fluorite vein, Parzan, Spanish central Pyrenees. Miner Depos 33:620–632. doi: 10.1007/s001260050177

Faure M, Rossi P, Gaché J, Melleton J, Frei D, Li X, Lin W (2014) Variscan orogeny in Corsica: New structural and geochronological insights, and its place in the Variscan geodynamic framework. Int J Earth Sci 103:1533–1551. doi: 10.1007/s00531-014-1031-8

Fert D (1976) Un aspect de la métallogénie du zinc et du plomb dans l'Ordovicien des Pyrénées Centrales : le district de Sentein (Ariège, Haute-Garonne). PhD Thesis, Univ Pierre Marie Curie 149p

Finkelman RB (1983) Modes of occurrence of trace elements and minerals in coal: an analytical approach

Fliervoet TF, Drury MR, Chopra PN (1999) Crystallographic preferred orientations and misorientations in some olivine rocks deformed by diffusion or dislocation creep. Tectonophysics 303:1–27. doi: 10.1016/S0040-1951(98)00250-9

Fonteilles M, Soler P, Demange M, Derré C, Krier-Schellen AD, Verkaeren J, Guy B, Zahm A (1989) The scheelite skarn deposit of Salau, Ariege, French Pyrenees. Econ Geol 84:1172–1209. doi: 10.2113/gsecongeo.84.5.1172

Fougerouse D, Micklethwaite S, Halfpenny A, Reddy SM, Cliff JB, Martin LAJ, Kilburn M, Guagliardo P, Ulrich S (2016a) The golden ark: Arsenopyrite crystal plasticity and the retention of gold through high strain and metamorphism. Terra Nov 28:181–187. doi: 10.1111/ter.12206

Fougerouse D, Micklethwaite S, Tomkins AG, Mei Y, Kilburn M, Guagliardo P, Fisher LA, Halfpenny A, Gee M, Paterson D, Howard DL (2016b) Gold remobilisation and formation of high grade ore shoots driven by dissolution-reprecipitation replacement and Ni substitution into auriferous arsenopyrite. Geochim Cosmochim Acta 178:143–159. doi: 10.1016/j.gca.2016.01.040

Fougerouse D, Reddy SM, Kirkland CL, Saxey DW, Rickard WD, Hough RM (2019) Time-resolved, defect-hosted, trace element mobility in deformed Witwatersrand pyrite. Geosci Front 10:55–63. doi: 10.1016/j.gsf.2018.03.010

Francotte J, Moreau J, Ottenburgs R, Levy C (1965) La briartite, une nouvelle espèce minérale. Bull Soc Fr minéralogie Cristallogr 432–437

Frenzel M, Bachmann K, Carvalho JRS, Relvas JMRS, Pacheco N, Gutzmer J (2019) The geometallurgical assessment of by-products—geochemical proxies for the complex mineralogical deportment of indium at Neves-Corvo, Portugal. Miner Depos 54:959–982. doi: 10.1007/s00126-018-0849-6

Frenzel M, Hirsch T, Gutzmer J (2016) Gallium, germanium, indium, and other trace and minor elements in sphalerite as a function of deposit type - A meta-analysis. Ore Geol Rev 76:52–78. doi: 10.1016/j.oregeorev.2015.12.017

Frenzel M, Ketris MP, Gutzmer J (2014) On the geological availability of germanium. Miner Depos 49:471–486. doi: 10.1007/s00126-013-0506-z

Frenzel M, Mikolajczak C, Reuter MA, Gutzmer J (2017) Quantifying the relative availability of high-tech by-product metals – The cases of gallium, germanium and indium. Resour Policy 52:327–335. doi: 10.1016/j.resourpol.2017.04.008

Frondel C, Ito J (1957) Geochemistry of Germanium in the Oxidized Zone of the Tsumeb Mine , South-West Africa. Am Mineral 42:

Frondel, Clifford, Strunz H (1960) Fleischerit und Itoite, zwei neue Germanium- Mineralien von Tsumeb. Neues Jahrb für Mineral 132–142

Fusswinkel T, Wagner T, Wälle M, Wenzel T, Heinrich CA, Markl G (2013) Fluid mixing forms basement-hosted Pb-Zn deposits: Insight from metal and halogen geochemistry of individual fluid inclusions. Geology 41:679–682. doi: 10.1130/G34092.1

Gagnon JE, Samson IM, Fryer BJ (2003) LA-ICP-MS analysis of fluid inclusions. Samson I, Anderson A, Marshall DD Fluid inclusions Anal Interpret Miner Assoc Canada, Vancouver 391–323

Gallard-Esquivel MC, Cepedal A, Fuertes-Fuente M, Martin-Izard A (2018) Enrichment in critical metals (In-Ge) and Te-Se in epithermal deposits of the 'La Carolina' district, San Luis, Argentina. Mineral Mag 82:S61–S87. doi: 10.1180/minmag.2017.081.105

García-Sansegundo J (1992) Estratigrafia y estructura de la Zona Axial Pirenaica en la Transversal del Valle de Aran y de la Alta Ribagorça. Publicación Espec del Boletín Geológico y Min España 102–103:1–290

Garcia-Sansegundo J, Alonso JL (1989) Stratigraphy and structure of the southeastern Garona Dome. Geodin Acta 3:127–134. doi: 10.1080/09853111.1989.11105180

García-Sansegundo J, Gavaldá J, Alonso JL (2004) Preuves de la discordance de l'Ordovicien supérieur dans la zone axiale des Pyrénées : Exemple du dôme de la Garonne (Espagne, France). Comptes Rendus - Geosci 336:1035–1040. doi: 10.1016/j.crte.2004.03.009

García-Sansegundo J, Martin-Izard A, Gavaldà J (2014) Structural control and geological significance of the Zn-Pb ores formed in the Benasque Pass area (Central Pyrenees) during the post-late Ordovician extensional event of the Gondwana margin. Ore Geol Rev 56:516–527. doi: 10.1016/j.oregeorev.2013.06.001

García-Sansegundo J, Merino JR, Santisteban RR, Leyva F (2013) Canejan-Vielha Mapa geologico 1:50 000. Inst Geol y Min Espana Primera ed:66p

Gasquet D, Bertrand JM, Paquette JL, Lehmann J, Ratzov G, Ascenção De Guedes RA, Tiepolo M, Boullier AM, Scaillet S, Nomade

S (2010) Miocene to Messinian deformation and hydrothermal activity in a pre-Alpine basement massif of the French western Alps: New U-Th-Pb and argon ages from the Lauzière massif. Bull la Soc Geol Fr 181:227–241. doi: 10.2113/gssgfbull.181.3.227

George LL, Cook NJ, Ciobanu CL (2016) Partitioning of trace elements in co-crystallized sphalerite-galena-chalcopyrite hydrothermal ores. Ore Geol Rev 77:97–116. doi: 10.1016/j.oregeorev.2016.02.009

Gibson GM, Hutton LJ, Holzschuh J (2017) Basin inversion and supercontinent assembly as drivers of sediment-hosted Pb–Zn mineralization in the Mount Isa region, northern Australia. J Geol Soc London 174:jgs2016-105. doi: 10.1144/jgs2016-105

Gibson GM, Nutman AP (2004) Detachment faulting and bimodal magmatism in the Palaeoproterozoic Willyama Supergroup, south-central Australia; keys to recognition of a multiply deformed Precambrian metamorphic core complex. J Geol Soc London 161, Part:55–66. doi: 10.1144/0016-764903-060

Gil-Pena I, Barnolas A, Sanz-Lopez J, Garcia-Sansegundo J, Palau J (2001) Discontinuidad sedimentaria del Ordovicico terminal en los Pirineos centrales. Geogaceta 29:4p

Gill JE (1969) Experimental deformation and annealing of sulfides and interpretation of ore textures. Econ Geol 64:500–508. doi: 10.2113/gsecongeo.64.5.500

Gilligan LB, Marshall B (1987) Textural evidence for remobilization in metamorphic environments. Ore Geol Rev 2:205–229. doi: 10.1016/0169-1368(87)90029-1

Gleizes G, Crevon G, Asrat A, Barbey P (2006) Structure, age and mode of emplacement of the Hercynian Bordères-Louron pluton (Central Pyrenees, France). Int J Earth Sci 95:1039–1052. doi: 10.1007/s00531-006-0088-4

Goffin V, Evrard M, Pirard E (2015) Critical metals in sphalerites from Belgian MVT deposits. Proc 13th SGA Bienn Meet 1–4

Golberg JM, Leyreloup AF (1990) High temperature-low pressure Cretaceous metamorphism related to crustal thinning (Eastern North Pyrenean Zone, France). Contrib to Mineral Petrol 104:194–207. doi: 10.1007/BF00306443

Goldschmidt VM (1954) Geochemistry. Soil Sci 78:156

Goldschmidt VM, Peters C (1933) Über die Anreicherung seltener Elemente in Steinkohlen. Nachrichten von der Gesellschaft der Wissenschaften zu Göttingen Math Phys Klasse 4:371–387

Goldstein RH, Reynolds TJ (1994) Systematics of Fluid Inclusions in Diagenetic Minerals. SEPM Short Course 31 1–213

Gonçalves GO, Lana C, Scholz R, Buick IS, Gerdes A, Kamo SL, Corfu F, Marinho MM, Chaves AO, Valeriano C, Nalini HA (2016) An assessment of monazite from the Itambé pegmatite district for use as U-Pb isotope reference material for microanalysis and implications for the origin of the 'Moacyr' monazite. Chem Geol 424:30–50. doi: 10.1016/j.chemgeo.2015.12.019

Goodenough KM, Schilling J, Jonsson E, Kalvig P, Charles N, Tuduri J, Deady EA, Sadeghi M, Schiellerup H, Müller A, Bertrand G, Arvanitidis N, Eliopoulos DG, Shaw RA, Thrane K, Keulen N (2016) Europe's rare earth element resource potential: An overview of REE metallogenetic provinces and their geodynamic setting. Ore Geol Rev 72:838–856. doi: 10.1016/j.oregeorev.2015.09.019

Götze J, Plötze M, Graupner T, Hallbauer DK, Bray CJ (2004) Trace element incorporation into quartz: A combined study by ICP-MS, electron spin resonance, cathodoluminescence, capillary ion analysis, and gas chromatography. Geochim Cosmochim Acta 68:3741–3759. doi: 10.1016/j.gca.2004.01.003

Graf L, Skinner BJ, Bras J, Fagot M, Levade C, Couderc JJ (1981) Transmission Electron Microscopic observation of plastic deformation in experimentally deformed pyrite. Econ Geol 76:738–742

Graham GE, Kelley KD, Slack JF, Koenig AE (2009) Trace elements in Zn−Pb−Ag deposits and related stream sediments, Brooks Range Alaska, with implications for Tl as a pathfinder element. Geochemistry Explor Environ Anal 9:19–37. doi: 10.1144/1467-7873/08-177

Grand'Homme A, Janots E, Seydoux-Guillaume AM, Guillaume D, Bosse V, Magnin V (2016) Partial resetting of the U-Th-Pb systems in experimentally altered monazite: Nanoscale evidence of incomplete replacement. Geology 44:431–434. doi: 10.1130/G37770.1

Grant NT, Banks DA, McCaig AM, Yardley BWD (1990) Chemistry, source and behavior of fluids involved in alpine thrusting of the central Pyrenees. J Geophys Res 95:9123–9131. doi: 10.1029/JB095iB06p09123

Gratz JF, Misra KC (1987) Fluid inclusion study of the Gordonsville zinc deposit, central Tennessee. Econ Geol 82:1790–1804. doi: 10.2113/gsecongeo.82.7.1790

Guerrot C (2001) Datation du pluton des Eaux-Chaudes. Ternet Y, Majeste´-Menjoulas C, Cane´rot J, Baudin T, Co- cherie A, Guerr C, Ross P Not Explic Cart géol Fr (1/50,000), feuille Laruns-Somport (1069) BRGM, Orléans 59:

Guillong M, Heinrich CA (2007) Sensitivity enhancement in laser ablation ICP-MS using small amounts of hydrogen in the carrier gas. J Anal At Spectrom 22:1488–1494. doi: 10.1039/b709489b

Guillong M, Meier DL, Allan MM, Heinrich CA, Yardley BWD (2008) SILLS: A Matlab-Based program for the reduction of Laser Ablation ICP-MS data of homogeneous materials and inclusions. Mineral Assoc Canada Short Course 40:328–333

Guillope M, Poirier JP (1979) Dynamic Recrystallization During Creep of Single-Crystalline Halite: An Experimental Study. J Geophys Res 84:5557–5567

Guitard G (1964) Un exemple de structure en nappe de style pennique dans la chaîne hercynienne : les gneiss stratoïdes du Canigou (Pyrénées-Orientales). Compte Rendu Acad Sci Paris 258:4597–4599

Guitard G, Geyssant J, Laumonier B (1984) Les plissements hercyniens tardifs dans le Paléozoïque inférieur du versant nord du Canigou. 1re partie: analyse géométrique et chronologie des phases superposees. Relations avec le granite de Mont-Louis et le métamorphisme régional. Géologie la Fr 4:95–125

Gutiérrez-Alonso G, Fernández-Suárez J, Jeffries TE, Johnston ST, Pastor-Galán D, Murphy JB, Franco MP, Gonzalo JC (2011) Diachronous post-orogenic magmatism within a developing orocline in Iberia, European Variscides. Tectonics 30:. doi: 10.1029/2010TC002845

Gutiérrez-Alonso G, Fernández-Suárez J, López-Carmona A, Gärtner A (2018) Exhuming a cold case: The early granodiorites of the northwest Iberian Variscan belt-A Visean magmatic flare-up? Lithosphere 10:194–216. doi: 10.1130/L706.1

Hadadzadeh A, Mokdad F, Wells MA, Chen DL (2018) A new grain orientation spread approach to analyze the dynamic recrystallization behavior of a cast-homogenized Mg-Zn-Zr alloy using electron backscattered diffraction. Mater Sci Eng A 709:285–289. doi: 10.1016/j.msea.2017.10.062

Hall WE, Heyl A V. (1968) Distribution of minor elements in ore and host rock, Illinois-Kentucky fluorite district and upper Mississippi valley Zinc-Lead District. Econ Geol 63:655–670. doi: 10.2113/gsecongeo.63.6.655

Han R-S, Liu C-Q, Huang Z-L, Chen J, Ma D-Y, Lei L, Ma G-S (2006) Geological features and origin of the Huize carbonate-hosted Zn–Pb–(Ag) District, Yunnan, South China. Ore Geol Rev 31:360–383. doi: 10.1016/j.oregeorev.2006.03.003

Hao J, Wang Y, Guo Q, Zhao J, Li Y (2019) Structural Strategies for Germanium-Based Anode Materials to Enhance Lithium Storage. Part Part Syst Charact 1–30. doi: 10.1002/ppsc.201900248

Harańczyk C (1975) Morozeviczite and polkovicite, typochemical minerals of Mesozoic mineralization of the Fore-Sudeten monocline. Rudy i Met 20:288–293

Hariya Y, Wai CM (1970) The stability and phase transition of the system Fe2GeO4-Fe2SiO4. J Fac Sci Hokkaido Univ 14:355–363

Harlov DE, Wirth R, Hetherington CJ (2011) Fluid-mediated partial alteration in monazite: The role of coupled dissolution-reprecipitation in element redistribution and mass transfer. Contrib to Mineral Petrol 162:329–348. doi: 10.1007/s00410-010-0599-7

Harris DC, Sangster DF (1991) Minor element content of sphalerite, Nanisivik lead–zinc deposit, NWT

Harrison TM, Célérier J, Aikman AB, Hermann J, Heizler MT (2009) Diffusion of 40Ar in muscovite. Geochim Cosmochim Acta 73:1039–1051. doi: 10.1016/j.gca.2008.09.038

Hartevelt JJA (1970) Geology of the upper Segre and Valira Valleys, Central Pyrenees, Andorra/Spain. Leidse Geol Meded 45:167–236

Hawkins DP, Bowring SA (1997) U-Pb systematics of monazite and xenotime: Case studies from the Paleoproterozoic of the Grand Canyon, Arizona. Contrib to Mineral Petrol 127:87–103. doi: 10.1007/s004100050267

Haydon RC, Mcconachy GW (1987) The Stratigraphic Setting of Pb-Zn-Ag Mineralization at Broken Hill. Econ Geol 82:826–856. doi: 10.2113/gsecongeo.82.4.826

Hazarika P, Upadhyay D, Mishra B (2013) Contrasting geochronological evolution of the Rajpura-Dariba and Rampura-Agucha metamorphosed Zn-Pb deposit, Aravalli-Delhi Belt, India. J Asian Earth Sci 73:429–439. doi: 10.1016/j.jseaes.2013.04.047

Hedenquist JW (1991) Boiling and dilution in the shallow portion of the Waiotapu geothermal system, New Zealand. Geochim Cosmochim Acta 55:2753–2765. doi: 10.1016/0016-7037(91)90442-8

Heijlen W, Banks DA, Muchez P, Stensgard BM, Yardley BWD (2008) The nature of mineralizing fluids of the Kipushi Zn-Cu deposit, Katanga, Democratic Repubic of Congo: Quantitative fluid inclusion analysis using laser ablation ICP-MS and bulk crush-leach methods. Econ Geol 103:1459–1482. doi: 10.2113/gsecongeo.103.7.1459

Heimann A, Spry PG, Teale GS, Leyh WR, Conor CHH, Mora G, O'Brien JJ (2013) Geochemistry and genesis of low-grade metasediment-hosted Zn-Pb-Ag mineralization, southern Proterozoic Curnamona Province, Australia. J Geochemical Explor 128:97–116. doi: 10.1016/j.gexplo.2013.02.007

Henderson IHC, McCaig AM (1996) Fluid pressure and salinity variations in shear zone-related veins, central Pyrenees, France: Implications for the fault-valve model. Tectonophysics 262:321–348. doi: 10.1016/0040-1951(96)00018-2

Henjes-Kunst E, Raith JG, Boyce AJ (2017a) Micro-scale sulfur isotope and chemical variations in sphalerite from the Bleiberg Pb-Zn deposit, Eastern Alps, Austria. Ore Geol Rev 90:52–62. doi: 10.1016/j.oregeorev.2017.10.020

Henjes-Kunst E, Raith JG, Boyce AJ (2017b) Micro-scale sulfur isotope and chemical variations in sphalerite from the Bleiberg Pb-Zn deposit, Eastern Alps, Austria. Ore Geol Rev 90:52–62. doi: 10.1016/j.oregeorev.2017.10.020

Hirth G, Tullis J (1992) Dislocation creep regimes in quartz aggregates. J Struct Geol 14:145–159. doi: 10.1016/0191-8141(92)90053-Y

Hitzman MW (1986) Geology of the Ruby Creek Copper Deposit, Southwestern Brooks Range, Alaska. Econ Geol 81:1644–1674

Hitzman MW, Reynolds NA, Sangster DF, Allen CR, Carman CE (2003) Classification, genesis, and exploration guides for nonsulfide zinc deposits. Econ Geol 98:685–714. doi: 10.2113/gsecongeo.98.4.685

Hobbs BE, Walshe JL, Ord A, Zhang Y, Carr GC (1998) The Broken Hill orebody: A high temperature, high pressure scenario. Aust Geol Surv Organ Rec 1998 2:98–103

Hofmann AB, Knill DM (1996) Geochemistry and genesis of the lengenbach Pb–Zn–As–Tl–Ba-mineralization, Binn Valley, Switzerland. Miner Depos 31:319–339

Hofmann BA (1994) Formation of a sulfide melt during Alpine metamorphism of the Lengenbach polymetallic sulfide mineralization, Binntal, Switzerland. Miner Depos 29:439–442. doi: 10.1007/BF01886964

Höll R, Kling M, Schroll E (2007) Metallogenesis of germanium-A review. Ore Geol Rev 30:145–180. doi: 10.1016/j.oregeorev.2005.07.034

Horn S, Dziggel A, Kolb J, Sindern S (2018) Textural characteristics and trace element distribution in carbonate-hosted Zn-Pb-Ag ores at the Paleoproterozoic Black Angel deposit, central West Greenland. Miner Depos 54:507–524. doi: 10.1007/s00126-018-0821-5

Hower JC, Berti D, Hochella MF, Rimmer SM, Taulbee DN (2018) Submicron-scale mineralogy of lithotypes and the implications for trace element associations: Blue Gem coal, Knox County, Kentucky. Int J Coal Geol 192:73–82. doi: 10.1016/j.coal.2018.04.006

Hower JC, Ruppert LF, Williams DA (2002) Controls on boron and germanium distribution in the low-sulfur Amos coal bed, Western Kentucky coalfield, USA. Int J Coal Geol 53:27–42. doi: 10.1016/S0166-5162(02)00151-9

Hu RZ, Qi HW, Zhou MF, Su WC, Bi XW, Peng JT, Zhong H (2009) Geological and geochemical constraints on the origin of the giant Lincang coal seam-hosted germanium deposit, Yunnan, SW China: A review. Ore Geol Rev 36:221–234. doi: 10.1016/j.oregeorev.2009.02.007

Huang M, Li S, Cai P, Hou G, Su TI, Chen W, Hong CY, Pan D (2018) Germanium on silicon avalanche photodiode. IEEE J Sel Top Quantum Electron 24:1–11. doi: 10.1109/JSTQE.2017.2749958

Hughes MJ (1987) The Tsumeb ore body, Namibia, and related dolostone-hosted base metal ore deposits of Central Africa. Ph D Thesis Univ Witwatersrand, Johannesbg p448

Hurai V, Paquette J-L, Huraiová M, Konečný P (2010) Age of deep crustal magmatic chambers in the intra-Carpathian back-arc basin inferred from LA-ICPMS U-Th-Pb dating of zircon and monazite from igneous xenoliths in alkali basalts. J Volcanol Geotherm Res 198:275–287

Hurai V, Paquette JL, Huraiová M, Sabol M (2012) U-Pb geochronology of zircons from fossiliferous sediments of the Hajnáčka i maar (Slovakia) type locality of the MN 16a biostratigraphic subzone. Geol Mag 149:989–1000. doi: 10.1017/S0016756812000106

Huston DL, Stevens B, Southgate PN, Muhling P, Wyborn L (2006) Australian Zn-Pb-Ag Ore-forming systems: A review and analysis. Econ Geol 101:1117–1157. doi: 10.2113/gsecongeo.101.6.1117

Intiomale MM, Oosterbosch R (1974) Géologie et géochimie du gisement de Kipushi, Zaïre. Bartholomé P. Gisements Stratif. Prov. cupriferes. Centen. Société Géologique Belgique 123–164

Jackson SE, Pearson NJ, Griffin WL, Belousova EA (2004) The application of laser ablation-inductively coupled plasma-mass spectrometry to in situ U-Pb zircon geochronology. Chem Geol 211:47–69. doi: 10.1016/j.chemgeo.2004.06.017

Jaffey AH, Flynn KF, Glendenin LE, Bentley WC, Essling AM (1971) Precision measurement of half-lives and specific activities of U235 and U238. Phys Rev C 4:1889–1906. doi: 10.1103/PhysRevC.4.1889

Jambor JL, Roberts AC, Groat LA, Stanley CJ, Criddle AJ, Feinglos MN (2007) Calvertite, Cu5Ge0.5S4, A new mineral species

from Tsumeb, Namibia. Can Mineral 45:1519–1523

Jastrzębski M, Machowiak K, Krzemińska E, Lang Farmer G, Larionov AN, Murtezi M, Majka J, Sergeev S, Ripley EM, Whitehouse M (2018) Geochronology, petrogenesis and geodynamic significance of the Visean igneous rocks in the Central Sudetes, northeastern Bohemian Massif. Lithos 316–317:385–405. doi: 10.1016/j.lithos.2018.07.034

Jochum KP, Weis U, Stoll B, Kuzmin D, Yang Q, Raczek I, Jacob DE, Stracke A, Birbaum K, Frick DA, Günther D, Enzweiler J (2011) Determination of reference values for NIST SRM 610-617 glasses following ISO guidelines. Geostand Geoanalytical Res 35:397–429. doi: 10.1111/j.1751-908X.2011.00120.x

Johan Z (1988) Indium and germanium in the structure of sphalerite: an example of coupled substitution with Copper. Mineral Petrol 39:211–229. doi: 10.1007/BF01163036

Johan Z, Oudin E (1986) Présence de grenats, Ca3 Ga (GeO4)3, Ca3 Al (sub 2) [(Ge,Si)O4]3 et d'un équivalent ferrifere, germanifere et gallifere de la sapphirine, Fe4 (Ga,Sn,Fe)4 (Ga,Ge)6 O20, dans la blende des gisements de la zone axiale pyrénéenne. Conditions de formation des. CR Acad Sc Paris 9:811–816

Johan Z, Oudin E, Picot P (1983) Analogues germanifères et gallifères des silicates et oxydes dans les gisements de zinc des Pyrénées centrales, France; argutite et carboirite, deux nouvelles espèces minérales. TMPM Tschermaks Mineral und Petrogr Mitteilungen 31:97–119. doi: 10.1007/BF01084764

Johnson CA, Cardellach E, Tritlla J, Hanan BB (1996) Cierco Pb-Zn-Ag Vein Deposits: Isotopic and Fluid Inclusion Evidence for Formation during the Mesozoic Extension in the Pyrenees of Spain. Econ Geol 91:497–506. doi: 10.5962/bhl.title.18736

Jolivet L, Leprince M, Moncayo S, Sorbier L, Lienemann C (2019) Spectrochimica Acta Part B Review of the recent advances and applications of LIBS-based imaging. Spectrochim Acta Part B 151:41–53. doi: 10.1016/j.sab.2018.11.008

Jonsson E, Högdahl K, Majka J, Lindeberg T (2013) Roquesite and associated indium-bearing sulfides from a paleoproterozoic carbonate-hosted mineralization: Lindbom's prospect, Bergslagen, Sweden. Can Mineral 51:629–641. doi: 10.3749/canmin.51.4.629

Joseph Canérot (1991) Comparative study of the Eastern Iberides (Spain) and the Western Pyrenees (France) Mesozoic basins. Palaeogeogr Palaeoclimatol Palaeoecol 87:1–28

Julliot JY, Volfinger M, Robert JL (1987) Mineralogy Petrology Experimental Study of Carboirite and Related Phases in the System GeO2-SiO2-AI203-FeO-H20 at P up to 2 kbar. Mineral Petrol 36:51–69

Kamona AF, Friedrich GH (2007) Geology, mineralogy and stable isotope geochemistry of the Kabwe carbonate-hosted Pb-Zn deposit, Central Zambia. Ore Geol Rev 30:217–243. doi: 10.1016/j.oregeorev.2006.02.003

Kamona AF, Lévêque J, Friedrich G, Haack U (1999) Lead isotopes of the carbonate-hosted Kabwe, Tsumeb, and Kipushi Pb-Zn-Cu sulphide deposits in relation to Pan African orogenesis in the Damaran-Lufilian Fold Belt of Central Africa. Miner Depos 34:273–283. doi: 10.1007/s001260050203

Kampmann TC, Jansson NF, Stephens MB, Olin PH, Gilbert S, Wanhainen C (2018) Syn-tectonic sulphide remobilization and trace element redistribution at the Falun pyritic Zn-Pb-Cu-(Au-Ag) sulphide deposit, Bergslagen, Sweden. Ore Geol Rev 96:48–71. doi: 10.1016/j.oregeorev.2018.04.010

Kampunzu AB, Cailteux JLH, Kamona AF, Intiomale MM, Melcher F (2009) Sediment-hosted Zn-Pb-Cu deposits in the Central African Copperbelt. Ore Geol Rev 35:263–297. doi: 10.1016/j.oregeorev.2009.02.003

Keller, P., Dunn PJ (1986) (1986) Mathewrogersit, ein neues Bleisilikatmineral von Tsumeb, Namibia. Neues Jahrb für Mineral 203–208

Keller P, Hess H, Dunn PJ (1981) Otjisumeit, PbGe4O9, ein neues Mineral aus Tsumeb, Namibia. Neues Jahrb Miner 49–51

Kelley KD, Jennings S (2004) A special issue devoted to barite and Zn-Pb-Ag deposits in the Red Dog district, Western Brooks Range, northern Alaska. Econ Geol 99:1267–1280. doi: 10.2113/gsecongeo.99.7.1267

Kelly WC, Clark BR (1975) Sulfide deformation studies: III. Experimental deformation of chalcopyrite to 2,000 bars and 500??C. Econ Geol 70:431–453. doi: 10.2113/gsecongeo.70.3.431

Kesler SE, Richard Kyle J, Appold MS, Huston TJ, Walter LM, Martini AM (1995) Na-Cl-Br systematics of mineralizing brines in Mississippi Valley–type deposits. Geology 23:641–644. doi: 10.1130/0091-7613(1995)023<0641:ncbsom>2.3.co;2

Kilzi MA, Grégoire M, Bosse V, Benoît M, Driouch Y, de Saint Blanquat M, Debat P (2016) Geochemistry and zircon U-Pb geochronology of the ultramafic and mafic rocks emplaced within the anatectic series of the Variscan Pyrenees: The example of the Gavarnie-Heas dome (France). Comptes Rendus - Geosci 348:107–115. doi: 10.1016/j.crte.2015.06.014

Kleinsmiede WFJ (1960) Geology of the Valle de Aran (Central Pyrenees). Leidse Geol Meded 25:129–245

Klinger L, Rabkin E (1999) Beyond the fisher model of grain boundary diffusion: Effect of structural inhomogeneity in the bulk. Acta Mater 47:725–734. doi: 10.1016/S1359-6454(98)00420-0

Kollenberg W, Siemes H (1983) Experimental deformation of sphalerite-garnet ore under a confining pressure of 300 MPa and at temperatures between 250° C and 300° C. Deform Multi-Phase Part Contain Mater Mater Sci (Eds JB Bild N Hansen A Horsewell, T Leffers, H Liholt) 351–356

Komuro K, Kajiwara Y (2004) Germanium-bearing colusite in siliceous black ore from the Ezuri Kuroko deposit, Hokuroku district, Japan. Resour Geol 54:447–452. doi: 10.1111/j.1751-3928.2004.tb00220.x

Kontonikas-Charos A, Ciobanu CL, Cook NJ, Ehrig K, Ismail R, Krneta S, Basak A (2018) Feldspar mineralogy and rare-earth element (re) mobilization in iron-oxide copper gold systems from South Australia : a nanoscale study. Mineral Mag 82:173–197

Kouzmanov K (2001) Genèse des concentrations en métaux de base et précieux de Radka et Elshitsa (zone de Sredna Gora, Bulgarie) : une approche par l'étude minéralogique, isotopique et des inclusions fluides. Ph D Thesis Univ d'Orléans 289

Kouzmanov K, Bailly L, Ramboz C, Rouer O, Bény JM (2002) Morphology, origin and infrared microthermometry of fluid inclusions in pyrite from the Radka epithermal copper deposit, Srednogorie zone, Bulgaria. Miner Depos 37:599–613. doi: 10.1007/s00126-002-0270-y

Kroner U, Romer RL (2013) Two plates - Many subduction zones: The Variscan orogeny reconsidered. Gondwana Res 24:298–329. doi: 10.1016/j.gr.2013.03.001

Kyle JR, Li N (2002) Jinding : A Giant Tertiary Sandstone-Hosted Zn-Pb deposit, Yunnan, China. SEG Newsl 50:1–9

Laforet C, Oudin E, Picot P, Pierrot R, Pillard F (1981) Métallogénie régionale Utilisation des paragenèses minéralogiques et des minéraux traceurs. Bur Rech Geol Minieres Rapp 80 SGN175:33p.

Lagabrielle Y, Bodinier JL (2008) Submarine reworking of exhumed subcontinental mantle rocks: Field evidence from the Lherz peridotites, French Pyrenees. Terra Nov 20:11–21. doi: 10.1111/j.1365-3121.2007.00781.x

Lagabrielle Y, Labaume P, De Saint Blanquat M (2010) Mantle exhumation, crustal denudation, and gravity tectonics during Cretaceous rifting in the Pyrenean realm (SW Europe): Insights from the geological setting of the lherzolite bodies. Tectonics 29:1–26. doi: 10.1029/2009TC002588

Large RR, Bull SW, McGoldrick PJ, Walters S, Derrick GM, Carr GR (2005) Stratiform and Strata-Bound Zn-Pb-Ag Deposits in

Proterozoic Sedimentary Basins, Northern Australia. Econ Geol 100th Anniv Vol 931–963

Large RR, Danyushevsky L, Hollit C, Maslennikov V, Meffre S, Gilbert S, Bull S, Scott R, Emsbo P, Thomas H, Singh B, Foster J (2009) Gold and Trace Element Zonation in Pyrite Using a Laser Imaging Technique : Implications for the Timing of Gold in Orogenic and Carlin-Style Sediment-Hosted Deposits. Econ Geol 104:635–668

Larocque ACL, Hodgson CJ, Lafleur P-J (1993) Gold Distribution in the Mobrun Volcanic-Associated Massive Sulfide Deposit, Noranda, Quebec: A Preliminary Evaluation of the Role of Metamorphic Remobilization. Econ Geol 88:1443–1459

Laumonier B (2008) Les Pyrénées pré-hercyniennes et hercyniennes. CANÉROTCANÉROT J, COLIN J-P, PLATEL J-P BILOTTE M (dir) Pyrénées d'hier d'aujourd'hui, Pau, 20-21 Sept 2008 Éd Atl 23-35 23–35

Laumonier B, Le Bayon B, Calvet M (2015) Carte géol. France (1/50 000), feuille Prats-de-Mollo-la-Preste (1099). BRGM Not Explic par Laumonier B, Calvet M, Le Bayon B, Barbey P, Lenoble J-L 189p

Laumonier B, Marignac C, Kister P (2010) Polymétamorphisme et évolution crustale dans les Pyrénées orientales pendant l'orogenèse varisque au Carbonifère supérieur. Bull la Société géologique Fr 181:411–428

Laurent O, Couzinié S, Zeh A, Vanderhaeghe O, Moyen JF, Villaros A, Gardien V, Chelle-Michou C (2017) Protracted, coeval crust and mantle melting during Variscan late-orogenic evolution: U–Pb dating in the eastern French Massif Central. Int J Earth Sci 106:421–451. doi: 10.1007/s00531-016-1434-9

Lawrence LJ (1973) Polymetamorphism of the sulphide ores of Broken Hill, NSW, Australia. Miner Depos 8:211–236

Laznicka P (1999) Quantitative Relationships among Giant Deposits of Metals. Econ Geol 94:455–473

Laznicka P (2014) Giant metallic deposits-A century of progress. Ore Geol Rev 62:259–314. doi: 10.1016/j.oregeorev.2014.03.002

Le Pichon X, Bonnin J, Sibuet J-C (1970) La faille nord-pyrénéenne : faille transformante liée à l'ouverture du golfe de gascogne. Compte Rendu Acad Sci Paris 271:1941–1944

Leach DL (2005) Sediment-Hosted Lead-Zinc Deposits : A Global Perspective. Econ Geol 561–607. doi: 978-1-887483-01-8

Leach DL, Macquar JC, Lagneau V, Leventhal JS, Emsbo P, Premo W (2006) Precipitation of lead-zinc ores in the Mississippi Valley type deposit at Treves, cevennes region of southern France. Geofluids 6:24–44. doi: 10.1111/j.1468-8123.2006.00126.x

Leach DL, Marsh E, Emsbo P, Rombach CS, Kelley KD, Anthony M (2004) Nature of hydrothermal fluids at the shale-hosted Red Dog Zn-Pb-Ag deposits, Brooks Range, Alaska. Econ Geol 99:1449–1480. doi: 10.2113/gsecongeo.99.7.1449

Leach DL, Song YC, Hou ZQ (2017) The world-class Jinding Zn–Pb deposit: ore formation in an evaporite dome, Lanping Basin, Yunnan, China. Miner Depos 52:281–296. doi: 10.1007/s00126-016-0668-6

Lemirre B, Cochelin B, Duchene S, de Saint Blanquat M, Poujol M (2019) Origin and duration of late orogenic magmatism in the foreland of the Variscan belt (Lesponne — Chiroulet — Neouvielle area, French Pyrenees). Lithos 336–337:183–201. doi: 10.1016/j.lithos.2019.03.037

Li J, Zhuang X, Querol X, Font O, Izquierdo M, Wang Z (2014) New data on mineralogy and geochemistry of high-Ge coals in the Yimin coalfield, Inner Mongolia, China. Int J Coal Geol 125:10–21. doi: 10.1016/j.coal.2014.01.006

Li W, Audétat A, Zhang J (2015) The role of evaporites in the formation of magnetite-apatite deposits along the Middle and Lower Yangtze River, China: Evidence from LA-ICP-MS analysis of fluid inclusions. Ore Geol Rev 67:264–278. doi: 10.1016/j.oregeorev.2014.12.003

Licht C, Peiró LT, Villalba G (2015) Global substance flow analysis of gallium, germanium, and indium: Quantification of extraction, uses, and dissipative losses within their anthropogenic cycles. J Ind Ecol 19:890–903. doi: 10.1111/jiec.12287

Liu X, Liu Y, Harris MM, Li J, Wang K, Chen J (2018) Germanium nanoparticles supported by 3D ordered macroporous nickel frameworks as high-performance free-standing anodes for Li-ion batteries. Chem Eng J 354:616–622. doi: 10.1016/j.cej.2018.08.056

Llopis Llado N (1965) Sur le Paleozoique inferieur de l'Andorre. Bull la Soc Geol Fr 7:652–659

Lockington JA, Cook NJ, Ciobanu CL (2014) Trace and minor elements in sphalerite from metamorphosed sulphide deposits. Mineral Petrol 108:873–890. doi: 10.1007/s00710-014-0346-2

Lombaard AF, Gunzel A, Innes J, Kruger TL (1986) The Tsumeb lead-copper-zinc-silver deposit, south west Africa / Namibia. Miner Depos South Africa 1761–1787

Lopez-Sanchez MA, Aleinikoff JN, Marcos A, Martínez FJ, Llana-Fúnez S (2016) An example of low-Th/U zircon overgrowths of magmatic origin in a late orogenic variscan intrusion: The San Ciprián massif (NW Spain). J Geol Soc London 173:282–291. doi: 10.1144/jgs2015-071

Lopez-Sanchez MA, García-Sansegundo J, Martínez FJ (2018) The significance of early Permian and early Carboniferous U–Pb zircon ages in the Bossòst and Lys-Caillaouas granitoids (Pyrenean Axial Zone). Geol J 1–16. doi: 10.1002/gj.3283

Luais B (2007) Isotopic fractionation of germanium in iron meteorites: Significance for nebular condensation, core formation and impact processes. Earth Planet Sci Lett 262:21–36. doi: 10.1016/j.epsl.2007.06.031

Luais B, Framboisier X, Carignan J, Ludden JN (2000) Analytical development of Ge isotope nalysis using multi-collector plasma source mass spectrometery: Isotope MC-HEX-ICP_MS (Micromass). Geoanalysis 2000 - Symp B 994:45–46

Ludwig KR (2001) User's manual for Isoplot/Ex Version 2.49, a geochronological toolkit for Microsoft Excel. Berkeley Geochronological Center, Spec Publ 1a, Berkeley, USA, 55p

MacDonald R, Bagiński B, Dzierzanqwski P, Fettes DJ, Upton BGJ (2013) Chevkinite-group minerals in uk Palaeogene granites: Underestimated ree-bearing accessory phases. Can Mineral 51:333–347. doi: 10.3749/canmin.51.2.333

Macquar JC, Lagny P (1981) Minéralisations Pb-Zn 'Sous Inconformité' des Series de Plates-Formes Carbonatées. Exemple du Gisement de Trèves (Gard, France). Relations entre Dolomitisations, Dissolutions et Minéralisations. Miner Depos 16:283–307. doi: 10.1007/BF00202741

Majesté-Menjoulàs C, Debon F, P. Barrèr (1999) Notice explicative, Carte géol. France (1/50 000), feuille Gavarnie (1082). Orléans : BRGM. Cart géologique par C Majesté-Menjoulàs, F Debon, avec la Collab Y Driouch, H Flachère, H Moreau, J Valéro, Y Ternet (1999) 158p

Marcoux E (1986a) Isotope du plomb et paragénèses métalliques, traceurs de l'histoire des gites mineraux. Bur. Rech. Geol. Minière 117:1–289

Marcoux E (1986b) Isotope du plomb et paragénèses métalliques, traceurs de l'histoire des gites mineraux. Bur Rech Geol Minière 117:1–289

Marcoux E, Joubert M, Lescuyer J-L (1991a) Origine des minéralisations stratiformes de la bordure du Canigou (Pyrénées-orientales, France): apport de la géochimie isotopique du plomb. CR Acad Sci Paris 312:281–287

Marcoux E, Joubert M, Lescuyer JL (1991b) Origine des mineralisations stratiformes de la bordere du Canigou (Pyrenees orientales, France): apport de la geochimie isotopique du plomb. Compte Rendu Acad Sci Paris II 312,II,281:281–287

Marcoux E, Moelo Y (1991) Lead isotope geochemistry and paragenetic study of inheritance phenomena in metallogenesis: examples from base metal sulfide deposits in France. Econ Geol 86:106–120. doi: 10.2113/gsecongeo.86.1.106

Marshall B, Gilligan LB (1993) Remobilization, syn-tectonic processes and massive sulphide deposits. Ore Geol Rev 8:39–64. doi: 10.1016/0169-1368(93)90027-V

Marshall B, Gilligan LB (1987) An introduction to remobilization: Information from ore-body geometry and experimental considerations. Ore Geol Rev 2:87–131. doi: 10.1016/0169-1368(87)90025-4

Marshall B, Vokes FM, Larocque ACL (1998) Regional metamorphic remobilization - upgrading and formation of ore deposits. Econ Geol 11:20

Martín-Closas C, Trias S, Casas JM (2018) New palaeobotanical data from carboniferous culm deposits constrain the age of the variscan deformation in the eastern pyrenees. Geol Acta 16:107–123. doi: 10.1344/GeologicaActa2018.16.2.1

Martín-gonzález F, Marzo M, Mercedes-martín R, Ortí F, Pérez-lópez A, Pérez-valera F, Pérez-valera JA, Plasencia P, Ramos E, Rodríguez-méndez L, Ronchi A, Salas R, Suárez-rodríguez Á, Tubía JM, Ubide T (2019) Permian-Triassic Rifting Stage. Geol Iberia A Geodyn Approach 29–112. doi: 10.1007/978-3-030-11295-0

Martinez Catalan JR (2011) Are the oroclines of the Variscan belt related to late Variscan strike-slip tectonics? Terra Nov 23:241–247. doi: 10.1111/j.1365-3121.2011.01005.x

Martínez FJ, Dietsch C, Aleinikoff J, Cirés J, Arboleya ML, Reche J, Gómez-Gras D (2015) Provenance, age, and tectonic evolution of Variscan flysch, southeastern France and northeastern Spain, based on zircon geochronology. Geol Soc Am Bull 128:842–859. doi: 10.1130/b31316.1

Martínez FJ, Iriondo A, Dietsch C, Aleinikoff JN, Peucat JJ, Cirès J, Reche J, Capdevila R (2011) U-Pb SHRIMP-RG zircon ages and Nd signature of lower Paleozoic rifting-related magmatism in the Variscan basement of the Eastern Pyrenees. Lithos 127:10–23. doi: 10.1016/j.lithos.2011.08.004

Martínez FJ, Reche J, Iriondo A (2008) U-Pb Shrimp-RG zircon ages of Variscan igneous rocks from the Guilleries massif (NE Iberia pre-Mesozoic basement). Geological implications. Comptes Rendus - Geosci 340:223–232. doi: 10.1016/j.crte.2007.12.006

Mastalerz M, Drobniak A (2012) Gallium and germanium in selected Indiana coals. Int J Coal Geol 94:302–313. doi: 10.1016/j.coal.2011.09.007

Matte P (2001) The Variscan collage and orogeny (480–290 Ma) and the tectonic definition of the Armorica microplate: a review - Matte - 2003 - Terra Nova - Wiley Online Library. Terra Nov 13:122–128

Matte P (2002) Les plis hercyniens kilométriques couchés vers l'ouest-sud-ouest dans la région du pic du Midi d'Ossau-col du Somport (zone axiale des Pyrénées occidentales). Comptes Rendus - Geosci 334:773–779. doi: 10.1016/S1631-0713(02)01808-4

Matte P (1969) Le problème du passage de la schistosité horizontale à la schistosité verticale dans le dôme de la Garonne (Paléozoïque des Pyrénées Centrales). Compte Rendu Acad Sci Paris II 268:Série D-1841-1844

Matte P, Zhi QX (1988) Decollements in slate belts, examples from the European variscides and the Qin Ling Belt of Central China. Geol Rundschau 77:227–238. doi: 10.1007/BF01848686

Maurel O (2003) L'exhumation de la Zone Axiale des Pyrénées orientales : Une approche thermo-chronologique multi-méthodes du rôle des failles

Mavrogenes JA, MacIntoshi IW, Ellis AD (2001) Partial melting of the broken hill galena-sphalerite ore: Experimental studies in the system PbS-FeS-ZnS-(Ag2S). Econ Geol 96:205–210. doi: 10.2113/gsecongeo.96.1.205

McCaffrey MA, Lazar B, Holland HD (1987) The Evaporation Path of Seawater and the Coprecipitation of Br- and K+ with Halite. J Sediment Res Vol. 57:928–937. doi: 10.1306/212f8cab-2b24-11d7-8648000102c1865d

McCaig AM, Miller JA (1986) 40Ar-39Ar age of Mylonites along the Merens fault, Central Pyrenees. Tectonophysics 129:149–172

McCaig AM, Tritlla J, Banks DA (2000) Fluid flow patterns during Pyrenean thrusting. J Geochemical Explor 70:539–543

McClay KR (1991) Deformation of stratiform ZnPb(-barite) deposits in the northern Canadian Cordillera. Ore Geol Rev 6:435–462. doi: 10.1016/0169-1368(91)90040-E

McClay KR, Atkinson BK (1977) Experimentally induced kinking and annealing of single crystals of galena. Tectonophysics 39:175–189

McClay KR, Ellis PG (1983) Deformation and Recrystallization of Pyrite. Mineral Mag 47:527–538. doi: 10.1180/minmag.1983.047.345.14

McClay KR, Ellis PG (1984) Deformation of Pyrite. Econ Geol 79:400–403

McDonald AM, Zhe W, Ames DE, Ross KC, Kjarsgaard IM, Good DJ (2017) Palladogermanide, IMA 2016-086. CNMNC Newslet- ter No. Eur J Mineral 35:150. doi: 10.1127/ejm/2019/0031-2852

Mckinney M, Brown I, Allan G, Ken L (2006) Tschudi Copper Deposit Geological Modelling and Mineral Resource Estimate

Melcher F (2003) The Otavi Mountain Land in Nambia: Tsumeb, Germanium and Snowball Earth. MittOsterrMinerGes 148:413–435

Melcher F, Buchholz P (2013) Germanium. Gunn G Crit Met Handbook Wiley- Blackwell, Chicester, UK 8. doi: 10.1515/9783110800487.550

Melcher F, Oberthür T, Rammlmair D (2006) Geochemical and mineralogical distribution of germanium in the Khusib Springs Cu-Zn-Pb-Ag sulfide deposit, Otavi Mountain Land, Namibia. Ore Geol Rev 28:32–56. doi: 10.1016/j.oregeorev.2005.04.006

Melcher F, Onuk P (2019) Potential of Critical High-technology Metals in Eastern Alpine Base Metal Sulfide Ores. Berg- und Hüttenmännische Monatshefte 1–6. doi: 10.1007/s00501-018-0818-5

Meng YM, Qi HW, Hu RZ (2015) Determination of germanium isotopic compositions of sulfides by hydride generation MC-ICP-MS and its application to the Pb-Zn deposits in SW China. Ore Geol Rev 65:1095–1109. doi: 10.1016/j.oregeorev.2014.04.008

Merlino S, Orlandi P (2001) Carraraite and zaccagnaite, two new minerals from the Carrara marble quarries: Their chemical compositions, physical properties, and structural features. Am Mineral 86:1293–1301. doi: 10.2138/am-2001-1017

Mey PHW (1967) The geology of the upper Ribagorzana and Baliera granodiorite Permo-Triásico Permo-Triásicas. Leidse Geol Meded 41:153–220

Mezger JE (2005) Comparison of the western Aston-Hospitalet and the Bossòst domes: Evidence for polymetamorphism and its implications for the Variscan tectonic evolution of the Axial Zone of the Pyrenees. J Virtual Explor 19:1–19. doi: 10.3809/jvirtex.2005.00122

Mezger JE (2009) Transpressional tectonic setting during the main Variscan deformation: Evidence from four structural levels in the Bossòst and Aston-Hospitalet mantled gneiss domes, central Axial Zone, Pvrenees. Bull la Soc Geol Fr 180:199–207.

doi: 10.2113/gssgfbull.180.3.199

Mezger JE, Gerdes A (2016) Early Variscan (Visean) granites in the core of central Pyrenean gneiss domes: Implications from laser ablation U-Pb and Th-Pb studies. Gondwana Res 29:181–198. doi: 10.1016/j.gr.2014.11.010

Mezger JE, Passchier CW (2003) Polymetamorphism and ductile deformation of staurolite–cordierite schist of the Bossòst dome: indication for Variscan extension in the Axial Zone of the central Pyrenees. Geol Mag 140:595–612. doi: 10.1017/S0016756803008112

Mezger JE, Passchier CW, Régnier J-L (2004) Metastable staurolite–cordierite assemblage of the Bossòst dome: Late Variscan decompression and polyphase metamorphism in the Axial Zone of the central Pyrenees. Comptes Rendus Geosci 336:827–837. doi: 10.1016/j.crte.2003.12.024

Mezger JE, Régnier JL (2016) Stable staurolite-cordierite assemblages in K-poor metapelitic schists in Aston and Hospitalet gneiss domes of the central Pyrenees (France, Andorra). J Metamorph Geol 34:167–190. doi: 10.1111/jmg.12177

Mezger JE, Schnapperelle S, Rölke C (2012) Evolution of the Central Pyrenean Mérens fault controlled by near collision of two gneiss domes. Jahrb für Geowissenschaften 34:11–29

Michard A (1966) Les minéralisations Pb-Zn du PER de Tuq de Roquefort (Hte-Garonne, Ariège). BRGM Rep DRMM66 A-1:32

Michard A (1969) Per du tuc de roquefort (Haute-Garonne)-Résultat de la campagne 1968. BRGM Rep 69RME 011R:32

Militon C (1987) Métallogénie polyphasée à Zn, Pb, Ba, F et Mg, Fe de ma région de Gèdre-Gavarnie- Barroude (Hautes-Pyrénées). Ph D Thesis Univ d'Orléans 413p

Minceva-Stefanova J (1993) A Morphological SEM Study of Wurtzite-Sphalerite Relationships in Specimens from Zvezdel, Bulgaria. Mineral Petrol 49:119–126

Mondillo N, Arfè G, Herrington R, Boni M, Wilkinson C, Mormone A (2018a) Germanium enrichment in supergene settings: evidence from the Cristal nonsulfide Zn prospect, Bongará district, northern Peru. Miner Depos 53:155–169. doi: 10.1007/s00126-017-0781-1

Mondillo N, Herrington R, Boyce AJ, Wilkinson C, Santoro L, M. Rumsey (2018b) Critical elements in non-sulfide Zn deposits : a reanalysis of the Kabwe Zn-Pb ores (central Zambia). Mineral Mag 82(S1):89–114. doi: 10.1180/minmag.2017.081.038

Monteiro SLV, Bettencourt SJ, Juliani C, Oliveira TF de (2006) Geology, petrography, and mineral chemistry of the Vazante non-sulfide and Ambrosia and Fagundes sulfide-rich carbonate-hosted Zn–(Pb) deposits, Minas Gerais, Brazil. Ore Geol Rev 28:201–234. doi: 10.1016/j.oregeorev.2005.03.005

Moore DW, Young LE, Modene JS, Plahuta JT (1986) Geologic setting and genesis of the Red Dog zinc-lead-silver deposit, western Brooks Range, Alaska. Econ Geol 81:1696–1727. doi: 10.2113/gsecongeo.81.7.1696

Morales-Ruano S, Touray J-C, Barbanson L, Hach-Ali PF (1996) Primary cavities with incompatible fluid fillings in Ge-bearing sphalerite from Cerro del Toro, Alpujarride (Spain). Econ Geol 91:460–465

Morey GW (1957) The solubility of solids in gases. Econ Geol 52:225–251

Mortlock RA, Frohlich PN (1987) Continental weathering of germanium: Ge Si in the global river discharge. Geochim Cosmochim Acta 51:2075–2082. doi: 10.1016/0016-7037(87)90257-2

Moskalyk RR (2004) Review of germanium processing worldwide. Miner Eng 17:393–402. doi: 10.1016/j.mineng.2003.11.014

Munoz JA (1993) Estructura alpina i herciniana a la vora sud de la Zona Axial del Pirineu oriental. Monografies núm. 1. Monogr

núm 1 Publicació del Serv Geològic Catalunya General Catalunya, Dep Política Territ i Obres Públiques, Serv Geol Catalunya, Barcelona 227p

Munoz M, Baron S, Boucher A, Béziat D, Salvi S (2016) Mesozoic vein-type Pb–Zn mineralization in the Pyrenees: Lead isotopic and fluid inclusion evidence from the Les Argentières and Lacore deposits. Comptes Rendus Geosci 348:322–332. doi: 10.1016/j.crte.2015.07.001

Munoz M, Boyce A, Courjault-Rade P, Fallick A, Tollon F (1997) Le filon (Zn, F) de Peyrebrune (SW Massif central, France): caractérisation géochimique des fluides au cours du Mésozoïque à la bordure orientale du bassin d'Aquitaine. Compte Rendu Acad Sci Paris t. 324:899–906

Munoz M, Boyce AJ, Courjault-Rade P, Fallick AE, Tollon F (1994) Multi-stage fluid incursion in the Palaeozoic basement-hosted Saint-Salvy ore deposit (NW Montagne Noire, southern France). Appl Geochemistry 9:609–626. doi: 10.1016/0883-2927(94)90022-1

Munoz M, Boyce AJ, Courjault-Rade P, Fallick AE, Tollon F (1999) Continental basinal origin of ore fluids from southwestern Massif central fluorite veins (Albigeois, France): Evidence from fluid inclusion and stable isotope analyses. Appl Geochemistry 14:447–458. doi: 10.1016/S0883-2927(98)00070-5

Murakami H, Ishihara S (2013) Trace elements of Indium-bearing sphalerite from tin-polymetallic deposits in Bolivia, China and Japan: A femto-second LA-ICPMS study. Ore Geol Rev 53:223–243. doi: 10.1016/j.oregeorev.2013.01.010

Murciego A, Pascua MI, Babkine J, Dusausoy Y, Medenbach O, Bernhardt H-J (2014) Barquillite, Cu2(Cd, Fe)GeS4, a new mineral from the Barquilla deposit, Salamanca, Spain. Eur J Mineral 11:111–118. doi: 10.1127/ejm/11/1/0111

Murphy TE (2004) Structural and stratigraphic controls on mineralization at the George Fisher Zn-Pb-Ag Deposit, northwest Queensland, Australia. Ph D Thesis, James Cook Univ 1–423

Nassar NT, Graedel TE, Harper EM (2015) By-product metals are technologically essential but have problematic supply. Sci Adv 1:1–11. doi: 10.1126/sciadv.1400180

Navidad M, Castiñeiras P, Casas JM, Liesa M, Belousova E, Proenza J, Aiglsperger T (2018) Ordovician magmatism in the Eastern Pyrenees: Implications for the geodynamic evolution of northern Gondwana. Lithos 314–315:479–496. doi: 10.1016/j.lithos.2018.06.019

Neuser RD (1995) A new high-intensity cathodoluminescence microscope and its application to weakly luminescing minerals. Bochumer Geol und Geotech Arb 44:116–118

Nicol N (1997) Etude structurale des minéralisations Zn-Pb du Paléozoïque du dôme de Pierrefitte (Hautes-Pyrénées). Goniométrie de texture appliquée aux minéraux transparents et opaques. PhD Thesis Univ Orléans 318p

Nicol N, Legendre O, Charvet J (1997) Les minéralisations Zn-Pb de la série paléozoïque de Pierrefitte (Hautes-Pyrénées) dans la succession des évènements tectoniques hercyniens. CR Acad Sci Paris 324:453–460

Oberc-Dziedzic T, Kryza R, Pin C (2015) Variscan granitoids related to shear zones and faults: examples from the Central Sudetes (Bohemian Massif) and the Middle Odra Fault Zone. Int J Earth Sci 104:1139–1166. doi: 10.1007/s00531-015-1153-7

Oliveira JT, Pereira Z, Carvalho P, Pacheco N, Korn D (2004) Stratigraphy of the tectonically imbricated lithological succession of the Neves Corvo mine area , Iberian Pyrite Belt , Portugal. Miner Depos 39:422–436. doi: 10.1007/s00126-004-0415-2

Origlieri MJ, Downs RT (2013) Schaurteite, Ca3Ge(SO4)2(OH) 6·3H2O. Acta Crystallogr Sect E Struct Reports Online 69:0–6. doi: 10.1107/S1600536812050945

Origlieri MJ, Yang H, Downs RT, Posner ES, Domanik KJ, Pinch WW (2012) The crystal structure of bartelkeite, with a revised

chemical formula, PbFeGeVI(Ge2IVO7)(OH)2{middle dot}H2O, isotypic with high-pressure P21/m lawsonite. Am Mineral 97:1812–1815. doi: 10.2138/am.2012.4269

Ostendorf J, Henjes-Kunst F, Schneider J, Melcher F, Gutzmer J (2017) Genesis of the carbonate-hosted tres marias Zn-Pb-(Ge) deposit, Mexico: Constraints from Rb-Sr sphalerite geochronology and Pb isotopes. Econ Geol 112:1075–1087. doi: 10.5382/econgeo.2017.4502

Ostkamp M, Schnapperelle S, Mertmann D (2019) Strukturgeologische Charakterisierung der Mérens Scher-und Störungszone bei Mérens-les-Vals (französische Pyrenäen). Hallesches Jahrb für Geowissenschaften 42:69–111

Ottemann VJ, Nuber B (1972) Brunogeierit, ein Germanium-Ferritspinell von Tsumeb. Neues Jahrb für Mineral - Monatshefte 263–267

Oudin E (1982) Minéralogie des Pyrénées Centrales. Bur Rech Géologiques Minières Rapp 82 SGN189:38p.

Oudin E, Pouit G, Tollon F (1988) Les minéraux en trace de Ni-Co, Sn, Ge-Ga, Pb-Sb, Ag et Au témoins de l'évolution de l'hydrothermalisme de l'Ordovicien au Dévonien dans les minéralisations zincifères des Pyrénées Centrales. Bull minéralogique 111:49–63

Ovejero Zappino G (1991) Mineralizaciones Zn-Pb ordovícicas del anticlinorio de Bossost. Yacimientos de Liat y Victoria. Valle de Arán. Pirineo (España). Boletín Geológico y Minero 102–3:356–377

Ovejero Zappino G (1987) Mineralizaciones Zn-Pb del Ordovicico Superior del Valle de Aran (Anticlinorio de Bossost). Pireneo de Lerida (Espana). Bol Soc Esp Mineral 10:35–37

Paar WH, Putz H, Paar WH, Putz H (2005) Germanium associated with epithermal mineralization : examples from Bolivia and Argentina. In: Conference paper: Eight biennial SGA Meeting Beijing/China/18-21 August 2005. p 4

Paar WH, Roberts AC, Berlepsch P, Armbruster T, Topa D, Zagler G (2004) PUTZITE, (Cu4.7Ag3.3)?8GeS6, A NEW MINERAL SPECIES FROM CAPILLITAS, CATAMARCA, ARGENTINA: DESCRIPTION AND CRYSTAL STRUCTURE. Can Mineral 42:1757–1769

Padel M, Álvaro JJ, Casas JM, Clausen S, Poujol M, Sánchez-García T (2018) Cadomian volcanosedimentary complexes across the Ediacaran–Cambrian transition of the Eastern Pyrenees, southwestern Europe. Int J Earth Sci 107:1579–1601. doi: 10.1007/s00531-017-1559-5

Palero-Fernández FJ, Martín-Izard A (2005) Trace element contents in galena and sphalerite from ore deposits of the Alcudia Valley mineral field (Eastern Sierra Morena, Spain). J Geochemical Explor 86:1–25. doi: 10.1016/j.gexplo.2005.03.001

Papise J (1928) Occurrence of Germanium in Topaz. Science (80-) 68:350–351. doi: 10.1126/science.68.1763.350

Paquette JL, Gleizes G, Leblanc D, Bouchez JL (1997) Le granite de Bassies (Pyrénées): un pluton syntectonique d'âge westphalien. Géochronologie U– Pb sur zircons. Compte Rendu Acad Sci Paris 324:387–392

Paquette JL, Piro JL, Devidal JL, Bosse V, Didier A (2014) Sensitivity enhancement in LA-ICP-MS by N2 addition to carrier gas: application to radiometric dating of U-Th- bearing minerals. Agil ICP-MS J 58:4–5

Paquette JL, Tiepolo M (2007) High resolution (5 µm) U-Th-Pb isotope dating of monazite with excimer laser ablation (ELA)-ICPMS. Chem Geol 240:222–237. doi: 10.1016/j.chemgeo.2007.02.014

Pascua MI, Murciego A, Pellitero E, Babkine J, Dusausoy Y (1997) Sn-Ge-Gd-Cu-Fe-Bearing sulfides and sulfosalts from the Barquilla deposit, Salamanca, Spain. Can Mineral 35:39–52

Passchier C, Trouw R (1996) Microtectonics

Pearce NJG, Perkins WT, Westgate JA, Jackson SE, Neal CR, Chenery SP, Gorton MP (1997) A Compilation of New and Published Major and Trace Element Data for NIST SRM 610 and NIST SRM 612 Glass Reference Materials. Geostand Newsl 21:1–30

Pesquera A, Velasco F (1989) The arditurri Pb-Zn-F-Ba deposit (Cinco Villas massif, Basque Pyrenees): A deformed and metamorphosed stratiform deposit. Miner Depos 24:199–209. doi: 10.1007/BF00206443

Pesquera A, Velasco F (1993) Ore Metamorphism in Sulfide Mineralizations from the Cinco Villas Massif (Western Pyrenees, Spain). Econ Geol 88:266–282

Piazolo S, La Fontaine A, Trimby P, Harley S, Yang L, Armstrong R, Cairney JM (2016) Deformation-induced trace element redistribution in zircon revealed using atom probe tomography. Nat Commun 7:10490. doi: 10.1038/ncomms10490

Pirrie D, Butcher AR, Power MR, Gottlieb P, Miller GL (2004) Rapid quantitative mineral and phase analysis using automated scanning electron microscopy (QemSCAN); potential applications in forensic geoscience. Geol Soc London, Spec Publ 232:123–136. doi: 10.1144/gsl.sp.2004.232.01.12

Pitcairn IK, Olivo GR, Teagle DAH, Craw D (2010) Sulfide Evolution During Prograde Metamorphism of the Otago and Alpine Schists, New Zealand. Can Mineral 48:1267–1295. doi: 10.3749/canmin.48.5.1267

Plimer IR (1987) Remobilization in high-grade-metamorphic environments. Ore Geol Rev 2:231–245

Plümper O, King HE, Vollmer C, Ramasse Q, Jung H, Austrheim H (2012) The legacy of crystal-plastic deformation in olivine: High-diffusivity pathways during serpentinization. Contrib to Mineral Petrol 163:701–724. doi: 10.1007/s00410-011-0695-3

Poitrenaud T (2018) Le gisement périgranitique à tungstène et or de Salau (Pyrénées, France), histoire polyphasée d'un système minéralisé tardi-varisque. Ph D Thesis Univ d'Orléans 491

Pokrovski GS, Borisova AY, Harrichoury JC (2008) The effect of sulfur on vapor-liquid fractionation of metals in hydrothermal systems. Earth Planet Sci Lett 266:345–362. doi: 10.1016/j.epsl.2007.11.023

Pokrovski GS, Roux J, Hazemann JL, Testemale D (2005) An X-ray absorption spectroscopy study of argutite solubility and aqueous Ge(IV) speciation in hydrothermal fluids to 500 °C and 400 bar. Chem Geol 217:127–145. doi: 10.1016/j.chemgeo.2005.01.006

Pokrovski GS, Schott J (1998a) Thermodynamic properties of aqueous Ge(IV) hydroxide complexes from 25 to 350°C: Implications for the behavior of germanium and the Ge/Si ratio in hydrothermal fluids. Geochim Cosmochim Acta 62:1631–1642

Pokrovski GS, Schott J (1998b) Experimental study of the complexation of silicon and germanium with aqueous organic species: Implications for germanium and silicon transport and Ge/Si ratio in natural waters. Geochim Cosmochim Acta 62:3413–3428

Pouget P (1991) Hercynian Tectonometamorphic Evolution of the Bosost Dome (French Spanish Central Pyrenees). J Geol Soc London 148:299–314. doi: 10.1144/gsjgs.148.2.0299

Pouit G (1985) Les minéralisations Zn (Pb) Ba du Paléozoïque des Pyrénées Centrales : Une mise au point et un compte rendu des missions 1984. Bur Rech Géologiques Minières Rapp 85 DAM037:72

Pouit G (1978) Différents Modeles de Mineralisations «Hydrothermale Sédimentaire », à Zn (Pb) du Paléozoïque des Pyrénees Centrales. Miner Depos 13:411–421

Pouit G (1974) Les minéralisations Zn-Pb dans l'Ordovicien des Pyrénées centrales-Etude préliminaire. Rapp BRGM 74 SGN 122:50

Pouit G (1986) Les minéralisations Zn-Pb exhalatives sédimentaires de Bentaillou et de l 'anticlinorium paléozoïque de Bosost (Pyrénées ariégeoises, France). Chron la Rech minière 485:3–16

Pouit G, Bois JP (1986a) Arrens Zn (Pb), Ba Devonian deposit , Pyrénées , France : an exhalative-sedimentary-type deposit similar to Meggen. Miner Depos 21:181–189

Pouit G, Bois JP (1980) Les minéralisations Zn (Pb) du Nerbiou (Pyrénées centrales) – Etat des connaissances et extensions possibles. BRGM 80 RDM 011:21

Pouit G, Bois JP (1986b) Arrens Zn (Pb), Ba Devonian deposit, Pyrénées, France: an exhalative-sedimentary-type deposit similar to Meggen. Miner Depos 21:181–189

Pouit G, Fortuné J-P (1980) Métallogénie comparée des Pyrénées et du Sud du Massif-central. In: 26ème congrès géologique international. p 61p

Poujol M, Boulvais P, Kosler J (2010) Regional-scale Cretaceous albitization in the Pyrenees: Evidence from in situ U-Th-Pb dating of monazite, titanite and zircon. J Geol Soc London 167:751–767. doi: 10.1144/0016-76492009-144

Prokin VA, Buslaev FP (1999) Massive copper–zinc sulphide deposits in the Urals. Ore Geol Rev 14:1–69. doi: http://dx.doi.org/10.1016/S0169-1368(98)00014-6

Pufahl O (1922) 'Germanit', ein Germanium-Mineral und -Erz von Tsumeb, Südwest-Afrika. Met und Erz 19:324–325

Pufhal O (1922) 'Germanit', ein Germanium-Mineral und -Erz von Tsumeb, Südwest-Afrika. Met und Erz, Halle 19:324–325

Puigdefàbregas C, Souquet P (1986) Tecto-sedimentary cycles and depositional sequences of the Mesozoic and Tertiary from the Pyrenees. Tectonophysics 129:173–203. doi: 10.1016/0040-1951(86)90251-9

Pujals I (1992) Las mineralizaciones de sulfuros en el Cambro-Ordovicico de la Val d'Aran (Pirineo Central, Lérida). PhD Thesis, Univ Autónoma Barcelona 294p

Putz H, Paar WH, Topa D, Makovicky E, Roberts AC (2006) Catamarcaite, Cu6GeWS8, a new germanium sulfide mineral species from Capillitas, Catamarca, Argentina: Description, paragenesis and crystal structure. Can Mineral 44:1481–1497. doi: 10.2113/gscanmin.44.6.1481

Qi H-W, Rouxel O, Hu RZ, Bi XW, Wen HJ (2011) Germanium isotopic systematics in Ge-rich coal from the Lincang Ge deposit, Yunnan, Southwestern China. Chem Geol 286:252–265. doi: 10.1016/j.chemgeo.2011.05.011

Quesnel B, Boiron M-C, Cathelineau M, Truche L, Rigaudier T, Bardoux G, Agrinier P, de Saint Blanquat M, Masini E, Gaucher EC (2019) Nature and Origin of Mineralizing Fluids in Hyperextensional Systems: The Case of Cretaceous Mg Metasomatism in the Pyrenees. Geofluids 2019:1–18. doi: 10.1155/2019/7213050

Ramboz C, Pichavant M, Weisbrod A (1982) Fluid immiscibility in natural processes: Use and misuse of fluid inclusion data. II. Interpretation of fluid inclusion data in terms of immiscibility. Chem Geol 37:29–48. doi: 10.1016/0009-2541(82)90065-1

Ramdohr P (1969) The ore minerals and their intergrowths. Pergamon Press Ltd, Head Hill Hall, Oxford 4 5 Fitzroy Square, London W 1 1179

Reddy SM, Hough RM (2013) Microstructural evolution and trace element mobility in Witwatersrand pyrite. Contrib to Mineral Petrol 166:1269–1284. doi: 10.1007/s00410-013-0925-y

Reddy SM, Timms NE, Pantleon W, Trimby P (2007) Quantitative characterization of plastic deformation of zircon and geological implications. Contrib to Mineral Petrol 153:625–645. doi: 10.1007/s00410-006-0174-4

Reiser FKM, Rosa DRN, Pinto ÃMM, Carvalho JRS, Matos JX, Guimaraes FMG, Alves LC, de Oliveira DPS (2011) Mineralogy and geochemistry of tin- and germanium-bearing copper ore, Barrigao re-mobilized vein deposit, Iberian Pyrite Belt, Portugal. Int Geol Rev 53:1212–1238. doi: 10.1080/00206811003683168

Renne PR, Swisher CC, Deino AL, Karner DB, Owens TL, DePaolo DJ (1998) Intercalibration of standards, absolute ages and uncertainties in 40Ar/39Ar dating'. Chem Geol 145:117–152. doi: 10.1016/s0009-2541(98)00047-3

Reyx J (1973) Relations entre tectonique, métamorphisme de contact et concentrations metalliques dans le secteur des anciennes mines d'Arre et Anglas (Hautes-Pyrénées - Pyrénées atlantiques). Ph D Thesis, Univ Paris VI 83p

Ringwood AE (1955) The principles governing trace element distribution during magmatic crystallization Part I: The influence of electronegativity. Geochim Cosmochim Acta 7:

Roberts AC, Seward TM, Reusser E, Carpenter GJC, Grice JD, Clark SM, Marcus MA (2004) Eyselite, Fe3+Ge4+ 3O7(OH), a new mineral species from Tsumeb, Namibia. Can Mineral 42:1771–1776

Roberts MP, Pin C, Clemens JD, Paquette J, Ge PDE (2000a) Petrogenesis of Mafic to Felsic Plutonic Rock Associations : the Calc-alkaline Quérigut Complex, French Pyrenees. J Petrol 41:809–844

Roberts MP, Pin C, Clemens JD, Paquette JL (2000b) Petrogenesis of Mafic to Felsic Plutonic Rock Associations: the Calc-alkaline Querigut Complex, French Pyrenees. J Petrol 41:809–844. doi: 10.1093/petrology/41.6.809

Rodríguez-Méndez L, Cuevas J, Tubía JM (2016) Post-Variscan basin evolution in the central Pyrenees: Insights from the Stephanian-Permian Anayet Basin. Comptes Rendus - Geosci 348:333–341. doi: 10.1016/j.crte.2015.11.006

Roedder E (1984) Fluid inclusions. Mineral Soc Am 646p

Roig JY, Faure M, Ledru P (1996) Polyphase wrench tectonics in the southern french Massif Central: Kinematic inferences from pre- And syntectonic granitoids. Int J Earth Sci 85:138–153

Rosenberg CL, Stünitz H (2003) Deformation and recrystallization of plagioclase along a temperature gradient: An example from the Bergell tonalite. J Struct Geol 25:389–408. doi: 10.1016/S0191-8141(02)00036-6

Ruiz AG, Sola PC, Palmerola NM (2018) Germanium: Current and Novel Recovery Processes. Lee, S, ed, Adv Mater Device Appl with Ger London, IntechOpen Ltd Chapter 2:p.9-29. doi: 10.5772/INTECHOPEN.77997

Sahlström F, Arribas A, Dirks P, Corral I, Chang Z (2017a) Mineralogical Distribution of Germanium, Gallium and Indium at the Mt Carlton High-Sulfidation Epithermal Deposit, NE Australia, and Comparison with Similar Deposits Worldwide. Minerals 7:213. doi: 10.3390/min7110213

Sahlström F, Blake K, Corral I, Chang Z (2017b) Hyperspectral cathodoluminescence study of indium-bearing sphalerite from the Mt Carlton high-sulphidation epithermal deposit, Queensland, Australia. Eur J Mineral 29:985–993. doi: 10.1127/ejm/2017/0029-2660

Saini-Eidukat B, Melcher F, Lodziak J (2009) Zinc-germanium ores of the Tres Marias Mine, Chihuahua, Mexico. Miner Depos 44:363–370. doi: 10.1007/s00126-008-0222-2

Sancey L, Motto-Ros V, Busser B, Kotb S, Benoit JM, Piednoir A, Lux F, Tillement O, Panczer G, Yu J (2014) Laser spectrometry for multi-elemental imaging of biological tissues. Sci Rep 4:1–8. doi: 10.1038/srep06065

Schaltegger U (1997) Magma pulses in the central Variscan belt: episodic melt generation and emplacement during lithospheric thinning. Terra Nov 9:242–245. doi: 10.1111/j.1365-3121.1997.tb00021.x

Schärer U, De Parseval P, Polvé M, De Saint Blanquat M (1999) Formation of the Trimouns talc-chlorite deposit (Pyrenees) from

persistent hydrothermal activity between 112 and 97 Ma. Terra Nov 11:30–37. doi: 10.1046/j.1365-3121.1999.00224.x

Schlöglova K, Wälle M, Heinrich CA (2017) LA-ICP-MS analysis of fluid inclusions: Contamination effects challenging micro-analysis of elements close to their detection limit. J Anal At Spectrom 32:1052–1063. doi: 10.1039/c7ja00022g

Schlüter J, Geisler T, Pohl D, Stephan T (2010) Krieselite, Al₂GeO₄(F,OH)₂: A new mineral from the Tsumeb mine, Namibia, representing the Ge analogue of topaz. Neues Jahrb für Mineral - Abhandlungen 187:33–40. doi: 10.1127/0077-7757/2010/0160

Schneider J, Melcher F, Brauns M (2007) Concordant ages for the giant Kipushi base metal deposit (DR Congo) from direct Rb-Sr and Re-Os dating of sulfides. Miner Depos 42:791–797. doi: 10.1007/s00126-007-0158-y

Schroll E (1996) The Triassic carbonate-hosted Pb-Zn mineralization in the Alps (Europe): The genetic position of Bleiberg type deposits. Spec Publ Soc Econ Geol 182–194

Schwarz-Schampera U, Herzig PM (2002) Indium: Geology, Mineralogy, and Economics. Springer 1–237

Scott RJ, Meffre S, Woodhead J, Gilbert SE, Berry RF, Emsbo P (2009) Development of framboidal pyrite during diagenesis, low-grade regional metamorphism, and hydrothermal alteration. Econ Geol 104:1143–1168. doi: 10.2113/gsecongeo.104.8.1143

Scott SD, Barnes HL (1972) Sphalerite-wurtzite equilibria and stoichiometry. Geochim Cosmochim Acta 36:1275–1295. doi: 10.1016/0016-7037(72)90049-X

Seguret M, Proust F (1968) Tectonique hercynienne des Pyrenees centrales: signification des schistosités redressées, chronologie des déformations. Compte Rendu Acad Sci Paris 266:984–987

Seifert T, Sandmann D (2006) Mineralogy and geochemistry of indium-bearing polymetallic vein-type deposits: Implications for host minerals from the Freiberg district Eastern Erzgebirge, Germany. Ore Geol Rev 28:1–31. doi: 10.1016/j.oregeorev.2005.04.005

Seo JH, Guillong M, Aerts M, Zajacz Z, Heinrich CA (2011) Microanalysis of S, Cl, and Br in fluid inclusions by LA-ICP-MS. Chem Geol 284:35–44. doi: 10.1016/j.chemgeo.2011.02.003

Seredin V V. (2012) From coal science to metal production and environmental protection: A new story of success. Int J Coal Geol 90–91:1–3. doi: 10.1016/j.coal.2011.11.006

Seredin V V., Finkelman RB (2008) Metalliferous coals: A review of the main genetic and geochemical types. Int J Coal Geol 76:253–289. doi: 10.1016/j.coal.2008.07.016

Seredin V V (2003) Anomalous Concentrations of Trace Elements in the Spetsugli Germanium Deposit (Pavlovka Brown Coal Deposit, Southern Primorye): Communication 2. Rubidium and Cesium. Lithol Miner Resour 38:233–241. doi: 10.1023/A:1023931702843

Seydoux-Guillaume AM, Montel JM, Bingen B, Bosse V, de Parseval P, Paquette JL, Janots E, Wirth R (2012) Low-temperature alteration of monazite: Fluid mediated coupled dissolution-precipitation, irradiation damage, and disturbance of the U-Pb and Th-Pb chronometers. Chem Geol 330–331:140–158. doi: 10.1016/j.chemgeo.2012.07.031

Seydoux-Guillaume AM, Paquette JL, Wiedenbeck M, Montel JM, Heinrich W (2002) Experimental resetting of the U-Th-Pb systems in monazite. Chem Geol 191:165–181. doi: 10.1016/S0009-2541(02)00155-9

Shannon BYRD, H M, Baur NH, Gibbs OH, Eu M, Cu V (1976) Revised Effective Ionic Radii and Systematic Studies of Interatomie Distances in Halides and Chaleogenides Central Research and Development Department , Experimental Station , E . L Du Pont de Nemours The effective ionic radii of Shannon & Prewitt [Acta. Acta cryst 32:751–767

Shi JX, Yi FH, Wen QD (1983) The rock-ore characteristics and mineralisation of Jinding lead–zinc deposit, Lanping. J Yunnan Geol 1983

Shimizu T, Morishita Y (2012) Petrography, chemistry, and near-infrared microthermometry of indium-bearing sphalerite from the Toyoha polymetallic deposit, Japan. Econ Geol 107:723–735. doi: 10.2113/econgeo.107.4.723

Siemes H (1976) Recovery and recrystallization of experimentally deformed galena. Econ Geol 71:763–771. doi: 10.2113/gsecongeo.71.4.763

Siemes H, Borges B (1979) Experimental deformation of sphalerite single crystals under confining pressures of 3000 and 5000 bars at temperatures between 25°C and 450°C. N Jb Miner Abb 134:288–304

Siemes H, Hennig-Michaeli C (1985) Ore Minerais. Prefer Orientat Deform Met rocks, an Introd to Mod texture Anal (Ed HR Wenk Acad Press Orlando 335–360

Siemes H, Hennig-Michaeli C, Martens L (1991) The importance of deformation experiments on minerals for the interpretation of metamorphic ore textures. Ore Geol Rev 6:475–483. doi: 10.1016/0169-1368(91)90042-6

Siemes H, Saynisch HJ, Borges B (1973) Experimentelle Verformung von Zinkblendeeinkristallen bei Raumtemperatur und 5000 bar Manteldruck. N Jb Miner Abb 119:65–82

Smith KS, Huyck HLO (1999) An Overview of the Abundance, Relative Mobility, Bioavailability, and Human Toxicity of Metals. Plumlee, GS, Logsdon, MJ, eds, Environ Geochemistry Miner Depos Rev Econ Geol Vol. 6A:29–70

Song XX (1984) Minor elements and ore genesis of the Fankou Lead - Zinc deposit, China. Miner Depos 19:95–104

Soref R (2010) Mid-infrared photonics in silicon and germanium. Nat Publ Gr 4:495–497. doi: 10.1038/nphoton.2010.171

Soula JC, Debat P, Deramond J, Pouget P (1986) The Geological Evolution of the Pyrenees A dynamic model of the structural evolution of the Hercynian Pyrenees. Tectonophysics 129:29–51. doi: 10.1016/0040-1951(86)90244-1

Spiridonov EM (2003) Maikainite Cu20(Fe,Cu)6Mo2Ge6S32 and ovamboite Cu20(Fe,Cu,Zn)6W2Ge6S32: New minerals in massive sulfide base metal ores. Dokl Earth Sci 393A:1329–1332

Spiridonov EM, Kachalovskaya VM, Kovachev VV, Krapiva LY (1992) Germanocolusite Cu26V2(Ge, As)6S32 — a new mineral. Vestn Mosk Univ 4:50–54 (in Russian)

Spry PG, Plimer IR, Teale GS (2008) Did the giant Broken Hill (Australia) Zn-Pb-Ag deposit melt? Ore Geol Rev 34:223–241. doi: 10.1016/j.oregeorev.2007.11.001

Stampfii GM, von Raumer JF, Borel GD (2007) Paleozoic evolution of pre-Variscan terranes: From Gondwana to the Variscan collision. Spec Pap 364 Variscan-Appalachian Dyn Build late Paleoz basement 263–280. doi: 10.1130/0-8137-2364-7.263

Stampfli GM, Hochard C, Vérard C, Wilhem C, vonRaumer J (2013) The formation of Pangea. Tectonophysics 593:1–19. doi: 10.1016/j.tecto.2013.02.037

Stanton RL (1964) Textures of stratiform ores. Nature 202:173–174

Stanton RL, Gorman H (1968) A phenomenological study of grain boundary migration in some common sulfides. Econ Geol 63:907–923. doi: 10.2113/gsecongeo.63.8.907

Steele-MacInnis M (2018) Fluid inclusions in the system H2O-NaCl-CO2: An algorithm to determine composition, density and isochore. Chem Geol 498:31–44. doi: 10.1016/j.chemgeo.2018.08.022

Steele-MacInnis M, Bodnar RJ, Naden J (2011) Numerical model to determine the composition of H2O – NaCl – CaCl2 fluid

inclusions based on microthermometric and microanalytical data. Geochemica Cosmochim Acta 75:21–40. doi: 10.1016/j.gca.2010.10.002

Steele-MacInnis M, Lecumberri-Sanchez P, Bodnar RJ (2012) HokieFlincs_H2O-NaCl: A Microsoft Excel spreadsheet for interpreting microthermometric data from fluid inclusions based on the PVTX properties of H2O-NaCl. Comput Geosci 49:334–337. doi: 10.1016/j.cageo.2012.01.022

Steiger RH, Jäger E (1977) Submission on Geochronology: Convention on the use of decay constants in geo- and cosmochronology. Earth Planet Sci Lett 36:359–362

Stoffell B, Appold MS, Wilkinson JJ, Mcclean NA, Jeffries TE (2008) Geochemistry and evolution of mississippi valley-type mineralizing brines from the Tri-State and Northern Arkansas districts determined by LA-ICP-MS microanalysis of fluid inclusions. Econ Geol 103:1411–1435. doi: 10.2113/gsecongeo.103.7.1411

Strunz H, Giglio M (1961) Die Kristallstruktur von Stottit Fe[Ge(OH)6]. Acta Crystallogr 14:205–208. doi: 10.1107/s0365110x61000723

Strunz H, Söhnge G, Geier BH (1958) Stottit, ein neues germanium -mineral, und seine paragenese in Tsumeb. Neues Jahrb für Mineral 85–96

Stünitz H, Fitz Gerald JD (1993) Deformation of granitoids at low metamorphic grade. I: Reactions and grain size reduction. Tectonophysics 221:299–324. doi: 10.1016/0040-1951(93)90164-F

Subias I, Fanlo I, Yuste A, Fernandez-Nieto C (1999) The Yenefrito Pb-Zn mine (Spanish Central Pyrenees): an example of superimposed metallogenetic events. Miner Depos 34:220–223

Subias I, Recio C, Fanlo I, Fernandez-Nieto C (1997) Stable isotope composition of F-Pb-Zn mineralization in the Valle de Tena (Spanish Central Pyrenees). Miner Depos 32:180–188

Tamăş CG, Bailly L, Ghergari L, O'Connor G, Minuţ A (2006) New occurrences of tellurides and argyrodite in Roşia Montană, Apuseni Mountains, Romania, and their metallogenic significance. Can Mineral 44:367–383. doi: 10.2113/gscanmin.44.2.367

Tamas CG, Grobety B, Bailly L, Bernhards H-J, Minut A (2014) Alburnite, Ag8GeTe2S4, a new mineral species from the Roşia Montana Au-Ag epithermal deposit, Apuseni Mountains, Romania. Am Mineral 99:57–64. doi: 10.2113/gscanmin.38.5.1233

Taylor CD, Sutley SJ, Lichte FE (2010) Mineralogical , Textural , and Metal Residence Studies of Primary , Recrystallized , and Remobilized Ores of the Greens Creek Deposit. Geol Geochemistry Genes Greens Creek Massive Sulfide Depos Admir Island, Southeast Alaska, Geol Surv Prof Pap 1763 183–236

Taylor S., McLennan S. (1995) The geochemical evolution of the continental crust. Rev Geophys 33:241–265. doi: 10.1029/95RG00262

Ternet Y, Majesté-Menjoulas C, Canérot J, Baudin T, Cocherie A, Guerrot C, Rossi P (2004) Carte géologique de la France - 1/50 000. Feuille 1069, Laruns-Somport. Ed du BRGM Serv géologique Natl 1–195

Tomascak PB, Krogstad EJ, Walker RJ (1996) U-Pb Monazite Geochronology of Granitic Rocks from Maine: Implications for Late Paleozoic Tectonics in the Northern Appalachians. J Geol 104:185–195. doi: 10.1086/629813

Tomkins AG, Mavrogenes JA (2001) Redistribution of gold within arsenopyrite and löllingite during pro- and retrograde metamorphism: Application to timing of mineralization. Econ Geol 96:525–534. doi: 10.2113/gsecongeo.96.3.525

Torres B, Melgarejo J-C, Torro L, Camprubi A, Castillo-Oliver M, Artiaga D, Campeny M, Tauler E, Jimenez-Franco A, Alfonso P, Arce-Burgoa OR (2019) The Poopó Polymetallic Epithermal Deposit, Bolivia: Mineralogy, Genetic Constraints, and

Distribution of Critical Elements. Minerals 9:472. doi: 10.3390/min9080472

Tourigny G, Doucet D, Bourget A (1993) Geology of the Bousquet 2 mine: an example of a deformed, gold- bearing, polymetallic sulfide deposit. Econ Geol 88:1578–1597. doi: 10.2113/gsecongeo.88.6.1578

U.S. Geological Survey (2019) Mineral Commodity Summaries 2019

Uenoi T, Scott SD, Kojima S (1996) Inversion between sphalerite and wurtzite-type structures in the system Zn-Fe-Ga-S. Can Mineral 34:949–958

Vaes JF (1948) La reniérite (anciennement appelee 'Bornite orange') un sulfure germanifère provenant de la Mine Prince- Léopold, Kipushi (Congo Belge). Ann la Soc G6o- Log Belgique 72:20–32

Valcke SLA, de Bresser JHP, Pennock GM, Drury MR (2014) Influence of deformation conditions on the development of heterogeneous recrystallization microstructures in experimentally deformed Carrara marble. Geol Soc London, Spec Publ 409:175–200. doi: 10.1144/sp409.4

Van Achterbergh E, Ryan CG, Griffin WL (2001) Glitter! User's manual. On-line Interact Data Reduct LA-ICPMS Microprobe 1–72

Van den Eeckhout B, Zwart HJ (1988) Hercynian crustal-scale extensional shear zone in the Pyrenees. Geology 16:135–138. doi: 10.1130/0091-7613(1988)016<0135:HCSESZ>2.3.CO;2

Van Wilderode J, Heijlen W, De Muynck D, Schneider J, Vanhaecke F, Muchez P (2013) The Kipushi Cu-Zn deposit (DR Congo) and its host rocks: A petrographical, stable isotope (O, C) and radiogenic isotope (Sr, Nd) study. J African Earth Sci 79:143–156. doi: 10.1016/j.jafrearsci.2012.11.011

Vassilev SV, Eskenazy GM, Tarassov MP, Dimov VI (1995a) Mineralogy and geochemistry of a vitrain lens with unique trace element content from the Vulche Pole coal deposit, Bulgaria. Geol Balc 25:111–124

Vassilev SV, Eskenazy GM, Tarassov MP, Dimov VI (1995b) Mineralogy and geochemistry of a vitrain lens with unique trace element content from the Vulche Pole coal deposit, Bulgaria. Geol Balanica 25:

Velasco F, Pesquera A, Arce R, Olmedo F (1987) A contribution to the ore genesis of the magnesite deposit of Eugui, Navarra (Spain). Miner Depos 22:33–41. doi: 10.1180/minmag.1967.036.278.23

Velasco F, Pesquera A, Herrero JM (1996) Lead isotope study of Zn-Pb ore deposits associated with the Basque-Cantabrian basin and Paleozoic basement, Northern Spain. Miner Depos 31:84–92. doi: 10.1007/BF00225398

Velásquez G, Béziat D, Salvi S, Siebenaller L, Borisova AY, Pokrovski GS, De Parseval P (2014) Formation and deformation of pyrite and implications for gold mineralization in the El Callao District, Venezuela. Econ Geol 109:457–486. doi: 10.2113/econgeo.109.2.457

Vergés J, Fernàndez M, Martìnez A (2002) The Pyrenean orogen: Pre-, syn-, and post-collisional evolution. J Virtual Explor 8:1–20. doi: 10.3809/jvirtex.2002.00058

Vernhet Y (1981) Les minéralisations zincifères de l'Ordovicien et du Dévonien du Val d'Orle (District de Sentein, Ariège) et de la région de Fourcaye (Val d'Aran, Espagne). Ph D Thesis, Univ Pierre Marie Curie 279p

Vic G, Billa M (2015) Potentiel minier des Pyrénées Rapport final. BRGM Rep 1–58

Viets J, Hopkins R, Miller B (1992) Variations in minor and trace metals in sphalerite from Mississipi Valley-type deposits of the Ozark Region: Genetic implications. Econ Geol 87:1897–1905

Viets JG, Nostra AF, Emsbo P (1996) Solute compositions of fluid inclusions in sphalerite from North American and European Mississippi Valley-type deposits: Ore fluids derived from evaporated seawater. Soc Econ Geol Spec Publ 4, Sangster DF Carbonate-Hosted Lead-Zinc Depos 465–482

Vikentyev I V., Belogub E V., Novoselov KA, Moloshag VP (2016a) Metamorphism of volcanogenic massive sulphide deposits in the Urals. Ore geology. Ore Geol Rev 34. doi: 10.1016/j.oregeorev.2016.10.032

Vikentyev I V., Belogub E V., Novoselov KA, Moloshag VP (2016b) Metamorphism of volcanogenic massive sulphide deposits in the Urals. Ore geology. Ore Geol Rev. doi: 10.1016/j.oregeorev.2016.10.032

Vilà M, Pin C, Liesa M, Enrique P (2007) LPHT metamorphism in a late orogenic transpressional setting, Albera Massif, NE Iberia: Implications for the geodynamic evolution of the Variscan Pyrenees. J Metamorph Geol 25:321–347. doi: 10.1111/j.1525-1314.2007.00698.x

Villars P, Calvert LD (1991) Pearson's handbook of crystallographic data for intermetallic phases

Vivien L, Osmond J, Fédéli J, Marris-morini D, Crozat P, Damlencourt J, Cassan E, Lecunff Y, Laval S (2009) 42 GHz p.i.n Germanium photodetector integrated in a silicon-on-insulator waveguide. Opt Express 17:6252–6257

Vukmanovic Z, Reddy SM, Godel B, Barnes SJ, Fiorentini ML, Barnes SJ, Kilburn MR (2014) Relationship between microstructures and grain-scale trace element distribution in komatiite-hosted magmatic sulphide ores. Lithos 184–187:42–61. doi: 10.1016/j.lithos.2013.10.037

Wagner T, Cook NJ (1998) Sphalerite remobilization during multistage hydrothermal mineralization events —examples from siderite-Pb-Zn-Cu-Sb veins, Rheinisches Schiefergebirge, Germany. Mineral Petrol 63:223–241. doi: 10.1007/BF01164152

Wagner T, Jonsson E, Boyce AJ (2005) Metamorphic ore remobilization in the Ha Sweden : constraints from mineralogical and small-scale sulphur isotope studies. Miner Depos 40:100–114. doi: 10.1007/s00126-005-0463-2

Wagner T, Klemd R, Wenzel T, Mattsson B (2007) Gold upgrading in metamorphosed massive sulfide ore deposits: Direct evidence from laser-ablation-inductively coupled plasma-mass spectrometry analysis of invisible gold. Geology 35:775–778. doi: 10.1130/G23739A.1

Wagner T, Monecke T (2005) Germanium-bearing colusite from the Waterloo volcanic-rock-hosted massive sulfide deposit, Australia: Crystal chemistry and formation of colusite-group minerals. Can Mineral 43:655–669. doi: 10.2113/gscanmin.43.2.655

Wagner T, Schneider J (2002) Lead isotope systematics of vein-type antimony mineralization, Rheinisches Schiefergebirge, Germany: A case history of complex reaction and remobilization processes. Miner Depos 37:185–197. doi: 10.1007/s00126-001-0211-1

Walter LM, Stueber AM, Huston TJ (1990) Br-Cl-Na systematics in Illinois basin fluids: Constraints on fluid origin and evolution. Geology 18:315–318. doi: 10.1130/0091-7613(1990)018<0315:BCNSII>2.3.CO;2

Walters S, Bailey A (1998) Geology and Mineralization of the Cannington Ag-Pb-Zn Deposit: An Example of Broken Hill-Type Mineralization in the Eastern Succession, Mount Isa Inlier, Australia. Econ Geol 93:1307–1329. doi: 10.1016/j.precamres.2007.08.009

Wang JB, Li CY, Chen X (1992) Wang JB, Li CY, Chen X (1992) A new genetic model for the Jinding lead-zinc deposit, Geol Explor Non-Ferrous Metals 1:200–206 (in Chinese with English abstract). Geol Explor Non-Ferrous Met 1:200–206

Warren H. V, Thompson RM (1945) Sphalerites from Western Canada. Econ Geol 40:309–335

Webster AE (2004) The Structural Evolution of the Broken Hill Pb-Zn-Ag Deposit , New South Wales, PhD Thesis University of Tasmania. PhD Thesis Univ Tasmania 1–430

Wei C, Huang Z, Yan Z, Hu Y, Ye L (2018) Trace Element Contents in Sphalerite from the Nayongzhi Zn-Pb Deposit, Northwestern Guizhou, China: Insights into Incorporation Mechanisms, Metallogenic Temperature and Ore Genesis. Minerals 8:490. doi: 10.3390/min8110490

Wei C, Ye L, Hu Y, Danyushevskiy L, Li Z, Huang Z (2019) Distribution and occurrence of Ge and related trace elements in sphalerite from the Lehong carbonate-hosted Zn-Pb deposit , northeastern Yunnan , China : Insights from SEM and LA-ICP-MS studies. Ore Geol Rev 115:103175. doi: 10.1016/j.oregeorev.2019.103175

Weisbach A (1886) Argyrodit , ein neues Silbererz. Neues Jahrb für Mineral 2:67–71

Went MR, Vos M, Kheifets AS (2006) Satellite structure in Auger and (e, 2 e) spectra of germanium. Radiat Phys Chem 75:1698–1703. doi: 10.1016/j.radphyschem.2006.09.003

Wenz ZJ, Appold MS, Shelton KL, Tesfaye S (2012) Geochemistry of Mississippi valley-type mineralizing fluids of the Ozark Plateau: A regional synthesis. Am J Sci 312:22–80. doi: 10.2475/01.2012.02

Wheeler J (1992) Importance of pressure solution and Coble creep in the deformation of polymineralic rocks. J Geophys Res 97:4579–4586

Wiedenbeck M, Allé P, Corfu F, Griffin WL, Meier M, Oberli F, Von Quadt A, Roddick JC, Spiegel W (1995) Three natural zircon standards for U-Th-Pb, Lu-Hf, trace element and REE analyses. Geostand Newsletters 19:1–23. doi: 10.1111/j.1751-908X.1995.tb00147.x

Wilkinson JJ (2013) Sediment-Hosted Zinc-Lead Mineralization: Processes and Perspectives: Processes and Perspectives, Treatise on Geochemistry, Second Edition. Elsevier, H Holland, K Turekian (ed), Amsterdam, Netherlands 219–249. doi: 10.1016/B978-0-08-095975-7.01109-8

Wilkinson JJ, Eyre SL, Boyce AJ (2005) Ore-forming processes in Irish-type carbonate-hosted Zn-Pb deposits: Evidence from mineralogy, chemistry, and isotopic composition of sulfides at the Lisheen Mine. Econ Geol 100:63–86. doi: 10.2113/100.1.0063

Wilkinson JJ, Stoffell B, Wilkinson CC, Jeffries TE, Appold MS (2009) Anomalously metal-rich fluids form hydrothermal ore deposits. Science (80-) 323:764–767. doi: 10.1126/science.1164436

Wilson SA, Ridley WI, Koenig AE (2002) Development of sulfide calibration standards for the laser ablation inductively-coupled plasma mass spectrometry technique. J Anal At Spectrom 17:406–409. doi: 10.1039/b108787h

Windh J (1995) Saddle Reef and Related Gold Mineralization, Hill End Gold Field, Australia: Evolution of an Auriferous Vein System during Progressive Deformation. Econ Geol 90:1764–1775

Working group on defining critical raw materials (2014) Report on Critical Raw Materials for the Eu Critical Raw Materials Profiles. Eur Commision 1–205. doi: Ref. Ares(2015)1819595 - 29/04/2015

Xue C, Zeng R, Liu S, Chi G, Qing H, Chen Y, Yang J, Wang D (2007) Geologic, fluid inclusion and isotopic characteristics of the Jinding Zn-Pb deposit, western Yunnan, South China: A review. Ore Geol Rev 31:337–359. doi: 10.1016/j.oregeorev.2005.04.007

Yalikun Y, Xue C, Symons DTA (2018) Paleomagnetic age and tectonic constraints on the genesis of the giant Jinding Zn-Pb deposit, Yunnan, China. Miner Depos 53:245–259. doi: 10.1007/s00126-017-0733-9

Yardley BWD (2005) Metal Concentrations in Crustal Fluids and Their Relationship to Ore Formation. Econ Geol 100:613–632

Ye L, Cook NJ, Ciobanu CL, Yuping L, Qian Z, Tiegeng L, Wei G, Yulong Y, Danyushevskiy L (2011) Trace and minor elements in sphalerite from base metal deposits in South China: A LA-ICPMS study. Ore Geol Rev 39:188–217. doi: 10.1016/j.oregeorev.2011.03.001

Ye L, Cook NJ, Liu T, Ciobanu CL, Gao W, Yang Y (2012) The Niujiaotang Cd-rich zinc deposit, Duyun, Guizhou province, southwest China: Ore genesis and mechanisms of cadmium concentration. Miner Depos 47:683–700. doi: 10.1007/s00126-011-0386-z

Ye L, Tiegeng L (1999) Sphalerite Chemistry, Niujiaotang Cd-Rich Zinc Deposit, Guizhou, Southwest China. Chinese J Geochemistry 18:62–68

Yun ST, So CS, Choi SH, Shelton KL, Koo JH (1993) Genetic environment of germanium-bearing gold-silver vein ores from the Wolyu mine, Republic of Korea. Miner Depos 28:107–121. doi: 10.1007/BF00196335

Zeng M, Zhang D, Zhang Z, Li T, Li C, Wei C (2018) Structural controls on the Lala iron-copper deposit of the Kangdian metallogenic province, southwestern China: Tectonic and metallogenic implications. Ore Geol Rev 97:35–54. doi: 10.1016/j.oregeorev.2018.04.028

Zheng Y, Zhang L, Chen Y jing, Hollings P, Chen H (2013) Metamorphosed Pb-Zn-(Ag) ores of the Keketale VMS deposit, NW China: Evidence from ore textures, fluid inclusions, geochronology and pyrite compositions. Ore Geol Rev 54:167–180. doi: 10.1016/j.oregeorev.2013.03.009

Zwart HJ (1963a) Metamorphic history of the Central Pyrenees, Part II, Valle de Aran. Leidse Geol Meded 28:321–376

Zwart HJ (1963b) The Structural Evolution of the Paleozoïc of the Pyrenees. Geol Rundschau 53:170–205

Zwart HJ (1979) The Geology of the Central Pyrenees. Leidse Geol Meded 50:1–74

11Supplementary materials

11.1 ARTICLE – Relationships between the occurrence of accessory Ge-minerals and sphalerite in Variscan Pb-Zn deposits of the Bossost anticlinorium, French Pyrenean Axial Zone: Chemistry, microstructures and ore-deposit setting – a first order textural and chemical approach

This section is devoted to the article "Relationships between the occurrence of accessory Ge-minerals and sphalerite in Variscan Pb-Zn deposits of the Bossost anticlinorium, French Pyrenean Axial Zone: Chemistry, microstructures and ore-deposit setting" published on February 15, 2018 in Ore Geology Review (95). The fully edited version of this article is available at the following link: https://www.sciencedirect.com/science/article/pii/S0169136817304523.

It was the first article published during the thesis and part of the results were collected during my Master internship (6 months). This paper presents a preliminary structural and chemical study with *in-situ* electro probe microanalyser (EPMA) and laser ablation inductively coupled plasma mass spectrometry (LA-ICP-MS) analyses on sphalerite and brunogeierite from three Vein-deposits (Argut, Pale Bidau, Pale de Rase). These deposits were interpreted in the previous chapter as Type 2b veins.

This study deciphers some of aspect of the Pyrenean sphalerite vein mineralization such as their structural patterns which demonstrate their epigenetic genesis even if they locally appear concordant to S_0-S_1 in two deposits (Argut-dessus and Pale de Rase). Microstructural analyses demonstrate an imprint of metamorphism/deformation on the sphalerite with possible recrystallization features observed on etched sphalerite, with small polygonal sphalerite crystals. Chemical analyses (EPMA and LA-ICP-MS) on sphalerite and brunogeierite describe a global poor Ge-Cu content in sphalerite lattice compare to brunogeierite which contain high Ge content (>29 wt.% Ge) and some trace elements (Cu, Ga; n=3). This study inferred the occurence of Ge remobilization during metamorphism and/or deformation. A global comparison with world-class Ge-deposits describe a paradox between sphalerite and Ge-minerals. When Ge-minerals occur, sphalerite appear globally depleted in Ge within the lattice whereas when Ge-minerals are absent, sphalerite contains relative high Ge in sphalerite (up to few thousands of ppm Ge).

Ore Geology Reviews 95 (2018) 1–19

Contents lists available at ScienceDirect

Ore Geology Reviews

journal homepage: www.elsevier.com/locate/oregeorev

Alexandre Cugerone[a,*], Bénédicte Cenki-Tok[a], Alain Chauvet[a], Elisabeth Le Goff[b], Laurent Bailly[c], Olivier Alard[a], Mael Allard[a]

[a] Géosciences Montpellier, UMR CNRS 5243, Université Montpellier, Place E. Bataillon, CC 60, F-34095 Montpellier, France

[b] BRGM, Bureau de Recherches Géologiques et Minières, Territorial Direction Languedoc-Roussillon, 1039 Rue de Pinville, 34000 Montpellier, France

[c] BRGM, Bureau de Recherches Géologiques et Minières, 3 Avenue Claude Guillemin, BP 36009, 45060 Orléans Cedex 2, France

Keywords: Germanium; Pyrenean Axial Zone; Sphalerite; Mineral chemistry; Sulfide textures

Received 9 June 2017; Received in revised form 2 February 2018; Accepted 11 February 2018 Available online 15 February 2018

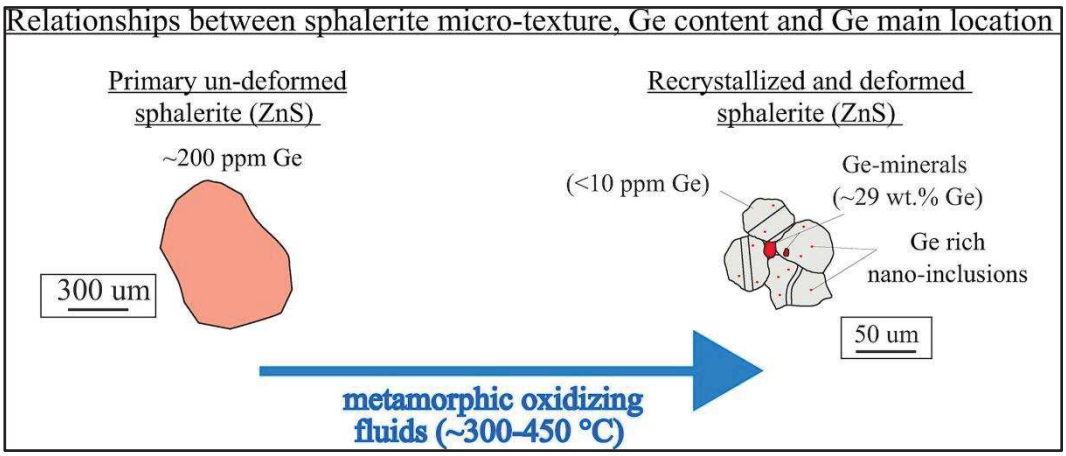

Figure 123. Graphical abstract describing the main purpose of the article

11.1.1 Abstract

The presence of unique accessory Ge-minerals (containing up to 70 wt% Ge) is a widespread phenomenon in Pb-Zn deposits of the Variscan Pyrenean Axial Zone (PAZ). Such a mode of occurrence is, however, rare worldwide with germanium more typically occurring as a trace component of sulfides, notably sphalerite (< 3200ppm), or in coal deposits (< 5570 ppm). The PAZ Pb-Zn deposits are thus an excellent target to unravel the processes and key factors controlling formation of mineralization highly concentrated in Ge. Three Pb-Zn deposits are studied here: Argut-dessus; Pale Bidau; and Pale de Rase. All three are located in Late Ordovician rocks within the PAZ Bossost anticlinorium. The main mineralization (Type 2) is localized in epigenetic veins with different geometries relative to host rocks and deformation. Textural analysis of sphalerite mineralization shows evidence for both recrystallization and deformation. Sphalerite is associated with muscovite or graphite and is the unique host for the discrete Ge-minerals in the studied samples. Brunogeierite ($GeFe_2O_4$) and argutite (GeO_2) occur almost universally at sphalerite grain boundaries. Laser ablation inductively coupled plasma-mass spectrometry analysis of sphalerite and brunogeierite show that sphalerite is relatively depleted in Ge (mean ~13 ± 3 ppm) and other trace elements such as Sb (~21 ± 2 ppm), Cu (~153 ± 23 ppm) and Ga (~127 ± 10 ppm) compared to brunogeierite (29–30 wt% Ge), which is also richer in Ga (~2406 ± 270 ppm) and Cu (~2438 ± 550 ppm). Collectively, these observations on this exceptional example of Ge enrichment highlight the role of oxidizing, moderate temperature (~< 450 °C) metamorphic fluids on the partitioning of Ge between discrete Ge-minerals and their sulfide hosts. Comparison with other Ge-deposits worldwide supports the hypothesis that low grade metamorphism and deformation may play a key role in the genesis and concentration of Ge-mineralization, especially in low-grade metamorphic Kipushi-type deposits in which discrete Ge-minerals are located immediately adjacent to recrystallized sulfides.

11.1.2 Introduction

Germanium (Ge) is one of twenty metals defined as critical by the European Union *(Working group on defining critical raw materials 2014*). It is extensively used in the optical fiber and photovoltaic industries. Even though Ge-bearing deposits occur in various geological settings, the element is predominantly found in trace contents within zinc and coal deposits (up to ~3200 and ~5570 ppm respectively; *Seredin and Finkelman 2008; Saini-Eidukat et al. 2009*). The largest Ge-deposits do not, however, exceed a few thousand tons of estimated metal resources, e.g., 2160 t Ge for the Tsumeb deposit, Namibia (*Lombaard et al. 1986*), or 1112 t Ge in the Yunnan coal province *(Höll et al. 2007; Hu et al. 2009*). Germanium has an average concentration of ~1.5 ppm in the continental crust (*Smith and Huyck 1999*) which is significantly higher than estimates for elements such as molybdenum or silver (respectively, 1.1 ppm and 0.07 ppm; *Laznicka 2014*). This paradox,

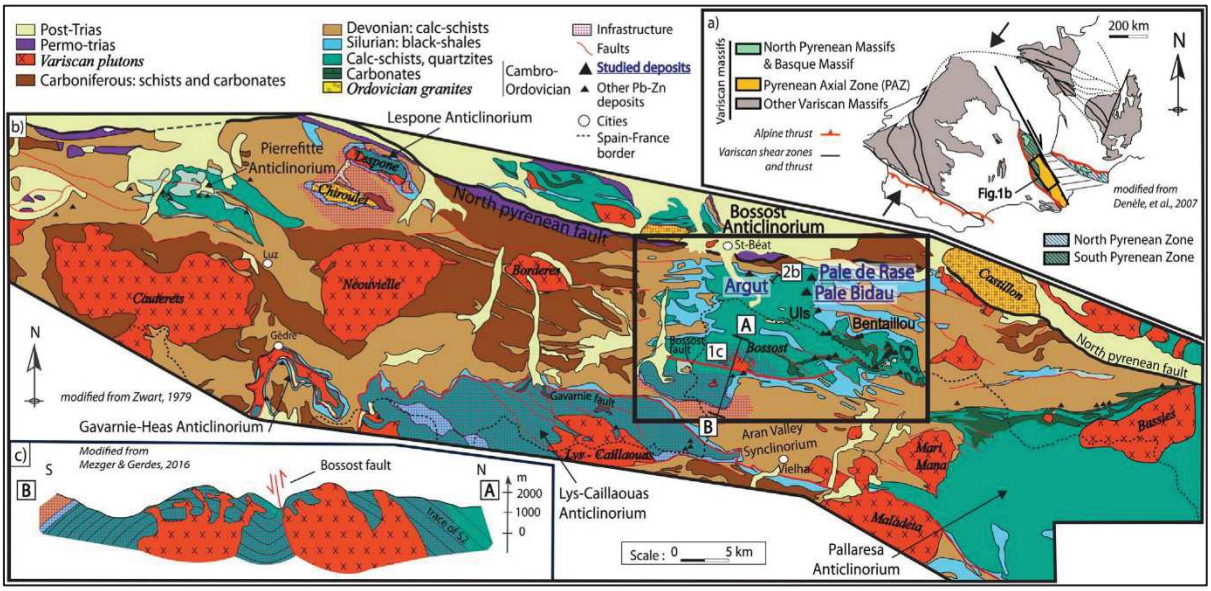

Figure 124 : a) Location of the Pyrenean Axial Zone (PAZ) within the Hercynian belt of Western Europe (modified from *Denèle et al., 2014*); b) Main Pb-Zn deposits in Paleozoic rocks of the Central PAZ, with the location of the studied Pb-Zn deposits (modified from *Zwart, 1979*). Location of the cross-sections shown in Figs. 1c and 2b; c) N-S cross-section of the Bossost dome (from *Mezger and Gerdes, 2016*).

i.e., the fact that Ge is relatively concentrated in the crust but does not appear as giant deposits, may explain why Ge deposits cannot be identified in a specific setting and instead occur in a diverse range of different environments.

Germanium mineralization may be linked to epigenetic or syngenetic ores even if (diagenetic)-epigenetic deposits hosted in sedimentary sequences typically provide for a greater

enrichment (i.e., coal, Mississippi Valley Type (MVT) and Kipushi-type deposits). Germanium can readily partition into sulfides, oxides, silicate minerals or organic matter, at a large range of concentration, from trace to major contents. Processes of Ge concentration remain poorly constrained but appear linked to low-temperature hydrothermal fluids (*Höll et al. 2007*). The source of Ge is still unclear in most of the Ge-deposits even if few Ge anomalies may be found in granites or black shales *(Belissont 2016)* associated with Ge ores. Post-mineralization processes, notably metamorphic recrystallization, can impact on Ge mineralization as Frenzel et al. (2016) showed that Ge concentration in sphalerite decreases with increasing metamorphic grade (< 310 °C) affecting the PbZn deposits.

In the Pyrenean Axial Zone (PAZ, Figure 124A), the main metallic resources (Zn, Pb, Fe, Cu, Mn) are located in metasedimentary rocks of Paleozoic age (Figure 124B; *Vic and Billa 2015*), especially in Cambro-Devonian units that make up several metamorphic domes (Pierrefitte, Lys, Gavarnie; Pallaresa, Bossost etc.; Figure 124B). Several events generating Pb-Zn mineralization in the PAZ have been proposed and continue to be debated, including Middle-Late Ordovician, Lower or Late Devonian, Carboniferous (Variscan) and Late-Triassic/Late-Jurassic ages (Marcoux et al. 1991a; Nicol et al. 1997; García-Sansegundo et al. 2014; Munoz et al. 2016). The two oldest events are considered as SEDEX-type by *Bois et al. (1976)* and *Pouit (1985)*. More than 150 individual Pb-Zn deposits are identified in the French and Spanish parts of the PAZ within 40 different mineralized districts (*Oudin et al. 1988*). Production did, however, not exceed 300,000 tons of Zn in the French deposits (*http://sigminesfrance.brgm.fr/*).

The frequent and widespread occurrence of discrete Ge-minerals in the PAZ Pb-Zn deposits (Figure 124B) is quite uncommon in comparison with other deposits worldwide. More usually, whenever Ge is present, it is enriched in the sphalerite (ZnS) lattice rather than as independent Ge-minerals (Reyx 1973; Laforet et al. 1981; Johan et al. 1983; Bernstein 1985; Cook et al. 2009b, 2015). These Ge-minerals may be brunogeierite ($GeFe_2O_4$), argutite (GeO_2), Ge-chloritoid (carboirite, $FeA1_2GeO_5(OH)_2$), rare briartite ($Cu_2(Fe, Zn)GeS_4$), as well as Gebearing lepidomelane, titanite, garnet, zoisite, chlorite, quartz, allanite, and magnetite (*Laforet et al. 1981; Johan et al. 1983; Bernstein 1985; Johan and Oudin 1986; Pouit and Bois 1986b*). The formation of Ge-minerals in the Pyrenean deposits is poorly documented until now except for *Aye et al. (1978)* and *Johan and Oudin (1986)* who suggested a possible link with regional metamorphism, based on paragenetic analysis.

The aim of this study is firstly to decipher the processes leading to genesis of Argut-dessus (AD), Pale Bidau (PB) and Pale de Rase (PR) PbZn(-Ge) deposits located in the PAZ Bossost

anticlinorium, and secondly, to compare their features with those of other Ge-occurrences worldwide. We focus on: (i) the structural setting of the three deposits within the regional tectonic framework; (ii) the mineralogy and microstructures of 38 representative samples; and (iii) the chemistry of sphalerite and accessory Ge-minerals in order to highlight the role of metamorphism and deformation in ore genesis.

11.1.3 Geological and structural setting

The Pyrenean Axial Zone (PAZ) belongs to the West-European Variscan belt which was involved in the Pyrenean orogenic cycle (Figure 124A). It is composed of Paleozoic metasedimentary rocks intruded by Ordovician granites which were metamorphosed and deformed during the Variscan orogeny (Aston, Hospitalet, and Canigou gneiss; *Denèle et al. 2014*). Two structural domains are present in the PAZ (*Zwart 1963b, 1979*): (i) the Infrastructure consists of high grade metamorphic rocks presenting moderately dipping foliation patterns. Numerous domes are present in the PAZ like the Bossost, Lys Caillaouas, or Aston, Hospitalet and Canigou (Figure 124B; *Zwart 1979; Denèle 2007; Denèle et al. 2008)*. Formation of these domes is associated with emplacement of late-Carboniferous granitoids (i.e., Lys, Maladeta, Bassies, Bossost; (*Kleinsmiede 1960; Zwart 1963a; Garcia-Sansegundo and Alonso 1989; Mezger and Passchier 2003; Mezger 2005*); ii) the Superstructure is composed of low-grade metamorphic rocks and present steep folds and fabrics *(Zwart 1963b; Cochelin 2016*). The main tectono-metamorphic events recorded in the PAZ are considered as Variscan (ca. 300–325 Ma, *Evans et al. 1998; Denèle et al. 2014)*.

This study focuses on the Bossost anticlinorium (Figure 124C). The study focuses on the northern part of the Bossost anticlinorium which is composed of Cambrian to Devonian rocks and is part of the Superstructure (Figure 124B). The southern part of the anticlinorium forms the Aran valley synclinorium and the northern part is bounded by the North-Pyrenean Fault (Figure 124B). It is composed of a late-Variscan intrusive leucocratic muscovite-hornblende granite forming the core of a metamorphic dome (Infrastructure) within a larger anticlinorium of Cambro-Devonian metasedimentary rocks *(Kleinsmiede 1960; Zwart 1963b; Garcia-Sansegundo and Alonso 1989*).

Four stages of deformation are recorded in the Superstructure of the Bossost anticlinorium. (1) A first Variscan deformation (D1) linked to formation of a discrete Pre-Upper Ordovician slaty cleavage (S1). D1 is poorly preserved due to superposition of intensive late events *(Garcia-Sansegundo and Alonso 1989*). (2) D2 is expressed by F2 recumbent north-facing folds associated with a sub-horizontal axial planar S2 cleavage *(Matte 1969; Garcia-Sansegundo and Alonso 1989)*. A regional metamorphism linked to MP/MT crustal thickening is synchronous with D2. Metamorphism is

epizonal *(Pouit 1974; Johan and Oudin 1986)*. (3) D3 is locally expressed with S3 cleavage and F3 crenulation folds (*Aerden 1994; Mezger and Passchier 2003*). At regional scale, *Aerden (1994)* describes D3 deformation patterns (which he named D2) as related to N-S compression and crustal thickening. A decollement is inferred at the base of Silurian black-shales *(Zwart 1979; Matte and Zhi 1988; Mezger and Passchier 2003*) with tight north-vergent folds. (4) Alpine Upper Cretaceous to Miocene D4 deformation is locally present and essentially reactivates E-W Variscan faults like the Gavarnie Fault *(García-Sansegundo et al. 2014)*, the Merens mylonitic zone *(Zwart 1979; Mezger et al. 2012; Denèle et al. 2014*) and in the area of interest here, the Bossost Fault (*Zwart 1979*)

The three studied Pb-Zn(-Ge) deposits (Argut-Dessus, Pale Bidau and Pale de Rase) are located within the northernmost part of the Bossost anticlinorium (Figure 125A). Sulfide mineralogy is dominated by sphalerite and galena. These deposits are relatively small with historical production of about 2000–3000 tons of Zn and less than 1000 tons of Pb *(Michard 1966, 1969; Chaput M. and Michard A. 1967; BRGM 1984)*. The AD and PR deposits are hosted by schists, meta-siltstones and metaconglomerates (Figure 125B). The PB deposit is hosted by grey schists locally alternating with dm-scale siltstones that represent lower parts of the Late Ordovician (o5) compared to those of the AD and PR deposits (Figure 125B; *Pouit 1974*). These three deposits occur in Late Ordovician units affected by low-grade metamorphism with the appearance of sericite or muscovite and chlorite in the host schists (*Chaput M. and Michard A. 1967; Pouit 1974; Johan and Oudin 1986)*.

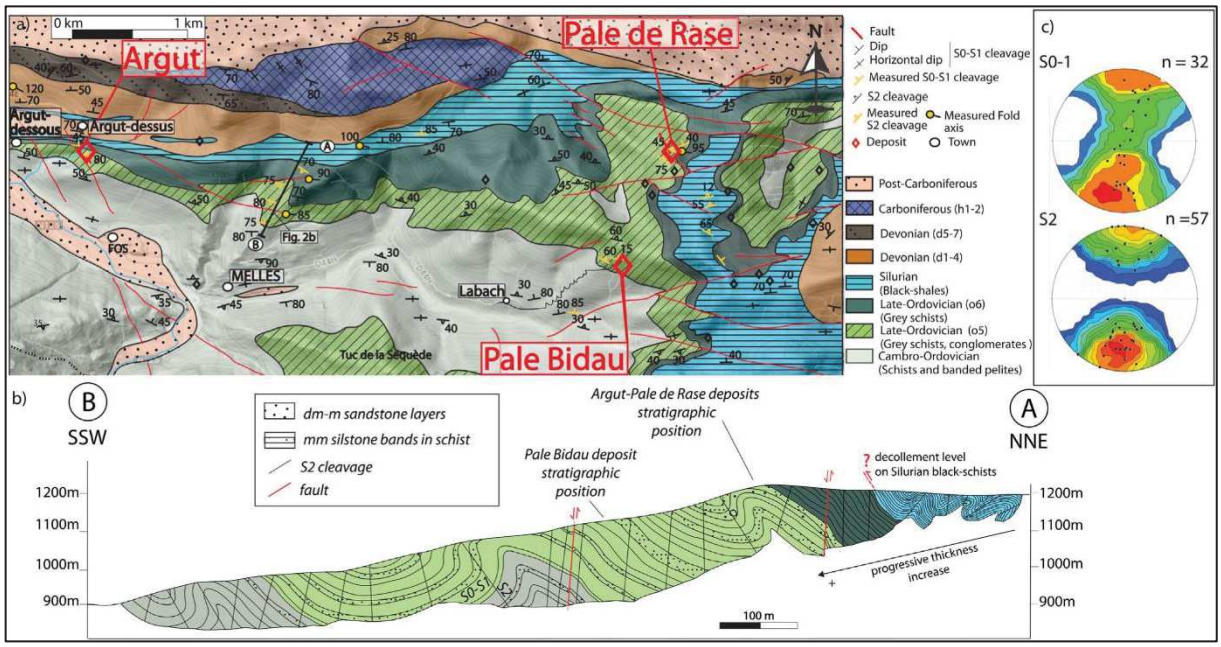

Figure 125. a) Regional structural map for the northern part of the Bossost anticlinorium (compiled from the geological map and our own data). Structural positions of Argut-dessus (AD), Pale Bidau (PB) and Pale de Rase (PR) deposits are indicated in red. Location of the cross-section shown as Figure 125B is indicated; b) NNE-SSW structural cross-section near Melles in Cambro- Silurian rocks. c) Pole figures of S0-S1 and S2 measurements. (For interpretation of the references to colour in this figure legend, the reader is referred to the web version of this article.)

11.1.4 Methods

Samples were collected in situ in underground galleries, outcrops and rarely in mine dumps. 38 polished thin sections (30 and 100 μm) were studied. 21 of these contained sphalerite. One polished section from the BRGM collection (sample 32362 from the AD deposit) was included in the study. Microanalysis was carried out using a FEI Quanta FEG 100 Scanning electron microscope (SEM) and a Cameca SX100 electron microprobe analyzer (EMPA) at the Service inter-regional Microsonde-Sud, Montpellier. Major, minor and trace elements were measured with a beam current of 100nA and accelerating voltage of 20 kV. 14 elements were analyzed: standards, spectral lines, and spectrometers were as follows: Zn (Zn, Lα, TAP); S (FeS2,Kα, PET); Fe (Fe2O3,Kα, LLif); Cd(CdS, Lα, LPET); Ge (Ge, Kα, LLif); Sb (GaSb, Lα, LPET); Cu (CuS, Kα, LLif); Ga (GaSb, Kα, LLif); Ag (Ag, Lα, LPET); Mn (Mn, Kα, LPET); Sn (Sn, Lα, PET); Pb (Pb, Mα, PET); As (GaAs, Lα, TAP); Si (CaSiO3,Kα, TAP). Peak count times ranged from 30 to 240 s (240 s for Ge). Germanium is analyzed on 2 LLif monochromators. The limit of de- tection for Ge, calculated by internal Cameca procedures, is reduced to 84 ppm. Gallium, As, Ag, Pb, Sn, Sb, and Mn were below detection limit and are not reported in the data tables.

Laser ablation inductively coupled plasma-mass spectrometry (LA-ICP-MS) was used to determine trace elements concentrations in sphalerite and brunogeierite. Analyses were carried out using an Excimer CompEx 102 coupled with a ThermoFinnigan Element XR available at the OSU-OREME Montpellier. Analytical setting is modified from *Belissont et al. (2014)*. Laser ablation was performed with a constant 5 Hz pulse rate at 90 mJ laser energy. Ablation was performed with different spot diameters: 26 μm for sphalerite and 5 μm for brunogeierite. Total acquisition time was limited to 300 s including 180 s of background measurement (laser off) followed by 60 s of signal acquisition and 60 s of washout time. Zinc or Fe contents measured with EMPA were used as internal calibration for sphalerite or brunogeierite, respectively. MASS 1 (synthetic polymetallic sulfide) with a Ge con- centration of 57.8 ± 2.6 ppm (S. Wilson, pers. comm.) was used as external standard. The following isotopes were measured: 64Zn; 34S; 55Mn; 57Fe; 59Co; 61Ni; 118Sn; 75As; 63Cu; 69Ga; 74Ge; 107Ag; 110Cd; 115In; 121Sb; and 208Pb. Data were processed using the Glitter 4.0 software package *(Van Achterbergh et al. 2001)*. Twenty-nine spot analyses were made on sphalerite from three different samples, one from each of the three deposits (14 spots on PB sample PB08; 9 spots on AD sample AD12; 6 spots on PR sample PR01). Three spot analyses were made on brunogeierite (sample PB08). The mean minimum detection limit for Ge was ~1.1 ppm for sphalerite and 170 ppm for brunogeierite.

11.1.5 Structural and petrological study of the PAZ Pb-Zn(-Ge) deposits

11.1.5.1 Structural study

In the three studied deposits, two main cleavages are present. Both cleavages are roughly oriented N090-120°E (Figure 125A) across the entire study area and exhibit various dip angles (Figure 125C). A first cleavage (here termed S1) is weakly developed and transposes the stratification S0. It is observed within most outcrops except when a second cleavage overprint (S2) is strong. According to the NNE-SSW cross-section (Figure 125B), S0-1 cleavage is affected by cm- to dm-scale E-W trending asymmetric F2 folds (Figure 126A). S2 cleavage is always strongly dipping or vertical (Figs. 2c and 3a), intensively developed and locally erases all pre-existing structures. Regional structuration is essentially related to south-verging asymmetric F2 folds. This D2 deformation is the D3 deformation described in *Garcia-Sansegundo and Alonso (1989)*. In contrast, Silurian black-shale in the north of the Bossost anticlinorium display north-vergent E-W trending F2 tight folds (Figure 125B) and may be considered as a decollement layer with the Silurian level as suggested by *Zwart (1979)* and *Matte and Zhi (1988)*.

11.1.5.2 Macroscopic description of the mineralization

Two types of mineralized structures are observed. The first (type 1) consists of μm- to cm-scale disseminated sulfides within the stratigraphic sequence. This type occurs especially at PB and AD but is minor in PR. The second mineralization type (type 2) consists of dm- to m scale veins and represents the main exploited orebodies in PB and AD. These are particularly well-developed within the lithologies affected by D2 deformation. Geometries of these veins vary and can be sub-parallel to S0-1 and affected by S2 (Figure 126B-D), or sub-parallel to S2 and crosscutting S0-S1 (Figure 126E-F). Mineralization appears larger and better developed when crossing competent, relatively coarse beds such as siltstone-conglomerates (PR and AD) or siltstones (PB) and tends to be parallel to S2 in this case. In AD, and especially PB, mineralization is essentially sub-parallel to S2 in coarse beds, or parallel to S0-1 in schists (Figure 126C). This sulfide-rich mineralization forms veins up to several tens of cm thick (Figure 126E-F). The vein gangue is composed of quartz and carbonate with local brecciated domains (Figure 126E) Erosive box-work structures are often present in sphalerite or pyrite mineralization with the formation of cubic cavities (Figure 126C-D) in quartz gangue. It evidences macro-overgrowth structures of sphalerite in gangue minerals (seen in section in Figure 126C). These box-work structures and associated mineralized bodies are preferentially located within the dm-scale levels of siltstone. In AD, type 2 mineralization is locally composed of sphalerite boxwork (in schist-siltstone levels; Figure 126C), or present in N040trending fractures (Table 7). PR deposit contains type 2 mineralization essentially observed parallel to stratification (Figure 126B), which is deformed by the S2-corridor. This mineralization may be offset by barren normal faulting (Figure 126B). Minor sphalerite mineralization is also present in N050-trending fractures (Table 7).

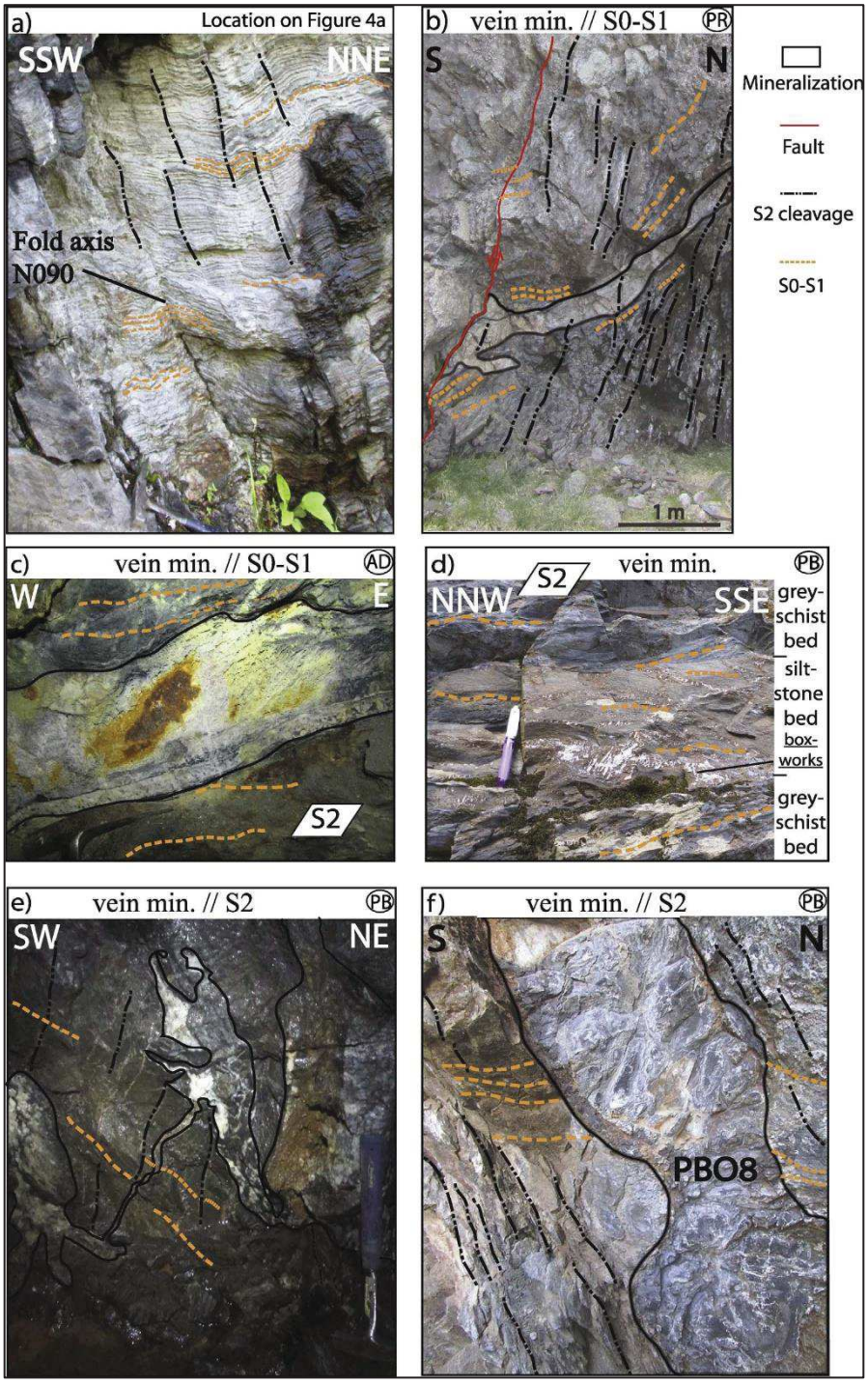

Figure 126. Outcrop photographs from the three studied PAZ deposits: a) Folded Late Ordovician (o5) grey schists in the northern Bossost anticlinorium; b) Stratiform type 2 mineralization in Pale de Rase (PR); c) Type-2 vein mineralization (boxworks) parallel to S0-S1 in Argut-dessus (AD); d) Boxworks in Pale Bidau (PB) preferentially within Late Ordovician (o5) siltstone bed; e) Type-2 vein mineralization parallel to S2 in Pale Bidau (PB) gallery; f) Type-2 vein mineralization in Pale Bidau (PB) with position of sample PB08.

11.1.5.3 Micro-structure, mineralogy and texture of mineralization

11.1.5.3.1 Mineralogy

Type 1 (stratiform) mineralization is essentially composed of an assemblage of disseminated pyrite and brown sphalerite (Fig. 4a, b; MEL-1; AD01; AD03).

Type 2 (vein) mineralization (samples PB08, PR01, MEL-1, AD06, AD12, AD16, AD20, and AD32362) is mainly composed of massive brown sphalerite (≅80%), galena, minor pyrite, and arsenopyrite (Figure 127A, C and D). Pyrrhotite, chalcopyrite, tennantite-tetrahedrite, Pb-Bisulfosalts and magnetite occur rarely (Figure 128). The presence of graphite, chlorite and frequent metamorphic muscovite associated with sphalerite is noteworthy. Germanium oxides (brunogeierite and rare argutite) can be observed only in the PB and AD samples. Gangue minerals are composed of quartz and carbonate minerals (Figure 128).

Locality		AD (Argut-dessus)	PR (Pale de Rase)	PB (Pale Bidau)
Host rocks		Conglomerates/siltstone/schists		siltstones-calc-schists
Type 1	Structure/Deformation	parallel to S0-1 deformed with asymetric E-W folds	parallel to S0-1 deformed with asymetric E-W folds	only boxworks
	Samples	AD01, AD03, MEL4	/	PBO3-PB10
	Mineralogy	Py + Sp		
Type 2	Structure/Deformation	parallel to S2 or S0-S1, N040 fractures	parallel to S2 or S0-S1, N050 fractures	parallel to S2, minor parallel to S0-S1
	Samples	AD06, AD12, AD17, AD20	PR01, PR02, PR03, PR04	PBO3, PB08, PB10
	Mineralogy Mineralization	Sp + Gn + Py + Ccp + Po + Apy ± Ms. ± Gr + Ge mineralization	Py ± Ms. ± Chl ± Gr	Sp + Gn + Py + Chl + Ge mineralization ± Ms. ± Chl ± Gr
	Gangue	Qz + (Ca-Fe-Mg) Cb	Qz + (Ca-Fe-Mg) Cb	Qz + (Ca-Fe-Mg) Cb

Mineral abbreviations: Sp: sphalerite; Gn: galena/Py: pyrite/Ccp: chalcopyrite/Po: pyrrhotite/Apy: arsenopyrite/Ms: muscovite/Chl: chlorite/Gr: graphite/Qz: quartz/Cb: carbonate.

Table 7 : Geological characteristic of the three studied Pb-Zn deposits and the two types of mineralizations.

11.1.5.3.2 Textures

Quartz and carbonates display comb textures in type 2 vein mineralization. Brecciated textures are locally present in vein mineralization (PB). Generally, carbonates are present as coarse (> 2 mm) grains that are intensely fractured with curved continuous thick twins, and locally filled with sphalerite. Two generations of quartz are recognized. The earlier one occurs as coarse deformed grains, and is affected by stylolites, whereas the second occurs as overgrowth at the contact with sulfide minerals. Early quartz is rounded or presents comb textures. Stylolites are locally filled with sulfide mineralization. Muscovite is associated with sphalerite at grain boundaries, or as inclusions (Figure 129A).

Two different pyrite textures are present: Py1 appears in beds or as disseminated xenomorphic dull yellow crystals (Figure 129B) compared to shiny automorphic Py2 in vein

structures. Intervals containing Py1 are folded and graded beds of pyrite are present (Figure 127C andFigure 129C); pressure shadows appear locally. Locally, rare isolated and elongate Py1 crystals parallel to S0-S1 are present. Framboidal cores are apparent in Py1. Py2 appear often orientated perpendicular to vein boundaries (Figure 129C).

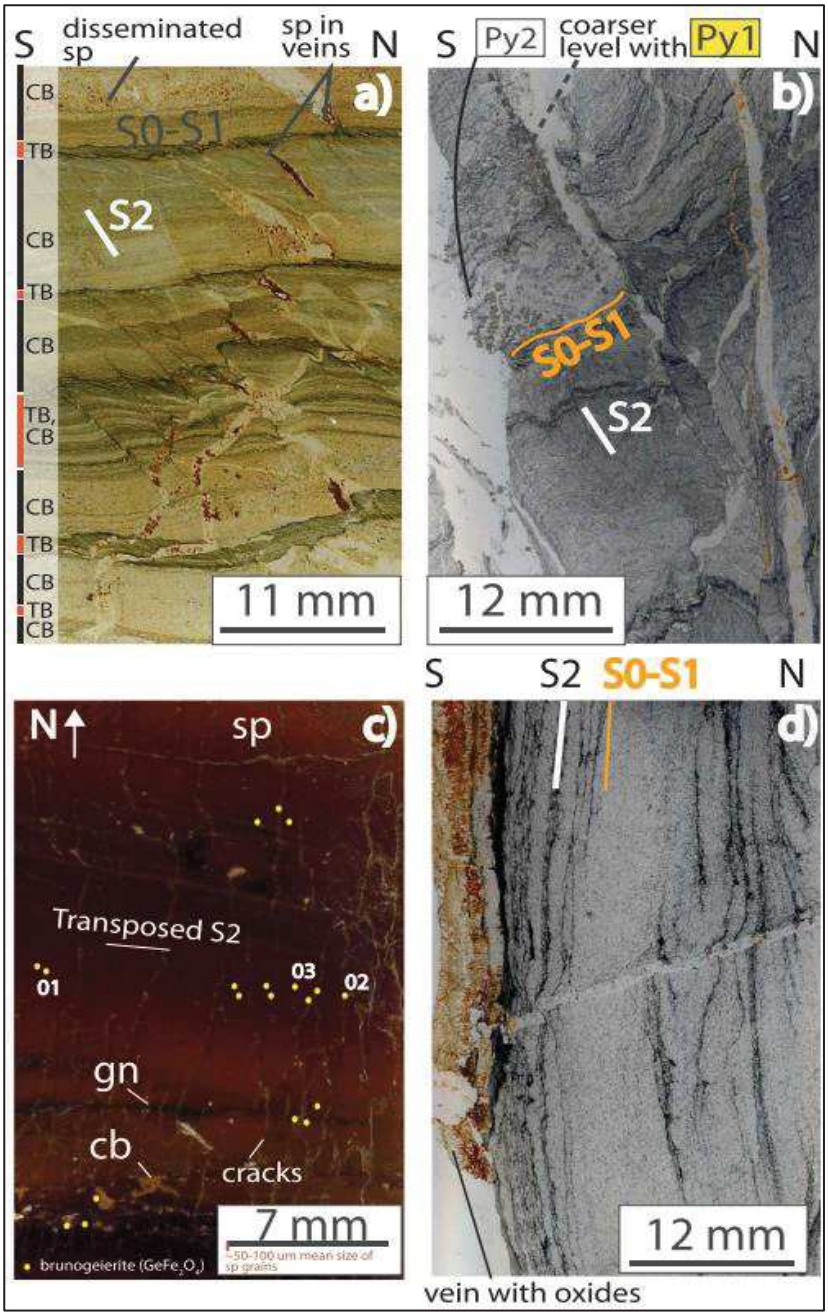

Figure 127 : Microphotographs of different structures in thin section a) Relationships between lithologies, S2 cleavage and mineralizations (TB: thin beds; CB: coarse beds); b) Relationships between pyrite mineralization, S0-S1 and S2 cleavages. Note that S0-S1 and S2 are perpendicular; c) Location of grains of brunogeierite in sphalerite (sp) with galena (gn) and Fecarbonates (cb) also present (Pale Bidau, sample PB08). Numbers associated with brunogeierite crystals refer to the LA-ICP-MS analyses given in Table 8b; d) Relationships between vein mineralization, S0-S1 and S2 cleavages. S0-S1 and S2 are parallel.

Galena occurs systematically at sphalerite grain boundaries. It exhibits rounded-lensoid habit or foamy texture (Figure 129D) after etching with HCl-thiourea solution (composition in *Brebrick and Scanlon 1957)*. Triangular cleavage pits from polishing are locally curved.

In the three different deposits, sphalerite from vein mineralization (type 2), as well as disseminated mineralization (type 1), appears as fine grains (< 50 μm; Figure 129D-G). Sphalerite in veins is generally late compared to quartz and carbonate gangue. After etching sphalerite with hypochlorous acid HClO, two intimately associated textures appear in type 2 mineralization from the three deposits: (1) fine grains (< 50 μm) frequently exhibit polygonal aspects or foam texture with dihedral 120° angles and equidimensional size (Figure 129D-G). Regular twinning in these grains shows no apparent deformation (Figure 129E-F). (2) coarser grains (> 80 μm) with irregular

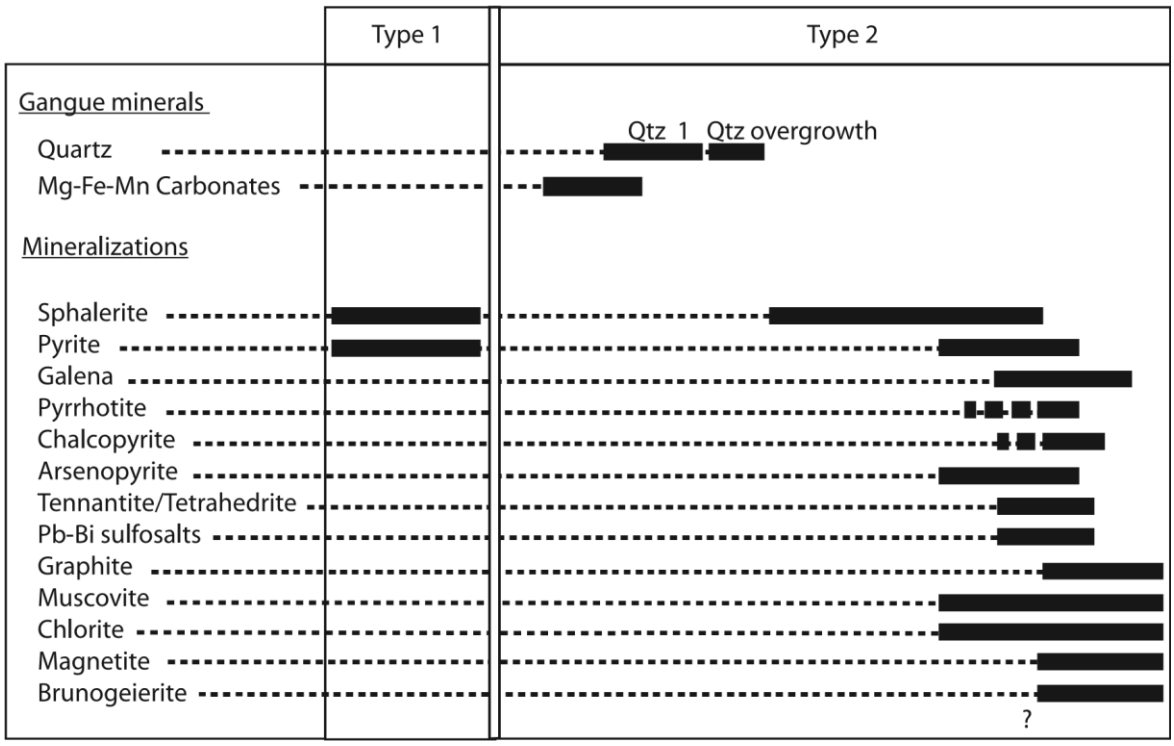

Figure 128 Paragenetic succession of ore and gangue minerals in stratiform and vein mineralizations in the three PAZ studied deposits.

shape frequently display deformed folded twins (Figure 129E; coarse grain in image center). Sphalerite can be dark or light brown. The difference in color is due to variable Fe content in PB deposit (see Section *Sphalerite chemistry*).

Brunogeierite and argutite are abundant and exclusively associated with sphalerite. Carboirite has been previously reported from the AD deposit (*Oudin 1982*) but the phase was not

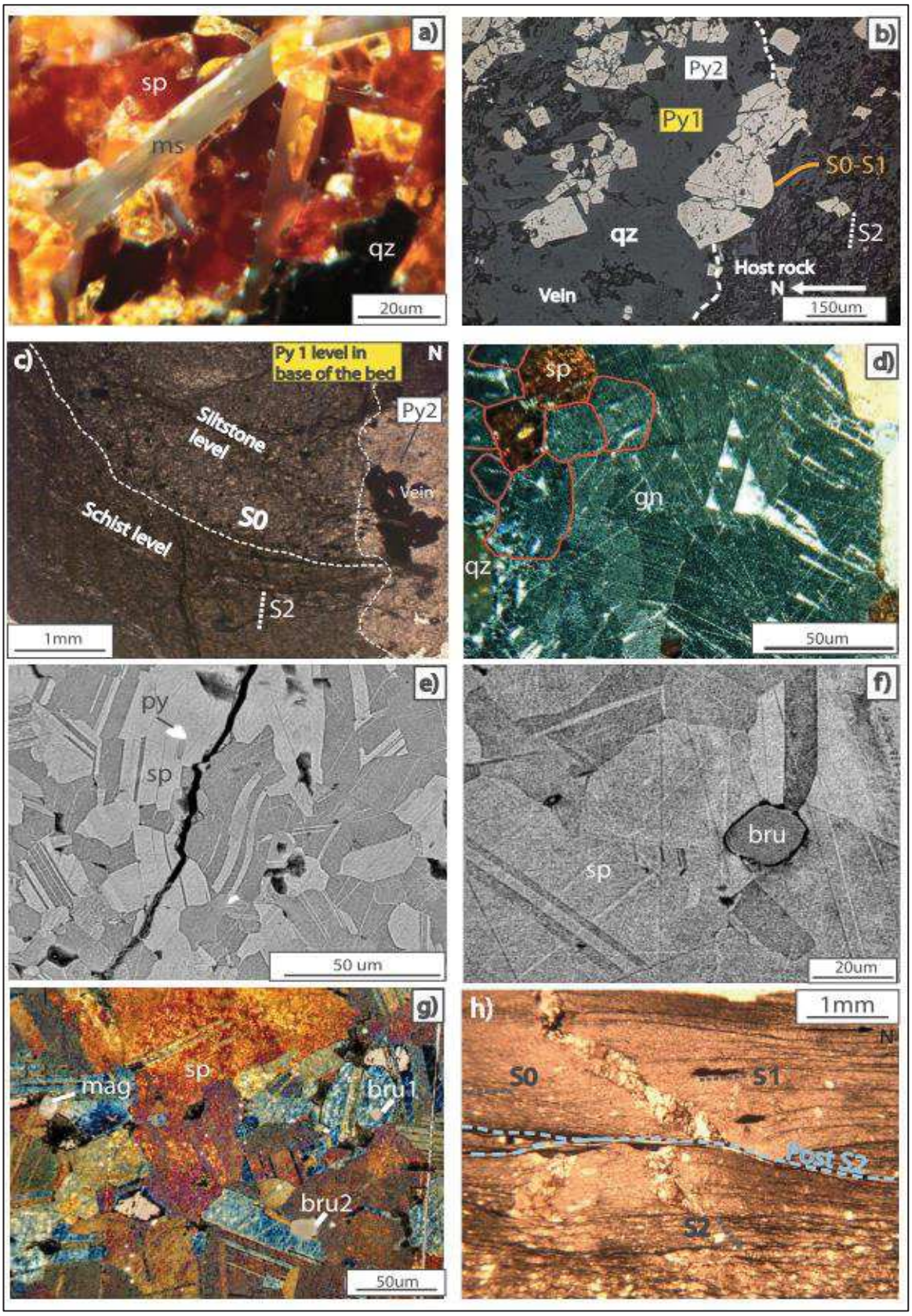

Figure 129 : Microphotographs showing characteristic textures in sulfide mineralization. a) Microtexture of sphalerite (sp) associated with muscovite (ms) and quartz (qz). Sphalerite grains present rounded habitus (crossed nicols, sample AD06). b) Different textures of pyrite: bright and automorphic texture preferentially in vein and dull yellow, less automorphic texture preferentially in host rock with the presence of framboidal cores (sample AD03). c) Different textures of pyrite : bright and automorph texture in vein and dull yellow less automorph texture in host rock with the presence of framboïdal cores (sample AD03). d) Rounded small grains of galena (gn) associated with polygonal sphalerite (sp) (etched with HCl-thiourea solution, sample AD12). e) Sphalerite grains with recrystallized (small and undeformed twins) and deformed (deformation twin in coarser grain, in the center of the picture) textures (etched with HClO; 32362 from AD; SEM). f) Brunogeierite (bru) at sphalerite grain boundary (etched with HClO; AD12; SEM color inverted). g) Two brunogeierite (bru1 and bru2) and one magnetite inclusions in sphalerite. Bru2 is in boundary position in sphalerite, bru1is in intermediate position. Magnetite has a low Ge-content (< 600 ppm GeO2) (sample AD12). Minerals abbreviations from *Whitney and Evans (2010)*. h) Relationships between S0 stratification, S1 cleavage observed locally with elongated iron-oxide grains, and S2 main cleavage parallel to mineralization (quartz, carbonates and iron-oxides) (sample PB10). (For interpretation of the references to colour in this figure legend, the reader is referred to the web version of this article.)

observed in our samples. Brunogeierite and argutite grains are rounded, dark grey, < 20 μm in size, and mainly located at sphalerite grain boundaries (Figure 129F). Sixtysix Ge-minerals were detected with SEM (63 brunogeierite and 3 argutite) in thin sections from PB and PR deposits. Among these, 36 appear at sphalerite grains boundaries (Figure 129F, g, bru2) with size ranging between 5 and 20 μm. Twenty-four are close to sphalerite grain boundaries (Figure 129G, bru1) in intermediate position and 6 (≅5 μm) are included within sphalerite grain cores. Argutite was found in AD sphalerite (sample AD12) as grains smaller than 3 μm in diameter. In the PB samples (PB08), 10 aligned brunogeierite inclusions were observed within dark brown sphalerite close to the light brown sphalerite and aligned parallel to S2.

11.1.5.3.3 Micro-structures

In thin section, S0-S1 is readily identified because of lithological changes and superposition of S1 on S0 is marked by elongate oxide disseminations (Figure 129H). When cross-cutting fine-grained beds, type 2 vein-mineralization tends to disappear or become parallel to S0-S1. But like at the macroscopic scale, when crosscutting coarser beds, the veins are typically larger, and mineralization tends to be parallel to S2 (Figure 127B-C). Continuous veins can appear with both geometries (Figure 127A) and present deformational imprint, but many are exclusively parallel to S2 cleavage (Figure 127B-D). Figure 127D shows that, within zones in which S2 is dominant, S0-1 is vertical and parallel to S2, as a response to folding.

11.1.6 Mineral chemistry

11.1.6.1 Germanium minerals

EMPA analysis was performed on 28 < 15 μm-sized brunogeierite grains from AD (AD05, n = 3; AD06, n = 5, AD12, n = 10) and PB (PB08, n = 10) (Table 8A). Due to small grain size, two attempts to obtain analyses of argutite were unsuccessful. No visible compositional zoning in these minerals was observed.

The chemistry of major and minor elements in brunogeierite is summarized in Table 8A. In one sample from PB and three from AD, GeO_2 and FeO vary in the range of a few wt.% (Figure 130). A slight depletion in GeO_2 can be noticed within grains in intermediate position with a mean of 38.7 ± 0.3 wt% GeO_2 compared to grains at sphalerite grain boundaries (mean 40.5 ± 0.4 wt% GeO_2). Low FeO contents for brunogeierite in intermediate positions is linked to a relative enrichment in ZnO (up to 1.6 wt% ZnO).

LA-ICP-MS analyzes on 3 brunogeierite crystals from PB (PB08) are given in Table 8B. Mean Ge content is 28.0 ± 3.0 wt% Ge (40 ± 4 wt % GeO_2). For Co, Cu, Ga, Ag, Sn, Sb, and Pb, results are not in agreement with the

Brunogeierite (GeFe2O4) EMPA		SO2	ZnO	FeO	Ga2O3	GeO2	As2O3	SiO2
Pale Bidau (PB, n = 10) PB08	n	10	8	10	4	10	10	10
	Mean (wt-ox%)	0.25	0.49	56.80	0.04	39.83	0.19	0.12
	SD (wt-ox%)	0.11	0.20	0.32	0.02	0.68	0.03	0.01
	LOD (ppm)	442	1579	392	354	676	410	104
Argut-dessus (AD, n = 18) AD05-AD06-AD12	n	18	12	18	6	18	18	18
	Mean (wt-ox%)	0.50	0.78	56.20	0.01	39.96	0.17	0.12
	SD (wt-ox%)	0.14	0.33	0.33	0.03	0.58	0.04	0.01
	LOD (ppm)	331	1609	379	547	683	435	100

Brunogeierite (GeFe2O4) LA-ICP-MS		Co (ppm)	Cu (ppm)	Ga (ppm)	Ge (%)	Ag (ppm)	Sn (ppm)	Sb (ppm)	Pb (ppm)
PB08 – 1	Contents	3965.8	2907	3018.9	26.7	225.4	256.2	327.3	1717
	SD	1152	850	402	2.9	146	383	125	297
PB08 – 2	Contents	4511.4	1906.6	1788.7	27.4	195.7	114.8	30.8	423.1
	SD	1124	534	223	3.2	38	362	41	66
PB08 – 3	Contents	4257	2502.3	2412	30	214	214	122	570
	SD	1202	586	325	3.1	84	349	69	75
Mean		4244.7	2438.6	2406.5	28	211.7	195	160	903.4
LOD		340	369	72	383	73	90	12	9

n: number of measurements with higher contents than the limit of detection.
LOD: Limit of detection; SD: Standard Deviation.

Table 8 : a) EPMA analyzes of 28 brunogeierite (GeFe2O4) crystals in weight-oxide % (structural formula normalized to 4 oxides). b) LA-ICP-MS analyzes of 3 brunogeierite ($GeFe_2O_4$) crystals in weight % for different elements (Co, Cu, Ga, Ge, Ag, Sn, Sb, Pb) (PBO8 sample).

EMPA data which showed these elements to be below detection limits. This may be either a matrix effect (use of the MASS-1 sulfide standard to analyse brunogeierite), or more likely indicative of

Sphalerite (ZnS) EMPA		S	Zn	Fe	Cu	Ge	Cd	Si
Pale Bidau (PB) (n = 14)	n	14	14	14	3	2	14	14
	Mean (wt%)	33.14	61.15	4.03	0.02	0.01	0.20	0.05
	SD (wt%)	0.57	0.97	0.04	0.02	0.01	0.01	0.003
	LOD (ppm)	483	2266	342	541	84	110	32
Argut-dessus (AD) (n = 24)	n	24	24	24	2	5	24	24
	Mean (wt%)	34.18	59.21	5.53	0.01	0.01	0.17	0.06
	SD (wt%)	0.12	0.27	0.32	0.02	0.37	0.13	0.01
	LOD (ppm)	342	1529	347	487	88	426	107
Pale de Rase (PR) (n = 11)	n	11	11	11	1	0	11	11
	Mean (wt%)	33.86	58.99	5.74	0.03	< LOD	0.18	0.07
	SD (wt%)	0.57	0.95	0.12	0.05	< LOD	0.04	0.01
	LOD (ppm)	484	2313	348	544	84	422	106

Sphalerite (ZnS) LA-ICP-MS		Mn (ppm)	Fe (%)	Co (ppm)	Cu (ppm)	Ga (ppm)	Ge (ppm)	Ag (ppm)	Cd (ppm)	In (ppm)	Sb (ppm)	Sn (ppm)	Pb (ppm)
Argut-dessus (AD12; n = 9)	Mean	51.5	3.7	79.1	206.7	75.3	32.1	165.7	2347	0.8	29.4	11.4	174.0
	Median	59.1	3.8	72.7	112.9	45.6	11.9	55.1	2170.7	0.8	33.1	< LOD	32.6
	Min	23.6	0.9	25.3	< LOD	10.9	2.3	11.1	2119.1	0.3	2.4	< LOD	22.7
	Max	78.3	6.4	154.2	619.4	320.9	102.2	418.4	2906.4	1.6	54.7	20.9	523.7
	1 σ	16	0.2	11	41	18	14	33	395	0.5	4	6	76
Pale Bidau (PB08; n = 14)	Mean	33.2	5.2	181.4	184.5	206.3	11.8	27.6	2575.9	0.5	19.9	19	203.6
	Median	31.9	5.5	171.8	167.5	244.1	4.8	25.7	2671.5	0.3	17.7	16.8	46.8
	Min	19.8	2.8	86.9	51.2	30.5	0.8	6.6	1980.7	0.2	4.5	5.2	11.1
	Max	51.7	6.6	235.6	653.4	332.5	80.5	51.1	3105.2	1.9	44.7	47.8	2297.0
	1 σ	6	0.3	19	42	47	32	6	432	0.5	3	4	130
Pale de Rase (PR01; n = 6)	Mean	42.9	7.7	38.7	17.9	17.3	< LOD	10.5	2774.5	1.1	9.8	< LOD	4.7
	Median	49.1	8.5	43.1	16.9	10.8	< LOD	4.4	2692.6	1.1	2.3	< LOD	1.4
	Min	7.7	3.6	16.2	7.5	5.1	< LOD	3.2	2651.4	1.1	1	< LOD	0.6
	Max	63.7	10.1	48.5	36.4	44.1	1.1	41.1	3096.1	1.2	46.3	1.3	21.3
	1 σ	5	0.5	4	4	4	1	2	465	0.4	0.4	2	2
Mean (total)		40.1	5.2	121.6	153.2	127.5	13	65.0	2546	0.7	20.6	13.9	153.3
Detection limite (mean)		4.46	0.04	1.64	2.79	0.51	1.13	0.15	3.78	0.1	0.2	3.6	0.06

n: number of measurements with higher contents than the limit of detection.
LOD: Limit of detection; SD: Standard Deviation.

Table 9 : a) EPMA analyzes of sphalerite (ZnS, n=49) in weight%. Mean limit of detection for Ge is 84 ppm for the entire dataset. b) LA-ICP-MS analyzes of sphalerite (ZnS, n=29) in weight ppm or% for different elements (Mn, Fe, Co, Cu, Ga, Ge, Ag, Cd, In, Sb, Sn, Pb).

the presence of micro- to nanoscale inclusions carrying these elements below the surface, which are intercepted during ablation. The higher Cu content may, for example, be explained by the presence of Cu-rich inclusions in sphalerite in textural contact with brunogeierite which can be observed by SEM.

11.1.6.2 Sphalerite

Forty-nine EMPA (Table 9A) and twenty-nine LA-ICP-MS (Table 9B) analyses were performed on type 2 sphalerite crystals from the three studied deposits.

Principal component analyzes (PCA) applied to the entire dataset of LA-ICP-MS analyzes show element distributions and spot representations in the PC1 and PC2 plane (Figure 131). PCA helps to highlight interelement correlations *(Belissont et al. 2014; Frenzel et al. 2016)*. Each arrow represents a variable or an element. The length of the arrow gives an indication of the elemental representivity in the dataset and the small angle between arrows indicates a correlation between these elements. The PC1–PC2 space carries 63% of the total dataset variance. Figure 131 reveals the high depletion in all elements except for Cd, Fe and In within sphalerite from the PR deposit compared to PB and AD. The PB and AD deposits display larger variations in Cd (1980 ± 420 to 3105 ± 410 ppm Cd) and In (below limit of detection to 1.9 ± 0.5 ppm In) compared to PR with Cd contents ranging from 2650 ± 522 to 3096 ± 510 ppm Cd, and In contents ranging from 1.09 ± 0.4 to 1.17 ± 0.4 ppm In.

The entire dataset shows a positive correlation between Sb and Ag, and another correlation between Ge and Sn in sphalerite. No correlation between Ge and Ga is observed. Correlations between Pb and Cu, Ag, Sb are remarkable, and are almost certainly related to the small inclusions that can be observed on the time-resolved LA-ICP-MS depth spectra (Figure 132A).

Variability in Fe and Ge within the entire dataset is explored in Figure 132B and is detailed for each deposit. PB deposit contains brown dark and light zones in sphalerite (Figure 127C). LA-ICP-MS analyzes show enrichment in Fe (~5.8 ± 0.3 wt%) within dark domains compared to lighter ones (~4.0 ± 0.3 wt%). In this sphalerite, the light brown domains show greater variation in Ge than the darker zones (Figure 132B) with concentrations ranging between 0.75 ± 0.4 and 80 ± 1 ppm Ge. Germanium concentrations in dark brown domains concentrations are consistently < 10 ± 1 ppm. These large variations of Ge in sphalerite appear localized and seem associated with the presence of Ge- and GeSn-Cu-bearing inclusions (Figure 132A). Small inclusions of Pb-Ag-Sn-Sb are also often recognizable on the time-resolved LA-ICP-MS depth spectra (Figure 132A).

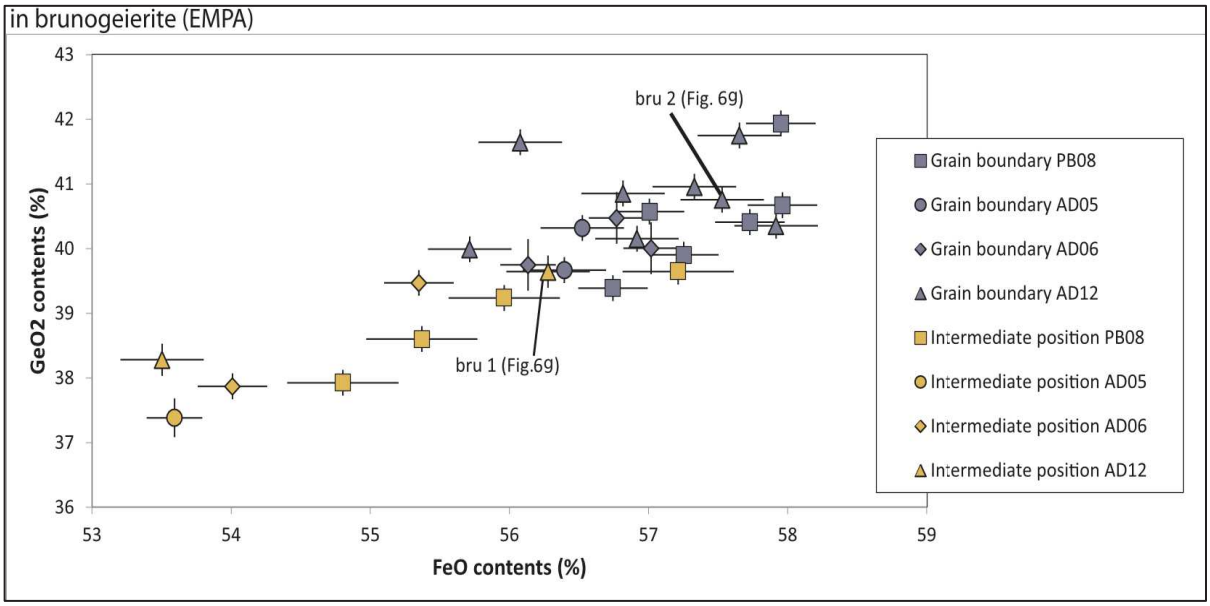

Figure 130 : Diagram showing GeO_2 and FeO contents in 28 brunogeierite grains from the three different deposits (EMPA data) and in different textural position according to sphalerite grains. 1σ errors are represented for each data point. Blue – brunogeierite located at sphalerite grain boundaries; orange – brunogeierite in intermediate position. Low FeO content for brunogeierite in intermediate position is linked to a corresponding enrichment in ZnO. (For interpretation of the references to colour in this figure legend, the reader is referred to the web version of this article).

In the AD samples, no color differences are visible in brown sphalerite in plane-polarized light; these are depleted in Fe (3.68 ± 0.2 wt % Fe). Similarly, larger variations in Ge (Figure 132B) appear in sphalerite with concentration ranging from 0.5 ± 0.6 to 102 ± 1 ppm Ge. These variations are systematically associated with small inclusions of Ge-minerals, and locally associated with Sn and/or Cu. Compared to PB, sphalerite from the AD deposit has lower mean concentrations of Co, Ga, and Pb, and higher mean concentrations of Ag, Sb, Mn and Ge.

In the PR samples, sphalerite appears red-brown in plane-polarized light and has the highest Fe content (7.67 ± 0.5 wt% Fe). Sphalerite from PR does not contain accessory Ge-minerals (sample PR01). It is significantly depleted in all analyzed elements relative to AD and PB (Table 9A and B) and especially so in Ge with contents below the minimum limit of detection (1.1 ppm).

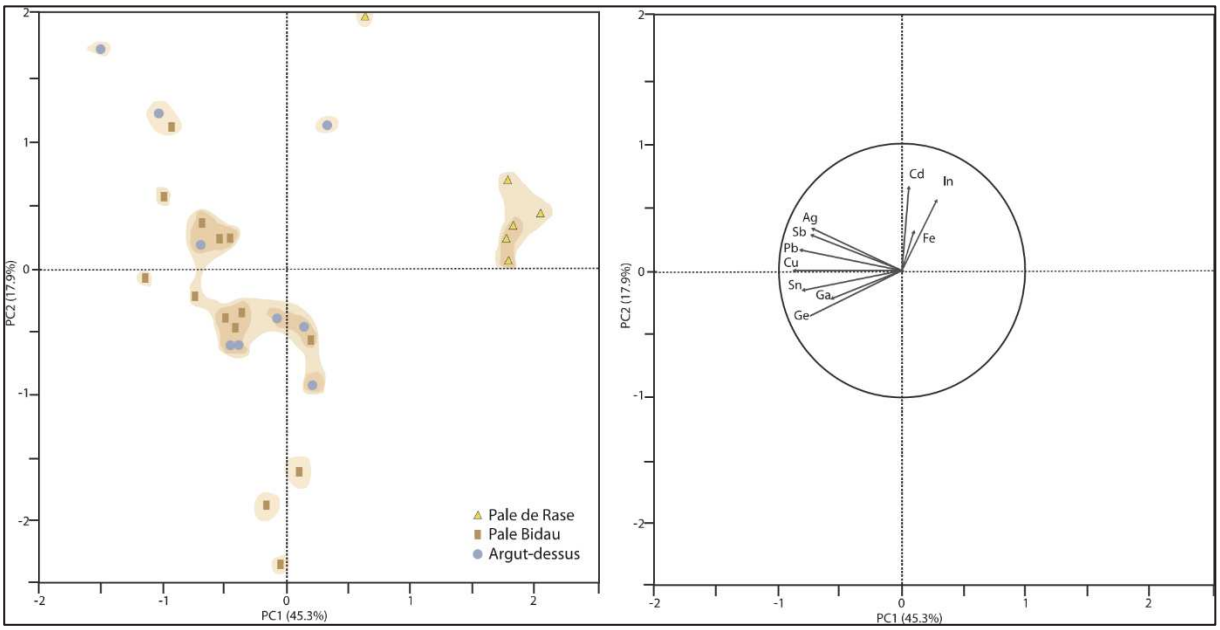

Figure 131 : Principal component analysis of the LA-ICP-MS log-transformed dataset of trace element contents in sphalerite from the Pale Bidau, Argut-dessus and Pale de Rase deposits. Circle of correlation and related covariance biplots. Arrow length is important to correlate element; if the arrow is short, the representation is poor (loadings close to 0) but if arrow is long (close to circle line), the representation is good (loadings close to −1; 1). The second parameter is the angle between two arrows. It is related to the covariance between the concentrations of elements: if the angle is close to 0°, element concentrations correlate positively. If it is close to 90°, these do not correlate, and if it is close to 180° they are negatively correlated.

11.1.7 Discussion

11.1.7.1 Genetic model for the three studied deposits and formation of Ge-minerals

11.1.7.1.1 Structural context of the studied mineralization

Relationships between structures and mineralization are represented on the schematic diagrams shown as Figure 133 and Figure 134 (at macroscopic and microscopic scales, respectively). The location and characteristics of each deposit with respect to deformational structures are indicated taking the specific lithologies that host the mineralization into account. In all three studied deposits, mineralization is present essentially within type-2 veins dominated by Zn- and Pb-sulfides (Figure 133), with different geometries linked to rock competence and S2 cleavage. The lithological

and structural control on vein geometry is strong (Figure 134). Disseminated mineralization within the Late-Ordovician stratigraphic sequence (type 1) is rare in the studied samples (Fig. 10).

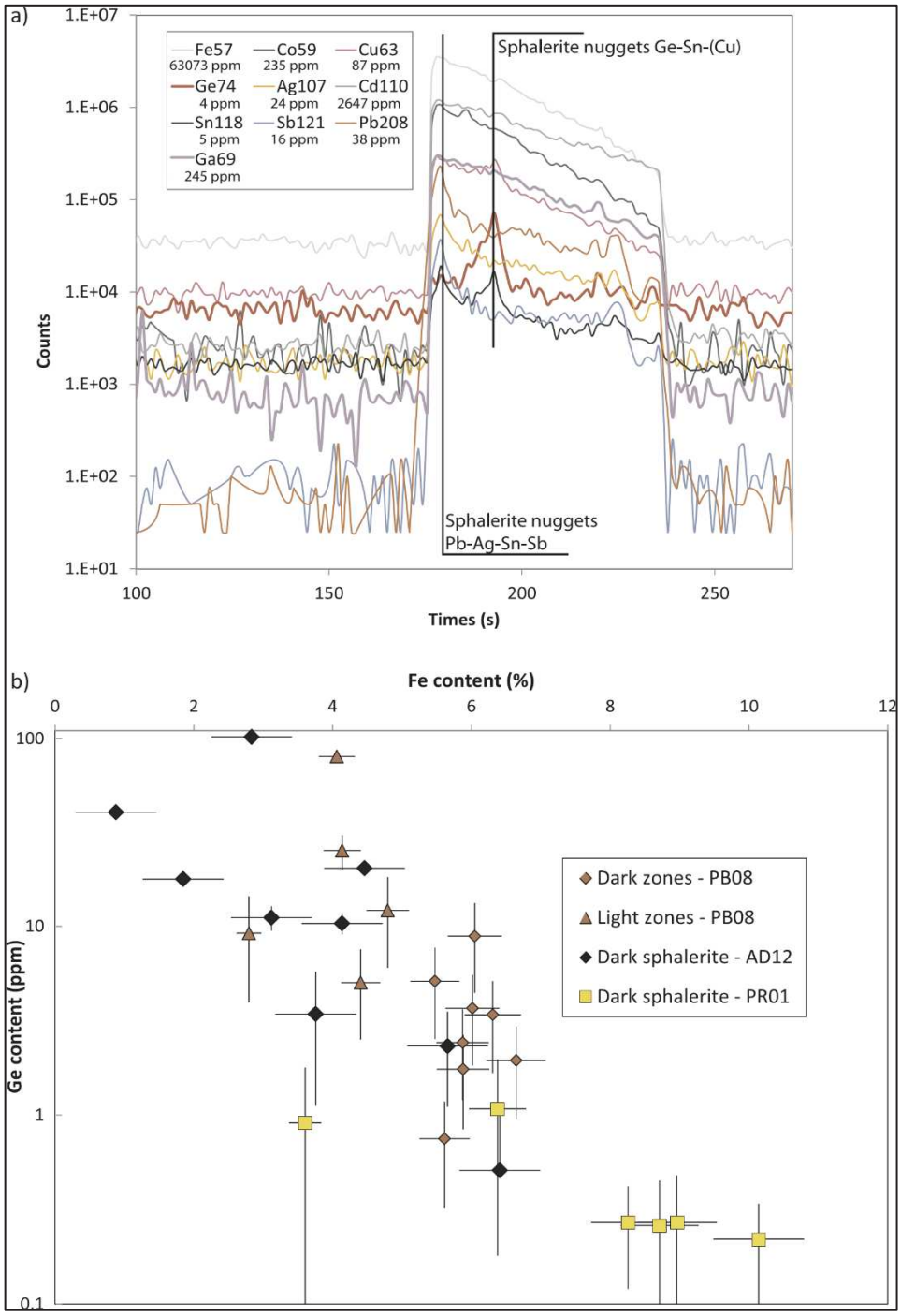

Figure 132 : a) Representative single-spot LA-ICP-MS spectra for selected elements in sphalerite. Nuggets or small inclusions can be detected for elements like Ge-Sn(-Cu) or Pb-Ag-Sn-Cu. b) Comparison of Ge and Fe wt.% contents in sphalerite from the three studied deposits. For PB deposit, analyzes in dark and light domains in sphalerite are presented. 1σ errors are represented for each data point.

According to *Bois et al. (1976)* and *Pouit (1985)*, pre-Silurian mineralization events for Ordovician-hosted ores are considered of SEDEX-type. The Pb-Zn ores are considered syngenetic with concordant mineralization, or epigenetic for discordant ore (*Bois et al. 1976*) and are only weakly remobilized. In the three deposits, only the minor type 1 disseminated mineralization is syngenetic and strictly concordant with stratification. This study shows that type 2 vein mineralization sub-parallel and oblique to stratification must be linked to an epigenetic hydrothermal event. Vein geometry is linked to rock grain size and the presence of S0-S1 and S2 deformation imprints. Ore concordant to S0-S1 is often present in schists but tends to be discordant to S0-S1 and parallel to S2 cleavage in coarser rocks (siltstones to conglomerates, Figure 133 and Figure 134). These observations clearly indicate a post-Ordovician vein-like emplacement

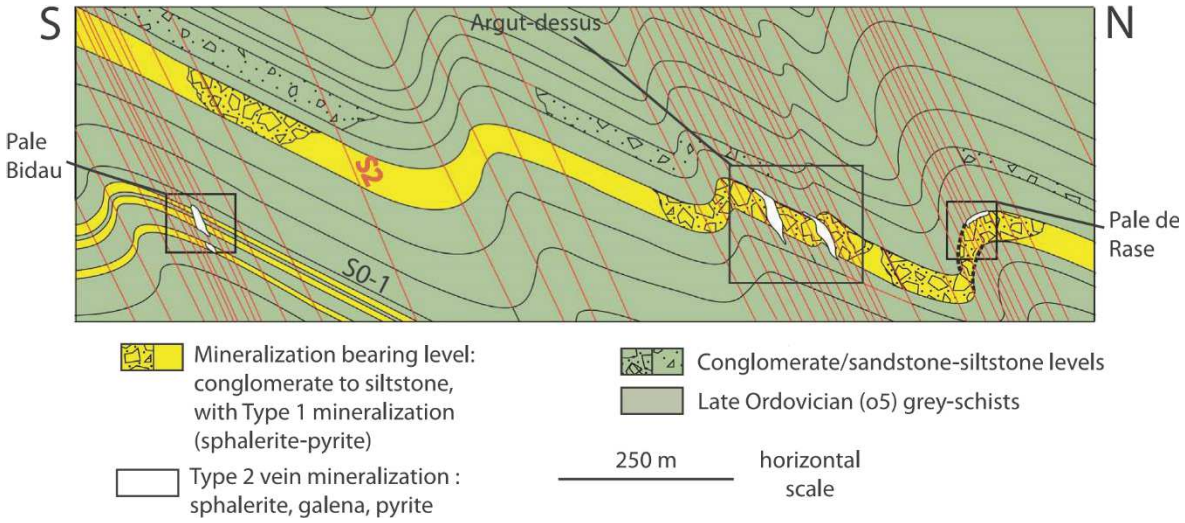

Figure 133 : Schematic N-S regional sketch of structural relationships between mineralization, bedding and cleavage at macroscopic scale.

of type 2 Pb-Zn-(Ge) mineralization.

11.1.7.1.2 The role of metamorphism and recrystallization in the genesis of Ge-minerals

This study shows that Ge mineralization is concentrated in accessory Ge-minerals in the three deposits. Ge-minerals are widespread in the PAZ deposits with > 44 deposits known to contain independent Ge-minerals (*Oudin 1982*). Such minerals are, however, absent in the Aulus-Les Argentieres deposit (*Oudin 1982*) which has been recently associated with a post-Variscan mineralization event (Munoz et al. 2016). In most deposits, sphalerite is depleted in many trace elements, particularly in Ge (mean value < 13 ± 1 ppm) and shows evidence of deformation and recrystallization (Figure 129D and E,Figure 130 and Figure 136). These recrystallization/deformation textures seem widespread in PAZ deposits (*Nicol et al. 1997*), and in

Basque Massifs *(Pesquera and Velasco 1989, 1993)*. PR sphalerite is even more depleted in Ge and other trace elements (except for Fe, Cd and In) than the other two deposits. No Ge-mineral is reported in this sphalerite. Bulk chemistry was probably primarily poor in these elements, as PR presents the same mineralization type and sphalerite texture as the two other deposits.

Fe-rich zones in a set of sphalerite crystals are present (darker sphalerite, Figure 127C) but no compositional zoning at crystal scale is reported as in Ge-minerals. Nevertheless, higher values of Ge and elements like Sn or Cu appear locally in rare nano-inclusions within sphalerite or attached to brunogeierite. Dark brown domains in PB08 which host the majority of brunogeierite grains

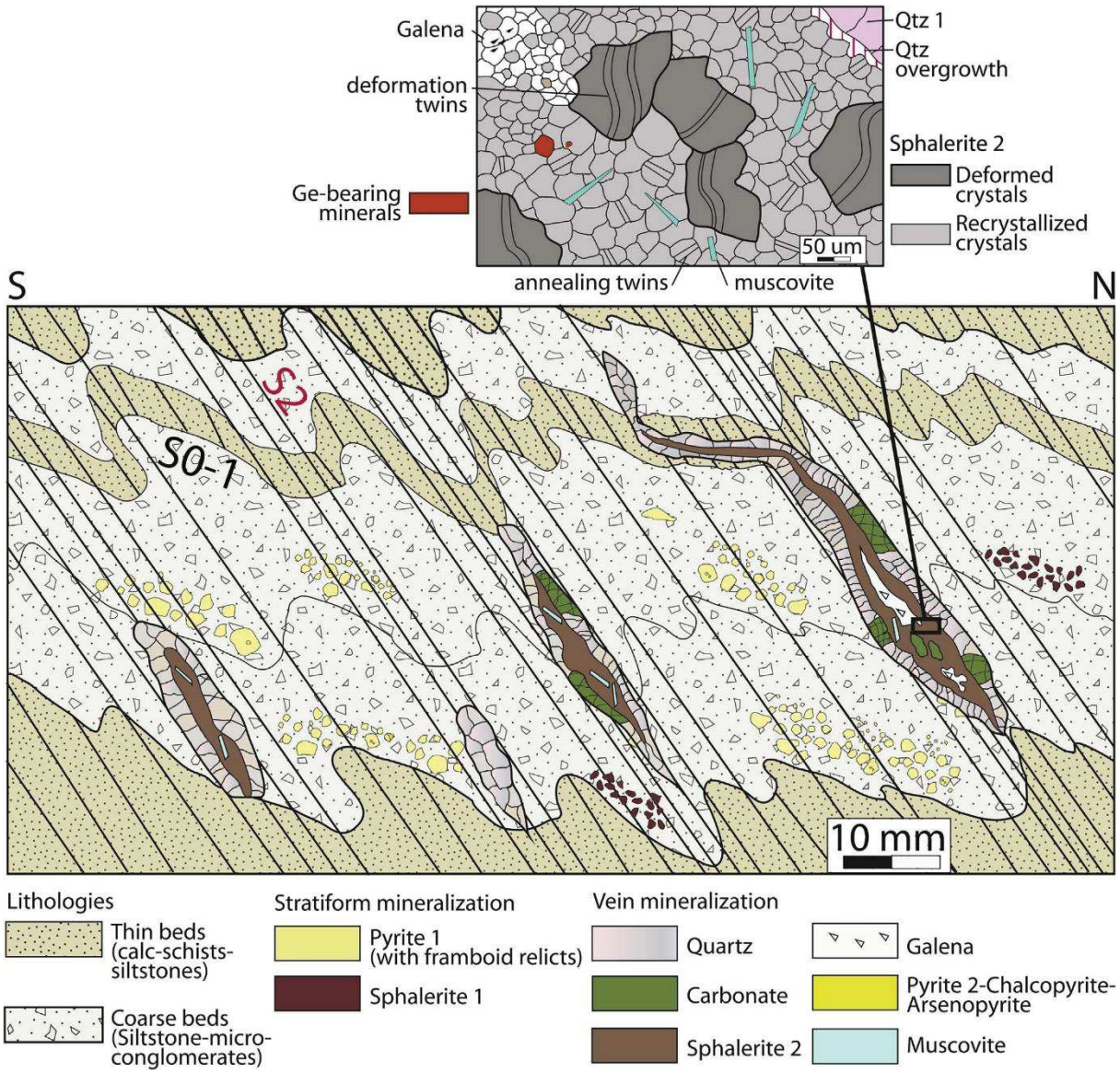

Figure 134 : Schematic sketch showing relationships between host-rocks, type-1 and 2 mineralizations at microscopic scale. Ge-bearing minerals are represented in the insert.

(Figure 127C) do not display large variations in the concentrations of these elements and have a consistently low Ge content (< 1.1 ± 1 ppm, Figure 132B). The presence of Ge(-Cu) nano-inclusions in an otherwise Ge-poor sphalerite is reported from the Kipushi Cu–Zn–(Ge–Pb) deposit, D.R. Congo (*Belissont et al. 2016*). PAZ Germanium-minerals like brunogeierite (~30% Ge), or argutite (~70% Ge), are only hosted in sphalerite and preferentially located at sphalerite grain boundaries.

The observed sphalerite-dominant mineral assemblage in host metasedimentary rocks dominated by graphite, muscovite and chlorite. This assemblage corresponds to a pressure–temperature paragenesis characteristic of the greenschist facies (ca. 300–450 °C) as inferred by *Pouit (1974)* and *Johan and Oudin (1986)*. Recent work on metamorphic conditions of the PAZ Superstructure indicates that maximum metamorphic temperatures were 350–400 °C (*Cochelin 2016*) concordant with greenschist facies conditions. Low temperature processes are considered to account for Ge-enrichment in sulfides such as sphalerite (*Belissont 2016; Frenzel et al. 2016*). Above 150–200 °C, Germanium incorporation in sphalerite decrease with increase in temperature (*Belissont 2016*). Metamorphic conditions above 300 °C seem to affect and reduce the Ge (and Ga) concentrations in sphalerite *(Frenzel et al. 2016)*. Chemical analyses in this study show a generally depleted sphalerite which is coherent with greenschist facies conditions (300–450 °C).

Formation of independent Ge-minerals (spinel as brunogeierite and oxides as argutite in the PAZ deposits) is likely triggered by low-grade metamorphic processes. During metamorphic recrystallization processes, Germanium would be expelled from the ZnS lattice, and concentrated into Ge-minerals preferentially nucleating at sphalerite grain boundaries. Trace element remobilization during low grade-metamorphism and recrystallization is well-documented for many elements in sphalerite (Au, Ag, Cu, Mn, etc.; *Brugger and Giere 2000; Pitcairn et al. 2010; Taylor et al. 2010; Zheng et al. 2013; Lockington et al. 2014)* and proposed for Ge-mineralization in *(Morales-Ruano et al. 1996)*. Syn-metamorphic recrystallization and release of trace elements may be responsible for formation of diverse accessory minerals paragenesis (*Cook 1996; Hofmann and Knill 1996; Cook et al. 1998; Marshall et al. 1998; Eremin et al. 2007; Taylor et al. 2010*). fO_2 and fS_2 conditions may play a key role as well in the remobilization of element like Ge, as this will control which Ge-mineral crystallizes. High fO_2 (and low fS_2) has an essential impact on remobilization of Ge in sphalerite to form Ge oxide, which is thermodynamically stable under highly oxidizing conditions *(Bernstein 1985; Johan and Oudin 1986*). The impact of fO_2 on the stability of brunogeierite has been explored by *Hariya and Wai (1970)*. They confirmed the stability of brunogeierite at high fO_2 above the wurtzite-magnetite buffer ($fO_2 = > 10^{-15}$ at 800 °C). *Bernstein (1985)* describes a phase diagram with GeO_2

stable at high fO_2 and shows a widening of the GeO_2 stability field when temperature decreases. On the contrary, high fS_2 would rather stabilize Ge-sulfides, as in Kipushi type deposits. For example, *Melcher et al. (2006)* showed that ore formation in Khusib Springs Ge-deposit (Kipushi type) is linked to highly saline hot fluids (up to 370 °C) with high fS_2.

Therefore, in the present case, it is expected that Ge would originate from primary trace level enrichment in sphalerite associated with strong Ge partitioning into independent Ge-minerals during sulfide recrystallization under greenschist facies conditions that renders the recrystallized sphalerite depleted in Ge. Semi-quantitative evaluation shows that the proportion of Ge by mass in accessory Ge-minerals is seven times that of Ge in the sphalerite host (PB08, Figure 127C). For this evaluation, nineteen brunogeierite grains (30 wt% Ge) were considered with an average diameter of 10 µm, and the rest of the thin section is considered as pure sphalerite with a mean content of 30 ppm Ge. A density of 5.2 $g \cdot cm^{-3}$ is assumed for sphalerite and 4.1 $g \cdot cm^{-3}$ for brunogeierite (spinel group). Considering the same sphalerite volume and a closed system, a primary (pre-recrystallization) Ge content in sphalerite can be estimated. A maximum amount of Ge in PB08 sphalerite is 227 ppm.

Two additional hypotheses of formation may be considered: Is it only an enrichment of primary accessory minerals or a complete neoformation of Ge-minerals, both processes assisted by metamorphic fluids? *Bernstein (1985)* and *Ottemann and Nuber (1972)* report solid solution between brunogeierite and magnetite because of frequently observed enrichment in Ge within magnetite. In Ga-bearing magnetite close to brunogeierite crystals, Ge is reported from Pyrenean deposits with concentrations exceeding 4000 ppm *(Johan et al. 1983)*. In addition, a large paragenesis of Ge-minerals is described (*Johan et al. 1983; Oudin et al. 1988)*. These observations could indicate that PAZ Ge-minerals result from the enrichment of a primary mineral (magnetite in the case of brunogeierite). Nevertheless, Ge-mineral neoformation associated with metamorphic fluids may also play a key role with formation of Ge-minerals like argutite (70 wt% Ge) in high oxidizing conditions.

11.1.7.2 Chemistry

Sphalerite from the studied deposits is largely depleted in Ge with mean concentration of 13 ± 1 ppm (Figure 135). Classically in sulfide-rich environments, Ge is found as traces in sphalerite, as presented in Figure 135. These well-known and documented Pb-Zn(-Ge) deposit-type are MVT deposits (< 3200 ppm Ge in Tres Marias, Mexico, *Saini-Eidukat et al. 2009*), SEDEX (< 723 ppm Ge in Anarraaq, *Graham et al. 2009*) or in polymetallic vein deposits (up to 2576 ppm Ge in Saint-

Salvy, *Belissont et al. 2014*). In such deposits, fluid temperature is generally low and below 200 °C *(Viets et al. 1992; Kelley and Jennings 2004; Leach et al. 2004; Belissont et al. 2014; Bonnet 2014)*.

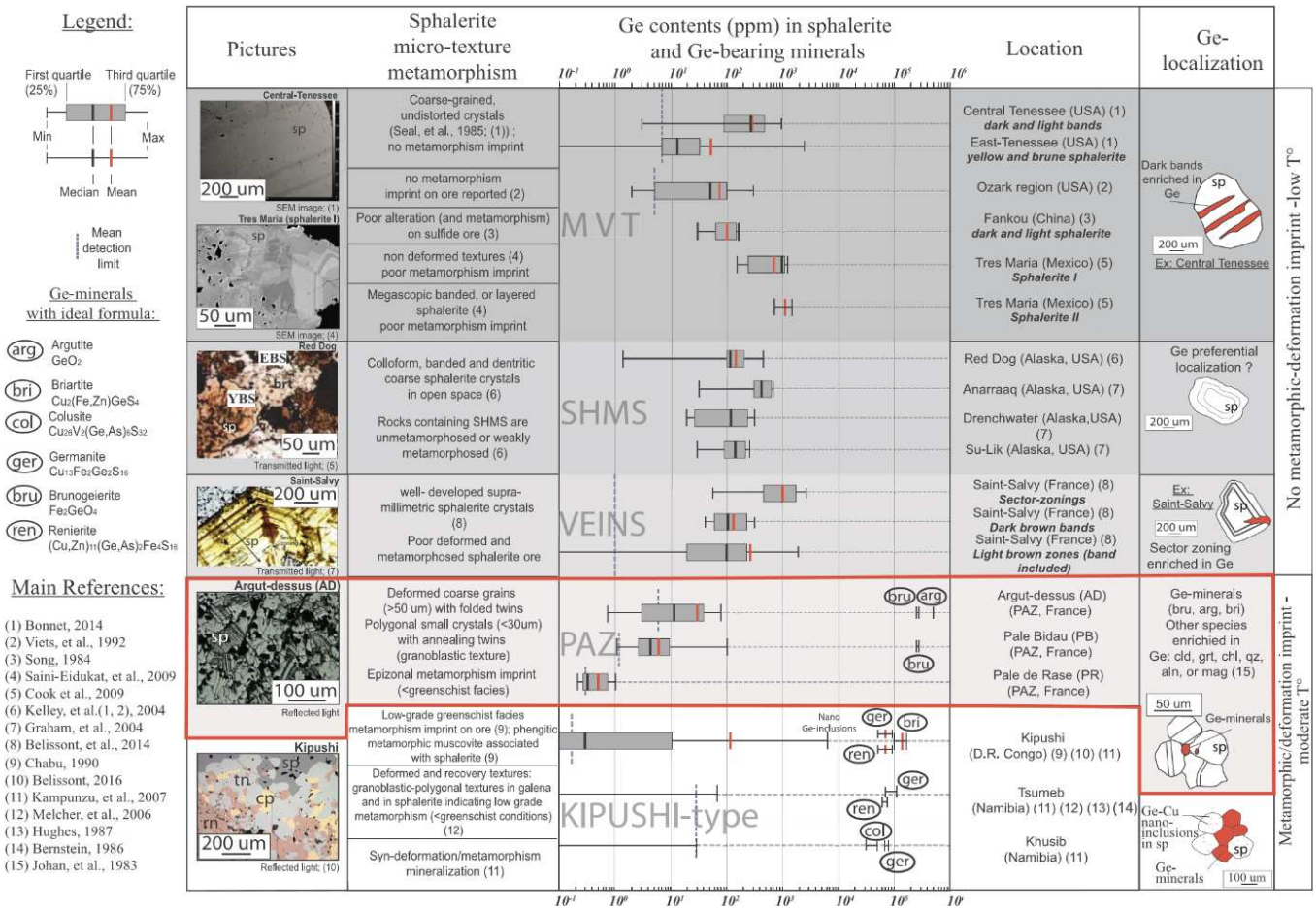

Figure 135 : Synthesis of the characteristics of the four main Ge-bearing deposit-types and PAZ deposits (red frame) based on several criteria: deposit-setting, ore texture (sphalerite), metamorphic imprint, and main Ge-concentration. Abbreviations: YBS: yellow-brown sphalerite; EBS: early-brown sphalerite; sp: sphalerite; gn: galena; tn: tennantite, rn: renierite, cp: chalcopyrite, brt: baryte. (For interpretation of the references to colour in this figure legend, the reader is referred to the web version of this article.) (See above-mentioned references for further information.)

In Ge-rich environments, sphalerite depleted in Ge can be found in Kipushi type deposits (0.3 ppm Ge, main mode in Kipushi deposit, *Belissont (2016)*; Figure 135). Also, similar to PAZ deposits, discrete Ge-minerals are reported from Kipushi-type deposits *(De Vos et al. 1974; Lombaard et al. 1986; Melcher et al. 2006*). These are, however, mostly Ge-sulfides such as germanite (9.1% Ge), renierite (6.58% Ge), or briartite (18.6% Ge), even if brunogeierite has been reported from the Tsumeb (Kipushi-type) deposit (*Lombaard et al. 1986*). The occurrence of Ge-sulfides is also reported from a range of other deposit types, including epithermal deposits (Figure 136; *Yun et al. 1993; Kouzmanov 2001; Bailly et al. 2005; Putz et al. 2006)* and VHMS deposits (Figure 136;

Tourigny et al. 1993; Komuro and Kajiwara 2004; Wagner and Monecke 2005; Vikentyev et al. 2016). Fluid temperatures associated with the mineralization event are relatively moderate, between 250 and 400 °C *(Lombaard et al. 1986; Bailly et al. 2005; Melcher et al. 2006; Kampunzu et al. 2009)* and are similar to the temperatures of metamorphic fluids in studied PAZ deposits (300–450 °C). Nevertheless fS_2 is clearly higher than in the PAZ deposits (*Bernstein 1985; Melcher et al. 2006*). High fS_2 controls formation of Ge-sulfides rather than Ge-oxides which are thermodynamically stable under high oxidizing conditions. Even though they share many similarities, variability in redox conditions may explain the difference between Kipushi and PAZ deposits (crystallization of Ge-sulfides rather than Ge-oxides, respectively).

11.1.7.3 Tectono-metamorphic setting

Figure 136 shows the large diversity of settings for Ge-bearing deposits and locates the PAZ studied deposits. According to their structural-lithological settings, the three studied have some similarities with either reworked SEDEX, vein type, or Kipushi-type deposits. Sedimentary-

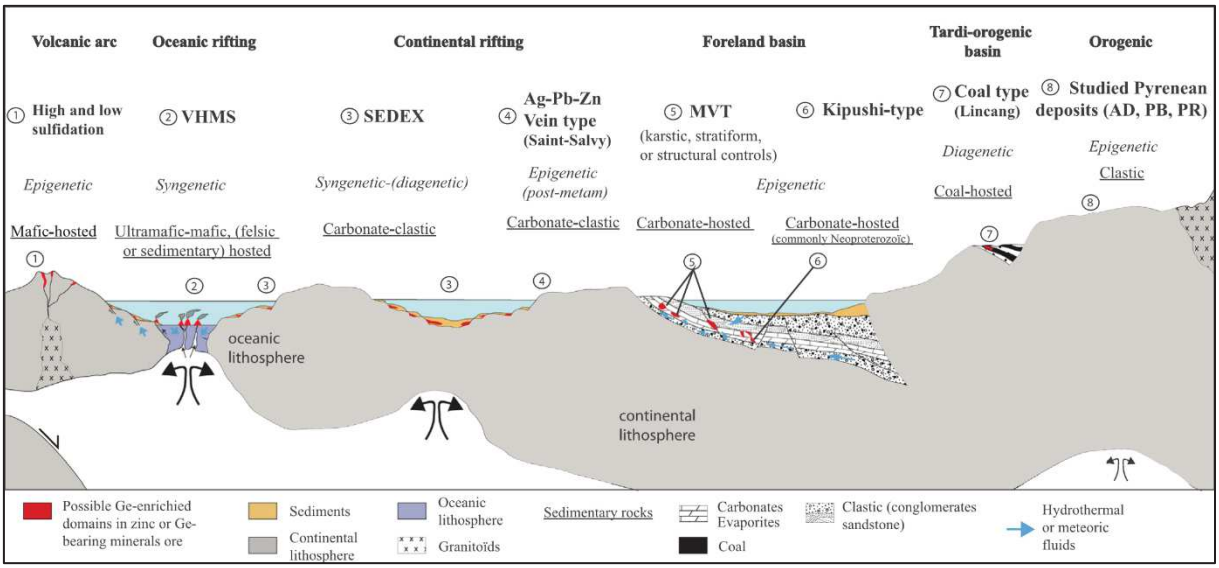

Figure 136 : Geodynamic sketch diagrams showing the geologic environments of the main Ge-bearing ore deposits worldwide: high = and low-sulfidation epithermal; VHMS; SEDEX; polymetallic Ag-Pb-Zn veins (Saint-Salvy); MVT; Kipushi-type; coal (Lincang) deposits; and the studied PAZ deposits.

exhalative (SEDEX) Pb-Zn (and Ge) mineralization is linked to circulation of syngenetic to diagenetic fluids in continental crust (Figure 136; *Wilkinson 2013*). The studied veins are clearly epigenetic and cannot be associated with syn- to diagenetic mineralization of SEDEX type. The three studied deposits are structurally closer to Ag-Pb-Zn(-Cu) vein type deposits which intersect meta-sedimentary or magmatic basement (Figure 136) in various tectonic settings *(Munoz et al. 1994;*

Schwarz-Schampera and Herzig 2002; Höll et al. 2007). Despite this, the deformational-metamorphic imprint recorded in the studied PAZ deposits, has not been reported for polymetallic sulfide vein mineralization (Figure 136). In Kipushi-type deposits, micro-textures of the mineralization tend to display a similar recrystallization and deformation imprint on sphalerite (Figure 136; *Hughes 1987; Chabu 1989; Kamona and Friedrich 2007; Heijlen et al. 2008)*. Nevertheless, from a structural point of view, Kipushi-type mineralization is different from the studied deposits because the orebodies are polymetallic, characteristically pipe/tube like or tabular, and are hosted in carbonate rocks (Figure 136; *Höll et al. 2007)*.

11.1.8 Conclusions

This study highlights the unique occurrence of Ge-minerals in three representative PAZ deposits and shows the major role played by recrystallization processes associated with low-grade metamorphism and deformation, on the formation of the Ge-minerals. During Variscan regional metamorphism, primary sphalerite underwent recrystallization and Ge was expelled from the ZnS lattice under the presence of highly oxidizing metamorphic fluids and moderate temperature (~300–450 °C). Probable enrichment of pre-existing accessory minerals (e.g. magnetite for brunogeierite), and neoformation of minerals (argutite) leading to the observed Ge-mineral paragenesis. The fact that certain minerals like argutite or Ge-chloritoid (carboirite) are described only from the Pyrenees testifies a unique mode of formation. The three studied PAZ mineralizations share some similarities with Kipushi-type mineralization (Figure 135) including the occurrence of Ge-minerals, similar recrystallization-deformation imprint under greenschist facies conditions, and the presence of sphalerite which is depleted in Ge. The occurrence of Ge-sulfides paragenesis in Kipushi may be linked to fluid composition with higher fS_2 and medium fO_2 compared to PAZ deposits.

Finally, the likely source of Ge is still largely unresolved for Ge-deposits (*Belissont 2016*). This issue may be potentially addressed by a study of organic-rich levels within the associated Late-Ordovician or Silurian rocks. Furthermore, a variety of ages are reported for different deposits in the PAZ, ranging from Middle-Late Ordovician, through Lower or Late Devonian and Carboniferous (Variscan), to Late-Triassic/ Late-Jurassic. A detailed study of other PAZ deposits displaying different tectono-metamorphic imprints and occurrence of Ge mineralization would be essential to understand the hydrothermal mobility of strategic metals during the Variscan orogeny.

11.1.9 Acknowledgments

The authors thank the French Geological Survey (Bureau de Recherches Géologiques et Minières; BRGM) for funding through the national program "Référentiel Géologique de France" (RGF-Pyrénées). We acknowledge Christophe Nevado and Doriane Delmas for thin section preparation, Bernard Boyer and Olivier Bruguier for respectively, their involvement in EMPA (Service inter-régional Microsonde-Sud, Montpellier) and LA-ICP-MS analysis (Plateforme AETE, OSU-OREME, Montpellier). The authors are thankful for the editorial handling of Cristiana L. Ciobanu and for the constructive comments of five anonymous reviewers.

11.1.10 References

Aerden, D.G.A.M., 1994. Kinematics of orogenic collapse in the Variscan Pyrenees de- duced from microstructures in porphyroblastic rocks from the Lys-Caillaouas massif. Tectonophysics 238, 139–160. http://dx.doi.org/10.1016/0040-1951(94)90053-1.

Aye, F., Bouladon, J., Picot, P., Pouit, G., 1978. Quelques exemples d'apport de la minéralogie à la connaissance et à la recherche des gîtes minéraux. Bull. Mineral. 101, 139–147.

Bailly, L., Tamas, C.-G., Minut, A., 2005. Te-Rich argyrodite occurrence in Rosia Montana ore deposit, Apuseni Mountains. Romani. C. R. Geosci. Geomaterials, Ore Depos. 337, 755–762. http://dx.doi.org/10.1016/j.crte.2005.03.011.

Bélissont, R., 2016. Germanium and related elements in sulphide minerals: crystal chemistry, incorporation and isotope fractionation, Ph. D Thesis Univ. Lorraine- Georessources-CRPG, 210p.

Bélissont, R., Boiron, M.C., Luais, B., Cathelineau, M., 2014. LA-ICP-MS analyses of minor and trace elements and bulk Ge isotopes in zoned Ge-rich sphalerites from the Noailhac - Saint-Salvy deposit (France): Insights into incorporation mechanisms and ore deposition processes. Geochim. Cosmochim. Acta 126, 518–540. http://dx.doi.org/10.1016/j.gca.2013.10.052.

Bélissont, R., Munoz, M., Boiron, M.C., Luais, B., Mathon, O., 2016. Distribution and oxidation state of Ge, Cu and Fe in sphalerite by u-XRF and K-edge u-XANES: Insights into Ge incorporation, partitioning and isotopic fractionation. Geochim. Cosmochim. Acta 177, 298–314. http://dx.doi.org/10.1016/j.gca.2016.01.001.

Bernstein, L.R., 1985. Germanium geochemistry and mineralogy. Geochim. Cosmochim. Acta 49, 2409–2422. http://dx.doi.org/10.1016/0016-7037(85)90241-8.

Bernstein, L.R., 1986. Renierite, Cu10ZnGe2Fe4S16- Cu11GeAsFe4S16: a coupled solid solution series. Am. Mineral. 71, 210.

Bois, J.P., Pouit, G., Gros, Y., Guérangé, B., Picot, P., 1976. Les minéralisations de Zn (Pb) de l'anticlinorium de Pierrefitte: un exemple de gisements hydrothermaux et sédimentaires associés au volcanisme dans le Paléozoïque des Pyrénées centrales. Bull. BRGM 2, 543–567.

Bonnet, J., 2014. Distribution et contrôle cristallographique des éléments Ge, Ga et Cd dans les sphalérites des gisements de type Mississippi Valley dans les districts de Central et East Tennessee, USA. Ph. D Thesis Univ. Lorraine-Georessources 204p.

Brebrick, R.F., Scanlon, W.W., 1957. Chemical Etches and Etch Pit Patterns on PbS Crystals. J. Chem. Phys. 27, 607. http://dx.doi.org/10.1063/1.1743796.

BRGM, 1984. Les gisements de Pb-Zn français (situation en 1977). BRGM Intern. Rep. 1–278.

Brugger, J., Giere, R., 2000. Origin and distribution of some trace elements in meta- morphosed Fe-Mn deposits, Val Ferrara, Eastern Swiss Alps. Can. Mineral. 38, 1075–1101. http://dx.doi.org/10.2113/gscanmin.38.5.1075.

Chabu, M., 1990, Metamorphism of the Kipushi carbonate hosted Zn-Pb-Cu deposit (Shaba, Zaire), Regional metamorphism of Ore deposits and genetic implications, Proceedings of the 28th International Geology Congress, 9–19 July, 1989, VSP: Utrecht, Netherlands, 27–47.

Chaput, M., Michard, A., 1967. L'Ordovicien supérieur d'Argut et ses minéralisations Pb- Zn. BRGM Rep. DRMM67 A-9, 38.

Cochelin, B., 2016. Champ de déformation du socle Paléozoïque des Pyrénées, PhD Thesis Université Toulouse 3 Paul Sabatier. 244p.

Cook, N.J., 1996. Mineralogy of the sulphide deposits at Sulitjelma, northern Norway. Ore Geol. Rev. 303–338. http://dx.doi.org/10.1016/S0169-1368(96)00009-1.

Cook, N.J., Spry, P.G., Vokes, F.M., 1998. Mineralogy and textural relationships among sulphosalts and related minerals in the Bleikvassli Zn-Pb-(Cu) deposit, Nordland. Norway. Miner. Depos. 34, 35–56. http://dx.doi.org/10.1007/s001260050184.

Cook, N.J., Ciobanu, C.L., Pring, A., Skinner, W., Shimizu, M., Danyushevsky, L., Saini- Eidukat, B., Melcher, F., 2009. Trace and minor elements in sphalerite: a LA-ICPMS study. Geochim. Cosmochim. Acta 73, 4761–4791. http://dx.doi.org/10.1016/j.gca. 2009.05.045.

Cook, N.J., Etschmann, B., Ciobanu, C.L., Geraki, K., Howard, D.L., Williams, T., Rae, N., Pring, A., Chen, G., Johannessen, B., Brugger, J., 2015. Distribution and substitution mechanism of Ge in a Ge-(Fe)-bearing sphalerite. Minerals 5, 117–132.

De Vos, W., Viaene, W., Moreau, J., Wautier, J., 1974. Minéralogie du gisement de Kipushi Shaba, Zaïre. Annales de la Société géologique de Belgique [En ligne], Publ. spéciales Gisements Stratif. Prov. cuprifères – Centen. la Société Géologique Belgique, 1–20.

Denèle, Y., 2007, Formation des dômes gneissiques hercyniens dans les Pyrénées: exemple du massif de l 'Aston-Hospitalet Formation des dômes gneissiques hercyniens dans les Pyrénées: exemple du massif de l'Aston-Hospitalet, Ph. D. Thesis Univ. Toulouse, 300p007.

Denèle, Y., Olivier, P., Gleizes, G., 2008. Progressive deformation of a zone of magma transfer in a transpressional regime: the Variscan Mérens shear zone (Pyrenees, France). J. Struct. Geol. 30, 1138–1149. http://dx.doi.org/10.1016/j.jsg.2008.05. 006.

Denèle, Y., Laumonier, B., Paquette, J.-L., Olivier, P., Gleizes, G., Barbey, P., 2014. Timing of granite emplacement, crustal flow and gneiss dome forma-tion in the Variscan segment of the Pyrenees. Geol. Soc. London Spec. Publ. 405, 265–287. http://dx.doi. org/10.1144/SP405.5.

Eremin, N.I., Sergeeva, N.E., Dergachev, A.L., 2007. Rare minerals from massive sulfide ores: typomorphic features and geochemical trend. Moscow Univ. Geol. Bull. 62, 98–106. http://dx.doi.org/10.3103/S0145875207020044.

European Commission, 2014. The European Critical Raw Materials review, European Commission Memo/14/377 (Brussels), 1–7p.

Evans, N.G., Gleizes, G., Leblanc, D., Bouchez, J.L., 1998. Syntectonic emplacement of the Maladeta granite (Pyrenees) deduced from relationships between Hercynian de- formation and contact metamorphism. J. Geol. Soc. London 155, 209–216. http://dx. doi.org/10.1144/gsjgs.155.1.0209.

Frenzel, M., Hirsch, T., Gutzmer, J., 2016. Gallium, germanium, indium, and other trace and minor elements in sphalerite as a function of deposit type – A meta-analysis. Ore Geol. Rev. 76, 52–78. http://dx.doi.org/10.1016/j.oregeorev.2015.12.017. Garcia-Sansegundo, J., Alonso, J.L., 1989. Stratigraphy and structure of the southeastern Garona Dome. Geodin. Acta 3, 127–134. http://dx.doi.org/10.1080/09853111.1989. 11105180.

García-Sansegundo, J., Martin-Izard, A., Gavaldà, J., 2014. Structural control and geo- logical significance of the Zn-Pb ores formed in the Benasque Pass area (Central Pyrenees) during the post-late Ordovician extensional event of the Gondwana margin. Ore Geol. Rev. 56, 516–527. http://dx.doi.org/10.1016/j.oregeorev.2013. 06.001.

Graham, G.E., Kelley, K.D., Slack, J.F., Koenig, A.E., 2009. Trace elements in Zn−Pb−Ag deposits and related stream sediments, Brooks Range Alaska, with implications for Tl as a pathfinder element. Geochem. Explor. Environ. Anal. 9, 19–37. http://dx.doi. org/10.1144/1467-7873/08-177.

Hariya, Y., Wai, C.M., 1970. The stability and phase transition of the system Fe2GeO4- Fe2SiO4. J. Fac. Sci. Hokkaido Univ. 14, 355–363.

Heijlen, W., Banks, D.A., Muchez, P., Stensgard, B.M., Yardley, B.W.D., 2008. The nature of mineralizing fluids of the Kipushi Zn-Cu deposit, Katanga, Democratic Repubic of Congo: Quantitative fluid inclusion analysis using laser ablation ICP-MS and bulk crush-leach methods. Econ. Geol. 103, 1459–1482. http://dx.doi.org/10.2113/ gsecongeo.103.7.1459.

Hofmann, A.B., Knill, D.M., 1996. Geochemistry and genesis of the Lengenbach Pb–Zn–As–Tl–Ba-mineralization, Binn Valley, Switzerland. Miner. Depos. 31, 319–339. http://dx.doi.org/10.1007/BF02280795.

Höll, R., Kling, M., Schroll, E., 2007. Metallogenesis of germanium – A review. Ore Geol. Rev. 30, 145–180. http://dx.doi.org/10.1016/j.oregeorev.2005.07.034.

Hu, R.Z., Qi, H.W., Zhou, M.F., Su, W.C., Bi, X.W., Peng, J.T., Zhong, H., 2009. Geological and geochemical constraints on the origin of the giant Lincang coal seam-hosted germanium deposit, Yunnan, SW China: a review. Ore Geol. Rev. 36, 221–234. http://dx.doi.org/10.1016/j.oregeorev.2009.02.007.

Hughes, M.J., 1987. The Tsumeb ore body, Namibia, and related dolostone-hosted base metal ore deposits of Central Africa. Ph. D Thesis Univ. Witwatersrand, Johannesburg. 448p.

Johan, Z., Oudin, E., 1986. Présence de grenats, Ca3 Ga (GeO4)3, Ca3 Al (sub 2) [(Ge, Si) O4]3 et d'un équivalent ferrifere, germanifere et gallifere de la sapphirine, Fe4 (Ga, Sn, Fe)4 (Ga, Ge)6 O20, dans la blende des gisements de la zone axiale pyrénéenne. Conditions de formation des phases germanifères et gallifères. C.R. Acad. Sc. Paris 9, 811–816.

Johan, Z., Oudin, E., Picot, P., 1983. Analogues germanifères et gallifères des silicates et oxydes dans les gisements de zinc des Pyrénées centrales, France; argutite et car- boirite, deux nouvelles espèces minérales. TMPM Tschermaks Mineral. und Petrogr. Mitteilungen 31, 97–119. http://dx.doi.org/10.1007/BF01084764.

Kamona, A.F., Friedrich, G.H., 2007. Geology, mineralogy and stable isotope geochem- istry of the Kabwe carbonate-hosted Pb-Zn deposit, Central Zambia. Ore Geol. Rev. 30, 217–243. http://dx.doi.org/10.1016/j.oregeorev.2006.02.003.

Kampunzu, A.B., Cailteux, J.L.H., Kamona, A.F., Intiomale, M.M., Melcher, F., 2009. Sediment-hosted Zn-Pb-Cu deposits in the Central African Copperbelt. Ore Geol. Rev. 35, 263–297. http://dx.doi.org/10.1016/j.oregeorev.2009.02.003.

Kelley, K.D., Jennings, S., 2004. A special issue devoted to barite and Zn-Pb-Ag deposits in the Red Dog district, Western Brooks Range, northern Alaska. Econ. Geol. 99, 1267–1280. http://dx.doi.org/10.2113/gsecongeo.99.7.1267.

Kelley, K.D., Leach, D.L., Johnson, C.A., Clark, J.L., Fayek, M., Slack, J.F., Anderson, V.M., Ayuso, R.A., Ridley, W.I., 2004. Textural, Compositional, and Sulfur Isotope Variations of Sulfide Minerals in the Red Dog Zn-Pb-Ag Deposits, Brooks Range, Alaska. Implications Ore Form. Econ. Geol. 99, 1509–1532. http://dx.doi.org/10. 2113/99.7.1509.

Kleinsmiede, W.F.J., 1960. Geology of the Valle de Arán (Central Pyrenees). Leidse Geol. Meded. 25, 129–245.

Komuro, K., Kajiwara, Y., 2004. Germanium-bearing colusite in siliceous black ore from the Ezuri Kuroko deposit, Hokuroku district, Japan. Resour. Geol. 54, 447–452. http://dx.doi.org/10.1111/j.1751-3928.2004.tb00220.x.

Kouzmanov, K., 2001. Genèse des concentrations en métaux de base et précieux de Radka et Elshitsa (zone de Sredna Gora, Bulgarie) : une approche par l'étude minéralogique, isotopique et des inclusions fluides. Ph. D Thesis Université d'Orléans, 289p.

Laforet, C., Oudin, E., Picot, P., Pierrot, R., Pillard, F., 1981. Métallogénie régionale Utilisation des paragenèses minéralogiques et des minéraux traceurs. Rapp. BRGM 80 (SGN175), 33.

Laznicka, P., 2014. Giant metallic deposits-A century of progress. Ore Geol. Rev. 62, 259–314. http://dx.doi.org/10.1016/j.oregeorev.2014.03.002.

Leach, D.L., Marsh, E., Emsbo, P., Rombach, C.S., Kelley, K.D., Anthony, M., 2004. Nature of hydrothermal fluids at the shale-hosted Red Dog Zn-Pb-Ag deposits, Brooks Range, Alaska. Econ. Geol. 99, 1449–1480. http://dx.doi.org/10.2113/gsecongeo.99.7. 1449.

Lockington, J.A., Cook, N.J., Ciobanu, C.L., 2014. Trace and minor elements in sphalerite from metamorphosed sulphide deposits. Mineral. Petrol. 108, 873–890. http://dx. doi.org/10.1007/s00710-014-0346-2.

Lombaard, A.F., Günzel, A., Innes, J., Krüger, T.L., 1986. The Tsumeb lead–copper–- zinc–silver deposit, South West Africa/Namibia. In: In: Anhaeusser, C.R., Maske, S. (Eds.), Mineral Deposits of Southern Africa, vol. II. Geological Society of South Africa, Johannesburg, pp. 1761–1787.

Marcoux, E., Joubert, M., Lescuyer, J.L., 1991. Origine des minéralisations stratiformes de la bordure du Canigou (Pyrénées orientales. France); apport de la géochimie iso- topique du plomb. C. R. Acad. Sci. Paris 312, Ser. II, 281–287. doi:10.1016/0169- 1368(93)90027-V Marshall, B., Gilligan, L.B., 1993. Remobilization, syn-tectonic processes and massive sulphide deposits. Ore Geol. Rev. 8, 39–64. http://dx.doi.org/ 10.1016/0169-1368(93)90027-V.

Marshall, B., Vokes, F.M., Larocque, A.C.L., 1998. Regional metamorphic remobilization - upgrading and formation of ore deposits. Econ. Geol. 11, 20.

Matte, P., 1969. Le problème du passage de la schistosité horizontale à la schistosité verticale dans le dôme de la Garonne (Paléozoïque des Pyrénées Centrales). Compte Rendu Acad. Sci. Paris II 268, Série D-1841-1844.

Matte, P., Zhi, Q.X., 1988. Decollements in slate belts, examples from the European variscides and the Qin Ling Belt of Central China. Geol. Rundschau 77, 227–238. http://dx.doi.org/10.1007/BF01848686.

Melcher, F., Oberthür, T., Rammlmair, D., 2006. Geochemical and mineralogical dis- tribution of germanium in the Khusib Springs Cu-Zn-Pb-Ag sulfide deposit, Otavi Mountain Land,Namibia. Ore Geol. Rev. 28, 32–56. http://dx.doi.org/10.1016/j. oregeorev.2005.04.006.

Mezger, J.E., 2005. Comparison of the western Aston-Hospitalet and the Bossòst domes: Evidence for polymetamorphism and its implications for the Variscan tectonic evo- lution of the Axial Zone of the Pyrenees, Jour. Virt. Explor., Electronic Edition, ISSN 1 441–81 42, Volume 19, Paper 6, pp. 1–19, doi: http://dx.doi.org/10.3809/jvirtex. 2005.00122.

Mezger, J.E., Gerdes, A., 2016. Early Variscan (Visean) granites in the core of central Pyrenean gneiss domes: Implications from laser ablation U-Pb and Th-Pb studies. Gondwana Res. 29, 181–198. http://dx.doi.org/10.1016/j.gr.2014.11.010.

Mezger, J.E., Passchier, C.W., 2003. Polymetamorphism and ductile deformation of staurolite–cordierite schist of the Bossòst dome: indication for Variscan extension in the Axial Zone of the central Pyrenees. Geol. Mag. 140, 595–612. http://dx.doi.org/ 10.1017/S0016756803008112.

Mezger, J.E., Schnapperelle, S., Rölke, C., 2012. Evolution of the Central Pyrenean Mérens fault controlled by near collision of two gneiss domes, Hallesches Jahrbuch für Geowissenschaften. Halle, S, Bd. 34 (2012), 11–30.

Michard, A., 1966. Les minéralisations Pb-Zn du PER de Tuq de Roquefort (Hte-Garonne, Ariège). BRGM Rep. DRMM66 A-1, 32.

Michard, A., 1969. Per du tuc de roquefort (Haute-Garonne)-Résultat de la campagne 1968. BRGM Rep. 69RME 011R, 32.

Morales-Ruano, S., Touray, J.-C., Barbenson, L., Hach-Ali, P.F., 1996. Primary cavities with incompatible fluid fillings in Ge-bearing sphalerite from Cerro del Toro, Alpujarride (Spain). Econ. Geol. 91, 460–465. http://dx.doi.org/10.2113/gsecongeo. 91.2.460.

Munoz, M., Boyce, A.J., Courjault-Rade, P., Fallick, A.E., Tollon, F., 1994. Multi-stage fluid incursion in the Palaeozoic basement-hosted Saint-Salvy ore deposit (NW Montagne Noire, southern France). Appl. Geochem. 9, 609–626. http://dx.doi.org/ 10.1016/0883-2927(94)90022-1.

Munoz, M., Baron, S., Boucher, A., Béziat, D., Salvi, S., 2015. Mesozoic vein-type Pb–Zn mineralization in the Pyrenees: Lead isotopic and fluid inclusion evidence from the Les Argentières and Lacore deposits. Comptes Rendus Geosci. 348, 322–332. http:// dx.doi.org/10.1016/j.crte.2015.07.001.

Nicol, N., Legendre, O., Charvet, J., 1997. Les minéralisations Zn–Pb de la série paléozoïque de Pierrefitte (Hautes-Pyrénées) dans la succession des évènements tectoniques hercyniens. C. R. Acad. Sci. Paris 324, Ser. IIa, 453–460.

Otteman, J., Nuber, B., 1972. Brunogeierit, ein Germanium-Ferritspinell von Tsumeb. Neu Jb Mineral, Mh 263–267.

Oudin, E., 1982. Minéralogie des Pyrénées Centrales (Annexe III). BRGM Rapport 82 (SGN189), 1–102.

Oudin, E., Pouit, G., Tollon, F., 1988. Les minéraux en trace de Ni-Co, Sn, Ge-Ga, Pb-Sb, Ag et Au témoins de l'évolution de l'hydrothermalisme de l'Ordovicien au Dévonien dans les minéralisations zincifères des Pyrénées Centrales. Bull. Minéral. 111, 49–63.

Pesquera, A., Velasco, F., 1989. The arditurri Pb-Zn-F-Ba deposit (Cinco Villas massif, Basque Pyrenees): a deformed and metamorphosed stratiform deposit. Miner. Depos. 24, 199–209. http://dx.doi.org/10.1007/BF00206443.

Pesquera, A., Velasco, F., 1993. Ore Metamorphism in Sulfide Mineralizations from the Cinco Villas Massif (Western Pyrenees, Spain). Econ. Geol. 88, 266–282. http://dx. doi.org/10.2113/gsecongeo.88.2.266.

Pitcairn, I.K., Olivo, G.R., Teagle, D.A.H., Craw, D., 2010. Sulfide evolution during pro- grade metamorphism of the otago and alpine schists, New Zealand. Can. Mineral. 48, 1267–1295. http://dx.doi.org/10.3749/canmin.48.5.1267.

Pouit, G., 1974. Les minéralisations Zn-Pb dans l'Ordovicien des Pyrénées centrales-Etude préliminaire. Rapp. BRGM, BRGM74 SGN 122, 1–50.

Pouit, G., 1985. Les minéralisations Zn (Pb) Ba du Paléozoïque des Pyrénées Centrales : Une mise au point et un compte rendu des missions 1984. Rapp. BRGM, BRGM85 DAM037, 1–72.

Pouit, G., Bois, J., 1986. Arrens Zn (Pb), Ba Devonian deposit, Pyrénées, France: an ex- halative-sedimentary-type deposit similar to Meggen. Miner. Depos. 21, 181–189. http://dx.doi.org/10.1007/BF00199798.

Putz, H., Paar, W.H., Topa, D., Makovicky, E., Roberts, A.C., 2006. Catamarcaite, Cu6GeWS8, a new germanium sulfide mineral species from Capillitas, Catamarca, Argentina: Description, paragenesis and crystal structure. Can. Miner. 44, 1481–1497. http://dx.doi.org/10.2113/gscanmin.44.6.1481.

Reyx, J., 1973. Relations entre tectonique, métamorphisme de contact et concentrations métalliques dans le secteur des anciennes mines d'Arre et d'Anglas – Ph. D Thesis. Univ. de Paris VI.

Saini-Eidukat, B., Melcher, F., Lodziak, J., 2009. Zinc-germanium ores of the Tres Marias Mine, Chihuahua, Mexico. Miner. Depos. 44, 363–370. http://dx.doi.org/10.1007/ s00126-008-0222-2.

Schwarz-Schampera, U., Herzig, P.M., 2002, Indium: Geology, Mineralogy, and Economics, Springer, 1–237.

Seredin, V.V., Finkelman, R.B., 2008. Metalliferous coals: a review of the main genetic and geochemical types. Int. J. Coal Geol. 76, 253–289. http://dx.doi.org/10.1016/j. coal.2008.07.016.

Smith, K.S., Huyck, H.L.O., 1999. An overview of the abundance, relative mobility, bioavailability, and human toxicity of metals. Rev. Econ. Geol. Environ. Geochemistry Miner. Depos. 6A, 29–70.

Song, X.X., 1984. Minor elements and ore genesis of the Fankou Lead – Zinc deposit, China. Miner. Deposita 19, 95–104. http://dx.doi.org/10.1007/BF00204667.

Taylor, C.D., Sutley, S.J., Lichte, F.E., 2010. Mineralogical, textural, and metal residence studies of primary, recrystallized, and remobilized ores of the greens creek deposit. geology, geochemistry and genesis of the greens creek massive sulfide deposit, ad- miratly Island, Southeastern Alaska. Geol. Surv. Prof. Pap. 1763, 183–236.

Tourigny, G., Doucet, D., Bourget, A., 1993. Geology of the Bousquet 2 mine: an example of a deformed, gold- bearing, polymetallic sulfide deposit. Econ. Geol. 88, 1578–1597. http://dx.doi.org/10.2113/gsecongeo.88.6.1578.

Van Achterbergh, E., Ryan, C.G., Jackson, S.E., Griffin, W., 2001, Data reduction software for LA-ICP-MS, Sylvester, P., ed., Laser ablation-ICPMS in the Earth Science, Mineralogical Association of Canada, v. 29, p. 239–243.

Vic, G., Billa, M., 2015. Potentiel minier des Pyrénées – Rapp. BRGM 1–58. Viets, J., Hopkins, R., Miller, B., 1992. Variations in minor and trace metals in sphalerite from Mississipi Valley-type deposits of the Ozark Region: genetic implications. Econ. Geol. 87, 1897–1905. http://dx.doi.org/10.2113/gsecongeo.88.5.1281.

Vikentyev, I.V., Belogub, E.V., Novoselov, K.A., Moloshag, V.P., 2016. Metamorphism of volcanogenic massive sulphide deposits in the Urals. Ore Geol. Ore Geol. Rev. 1–34. http://dx.doi.org/10.1016/j.oregeorev.2016.10.032.

Wagner, T., Monecke, T., 2005. Germanium-bearing colusite from the Waterloo volcanic- rock-hosted massive sulfide deposit, Australia: crystal chemistry and formation of colusite-group minerals. Can. Mineral. 43, 655–669. http://dx.doi.org/10.2113/ gscanmin.43.2.655.

Whitney, D.L., Evans, B.W., 2010. Abbreviations for names of rock-forming minerals. Am. Mineral. 95, 185–187. http://dx.doi.org/10.2138/am.2010.3371.

Wilkinson, J.J., 2013. Sediment-Hosted Zinc-Lead Mineralization: Processes and Perspectives: Processes and Perspectives, 2nd ed, Treatise on Geochemistry: second Edition. Elsevier Ltd. 219–249. doi: http://dx.doi.org/10.1016/B978-0-08-095975-7. 01109-8.

Yun, S.T., So, C.S., Choi, S.H., Shelton, K.L., Koo, J.H., 1993. Genetic environment of germanium-bearing gold-silver vein ores from the Wolyu mine, Republic of Korea. Miner. Depos. 28, 107–121. http://dx.doi.org/10.1007/BF00196335.

Zheng, Y., Zhang, L., Chen, Y., Hollings, P., Chen, H., 2013. Metamorphosed Pb-Zn-(Ag) ores of the Keketale VMS deposit, NW China: Evidence from ore textures, fluid in- clusions, geochronology and pyrite compositions. Ore Geol. Rev. 54, 167–180. http://dx.doi.org/10.1016/j.oregeorev.2013.03.009.

Zwart, H.J., 1963. The structural evolution of the Paleozoic of the Pyrenees. Geol. Rundschau 53, 170–205.

Zwart, H.J., 1963a. Metamorphic history of the Central Pyrenees, Part II. Valle deArán, sheet 4. Leidse Geol. Meded. 28, 321–376.

Zwart, H.J., 1979. The Geology of the Central Pyrenees. Leidse Geol. Meded. 50, 1–74

11.2 Sample description

Table 10 Complete sample list (n=329; abbréviations: FI: fluid inclusions)

N° sample	Deposit	Locality	Location precision	Orientation	Description	Sphalerite vol.%	FI	EBSD		QEMSCAN
NER01	Nerbiou	Outcrop		N120 verti	Calcaire avec niveaux sulfuré	<10				
NER02	Nerbiou	Outcrop		N140 verti	Quartz-carbonate avec sphalerite	<10				
NER03	Nerbiou	Outcrop		N140 verti	Quartz-carbonate avec sphalerite	<10				
NER04	Nerbiou	Outcrop		N046 verti	Calcaire blanc	<1				
NER05	Nerbiou	Outcrop		N120 verti	Peu de quartz?	<1				
NER06	Nerbiou	Underground galleries		N120 verti	Schistes carbonaté avec veine de quartz?	<1				
NER07	Nerbiou	Underground galleries		N120 verti	Schiste avec veine de carbonate+sphal?	<10				
NER08	Nerbiou	Underground galleries		n.o.	Structures de courant?	<1				
NER09	Nerbiou	Underground galleries		n.o.	Minéraux aciculaires	<1				
NER10	Nerbiou	Underground galleries		N080 verti	Niveaux sphalerite	10_20				
NER11	Nerbiou	Underground galleries		N165 horiz	Schiste noir avec veine de quartz	<1				
NER12	Nerbiou	Underground galleries		N140 75NE	-	-				
NER13	Nerbiou	Underground galleries		N160 verti	Carbonate	<1				
NER14	Nerbiou	Underground galleries		N120 verti	Eponte de la veine de quartz-sphalerite	<10				
NER15	Nerbiou	Underground galleries		N010 verti	Calcaire rubané avec petits sulfures	<10				
NER16	Nerbiou	Underground galleries		N040 verti	Calcaire rubané avec sulfures	<10				
PIE01	Vieille-mine	Underground galleries		N045 verti						
PIE02	Vieille-mine	Underground galleries		N140 50S0						QEMSCAN
PIE03	Vieille-mine	Underground galleries		N70 80SO						
PIE04	Vieille-mine	Underground galleries		N160 verti						
PIE05	Vieille-mine	Underground galleries		N020 verti						

PIE06	Vieille-mine	Underground galleries		N020 verti						
PIE07	Vieille-mine	Underground galleries		N030 verti						
PIE08	Vieille-mine	Underground galleries		N00 verti						
PIE09	Vieille-mine	Underground galleries		N010 verti						
PIE10	Vieille-mine	Underground galleries		N010 verti						
PIE11	Vieille-mine	Underground galleries		N010 verti						
PIE12	Vieille-mine	Underground galleries		N100 verti						
PIE13	Vieille-mine	Underground galleries		N010 verti						
PIE14	Vieille-mine	Underground galleries		N080 verti						
PIE15	Vieille-mine	Underground galleries		N100 verti						
PIE16	Vieille-mine	Underground galleries		N010 verti						
ISA01	Isaby	Outcrop		N080 verti						
ISA02	Isaby	Outcrop		N085 verti						
ISA03	Isaby	Outcrop		N080 verti						
ISA04	Isaby	Outcrop		N080 verti						
ISA05	Isaby	Outcrop		N090 verti						
ISA06	Isaby	Outcrop		N080 verti						
GAR01	Garaoulere	Underground galleries		N090 verti						
GAR02	Garaoulere	Underground galleries		N040 verti						
GAR03	Garaoulere	Underground galleries		N140 verti						
GAR04	Garaoulere	Underground galleries		N164 verti						
GAR05	Garaoulere	Underground galleries		N110 verti						
COU01	Couledous	Underground galleries		N040 verti						
COU02	Couledous	Underground galleries		N160 verti						
COU03	Couledous	Underground galleries		N030 80NE						
COU04	Couledous	Underground galleries		N95 45NO						
COU05	Couledous	Underground galleries		N75 verti			I F			
COU06	Couledous	Underground galleries		N70 verti						

COU07	Couledous	Underground galleries		N090 verti						
COU08	Couledous	Underground galleries		N080 verti						
COU09	Couledous	Underground galleries		N060 verti						
COU10	Couledous	Underground galleries		N090 verti						
ARS01	Arrens	Outcrop		N080 verti						
ARS02	Arrens	Outcrop		n.o.			IF			QEMSCAN
ARS03	Arrens	Outcrop		n.o.						
ARS04	Arrens	Outcrop		n.o.						
ARS05	Arrens	Outcrop		n.o.						
ARS06	Arrens	Outcrop		n.o.						
EST01	Estaings	Outcrop		n.o.						
EST01b	Estaings	Outcrop		N080 50SO						
EST02	Estaings	Outcrop		N160 verti						
EST03	Estaings	Outcrop		N090 verti						
EST04	Estaings	Outcrop		N060 verti						
EST05	Estaings	Outcrop		N130 verti						
EST06	Estaings	Outcrop		N060 verti						
EST07	Estaings	Outcrop		N110 80N						
EST08	Estaings	Outcrop		N120 verti						
EST09	Estaings	Outcrop		N020 verti						
EST10	Estaings	Outcrop		N090 verti						
EST11	Estaings	Outcrop		n.o.						
EST12a	Estaings	Outcrop		N150 verti						
EST12b	Estaings	Outcrop		N090 verti						
EST13	Estaings	Outcrop		N090 verti						
EST14	Estaings	Outcrop		N75 55N						
EST15	Estaings	Outcrop		N090 verti						
EST16	Estaings	Outcrop		N090 verti						
EST17	Estaings	Outcrop		n.o.						
EST18	Estaings	Outcrop		N150 verti						
EST19	Estaings	Outcrop		N020 verti						
EST20	Estaings	Outcrop		N140 verti						
EST21	Estaings	Outcrop		N020 verti						
EST22	Estaings	Outcrop		n.o						
EST23	Estaings	Outcrop		N090 verti						
AUL01	Aulus-Les Argentieres	Outcrop		N140 verti		75	IF			QEMSCAN
AUL02	Aulus-Les Argentieres	Outcrop		N090 verti						
AUL03	Aulus-Les Argentieres	Outcrop		N00 verti						
AUL04	Aulus-Les Argentieres	Outcrop		N170 verti						
AUL05	Aulus-Les Argentieres	Outcrop		N100 verti						

AUL06	Aulus-Les Argentieres	Outcrop		N150 50S						
AUL07	Aulus-Les Argentieres	Outcrop		n.o.						
AUL08	Aulus-Les Argentieres	Outcrop		N020 verti						
AUL09	Aulus-Les Argentieres	Outcrop		N175 verti						
AUL10	Aulus-Les Argentieres	Outcrop		N110 verti						
AUL11	Aulus-Les Argentieres	Outcrop		N060 verti						
AUL12	Aulus-Les Argentieres	Outcrop		N110 50N						
AUL13	Aulus-Les Argentieres	Outcrop		N015 verti						
AUL14	Aulus-Les Argentieres	Outcrop		N120 verti						
AUL15	Aulus-Les Argentieres	Outcrop		n.o.						
AUL16	Aulus-Les Argentieres	Outcrop		N080 verti						
LAS01	Aulus-Les Argentieres	Outcrop		N010 verti						
LAS02	Aulus-Les Argentieres	Outcrop		N010 verti						
CAR01	Carboire	Outcrop		N100 verti						
CAR02	Carboire	Outcrop		N090 verti						
CAR03	Carboire	Outcrop		N090 verti						
ANG01	Anglas	Outcrop		N140 horizontal						
ANG02	Anglas	Outcrop		N060 verti						
ANG03	Anglas	Outcrop		N060 verti						
ANG04	Anglas	Outcrop		N060 verti						
ANG05	Anglas	Outcrop		N080 horizontal						
ANG06	Anglas	Outcrop		N60 70S						
ANG07	Anglas	Outcrop		N140 verti						
ANG08	Anglas	Outcrop		N020 verti						
ANGbonus	Anglas	Outcrop		n.o.						
ANG09	Anglas	Outcrop		N070 verti						
ANG10	Anglas	Outcrop		N040 verti						
ANG11	Anglas	Outcrop		N140 verti						
ANG12	Anglas	Outcrop		N180 verti				EBSD	1	QEMSCAN
ANG13	Anglas	Outcrop		N100 verti			IF	EBSD	1	
ANG14	Anglas	Outcrop		N010 verti						
ANG15a	Anglas	Outcrop		N100 verti						

ANG15b	Anglas	Outcrop		N100 verti						
ANG15c	Anglas	Outcrop		N100 verti						
ANG15d	Anglas	Outcrop		N100 verti						
ANG16	Anglas	Outcrop		n.o.						
ANG17	Anglas	Outcrop		N090 verti						
ANG18	Anglas	Outcrop		N090 verti						
ANG19	Anglas	Outcrop		N090 verti						
ANG20	Anglas	Outcrop		N010 verti						
ANG21	Anglas	Outcrop		n.o.						
ANG22	Anglas	Outcrop		N100 verti						
ANG23	Anglas	Outcrop		N065 verti						
ANG24	Anglas	Outcrop		N100 verti						
ANG25	Anglas	Outcrop		N120 verti						
ANG26	Anglas	Outcrop		N100 verti						
ANG27	Anglas	Outcrop		N090 verti						
ANG28	Anglas	Outcrop		N020 verti						
ANG29	Anglas	Outcrop		N010 verti						
ARR01	Arre	Underground galleries		N160 verti						
ARR02	Arre	Underground galleries		N140 verti						
ARR03	Arre	Underground galleries		N040 verti				EBSD	4	QEMSCAN
ARR04	Arre	Underground galleries		N040 verti						
ARR05	Arre	Underground galleries		N030 verti						
ARR06	Arre	Underground galleries		N070 80S						
ARR07	Arre	Underground galleries		N070 verti						
CRA01	Crabioules	Underground galleries		N120 verti						
CRA02	Crabioules	Underground galleries		N00 verti			IF			
CRA03	Crabioules	Underground galleries		N304 42SE						
CRA04	Crabioules	Underground galleries		N125 verti						
CRA05	Crabioules	Underground galleries		N310 verti						
CRA06	Crabioules	Underground galleries		N030 verti						
CRA07	Crabioules	Underground galleries		N340 verti						
CRA08	Crabioules	Underground galleries		N340 verti						
CRA09	Crabioules	Underground galleries		N320 verti						

CRA10	Crabioules	Underground galleries		n.o.						
LIA01	Liat	Underground galleries		N120 verti						
LIA02	Liat	Underground galleries		N00 verti						
LIA03	Liat	Underground galleries		N304 42SE						
LIA04	Liat	Underground galleries		N125 verti						
LIA05	Liat	Underground galleries		N310 verti						
LIA06	Liat	Underground galleries		N030 verti						
LIA07	Liat	Underground galleries		N340 verti						
LIA08	Liat	Underground galleries		N340 verti						
LIA09	Liat	Underground galleries		N320 verti						
LIA10	Liat	Underground galleries		n.o.						
LIA11	Liat	Underground galleries		n.o.						
LIA11b	Liat	Underground galleries		n.o.						
LIA12	Liat	Underground galleries		N00 verti	Sphal dans autre plan	15%				
LIA13	Liat	Underground galleries		N120 verti	Schistos multiples	0				
LIA14	Liat	Underground galleries		N150 verti	Sphal sub-horizontale	20%		EBSD	1	
LIA15	Liat	Underground galleries		N050 verti	Sphal dans calcaire	50%				
LIA16a	Liat	Underground galleries		N280 verti			IF			QEMSCAN
LIA16b	Liat	Underground galleries		N00 verti						
LIA16c	Liat	Underground galleries		N050 verti						
LIA16d	Liat	Underground galleries		N095 verti						
LIA17	Liat	Underground galleries		N188 verti						
LIA18	Liat	Underground galleries		n.o.						
LIA19	Liat	Underground galleries		N220 verti		90		EBSD	1	
LIA20	Liat	Underground galleries		n.o.						

LIA21	Liat	Underground galleries		N110 verti						
MARG01	Margalida	Outcrop		N120 verti						
MARG02	Margalida	Outcrop		N120 verti						
MARG03	Margalida	Outcrop		N120 verti						
MARG04	Margalida	Outcrop		N150 verti						
MARG05	Margalida	Outcrop		N120 verti						
MARG06	Margalida	Outcrop		N280 verti			IF	EBSD	1	QEMSCAN
MARG07	Margalida	Outcrop	BO33	N330 60E	Nicveau de pegmatite					
MARG08	Margalida	Outcrop	BO34	N330 60E	Pegmatite avec encaissant					
MARG09	Margalida	Outcrop	BO35	N105 verti	Quartzite close to mylonite					
MARG10	Margalida	Outcrop	BO36	N117 80S	oxidized breccia					
VIC01	Victoria	Underground galleries		N120 verti						
VIC02	Victoria	Underground galleries		N110 verti						
VIC03	Victoria	Underground galleries		N120 verti						
VIC04	Victoria	Underground galleries		N120 verti	schiste (dans minéralization)					
VIC05	Victoria	Underground galleries		N120 verti						
VIC06	Victoria	Underground galleries		N120 verti						
VIC07	Victoria	Underground galleries		N120 60S						
VIC08	Victoria	Underground galleries		N160 68N						
VIC09	Victoria	Underground galleries		N152 verti						
VIC10	Victoria	Underground galleries		N150 verti						
VIC11	Victoria	Underground galleries		N150 verti						
VIC12	Victoria	Underground galleries		n.o.			IF	EBSD	2	QEMSCAN
VIC13	Victoria	Underground galleries		N150 verti	Schistes metam avec grenats					
VIC14	Victoria	Underground galleries		N125 verti	Schistes					
VIC15	Victoria	Underground galleries		N220 verti	Schistes					
URE01	Urets	Underground galleries		N090 verti	Sphal en lits	40	IF			
URE02	Urets	Underground galleries		N050 verti	Sphal+Cpy	30				

URE03	Urets	Underground galleries		n.o.	Cpy	10				QEMSCAN
URE04	Urets	Underground galleries		n.o.	Lits quartzeux	10				
BEN01	Bentaillou	Underground galleries	Salle du coffre proche	N130 verti	Sphalerite	70				
BEN02	Bentaillou	Underground galleries	Pilier grande salle	N050 verti	Sphalerite	60				
BEN03	Bentaillou	Underground galleries	Pilier grande salle	N160 verti	Quartz N160	10				
BEN04	Bentaillou	Underground galleries	Pont de pierre	N050 verti	Calcaire et schistes	10				
BEN05	Bentaillou	Underground galleries	Galerie Narbonne	N060 verti	Calcaire de Bentaillou	10				
BEN06	Bentaillou	Underground galleries	Galerie Narbonne	N120 verti	Calcaire	10				
BEN07	Bentaillou	Underground galleries	Proche Saint Jean	N110 verti	Sphalerite et schistes noirs (gros ech)	80	IF	EBSD	3	QEMSCAN
BEN08	Bentaillou	Underground galleries	Lentilles extérieures	N035 verti	Sphalerite-Quartz	60				
BEN09	Bentaillou	Underground galleries	Galerie du haut extérieure	N110 verti	Sphalerite	80				
BEN10	Bentaillou	Underground galleries	Galerie du haut extérieure	N040 verti	Sphalerite	80				
BEN11	Bentaillou	Underground galleries	Lentille oxydée proche Martel	N115 verti	Quartz, sphalerite	30				
BEN12	Bentaillou	Underground galleries	Plan incliné 01	N060 verti	Sphalerite dans filon	20				
BEN13	Bentaillou	Underground galleries	Cavité	N060 verti	Sphal et schistes	30				
BEN14	Bentaillou	Underground galleries	Proche plan incliné 1	N100 verti	Quartz fracture N020	10				
BEN15	Bentaillou	Underground galleries	Galerie du haut intérieure	N100 verti	Sphalerite et calcaire	50				
BEN16	Bentaillou	Underground galleries	Viva Estaline-proche sortie Saint Jean	N150 verti	Galène mm avec sphalerite	90				

BEN17	Bentaillou	Underground galleries		N305 verti		20				
BEN18	Bentaillou	Outcrop		N115 verti	Microconglomerat	10				
BEN19	Bentaillou	Underground galleries	Cigalere	N340 verti	Calcaire	10				
BEN20	Bentaillou	Underground galleries	Route d'Urets	N00 verti	Sphal et encaissant	50				
BEN21	Bentaillou	Underground galleries	Route d'Urets	n.o.	Sphal et encaissant	50				
FOU01	Fourcaye	Underground galleries		N230 verti	Sphal+grenat+schistes	60				
CIE01	Cierco	Underground galleries		N10 verti						
CIE02	Cierco	Underground galleries		n.o.	Quartz					
CIE03	Cierco	Underground galleries		N90 50S						
CIE04	Cierco	Underground galleries		N045 verti	Sphalerite quartz	50				
CIE05	Cierco	Underground galleries		n.o.						
CIE06	Cierco	Underground galleries		n.o.	granite					
CIE07	Cierco	Underground galleries		n.o.						
SOL01	Solitaria	Underground galleries		N120 verti	Sphalerite encaissant					
SOL02	Solitaria	Underground galleries		N120 verti	Sphalerite encaissant					
SOL03	Solitaria	Underground galleries		N120 verti	Sphalerite encaissant					
SOL04	Solitaria	Underground galleries		N120 verti	Sphalerite encaissant					
SOL05	Solitaria	Underground galleries		n.o.						
SOL06	Solitaria	Underground galleries		n.o.						
BO1	Pale Bidau	Underground galleries	Filon+encai		PB01					
BO2	Pale Bidau	Underground galleries	Filon+encai		PB02					
BO3	Pale Bidau	Underground galleries	encaissant		PB03					
BO4	Pale Bidau	Underground galleries	encaissant vein		PB04					
BO5	Pale Bidau	Underground galleries	cont encai-filon		PB05					
BO6-7	Pale Bidau	Underground galleries	cœur filon		PB06					

BO8	Pale Bidau	Underground galleries	encaissant		PB07					
BO9	Pale Bidau	Outcrop/gallery	Sphalerite		PB08	95	IF	EBSD	4	QEMSCAN
BO9-2	Pale Bidau	Outcrop/gallery	Sphalerite			90				
BO9-3	Pale Bidau	Outcrop/gallery				20				
BO9-4	Pale Bidau	Outcrop/gallery	Boxwork			20				
BO9-5	Pale Bidau	Outcrop/gallery		<		60				
BO9-6	Pale Bidau	Outcrop/gallery	breccia			60				
BO9-7	Pale Bidau	Outcrop/gallery				60				
BO9-8	Pale Bidau	Outcrop/gallery				30				
BO10	Pale Bidau	Underground galleries	boxworks		PB09	0	IF			
BO11	Pale Bidau	Underground galleries	strati tranch		PB10					
BO12	Pale Bidau	Underground galleries	relat Qtz-carb-sulf		PB11	0	IF			
BO13	Pale Bidau	Underground galleries	boxworks		PB12					
BO14	Pale de Rase	Outcrop/gallery	sphal niv		PB13	15	IF			
BO15	Pale de Rase	Outcrop/gallery	Py niv		PB14					
BO17	Pale de Rase	Outcrop/gallery	Py		PB15					
BO18	Pale de Rase	Outcrop/gallery	Qtz en peigne		PB16	0	IF			
BO20	Argut	Underground galleries	Ar1: fond gal		AD01					
BO21	Argut	Underground galleries	Ar1 :enc filon		AD02					
BO22	Argut	Underground galleries	Ar1: ext filon		AD03					
BO23	Argut	Underground galleries	Ar1: filon		AD04					
BO24	Argut	Underground galleries	Ar2: gauche entrée		AD05	30	IF	EBSD	2	
BO25	Argut	Underground galleries	Ar2: fracture		AD06	80	IF			
BO26	Argut	Underground galleries	Ar2 : entrée		AD07					
BO27a	Argut	Underground galleries	Ar2: Milieu gal		AD08					
BO27b	Argut	Underground galleries	Ar2: Milieu gal		AD09					
BO28	Argut	Underground galleries	Ar3: Boxworks		AD10	30	IF			
BO29a	Argut	Outcrop/gallery	Déblais	n.o.	PR01	40	IF			
BO29b	Argut	Outcrop/gallery	Déblais	n.o.	PR02					
BO30	Argut	Outcrop/gallery	Déblais	n.o.	PR03					

BO31	Argut	Outcrop/gallery	Déblais	n.o.	PR04					
BO32	Argut	Outcrop/gallery	Déblais	n.o.	PR05	40	I F			QEMSCAN
BO33a	Argut	Outcrop/gallery	Déblais	n.o.	PR06					
BO33b	Argut	Outcrop/gallery	Déblais	n.o.	PR07	40				QEMSCAN
BO34	Argut	Outcrop/gallery	Déblais	n.o.	PR08					
BO35	Argut	Outcrop/gallery	Déblais	n.o.	PR09					
BO36	Argut	Outcrop/gallery	Déblais	n.o.	PR10	20	I F			
BO37	Argut	Outcrop/gallery	Déblais	n.o.	PR11					
BO38	Argut	Outcrop/gallery	Déblais	n.o.	PR12					
Metamorphic study										
BOS01	Bossost			N080 verti	schistes de bas degré Lez					
BOS02	Bossost			N090 80N	schistes de bas degré Argut					
BOS03	Bossost			N102 76N	schistes noirs					
BOS04	Bossost			N104 88N	schistes noirs					
BOS05	Bossost			N120 75S	schiste gréseux					
BOS06	Bossost			N100 verti	schiste gréseux					
BOS07	Bossost			N092 75S	schistes (rte de Melles)					
BOS08	Bossost			N040 verti	schistes (long RN)					
BOS09	Bossost			N230 verti	schistes (en face du barrage)					
BOS10	Bossost			N090 80N	Métapélite avec S2 très marquée (frontière)					
BOS11	Bossost			N088 verti	Métapélites (Pontaut)					
BOS12	Bossost			N108 68S	Métapélite à crd st (croisement Bausen)					
BOS12b	Bossost			N112 10N?	Métapélite à crd st (croisement Bausen)					
BOS13	Bossost			N150 verti	cornéennes foliées à biotite					
BOS14	Bossost			N140 60N	cornéennes foliées à biotite					
BOS15	Bossost			N140 verti	granite non déformé					
BOS16	Bossost			n.o.	schistes à grt-std (Mardalida)					
BOS17a	Bossost			N050 verti	schiste à std crd (Arres)					
BOS17b	Bossost			n.o	schiste à std crd (Arres)					

BOS18	Bossost			N120 verti	schistes à crd-std (Arres)					
BOS19	Bossost			N050 verti	granite (Arres)					
BOS20	Bossost			N110 verti	veine de quartz dans schiste (Arres)					
BOS21	Bossost			N060 verti	pegmatites					
BOS22	Bossost			N090 verti	lentille schisteuses avec minéraux metam					
BOS23	Bossost			N108 verti	mylonites dans la faille					
BOS24	Bossost			n.o	pegmatite et mylonite					
BOS25	Bossost			N12 24N	brèches					
BOS26	Bossost			N080 verti	schistes noirs déformées					
BOS27	Bossost			N96 20S	schistes noirs déformées					
BOS28	Bossost			N96 20S	schistes noirs					
BOS29	Bossost			N90 verti	schistes très déformés					
BOS30	Bossost			n.o.	métapellites					
BOS31	Bossost			n.o.	granite					
BOS32a	Bossost			n.o.	granite					
MEL01	Bossost			n.o.	schistes déformés silurien (Melles)					
MEL02	Bossost			n.o.	schistes silurien pyriteux (Melles)					
MEL03	Bossost			n.o.	alternance schistes et niveaux gréseux (schistes rubanés) (Melles)					
MEL04	Bossost			n.o.	alternance schistes et niveaux gréseux (schistes rubanés) (Melles)					
Other deposits										
M4	Saint-Salvy			n.o.	Sphalerite siderite schists (M4)	70		1		
SCH M1-2	Saint-Salvy			n.o.	Sphalerite stratiform (M1-2)	30				
MAL	Les Malines			n.o.	Sphalerite in breccia	30				

11.3 EPMA analytical conditions

Table 11. EPMA analytical conditions in order to maximize detection of Ge in sphalerite (all EPMA sphalerite data)

EPMA analytical conditions							
Spectrometers	Elements / Lines	Position	Reference material	Beam current (nA)	Acceleration voltage (kV)	Counting time (ms)	Mean limit of detection (LOD-ppm)
Sp4	S Ka	4 PET	FeS_2	10	20	30	415
Sp1	Zn La	1 TAP	Zn	10	20	30	1151
Sp3	Fe Ka	3 LLIF	Fe_2O_3	100	20	30	168
Sp3	Cu Ka	3 LLIF	Cu_2O_3	100	20	60	123
Sp3	Ge Ka	3 LLIF	Ge	100	20	240	85
Sp2	Cd La	2 LPET	CdS	100	20	60	300
Sp2	Sb La	2 LPET	GaSb	100	20	30	165
Sp1	Si Ka	1 TAP	Wollastonite	100	20	180	30

11.4 EPMA Sphalerite – relative to section 11.1

Table 12. EMPA in-situ measurements on sphalerite from Pale Bidau, Argut-dessus and Pale de Rase deposits (section 11.1 – Ore Geology Review; LOD: limit of detection)

Deposit	Sample	S (wt. %)	Zn (wt. %)	Fe (wt. %)	Cd (ppm)	Cu (ppm)	Ge (ppm)	Si (ppm)	Sb (ppm)	Total
Pale Bidau	BO9	33.58	60.56	4.49	1470	110	132	505	<LOD	98.90
	BO9	33.27	61.83	3.08	1438	40	132	505	<LOD	98.43
	BO9	33.75	60.80	4.10	2130	150	<LOD	450	<LOD	98.99
	BO9	32.93	60.84	3.99	2344	419	115	505	183	98.15
	BO9	33.15	61.07	4.20	1898	246	<LOD	535	<LOD	98.87
	BO9	33.22	61.13	4.04	2026	43	117	500	<LOD	98.67
	BO9	33.32	60.76	4.13	2068	277	<LOD	544	187	98.60
	BO9	33.45	61.13	3.97	1768	113	<LOD	577	<LOD	98.84
	BO9	33.12	61.33	3.91	1997	302	368	529	<LOD	98.70
	BO9	33.21	61.18	4.04	1989	0	216	552	<LOD	98.70
	BO9	32.89	60.82	4.09	2085	131	86	513	<LOD	98.18
	BO9	32.47	61.54	4.39	1885	309	<LOD	469	336	98.97
	BO9	32.95	61.57	3.96	2120	1	117	504	<LOD	98.79
	BO9	32.68	61.55	4.01	2289	5	180	476	<LOD	98.54
Argut-dessus	BO29b	34.86	60.16	4.61	1542	<LOD	188	563	<LOD	99.87
	BO29b	33.82	59.03	5.36	1571	<LOD	<LOD	1000	<LOD	98.69
	BO29b	34.34	59.71	4.69	1758	<LOD	188	792	<LOD	99.07
	BO29b	34.19	60.11	4.56	1812	<LOD	251	821	<LOD	99.19
	BO29b	34.41	59.50	4.82	1586	<LOD	122	1027	<LOD	99.17
	BO29b	33.41	59.62	4.91	1584	<LOD	176	678	176	98.37
	BO29b	34.02	60.54	5.00	1489	121	235	629	304	100.08
	BO29b	34.61	59.02	4.65	967	238	141	631	<LOD	98.50
	BO29b	34.05	61.00	4.45	1809	<LOD	192	404	<LOD	99.79

	BO29b	34.63	59.14	5.96	1753	84	209	475	<LOD	100.02
	BO29b	34.42	59.12	6.02	1740	214	178	486	222	99.87
	BO29b	34.38	58.78	6.25	1616	<LOD	<LOD	432	<LOD	99.63
	BO29b	34.45	59.10	5.97	1509	184	50	341	281	99.83
	BO24	34.36	60.34	4.33	1758	446	216	452	<LOD	99.39
	BO24	34.20	60.93	4.39	1948	32	234	546	<LOD	99.82
	BO24	34.40	60.63	4.31	2181	<LOD	89	463	<LOD	99.63
	BO24	34.54	57.12	7.83	1770	196	<LOD	476	<LOD	99.79
	BO24	34.45	56.18	8.03	1802	332	<LOD	552	<LOD	98.97
	BO24	34.64	56.88	7.95	1960	158	196	455	<LOD	99.81
Pale de Rase	BO14	32.33	58.43	6.32	1925	140	319	576	<LOD	97.38
	BO14	33.16	59.97	6.27	1939	258	80	643	<LOD	99.71
	BO14	33.23	57.82	6.80	1915	<LOD	369	521	<LOD	98.16
	BO14	32.75	59.67	5.76	2045	200	506	824	<LOD	98.59
	BO14	34.61	58.84	6.17	1697	<LOD	346	501	<LOD	99.88
	BO14	34.64	58.90	5.36	1624	431	107	1041	<LOD	99.24
	BO14	34.55	60.36	5.41	1571	383	164	541	<LOD	100.61
	BO14	34.52	59.49	5.21	1433	478	127	503	<LOD	99.49
	BO14	34.03	58.72	5.23	1386	403	<LOD	2024	<LOD	98.40
	BO14	34.34	59.47	5.25	2849	508	<LOD	473	200	99.49
	BO14	34.26	60.19	5.33	1327	267	99	491	181	100.06

11.5 EPMA Sphalerite – relative to section 5.1

Table 13. EPMA in-situ measurements on sphalerite from Arre, Anglas, Pale Bidau deposits (section 5.1 – Geology; LOD: Limit of detection). Values for Ge and Cu below limit of detection are shown.

Texture	Deposit	S (wt. %)	Zn (wt. %)	Fe (wt. %)	Cd (ppm)	Cu (ppm)	Ge (ppm)	Si (ppm)	Sb (ppm)	Total (wt. %)
Recrystallized grains (n=33)	Arre	33.51	61.98	2.78	1019	291	103	785	<LOD	98.41
		33.51	62.17	2.73	1145	189	94	834	<LOD	98.54
		33.70	61.98	2.74	961	119	54	774	<LOD	98.54
		33.45	62.36	2.51	1105	119	36	679	<LOD	98.44
		33.64	62.29	2.51	1211	177	35	717	<LOD	98.59
		33.71	62.24	2.51	985	120	78	679	<LOD	98.58
		33.82	62.30	2.49	1113	161	11	726	<LOD	98.74
		33.53	62.39	2.46	1198	169	67	697	<LOD	98.52
		33.54	62.54	2.51	1078	254	34	723	<LOD	98.72
		33.36	62.45	2.46	1181	208	42	697	<LOD	98.41
		33.58	62.48	2.47	968	148	26	656	<LOD	98.64
	Anglas	33.31	61.98	3.57	1065	237	62	583	<LOD	98.99
		33.35	61.97	3.55	1150	227	23	553	<LOD	99.00
		33.66	61.98	3.55	1151	256	11	572	<LOD	99.33
		33.55	61.73	3.68	1156	222	52	622	<LOD	99.09
		33.66	61.83	3.57	1175	274	6	567	<LOD	99.21
		33.23	61.93	3.49	998	320	37	564	<LOD	98.79
		33.23	61.53	3.56	1113	247	3	595	<LOD	98.46
		33.51	60.91	4.22	778	241	86	594	<LOD	98.75
		33.60	61.58	4.26	1255	311	94	582	<LOD	99.61
		33.69	61.29	4.27	1336	327	21	578	<LOD	99.42
		33.85	61.52	4.22	1067	254	83	584	<LOD	99.73
		34.10	60.80	4.25	1143	230	46	552	<LOD	99.30
	Pale Bidau	34.41	62.11	3.51	1666	81	26	<LOD	<LOD	100.20
		34.55	61.26	3.53	1788	17	51	78	<LOD	99.53
		34.63	61.27	3.35	1766	10	31	57	<LOD	99.44
		34.96	61.53	3.35	1766	29	15	52	<LOD	100.02
		34.09	62.49	3.34	1766	148	61	417	<LOD	100.12
		34.15	63.06	3.25	1817	176	108	465	<LOD	100.67
		34.25	62.91	3.25	1519	109	107	490	<LOD	100.58
		34.12	62.97	3.27	1636	293	83	436	<LOD	100.56
		34.09	62.84	3.26	1811	218	86	422	<LOD	100.39
		35.10	62.42	3.14	1847	239	85	418	<LOD	100.87
Dark parent	Arre	33.45	62.20	2.71	1010	964	309	765	<LOD	98.59
		33.55	62.06	2.71	1170	824	314	807	<LOD	98.54
		33.50	61.84	2.68	1013	990	358	823	<LOD	98.26

		33.39	61.73	2.84	1038	1452	535	785	<LOD	98.26
		33.42	62.05	2.48	991	1507	536	758	<LOD	98.26
		33.35	62.34	2.49	981	1712	592	739	<LOD	98.50
		33.42	61.98	2.51	1239	1702	550	733	<LOD	98.26
		33.32	61.95	2.48	1034	1628	647	729	<LOD	98.08
		33.69	62.03	2.48	1092	1182	433	732	<LOD	98.47
		33.46	62.02	2.43	1132	1154	410	745	<LOD	98.17
		33.13	62.89	2.48	1120	1519	564	721	<LOD	98.82
		33.13	62.88	2.51	890	1095	318	717	<LOD	98.75
		33.25	62.46	2.49	1147	456	157	780	<LOD	98.37
		33.20	62.75	2.49	1062	461	180	835	<LOD	98.61
		33.51	62.48	2.56	1112	1513	590	699	<LOD	98.88
		33.34	62.27	2.51	1147	1488	544	762	<LOD	98.44
		33.40	62.24	2.65	1196	1539	545	750	<LOD	98.63
		33.34	62.31	2.69	1315	1535	607	781	<LOD	98.68
	Anglas	32.76	61.29	3.95	1042	515	281	444	<LOD	98.19
		33.52	60.52	4.06	965	957	383	739	<LOD	98.32
		33.63	60.78	3.71	1049	1585	540	765	<LOD	98.43
		33.50	61.58	3.48	975	865	222	582	<LOD	98.77
		33.48	61.86	2.91	1071	1085	404	599	232	98.51
		33.44	62.12	2.90	1073	1199	311	584	322	98.71
		33.60	61.22	3.71	1053	871	267	582	202	98.75
		33.42	61.29	3.64	975	735	252	595	<LOD	98.54
		33.50	60.95	3.94	1034	504	162	596	<LOD	98.56
		33.63	60.54	4.18	1192	964	316	588	<LOD	98.59
		33.51	60.34	4.08	954	986	281	598	<LOD	98.16
		33.56	60.39	4.16	961	1053	314	603	207	98.34
		33.74	60.38	4.12	938	988	273	578	234	98.46
		33.66	60.67	4.16	1127	797	277	593	<LOD	98.71
		33.73	60.45	4.16	1114	841	235	583	262	98.56
Light parent grains (n=36; wt)	Arre	33.57	62.56	2.68	1102	219	26	800	<LOD	98.94
		33.47	62.21	2.69	1138	168	8	771	<LOD	98.50
		33.39	62.60	2.70	871	214	70	814	<LOD	98.81
		33.25	62.96	2.52	1260	225	10	671	<LOD	98.88
		33.17	62.72	2.51	1135	236	29	696	<LOD	98.54
		33.48	62.56	2.59	970	166	130	680	<LOD	98.75
		33.43	62.53	2.61	1172	184	23	735	<LOD	98.70
	Anglas	33.57	61.15	3.82	1065	565	177	636	<LOD	98.71
		33.10	61.06	3.51	1229	508	127	823	<LOD	97.85
		33.75	61.98	3.43	1101	527	146	598	<LOD	99.34
		33.57	62.22	3.01	1284	577	78	563	<LOD	98.99
		33.46	62.00	2.95	1012	525	71	584	<LOD	98.57
		33.36	62.95	2.91	975	633	170	590	<LOD	99.40
		33.54	62.53	2.99	1360	252	68	597	<LOD	99.23

		33.55	62.32	2.91	1081	294	87	620	<LOD	98.93
		33.41	62.22	2.89	1043	307	77	601	<LOD	98.67
		33.40	61.47	3.92	1035	381	110	603	<LOD	98.94
		33.36	61.61	3.61	1062	319	0	565	<LOD	98.72
		33.21	61.43	3.60	981	239	14	577	<LOD	98.36
	Pale Bidau	33.88	62.68	3.45	1665	114	1	77	<LOD	100.20
		33.87	62.64	3.46	1665	140	115	447	<LOD	100.16
		33.58	62.99	3.51	1725	89	150	444	<LOD	100.27
		33.65	62.96	3.52	1679	<LOD	105	447	<LOD	100.31
		33.65	62.99	3.54	1624	<LOD	103	451	<LOD	100.35
		34.16	62.55	3.54	1869	<LOD	98	432	<LOD	100.46
		34.09	62.70	3.61	1737	<LOD	<LOD	468	<LOD	100.58
		33.98	62.75	3.71	1901	<LOD	106	437	<LOD	100.65
		33.97	62.64	3.70	1582	<LOD	128	419	<LOD	100.48
		34.25	62.34	3.79	2016	<LOD	82	455	<LOD	100.59
		34.23	62.68	3.75	1878	100	121	466	<LOD	100.87
		34.11	62.34	3.68	1839	102	85	441	<LOD	100.33
		34.11	62.30	3.96	2015	185	122	398	<LOD	100.61
		33.99	61.95	4.09	2019	194	189	430	<LOD	100.27
		34.15	61.74	4.05	2066	169	125	433	<LOD	100.18
		34.03	62.55	3.33	1639	5	152	476	<LOD	100.09
		34.24	62.57	3.24	1683	261	148	433	<LOD	100.25

11.6 EPMA Brunogeierite (in oxides) – relative to section 5

Table 14. EPMA in-situ measurements on brunogeierite (ideal formulae: $GeFe_2O_4$) from Pale Bidau (BO9) and Argut-dessus (BO24-BO25-BO29b) deposits

Samples & n° inc. (wt. %)	SO2	ZnO	FeO	CuO	Ga_2O_3	GeO_2	As_2O_3	Ag_2O	CdO	SnO	MnO	Sb_2O_3	PbO	SiO_2	Total
BO9-inclusion2	0.21	0.29	57.25	<LOD	<LOD	39.91	0.20	<LOD	<LOD	<LOD	<LOD	<LOD	<LOD	0.18	98.08
BO9-inclusion1	0.04	0.06	57.95	<LOD	0.04	41.94	0.15	<LOD	<LOD	<LOD	<LOD	0.03	0.04	0.14	100.39
BO9-inclusion3	0.10	0.06	56.74	<LOD	<LOD	39.39	0.22	<LOD	<LOD	<LOD	<LOD	0.03	<LOD	0.10	96.66
BO9-inclusion4	0.07	0.03	57.21	0.02	0.09	39.65	0.21	0.02	<LOD	<LOD	<LOD	<LOD	<LOD	0.10	97.42
BO9-inclusion5	0.28	0.32	54.80	<LOD	0.20	37.93	0.20	<LOD	<LOD	<LOD	<LOD	<LOD	<LOD	0.10	93.87
BO9-inclusion6	0.30	0.35	55.96	<LOD	<LOD	39.24	0.18	<LOD	<LOD	0.03	<LOD	<LOD	<LOD	0.12	96.19
BO9-inclusion7	1.22	3.72	55.37	<LOD	<LOD	38.60	0.18	<LOD	<LOD	<LOD	<LOD	<LOD	0.06	0.11	99.30
BO9-inclusion8	0.04	<LOD	57.73	<LOD	<LOD	40.41	0.22	<LOD	<LOD	<LOD	<LOD	<LOD	<LOD	0.14	98.56
BO9-inclusion9	0.05	0.03	57.96	<LOD	<LOD	40.67	0.20	<LOD	<LOD	<LOD	<LOD	<LOD	<LOD	0.11	99.04
BO9-inclusion10	0.17	0.05	57.01	0.06	0.02	40.57	0.17	<LOD	<LOD	0.03	<LOD	<LOD	<LOD	0.13	98.22
BO29b-inclusion1c	0.18	0.33	56.28	<LOD	<LOD	39.64	0.18	<LOD	<LOD	<LOD	0.02	<LOD	<LOD	0.15	96.77
BO29b-inclusion1b	0.07	0.27	57.53	<LOD	0.03	40.76	0.17	<LOD	0.02	<LOD	<LOD	<LOD	<LOD	0.11	98.99
BO29b-inclusion2	0.18	0.06	57.65	0.02	0.02	41.75	0.11	<LOD	0.02	<LOD	<LOD	<LOD	<LOD	0.13	99.95
BO29b-inclusion3a	1.55	1.60	53.50	<LOD	0.02	38.28	0.15	<LOD	<LOD	<LOD	<LOD	<LOD	<LOD	0.12	113.64
BO29b-inclusion3c	0.20	0.02	56.92	<LOD	<LOD	40.15	0.19	<LOD	<LOD	<LOD	<LOD	<LOD	<LOD	0.11	97.60
BO29b-inclusion3d	1.42	3.74	55.71	<LOD	<LOD	39.99	0.15	<LOD	<LOD	<LOD	<LOD	<LOD	<LOD	0.10	101.12
BO29b-inclusion3e	0.18	0.33	56.08	<LOD	<LOD	41.64	0.18	<LOD	<LOD	<LOD	0.02	<LOD	<LOD	0.15	98.57
BO29b-inclusion3f	0.20	0.02	56.82	<LOD	<LOD	40.85	0.19	<LOD	<LOD	<LOD	<LOD	<LOD	<LOD	0.11	98.20
BO29b-inclusion3g	0.07	0.27	57.33	<LOD	0.03	40.96	0.17	<LOD	0.02	<LOD	<LOD	<LOD	<LOD	0.11	98.99
BO29b-inclusion3c	0.20	0.02	57.92	<LOD	<LOD	40.35	0.19	<LOD	<LOD	<LOD	<LOD	<LOD	<LOD	0.11	98.80
BO24-inclusion1	0.49	0.83	56.40	<LOD	<LOD	39.67	0.17	<LOD	<LOD	<LOD	<LOD	<LOD	<LOD	0.18	97.72
BO24-inclusion2a	1.11	3.09	56.52	<LOD	<LOD	40.32	0.17	<LOD	<LOD	<LOD	<LOD	0.02	<LOD	0.16	101.42

BO24-inclusion2b	0.02	0.05	53.59	0.03	<LOD	37.38	0.17	<LOD	0.02	<LOD	<LOD	<LOD	<LOD	<LOD	91.27
BO25-inclusion2a	1.85	1.19	54.01	<LOD	<LOD	37.87	0.15	<LOD	<LOD	<LOD	<LOD	0.03	<LOD	0.11	108.94
BO25-inclusion2b	0.18	0.03	57.02	0.02	<LOD	4<LOD	0.15	<LOD	<LOD	<LOD	<LOD	<LOD	<LOD	0.15	97.59
BO25-inclusion1a	0.68	0.21	56.13	<LOD	0.04	39.75	0.18	<LOD	<LOD	<LOD	0.02	<LOD	<LOD	0.13	97.16
BO25-inclusion 1c	0.62	1.04	56.77	<LOD	0.05	40.47	0.19	<LOD	<LOD	<LOD	<LOD	0.02	<LOD	0.12	99.29
BO25-inclusion3	3.43	0.83	55.35	0.04	<LOD	39.47	0.17	<LOD	0.04	<LOD	<LOD	<LOD	<LOD	0.13	99.48

11.7 LA-ICP-MS Sphalerite – relative to section 11.1

Table 15. LA-ICP-MS data on sphalerite from Pale Bidau, Pale de Rase and Argut-dessus (Ore Geology Review).

Contents (ppm)																
Deposit	**Samples**	**S34**	**Mn55**	**Fe57%**	**Fe57**	**Co59**	**Cu63**	**Zn64**	**Ga69**	**Ge74**	**Ag107**	**Cd110**	**In115**	**Sn118**	**Sb121**	**Pb208**
Pale Bidau	BO9	126388.5	32.1	5.9	58725.7	214.0	67.6	608374.5	100.8	2.4	13.6	1399.2	0.5	5.6	10.8	2297.0
		128644.2	31.8	6.0	60155.7	220.8	88.2	611343.8	125.6	3.7	14.8	1493.7	0.5	5.8	9.6	46.4
		143127.5	42.4	2.8	27939.5	86.9	68.8	611343.8	179.1	9.2	26.4	1590.6	1.0	14.1	21.4	97.5
		136629.8	33.2	4.1	41373.1	165.8	110.1	611343.8	158.0	25.2	13.3	1481.5	1.0	8.1	9.1	47.2
		133690.9	25.0	4.8	47931.6	173.0	305.7	608158.4	121.4	12.1	23.0	1460.7	0.3	13.1	14.0	58.8
		135046.5	28.3	6.3	63073.4	235.6	87.2	615444.2	122.5	3.4	13.0	1370.2	0.3	5.1	8.3	37.5
		129872.9	19.8	4.4	44035.8	157.2	56.5	618257.6	68.5	5.0	20.2	1092.3	1.9	7.1	15.9	47.3
		128249.2	51.7	6.6	66445.2	163.7	25.5	605627.8	28.1	2.0	7.9	1012.6	0.2	2.6	6.9	25.3
		133706.7	49.9	6.0	60482.8	148.5	41.7	605627.8	42.7	8.9	8.4	1030.3	0.2	3.2	5.7	23.9
		124910.1	30.6	4.1	40602.5	165.2	24.1	610223.9	37.7	80.5	3.6	1124.8	0.2	2.1	2.3	12.6
		134374.0	32.9	5.6	56129.2	215.1	91.8	611343.8	154.7	0.8	4.7	1404.7	0.3	1.8	2.2	11.1
		132479.8	32.1	5.9	58800.1	219.0	96.7	611343.8	149.2	1.8	10.9	1378.5	0.3	3.8	6.1	32.2
		128925.6	29.6	5.5	54743.7	204.5	101.8	611343.8	146.8	5.1	21.3	1347.3	0.4	7.1	12.4	55.1
		134855.7	25.0	4.8	47858.4	170.7	29.4	615543.0	15.3	4.6	19.9	1368.2	0.2	9.2	16.1	59.2
Argut-dessus	BO29b	141922.6	23.6	4.5	44593.6	<6,84	113.7	607466.7	34.9	20.3	8.1	1158.5	0.6	<1,70	6.6	92.1
		148126.1	78.3	6.4	64086.4	63.6	24.1	631567.9	38.9	0.5	27.7	1321.8	1.0	<0,14	27.5	29.4
		143748.8	59.1	5.7	56569.8	125.8	89.0	630468.9	162.7	2.3	31.1	1095.3	0.3	0.6	20.4	23.0
		155935.0	28.8	3.8	37561.5	68.1	14.3	616223.5	24.6	3.4	21.9	1108.6	0.4	<0,28	16.4	22.7
		165004.0	<22,33	2.8	28325.0	154.2	278.0	621279.1	32.1	102.2	212.6	1454.9	1.6	13.6	25.8	523.7
		151638.5	37.6	3.1	31182.6	77.3	52.3	622698.7	16.5	11.1	161.8	1235.8	<0,39	<2,80	5.9	342.0
		163559.5	66.5	4.1	41350.3	87.7	101.3	632516.7	17.8	10.4	227.2	1263.0	1.0	3.0	22.6	475.4
		159045.1	<54,66	0.9	8772.4	25.3	<37,84	632516.7	10.9	40.2	<9,46	1119.5	<1,46	<9,72	2.8	32.6

		158822.8	66.6	1.8	18465.3	30.8	<17,44	622698.7	5.1	17.8	21.7	1096.2	<0,61	7.1	0.9	25.5
Pale de Rase	BO14	134823.7	55.6	9.0	89610.2	44.3	3.2	597556.3	3.1	0.3	2.4	1382.1	1.2	0.4	1.1	1.0
		134761.4	48.6	8.3	82556.2	42.1	3.1	597556.3	2.6	0.3	3.6	1367.0	1.1	0.4	2.3	2.6
		133414.6	49.7	8.7	87109.6	44.1	5.7	597556.3	7.9	0.3	2.4	1390.9	1.1	0.4	1.1	1.4
		137659.0	31.9	6.4	63758.1	36.8	9.9	597556.3	22.8	1.1	2.3	1460.5	1.1	<0,19	0.5	0.6
		141004.7	63.7	10.1	101394.4	48.5	9.4	597555.5	13.9	0.2	3.0	1381.7	1.1	0.3	1.2	1.5
		135313.6	7.7	3.6	36042.0	16.2	14.4	603856.4	2.3	0.9	21.1	1588.4	1.1	0.4	23.4	21.3
Detection limit (ppm)																
Deposit	**Samples**	**S34**	**Mn55**	**Fe57%**	**Fe57**	**Co59**	**Cu63**	**Zn64**	**Ga69**	**Ge74**	**Ag107**	**Cd110**	**In115**	**Sn118**	**Sb121**	**Pb208**
Pale Bidau	BO9	20.7	0.2	0.1	13.6	0.1	0.1	0.2	0.1	0.1	0.1	0.1	0.1	0.1	0.0	0.1
		28.3	0.2	0.1	18.6	0.1	0.1	0.3	0.1	0.1	0.1	0.1	0.1	0.1	0.0	0.1
		1638.1	13.1	0.1	1100.6	3.3	6.3	19.0	1.8	8.7	1.4	7.9	0.2	1.7	0.3	0.2
		1031.1	8.3	0.1	700.6	2.1	4.2	11.1	1.1	5.5	0.9	5.0	0.1	1.1	0.2	0.1
		52.6	0.4	0.1	37.1	0.1	0.2	0.6	0.1	0.3	0.1	0.3	0.1	0.1	0.1	0.1
		28.7	0.2	0.1	20.8	0.1	0.1	0.5	0.1	0.2	0.0	0.2	0.1	0.1	0.1	0.1
		28.1	0.2	0.1	20.1	0.1	0.1	0.5	0.1	0.2	0.0	0.2	0.1	0.1	0.1	0.1
		19.1	0.2	0.1	13.8	0.1	0.1	0.4	0.1	0.1	0.0	0.1	0.1	0.1	0.1	0.1
		24.4	0.2	0.1	17.7	0.1	0.1	0.5	0.1	0.1	0.0	0.2	0.1	0.1	0.1	0.1
		27.0	0.2	0.1	20.1	0.1	0.1	0.6	0.1	0.2	0.0	0.2	0.1	0.1	0.1	0.1
		26.4	0.2	0.1	20.0	0.1	0.1	0.6	0.1	0.2	0.0	0.2	0.1	0.1	0.1	0.1
		27.2	0.2	0.1	20.2	0.1	0.1	0.6	0.1	0.2	0.0	0.2	0.1	0.1	0.1	0.1
		25.5	0.2	0.1	19.3	0.1	0.1	0.6	0.1	0.1	0.0	0.2	0.1	0.1	0.1	0.1
		43.2	0.4	0.1	32.9	0.1	0.2	1.0	0.1	0.3	0.1	0.3	0.1	0.1	0.1	0.1
Pale Bidau	BO29b	1139.5	9.3	0.1	851.3	6.8	5.4	21.7	1.3	6.4	1.3	7.4	0.2	1.7	0.2	0.1
		89.0	0.7	0.1	66.1	0.3	0.4	1.7	0.1	0.5	0.1	0.6	0.0	0.1	0.1	0.1
		38.9	0.3	0.1	29.2	0.1	0.2	0.8	0.1	0.2	0.1	0.3	0.0	0.1	0.1	0.1
		177.1	1.5	0.1	135.2	0.6	1.0	3.6	0.2	1.1	0.2	1.4	0.0	0.3	0.1	0.1
		2627.3	22.3	0.2	1961.5	7.9	15.1	54.1	3.5	16.2	3.8	21.3	0.6	3.9	0.5	0.3
		1831.8	15.3	0.1	1377.1	5.4	10.3	35.3	2.3	11.1	2.6	14.2	0.4	2.8	0.4	0.2
		1713.0	14.5	0.1	1250.5	5.2	9.8	32.3	2.3	10.4	2.5	13.6	0.3	2.6	0.4	0.2
		6459.6	54.7	0.5	4932.9	19.1	37.8	122.4	8.5	40.2	9.5	52.9	1.5	9.7	1.5	0.7

		2833.7	24.4	0.2	2163.5	8.6	17.4	54.2	4.0	17.8	4.3	23.8	0.6	4.1	0.7	0.3
Pale de Rase	BO14	41.3	0.4	0.1	31.7	0.1	0.3	0.8	0.1	0.3	0.1	0.3	0.1	0.1	0.1	0.1
		41.8	0.4	0.1	32.4	0.1	0.3	0.9	0.1	0.3	0.1	0.4	0.1	0.1	0.1	0.1
		41.4	0.4	0.1	32.4	0.1	0.3	1.0	0.1	0.3	0.1	0.4	0.1	0.1	0.1	0.1
		126.5	1.3	0.1	100.7	0.4	0.8	3.2	0.2	0.8	0.2	1.1	0.1	0.2	0.1	0.1
		34.0	0.4	0.1	26.9	0.1	0.2	0.8	0.1	0.2	0.1	0.3	0.1	0.1	0.1	0.1
		142.2	1.5	0.1	112.9	0.4	0.9	3.6	0.2	0.9	0.2	1.3	0.1	0.2	0.1	0.1
1 sigma error																
Deposit	**Samples**	**S34**	**Mn55**	**Fe57%**	**Fe57**	**Co59**	**Cu63**	**Zn64**	**Ga69**	**Ge74**	**Ag107**	**Cd110**	**In115**	**Sn118**	**Sb121**	**Pb208**
Pale Bidau	BO9	26912.99	4.01	0.3779856	37798.56	21.67	33.29	19238.83	46.87	1.22	6.31	546.03	0.21	2.44	4.42	10027.4
		27393.2	4.0	0.4	38718.9	22.4	43.5	19332.7	58.4	1.9	6.9	582.9	0.2	2.5	3.9	20.3
		30591.2	18.2	0.2	18080.3	12.3	35.3	19366.9	83.6	5.2	12.6	621.9	0.6	6.7	8.9	42.7
		29157.1	12.9	0.3	26674.6	19.0	54.9	19354.7	73.6	5.3	6.4	578.9	0.5	3.9	3.8	20.7
		28469.8	3.2	0.3	30852.9	17.7	150.6	19233.6	56.4	6.1	10.7	570.1	0.1	5.7	5.7	25.7
		28757.1	3.6	0.4	40597.5	23.9	43.0	19462.9	56.9	1.7	6.1	534.7	0.1	2.2	3.4	16.4
		27655.0	2.5	0.3	28343.6	15.9	27.8	19551.4	31.9	2.5	9.4	426.3	0.7	3.1	6.5	20.7
		27309.6	6.5	0.4	42767.5	16.6	12.6	19152.3	13.1	1.0	3.7	395.2	0.1	1.1	2.8	11.1
		28471.1	6.2	0.4	38929.3	15.0	20.6	19151.8	19.9	4.4	3.9	402.1	0.1	1.4	2.3	10.5
		26599.0	3.9	0.3	26134.6	16.8	11.9	19298.0	17.5	4.0	1.7	439.0	0.1	0.9	1.0	5.5
		28613.7	4.1	0.4	36127.7	21.8	45.3	19333.0	71.9	0.4	2.2	548.2	0.1	0.8	0.9	4.9
		28210.4	4.0	0.4	37846.8	22.2	47.7	19333.0	69.3	0.9	5.0	538.0	0.1	1.7	2.5	14.1
		27454.0	3.7	0.4	35236.3	20.8	50.2	19333.3	68.2	2.6	9.9	525.8	0.1	3.1	5.1	24.0
		28716.5	3.2	0.3	30804.5	17.3	14.5	19466.0	7.1	2.3	9.3	533.9	0.1	4.0	6.6	25.9
Pale Bidau	BO29b	30334.0	16.3	0.3	28791.2	11.6	57.4	19254.8	16.8	1.5	4.6	453.7	0.5	3.3	2.9	40.3
		31543.5	9.8	0.4	41250.6	6.6	11.9	19973.7	18.1	0.6	12.9	515.9	0.4	0.2	11.3	12.8
		30610.2	7.4	0.4	36411.5	12.8	43.9	19938.0	75.7	1.2	14.5	427.5	0.1	0.3	8.3	10.0
		33210.3	4.2	0.2	24182.2	7.4	7.2	19491.4	11.5	2.3	10.2	432.8	0.2	0.4	6.7	9.9
		35449.3	33.1	0.2	18561.3	25.2	139.9	19733.3	16.6	5.8	99.4	571.3	1.2	8.6	10.9	228.9
		32358.1	15.0	0.2	20135.7	10.9	27.7	19713.5	8.1	1.6	75.3	483.1	0.4	2.6	2.5	149.4
		34934.7	20.2	0.3	26703.0	13.5	51.9	20039.3	9.0	1.3	105.8	494.3	0.7	3.5	9.4	207.7
		33979.3	22.5	0.1	6008.3	8.5	15.7	20009.9	6.2	1.7	5.3	437.6	0.7	4.5	1.3	14.3

		33863.8	15.8	0.1	11953.2	6.0	10.3	19699.6	3.3	1.4	10.4	428.2	0.4	3.9	0.6	11.2
Pale de Rase	BO14	28708.9	6.9	0.6	57676.8	4.5	1.6	18896.5	1.4	0.2	1.1	539.4	0.5	0.2	0.5	0.5
		28695.7	6.1	0.5	53136.5	4.3	1.6	18896.6	1.2	0.2	1.7	533.5	0.4	0.2	0.9	1.1
		28408.9	6.2	0.6	56067.3	4.5	2.8	18896.6	3.7	0.2	1.1	542.8	0.4	0.2	0.5	0.6
		29314.3	4.2	0.4	41039.0	3.9	5.0	18897.8	10.6	0.9	1.1	570.0	0.4	0.2	0.2	0.3
		30025.4	7.9	0.7	65262.0	5.0	4.6	18896.8	6.5	0.1	1.4	539.2	0.4	0.2	0.5	0.6
		28814.9	1.6	0.2	23199.9	1.8	7.1	19097.0	1.1	0.9	9.8	619.9	0.5	0.2	9.5	9.3

11.8 LA-ICP-MS Sphalerite – relative to section 5.2

Table 16. LA-ICP-MS data on sphalerite from Anglas, Arre, Pale Bidau, Victoria, Margalida and Bentaillou (Mineralium deposita)

Content (ppm)																
Deposit	**Texture**	**S34**	**Mn55**	**Fe57**	**Co59**	**Cu63**	**Zn64**	**Ga69**	**Ga71**	**Ge74**	**Ag107**	**Cd111**	**In115**	**Sn118**	**Sb121**	**Pb208**
Anglas	Recrystallized grains	236254	194.6	25101	137.3	94.5	604453	32.4	32.7	33.0	2.3	1021	1.60	1.9	12.6	23.3
		261026	92.3	12730	103.1	28.8	606147	28.3	25.2	16.7	1.9	905	1.44	2.8	10.0	20.2
		230995	230.2	29757	172.5	53.8	605813	31.6	30.5	40.7	2.2	1029	1.73	1.1	8.5	22.7
		240436	195.9	25557	142.9	49.4	602939	31.1	30.8	62.1	1.7	999	1.84	1.0	6.1	20.1
		233791	197.0	25175	142.1	50.0	605185	40.3	40.0	13.1	1.6	997	1.50	0.8	6.5	16.6
		233964	200.5	25674	145.0	60.1	608009	52.3	52.6	40.2	1.6	1001	1.51	0.8	6.1	13.7
		227425	96.9	14845	104.3	48.6	599784	32.7	32.4	5.7	2.3	1050	<LOD	2.6	6.2	23.8
		234058	149.9	22447	152.9	72.0	599784	38.7	38.3	1.7	2.8	1023	<LOD	2.4	7.1	29.1
		242049	158.6	23444	160.7	50.4	615660	29.3	29.4	3.4	1.9	1003	<LOD	1.3	9.1	21.0
		244191	166.6	24269	165.8	49.4	612817	35.9	34.6	19.6	1.9	993	<LOD	0.9	3.7	13.9
		234517	128.7	19378	139.4	63.7	613270	41.8	41.3	1.4	3.5	982	<LOD	1.4	5.9	22.3
		248446	151.5	22796	143.4	67.2	620020	24.3	24.4	4.3	2.8	1032	0.64	7.7	12.5	38.3
		241187	139.1	20743	130.8	50.7	615250	20.3	20.4	3.0	2.1	1027	0.61	7.5	7.4	24.7
		250083	159.7	22326	134.5	40.9	616078	25.0	24.5	1.5	1.8	918	0.47	0.6	5.9	12.7

		248000	155.8	22010	131.8	44.3	614253	24.3	24.1	0.8	2.2	929	0.55	0.7	5.2	22.7
Arre	Recrystallized grains	249315	18.6	16916	144.7	33.9	627187	9.4	9.2	7.9	5.0	1166	0.05	1.0	7.8	37.7
		261254	18.0	21798	163.6	10.3	623044	0.6	0.5	1.5	1.3	1092	0.03	0.3	2.5	2.9
		249144	19.4	20265	169.4	20.2	619786	0.3	0.4	1.7	2.5	1057	<LOD	0.4	2.4	9.8
		258107	23.8	22067	172.7	35.0	621670	2.9	2.7	4.2	4.6	1098	<LOD	1.2	8.2	30.6
		249629	22.0	21919	170.2	34.7	619784	5.4	5.2	3.8	3.7	1128	<LOD	1.1	5.2	25.5
		275506	19.0	18962	160.4	27.3	623593	4.7	4.4	4.9	3.8	1092	<LOD	0.8	5.3	20.5
		271844	20.3	18037	153.9	30.8	622920	5.0	4.4	5.4	4.3	1087	<LOD	0.6	6.4	23.4
		260366	18.4	18045	158.8	24.9	622403	4.0	3.8	2.2	3.7	1060	<LOD	0.6	4.6	19.1
		275685	16.2	17206	155.6	17.1	622974	5.9	5.6	1.1	1.7	1036	<LOD	0.6	2.8	10.5
		256573	13.7	14117	128.2	24.7	623857	6.5	6.5	3.9	3.2	1073	<LOD	0.6	5.9	17.2
		261417	20.6	17911	154.6	44.6	625399	6.9	6.5	8.4	5.8	1080	<LOD	1.3	9.8	37.2
		268070	18.5	19097	165.0	35.9	624462	6.3	6.1	4.7	4.8	1062	<LOD	1.0	10.0	31.4
		263132	17.0	15257	136.2	49.5	624801	5.2	5.2	12.8	7.0	1046	<LOD	1.3	12.0	49.3
		274645	17.4	20273	170.8	17.2	622447	0.7	0.3	1.5	2.0	1103	<LOD	0.6	2.4	10.1
Pale Bidau	Recrystallized grains	230212	22.7	21349	129.9	42.5	625499	31.6	32.0	3.7	12.9	1526	2.22	6.1	15.2	38.4
		226130	23.8	22637	139.9	43.5	624932	26.8	27.4	4.8	15.5	1534	1.97	7.5	16.5	40.1
		225249	25.1	24145	145.5	52.1	624932	33.9	34.5	4.7	16.0	1527	2.00	7.2	16.5	43.5
		232305	20.9	21808	133.0	35.7	624932	30.9	31.7	3.0	9.8	1561	2.15	5.0	11.0	27.1
		229688	21.4	21236	133.6	77.5	630610	76.2	78.2	5.3	13.8	1500	1.04	7.0	16.7	32.2
		233949	27.1	21959	142.7	114.3	629137	101.6	104.3	5.1	24.7	1501	0.96	11.5	34.6	9420.7
		231902	23.2	20602	135.1	128.3	629729	148.8	152.8	3.2	14.8	1531	0.66	5.4	16.2	1872.3
		230219	25.6	21083	140.6	141.3	628380	156.4	159.1	5.0	19.3	1569	0.51	6.4	19.5	144.5
		232679	22.9	18938	126.1	114.8	625653	153.9	157.6	1.7	7.1	1546	0.49	2.3	6.5	189.3
		231699	20.9	21201	138.6	88.8	629729	109.0	111.6	0.5	4.8	1515	0.73	1.8	2.8	14.8
		220895	26.4	22434	147.9	150.4	624172	146.5	151.4	4.5	21.2	1546	0.54	6.9	20.9	41.6
		234495	26.4	20781	142.8	123.0	621274	142.9	148.0	1.8	9.1	1526	0.45	2.8	8.3	22.2
Anglas	Dark domains-coarse grains	223644	158.5	22736	116.1	520.3	592870	11.2	10.9	257.6	2.8	944	<LOD	0.4	41.9	12.1
		230354	167.8	23308	117.9	655.8	605197	17.0	16.6	324.5	3.9	968	<LOD	0.4	110.4	49.1
		226912	151.2	22887	123.2	575.1	611468	40.9	41.0	232.0	3.2	964	<LOD	0.2	108.6	51.7
		232250	135.8	21026	112.5	660.9	607757	45.6	45.7	289.9	3.8	955	<LOD	0.4	128.2	44.7
		235823	152.2	23886	126.5	609.5	607757	42.2	42.3	253.1	3.6	962	<LOD	0.3	183.2	53.6

		233786	182.9	24621	139.8	396.7	605354	37.9	38.3	181.9	2.5	995	2.43	7.4	35.0	21.1
		234014	179.3	23991	137.3	595.5	603422	23.9	24.2	268.1	3.1	977	3.31	21.0	96.7	45.1
		233053	179.5	24033	137.3	378.8	603906	13.7	13.4	200.2	2.3	967	2.80	20.4	32.6	14.1
		238896	184.3	24762	139.9	308.8	603777	18.8	18.9	228.0	2.8	973	2.25	18.6	14.4	20.4
		237785	217.9	28642	156.5	291.0	606726	24.4	24.7	194.0	2.2	982	1.88	6.6	32.5	16.9
		234951	132.0	21614	159.0	720.9	610619	68.6	67.7	337.8	9.5	975	0.38	4.4	14.2	65.1
		244286	134.4	21530	147.6	455.2	619818	128.6	128.3	224.7	4.6	969	1.80	38.5	2.0	11.3
		246020	147.6	21769	135.7	537.7	612171	38.9	39.0	252.0	3.3	972	0.37	3.2	99.4	46.9
		243576	146.8	21977	133.0	533.5	612853	19.4	20.0	235.1	3.2	965	<LOD	2.2	145.0	78.3
		249023	173.8	23773	134.5	228.4	609509	35.7	35.4	102.3	2.8	1003	<LOD	0.5	7.4	2.8
		245626	81.9	17935	131.7	698.0	618606	20.6	20.5	294.1	3.5	925	<LOD	0.2	217.2	108.0
		250329	83.9	18202	132.6	840.6	621169	30.4	30.0	364.4	3.8	905	<LOD	0.1	218.4	89.7
		248434	103.2	19357	134.3	653.5	619505	72.2	72.4	401.1	3.9	936	0.08	3.3	54.4	16.0
Arre	Dark domains-coarse grains	247319	15.9	15519	133.3	552.7	627486	7.8	7.8	305.4	3.2	1155	<LOD	3.7	3.6	16.1
		245895	18.1	16521	140.6	1019.5	624812	8.3	7.9	511.2	3.2	1151	<LOD	3.1	2.6	9.5
		250692	17.4	16544	138.7	905.6	622664	5.6	5.6	432.8	2.9	1153	0.05	3.0	2.1	10.6
		251376	15.3	17154	135.7	461.3	621952	4.9	4.9	227.1	2.6	1121	<LOD	0.2	7.0	2.2
		249074	16.7	18304	147.3	522.9	620573	6.1	5.6	246.6	2.6	1099	<LOD	0.3	8.7	2.3
		261244	18.4	20554	164.7	558.6	626458	0.5	0.1	241.1	2.2	1085	<LOD	0.2	1.2	1.5
		259861	19.6	21798	170.7	1120.1	625362	4.5	4.6	480.9	2.5	1116	<LOD	5.3	2.8	7.2
		248541	14.4	15972	139.3	761.9	620538	7.8	7.7	386.9	2.2	1121	<LOD	6.4	1.8	6.3
		253391	13.1	16179	143.1	1175.4	623367	8.3	8.3	579.6	2.5	1089	<LOD	1.0	5.1	3.2
		257654	15.7	18341	161.0	1265.4	619794	6.9	6.6	540.8	3.0	1096	0.06	1.6	3.1	4.1
		252882	15.4	17874	157.2	1225.0	617456	9.7	9.6	525.1	2.4	1071	<LOD	2.9	1.9	3.4
		254546	16.2	17896	159.2	1040.1	620317	10.3	10.0	460.7	4.6	1089	<LOD	10.0	5.6	24.8
		266281	15.1	17565	158.8	869.2	620189	11.3	10.5	431.7	3.4	1051	<LOD	8.8	2.6	15.5
		274499	15.5	17236	155.0	1127.5	618876	5.2	5.2	519.8	2.8	1009	<LOD	0.4	4.4	3.8
		270724	14.8	17485	153.7	908.5	618790	5.4	5.1	404.3	3.3	1011	<LOD	2.5	2.8	7.6
		291187	18.0	20585	160.0	1222.7	625592	6.0	5.6	507.3	6.1	1073	<LOD	0.6	6.0	5.0
		260770	19.0	21088	164.9	1012.4	625253	5.0	4.3	415.2	4.8	1115	0.04	0.5	12.4	5.9
Pale Bidau	Dark domains-	228422	20.8	20311	131.5	220.5	629729	119.7	122.9	145.9	7.0	1498	0.78	7.4	4.3	20.9
		228410	18.6	20300	110.3	209.3	629718	109.3	111.7	134.7	4.3	1487	0.21	5.0	4.9	9.7

Pale Bidau	coarse grains	228433	25.3	20322	132.6	231.6	629740	124.3	134.0	157.0	7.2	1509	0.52	27.3	5.3	32.0
		228473	22.3	20362	172.7	269.3	629780	142.3	174.1	197.1	8.5	1549	0.42	3.0	8.3	48.3
Anglas	Light domains-coarse grains	240197	124.7	21114	156.2	251.9	615298	60.4	60.9	111.0	4.0	967	0.21	3.8	4.2	33.5
		246638	88.7	18973	148.9	242.4	615787	95.3	95.5	75.8	3.7	951	0.21	11.8	5.7	3.7
		244049	77.9	18126	142.2	190.5	622179	82.9	82.2	61.2	1.5	933	0.02	0.9	5.1	1.9
		243835	173.1	23585	133.0	201.7	611658	47.6	47.4	136.7	1.7	1002	0.02	0.9	11.8	3.8
		251632	83.9	18016	133.8	55.6	620287	4.5	4.2	19.4	3.1	912	0.02	0.1	2.2	15.1
		250491	90.7	18450	131.8	77.3	623235	5.4	5.3	22.1	5.3	917	0.02	0.4	3.9	47.6
		249531	91.3	18624	134.7	66.3	622196	3.9	3.7	18.1	4.2	946	0.02	0.4	3.9	40.3
Arre	Light domains-coarse grains	241439	18.9	16772	150.5	101.6	624619	15.6	15.5	40.7	4.5	1181	0.03	1.3	5.6	31.1
		251389	19.2	16600	136.8	61.7	624557	8.8	8.5	20.0	3.8	1202	0.02	1.1	5.1	27.6
		247688	18.4	20406	158.4	185.5	622585	6.9	6.8	73.7	2.2	1114	0.02	0.2	8.7	2.4
		276263	19.2	19678	162.4	102.5	623083	8.4	8.6	36.0	3.4	1095	0.07	1.2	5.0	20.1
		278605	18.9	20692	171.4	229.7	625253	7.4	6.0	95.5	1.4	1085	0.02	1.6	1.1	2.4
Pale Bidau	Light domains-coarse grains	227075	22.7	26710	142.6	20.0	626392	13.6	13.8	0.4	4.3	1586	4.40	2.3	4.4	12.1
		225048	26.0	26058	141.7	11.1	629854	5.7	5.5	0.2	1.5	1585	6.21	1.1	0.8	3.2
		218609	24.1	24584	130.5	7.8	629646	2.4	2.4	0.2	1.6	1584	6.09	1.0	0.8	3.0
		223587	22.8	24540	132.5	9.7	629914	2.3	2.2	0.3	2.5	1573	5.34	1.7	2.0	8.3
		222428	23.1	26700	143.3	4.7	625508	1.4	1.3	0.1	1.3	1558	2.57	1.0	0.3	1.9
		224490	24.4	24956	136.6	13.0	626989	5.7	5.4	1.0	3.4	1583	3.83	2.2	3.3	12.2
		227441	23.4	25064	137.7	12.7	627549	10.5	10.5	0.2	1.8	1602	4.27	1.2	1.2	4.3
		226121	27.4	27953	154.5	15.2	626354	6.1	6.0	0.2	3.3	1635	4.70	1.8	2.7	10.6
		229276	29.7	27976	157.7	10.6	623396	5.7	5.4	0.2	1.9	1658	3.68	1.4	1.0	5.4
		233230	27.5	27680	154.6	10.7	626797	6.5	6.3	0.2	1.5	1634	4.63	1.0	0.9	3.4
		225045	24.4	26246	147.8	11.6	623429	9.0	9.2	0.1	1.4	1577	3.87	0.7	0.6	2.6
		229823	34.3	29740	175.9	59.1	622995	53.0	53.8	3.0	9.1	1756	0.13	4.7	7.2	24.2
		227187	31.5	30501	184.6	106.9	619529	125.0	127.9	0.5	2.0	1787	0.37	0.7	0.7	3.7
		230037	32.3	30200	183.3	108.0	617428	129.7	131.8	0.1	2.0	1827	0.36	0.8	0.5	3.2
Victoria	Recrystallized grains	243037	256.6	26504	92.3	12.1	611699	1.2	0.8	<LOD	8.5	919	0.60	1.8	3.7	41.8
		249431	252.3	25239	89.8	7.8	608276	1.2	1.0	<LOD	5.4	913	0.52	1.4	3.5	27.0
		248918	267.4	26750	90.1	18.6	606274	0.8	0.6	<LOD	13.8	949	0.55	2.4	7.1	70.9
		245215	262.5	25630	91.7	16.5	610786	0.9	0.6	<LOD	12.2	945	0.55	2.3	6.6	62.9

Victoria		242942	260.0	27069	88.4	8.9	607974	1.3	1.2	<LOD	4.9	940	0.52	1.4	2.6	25.6
		256952	267.7	26930	91.3	15.1	610250	0.9	0.7	<LOD	11.1	943	0.59	2.5	6.2	56.2
		260557	268.9	26568	98.1	23.5	608419	1.4	1.2	<LOD	14.6	948	0.62	2.5	7.8	73.1
	Coarse grains	242840	472.7	47426	164.7	10.5	577633	9.8	9.7	<LOD	1.2	1523	0.76	0.4	0.2	2.5
		246682	468.9	47191	166.5	20.1	576163	11.3	10.6	<LOD	4.5	1481	0.68	0.6	2.2	18.3
		251850	504.7	50536	178.1	15.0	576952	15.0	14.7	<LOD	0.9	1434	0.74	0.2	<LOD	0.6
		247505	552.0	52251	183.9	16.4	578123	14.5	14.2	<LOD	1.2	1495	0.79	0.1	0.2	2.3
Margalida	Recrystallized grains	227831	229.8	54427	89.4	10.8	582370	2.8	2.7	<LOD	9.9	1551	<LOD	0.4	7.0	8.0
		230817	230.3	53552	84.7	5.1	589102	1.8	2.1	<LOD	1.8	1492	<LOD	0.1	0.2	1.5
		232839	236.2	53617	83.7	6.3	589342	2.0	1.8	<LOD	2.3	1511	<LOD	0.2	0.2	1.1
		238177	209.7	50563	80.6	25.1	590879	4.4	5.1	<LOD	23.2	1485	<LOD	0.7	17.0	17.9
		241715	216.2	52050	81.5	17.2	584966	5.4	5.4	<LOD	13.4	1489	<LOD	0.4	8.6	11.0
		245613	226.8	48860	79.3	17.9	584856	5.1	5.5	<LOD	11.5	1542	<LOD	0.4	6.4	11.4
		246778	208.1	47230	77.4	14.5	585846	1.8	1.8	<LOD	19.2	1520	<LOD	0.6	14.2	81.7
		252659	177.5	42421	70.3	22.1	583325	0.5	<LOD	<LOD	42.6	1578	<LOD	1.8	44.6	4.5
		255357	206.9	43397	73.4	9.9	583325	3.4	3.2	<LOD	3.7	1568	<LOD	0.3	1.0	3.7
Bentaillou	Coarse grains	250926	284.6	37709	94.5	4.6	593659	1.0	0.9	<LOD	0.8	2165	1.07	0.2	<LOD	<LOD
		251532	289.4	38062	94.2	5.4	591000	1.3	1.2	<LOD	0.8	2141	1.02	0.2	0.2	0.2
		250142	288.5	36512	95.9	8.8	593758	0.9	0.8	<LOD	6.3	2172	1.07	0.4	3.6	5.4
		254588	299.9	37486	95.7	4.8	591526	1.0	1.0	<LOD	0.8	2154	1.08	0.2	0.1	0.2
		251468	306.7	41096	99.6	4.2	593349	1.4	1.3	<LOD	0.7	2126	1.10	0.2	<LOD	<LOD
		247818	277.6	36674	90.7	3.9	593520	1.3	1.3	<LOD	0.7	2117	1.10	0.2	<LOD	<LOD
		246018	282.0	37676	93.5	7.6	593028	0.7	0.6	<LOD	3.8	2142	1.09	0.4	7.3	2.6
		253104	304.7	39491	96.6	3.0	590901	0.6	0.7	<LOD	0.8	2102	1.10	0.2	<LOD	<LOD
		254077	263.2	41446	87.0	2.5	589281	0.6	0.6	<LOD	0.8	2161	1.07	0.0	0.1	0.1
		253059	265.6	35366	84.2	3.0	592289	0.6	0.4	<LOD	0.9	2188	1.05	0.2	0.4	0.6
		250675	243.5	34996	80.3	2.5	589816	0.9	0.8	<LOD	0.8	2187	1.03	0.1	0.3	0.8
		252247	273.0	33720	80.9	2.5	590923	0.9	0.7	<LOD	0.8	2193	1.07	0.2	0.1	0.2
	Type 1 disseminated	209949	171.1	39404	100.4	12.0	592975	28.8	2.9	<LOD	4.6	1904	0.98	1.2	7.1	503.2
		203360	138.4	34550	72.8	7.6	584228	3.5	0.7	<LOD	2.9	1931	0.91	0.9	3.9	169.1
		204455	163.1	39556	87.7	69.8	589383	10.5	2.5	<LOD	10.2	1833	0.88	3.7	23.8	106.2
		206852	162.1	44964	95.9	23.9	588310	6.4	1.5	<LOD	7.6	1837	0.94	2.5	13.2	331.6

		213062	138.4	35202	80.0	39.8	591454	19.4	4.0	<LOD	10.6	1866	0.84	3.2	16.3	150.3
		200802	159.2	33096	81.5	14.8	589383	1.7	0.8	<LOD	2.5	1925	0.96	0.4	3.2	172.7
		207419	140.9	41611	89.1	37.5	589383	13.7	3.5	<LOD	12.0	1894	0.91	3.0	18.4	436.5
Detection limit (ppm)																
Deposit	Texture	S34	Mn55	Fe57	Co59	Cu63	Zn64	Ga69	Ga71	Ge74	Ag107	Cd111	In115	Sn118	Sb121	Pb208
Anglas	Recrystallized grains	86.5	0.20	12.90	0.27	0.16	0.73	0.07	0.03	0.15	0.02	0.11	0.01	0.05	0.01	0.015
		1527.2	3.70	233.61	4.63	2.86	12.42	1.31	0.47	2.71	0.32	1.90	0.23	0.80	0.23	0.088
		52.3	0.13	7.95	0.16	0.10	0.42	0.04	0.02	0.09	0.01	0.07	0.01	0.03	0.01	0.003
		79.8	0.19	11.94	0.24	0.15	0.65	0.07	0.03	0.14	0.02	0.11	0.01	0.04	0.01	0.004
		94.4	0.23	14.12	0.29	0.17	0.82	0.08	0.03	0.17	0.02	0.13	0.02	0.05	0.01	0.005
		97.4	0.23	14.47	0.30	0.18	0.83	0.08	0.03	0.17	0.02	0.14	0.02	0.05	0.01	0.005
		182.9	0.44	27.67	0.56	0.33	1.58	0.15	0.06	0.32	0.04	0.25	0.03	0.10	0.03	0.010
		90.5	0.22	13.95	0.29	0.17	0.82	0.08	0.03	0.16	0.02	0.13	0.01	0.05	0.01	0.005
		91.8	0.23	14.20	0.29	0.17	0.99	0.08	0.03	0.16	0.02	0.15	0.02	0.05	0.01	0.005
		78.0	0.19	12.03	0.25	0.15	0.79	0.07	0.03	0.14	0.02	0.12	0.01	0.04	0.01	0.004
		133.0	0.33	20.67	0.43	0.26	1.25	0.12	0.05	0.24	0.03	0.20	0.02	0.07	0.02	0.007
		94.8	0.24	14.56	0.32	0.18	1.00	0.09	0.03	0.17	0.02	0.16	0.02	0.05	0.01	0.005
		112.4	0.28	17.32	0.38	0.21	1.22	0.10	0.04	0.20	0.02	0.18	0.02	0.06	0.02	0.006
		102.7	0.25	16.06	0.35	0.20	1.05	0.10	0.04	0.19	0.02	0.16	0.02	0.05	0.02	0.005
		99.8	0.25	15.42	0.34	0.19	1.05	0.09	0.03	0.18	0.02	0.16	0.02	0.05	0.02	0.005
Arre	Recrystallized grains	91.1	0.17	15.43	0.41	0.21	0.47	0.11	0.02	0.17	0.03	0.10	0.02	0.06	0.01	0.006
		69.7	0.13	12.17	0.38	0.18	0.61	0.10	0.02	0.13	0.02	0.11	0.02	0.04	0.01	0.005
		72.9	0.13	12.74	0.39	0.19	0.67	0.10	0.02	0.13	0.03	0.13	0.02	0.04	0.01	0.005
		73.2	0.13	12.72	0.39	0.19	0.67	0.10	0.03	0.14	0.02	0.12	0.02	0.04	0.01	0.005
		63.3	0.11	10.73	0.34	0.16	0.59	0.09	0.02	0.12	0.02	0.11	0.01	0.04	0.01	0.005
		76.4	0.14	13.45	0.43	0.21	0.74	0.12	0.03	0.14	0.03	0.14	0.02	0.05	0.02	0.005
		83.7	0.15	14.74	0.47	0.23	0.82	0.13	0.03	0.16	0.03	0.15	0.02	0.05	0.02	0.006
		76.2	0.13	13.32	0.43	0.21	0.75	0.12	0.03	0.14	0.03	0.15	0.02	0.05	0.02	0.006
		81.4	0.15	14.97	0.48	0.23	0.85	0.13	0.03	0.16	0.03	0.16	0.02	0.05	0.02	0.006
		86.2	0.08	13.79	4.91	2.26	0.85	0.42	0.38	0.36	0.30	0.16	0.03	0.10	0.45	2.260
		79.9	0.14	13.87	0.45	0.22	0.80	0.12	0.03	0.15	0.03	0.15	0.02	0.05	0.02	0.006
		72.6	0.13	12.55	0.40	0.20	0.74	0.11	0.02	0.13	0.03	0.14	0.02	0.04	0.02	0.006

		72.4	0.10	12.45	5.28	4.47	0.73	0.39	0.35	0.86	0.64	0.15	0.04	0.15	0.91	6.470
		81.7	0.14	14.47	0.45	0.22	0.83	0.13	0.03	0.15	0.03	0.16	0.02	0.05	0.02	0.006
Pale Bidau	Recrystallized grains	84.4	0.19	14.08	0.24	0.15	0.79	0.08	0.03	0.17	0.02	0.14	0.01	0.04	0.01	0.007
		69.7	0.16	11.47	0.20	0.12	0.67	0.07	0.03	0.14	0.01	0.12	0.01	0.04	0.01	0.004
		57.6	0.13	9.46	0.17	0.10	0.56	0.05	0.02	0.12	0.01	0.10	0.01	0.03	0.01	0.003
		81.0	0.19	13.28	0.23	0.14	0.84	0.08	0.03	0.16	0.02	0.14	0.01	0.04	0.01	0.004
		72.5	0.16	11.87	0.21	0.13	0.77	0.07	0.03	0.14	0.01	0.13	0.01	0.04	0.01	0.004
		63.6	0.14	10.34	0.18	0.11	0.62	0.06	0.02	0.13	0.01	0.11	0.01	0.03	0.01	0.004
		82.1	0.19	13.29	0.23	0.14	0.81	0.08	0.03	0.16	0.02	0.14	0.01	0.04	0.01	0.013
		64.8	0.15	10.41	0.18	0.11	0.64	0.06	0.02	0.13	0.01	0.11	0.01	0.03	0.01	0.009
		92.0	0.21	14.77	0.26	0.16	0.92	0.09	0.04	0.18	0.02	0.16	0.01	0.05	0.01	0.010
		72.1	0.17	11.53	0.21	0.13	0.74	0.07	0.03	0.15	0.02	0.13	0.01	0.04	0.01	0.007
		51.0	0.12	8.10	0.15	0.09	0.54	0.05	0.02	0.10	0.01	0.09	0.01	0.03	0.01	0.004
		62.8	0.15	9.93	0.19	0.11	0.66	0.06	0.03	0.13	0.01	0.11	0.01	0.03	0.01	0.005
Anglas	Dark domains-coarse grains	100.3	0.22	14.07	0.28	0.17	0.46	0.08	0.03	0.16	0.02	0.08	0.01	0.06	0.01	0.005
		98.6	0.22	13.78	0.28	0.17	0.56	0.08	0.03	0.17	0.02	0.10	0.01	0.05	0.01	0.005
		76.8	0.17	11.00	0.22	0.13	0.48	0.06	0.02	0.13	0.02	0.08	0.01	0.04	0.01	0.004
		106.0	0.23	15.15	0.30	0.19	0.71	0.08	0.03	0.18	0.02	0.12	0.01	0.06	0.01	0.006
		71.2	0.16	10.23	0.21	0.12	0.52	0.06	0.02	0.12	0.01	0.09	0.01	0.04	0.01	0.004
		96.3	0.22	14.14	0.28	0.17	0.74	0.08	0.03	0.16	0.02	0.12	0.01	0.05	0.01	0.005
		91.9	0.21	13.53	0.27	0.17	0.73	0.08	0.03	0.16	0.02	0.11	0.01	0.05	0.01	0.005
		90.8	0.21	13.56	0.28	0.17	0.75	0.08	0.03	0.16	0.02	0.12	0.01	0.05	0.01	0.005
		86.1	0.20	12.95	0.27	0.16	0.77	0.07	0.03	0.15	0.02	0.11	0.01	0.05	0.01	0.004
		57.4	0.14	8.67	0.18	0.11	0.49	0.05	0.02	0.10	0.01	0.08	0.01	0.03	0.01	0.003
		93.5	0.23	14.52	0.31	0.18	0.97	0.08	0.03	0.17	0.02	0.15	0.02	0.05	0.01	0.005
		96.7	0.24	14.83	0.32	0.18	0.95	0.09	0.03	0.17	0.02	0.15	0.02	0.05	0.02	0.005
		95.2	0.24	14.83	0.32	0.18	1.01	0.09	0.03	0.17	0.02	0.16	0.02	0.05	0.01	0.005
		98.0	0.25	15.52	0.33	0.19	1.10	0.09	0.03	0.18	0.02	0.16	0.02	0.05	0.02	0.005
		95.5	0.24	14.78	0.32	0.18	0.99	0.09	0.03	0.17	0.02	0.15	0.02	0.05	0.02	0.005
		92.0	0.23	14.17	0.31	0.18	0.97	0.09	0.03	0.16	0.02	0.14	0.02	0.05	0.01	0.005
		99.8	0.24	15.27	0.34	0.19	1.14	0.09	0.03	0.18	0.02	0.17	0.02	0.05	0.02	0.005
		94.4	0.23	14.67	0.32	0.18	1.06	0.09	0.03	0.17	0.02	0.15	0.02	0.05	0.02	0.005
		109.6	0.20	18.55	0.54	0.27	0.75	0.14	0.03	0.20	0.04	0.15	0.02	0.07	0.02	0.007

Arre	Dark domains-coarse grains	93.4	0.17	15.93	0.47	0.23	0.70	0.12	0.03	0.18	0.03	0.14	0.02	0.06	0.01	0.007
		86.6	0.16	14.81	0.44	0.22	0.67	0.11	0.02	0.16	0.03	0.12	0.02	0.05	0.01	0.007
		109.9	0.20	18.80	0.55	0.27	0.88	0.14	0.03	0.20	0.04	0.16	0.02	0.07	0.02	0.008
		91.2	0.17	15.54	0.47	0.23	0.75	0.12	0.03	0.17	0.03	0.14	0.02	0.06	0.02	0.007
		74.4	0.13	12.83	0.40	0.20	0.67	0.11	0.03	0.14	0.03	0.12	0.02	0.05	0.01	0.006
		73.0	0.13	12.77	0.39	0.19	0.69	0.11	0.02	0.13	0.03	0.13	0.02	0.04	0.01	0.005
		102.5	0.18	17.80	0.55	0.27	0.97	0.15	0.04	0.19	0.04	0.18	0.02	0.06	0.02	0.007
		99.2	0.18	17.25	0.55	0.26	0.95	0.14	0.03	0.18	0.04	0.17	0.02	0.06	0.02	0.007
		73.9	0.13	12.94	0.40	0.19	0.74	0.11	0.02	0.14	0.03	0.13	0.02	0.05	0.01	0.005
		72.0	0.13	12.45	0.39	0.19	0.71	0.11	0.03	0.13	0.03	0.13	0.02	0.04	0.01	0.005
		76.9	0.14	13.30	0.42	0.20	0.77	0.11	0.03	0.14	0.03	0.15	0.02	0.05	0.02	0.005
		79.1	0.14	13.96	0.44	0.21	0.74	0.12	0.03	0.15	0.03	0.14	0.02	0.05	0.02	0.006
		77.4	0.14	13.60	0.40	0.21	0.74	0.12	0.03	0.14	0.03	0.14	0.02	0.05	0.02	0.006
		74.8	0.13	13.08	0.40	0.20	0.73	0.11	0.03	0.14	0.03	0.14	0.02	0.05	0.02	0.005
		78.0	0.14	13.65	0.45	0.21	0.81	0.13	0.03	0.14	0.03	0.15	0.02	0.05	0.02	0.005
		84.4	0.15	14.88	0.49	0.23	0.89	0.13	0.03	0.16	0.03	0.16	0.02	0.05	0.02	0.006
Pale Bidau	Dark domains-coarse grains	90.2	0.21	14.47	0.26	0.16	0.91	0.09	0.04	0.18	0.02	0.16	0.01	0.05	0.01	0.009
		79.0	0.20	3.27	0.26	0.16	0.91	0.09	0.04	0.18	0.02	0.18	0.01	0.05	0.01	0.009
		101.3	0.20	25.57	0.26	0.15	0.91	0.09	0.04	0.18	0.02	0.17	0.01	0.05	0.01	0.010
		141.4	0.19	65.67	0.26	0.17	0.91	0.09	0.04	0.18	0.02	0.16	0.01	0.05	0.01	0.009
Anglas	Light domains-coarse grains	94.2	0.24	14.47	0.31	0.18	0.89	0.09	0.03	0.17	0.02	0.14	0.02	0.05	0.01	0.005
		93.2	0.23	14.24	0.31	0.18	0.93	0.08	0.03	0.17	0.02	0.15	0.02	0.05	0.01	0.005
		92.3	0.23	14.20	0.31	0.18	0.94	0.09	0.03	0.17	0.02	0.14	0.02	0.05	0.01	0.004
		97.1	0.24	15.01	0.32	0.19	0.98	0.09	0.03	0.18	0.02	0.14	0.02	0.05	0.02	0.005
		98.8	0.24	15.29	0.34	0.19	1.08	0.09	0.03	0.18	0.02	0.17	0.02	0.05	0.02	0.005
		96.4	0.24	14.97	0.32	0.18	1.07	0.09	0.03	0.18	0.02	0.16	0.02	0.05	0.02	0.005
		98.2	0.24	15.14	0.34	0.19	1.15	0.09	0.04	0.17	0.02	0.16	0.02	0.05	0.02	0.005
Arre	Light domains-coarse grains	72.2	0.13	12.48	0.30	0.17	0.28	0.09	0.02	0.14	0.02	0.07	0.01	0.05	0.01	0.006
		91.1	0.17	15.43	0.41	0.21	0.47	0.11	0.02	0.17	0.03	0.10	0.02	0.06	0.01	0.006
		89.6	0.16	15.11	0.43	0.21	0.55	0.11	0.02	0.17	0.03	0.11	0.02	0.06	0.01	0.007
		71.9	0.13	12.43	0.37	0.18	0.61	0.10	0.02	0.13	0.02	0.11	0.02	0.04	0.01	0.005
		83.9	0.14	14.71	0.48	0.23	0.86	0.13	0.03	0.16	0.03	0.16	0.02	0.05	0.02	0.006
		72.4	0.15	12.26	0.16	0.11	0.35	0.06	0.02	0.14	0.01	0.06	0.01	0.04	0.01	0.004

Pale Bidau	Light domains-coarse grains	75.6	0.16	12.77	0.17	0.11	0.43	0.06	0.02	0.14	0.01	0.08	0.01	0.04	0.01	0.003
		95.0	0.20	16.12	0.22	0.15	0.62	0.08	0.03	0.18	0.02	0.11	0.01	0.05	0.01	0.004
		95.1	0.21	16.34	0.23	0.15	0.66	0.08	0.03	0.18	0.02	0.12	0.01	0.05	0.01	0.004
		72.8	0.16	12.43	0.18	0.11	0.53	0.06	0.02	0.14	0.01	0.09	0.01	0.04	0.01	0.004
		93.5	0.20	16.10	0.23	0.15	0.72	0.08	0.03	0.18	0.02	0.12	0.01	0.05	0.01	0.004
		101.5	0.22	17.26	0.26	0.17	0.81	0.09	0.04	0.20	0.02	0.14	0.01	0.05	0.01	0.005
		68.8	0.15	11.78	0.18	0.11	0.60	0.06	0.02	0.14	0.01	0.09	0.01	0.03	0.01	0.003
		75.2	0.17	12.91	0.20	0.13	0.66	0.07	0.03	0.15	0.01	0.11	0.01	0.04	0.01	0.003
		67.5	0.15	11.53	0.18	0.11	0.61	0.06	0.02	0.14	0.01	0.10	0.01	0.03	0.01	0.003
		72.8	0.16	12.46	0.20	0.12	0.66	0.07	0.03	0.14	0.01	0.11	0.01	0.04	0.01	0.003
		63.3	0.14	10.62	0.18	0.11	0.53	0.06	0.02	0.13	0.01	0.08	0.01	0.03	0.01	0.003
		66.1	0.15	11.04	0.18	0.12	0.58	0.06	0.02	0.13	0.01	0.10	0.01	0.03	0.01	0.003
		67.6	0.15	11.06	0.19	0.12	0.61	0.06	0.03	0.13	0.01	0.11	0.01	0.04	0.01	0.004
Victoria	Recrystallized grains	83.5	0.17	15.73	0.51	0.24	0.79	0.14	0.03	0.17	0.03	0.16	0.03	0.07	0.02	0.008
		96.5	0.20	17.78	0.61	0.27	0.91	0.16	0.04	0.20	0.04	0.20	0.03	0.08	0.02	0.009
		74.5	0.16	13.88	0.48	0.21	0.71	0.13	0.03	0.15	0.03	0.16	0.02	0.06	0.02	0.006
		81.7	0.17	15.31	0.53	0.23	0.86	0.14	0.03	0.17	0.03	0.17	0.03	0.07	0.02	0.007
		80.0	0.17	14.80	0.52	0.23	0.80	0.14	0.03	0.16	0.03	0.16	0.03	0.06	0.02	0.007
		80.7	0.17	15.19	0.53	0.23	0.82	0.14	0.03	0.17	0.03	0.17	0.03	0.06	0.02	0.005
		77.9	0.16	14.84	0.49	0.22	0.76	0.14	0.03	0.17	0.03	0.16	0.03	0.06	0.02	0.007
	Coarse grains	104.6	0.21	19.68	0.65	0.29	1.12	0.18	0.04	0.22	0.04	0.21	0.03	0.08	0.03	0.010
		100.1	0.21	18.85	0.65	0.28	1.00	0.17	0.04	0.21	0.04	0.20	0.03	0.08	0.03	0.008
		86.8	0.18	16.10	0.57	0.24	0.86	0.15	0.03	0.18	0.04	0.19	0.03	0.07	0.02	0.008
		93.0	0.19	17.49	0.62	0.26	0.94	0.17	0.04	0.20	0.04	0.21	0.03	0.07	0.02	0.008
Margalida	Recrystallized grains	102.0	0.17	15.21	15.20	0.91	0.93	0.63	0.39	0.31	0.42	0.24	0.03	0.12	0.50	2.100
		101.3	0.14	10.23	14.76	0.39	0.92	0.41	0.28	0.15	0.08	0.23	0.02	0.05	0.02	0.410
		95.6	0.12	14.23	15.08	0.50	0.92	0.47	0.25	0.18	0.11	0.23	0.02	0.06	0.03	0.320
		96.5	0.23	17.20	15.06	1.68	0.84	1.04	0.69	0.15	0.79	0.24	0.02	0.07	1.26	5.230
		96.8	0.28	17.30	15.84	1.23	0.52	1.32	0.77	0.18	0.48	0.25	0.02	0.07	0.67	3.350
		98.6	0.21	17.60	16.06	1.33	0.84	1.31	0.81	0.17	0.42	0.26	0.02	0.06	0.52	3.640
		100.2	0.23	17.80	16.33	1.14	0.54	0.49	0.29	0.18	0.69	0.28	0.03	0.07	1.18	27.35
		104.3	0.24	17.40	15.46	1.74	0.64	0.18	0.09	0.18	1.49	0.27	0.03	0.13	3.84	1.567
		93.0	0.27	14.60	17.55	0.89	0.63	1.04	0.55	0.16	0.15	0.21	0.02	0.06	0.10	1.410

Bentaillou	Coarse grains	72.2	0.16	10.72	0.21	0.15	0.57	0.07	0.03	0.13	0.02	0.11	0.01	0.05	0.01	0.005
		63.3	0.14	9.44	0.19	0.13	0.52	0.06	0.02	0.12	0.01	0.11	0.01	0.04	0.01	0.004
		77.7	0.17	11.76	0.23	0.16	0.65	0.07	0.03	0.15	0.02	0.14	0.01	0.05	0.01	0.005
		71.6	0.16	10.81	0.21	0.15	0.61	0.07	0.03	0.14	0.02	0.13	0.01	0.04	0.01	0.004
		60.4	0.14	9.24	0.18	0.13	0.53	0.06	0.02	0.11	0.01	0.11	0.01	0.04	0.01	0.004
		85.3	0.19	13.06	0.26	0.18	0.76	0.08	0.03	0.16	0.02	0.16	0.01	0.05	0.01	0.005
		82.2	0.19	12.75	0.25	0.17	0.74	0.08	0.03	0.16	0.02	0.16	0.01	0.05	0.01	0.005
		66.2	0.15	10.33	0.20	0.13	0.58	0.06	0.03	0.12	0.01	0.13	0.01	0.04	0.01	0.004
		69.4	0.16	10.89	0.21	0.14	0.62	0.07	0.03	0.14	0.01	0.13	0.01	0.05	0.01	0.005
		94.3	0.22	15.01	0.28	0.19	0.85	0.10	0.03	0.18	0.02	0.18	0.02	0.06	0.01	0.005
		88.0	0.21	13.95	0.27	0.18	0.80	0.09	0.03	0.17	0.02	0.17	0.02	0.05	0.01	0.005
		102.6	0.25	16.47	0.31	0.21	0.92	0.11	0.04	0.20	0.02	0.19	0.02	0.06	0.01	0.006
	Type 1 disseminated	494.0	1.36	114.64	1.83	1.25	4.63	0.64	0.24	1.09	0.13	0.90	0.10	0.34	0.09	0.030
		311.3	0.85	71.26	1.18	0.79	2.89	0.41	0.16	0.69	0.08	0.60	0.07	0.21	0.06	0.020
		304.1	0.83	68.89	1.23	0.76	2.83	0.40	0.15	0.67	0.08	0.58	0.06	0.20	0.06	0.020
		310.8	0.85	72.37	1.26	0.80	2.90	0.41	0.15	0.70	0.09	0.59	0.07	0.21	0.06	0.019
		492.5	1.34	112.62	2.02	1.25	4.66	0.66	0.23	1.10	0.13	0.87	0.11	0.33	0.09	0.028
		312.6	0.85	72.51	1.28	0.81	2.91	0.41	0.15	0.69	0.08	0.58	0.07	0.21	0.06	0.018
		541.6	1.48	123.82	2.23	1.36	5.04	0.72	0.26	1.21	0.15	1.02	0.12	0.36	0.10	0.033
1 sigma error (ppm)																
Deposit	**Texture**	**S34**	**Mn55**	**Fe57**	**Co59**	**Cu63**	**Zn64**	**Ga69**	**Ga71**	**Ge74**	**Ag107**	**Cd111**	**In115**	**Sn118**	**Sb121**	**Pb208**
Anglas	Recrystallized grains	35683.6	12.7	1813.4	5.7	8.0	19114.7	1.6	1.8	1.8	0.1	83.7	0.14	0.1	0.7	1.7
		39479.7	7.4	979.1	7.1	4.2	19175.5	2.2	2.0	3.2	0.4	75.7	0.31	0.9	0.7	1.6
		34890.4	15.0	2150.8	7.2	4.6	19158.1	1.5	1.7	2.3	0.2	84.4	0.16	0.1	0.5	1.7
		36317.4	12.8	1848.9	6.0	4.3	19067.5	1.5	1.8	3.4	0.1	82.1	0.17	0.1	0.3	1.5
		35310.9	12.9	1818.1	5.8	4.2	19137.8	1.9	2.2	0.7	0.1	81.7	0.13	0.1	0.3	1.2
		35337.2	13.1	1854.1	6.0	5.1	19227.1	2.5	2.9	2.2	0.1	82.1	0.13	0.1	0.3	1.0
		34351.9	6.4	1075.1	4.4	4.2	18967.6	1.6	1.9	0.5	0.2	86.2	0.05	0.2	0.3	1.7
		35351.4	9.8	1621.1	6.3	6.1	18967.0	1.8	2.1	0.1	0.2	83.9	0.04	0.2	0.4	2.1
		36558.2	10.4	1693.1	6.6	4.3	19469.0	1.4	1.6	0.2	0.1	82.3	0.04	0.1	0.5	1.5
		36883.7	10.9	1755.0	6.9	4.3	19379.7	1.8	2.0	1.2	0.1	81.5	0.05	0.1	0.2	1.0
		35421.3	8.4	1400.2	5.8	5.4	19393.6	2.0	2.3	0.2	0.2	80.6	0.04	0.1	0.3	1.6

		37524.5	9.9	1646.4	5.9	5.7	19606.9	1.2	1.4	0.3	0.2	84.6	0.06	0.5	0.6	2.8
		36428.8	9.1	1498.9	5.4	4.3	19456.2	1.0	1.2	0.3	0.1	84.3	0.06	0.5	0.4	1.8
		37771.8	10.4	1612.5	5.5	3.5	19482.2	1.2	1.4	0.2	0.1	75.3	0.04	0.1	0.3	0.9
		37457.1	10.2	1589.6	5.4	3.8	19424.5	1.2	1.3	0.1	0.1	76.2	0.05	0.1	0.3	1.6
Arre	Recrystallized grains	43783.2	1.1	833.5	5.4	3.0	19833.6	0.5	0.5	0.5	0.4	183.1	0.01	0.1	0.6	4.9
		45880.3	1.0	1074.5	6.2	1.0	19702.7	0.1	0.1	0.2	0.1	171.4	0.02	0.1	0.2	0.4
		43753.9	1.1	1000.0	6.4	1.8	19599.9	0.1	0.1	0.2	0.2	165.9	0.02	0.1	0.2	1.3
		45327.9	1.4	1088.4	6.5	3.1	19659.4	0.2	0.2	0.3	0.4	172.4	0.02	0.1	0.6	4.0
		43839.7	1.3	1082.9	6.5	3.1	19600.0	0.4	0.3	0.3	0.3	177.2	0.02	0.1	0.4	3.3
		48383.4	1.1	935.8	6.1	2.5	19720.2	0.3	0.3	0.4	0.4	171.4	0.02	0.1	0.4	2.7
		47740.8	1.2	891.5	5.9	2.8	19699.1	0.3	0.3	0.4	0.4	170.7	0.02	0.1	0.5	3.1
		45725.1	1.1	891.8	6.1	2.3	19682.8	0.3	0.3	0.3	0.3	166.5	0.02	0.1	0.4	2.5
		48415.7	1.0	851.7	6.0	1.6	19701.0	0.4	0.4	0.2	0.2	162.7	0.03	0.1	0.2	1.4
		256573.1	1.4	816.6	5.2	2.5	19702.3	6.5	6.5	3.9	3.2	1073.4	0.04	0.6	5.9	17.2
		45908.8	1.2	883.0	5.8	4.0	19777.2	0.4	0.4	0.5	0.5	169.6	0.02	0.1	0.7	4.9
		47078.7	1.1	945.3	6.3	3.3	19748.1	0.4	0.4	0.4	0.5	166.8	0.03	0.1	0.8	4.1
		263132.0	1.7	856.5	5.2	5.0	62480.6	5.2	5.2	1.3	7.0	1046.1	0.05	1.3	12.0	49.3
		48232.7	1.0	1001.8	6.5	1.6	19684.2	0.2	0.1	0.2	0.2	173.2	0.03	0.1	0.2	1.3
Pale Bidau	Recrystallized grains	22474.5	3.3	2190.4	18.5	7.3	19780.1	3.0	2.8	0.5	2.5	266.4	0.12	0.7	2.2	11.8
		22458.2	3.5	2356.9	20.3	7.7	19762.2	2.5	2.5	0.6	3.0	273.3	0.11	0.9	2.4	12.6
		22761.5	3.8	2551.6	21.6	9.4	19762.3	3.3	3.2	0.6	3.2	277.9	0.11	0.9	2.5	13.9
		23886.5	3.2	2338.9	20.1	6.6	19762.2	3.0	3.0	0.4	2.0	290.2	0.12	0.6	1.7	8.9
		24034.1	3.3	2311.8	20.5	4.5	19941.8	7.6	7.4	0.7	2.9	284.8	0.06	0.9	2.6	10.7
		24913.0	4.3	2426.4	22.4	1.8	19895.2	10.3	10.0	0.7	5.2	291.2	0.06	1.5	5.4	3213.3
		25132.1	3.8	2310.4	21.6	8.1	19913.9	15.3	14.9	0.4	3.2	303.4	0.04	0.7	2.6	652.6
		25391.5	4.2	2399.7	22.9	8.1	19871.3	16.4	15.8	0.7	4.3	317.6	0.03	0.8	3.2	51.5
		26116.4	3.9	2187.7	20.9	3.3	19785.1	16.4	15.9	0.3	1.6	319.7	0.03	0.3	1.1	68.9
		26929.5	3.7	2521.4	23.8	5.0	19913.9	12.0	11.6	0.1	1.1	326.8	0.05	0.3	0.5	5.6
		26123.7	4.7	2707.6	25.9	2.8	19738.5	16.4	16.1	0.7	5.1	340.5	0.04	1.0	3.7	16.1
		28213.2	4.8	2543.4	25.5	24.1	19646.6	16.2	16.0	0.3	2.3	343.3	0.03	0.4	1.5	8.8
Anglas		33778.4	10.3	1642.0	4.8	44.1	18748.3	0.5	0.6	13.8	0.2	77.4	0.01	0.0	2.1	0.9
		34791.9	11.0	1683.3	4.9	55.6	19138.1	0.8	0.9	17.3	0.2	79.3	0.01	0.0	5.6	3.6
		34272.0	9.9	1652.9	5.1	48.7	19336.4	2.0	2.3	12.4	0.2	79.1	0.01	0.0	5.5	3.7

Anglas	Dark domains-coarse grains	35078.2	8.9	1518.5	4.6	56.0	19219.1	2.2	2.5	15.5	0.2	78.3	0.01	0.0	6.5	3.2
		35618.1	9.9	1725.2	5.2	51.6	19219.1	2.0	2.3	13.5	0.2	78.9	0.01	0.0	9.3	3.9
		35310.3	11.9	1778.0	5.7	33.6	19143.1	1.8	2.1	9.7	0.2	81.6	0.21	0.5	1.8	1.5
		35344.7	11.7	1732.6	5.6	50.5	19082.0	1.1	1.3	14.3	0.2	80.1	0.29	1.3	4.9	3.3
		35199.6	11.7	1735.6	5.6	32.1	19097.3	0.7	0.8	10.7	0.1	79.3	0.24	1.3	1.7	1.0
		36081.9	12.0	1788.2	5.8	26.2	19093.2	0.9	1.1	12.2	0.2	79.8	0.19	1.2	0.7	1.5
		35914.7	14.2	2068.8	6.5	24.7	19186.6	1.2	1.4	10.4	0.1	80.6	0.16	0.4	1.7	1.2
		35486.3	8.6	1561.0	6.5	61.1	19309.6	3.3	3.7	18.0	0.6	79.9	0.04	0.3	0.7	4.7
		36896.1	8.8	1554.9	6.1	38.6	19600.5	6.1	7.1	12.0	0.3	79.4	0.16	2.4	0.1	0.8
		37158.0	9.6	1572.2	5.6	45.6	19358.7	1.9	2.2	13.5	0.2	79.7	0.04	0.2	5.1	3.4
		36788.9	9.6	1587.2	5.5	45.2	19380.3	0.9	1.1	12.6	0.2	79.1	0.02	0.1	7.4	5.7
		37611.6	11.3	1716.9	5.5	19.4	19274.5	1.7	2.0	5.5	0.2	82.2	0.02	0.0	0.4	0.2
		37098.5	5.4	1295.4	5.4	59.1	19562.2	1.0	1.1	15.7	0.2	75.8	0.01	0.0	11.0	7.8
		37808.9	5.5	1314.7	5.5	71.2	19643.2	1.5	1.7	19.5	0.2	74.2	0.01	0.0	11.1	6.5
		37522.6	6.7	1398.1	5.5	55.4	19590.6	3.4	4.0	21.4	0.2	76.7	0.01	0.2	2.8	1.2
Arre	Dark domains-coarse grains	43432.7	0.9	764.7	5.0	48.9	19843.0	0.4	0.4	16.6	0.3	181.4	0.01	0.3	0.3	2.1
		43182.6	1.0	813.8	5.3	90.2	19758.5	0.5	0.4	27.8	0.3	180.7	0.01	0.3	0.2	1.2
		44025.1	1.0	815.2	5.2	80.1	19690.6	0.3	0.3	23.5	0.3	181.0	0.01	0.3	0.2	1.4
		44145.1	0.9	844.9	5.1	40.8	19668.0	0.3	0.3	12.4	0.2	175.9	0.01	0.0	0.5	0.3
		43740.9	1.0	901.6	5.5	46.3	19624.4	0.4	0.3	13.4	0.2	172.6	0.01	0.0	0.7	0.3
		45878.2	1.1	1012.8	6.2	49.4	19810.6	0.1	0.0	13.1	0.2	170.3	0.01	0.0	0.1	0.2
		45635.4	1.1	1074.2	6.4	99.1	19776.0	0.3	0.3	26.2	0.2	175.1	0.02	0.5	0.2	0.9
		43647.2	0.8	786.9	5.2	67.4	19623.3	0.4	0.4	21.0	0.2	176.0	0.02	0.6	0.1	0.8
		44498.8	0.8	797.0	5.4	104.0	19712.8	0.5	0.4	31.5	0.2	170.9	0.02	0.1	0.4	0.4
		45248.3	0.9	905.3	6.1	112.0	19600.1	0.4	0.4	29.4	0.3	172.1	0.02	0.2	0.2	0.5
		44410.4	0.9	882.4	6.0	108.4	19526.2	0.6	0.5	28.6	0.2	168.2	0.02	0.3	0.2	0.5
		44703.0	1.0	884.5	6.1	92.0	19616.8	0.6	0.6	25.1	0.4	171.1	0.02	0.9	0.4	3.3
		46763.0	0.9	866.2	6.0	76.9	19612.4	0.6	0.6	23.5	0.3	165.1	0.02	0.8	0.2	2.0
		48206.5	0.9	850.9	5.9	99.8	19571.1	0.3	0.3	28.3	0.3	158.4	0.02	0.1	0.3	0.5
		47543.4	0.9	862.8	5.8	80.4	19568.3	0.3	0.3	22.0	0.3	158.7	0.02	0.2	0.2	1.0
		51137.6	1.1	1016.6	6.1	108.2	19783.6	0.4	0.3	27.6	0.6	168.5	0.02	0.1	0.5	0.7
		45796.2	1.1	1042.2	6.3	89.6	19773.0	0.4	0.3	22.7	0.5	175.1	0.03	0.1	0.9	0.8
		26092.6	3.6	2382.2	22.2	25.9	19914.4	12.9	12.6	19.9	1.6	316.4	0.06	1.0	0.7	7.8

Pale Bidau	Dark domains-coarse grains	26097.7	3.6	2381.2	22.3	23.5	19915.5	13.0	12.7	19.9	1.6	317.3	0.05	1.1	0.7	7.5
		26097.6	3.5	2387.3	22.1	21.3	19919.3	12.3	12.4	19.8	1.7	319.4	0.06	1.1	0.6	7.5
		26098.4	3.6	2382.8	22.6	26.3	19916.2	13.3	12.5	19.6	1.4	324.6	0.05	1.1	0.9	7.7
Anglas	Light domains-coarse grains	36278.5	8.1	1524.9	6.4	21.4	19457.6	2.9	3.4	5.9	0.2	79.3	0.02	0.3	0.2	2.4
		37251.4	5.8	1370.3	6.1	20.5	19473.0	4.5	5.3	4.1	0.2	78.0	0.02	0.8	0.3	0.3
		36860.3	5.1	1309.2	5.9	16.2	19675.2	3.9	4.5	3.3	0.1	76.5	0.01	0.1	0.3	0.1
		36828.1	11.3	1703.3	5.5	17.1	19342.5	2.3	2.6	7.3	0.1	82.2	0.01	0.1	0.6	0.3
		38005.7	5.5	1301.3	5.5	4.7	19615.3	0.2	0.3	1.1	0.2	74.8	0.01	0.0	0.1	1.1
		37833.3	5.9	1332.6	5.4	6.6	19708.6	0.3	0.3	1.2	0.3	75.2	0.01	0.0	0.2	3.4
		37688.4	6.0	1345.2	5.5	5.6	19675.7	0.2	0.2	1.0	0.3	77.6	0.01	0.0	0.2	2.9
Arre	Light domains-coarse grains	42400.5	1.1	827.2	5.7	9.0	19752.5	0.9	0.8	2.3	0.4	185.4	0.01	0.1	0.4	4.1
		44147.5	1.1	817.9	5.1	5.5	19750.4	0.5	0.4	1.1	0.3	188.6	0.01	0.1	0.4	3.6
		43497.6	1.0	1005.4	6.0	16.4	19688.1	0.4	0.4	4.0	0.2	174.8	0.01	0.0	0.7	0.3
		48516.5	1.1	971.4	6.2	9.1	19704.1	0.5	0.5	2.0	0.3	171.9	0.03	0.1	0.4	2.6
		48928.5	1.1	1023.5	6.6	20.4	19773.1	0.5	0.4	5.3	0.2	170.5	0.03	0.2	0.1	0.3
Pale Bidau	Light domains-coarse grains	17690.4	2.6	2286.5	15.8	2.6	19808.4	1.0	1.0	0.1	0.6	207.1	0.20	0.2	0.5	2.8
		17625.5	3.0	2235.2	15.8	1.5	19917.9	0.4	0.4	0.1	0.2	208.6	0.28	0.1	0.1	0.7
		17232.1	2.8	2115.9	14.7	1.0	19911.3	0.2	0.2	0.1	0.2	210.5	0.27	0.1	0.1	0.7
		17758.8	2.7	2122.2	15.0	1.3	19919.7	0.2	0.2	0.1	0.4	211.5	0.24	0.2	0.2	2.0
		17820.7	2.7	2322.9	16.4	0.7	19780.5	0.1	0.1	0.1	0.2	211.9	0.12	0.1	0.0	0.5
		18160.4	2.9	2186.5	15.8	1.8	19827.3	0.5	0.4	0.2	0.5	218.1	0.18	0.2	0.4	2.9
		18595.4	2.8	2213.8	16.1	1.8	19845.0	0.8	0.8	0.1	0.3	224.0	0.20	0.1	0.1	1.1
		18701.4	3.3	2491.8	18.4	2.1	19807.2	0.5	0.5	0.1	0.5	232.0	0.22	0.2	0.3	2.6
		19197.1	3.7	2518.8	19.0	1.5	19713.7	0.5	0.4	0.1	0.3	239.1	0.17	0.1	0.1	1.4
		19784.7	3.4	2519.3	18.9	1.6	19821.3	0.5	0.5	0.1	0.2	239.6	0.22	0.1	0.1	0.9
		19354.1	3.1	2416.2	18.3	1.7	19714.7	0.8	0.7	0.1	0.2	235.3	0.19	0.1	0.1	0.7
		21337.8	4.7	2922.5	23.8	0.4	19701.0	0.5	4.6	0.4	1.6	288.2	0.01	0.5	1.0	7.0
		21443.9	4.4	3040.2	25.4	0.5	19591.4	0.8	11.0	0.1	0.4	299.3	0.02	0.1	0.1	1.1
		22079.6	4.6	3053.7	25.7	0.2	19525.0	0.6	11.5	0.1	0.4	312.3	0.02	0.1	0.1	1.0
Victoria	Recrystallized Grains	25698.4	13.1	1668.0	5.6	1.0	19344.1	0.2	0.1	0.2	0.4	84.4	0.06	0.1	0.2	3.7
		26373.6	12.9	1587.4	5.4	0.7	19235.6	0.1	0.1	0.1	0.3	83.8	0.05	0.1	0.2	2.4
		26320.0	13.7	1683.3	5.4	1.5	19172.5	0.1	0.1	0.2	0.7	87.1	0.06	0.1	0.3	6.2

Victoria	Recrystallized grains	25928.1	13.4	1612.3	5.5	1.3	19315.1	0.1	0.1	0.1	0.6	86.7	0.06	0.1	0.3	5.5
		25688.0	13.3	1702.9	5.3	0.8	19226.2	0.2	0.1	0.1	0.3	86.3	0.05	0.1	0.1	2.3
		27169.6	13.7	1694.7	5.5	1.2	19298.3	0.2	0.1	0.2	0.6	86.6	0.06	0.1	0.3	5.0
		27550.4	13.8	1671.6	5.9	1.9	19240.3	0.2	0.1	0.2	0.7	87.0	0.06	0.1	0.4	6.4
	Coarse grains	25676.8	24.2	2981.6	9.9	0.9	18266.6	0.6	0.6	0.2	0.1	139.7	0.07	0.1	0.0	0.2
		26083.1	24.0	2967.0	10.0	1.6	18220.2	0.7	0.7	0.2	0.2	135.9	0.07	0.1	0.1	1.6
		26630.2	25.8	3178.1	10.7	1.2	18245.3	0.9	0.9	0.2	0.1	131.6	0.07	0.1	0.0	0.1
		26170.6	28.2	3285.6	11.0	1.3	18282.3	0.9	0.9	0.2	0.1	137.2	0.08	0.1	0.0	0.2
Margalida	Recrystallized grains	22783.1	23.0	5442.7	2.4	0.8	18284.3	2.8	2.7	0.1	9.9	137.6	0.02	0.4	7.0	8.0
		23081.7	23.0	5355.2	2.7	0.5	18287.0	1.8	2.1	0.1	1.8	137.5	0.01	0.1	0.2	1.5
		23283.9	23.6	5361.7	2.7	0.6	18284.4	2.0	1.8	0.0	2.3	134.2	0.06	0.2	0.2	1.1
		23817.7	21.0	5056.3	2.6	0.3	18281.2	4.4	5.1	0.1	23.2	124.6	0.05	0.7	17.0	17.9
		24171.5	21.6	5205.0	1.5	1.7	18294.3	2.4	5.4	0.3	13.4	117.4	0.03	0.4	8.6	11.0
		24561.3	22.7	4886.0	2.3	1.8	18284.2	2.1	5.5	0.3	11.5	137.1	0.01	0.4	6.4	11.4
		24677.4	20.8	4723.0	2.4	1.4	18287.5	1.8	1.8	0.1	19.2	139.4	0.10	0.6	14.2	81.7
		25265.9	17.7	4242.1	2.3	2.2	18288.4	0.5	0.5	0.7	12.6	135.4	0.09	1.8	14.6	4.5
		25535.7	20.7	4339.7	2.4	1.0	18282.3	3.4	3.2	0.2	3.7	137.3	0.07	0.3	1.0	3.7
Bentaillou	Coarse grains	31285.9	35.0	1334.6	8.9	0.7	18773.4	0.2	0.1	0.1	0.1	372.6	0.15	0.0	0.0	0.0
		32126.7	36.8	1356.6	9.1	0.8	18689.3	0.3	0.1	0.1	0.1	379.5	0.15	0.0	0.0	0.0
		32855.0	38.1	1312.1	9.6	1.3	18776.4	0.2	0.1	0.1	0.9	398.0	0.17	0.1	0.1	0.4
		34496.9	41.3	1360.3	9.9	0.8	18705.9	0.2	0.1	0.1	0.1	409.7	0.18	0.0	0.0	0.0
		35241.3	44.1	1507.9	10.7	0.7	18763.6	0.3	0.1	0.1	0.1	420.7	0.19	0.0	0.0	0.0
		35988.7	41.8	1361.4	10.1	0.7	18768.9	0.3	0.1	0.1	0.1	436.5	0.19	0.0	0.0	0.0
		37074.6	44.5	1417.3	10.8	1.3	18753.3	0.2	0.0	0.1	0.6	460.7	0.20	0.0	0.3	0.2
		39618.5	50.4	1507.5	11.7	0.6	18686.1	0.2	0.1	0.1	0.1	472.0	0.21	0.0	0.0	0.0
		41332.8	45.8	1606.7	10.9	0.5	18634.9	0.2	0.1	0.1	0.1	506.6	0.22	0.0	0.0	0.0
		42794.1	48.5	1393.1	11.0	0.6	18730.0	0.2	0.0	0.1	0.2	535.6	0.22	0.0	0.0	0.1
		44066.1	46.8	1403.0	10.9	0.5	18651.8	0.3	0.1	0.1	0.2	558.8	0.23	0.0	0.0	0.1
		46084.2	55.1	1375.8	11.5	0.5	18686.8	0.3	0.1	0.1	0.2	584.1	0.25	0.0	0.0	0.0
	Type 1 Disseminated	19052.3	18.1	2356.5	9.4	3.1	18753.5	1.5	0.3	0.9	0.9	188.7	0.16	0.3	0.3	73.0
		18446.3	14.6	2058.7	6.7	1.9	18475.7	0.3	0.1	0.5	0.5	191.1	0.13	0.2	0.2	24.5
		18549.9	17.2	2361.5	8.2	16.7	18639.4	0.7	0.3	0.6	1.9	181.6	0.14	0.3	0.8	15.4
		18764.8	17.1	2679.7	8.9	5.8	18605.1	0.5	0.2	0.5	1.4	181.9	0.14	0.3	0.5	48.1

	Type 1 disseminated	19333.6	14.6	2105.8	7.6	9.6	18705.2	1.1	0.4	0.9	2.0	184.9	0.15	0.4	0.6	21.8
		18216.4	16.8	1974.9	7.6	3.6	18639.0	0.4	0.2	0.6	0.5	190.6	0.14	0.2	0.2	25.1
		18840.0	15.0	2506.9	8.9	9.2	18642.4	1.2	0.5	1.4	2.3	188.1	0.20	0.5	0.8	63.3

11.9 Supplementary data relative to section 5.1

Figure 137. EDS Ge-map acquirred simultaneously as EBSD mapping which reffered to Figure 69.

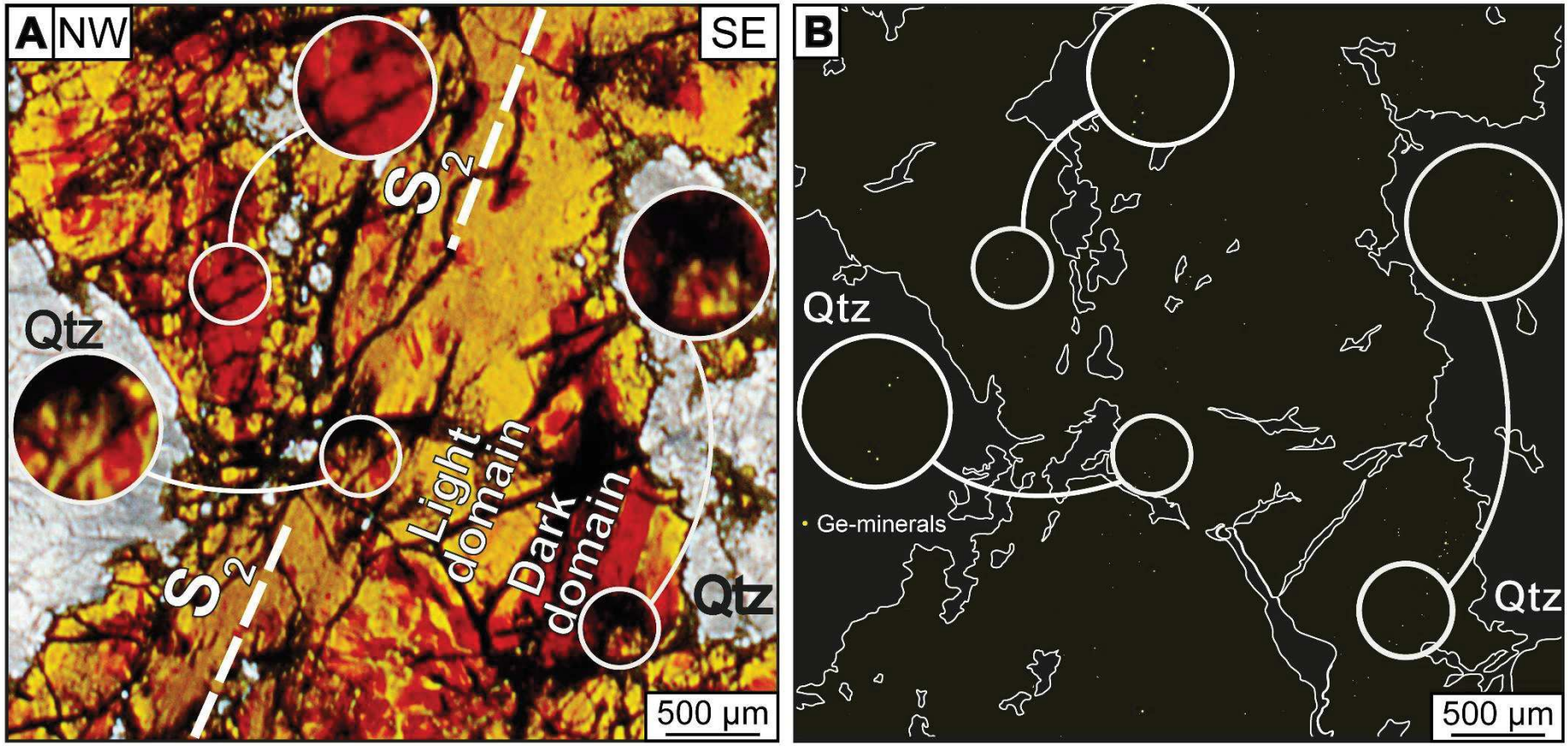

Figure 138. Sphalerite area from Figure 70. A. Sphalerite observed in transmitted plane polarized light with different zoom. B. Same area is analysed with EDS.

11.10 Supplementary data relative to section 5.2

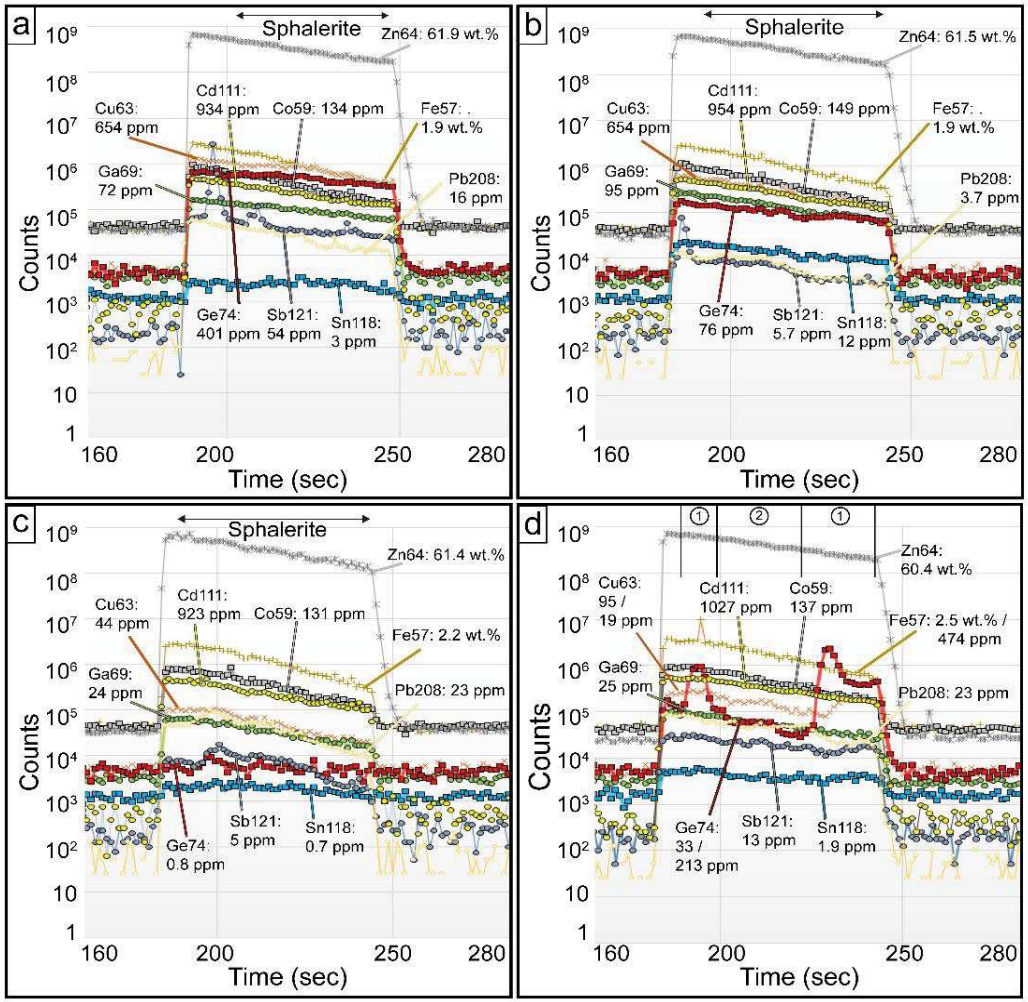

Figure 139. LA-ICP-MS spectra of sphalerite measurements

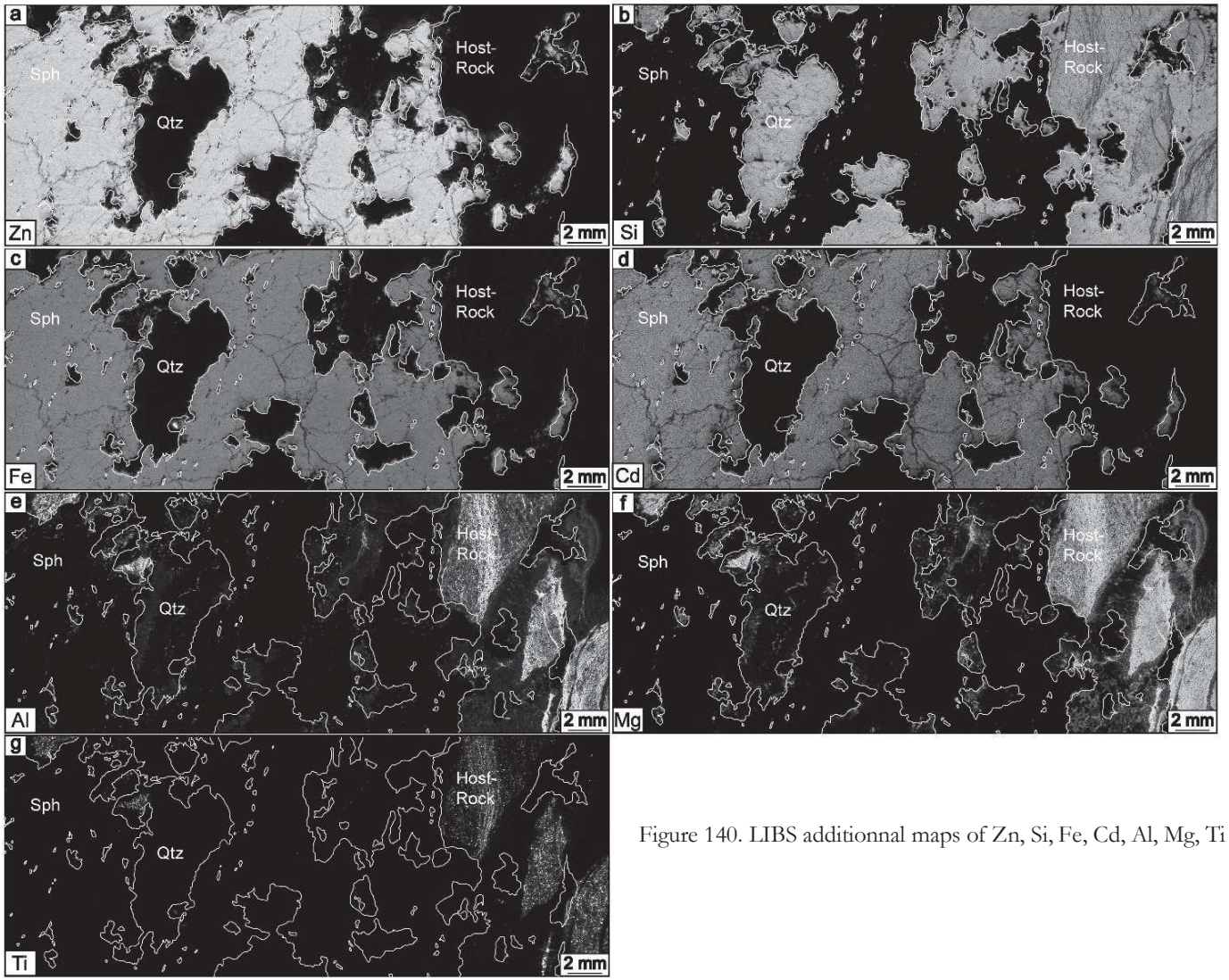

Figure 140. LIBS additionnal maps of Zn, Si, Fe, Cd, Al, Mg, Ti

Table 17 . Mass balance calculation on LIBS map for Ge content

	Ge distribution				
	Ge-minerals	**Sphalerite-noGe**	**Sphalerite-Ge**	**Total**	**Projection of a primary sph without Ge-minerals**
Sum pixels	49955	14464106	15633016	30147077	30097122
Volume (%)	0.1657	47.9785	51.8558	100.0000	99.8343
Density (g/cm3)	4.56	4.00	4.00		4.00
Weight	0.75	191.91	207.42	400.09	399.34
Weight (%)	0.19	47.97	51.84	100.00	99.81
[Ge] (ppm)	250000	20	400		**690**
Weight Ge (wt.%)	4.72	0.10	2.07	6.89	6.89
Ge fraction	68.49	1.39	30.12	100.00	

Table 18. Geothermometer results applied on trace elements in sphalerite (based on the GGIMFis geothermomether from *Frenzel et al., 2016*)

Deposit and textures		T° min mean	T° max mean	T° mean
Anglas	Recrystallized grains	199.9	220.5	210.2
	Dark domains-coarse grains	240.8	274.0	257.4
	Light domains-coarse grains	192.5	210.7	201.6
	All	211.1	235.1	223.1
Arre	Recrystallized grains	204.8	226.9	215.9
	Dark domains-coarse grains	261.7	301.4	281.6
	Light domains-coarse grains	240.7	273.9	257.3
	All	235.7	267.4	251.6
Pale Bidau	Recrystallized grains	212.0	236.3	224.1
	Dark domains-coarse grains	263.3	303.5	283.4
	Light domains-coarse grains	155.5	162.3	158.9
	All	210.2	234.0	222.1
Victoria	Recrystallized grains	107.7	113.8	110.8
	Coarse grains	119.5	122.8	121.2
	All	113.6	118.3	116.0
Margalida	Recrystallized grains	130.2	131.0	130.6
Bentaillou	Coarse grains	90.2	100.5	95.3
	Type 1 disseminated	148.2	152.7	150.5
	All	119.2	126.6	122.9

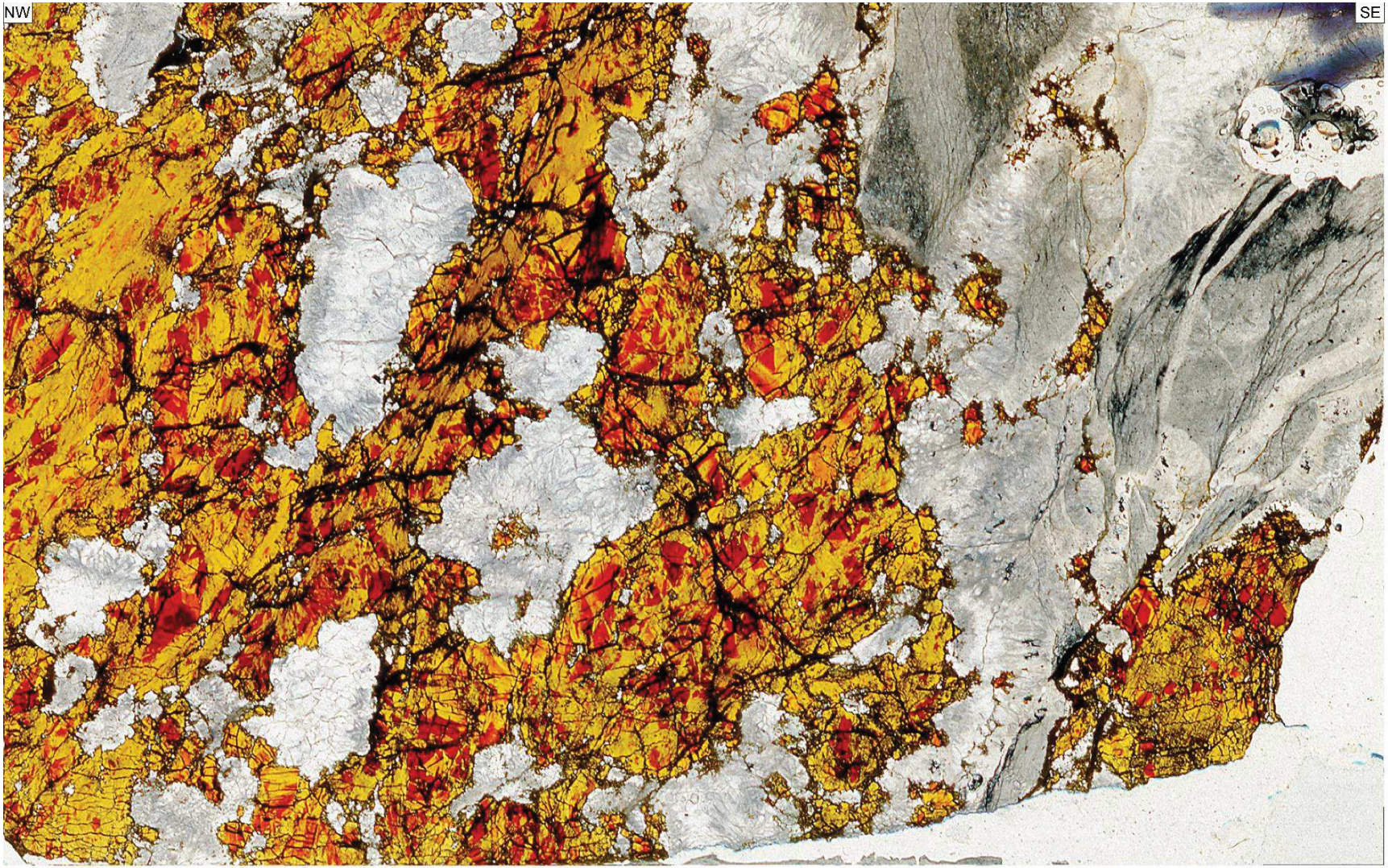

Figure 141. Sphalerite (brown-orange colors), quartz (white) and host-rock (grey-black at the right) from Arre in transmitted light

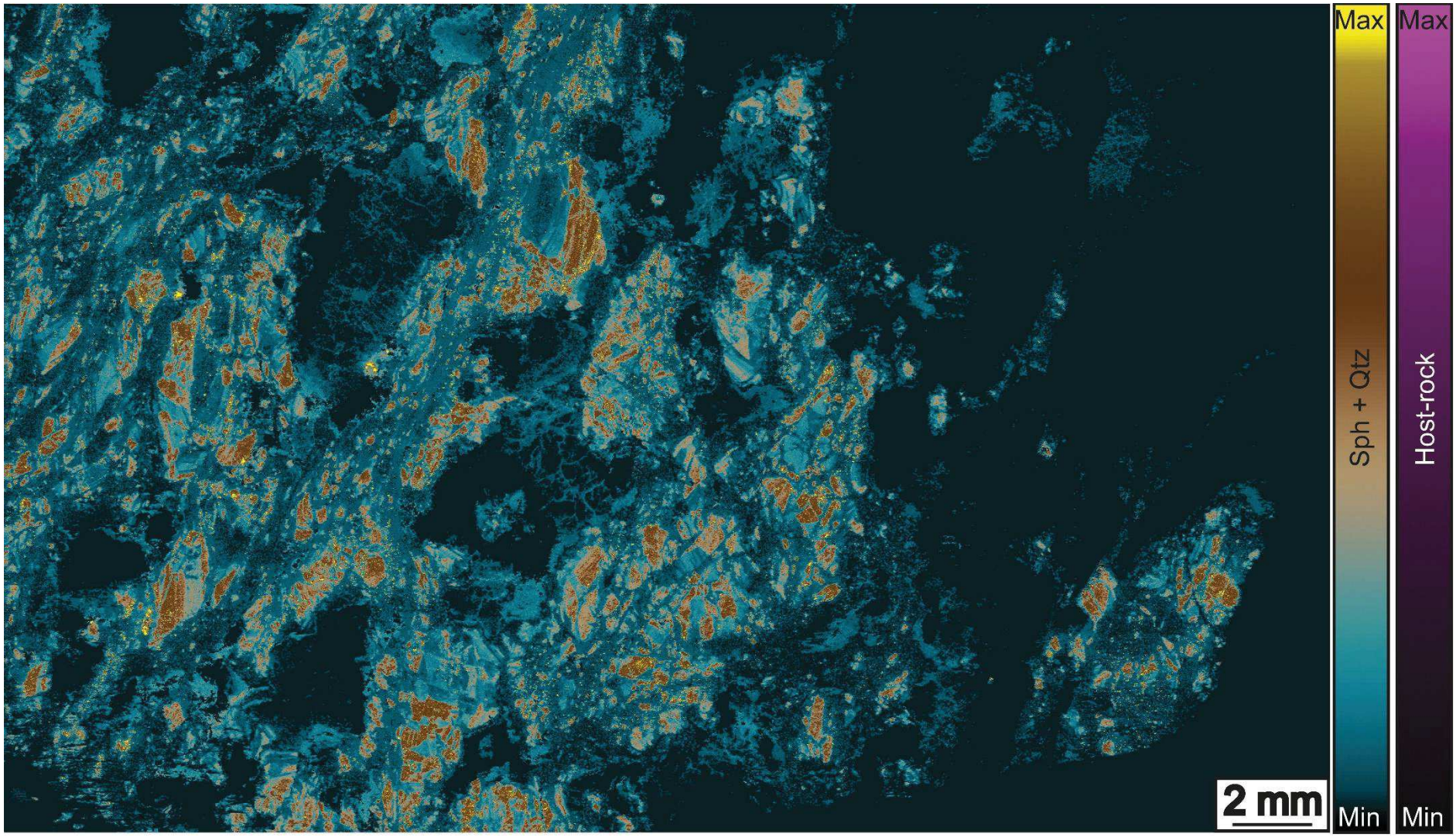

Figure 142. LIBS Ge map in sphalerite, quartz and host-rock of the same area as Figure 141.

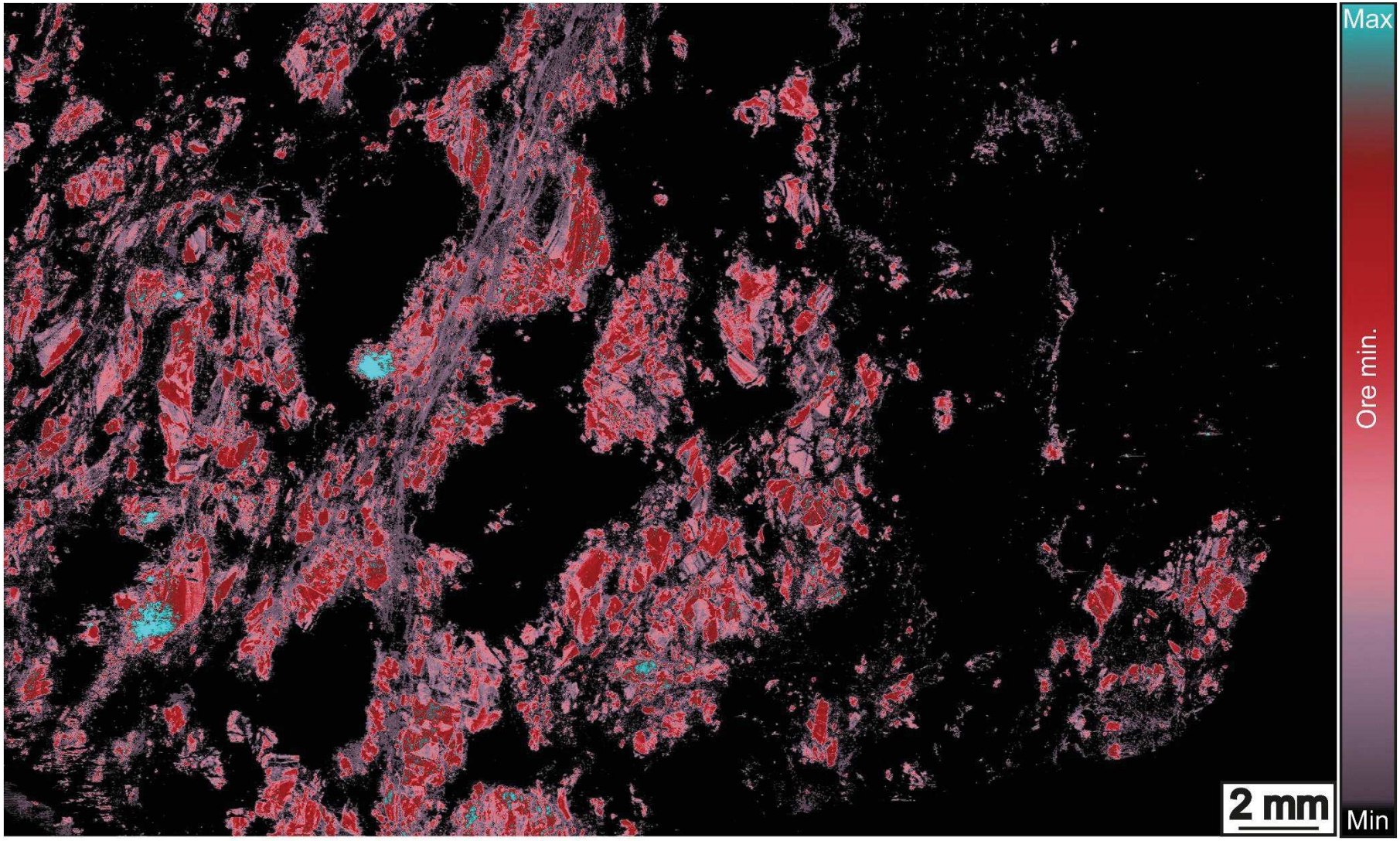

Figure 143. LIBS Cu map in sphalerite, quartz and host-rock of the same area as Figure 141

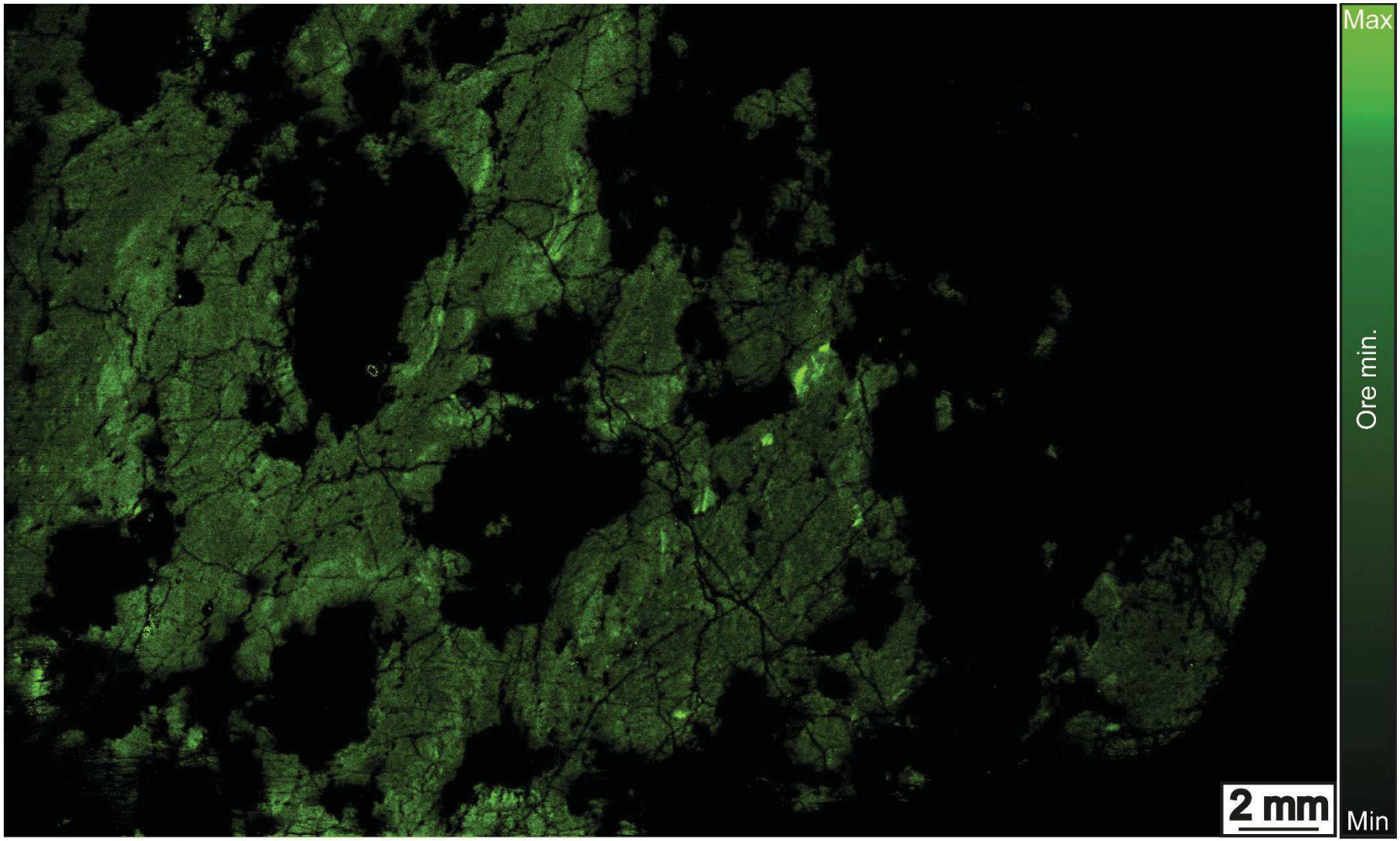

Figure 144. LIBS Ga map in sphalerite, quartz and host-rock of the same area as Figure 141

11.11 EBSD maps

Complete EBSD maps on sphalerite are presented in this section and for some of them are only present in this section.

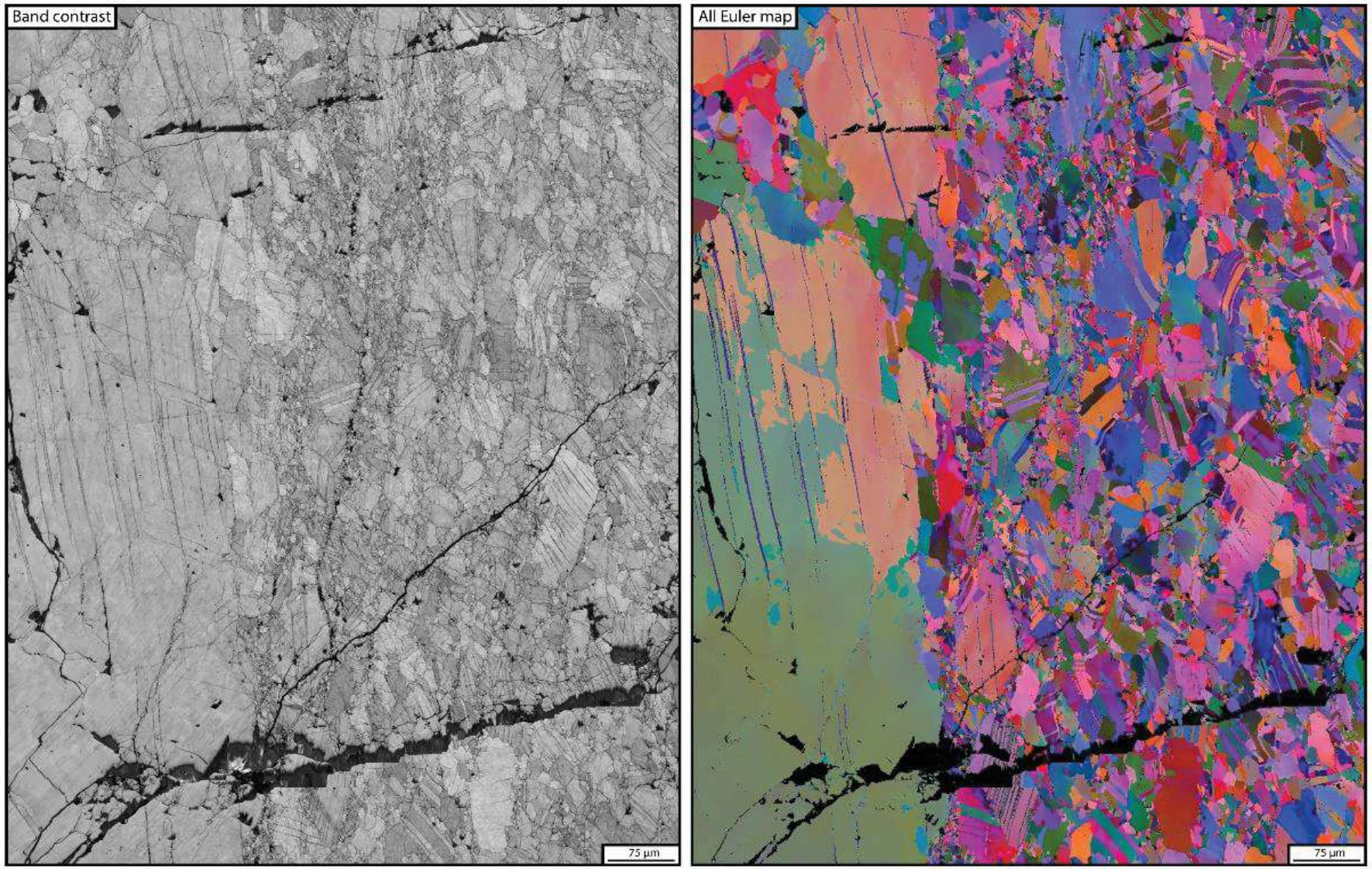

Figure 145. EBSD maps of Arre sphalerite (0.5 µm = step of measurment) with band contrast and all Euler maps.

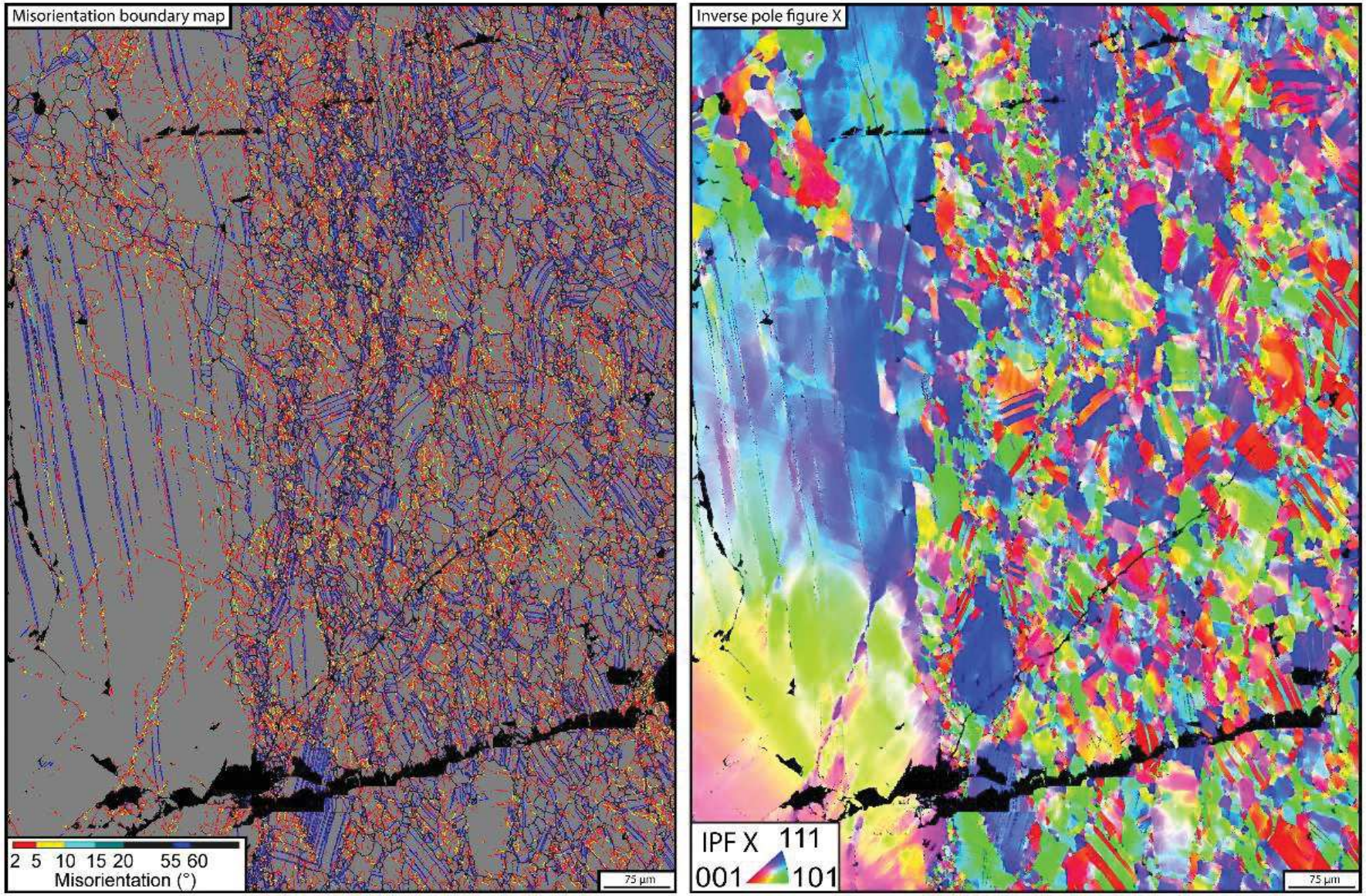

Figure 146. EBSD maps of Arre sphalerite (0.5 µm = step of measurment; same area as Figure 145) with misorientation boundary and inverse pole figure according to the X axis maps.

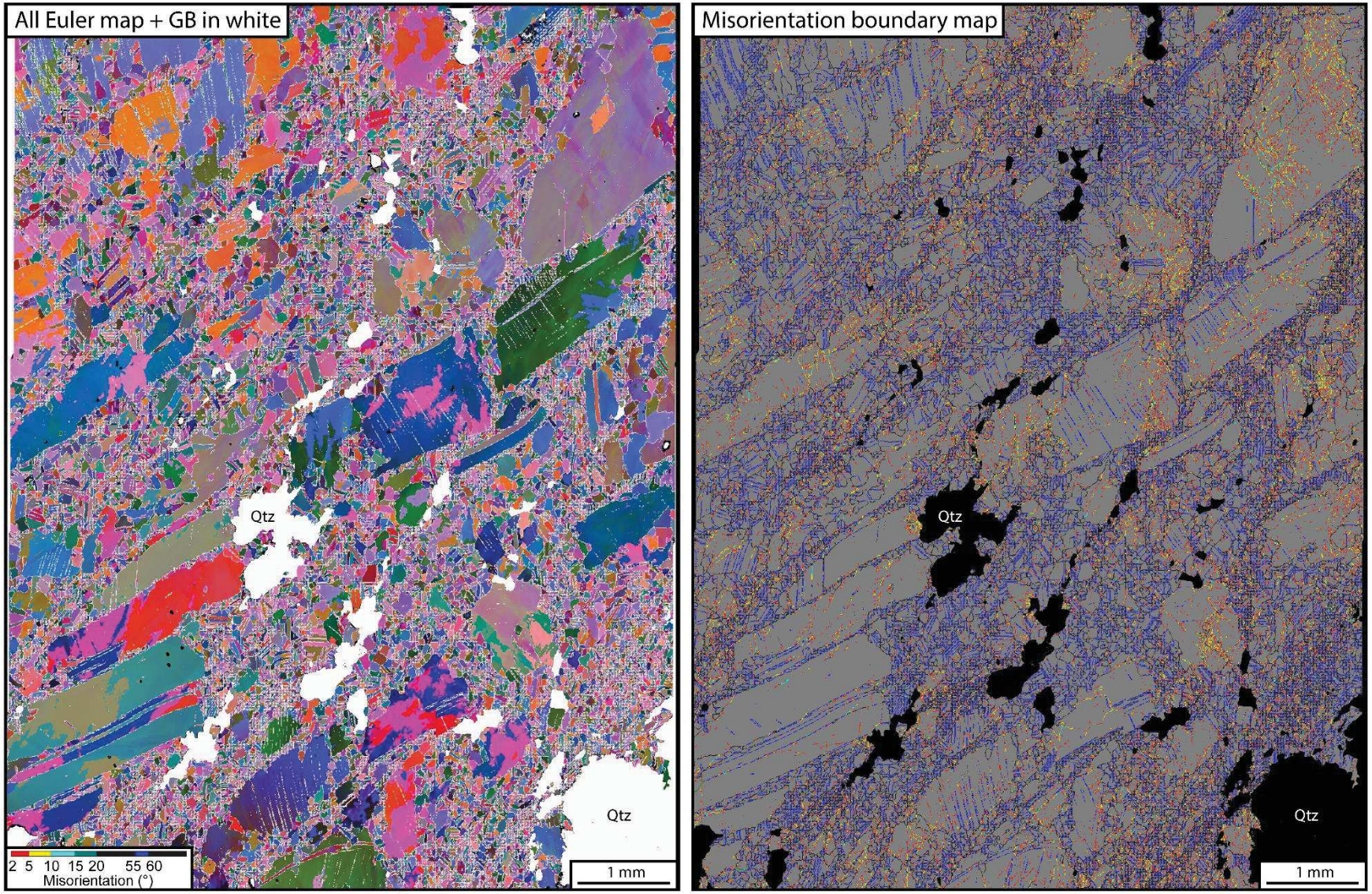

Figure 147. EBSD maps of Arre sphalerite (2.5 μm = step of measurment) with All Euler map with grain boundaries (>20°) and misorientation boundary map.

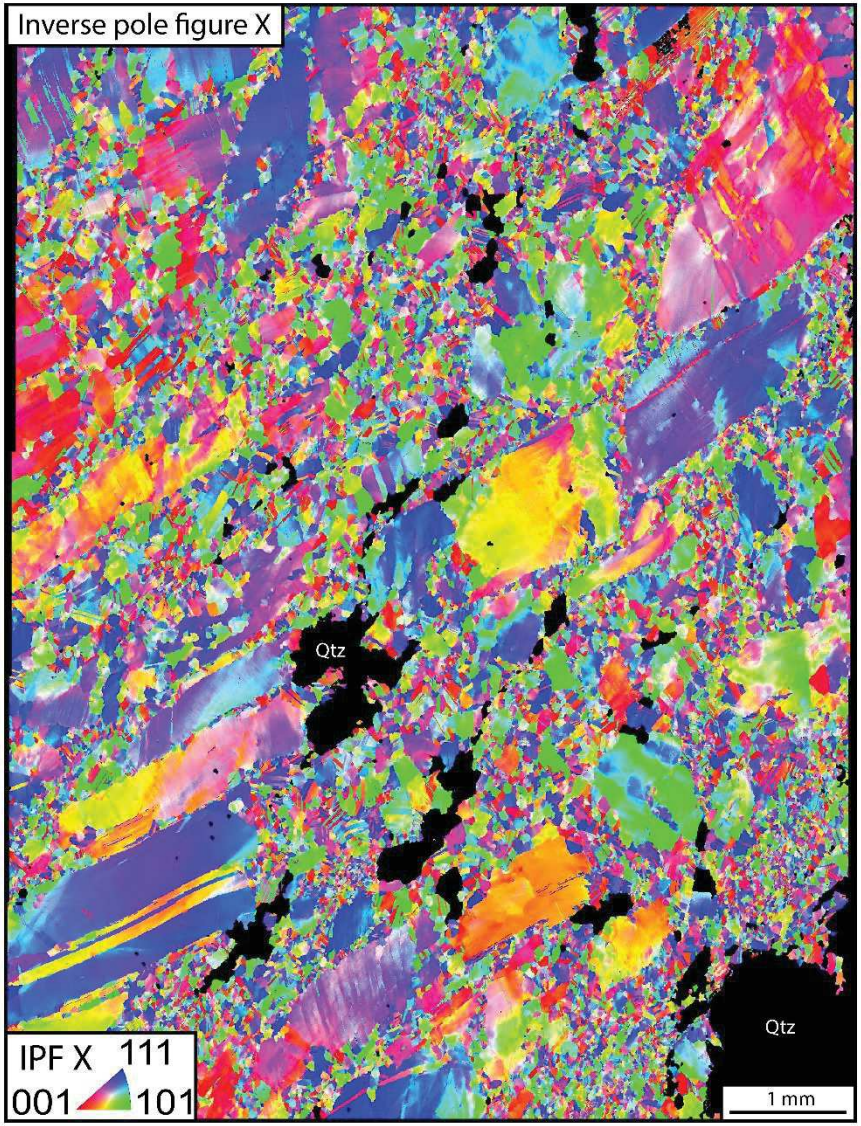

Figure 148. EBSD maps of Arre sphalerite (2.5 μm = step of measurment, same area as Figure 147) with inverse pole figure according to the X axis.

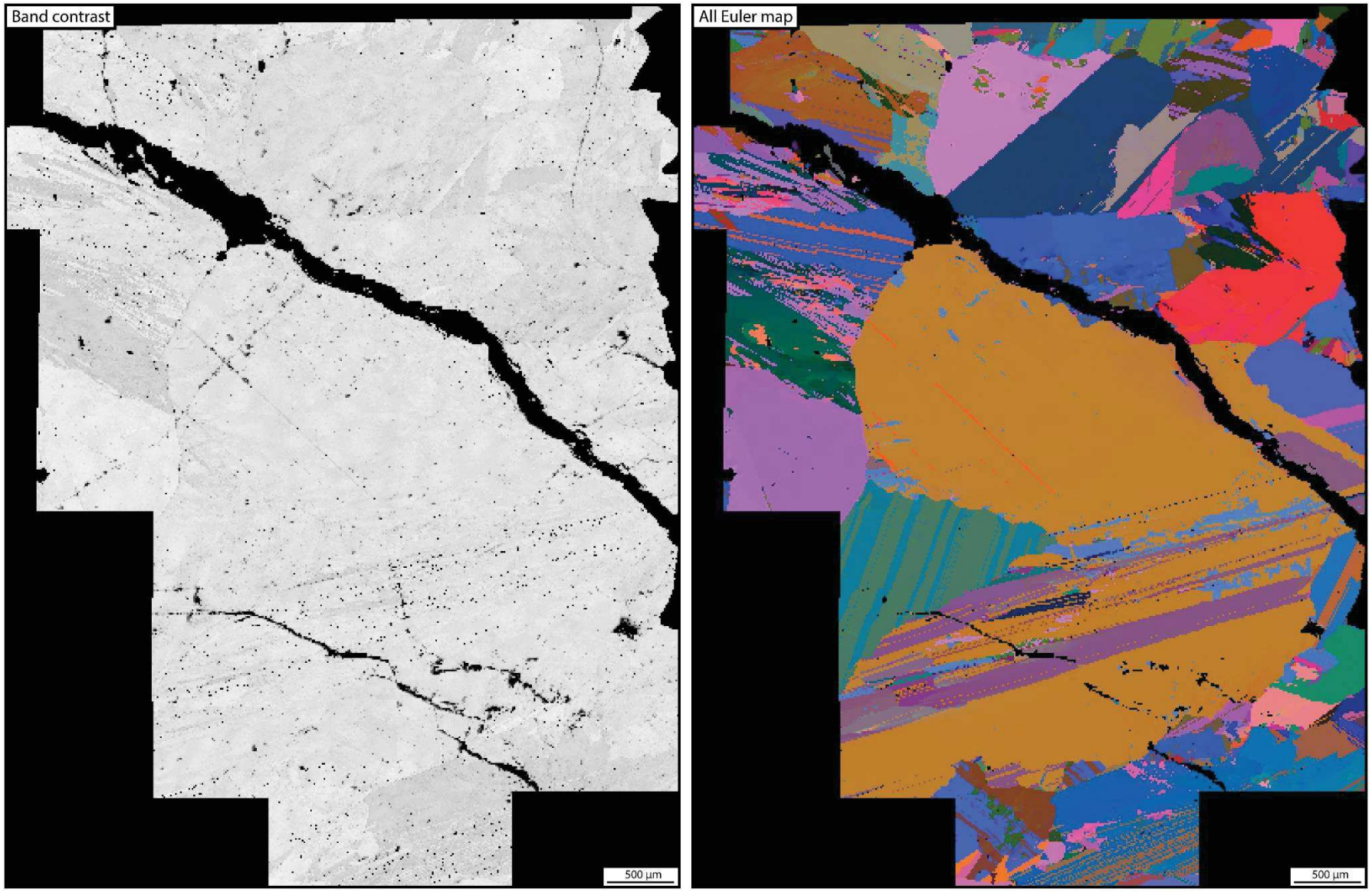

Figure 149. EBSD maps of Saint-Salvy sphalerite (5.7 µm = step of measurment) with band contrast and all Euler maps.

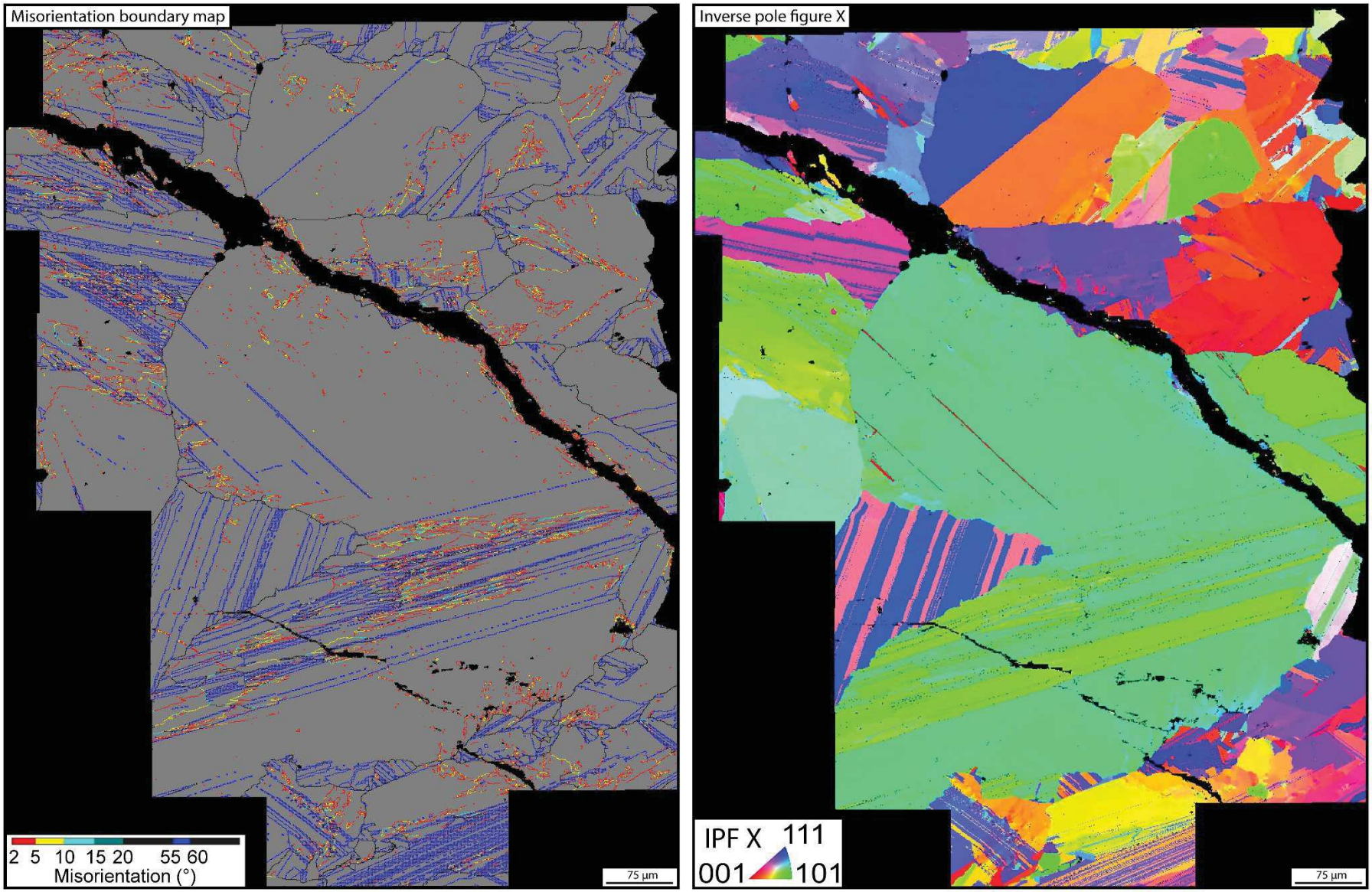

Figure 150.. EBSD maps of Saint-Salvy sphalerite (5.7 µm = step of measurment; same area as Figure 149) with misorientation boundary and inverse pole figure according to the X axis maps.

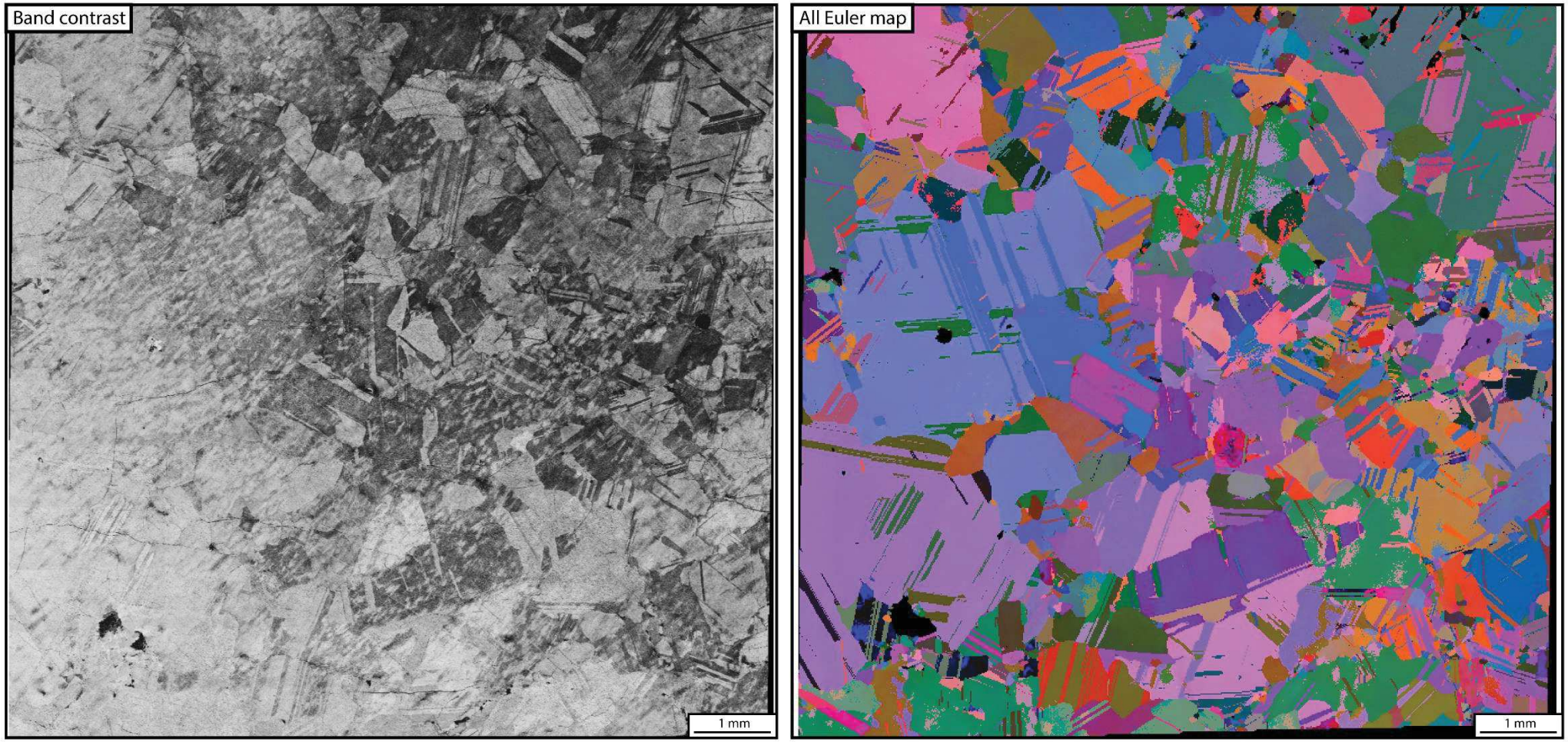

Figure 151. EBSD maps of Bentaillou sphalerite (6.5 μm = step of measurment) with band contrast and all Euler maps.

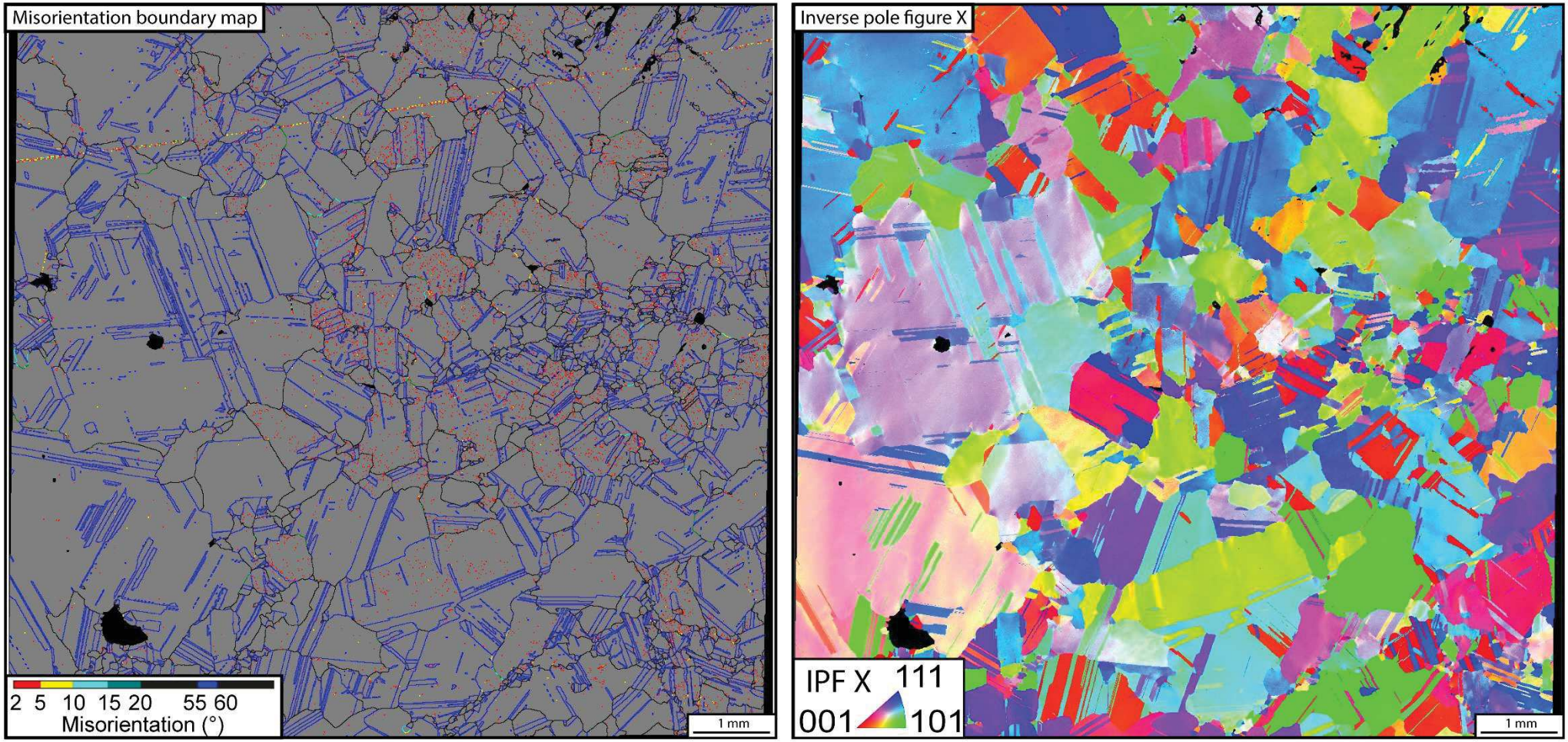

Figure 152 EBSD maps of Bentaillou sphalerite (6.5 µm = step of measurment; same area as Figure 151) with misorientation boundary and inverse pole figure according to the X axis maps.

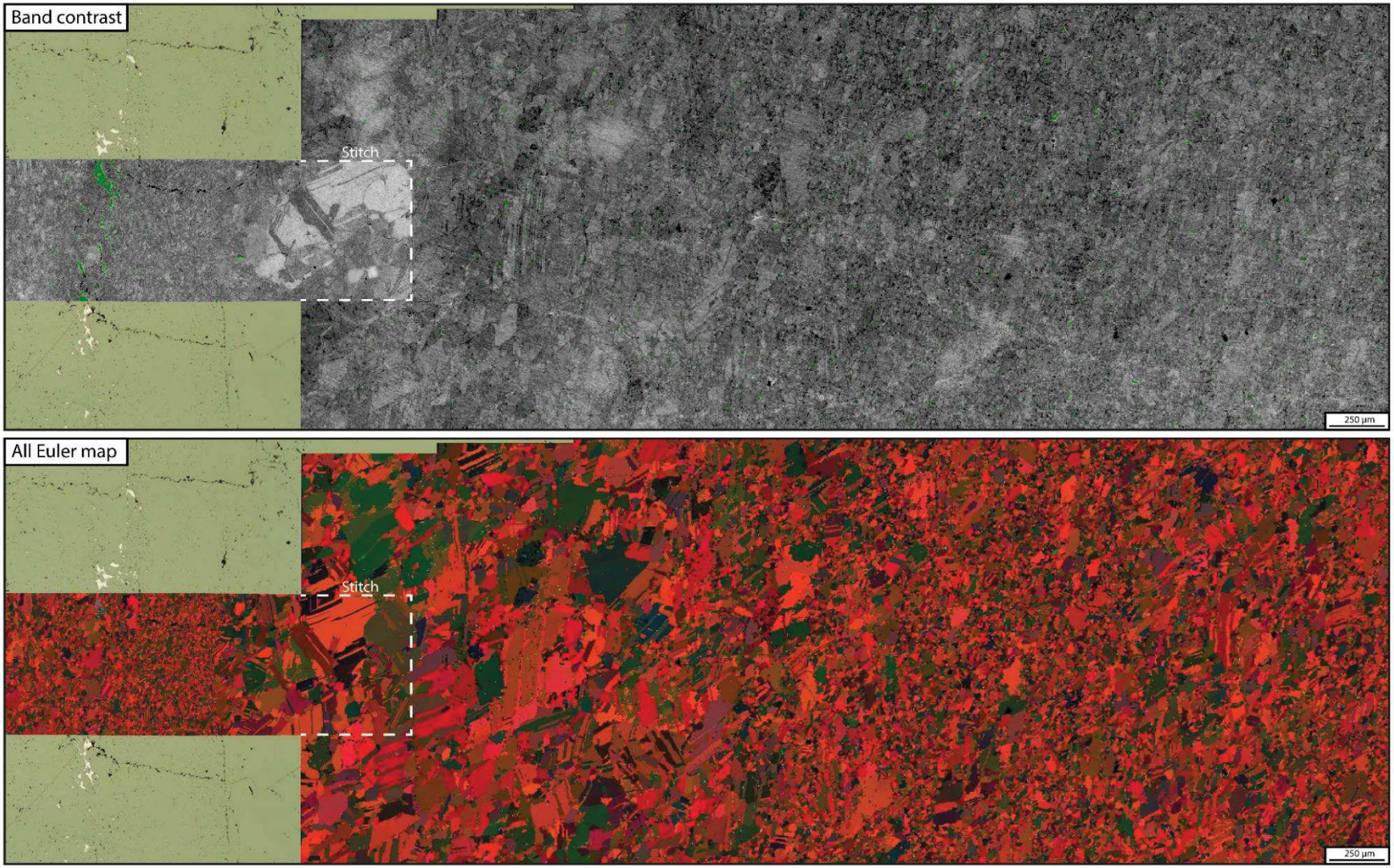

Figure 153. EBSD maps of Pale Bidau sphalerite (1.5 µm = step of measurment) with band contrast and all Euler maps superimposed on reflected light scan.

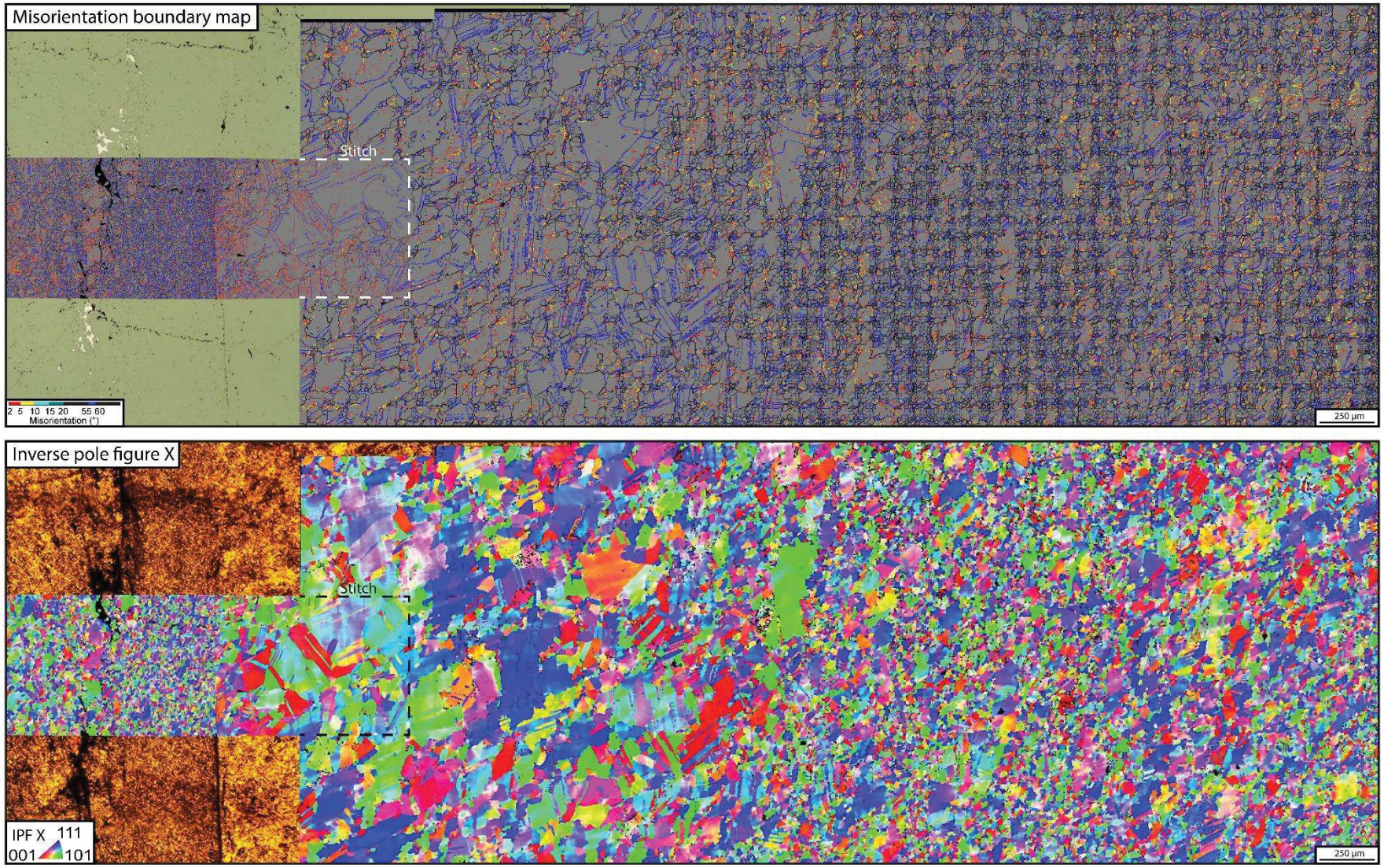

Figure 154. EBSD maps of Bentaillou sphalerite (1.5 µm = step of measurment; same area as Figure 153) with misorientation boundary and inverse pole figure according to the X axis maps superimposed on reflected light scan (on the top picture) and on transmitted plan polarized scan (on the bottom picture).

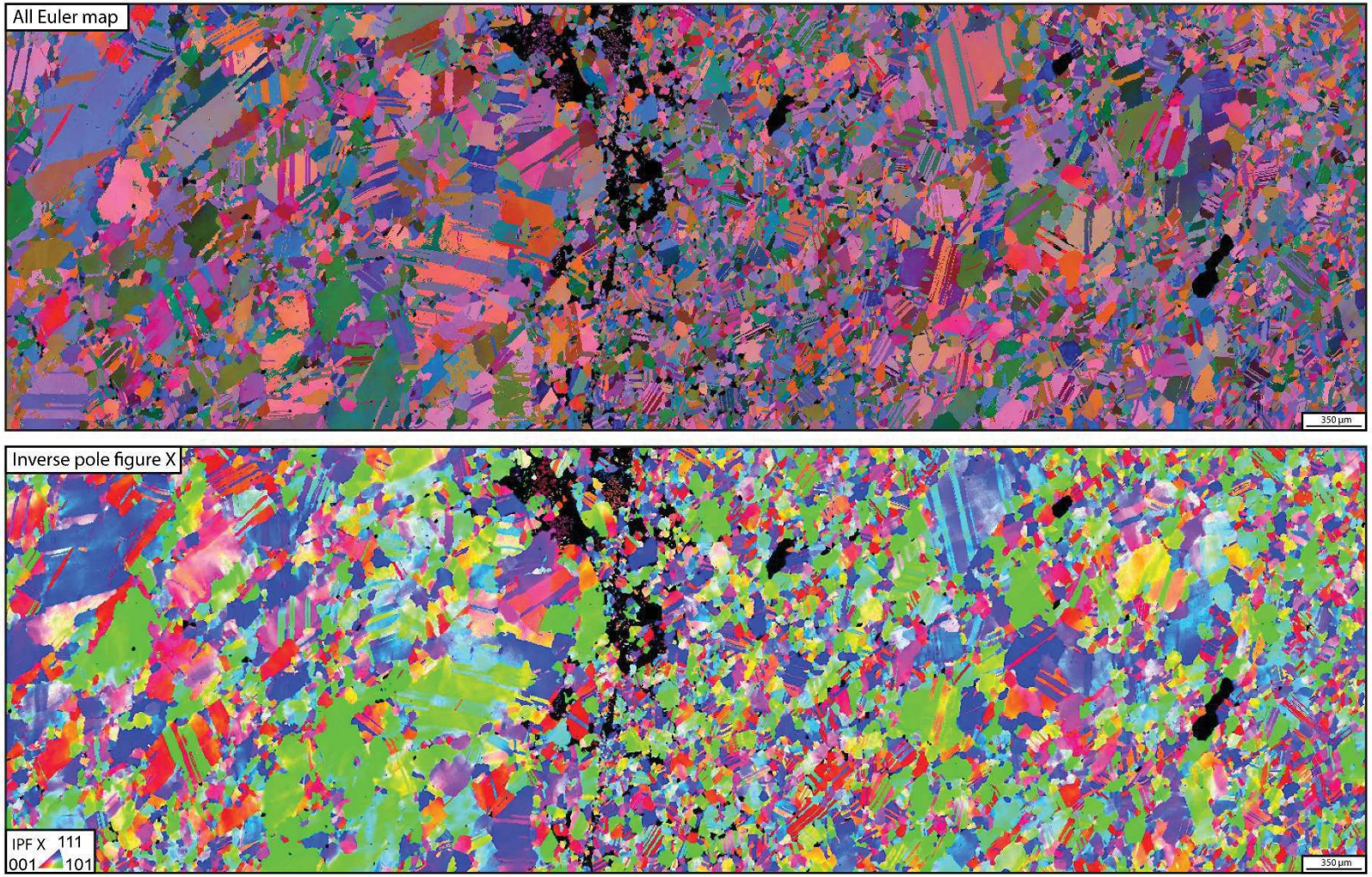

Figure 155. EBSD maps of Liat Vein sphalerite (3.5 µm = step of measurment) with all Euler map and inverse pole figure according to the X.

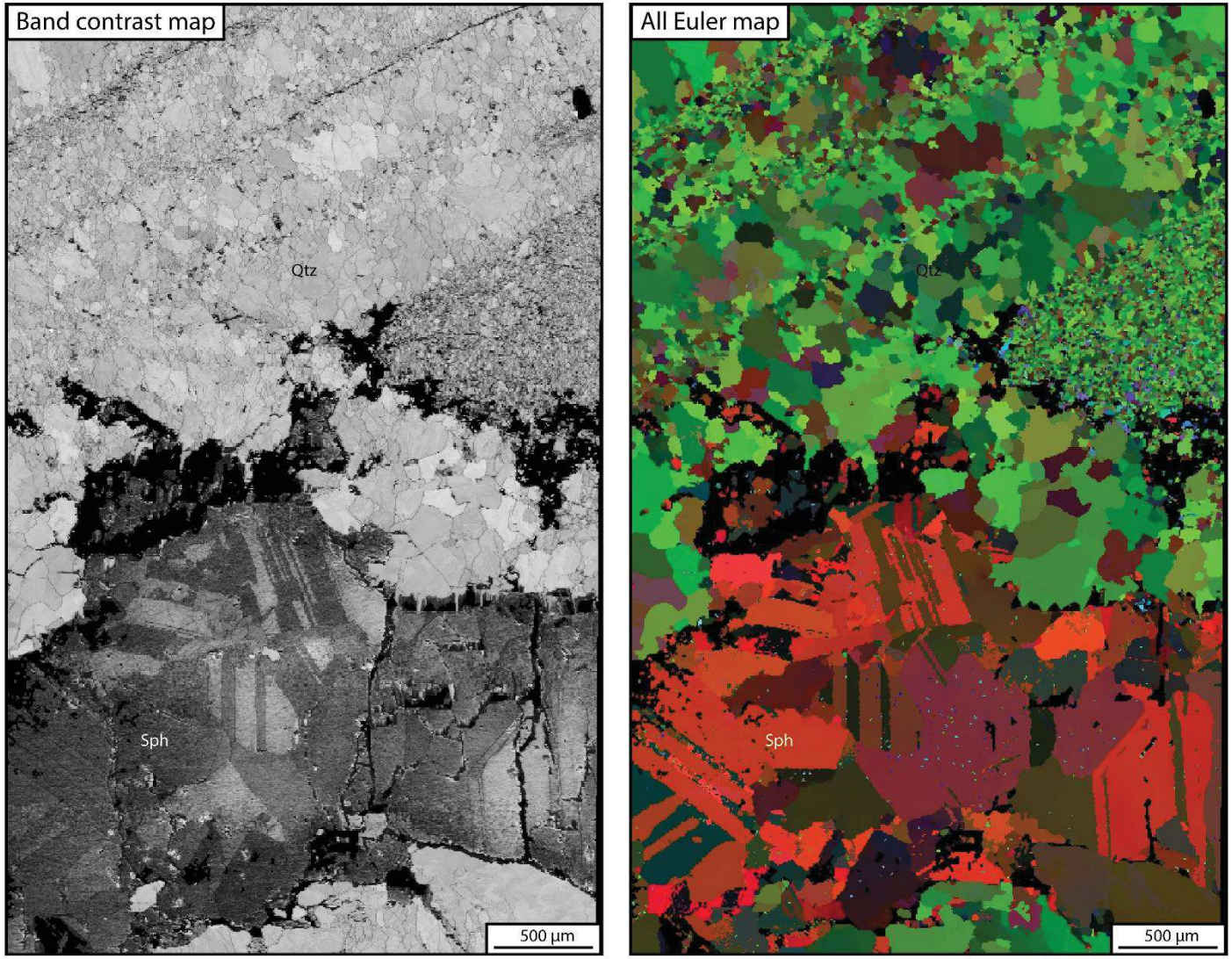

Figure 156. EBSD maps of Liat stratabound sphalerite (6 µm = step of measurment) with band contrast and all Euler map. Sphalérite is in the bottom area of the maps parallel to S_0-S_1.

Figure 157. EBSD map of Liat stratabound sphalerite (6 µm = step of measurment, same area as Figure 156) with inverse pole figure according to the X.

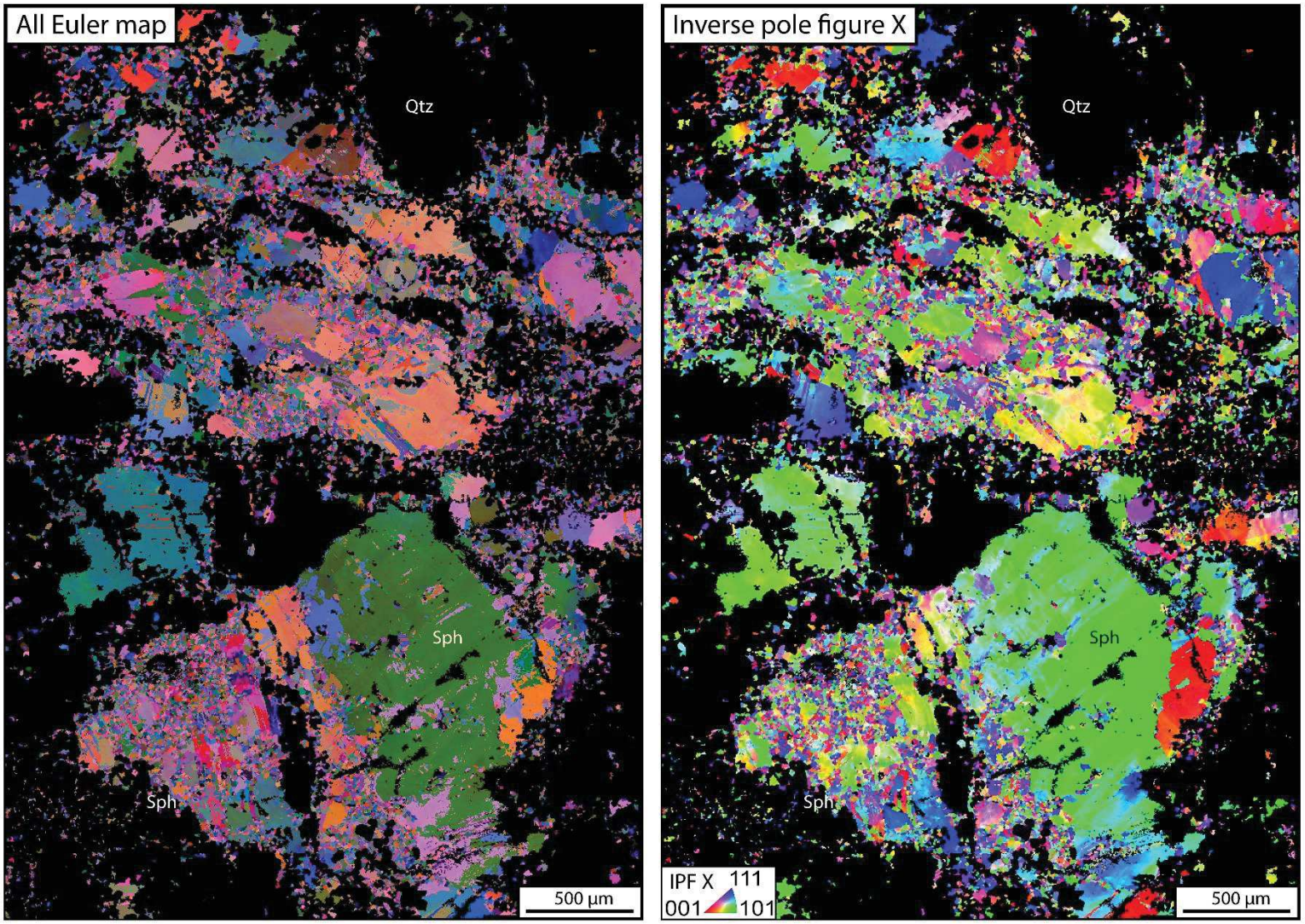

Figure 158. EBSD map of Cierco vein sphalerite (4 µm = step of measurment) with all Euler and inverse pole figure according to the X.

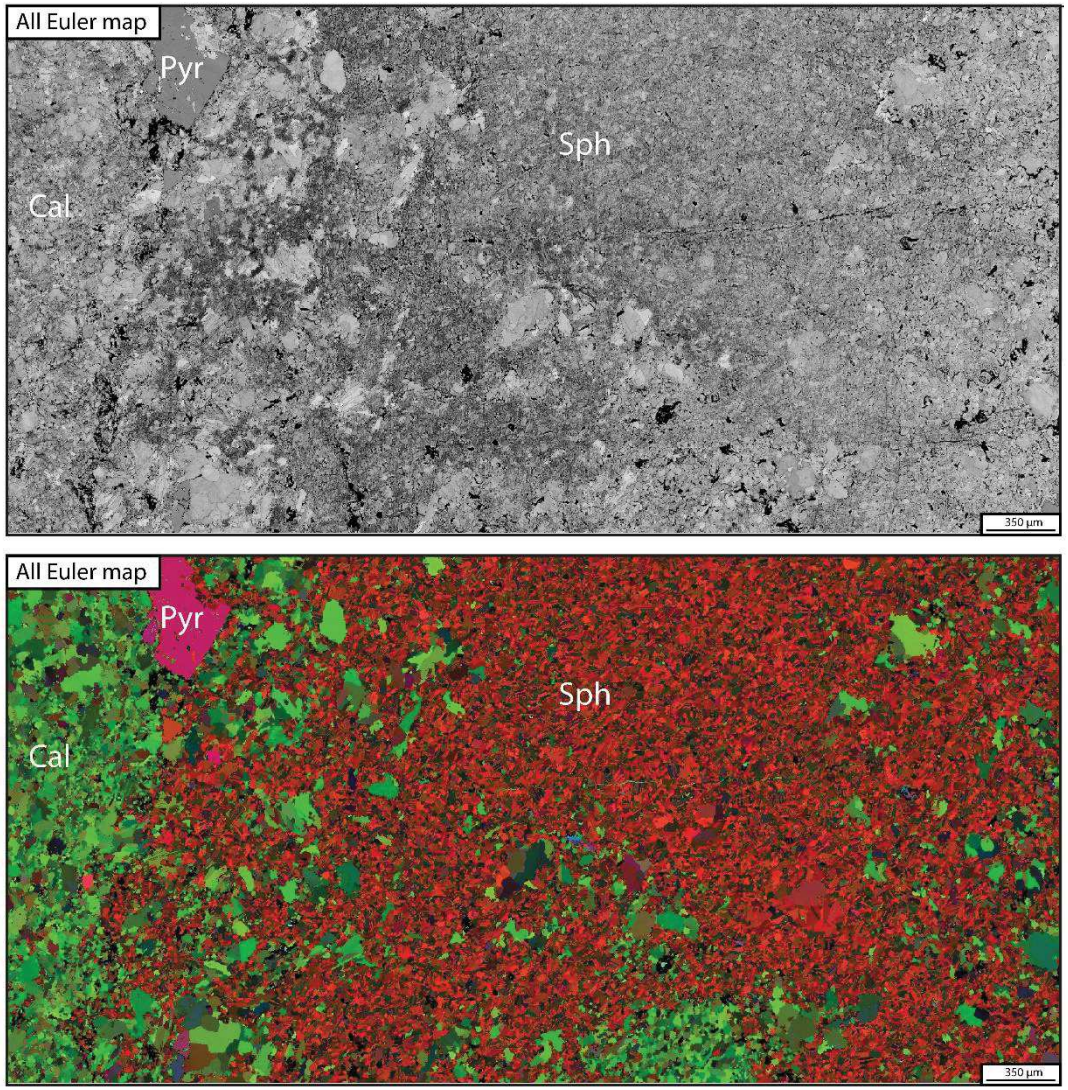

Figure 159. EBSD maps of Margalida stratabound sphalerite (5 µm = step of measurment) with band contrast and all Euler map.

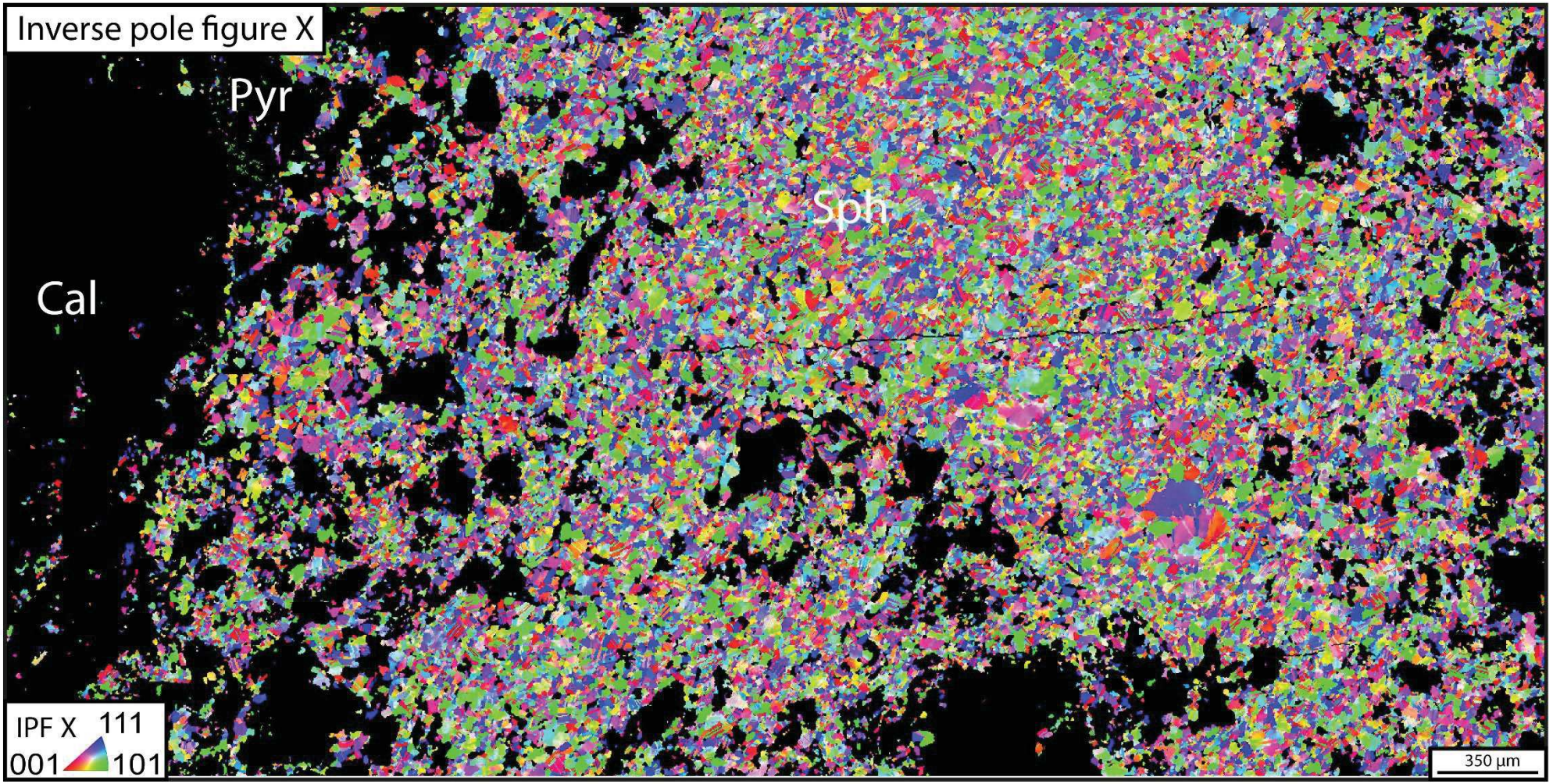

Figure 160. . EBSD maps of Margalida stratabound sphalerite (5 µm = step of measurment, same area as Figure 159) with inverse pole figure according to X axis.

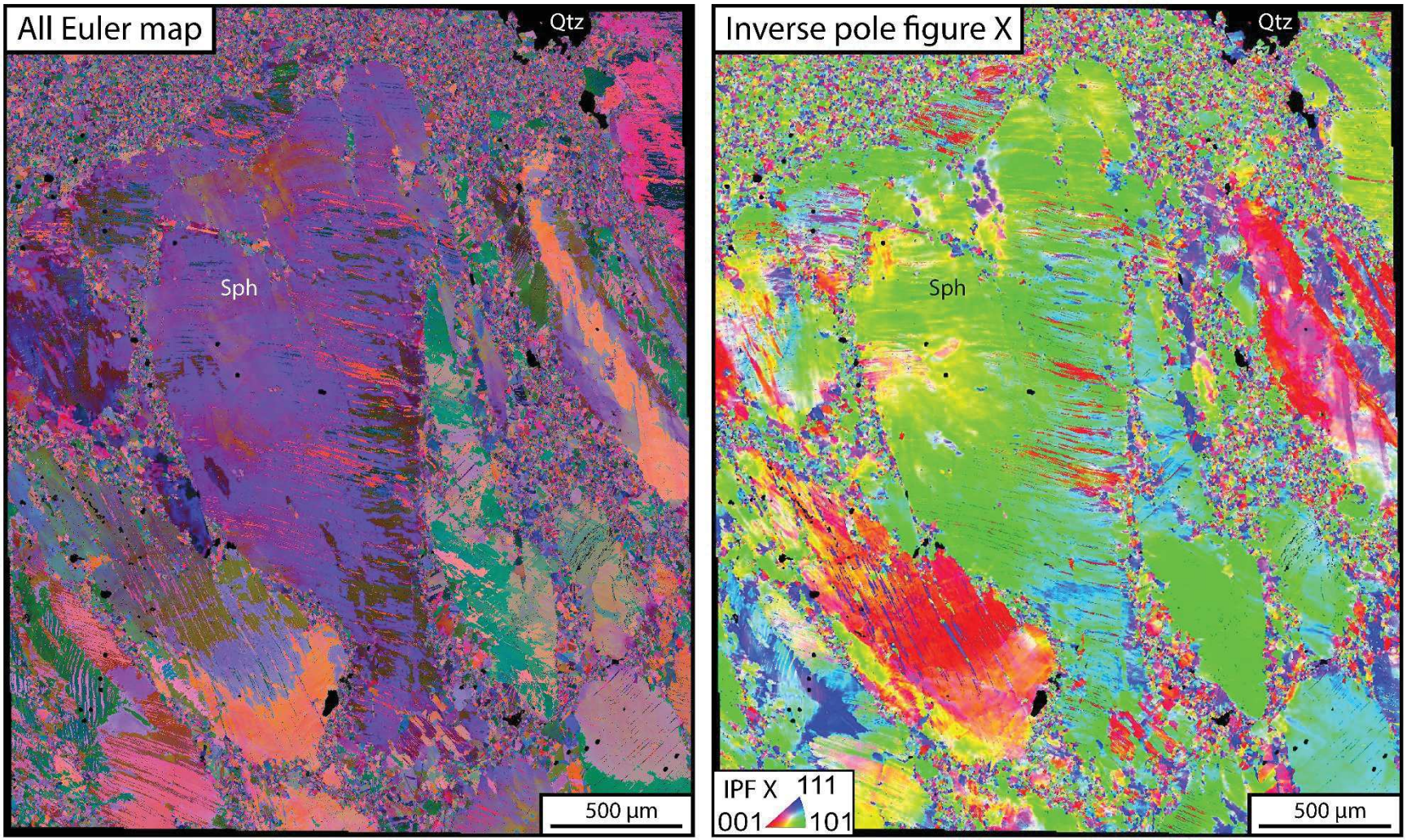

Figure 161. EBSD maps of Anglas sphalerite (3 µm = step of measurment) with all Euler map and inverse pole figure.

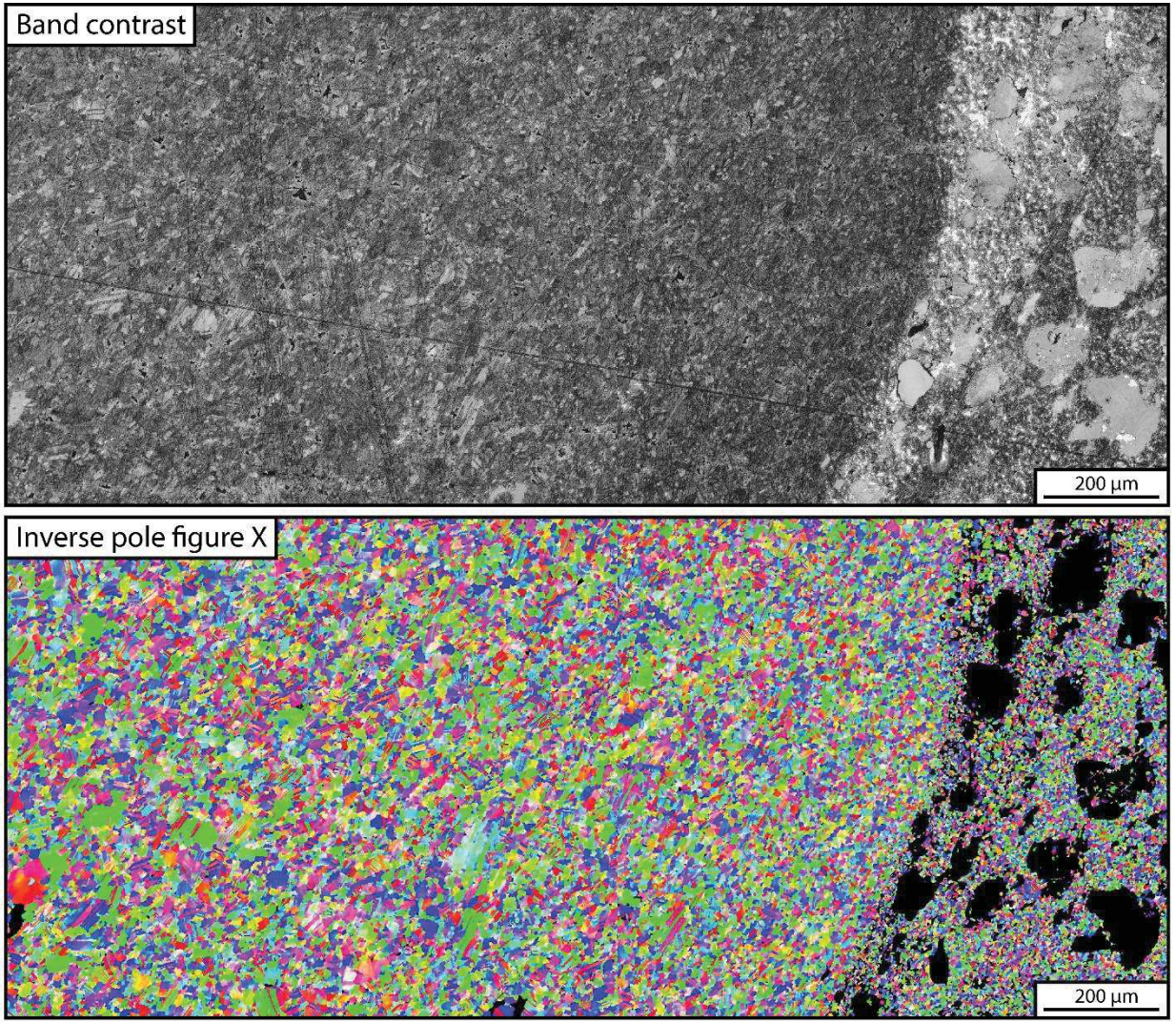

Figure 162. EBSD maps of Argut-dessus vein sphalerite (1 µm = step of measurment) with band contrast and inverse pole figure acording to X axis.

11.12 Fluid inclusions – Microthermometric data in quartz

Table 19. Fluid inclusions microthermometric analyses in **Crabioules (CR) sample** (CRA02 sample; in green: aqueous inclusions / in red: carbonic inclusions). Abbreviations: FIA: fluid inclusion assemblages; V/L ratio: vapor/liquid ratio; xCO2: CO2 proportion; Tc: freezing temperature; Tm: melting temperature; clath: clathrate; Th: homogenization temperature; Hal: halite; hh: hydrohalite; P@homog.: homogenization pressure.

Sample	n°chip	FIAs (CO2 red, H2O green)	Type (CO2 red, H2O green)	n° FI	Rapport V/L (%)	xCo2 (vol.%)	Size µm	Salt at T°=25 °C	Petro	TcCo2	Tc H2O	TmCo2	TmfH2O	TmlH2O	ThCO2	Tmclath	Salinity		ThH2O	TmHal or Thh	Thtotal	P @ homog.	rBULK	dP/dT
																	NaCl (wt.%)	CaCl2 (wt.%)				(bar)	(g/cm3)	(bar/°C)
CRA02-DP	Chip1	IF01	ii	1		15	15	No	Cluster	-100.7	-29.0	-66.3			-45.3	12					311			
CRA02-DP	Chip1	IF01	ii	2		15	20	No	Cluster	-103.3	-43.5	-63.5			-40.6	11					317			
CRA02-DP	Chip1	IF01	ii	3		15	20	No	Cluster	-103.5	-30.2	-65.8			-45.5	11					322			
CRA02-DP	Chip1	IF01	ii	4		15	20	No	Cluster	-108.5		-66.2			-39.2						317			
CRA02-DP	Chip1	IF02	i	1	10		8	Yes	Cracks		-60.2		-46.8	-26.8			22.5	10.8	227	198		11.8	1.1	19.8
CRA02-DP	Chip1	IF02	i	2	10		8	Yes	Cracks		-37.5			-22.0			29.5	2.1	224	198		11.8	1.1	19.7
CRA02-DP	Chip1	IF03	i	1	10		5	No	Cracks		-86.5		-39.5	-32.8			19.3	16.0	226	197		19.3	1.1	18.4
CRA02-DP	Chip1	IF03	i	2	10		10	No	Cracks		-82.0		-38.3	-28.6			20.8	12.9	239	193		25.2	1.1	17.7
CRA02-DP	Chip1	IF03	i	3	10		10	No	Cracks		-62.0		-28.4	-18.8			30.0	1.6	248	198		32.2	1.0	16.4
CRA02-DP	Chip1	IF04	i	1	10		10	No	Cracks		-80.7		-45.6	-28.9			21.1	13.1	215	198		16.2	1.1	18.9
CRA02-DP	Chip1	IF04	i	2	10		10	No	Cracks		-88.0		-46.0	-25.1			24.2	8.4	227	198		20.8	1.0	18.1
CRA02-DP	Chip1	IF04	ii	3		10	5	No	Cluster	-110.5		-71.5			-38.5	10					320			
CRA02-DP	Chip1	IF04	ii	4		10	5	No	Cluster	-107.2		-79.5			-37.0	10					321			
CRA02-DP	Chip1	IF04	i	5	10		8	No	Cracks		-86.2		-48.2	-22.2			26.62	4.90	229	190		23.9	1.0	16.6
CRA02-DP	Chip1	IF05	ii	6		15	10	No	Cluster	-103.2		-68.7			-39.2						311			
CRA02-DP	Chip1	IF05	ii	7		15	10	No	Cluster	-102.6		-68.2			-38.6						315			
CRA02-DP	Chip1	IF05	ii	8		10	10	No	Cluster	-102.1		-68.9			-38.2						312			

CRA02-DP	Chip2	IF06	ii	1		15	30	No	Cluster	-100.1	-71.6	-64.8		-23.5	2.1	-3					310			
CRA02-DP	Chip2	IF06	i	2	15		20	No	Cracks		-69.2		-44.2	-33.0			19.3	16.2	191	197		9.3	1.1	20.0
CRA02-DP	Chip2	IF06	i	3	15		8	Yes	Cracks		-78.3		-42.5	-24.6			24.8	7.5	193	198		11.8	1.1	19.7
CRA02-DP	Chip2	IF06	i	4	15		10	No	Cracks		-68.5		-42.3	-25.2			23.9	8.6	193	196		10.6	1.1	20.1
CRA02-DP	Chip2	IF06	i	5	15		8	No	Cracks		-67.9		-42.5	-22.5			28.4	3.3	193	198		11.0	1.1	20.0
CRA02-DP	Chip2	IF06	ii	6	15	15	15	No	Cracks	-99.3	-63.5			-25.6	5.2						306			
CRA02-DP	Chip2	IF06	ii	7		15	15	No	Cracks	-99.5	-63.2			-25.3	2.4						302			
CRA02-DP	Chip2	IF07	i	1	15		25	No	Cracks		-75.4		-43.5	-25.1			24.0	8.4	185	196		8.8	1.1	20.6
CRA02-DP	Chip2	IF07	i	2	15		20	Yes	Cracks		-75.2		-46.7	-30.2			20.3	14.2	212	196		11.3	1.1	19.9
CRA02-DP	Chip2	IF07	i	3	15		20	No	Cracks		-70.1		-46.8	-30.3			20.2	14.3	224	196		19.0	1.1	18.5
CRA02-DP	Chip2	IF07	i	4	15		10	No	Cracks		-74.5		-43.2	-26.3			22.8	10.2	195	196		11.0	1.1	19.9
CRA02-DP	Chip2	IF07	i	5	15		10	No	Cracks		-68.5		-44.6	-27.8			21.5	12.0	209	195		14.5	1.1	19.2
CRA02-DP	Chip2	IF08	i	1	15		15	No	Cracks		-80.7		-54.2	-44.2			20.1	19.3	172	227		4.3	1.2	20.8
CRA02-DP	Chip2	IF08	i	2	15		25	No	Cracks		-82.5		-52.5	-37.2			18.4	18.2	172	198		5.7	1.2	20.6
CRA02-DP	Chip2	IF08	ii	3	15	15	15	No	Cluster	-93.6		-63.9			-30.6	-2					315			
CRA02-DP	Chip2	IF08	i	4	15		10	No	Cracks		-81.5		-51.0	-43.9			18.4	20.0	174	209		4.7	1.2	20.6
CRA02-DP	Chip2	IF08	i	5	15		15	No	Cracks		-78.5		-52.6	-36.7			20.4	17.2	175	220		6.2	1.2	20.5
CRA02-DP	Chip2	IF08	i	6	15		35	Yes	Cracks		-83.9		-56.3	-27.0			21.4	11.3	188	185		8.7	1.1	20.6
CRA02-DP	Chip2	IF09	i	1	15		40	Yes	Cracks		-79.4		-59.2	-39.0			18.0	18.9	181	198		11.7	1.1	19.8
CRA02-DP	Chip2	IF09	i	2	15		15	Yes	Cracks		-80.7		-57.9	-36.1			18.6	17.7	180	198		11.8	1.1	19.7
CRA02-DP	Chip2	IF09	i	3	15		15	Yes	Cracks		-84.6		-58.5	-38.8			18.5	18.7	181	203		10.8	1.1	20.0
CRA02-DP	Chip2	IF09	i	4	15		15	Yes	Cracks		-83.8		-55.9	-35.8			18.5	17.7	181	196		11.3	1.1	19.9
CRA02-DP	Chip2	IF10	i	1	15		10	No	Cracks		-72.5		-54.2	-28.3			21.1	12.6	203	194		12.7	1.1	19.5
CRA02-DP	Chip2	IF10	i	2	15		25	No	Cracks		-75.2		-58.3	-32.1			19.5	15.6	204	196		12.6	1.1	19.4
CRA02-DP	Chip2	IF10	i	3	15		15	No	Cracks		-66.3		-52.1	-25.7			23.5	9.3	178	198		7.6	1.1	20.9
CRA02-DP	Chip2	IF10	i	4	15		20	No	Cracks		-78.7		-51.2	-31.3			19.9	15.0	176	197		6.8	1.1	20.8
CRA02-DP	Chip2	IF10	i	5	15		10	No	Cracks		-67.8		-49.3	-27.5			21.6	11.7	197	194		11.4	1.1	19.8

CRA02-DP	Chip2	IF11	i	1	15		15	No	Cracks		-73.8		-58.5	-28.4			21.2	12.6	188	196		9.3	1.1	20.3
CRA02-DP	Chip2	IF11	i	2	15		15	No	Cracks		-70.1		-55.6	-31.5			20.8	14.8	192	210		9.8	1.1	20.0
CRA02-DP	Chip2	IF11	i	3	15		10	No	Cracks		-75.8		-52.4	-29.3			20.5	13.5	192	194		10.1	1.1	20.1
CRA02-DP	Chip2	IF11	i	4	15		15	Yes	Cracks		-70.1		-55.4	-31.0			19.4	15.0	192	190		9.8	1.1	20.3
CRA02-DP	Chip2	IF11	i	5	15		15	Yes	Cracks		-79.3		-55.2	-32.2			19.2	15.8	179	192		10.4	1.1	20.1
CRA02-DP	Chip2	IF11	i	6	15		20	No	Cracks		-71.5		-57.1	-30.1			20.1	14.2	180	194		7.6	1.1	20.7
CRA02-DP	Chip2	IF11	i	7	15		15	No	Cracks		-78.5		-56.2	-30.5			20.7	14.3	172	203		6.3	1.1	21.1
CRA02-DP	Chip2	IF11	i	8	15		10	No	Cracks		-68.3		-50.7	-25.2			23.7	8.6	173	192		6.8	1.1	21.2
CRA02-DP	Chip2	IF11	i	9	15		10	No	Cracks		-68.9		-53.8	-26.8			21.7	11.0	180	187		7.8	1.1	20.8

Table 20. Fluid inclusions microthermometric analyses in **Pale de Rase (PR) sample** (BO18 sample; in green: aqueous inclusions). Abbreviations: FIA: fluid inclusion assemblages; V/L ratio: vapor/liquid ratio; xCO2: CO2 proportion; Tc: freezing temperature; Tm: melting temperature; clath: clathrate; Th: homogenization temperature; Hal: halite; hh: hydrohalite; P@homog.: homogenization pressure.

Sample	n°chip	FIAs (CO2 red, H2O green)	Type (CO2 red, H2O green)	n° FI	Rapport V/L (%)	xCo2 (vol.%)	Size µm	Salt at T°=25 °C	Petro	TcCo2	Tc H2O	TmCo2	TmfH2O	TmlH2O	ThCO2	Tmclath	Salinity		ThH2O	TmHalor Thh	Thtotal	P @ homog.	rBULK	dP/dT
																	NaCl (wt.%)	CaCl2 (wt.%)				(bar)	(g/cm3)	(bar/°C)
BO18 type2b	Chip1	IF01	iii	1	10		10	No	Primary		-52.6		-29.2	-3.5			5.7		243			33.6	0.9	13.7
BO18 type2b	Chip1	IF01	iii	2	10		10	No	Primary		-46.2		-28.8	-2.0			3.4		245			35.7	0.8	13.3
BO18 type2b	Chip1	IF01	iii	3	10		10	No	Primary		-46.4		-26.3	-0.5			0.9		255			43.0	0.8	12.7
BO18 type2b	Chip1	IF01	iii	4	10		10	No	Primary		-49.5		-27.2	-2.5			4.2		250			38.3	0.8	13.1
BO18 type2b	Chip1	IF01	iii	5	10		10	No	Primary		-45.8		-21.2	-2.8			4.6		248			37.3	0.8	13.3
BO18 type2b	Chip1	IF02	iii	1	10		10	No	Primary		-49.0		-26.3	-2.8			4.6		247			36.2	0.8	13.4
BO18 type2b	Chip1	IF02	iii	2	10		10	No	Primary		-48.6		-23.2	-1.2			2.1		229			27.1	0.8	14.1
BO18 type2b	Chip1	IF02	iii	3	10		10	No	Primary		-48.8		-24.3	-2.4			4.0		248			37.0	0.8	13.2
BO18 type2b	Chip1	IF02	iii	4	10		10	No	Primary		-53.2		-28.2	-2.5			4.2		216			20.6	0.9	14.9
BO18 type2b	Chip1	IF01.2	iii	1	15		15	No	Primary		-57.8		-28.2	-2.8			4.6		230			27.0	0.9	14.2
BO18 type2b	Chip1	IF01.2	iii	2	10		8	No	Primary		-58.0		-27.3	-3.2			5.3		235			29.4	0.9	14.0
BO18 type2b	Chip1	IF01.2	iii	3	15		8	No	Primary		-49.2		-28.3	-8.7			12.5		235			28.0	0.9	15.4
BO18 type2b	Chip1	IF01.2	iii	4	20		10	No	Primary		-51.9		-31.3	-2.5			4.2		248			36.9	0.8	13.3
BO18 type2b	Chip1	IF01.2	iii	5	15		6	No	Primary		-49.5		-21.9	-6.1			9.3		239			30.5	0.9	14.5
BO18 type2b	Chip1	IF01.2	iii	6	15		6	No	Primary		-47.9		-24.9	-6.5			9.9		239			30.7	0.9	14.6
BO18 type2b	Chip1	IF01.2	iii	7	10		8	No	Primary		-53.2		-28.2	-5.4			8.4		224			23.3	0.9	15.2
BO18 type2b	Chip1	IF01.2	iii	8	10		8	No	Primary		-52.1		-29.3	-2.0			3.4		235			29.8	0.8	13.9
BO18 type2b	Chip1	IF01.2	iii	9	15		8	No	Primary		-56.9		-24.9	-7.1			a		252			38.2	0.9	14.0
BO18 type2b	Chip1	IF01.2	iii	10	15		10	No	Primary		-50.8		-26.8	-6.5			9.9		236			28.8	0.9	14.8
BO18 type2b	Chip1	IF03	iii	1	10		25	No	Primary		-46.5		-29.5	-2.9			4.8		258			44.0	0.8	12.7

BO18 type2b	Chip1	IF03	iii	2	15		45	No	Primary		-44.9		-28.9	-2.2			3.7		255			42.1	0.8	12.8
BO18 type2b	Chip1	IF03	iii	3	10		15	No	Primary		-46.2		-28.7	-1.9			3.2		251			39.6	0.8	13.0
BO18 type2b	Chip1	IF03	iii	4	15		15	No	Primary		-44.4		-28.1	-0.7			1.2		252			40.6	0.8	12.9
BO18 type2b	Chip1	IF04	iii	1	10		20	No	Primary		-46.7		-25.8	-0.9			1.6		229			26.8	0.8	14.2
BO18 type2b	Chip1	IF04	iii	2	10		10	No	Primary		-45.2		-27.2	-1.9			3.2		239			31.7	0.8	13.7
BO18 type2b	Chip1	IF04	iii	3	10		10	No	Primary		-45.9		-29.1	-2.1			3.5		230			27.2	0.9	14.1
BO18 type2b	Chip1	IF04	iii	4	10		10	No	Primary		-47.8		-28.6	-1.7			2.9		232			28.4	0.8	14.0
BO18 type2b	Chip1	IF04	iii	5	10		10	No	Primary		-44.7		-27.9	-0.9			1.6		239			32.2	0.8	13.6
BO18 type2b	Chip1	IF05	iii	1	10		15	No	Primary		-48.2		-27.5	-0.7			1.2		243			34.5	0.8	13.4
BO18 type2b	Chip1	IF05	iii	2	15		15	No	Primary		-47.8		-26.9	-1.2			2.1		244			34.9	0.8	13.4
BO18 type2b	Chip1	IF05	iii	3	10		10	No	Primary		-45.1		-27.2	-2.3			3.9		251			39.4	0.8	13.0
BO18 type2b	Chip1	IF05	iii	4	10		10	No	Primary		-47.2		-26.3	-1.1			1.9		228			26.6	0.8	14.2
BO18 type2b	Chip1	IF05	iii	5	10		20	No	Primary		-47.3		-32.1	-1.2			2.1		252			40.6	0.8	12.9
BO18 type2b	Chip1	IF05	iii	6	10		20	No	Primary		-47.2		-26.1	-1.5			2.6		230			27.1	0.8	14.1
BO18 type2b	Chip1	IF06	iii	1	10		25	No	Primary		-44.3		-26.9	-1.6			2.7		261			46.9	0.8	12.4
BO18 type2b	Chip1	IF06	iii	2	10		15	No	Primary		-43.9		-28.2	-1.6			2.7		249			37.9	0.8	13.1
BO18 type2b	Chip1	IF06	iii	3	10		10	No	Primary		-48.2		-29.3	-0.8			1.4		246			36.7	0.8	13.2
BO18 type2b	Chip1	IF06	iii	4	10		10	No	Primary		-47.9		-27.9	-1.1			1.9		245			35.5	0.8	13.3
BO18 type2b	Chip1	IF07	iii	1	10		20	No	Primary		-56.1		-29.7	-3.1			5.1		202			15.7	0.9	15.7
BO18 type2b	Chip1	IF07	iii	2	15		30	No	Primary		-51.1		-31.4	-1.2			2.1		196			14.1	0.9	15.7
BO18 type2b	Chip1	IF07	iii	3	10		25	No	Primary		-46.5		-29.2	-1.6			2.7		208			17.9	0.9	15.2
BO18 type2b	Chip1	IF07	iii	4	10		15	No	Primary		-44.9		-28.2	-1.5			2.6		207			17.5	0.9	15.3
BO18 type2b	Chip1	IF07	iii	5	10		10	No	Primary		-46.9		-28.2	-0.9			1.6		207			17.6	0.9	15.3
BO18 type2b	Chip1	IF07	iii	6	10		15	No	Primary		-44.3		-27.8	-0.8			1.4		207			17.8	0.9	15.2
BO18 type2b	Chip1	IF08	iii	1	10		20	No	Primary		-47.9		-28.2	-0.6			1.1		231			28.3	0.8	14.0
BO18 type2b	Chip1	IF08	iii	2	15		15	No	Primary		-49.2		-29.5	-0.9			1.6		233			28.8	0.8	14.0
BO18 type2b	Chip1	IF08	iii	3	10		10	No	Primary		-44.5		-27.6	-0.8			1.4		242			34.0	0.8	13.5

BO18 type2b	Chip1	IF08	iii	4	10		10	No	Primary		-44.8		-28.1	-0.5			0.9		234			29.6	0.8	13.9
BO18 type2b	Chip1	IF08	iii	5	15		15	No	Primary		-47.8		-28.1	-1.1			1.9		233			29.0	0.8	13.9
BO18 type2b	Chip1	IF08	iii	6	10		10	No	Primary		-46.1		-27.9	-0.2			0.4		245			36.3	0.8	13.3
BO18 type2b	Chip1	IF08	iii	7	10		15	No	Primary		-48.2		-30.5	-0.5			0.9		245			36.0	0.8	13.3

Table 21. Fluid inclusions microthermometric analyses in **Pale Bidau (PB) sample** (BO10 and BO12 samples; in green: aqueous inclusions / in red: carbonic inclusions). Abbreviations: FIA: fluid inclusion assemblages; V/L ratio: vapor/liquid ratio; xCO2: CO2 proportion; Tc: freezing temperature; Tm: melting temperature; clath: clathrate; Th: homogenization temperature; Hal: halite; hh: hydrohalite; P@homog.: homogenization pressure.

Sample	n°chip	FIAs (CO2 red, H2O green)	Type (CO2 red, H2O green)	n° FI	Rapport V/L (%)	xCo2 (vol.%)	Size µm	Salt at T°=25 °C	Petro	TcCo2	Tc H2O	TmCo2	TmfH2O	TmlH2O	ThCO2	Tmclath	Salinity		ThH2O	TmHal or Thh	Thtotal	P @ homog.	rBULK	dP/dT
																	NaCl (wt.%)	CaCl2 (wt.%)				(bar)	(g/cm3)	(bar/°C)
BO10 type2b	Chip 1	IF03	iii	1	15		30	No	Pseudosecondary		-86.2		-33.2	-15.5			16.2		176			7.9	1.0	20.7
BO10 type2b	Chip 1	IF04	iii	1	10		15	No	Pseudosecondary		-35.0		-24.2	-18.3			27.6		190			9.7	1.1	20.2
BO10 type2b	Chip 1	IF04	ii	2		15	15	No	Pseudosecondary	-103.8	-27.2	-62.0	-18.3	-7.2	8.3	11	10.7				302			
BO10 type2b	Chip 1	IF04	iii	3	15		15	No	Pseudosecondary		-84.1		-35.5	18.5			26.5		177			7.4	1.1	21.0
BO10 type2b	Chip 1	IF04	iii	4	20		25	No	Pseudosecondary		-85.0		-33.0	-18.3			27.6		189			9.3	1.1	20.3
BO10 type2b	Chip 1	IF04	iii	5	20		25	No	Pseudosecondary		-41.4		-23.0	-7.5			11.1		206			16.3	0.9	16.8
BO10 type2b	Chip 1	IF04	ii	5bis	20		30	No	Pseudosecondary	-97.3	-34.8	-61.2	-31.2	-8.5	-2.3	0	12.3				305			
BO10 type2b	Chip 1	IF04	ii	6		20	30	No	Pseudosecondary	-101.4	-30.4	-61.3	-27.2	-7.2	9.4	9					306			
BO10 type2b	Chip 1	IF04	ii	7		15	20	No	Pseudosecondary	-103.2	-33.0	-59.5	-29.2	-7.3	9.6	10				-15	301			
BO10 type2b	Chip 1	IF04	ii	8		20	15	No	Pseudosecondary	-101.5	-32.4	-63.2	-29.5	-7.2	10.6	10				-15	304			
BO10 type2b	Chip 1	IF04	ii	9		10	30	No	Pseudosecondary	-83.2	-40.2	-58.9	-28.3	-7.2	14.2	0	10.7				304			
BO10 type2b	Chip 1	IF04	ii	10		10	15	No	Pseudosecondary	-102.3	-37.4	-57.3	-25.3	-5.2	23.2	9	8.1				308			
BO10 type2b	Chip 1	IF04	ii	11		15	25	No	Pseudosecondary	-98.0	-39.0	-58.5	-36.4	-20.5	6.7	3	9.7				310			
BO10 type2b	Chip 1	IF04	ii	12		10	15	No	Pseudosecondary	-97.8	-40.9	-59.1	-28.2	-10.5	-0.5	1	14.5				300			
BO10 type2b	Chip 1	IF04	ii	13		10	15	No	Pseudosecondary	-102.3	-38.2	-59.2	-29.5	-3.9	10.6	11					305			
BO10 type2b	Chip 1	IF05	iii	1	20		15	No	Pseudosecondary		-60.6		-34.8	-13.5			15.5		183	-15		9.4	1.0	19.9
BO10 type2b	Chip 1	IF07	iii	1	15		30	No	Pseudosecondary		-69.3		-42.3	-12.2			8.7		185	-15		9.8	1.0	19.5
BO10 type2b	Chip 1	IF07	iii	2	15		30	No	Pseudosecondary		-59.5		-27.9	-16.5			9.7		230	-16		23.5	1.0	17.2
BO10 type2b	Chip 1	IF07	iii	3	20		15	No	Pseudosecondary		-61.2		-31.4	-16.5			9.7		176			7.7	1.0	20.8
BO10 type2b	Chip 1	IF07	iii	4	20		15	No	Pseudosecondary		-58.3		-28.7	-16.2			9.5		189			10.5	1.0	19.9

BO10 type2b	Chip 1	IF07	ii	5		20	15	No	Pseudosecondary	-101.2	-37.8	-57.8	-27.3	-12.5	19.5	5	11.5				310			
BO10 type2b	Chip 1	IF07	iii	6	20		10	No	Pseudosecondary		-38.0		-28.5	-10.5			8.5		231			25.5	0.9	16.1
BO12 type2b	Chip 1	IF01	iii	1	15		15	No	Pseudosecondary		-49.0		-31.2	-4.7			7.4		279			59.7	0.8	12.0
BO12 type2b	Chip 1	IF01	iii	2	20		15	No	Pseudosecondary		-48.7		-28.6	-4.2			6.7		251			38.7	0.9	13.4
BO12 type2b	Chip 1	IF01	iii	3	20		15	No	Pseudosecondary		-48.5		-27.5	-7.2			10.7		266			47.6	0.9	13.3
BO12 type2b	Chip 1	IF01	iii	4	15		10	No	Pseudosecondary		-49.5		-29.5	-4.1			6.6		246			35.1	0.9	13.7
BO12 type2b	Chip 1	IF01	iii	5	15		15	No	Pseudosecondary		-47.5		-27.5	-4.6			7.3		279			60.3	0.8	12.0
BO12 type2b	Chip 1	IF01	iii	6	15		10	No	Pseudosecondary		-37.2		-27.2	-3.2			5.3		286			68.1	0.8	11.3
BO12 type2b	Chip 1	IF01	iii	9	10		15	No	Pseudosecondary		-48.9		-27.1	-6.8			10.2		276			56.5	0.9	12.6
BO12 type2b	Chip 1	IF01	iii	10	15		10	No	Pseudosecondary		-45.7		-24.2	-7.2			10.7		275			55.3	0.9	12.8
BO12 type2b	Chip 1	IF01	iii	11	15		15	No	Pseudosecondary		-48.2		-28.6	-8.2			11.9		274			53.9	0.9	13.1
BO12 type2b	Chip 1	IF01	iii	17	10		15	No	Pseudosecondary		-49.3		-27.7	-12.3			16.2		245			32.3	0.9	15.6
BO12 type2b	Chip 1	IF01b	iii	12	15		10	No	Secondary		-48.2		-24.5	-10.8			14.8		193			12.1	1.0	18.6
BO12 type2b	Chip 1	IF01b	iii	13	15		10	No	Secondary		-47.8		-25.7	-10.2			14.1		188			10.9	1.0	18.8
BO12 type2b	Chip 1	IF01b	iii	14	10		15	No	Secondary		-45.2		-28.6	-11.0			15.0		210			17.1	1.0	17.5
BO12 type2b	Chip 1	IF01b	iii	15	10		10	No	Secondary		-47.4		-29.1	-11.2			15.2		189			11.0	1.0	19.0
BO12 type2b	Chip 1	IF01b	iii	16	10		12	No	Secondary		-49.2		-31.5	-10.2			14.1		233			26.2	0.9	15.9
BO12 type2b	Chip 1	IF01b	iii	7	15		10	No	Secondary		-52.3		-24.5	-12.3			16.2		184			9.6	1.0	19.6
BO12 type2b	Chip 1	IF01b	iii	8	10		15	No	Secondary		-51.0		-23.2	-10.1			14.0		222			21.8	1.0	16.5
BO12 type2b	Chip 1	IF01c	ii	18		25	25	No	Pseudosecondary	-97.9	-43.6	-60.7	-24.5	-0.1	19.2	0	15.4				300			
BO12 type2b	Chip 1	IF01c	ii	19		25	20	No	Pseudosecondary	-98.2		-60.1			13.9	8	11.7				298			
BO12 type2b	Chip 1	IF01c	ii	20		25	16	No	Pseudosecondary	-107.4	-39.2	-62.1		-7.0	19.7	10	11.2				290			
BO12 type2b	Chip 1	IF01c	ii	21		25	15	No	Pseudosecondary	-96.7	-41.0	-60.4	-22.3	-8.2	16.1	10	11.2				300			
BO12 type2b	Chip 1	IF01c	ii	22		20	10	No	Pseudosecondary	-103.2	-33.3	-61.2			13.3	10	12.6				301			
BO12 type2b	Chip 1	IF01c	ii	23		25	10	No	Pseudosecondary	-100.3	-51.0	-61.4	-28.7	-5.3	16.2	9	12.5				301			
BO12 type2b	Chip 1	IF02	iii	1	10			No	Pseudosecondary		-43.2		-29.1	-11.1			15.1		285	-16		61.5	0.9	13.1
BO12 type2b	Chip 1	IF02	iii	2	10			No	Pseudosecondary		-46.6		-27.3	-10.8			14.8		208			16.2	1.0	17.6

BO12 type2b	Chip 1	IF02	iii	3	10			No	Pseudosecondary		-46.5		-26.8	-10.1			14.0		265			45.8	0.9	14.0
BO12 type2b	Chip 1	IF02	iii	4	10			No	Pseudosecondary		-46.8		-26.9	-10.2			14.1		310			89.6	0.8	11.7
BO12 type2b	Chip 1	IF02	iii	5	10			No	Pseudosecondary		-38.7		-23.9	-9.8			13.7		217	-18		19.8	1.0	16.8
BO12 type2b	Chip 1	IF02	iii	6	10			No	Pseudosecondary		-45.4		-27.1	-10.8			14.8		316	-17		96.0	0.8	11.5
BO12 type2b	Chip 1	IF02	iii	7	10			No	Pseudosecondary		-49.9		-27.8	-11.0			15.0		242			30.9	0.9	15.5
BO12 type2b	Chip 1	IF02	iii	8	10			No	Pseudosecondary		-49.6		-28.1	-11.2			15.2		266			46.1	0.9	14.2
BO12 type2b	Chip 1	IF02	iii	9	10			No	Pseudosecondary		-49.7		-28.0	-11.6			15.6		315			94.7	0.9	11.7
BO12 type2b	Chip 1	IF02	iii	10	10			No	Pseudosecondary		-48.1		-25.5	-10.8			14.8		233			26.2	0.9	16.1
BO12 type2b	Chip 1	IF02	iii	11	10			No	Pseudosecondary		-49.5		-29.5	-10.1			14.0		216			19.1	1.0	17.0
BO12 type2b	Chip 1	IF02	iii	12	10			No	Pseudosecondary		-52.1		-27.1	-10.3			14.3		225			22.9	0.9	16.4
BO12 type2b	Chip 1	IF03	iii	1	10			No	Pseudosecondary		-45.3		-29.5	-10.1			14.0		262			43.8	0.9	14.2
BO12 type2b	Chip 1	IF03	iii	2	10			No	Pseudosecondary		-47.2		-25.3	-9.8			13.7		256			39.8	0.9	14.4
BO12 type2b	Chip 1	IF03	iii	3	10			No	Pseudosecondary		-48.1		-27.5	-10.4			14.4		254	-15		38.3	0.9	14.7
BO12 type2b	Chip 1	IF03	iii	4	10			No	Pseudosecondary		-48.6		-25.4	-11.2			15.2		277			54.8	0.9	13.5
BO12 type2b	Chip 1	IF03	iii	5	10			No	Pseudosecondary		-52.1		-24.9	-10.1			14.0		248			34.4	0.9	15.0
BO12 type2b	Chip 1	IF03	iii	6	10			No	Pseudosecondary		-53.1		-30.1	-12.6			16.5		258			40.0	0.9	14.9
BO12 type2b	Chip 1	IF04	iii	1	10			No	Pseudosecondary		-49.8		-27.1	-11.4			15.4		322			104.4	0.8	11.3
BO12 type2b	Chip 1	IF04	iii	2	10			No	Pseudosecondary		-48.1		-25.7	-11.2			15.2		316			95.6	0.9	11.6
BO12 type2b	Chip 1	IF04	iii	3	10			No	Pseudosecondary		-46.9		-25.5	-11.5			15.5		285			61.1	0.9	13.2
BO12 type2b	Chip 1	IF04	iii	4	10			No	Pseudosecondary		-44.7		-26.5	-10.8			14.8		260			41.6	0.9	14.5
BO12 type2b	Chip 1	IF04	iii	5	10			No	Pseudosecondary		-51.2		-28.3	-10.9			14.9		238			29.0	0.9	15.7
BO12 type2b	Chip 1	IF04	iii	6	10			No	Pseudosecondary		-45.1		-24.5	-10.8			14.8		256			38.9	0.9	14.7
BO12 type2b	Chip 1	IF04	iii	7	10			No	Pseudosecondary		-37.8		-21.3	-9.5			13.4		228			24.2	0.9	16.0
BO12 type2b	Chip 1	IF05	iii	1	10			No	Pseudosecondary		-49.8		-28.7	-11.9			15.9		313			91.4	0.9	11.8
BO12 type2b	Chip 1	IF05	iii	2	10			No	Pseudosecondary		-48.2		-26.8	-11.5			15.5		242			30.4	0.9	15.7
BO12 type2b	Chip 1	IF05	iii	3	10			No	Pseudosecondary		-46.1		-24.2	-9.8			13.7		251			36.6	0.9	14.7
BO12 type2b	Chip 1	IF05	iii	4	10			No	Pseudosecondary		-49.1		-26.1	-10.4			14.4		322			104.3	0.8	11.1

BO12 type2b	Chip 1	IF05	iii	5	10			No	Pseudosecondary		-49.4		-24.5	-10.1			14.0		246			33.1	0.9	15.1

Table 22. Fluid inclusions microthermometric analyses in **Arre (AR) sample** (ARR06 sample, in green: aqueous inclusions / in red: carbonic inclusions). Abbreviations: FIA: fluid inclusion assemblages; V/L ratio: vapor/liquid ratio; xCO2: CO2 proportion; Tc: freezing temperature; Tm: melting temperature; clath: clathrate; Th: homogenization temperature; Hal: halite; hh: hydrohalite; P@homog.: homogenization pressure.

Sample	n°chip	FIAs (CO2 red, H2O green)	Type (CO2 red, H2O green)	n° FI	Rapport V/L (%)	xCo2 (vol.%)	Size µm	Salt at T°=25 °C	Petro	TcCo2	Tc H2O	TmCo2	TmfH2O	TmlH2O	ThCO2	Tmclath	Salinity		ThH2O	TmHal or Thh	Thtotal	P @ homog.	rBULK	dP/dT
																	NaCl (wt.%)	CaCl2 (wt.%)				(bar)	(g/cm3)	(bar/°C)
ARR06-DP	Chip 1	IF01	iii	1	10		25	No	Primary		-69.3		-41.2	-23.5			16.0	8.0	180	-24		8.1	1.1	20.8
ARR06-DP	Chip 1	IF01	iii	2	10		20	No	Primary		-64.5		-39.8	-21.5			13.0	9.5	170	-25		6.5	1.1	21.5
ARR06-DP	Chip 1	IF01	iii	3	10		15	No	Primary		-67.6		-37.8	-25.5			13.6	11.4	165	-24		5.6	1.1	21.7
ARR06-DP	Chip 1	IF01b	iii	4	15		15	No	Primary		-65.6		-40.7	-23.2			18.1	6.1	174	-22		6.9	1.1	21.3
ARR06-DP	Chip 1	IF01b	iii	5	10		10	No	Primary		-73.9		-44.3	-25.7			13.2	11.8	172	-25		6.6	1.1	21.3
ARR06-DP	Chip 1	IF01b	iii	6	10		15	No	Primary		-73.2		-41.4	-22.7			19.6	4.7	165	-20		5.7	1.1	21.8
ARR06-DP	Chip 1	IF01b	iii	7	15		10	No	Primary		-68.0		-44.9	-21.5			22.5	1.1	158	-21		4.7	1.1	22.3
ARR06-DP	Chip 1	IF01b	iii	8	15		10	No	Primary		-69.3		-46.3	-23.5			15.3	8.7	172	-24		6.7	1.1	21.3
ARR06-DP	Chip 1	IF01c	iii	8	15		10	No	Primary		-68.5		-46.4	-23.6			14.6	9.3	173	-25		6.7	1.1	21.3
ARR06-DP	Chip 1	IF01c	iii	8	15		10	No	Primary		-68.3		-46.3	-23.8			14.7	9.3	173	-25		6.8	1.1	21.3

ARR06-DP	Chip 1	IF01c	iii	9	15		10	No	Primary		-67.5		-38.5	-23.8			17.0	7.6	170	-21		6.4	1.1	21.5
ARR06-DP	Chip 1	IF02	iii	1	10		8	No	Primary		-71.5		-42.4	-23.1			13.6	9.9	184	-25		8.7	1.1	20.6
ARR06-DP	Chip 1	IF02	iii	2	10		10	No	Primary		-74.5		-45.7	-24.7			14.9	9.7	183	-24		8.6	1.1	20.6
ARR06-DP	Chip 1	IF02	iii	3	15		10	No	Primary		-72.0		-43.4	-24.5			15.3	9.3	183	-24		8.6	1.1	20.6
ARR06-DP	Chip 1	IF02	iii	4	10		10	No	Primary		-73.5		-43.2	-24.7			15.1	9.7	194	-23		10.9	1.1	20.0
ARR06-DP	Chip 1	IF03	iii	1	10		10	No	Primary		-68.2		-50.1	-25.2			14.7	10.7	185	-20		8.9	1.1	20.5
ARR06-DP	Chip 1	IF03	iii	2	10		10	No	Primary		-69.5		-51.0	-24.9			15.1	10.1	185	-21		8.9	1.1	20.5
ARR06-DP	Chip 1	IF03	iii	3	10		10	No	Primary		-70.1		-52.3	-25.1			14.2	10.6	201	-24		12.6	1.1	19.6
ARR06-DP	Chip 1	IF04	iii	1	10		15	No	Primary		-74.9		-46.8	-27.3			11.2	14.5	182	-25		8.2	1.1	20.7
ARR06-DP	Chip 1	IF04	iii	2	10		8	No	Primary		-71.7		-38.5	-25.8			13.1	12.0	173	-24		6.7	1.1	21.2
ARR06-DP	Chip 1	IF04	iii	3	10		10	No	Primary		-69.5		-47.7	-23.5			11.5	12.0	171	-26		6.5	1.1	21.4
ARR06-DP	Chip 1	IF04	iii	4	10		10	No	Primary		-66.4		-41.2	-21.2			15.2	7.3	191	-24		10.5	1.1	20.1
ARR06-DP	Chip 4	IF05	iii	1	10		10	No	Primary		-71.1		-58.2	-28.7			7.7	17.9	171	-30		6.1	1.1	21.3

ARR06-DP	Chip 4	IF05	iii	1	10		10	No	Primary		-71.3		-58.2	-28.5			10.0	16.2	171	-23		6.1	1.1	21.3
ARR06-DP	Chip4	IF05	iii	2	10		12	No	Primary		-70.3		-57.3	-28.1			10.4	15.6	175	-23		6.9	1.1	21.0
ARR06-DP	Chip 5	IF08	iii	1	10		12	No	Primary		-66.6		-46.7	-25.1			14.5	10.5	181	-22		8.1	1.1	20.8
ARR06-DP	Chip 5	IF08	iii	2	10		10	No	Primary		-70.8		-43.5	-27.2			11.2	14.4	166	-25		5.6	1.1	21.6
ARR06-DP	Chip 5	IF08	iii	3	10		10	No	Primary		-70.1		-45.4	-26.5			12.1	13.2	178	-25		7.5	1.1	20.9
ARR06-DP	Chip 5	IF08	iii	4	10		10	No	Primary		-69.5		-45.5	-26.6			11.8	13.4	173	-26		6.7	1.1	21.2
ARR06-DP	Chip 5	IF08	iii	5	10		10	No	Primary		-80.1		-52.1	-23.9			16.9	7.8	175	-21		7.2	1.1	21.2
ARR06-DP	Chip 5	IF08	iii	6	10		10	No	Primary		-69.1		-45.8	-26.5			12.2	13.2	168	-24		5.8	1.1	21.6
ARR06-DP	Chip 4	IF06	iii	1	15		20	No	Secondary cracks		-67.2		-49.5	-21.8			21.9	2.0	201	-20		13.0	1.1	19.5
ARR06-DP	Chip 4	IF06	iii	2	10		15	No	Secondary cracks		-71.0		-54.9	-26.4			12.3	13.0	144	-25		3.1	1.1	23.1
ARR06-DP	Chip 4	IF06	iii	3	10		20	No	Secondary cracks		-72.8		-49.3	-24.3			15.6	8.9	176	-24		7.3	1.1	21.1
ARR06-DP	Chip 4	IF06	iii	4	10		20	No	Secondary cracks		-59.7		-48.2	-24.3			15.9	8.8	175	-22		7.8	1.0	20.6
ARR06-DP	Chip 4	IF06	iii	5	10		12	No	Secondary cracks		-80.7		-59.2	-25.2			14.2	10.8	177	-23		7.3	1.1	21.0

ARR06-DP	Chip 4	IF06	iii	6	10		15	No	Secondary cracks		-72.2		-48.1	-24.3			10.8	13.0	165	-27		5.6	1.1	21.8
ARR06-DP	Chip 4	IF06	iii	7	10		10	No	Secondary cracks		-64.2		-47.0	-21.3			23.1	0.4	174	-20		7.2	1.1	21.2
ARR06-DP	Chip 4	IF06	iii	8	10		15	No	Secondary cracks		-73.8		-53.2	-27.6			10.7	15.0	151	-25		3.8	1.1	22.5
ARR06-DP	Chip 4	IF06	iii	9	10		15	No	Secondary cracks		-59.3		-29.3	-24.3			16.2	8.7	152	-20		4.3	1.1	22.6
ARR06-DP	Chip 4	IF07	iii	1	10		12	No	Secondary cracks		-61.2		-49.5	-22.6			19.9	4.4	177	-20		7.7	1.1	21.0
ARR06-DP	Chip 4	IF07	iii	2	15		15	No	Secondary cracks		-61.9		-45.6	-22.5			20.1	4.1	177	-20		7.8	1.1	21.0
ARR06-DP	Chip 4	IF07	iii	3	10		10	No	Secondary cracks		-55.2		-45.2	-22.4			20.3	3.8	180	-20		8.6	1.0	20.4
ARR06-DP	Chip 4	IF07	iii	4	10		20	No	Secondary cracks		-58.2		-47.1	-22.3			20.6	3.5	135	-20		2.6	1.1	23.9
ARR06-DP	Chip 4	IF07	iii	5	10		15	No	Secondary cracks		-62.5		-47.2	-22.8			19.3	5.0	190	-20		10.4	1.0	20.1
ARR06-DP	Chip 4	IF07	iii	6	15		12	No	Secondary cracks		-75.2		-52.3	-31.2			7.6	19.4	166	-25		5.4	1.1	21.4
ARR06-DP	Chip 4	IF09	iii	1	10		25	No	Secondary cracks		-74.2		-47.8	-32.2			6.9	20.4	200	-26		11.5	1.1	19.6
ARR06-DP	Chip 4	IF09	iii	2	15		25	No	Secondary cracks		-60.5		-48.0	-21.2			23.4	0.1	160	-20		5.0	1.1	22.2
ARR06-DP	Chip 4	IF09	iii	3	10		15	No	Secondary cracks		-71.2		-48.7	-25.7			13.3	11.8	160	-24		4.9	1.1	22.1

ARR06-DP	Chip 4	IF09	iii	4	10		15	No	Secondary cracks		-67.5		-48.4	-24.3			16.1	8.8	173	-21		6.7	1.1	21.3
ARR06-DP	Chip 4	IF09	iii	5	10		12	No	Secondary cracks		-75.9		-52.3	-28.2			10.2	15.8	163	-24		5.1	1.1	21.7
ARR06-DP	Chip 4	IF09	iii	6	10		12	No	Secondary cracks		-68.2		-45.2	-27.3			11.2	14.5	184	-24		8.5	1.1	20.6
ARR06-DP	Chip 4	IF09	iii	7	10		15	No	Secondary cracks		-84.5		-50.2	-26.9			12.0	13.8	175	-22		7.0	1.1	21.1
ARR06-DP	Chip 4	IF09	iii	8	10		20	No	Secondary cracks		-60.6		-52.5	-22.3			20.7	3.5	211	-19		15.9	1.0	18.8
ARR06-DP	Chip 4	IF09	iii	9	10		15	No	Secondary cracks		-74.1		-48.2	-26.9			11.7	13.9	165	-24		5.4	1.1	21.7
ARR06-DP	Chip 4	IF09	iii	10	10		15	No	Secondary cracks		-73.2		-50.2	-25.3			14.0	11.0	180	-23		7.9	1.1	20.8
ARR06-DP	Chip 4	IF09	iii	11	10		10	No	Secondary cracks		-65.9		-45.9	-22.1			17.9	5.4	184	-23		9.0	1.1	20.5
ARR06-DP	Chip 4	IF09	iii	12	10		10	No	Secondary cracks		-65.6		-46.2	-22.4			17.0	6.5	164	-23		5.6	1.1	21.9
ARR06-DP	Chip 4	IF10	iii	1	10		15	No	Secondary cracks		-83.1		-45.6	-25.2			14.0	10.8	180	-24		8.0	1.1	20.8
ARR06-DP	Chip 4	IF10	iii	2	10		15	No	Secondary cracks		-65.3		-50.1	-22.3			20.4	3.5	169	-21		6.3	1.1	21.5
ARR06-DP	Chip 4	IF10	iii	3	10		12	No	Secondary cracks		-72.9		-51.2	-22.7			19.6	4.7	167	-20		6.0	1.1	21.7
ARR06-DP	Chip 4	IF10	iii	4	10		15	No	Secondary cracks		-69.7		-50.3	-22.1			21.1	2.9	179	-20		8.1	1.1	20.8

ARR06-DP	Chip 4	IF10	iii	5	10		12	No	Secondary cracks		-71.5		-52.1	-23.2			18.4	6.0	174	-20		7.0	1.1	21.2
ARR06-DP	Chip 4	IF10	iii	6	10		10	No	Secondary cracks		-79.9		-50.5	-23.2			18.3	6.1	158	-21		4.7	1.1	22.3
ARR06-DP	Chip 4	IF10	iii	7	10		25	No	Secondary cracks		-72.6		-49.6	-21.6			12.5	10.0	180	-25		8.1	1.1	20.8
ARR06-DP	Chip 4	IF10	iii	8	10		30	No	Secondary cracks		-63.7		-48.5	-22.7			19.2	4.7	175	-22		7.4	1.1	21.1
ARR06-DP	Chip 4	IF10	iii	9	10		30	No	Secondary cracks		-66.5		-48.9	-22.4			14.2	9.0	170	-25		6.5	1.1	21.5
ARR06-DP	Chip 4	IF10	iii	10	10		30	No	Secondary cracks		-65.2		-48.3	-22.3			20.6	3.5	175	-20		7.4	1.1	21.1

Table 23. Fluid inclusions microthermometric analyses in **Argut-dessus (AD) sample** (BO25 sample, in green: aqueous inclusions / in red: carbonic inclusions). Abbreviations: FIA: fluid inclusion assemblages; V/L ratio: vapor/liquid ratio; xCO2: CO2 proportion; Tc: freezing temperature; Tm: melting temperature; clath: clathrate; Th: homogenization temperature; Hal: halite; hh: hydrohalite; P@homog.: homogenization pressure.

Sample	n°chip	FIAs (CO2 red, H2O green)	Type (CO2 red, H2O green)	n° FI	Rapport V/L (%)	xCo2 (vol.%)	Size µm	Salt at T°=25 °C	Petro	TcCo2	Tc H2O	TmCo2	TmfH2O	TmlH2O	ThCO2	Tmclath	Salinity		ThH2O	TmHal or Thh	Thtotal	P @ homog.	rBULK	dP/dT
																	NaCl (wt.%)	CaCl2 (wt.%)				(bar)	(g/cm3)	(bar/°C)
BO25	Chip1	IF01	iii	1	10		15	No	Primary		-35.7		-29.2	-8.2			11.9		238			19.3	1.1	18.4
BO25	Chip1	IF01	iii	2	10		10	No	Primary		-39.2		-34.4	-2.2			3.7		238			25.2	1.1	17.7
BO25	Chip1	IF01	iii	3	10		10	No	Primary		-47.3		-28.7	-7.2			10.7		239			32.2	1.0	16.4
BO25	Chip1	IF01	iii	4	10		10	No	Primary		-41.2		-28.2	-3.2			5.3		235			16.2	1.1	18.9
BO25	Chip1	IF01	iii	5	10		10	No	Primary		-42.3		-26.8	-4.5			7.2		242			20.8	1.0	18.1
BO25	Chip1	IF02	ii	1		80	15	No	Primary	-101.1		-58.1			9.4	9					290			
BO25	Chip1	IF02	ii	2		60	8	No	Primary	-100.8		-58.5			9.0	9					289			
BO25	Chip1	IF02	ii	3		75	10	No	Primary	-99.8		-58.2			14.9	15					291			
BO25	Chip1	IF03	ii	1		50	20	No	Primary	-96.5	-45.2	-56.5	-25.7	-3.2	9.6	11					298			
BO25	Chip1	IF03	ii	2		80	10	No	Primary	-100.2	-39.5	-57.6			10.9	11					296			
BO25	Chip1	IF03	ii	3		80	15	No	Primary	-100.8	-38.7	-57.2			4.3	8					295			
BO25	Chip1	IF03	ii	4		75	15	No	Primary	-101.0		-57.8			11.8	9					294			
BO25	Chip1	IF04	iii	1	10		15	No	Primary		-42.7		-22.4	-3.2			5.3		254			9.3	1.1	20.0
BO25	Chip1	IF04	iii	2	10		15	No	Primary		-44.8		-25.6	-2.3			3.9		283			11.8	1.1	19.7
BO25	Chip1	IF04	ii	3	10	40	15	No	Primary	-92.6	-39.2	-58.1	-27.2	-7.3	5.8	7	10.9				295			

BO25	Chip1	IF04	iii	4	10		10	No	Primary		-40.8		-21.2	-1.5			2.6		278			11.0	1.1	20.0
BO25	Chip2	IF05	ii	1		60	10	No	Primary	-96.2		-58.3	-24.0	-7.3	3.2	9					301			
BO25	Chip2	IF05	ii	2		70	8	No	Primary	-96.1		-57.5			8.5	10					300			
BO25	Chip2	IF05	ii	3		75	20	No	Primary	-93.9		-58.1			7.1	10					301			
BO25	Chip2	IF05	ii	4		60	15	No	Primary	-95.2		-57.5			2.1	11					299			
BO25	Chip2	IF05	ii	5		80	10	No	Primary	-96.1		-57.7			5.1	9					300			
BO25	Chip2	IF05	ii	6		70	10	No	Primary	-97.1		-57.0			6.1	3					300			
BO25	Chip2	IF06	ii	1		60	10	No	Primary	-94.9		-58.1			7.2	10					300			
BO25	Chip2	IF06	ii	2		70	10	No	Primary	-98.1	-34.5	-58.5			5.8	9					301			
BO25	Chip2	IF06	ii	3		60	10	No	Primary	-96.5	-35.1	-57.9			6.1	10					305			
BO25	Chip2	IF06	ii	4		60	15	No	Primary	-97.2		-57.2			10.1	9					301			
BO25	Chip2	IF06	ii	5		70	10	No	Primary	-99.5		-58.1			6.5	8					301			
BO25	Chip2	IF06	ii	6		70	10	No	Primary	-96.5		-57.5			3.5	6					300			
BO25	Chip2	IF07	iii	1	10		10	No	Primary		-47.3		-21.3	-3.5			5.7		232			8.7	1.1	20.6
BO25	Chip2	IF07	iii	2	10		10	No	Primary		-48.1		-22.0	-5.2			8.1		237			11.7	1.1	19.8
BO25	Chip2	IF08	ii	1		60	15	No	Primary	-97.8	-47.8	-57.2			11.7	10					300			
BO25	Chip2	IF08	ii	2		90	10	No	Primary	-97.5		-57.7			11.6	10					300			
BO25	Chip2	IF08	ii	3		90	10	No	Primary	-98.5		-58.0			11.7	9					301			
BO25	Chip2	IF08	ii	4		90	10	No	Primary	-97.9		-58.1			11.9	9					303			
BO25	Chip3	IF08	ii	5		80	10	No	Primary	-98.1		-57.8			12.5	9					305			
BO25	Chip4	IF08	ii	6		80	8	No	Primary	-98.8		-57.2			11.5	9					300			
BO25	Chip5	IF08	ii	7		90	8	No	Primary	-98.2		-57.2			11.6	9					300			

BO25	Chip6	IF09	ii	1		80	10	No	Primary	-95.1		-57.7			8.3	10					300			
BO25	Chip7	IF09	ii	2		60	10	No	Primary	-94.9		-58.2			8.4	10					301			
BO25	Chip8	IF10	iii	1	15		15	No	Primary		-39.2		-29.6	-8.9			12.7		252			9.8	1.1	20.0
BO25	Chip9	IF10	iii	2	10		10	No	Primary		-43.2		-31.3	-13.4			17.3		249			10.1	1.1	20.1

Table 24. Fluid inclusions microthermometric analyses in **Victoria (VT) sample** (VIC12 sample, in green: aqueous inclusions / in red: carbonic inclusions). Abbreviations: FIA: fluid inclusion assemblages; V/L ratio: vapor/liquid ratio; xCO2: CO2 proportion; Tc: freezing temperature; Tm: melting temperature; clath: clathrate; Th: homogenization temperature; Hal: halite; hh: hydrohalite; P@homog.: homogenization pressure.

Sample	n°chip	FIAs (CO2 red, H2O green)	Type (CO2 red, H2O green)	n° FI	Rapport V/L (%)	xCo2 (vol.%)	Size µm	Salt at T°=25 °C	Petro	TcCo2	Tc H2O	TmCo2	TmfH2O	TmlH2O	ThCO2	Tmclath	Salinity		ThH2O	TmHal or Thh	Thtotal	P @ homog.	rBULK	dP/dT
																	NaCl (wt.%)	CaCl2 (wt.%)				(bar)	(g/cm3)	(bar/°C)
VIC12	Chip 1	IF01	i	1	15		15	Yes (halite)	Secondary cracks		-81.0		-49.2	-28.3			20.4	12.8	222	184		9.8	1.1	20.3
VIC12	Chip 1	IF01	i	2	15		15	Yes (halite)	Secondary cracks		-102.0		-51.3	-29.3			20.0	13.7	224	186		10.4	1.1	20.1
VIC12	Chip 1	IF01	ii	3		40	10	No	Secondary cracks	-97.3	-49.2	-61.2	-42.4	-29.2	-16.1						301			
VIC12	Chip 1	IF01	ii	4		90	15	No	Secondary cracks	-103.0		-59.3			-16.1						305			
VIC12	Chip 1	IF01	i	5	10		15	No	Secondary cracks		-60.1		-41.2	-21.3			31.3	0.3	225	200		6.8	1.1	21.2
VIC12	Chip 1	IF01	i	6	10		10	No	Secondary cracks		-48.7		-37.2	-22.3			28.9	2.8	229	201		7.8	1.1	20.8
VIC12	Chip 1	IF01	i	7	10		10	No	Secondary cracks		-61.2		-39.3	-22.5			28.5	3.3	225	201		33.6	0.9	13.7
VIC12	Chip 1	IF01	i	8	10		15	No	Secondary cracks		-65.3		-49.6	-26.7			22.9	10.6	224	203		35.7	0.8	13.3
VIC12	Chip 1	IF01	i	9	10		15	No	Secondary cracks		-66.5		-53.5	-32.1			19.8	15.5	241	200		43.0	0.8	12.7
VIC12	Chip2	IF09	ii	1		70	10	No	Secondary cracks	-100.3	-42.0	-60.5			9.2	10					302			
VIC12	Chip2	IF09	ii	2		80	10	No	Secondary cracks	-100.6	-42.6	-59.5			9.6	9					305			
VIC12	Chip2	IF09	ii	3		80	10	No	Secondary cracks	-102.2	-39.5	-61.1			8.8	5					305			
VIC12	Chip2	IF09	ii	4		80	13	No	Secondary cracks	-102.7	-38.7	-61.3			9.0	11					300			
VIC12	Chip2	IF09	ii	5		80	15	No	Secondary cracks	-101.2	-38.4	-59.7			10.8	11					300			
VIC12	Chip2	IF09	ii	6		80	10	No	Secondary cracks	-104.3		-62.3			12.1	11					301			

VIC12	Chip2	IF09	ii	7		85	10	No	Secondary cracks	-97.4		-60.1			9.6	9					301			
VIC12	Chip2	IF09	i	8	15		16	No	Secondary cracks		-34.5		-22.1	-22.3			28.9	2.8	221	200		29.4	0.9	14.0
VIC12	Chip2	IF09	i	9	15		13	No	Secondary cracks		-35.3		-21.3	-22.6			28.2	3.5	219	200		28.0	0.9	15.4
VIC12	Chip2	IF10	ii	1		80	10	No	Secondary cracks	-102.7	-28.8	-60.5			12.3	12					300			
VIC12	Chip2	IF10	ii	2		85	10	No	Secondary cracks	-100.3		-63.2			11.3						301			
VIC12	Chip3	IF08	i	1	15		25	Yes (halite)	Secondary cracks		-72.8		-57.3	-41.0			19.5	18.8	224	208		30.7	0.9	14.6
VIC12	Chip3	IF08	i	2	15		20	Yes (halite)	Secondary cracks		-75.1		-54.5	-42.1			19.5	19.1	223	209		23.3	0.9	15.2
VIC12	Chip3	IF08	i	3	15		15	Yes (halite)	Secondary cracks		-68.5		-54.2	-40.5			19.4	18.8	224	198		29.8	0.8	13.9
VIC12	Chip3	IF08	i	4	15		10	Yes (halite)	Secondary cracks		-82.1		-55.2	-42.3			19.6	19.1	229	200		38.2	0.9	14.0
VIC12	Chip3	IF08	i	5	15		10	Yes (halite)	Secondary cracks		-74.2		-54.7	-42.7			19.3	19.3	251	200		28.8	0.9	14.8
VIC12	Chip3	IF08	i	6	15		15	Yes (halite)	Secondary cracks		-72.5		-54.5	-43.1			19.4	19.4	232	199		44.0	0.8	12.7
VIC12	Chip3	IF08	i	7	15		25	Yes (halite)	Secondary cracks		-81.2		-52.7	-41.8			20.6	18.6	235	200		42.1	0.8	12.8
VIC12	Chip3	IF08	i	8	15		15	Yes (halite)	Secondary cracks		-75.3		-54.1	-41.8			19.6	19.0	227	200		39.6	0.8	13.0
VIC12	Chip3	IF08	i	9	15		15	Yes (halite)	Secondary cracks		-72.5		-54.5	-41.2			18.8	19.2	222	200		40.6	0.8	12.9
VIC12	Chip3	IF08b	ii	1		90	10	No	Secondary cracks	-100.5		-57.8			-41.5	-7					314			
VIC12	Chip3	IF08b	ii	2		80	12	No	Secondary cracks	-103.2		-61.2			-34.5	-7					310			
VIC12	Chip3	IF08b	ii	3		80	15	No	Secondary cracks	-98.7		-60.5			-16.2	-7					311			
VIC12	Chip3	IF08b	i	4	15		15	Yes (halite)	Secondary cracks		-60.5		-50.7	-43.7			18.0	20.1	228	184		28.4	0.8	14.0
VIC12	Chip3	IF08b	i	5	15		15	Yes (halite)	Secondary cracks		-62.5		-52.3	-40.2			18.3	19.2	229	192		32.2	0.8	13.6
VIC12	Chip3	IF08b	ii	6		90	15	No	Secondary cracks	-97.5	-63.2			-40.0	-35.2	-6					322			
VIC12	Chip3	IF08c	ii	1		80	15	No	Secondary cracks	-82.2		-60.3			-34.3	-5					320			
VIC12	Chip3	IF08c	ii	2		90	10	No	Secondary cracks	-84.5		-60.1			-24.5	-5					317			

VIC12	Chip3	IF08c	ii	3		90	25	No	Secondary cracks	-84.3		-60.5			-40.3	-5					314			
VIC12	Chip3	IF08c	ii	4		80	15	No	Secondary cracks	-83.2		-61.2			-38.2	-5					311			
VIC12	Chip3	IF08c	ii	5		80	30	No	Secondary cracks	-84.6		-60.4			-32.3	-5					315			
VIC12	Chip3	IF08c	ii	6		90	10	No	Secondary cracks	-71.2		-59.8			-26.7	-5					317			
VIC12	Chip3	IF11	i	1	15		20	Yes (halite)	Secondary cracks		-60.1		-32.1	-23.1			27.4	4.6	231	201		37.9	0.8	13.1
VIC12	Chip3	IF11	i	2	15		15	Yes (halite)	Secondary cracks		-67.8		-48.2	-25.2			24.2	8.5	225	200		36.7	0.8	13.2
VIC12	Chip3	IF11	i	3	15		10	Yes (halite)	Secondary cracks		-62.4		-44.2	-25.1			24.3	8.4	227	199		35.5	0.8	13.3
VIC12	Chip3	IF11	i	4	15		10	Yes (halite)	Secondary cracks		-56.1		-45.6	-23.4			26.8	5.2	227	201		15.7	0.9	15.7
VIC12	Chip3	IF11	i	5	15		10	Yes (halite)	Secondary cracks		-58.5		-47.2	-23.4			26.7	5.3	222	200		14.1	0.9	15.7
VIC12	Chip3	IF11	i	6	15		10	Yes (halite)	Secondary cracks		-59.5		-48.3	-22.5			28.4	3.3	221	199		17.9	0.9	15.2

Table 25. Fluid inclusions microthermometric in **Margalida (MG) sample** (MARG06 sample, in green: aqueous inclusions / in red: carbonic inclusions).

Sample	n°chip	FIAs (CO2 red, H2O green)	Type (CO2 red, H2O green)	n° FI	Rapport V/L (%)	xCo2 (vol.%)	Size µm	Salt at T°=25 °C	Petro	TcCo2	Tc H2O	TmCo2	TmfH2O	TmlH2O	ThCO2	Tmclath	Salinity		ThH2O	TmHal or Thh	Thtotal	P @ homog.	rBULK	dP/dT
																	NaCl (wt.%)	CaCl2 (wt.%)				(bar)	(g/cm3)	(bar/°C)
MARG-06	Chip1	IF03	iii	1	10		8	No	Secondary cracks		-26.7			-2.5			4.2		347			17.5	0.9	15.3
MARG-06	Chip1	IF03	ii	2		60	15	No	Secondary cracks	-105.2	-25.5	-60.5			13.5	14					300			
MARG-06	Chip1	IF03	iii	3	10		10	No	Secondary cracks		-27.2			-0.7			1.2		328			17.8	0.9	15.2
MARG-06	Chip1	IF03	ii	4		80	10	No	Secondary cracks	-107.7	-25.5	-64.2			16.2	16					299			
MARG-06	Chip1	IF03	ii	5		50	15	No	Secondary cracks	-104.7	-26.5	-61.0	-11.5	-2.2	17.2	17					299			
MARG-06	Chip1	IF03	ii	6		50	15	No	Secondary cracks	-105.2	-27.2	-60.5	-15.2	-8.5	14.5	14					300			
MARG-06	Chip1	IF03	ii	7		30	10	No	Secondary cracks	-105.2	-35.2	-60.7	12.3	-4.5	13.2	11					299			
MARG-06	Chip1	IF03	iii	8	15		10	No	Secondary cracks		-26.7		-12.2	-3.5			5.7		336			29.0	0.8	13.9
MARG-06	Chip1	IF03	ii	9		60	10	No	Secondary cracks	-103.9	-28.7	-60.1	-14.2	-5.5	15.1	13					300			
MARG-06	Chip1	IF03	iii	10	10		8	No	Secondary cracks		-28.5		-10.8	-8.6			12.4		344			36.0	0.8	13.3
MARG-06	Chip1	IF04	iii	1	10		10	No	Secondary cracks		-26.4		-11.4	-4.3			6.9		340			7.9	1.0	20.7
MARG-06	Chip1	IF04	iii	2	15		10	No	Secondary cracks		-29.4		-10.8	-4.1			6.6		341			9.7	1.1	20.2
MARG-06	Chip1	IF04	ii	3		60	15	No	Secondary cracks	-102.3		-60.8			15.2	10					300			
MARG-06	Chip1	IF04	ii	4		60	10	No	Secondary cracks	-104.6	-27.6	-61.2			16.4	10					301			
MARG-06	Chip1	IF04	iii	5	10		15	No	Secondary cracks		-24.6		-11.0	-3.2			5.3		351			9.3	1.1	20.3
MARG-06	Chip1	IF04	iii	6	10		10	No	Secondary cracks		-24.9		-10.9	-5.1			8.0		352			16.3	0.9	16.8
MARG-06	Chip1	IF04	iii	7	10		10	No	Secondary cracks		-24.8		-11.7	-3.8			6.2		359			1.0		
MARG-06	Chip2	IF05	ii	1		50	15	No	Secondary cracks	-104.2	-25.5	-62.2	-12.3	-2.5	17.2	17					301			
MARG-06	Chip2	IF05	ii	2		60	8	No	Secondary cracks	-105.3	-25.5	-63.2			14.3	6					302			
MARG-06	Chip2	IF05	ii	3		40	8	No	Secondary cracks	-104.1		-62.2			15.4	7					303			
MARG-06	Chip2	IF05	ii	4		45	8	No	Secondary cracks	-103.7		-63.1			15.7	9					301			
MARG-06	Chip2	IF05	iii	5	10		8	No	Secondary cracks		-21.2		-11.2	-4.3			6.9		342			1.0		

MARG-06	Chip2	IF01	ii	1		60	15	No	Secondary cracks	-102.3		-62.1			14.9	9					302			
MARG-06	Chip2	IF01	ii	2		65	12	No	Secondary cracks	-102.5		-60.8			14.0	9					301			
MARG-06	Chip2	IF01	ii	3		60	15	No	Secondary cracks	-100.3		-61.3			16.3	10					300			
MARG-06	Chip2	IF01	iii	4	15		10	No	Secondary cracks		-28.1		-11.8	-4.3			6.9		341			9.4	1.0	19.9
MARG-06	Chip2	IF01	iii	5	10		10	No	Secondary cracks		-27.3		-11.4	-4.0			6.4		334			9.8	1.0	19.5
MARG-06	Chip2	IF01	iii	6	10		15	No	Secondary cracks		-26.8		-16.4	-3.2			5.3		337			23.5	1.0	17.2
MARG-06	Chip3	IF02	ii	1		65	20	No	Secondary cracks	-104.5	-40.5	-61.8	-19.5	-4.2	13.4	13					301			
MARG-06	Chip3	IF02	ii	2		65	10	No	Secondary cracks	-105.2	-41.2	-61.2	-22.3	-5.2	12.5	11					301			
MARG-06	Chip3	IF02	iii	3	15		10	No	Secondary cracks		-32.7		-12.5	-1.1			1.9		341			1.0		
MARG-06	Chip3	IF02	ii	4		70	10	No	Secondary cracks	-102.4	-26.5	-61.3	-19.5	-3.6	13.9	13					301			
MARG-06	Chip3	IF02	ii	5		75	10	No	Secondary cracks	-98.8	-27.1	-62.5	-13.6	-3.2	11.5	12					301			
MARG-06	Chip3	IF02	ii	6		80	15	No	Secondary cracks	-102.5	-25.6	-60.7	-12.6	-5.2	13.8	13					300			
MARG-06	Chip3	IF02	ii	7		75	10	No	Secondary cracks	-101.7	-26.2	-60.3	-12.8	-2.3	10.1	10					300			
MARG-06	Chip3	IF02	iii	8	10		8	No	Secondary cracks		-25.1		-7.2	-0.2			0.4		352			35.1	0.9	13.7
MARG-06	Chip3	IF02	iii	9	10		10	No	Secondary cracks		-31.8		-11.2	-2.5			4.2		347			60.3	0.8	12.0
MARG-06	Chip3	IF02	iii	10	15		10	No	Secondary cracks		-52.1		-33.0	-13.8			17.6		342			68.1	0.8	11.3
MARG-06	Chip4	IF06	iii	1	10		10	No	Secondary cracks		-42.5		-25.6	-7.2			10.7							
MARG-06	Chip4	IF06	ii	2		60	10	No	Secondary cracks	-106.8	-26.3	-62.1			15.3	10					300			
MARG-06	Chip4	IF06	ii	3		65	10	No	Secondary cracks	-109.3		-63.6			17.4	10					299			
MARG-06	Chip4	IF07	iii	1	10		12	No	Secondary cracks		-28.6		-12.8	-6.3			9.6		345			32.3	0.9	15.6
MARG-06	Chip4	IF07	iii	2	10		10	No	Secondary cracks		-47.4		-10.6	-4.8			7.6		351			12.1	1.0	18.6
MARG-06	Chip4	IF07	iii	3	10		15	No	Secondary cracks		-40.3		-13.4	-3.1			5.1		350			10.9	1.0	18.8
MARG-06	Chip4	IF07	iii	4	10		10	No	Secondary cracks		-35.6		-12.6	-3.5			5.7		341			17.1	1.0	17.5
MARG-06	Chip4	IF07	iii	5	10		10	No	Secondary cracks		-28.3		-18.2	-7.1			10.6		360			11.0	1.0	19.0
MARG-06	Chip4	IF07	ii	6		50	15	No	Secondary cracks	-100.3		-60.7			14.3	8					298			
MARG-06	Chip4	IF07	ii	7		55	15	No	Secondary cracks	-104.3		-61.5			12.3	8					300			

11.13 Fluid inclusions – LA-ICP-MS analyses (quartz host)

Table 26. LA-ICP-MS data on fluid inclusions in quartz (ppm) for Victoria (VIC12), Pale Bidau (BO10-BO12), Crabioulès (CRA02), Arre (ARR06) deposit. Abbreviations: FI: fluid inclusions.

Deposit	FI n°	FI assemblage	Li7	B11	Cl35	K39	Na23	Ca43	Mn55	Zn66	Br79	Rb85	Sr88	Cs133	Ba137	Pb208
Victoria	1n	5.0	307	964	171505	23172	134583	<LOD	<LOD	2499	3859	<LOD	1484	16	216	7999
Victoria	1n	5.0	<LOD	<LOD	<LOD	18103	96833	<LOD	<LOD	<LOD	<LOD	141	524	<35.673	<LOD	1717
Victoria	1n	5.0	357	<LOD	207804	5883	97456	<LOD	<LOD	<LOD	2266	33	2040	37	615	1233
Victoria	1n	5.0	<LOD	<LOD	<LOD	<LOD	103460	<LOD	16392	<LOD	<LOD	518	423	291	<LOD	6018
Victoria	1n	5.0	<LOD	<LOD	<LOD	53358	103463	<LOD	<LOD	<LOD	<LOD	124	369	<LOD	<LOD	8323
Victoria	1n	5.0	331	<LOD	210263	6588	98666	61955	<LOD	<LOD	8537	76	2726	40	452	<LOD
Victoria	1n	5.0	<LOD	<LOD	18657	<LOD	103463	<LOD	<LOD	<LOD	22448	<LOD	1760	<LOD	<LOD	<LOD
Victoria	2n	4.0	<LOD	<LOD	<LOD	9627	98456	<LOD	<LOD	<LOD	18719	96	4762	<LOD	408	156
Victoria	2n	4.0	<LOD	<LOD	286373	27257	103236	77756	930	<LOD	<LOD	69	1701	<LOD	381	8567
Victoria	2n	4.0	1056	<LOD	220333	6577	103463	<LOD	<LOD	<LOD	<LOD	<LOD	3318	<LOD	1145	281
Victoria	2n	4.0	<LOD	<LOD	<LOD	10708	103463	<LOD	<LOD	<LOD	5610	<LOD	2722	52	<LOD	397
Victoria	2n	4.0	<LOD	<LOD	<LOD	14588	102459	<LOD	<LOD	<LOD	<LOD	90	3509	95	688	<LOD
Victoria	2n	4.0	662	807	156646	25711	103453	<LOD	680	2220	4196	89	2317	<LOD	555	10141
Victoria	2n	4.0	888	<LOD	443682	21103	96584	16493	<LOD	2740	<LOD	206	3197	<LOD	1295	17517
Victoria	2n	4.0	<LOD	<LOD	41457	34356	102463	<LOD	1365	1023	10444	507	5711	86	1723	601
Victoria	2n	4.0	585	<LOD	169707	9727	103322	98762	586	1190	<LOD	167	2571	<LOD	198	<LOD
Victoria	2n	4.0	<LOD	14463	<LOD	18762	103463	<LOD	<LOD	<LOD	<LOD	<LOD	<LOD	<LOD	<LOD	1032
Victoria	2n	4.0	<LOD	<LOD	<LOD	7969	103463	<LOD	2520	2985	45985	93	5720	55	466	7669
Victoria	2n	4.0	<LOD	<LOD	<LOD	<LOD	102423	<LOD	<LOD	<LOD	<LOD	<LOD	<LOD	<LOD	<LOD	<LOD
Victoria	2n	4.0	<LOD	<LOD	301884	<LOD	103463	<LOD	5372	<LOD	25299	<LOD	<LOD	132	528	<LOD
Victoria	2n	4.0	<LOD	<LOD	740390	26036	96833	<LOD	10886	9762	83043	216	21171	289	3084	10296

Victoria	2n	4.0	<LOD	2977	449470	20242	123561	54227	1960	<LOD	3911	254	1879	64	616	10656
Victoria	2n	4.0	<LOD	<LOD	<LOD	<LOD	103463	<LOD	9057	<LOD	<LOD	348	3733	<LOD	<LOD	9305
Victoria	2n	4.0	<LOD	<LOD	<LOD	13356	103322	<LOD	3994	<LOD	<LOD	<LOD	276	61	<LOD	1276
Victoria	2n	4.0	427	1560	227456	8968	103463	<LOD	8715	7253	4761	118	5196	74	1092	9157
Victoria	2n	4.0	<LOD	<LOD	646536	19577	100321	<LOD	8363	12026	<LOD	<LOD	13129	229	1311	10029
Victoria	2n	4.0	<LOD	<LOD	763349	11988	103463	<LOD	9334	12303	9188	<LOD	7459	151	2300	6558
Victoria	4.0	1.0	<LOD	<LOD	<LOD	<LOD	103405	<LOD	<LOD	<LOD	<LOD	<LOD	3442	<LOD	<LOD	<LOD
Victoria	4.0	1.0	4538	<LOD	<LOD	<LOD	103312	<LOD	<LOD	<LOD	<LOD	453	2311	<LOD	<LOD	2679
Victoria	4.0	1.0	<LOD	<LOD	<LOD	<LOD	103463	<LOD	<LOD	<LOD	<LOD	<LOD	<LOD	861	<LOD	4613
Victoria	4.0	1.0	<LOD	<LOD	<LOD	13253	103463	<LOD	10332	10650	25149	<LOD	17080	272	2888	6270
Victoria	2.0	1.0	<LOD	<LOD	<LOD	6533	103463	16850	7684	7673	100548	<LOD	4882	67	1474	5848
Victoria	2.0	1.0	<LOD	<LOD	266971	<LOD	103463	<LOD	9237	10876	<LOD	<LOD	6323	<LOD	<LOD	3650
Victoria	2.0	1.0	<LOD	<LOD	657977	12462	93466	<LOD	2818	<LOD	<LOD	<LOD	8584	<LOD	<LOD	6663
Victoria	2.0	1.0	<LOD	<LOD	272537	<LOD	103463	<LOD	5683	4098	<LOD	<LOD	2910	<LOD	669	4431
Victoria	2.0	1.0	<LOD	<LOD	428686	6026	104563	<LOD	6005	10529	19580	197	7224	143	<LOD	10547
Victoria	2.0	1.0	1330	<LOD	579932	10948	103463	11117	4984	14815	20631	161	4649	191	890	10122
Victoria	1.0	1.0	1794	<LOD	337057	10411	103463	<LOD	7919	8198	10418	263	4571	<LOD	1182	11314
Victoria	1.0	1.0	<LOD	<LOD	156384	<LOD	123561	<LOD	3455	<LOD	<LOD	<LOD	859	<LOD	<LOD	4094
Victoria	1.0	1.0	<LOD	<LOD	<LOD	8368	123420	<LOD	4419	6028	<LOD	<LOD	7230	<LOD	1716	5596
Victoria	1.0	1.0	1055	<LOD	558121	10570	100322	20416	10555	8066	12650	297	11706	254	2298	10973
Victoria	1.0	1.0	97	<LOD	<LOD	5376	109853	54414	5500	5130	<LOD	63	5748	59	768	6179
Victoria	5.0	1.0	<LOD	<LOD	191191	5867	103463	<LOD	5724	5274	<LOD	<LOD	5762	92	982	5921
Victoria	5.0	1.0	<LOD	<LOD	515092	10893	103322	<LOD	3794	12017	33136	604	22773	667	6311	10222
Victoria	7.0	1.0	<LOD	<LOD	26572	12650	102356	12289	1354	9076	12829	<LOD	7252	154	1431	11999
Victoria	7.0	1.0	<LOD	<LOD	513486	4506	103463	<LOD	5266	1708	<LOD	220	3643	104	1663	5699
Victoria	7.0	1.0	<LOD	<LOD	190004	2614	103570	<LOD	4505	2747	<LOD	<LOD	2469	23	557	5996
Victoria	7.0	1.0	<LOD	<LOD	205390	5369	103463	<LOD	5617	<LOD	<LOD	<LOD	986	<LOD	<LOD	4363
Victoria	7.0	1.0	<LOD	<LOD	<LOD	<LOD	113560	<LOD	3286	<LOD	<LOD	229	558	26	1285	5665
Victoria	8.0	1.0	295	<LOD	496959	7619	103463	87347	7183	7203	2731	102	5941	66	1268	5780
Victoria	8.0	1.0	<LOD	<LOD	170591	5868	104623	<LOD	7100	5190	3360	64	3989	73	782	5122

Victoria	8.0	1.0	<LOD	<LOD	292972	6230	103463	98941	7709	7288	2187	46	4238	91	760	5893
Victoria	9.0	1.0	<LOD	<LOD	405163	10406	103463	<LOD	8067	8979	7599	<LOD	5996	99	1373	6298
Victoria	9.0	1.0	148	<LOD	382590	8586	100232	66308	8344	7025	2970	110	4375	88	987	6958
Victoria	9.0	1.0	<LOD	<LOD	293470	9454	103463	<LOD	7130	5726	<LOD	<LOD	4154	<LOD	<LOD	7035
Victoria	2b	2.0	2306	<LOD	725971	9228	103463	<LOD	5637	11066	<LOD	241	7101	179	1571	11915
Victoria	2b	2.0	<LOD	<LOD	276051	9090	124534	<LOD	8145	2887	<LOD	<LOD	4298	57	1108	5514
Victoria	2b	2.0	172	<LOD	433820	8137	104322	103341	7134	5917	4443	51	7004	89	1392	5381
Victoria	2b	2.0	276	<LOD	443248	12338	103463	88160	7825	10544	4173	149	7653	145	1477	8415
Victoria	2b	2.0	<LOD	<LOD	405345	10837	102256	15275	8591	11104	5260	200	8253	249	586	10107
Victoria	2b	2.0	254	<LOD	274404	9475	103463	40572	3065	9739	5024	50	7338	121	1263	5115
Victoria	2b	2.0	<LOD	<LOD	<LOD	13167	103463	<LOD	8419	10998	<LOD	<LOD	21851	335	7175	10903
Victoria	1c	3.0	<LOD	<LOD	<LOD	6849	103463	<LOD	<LOD	<LOD	<LOD	141	2423	<LOD	1707	360
Victoria	1c	3.0	<LOD	<LOD	<LOD	9922	124568	42616	2902	<LOD	<LOD	<LOD	3479	<LOD	964	<LOD
Victoria	1c	3.0	<LOD	<LOD	1108804	16871	103463	<LOD	<LOD	10576	<LOD	354	4650	<LOD	3146	17194
Victoria	2c	3.0	<LOD	<LOD	145505	12449	103447	64834	<LOD	<LOD	<LOD	903	4333	52	5303	<LOD
Victoria	2c	3.0	447	<LOD	201548	6026	100542	33719	432	<LOD	2290	45	2393	27	586	6490
Victoria	2c	3.0	<LOD	<LOD	<LOD	8342	103463	38879	<LOD	<LOD	<LOD	<LOD	3037	<LOD	683	10930
Victoria	3c	3.0	<LOD	<LOD	194440	18100	103463	<LOD	<LOD	<LOD	<LOD	218	2433	16	456	<LOD
Victoria	3c	3.0	<LOD	<LOD	147594	3270	103457	<LOD	<LOD	<LOD	5791	<LOD	3050	42	739	<LOD
Pale Bidau-PB12	18.0	1.0	<LOD	<LOD	64503	6469	51141	16330	6809	13676	<LOD	<LOD	412	184	728	5300
Pale Bidau-PB12	18.0	1.0	<LOD	<LOD	82416	4542	51141	<LOD	422	3320	1877	<LOD	604	88	309	4696
Pale Bidau-PB12	18.0	1.0	<LOD	<LOD	<LOD	<LOD	51141	<LOD	<LOD	<LOD	<LOD	<LOD	877	103	391	1224
Pale Bidau-PB12	2.0	2.0	96	612	21647	3276	26357	<LOD	<LOD	1779	468	28	946	50	374	698
Pale Bidau-PB12	2.0	2.0	<LOD	<LOD	101992	1351	26357	<LOD	<LOD	<LOD	<LOD	<LOD	729	51	312	276

Pale Bidau-PB12	2.0	2.0	<LOD	<LOD	<LOD	3123	26357	<LOD	<LOD	1470	<LOD	<LOD	465	<LOD	<LOD	857
Pale Bidau-PB12	2.0	2.0	<LOD	<LOD	164973	4522	26357	<LOD	<LOD	1315	6982	<LOD	1913	<LOD	1140	3010
Pale Bidau-PB12	19.0	2.0	1557	<LOD	360103	12036	47207	<LOD	9854	10667	27341	126	185	793	635	4008
Pale Bidau-PB12	19.0	2.0	1557	<LOD	360103	13024	47225	<LOD	7854	10452	27341	126	185	793	635	4008
Pale Bidau-PB12	19.0	2.0	<LOD	<LOD	<LOD	<LOD	47207	<LOD	<LOD	<LOD	<LOD	<LOD	<LOD	<LOD	<LOD	<LOD
Pale Bidau-PB12	19.0	2.0	<LOD	<LOD	<LOD	<LOD	47207	<LOD	<LOD	<LOD	<LOD	<LOD	<LOD	<LOD	<LOD	<LOD
Pale Bidau-PB12	20.0	2.0	<LOD	<LOD	<LOD	<LOD	47207	<LOD	<LOD	<LOD	<LOD	<LOD	<LOD	<LOD	<LOD	987
Pale Bidau-PB12	20.0	2.0	<LOD	<LOD	<LOD	<LOD	29111	<LOD	<LOD	<LOD	<LOD	<LOD	651	287	<LOD	390
Pale Bidau-PB12	1.0	2.0	225	<LOD	48767	2831	29111	<LOD	<LOD	1848	<LOD	16	1252	60	478	549
Pale Bidau-PB12	1.0	2.0	233	367	81075	5994	46814	<LOD	<LOD	<LOD	295	35	497	92	168	79
Pale Bidau-PB12	11.0	2.0	<LOD	<LOD	165798	17065	46814	<LOD	<LOD	15015	<LOD	93	193	89	<LOD	706
Pale Bidau-PB12	11.0	2.0	<LOD	<LOD	<LOD	7044	46814	<LOD	1313	<LOD	<LOD	48	674	<LOD	503	<LOD
Pale Bidau-PB12	11.0	2.0	<LOD	<LOD	<LOD	6994	59009	<LOD	<LOD	<LOD	<LOD	30	402	53	379	<LOD
Pale Bidau-PB12	13.0	3.0	541	1601	219876	6300	59009	<LOD	<LOD	<LOD	7854	<LOD	791	45	651	330
Pale Bidau-PB12	13.0	3.0	474	<LOD	428752	9991	59009	<LOD	<LOD	1386	8751	73	413	52	<LOD	2178

Pale Bidau-PB12	13.0	3.0	474	<LOD	<LOD	9991	59009	<LOD	<LOD	1386	<LOD	73	413	52	<LOD	2178
Pale Bidau-PB12	17.0	2.0	571	<LOD	162254	13236	63730	<LOD	<LOD	1157	3979	66	710	164	299	707
Pale Bidau-PB12	17.0	2.0	<LOD	<LOD	<LOD	13447	67664	<LOD	<LOD	<LOD	<LOD	<LOD	1190	80	1711	2063
Pale Bidau-PB12	19.0	2.0	<LOD	<LOD	<LOD	<LOD	47207	<LOD	<LOD	<LOD	<LOD	<LOD	526	<LOD	<LOD	885
Pale Bidau-PB12	22.0	2.0	<LOD	<LOD	<LOD	<LOD	29505	6529	113	<LOD	137	31	52	85	<LOD	238
Pale Bidau-PB12	22.0	2.0	<LOD	<LOD	<LOD	<LOD	29505	<LOD	<LOD	<LOD	<LOD	<LOD	<LOD	<LOD	<LOD	<LOD
Pale Bidau-PB12	22.0	2.0	1912	<LOD	<LOD	17650	51141	<LOD	<LOD	<LOD	30036	<LOD	222	111	747	<LOD
Pale Bidau-PB12	22.0	2.0	<LOD	<LOD	181078	15590	51141	<LOD	<LOD	<LOD	72553	<LOD	475	<LOD	<LOD	1428
Pale Bidau-PB12	22.0	2.0	929	<LOD	<LOD	<LOD	59009	19598	<LOD	<LOD	8200	97	259	41	628	260
Pale Bidau-PB12	22.0	2.0	<LOD	<LOD	<LOD	<LOD	59009	<LOD	<LOD	<LOD	<LOD	<LOD	<LOD	258	<LOD	<LOD
Pale Bidau-PB12	22.0	2.0	<LOD	3032	<LOD	9414	59015	16688	<LOD	<LOD	<LOD	<LOD	719	170	678	126
Pale Bidau-PB12	22.0	2.0	<LOD	<LOD	434755	8978	59009	<LOD	<LOD	<LOD	<LOD	<LOD	<LOD	40	<LOD	694
Pale Bidau-PB12	22.0	2.0	1969	<LOD	<LOD	49825	59009	<LOD	<LOD	<LOD	8107	<LOD	1828	506	980	226
Pale Bidau-PB12	22.0	2.0	<LOD	<LOD	273033	1566	59009	<LOD	<LOD	<LOD	<LOD	<LOD	<LOD	24	<LOD	124
Pale Bidau-PB12	7.0	3.0	<LOD	<LOD	-20646	13677	63730	<LOD	<LOD	<LOD	<LOD	<LOD	<LOD	749	<LOD	<LOD

Pale Bidau-PB12	10.0	2.0	141	807	32425	3838	24390	<LOD	<LOD	1123	1503	34	747	47	320	331
Pale Bidau-PB12	10.0	2.0	56267	5871	320358	13590	51141	<LOD	2826	<LOD	16722	4554	<LOD	<LOD	<LOD	<LOD
Pale Bidau-PB10	4a	1.0	<LOD	<LOD	43071	1863	25964	<LOD	<LOD	602	<LOD	26	1050	<LOD	1989	457
Pale Bidau-PB10	4a	1.0	<LOD	<LOD	<LOD	2322	25964	27671	516	2980	10020	23	1740	21	1800	1066
Pale Bidau-PB10	4a	1.0	100	<LOD	43617	3106	25964	<LOD	<LOD	588	2017	23	1031	24	966	505
Pale Bidau-PB10	5a	1.0	98	<LOD	45090	3267	28718	10356	338	484	1196	19	743	20	850	268
Pale Bidau-PB10	5a	1.0	<LOD	<LOD	43799	5057	28718	<LOD	444	18279	1580	31	1003	22	832	589
Pale Bidau-PB10	6a	1.0	74	<LOD	67311	4163	28718	8104	553	949	588	27	1401	26	1266	147
Pale Bidau-PB10	1a	1.0	108	<LOD	51596	2618	29111	13288	509	517	<LOD	9	1515	30	1322	568
Pale Bidau-PB10	1a	1.0	532	<LOD	57870	3563	29111	<LOD	<LOD	1049	2064	28	366	30	1167	209
Pale Bidau-PB10	1a	1.0	40	<LOD	66416	3531	29111	12096	469	727	684	23	1630	29	1686	686
Pale Bidau-PB10	1a	1.0	<LOD	<LOD	111850	2170	29111	<LOD	373	267	1744	<LOD	<LOD	18	336	746
Pale Bidau-PB10	7a	1.0	<LOD	<LOD	63263	994	28718	13898	294	2406	4678	<LOD	197	28	126	2092
Pale Bidau-PB10	5b	2.0	<LOD	<LOD	<LOD	1703	48388	<LOD	<LOD	931	5223	<LOD	<LOD	24	<LOD	126
Pale Bidau-PB10	5b	2.0	<LOD	2371	<LOD	5868	48388	<LOD	5842	12171	19082	<LOD	7716	32	1348	12138

Pale Bidau-PB10	6b	2.0	<LOD	<LOD	377181	3374	42093	<LOD	186	2858	4489	33	1219	26	679	4770
Pale Bidau-PB10	6b	2.0	<LOD	<LOD	<LOD	15615	42093	<LOD	<LOD	<LOD	23252	409	<LOD	<LOD	4258	<LOD
Pale Bidau-PB10	7b	2.0	<LOD	<LOD	<LOD	12613	42880	<LOD	<LOD	10870	<LOD	<LOD	18972	<LOD	17571	906
Pale Bidau-PB10	12b	2.0	<LOD	<LOD	289965	18467	57042	<LOD	4687	1126	17209	69	3728	34	3113	563
Pale Bidau-PB10	11b	2.0	545	<LOD	216472	15238	89301	<LOD	1402	2669	4588	58	2023	72	3414	1654
Pale Bidau-PB10	11b	2.0	<LOD	<LOD	<LOD	12061	89301	<LOD	<LOD	<LOD	16400	<LOD	2491	<LOD	<LOD	1265
Pale Bidau-PB10	2b	2.0	<LOD	<LOD	<LOD	6294	42093	<LOD	<LOD	955	3596	<LOD	877	<LOD	645	64
Pale Bidau-PB10	2b	2.0	176	247	80305	7738	42093	<LOD	110	764	<LOD	26	1155	28	1265	230
Pale Bidau-PB10	8b	2.0	<LOD	3554	452963	6735	42093	<LOD	1651	<LOD	<LOD	<LOD	<LOD	<LOD	<LOD	399
Pale Bidau-PB10	1b	3.0	217	1734	52653	3197	10622	<LOD	<LOD	<LOD	1280	19	7	4	97	11
Pale Bidau-PB10	4b	3.0	250	<LOD	251655	14557	108577	25602	1955	1830	2070	110	685	93	6380	1381
Pale Bidau-PB10	4b	3.0	<LOD	<LOD	371389	14897	108577	<LOD	<LOD	5253	<LOD	<LOD	1900	<LOD	1833	1038
Pale Bidau-PB10	4b	3.0	11228	<LOD	311003	9296	108577	<LOD	<LOD	<LOD	<LOD	<LOD	1794	<LOD	<LOD	<LOD
Pale Bidau-PB10	4b	3.0	<LOD	<LOD	<LOD	10479	108577	<LOD	<LOD	<LOD	<LOD	<LOD	1288	<LOD	6077	2589
Pale Bidau-PB10	3b	3.0	1226	<LOD	133604	14510	104250	<LOD	3363	1929	3652	145	342	2370	3719	1634

Pale Bidau-PB10	3b	3.0	908	<LOD	172569	10105	104250	<LOD	<LOD	<LOD	4182	50	425	88	654	<LOD
Pale Bidau-PB10	13b	2.0	486	<LOD	<LOD	4556	24784	<LOD	997	1088	<LOD	<LOD	737	32	772	<LOD
Pale Bidau-PB10	13b	2.0	51	<LOD	61917	4048	24784	16730	917	774	701	29	1614	29	1788	675
Pale Bidau-PB10	9b	2.0	11	<LOD	5277	235	3541	636	25	16	60	2	161	1	60	82
Crabioules	1a	1.0	3042	<LOD	<LOD	12680	98349	<LOD	<LOD	9817	<LOD	<LOD	360	<LOD	<LOD	2221
Crabioules	3a	1.0	<LOD	<LOD	<LOD	13264	98349	<LOD	3334	12846	12096	<LOD	4740	<LOD	<LOD	10623
Crabioules	2a	1.0	<LOD	<LOD	<LOD	<LOD	98349	<LOD	<LOD	<LOD	<LOD	<LOD	<LOD	<LOD	<LOD	5284
Crabioules	4a	1.0	8239	<LOD	297919	<LOD	98349	<LOD	<LOD	<LOD	35384	<LOD	5221	<LOD	<LOD	694
Crabioules	1b	2.0	<LOD	<LOD	137468	15810	103069	28042	3087	<1208.788	21820	50	7081	56	1093	157
Crabioules	1b	2.0	485	236	308154	12109	103046	74432	865	639	1355	81	2943	159	524	688
Crabioules	1b	2.0	751	<LOD	759921	19569	103069	17300	<LOD	<LOD	7856	105	3847	66	1152	175
Crabioules	1b	2.0	1607	<LOD	191391	9596	103346	<LOD	2634	10333	24647	<LOD	5058	128	<LOD	778
Crabioules	1b	2.0	636	610	267110	12691	103064	83412	730	749	<LOD	82	3945	142	705	720
Crabioules	1b	2.0	<LOD	<LOD	323140	16471	103069	<LOD	5861	<LOD	22942	<LOD	1331	304	2792	1105
Crabioules	1b	2.0	2094	<LOD	495487	13458	103346	<LOD	<LOD	<LOD	<LOD	156	1787	186	633	557
Crabioules	1b	2.0	817	476	403855	15870	103069	69351	1596	835	2144	93	3208	283	904	893
Crabioules	2b	2.0	<LOD	<LOD	158260	111586	103069	<LOD	<LOD	8014	24767	<LOD	<LOD	<LOD	<LOD	584
Crabioules	2b	2.0	426	<LOD	274887	13093	103069	38844	<LOD	701	1905	83	3063	183	528	447
Crabioules	2b	2.0	640	207	400740	13849	103069	81749	556	864	1441	113	3988	169	817	869
Crabioules	2b	2.0	<LOD	<LOD	550408	12370	103069	<LOD	<LOD	<LOD	9604	161	1887	129	451	618
Crabioules	2n	2.0	1070	<LOD	187955	13888	98349	106165	1275	<LOD	5132	<LOD	3555	154	749	593
Crabioules	2n	2.0	2249	<LOD	<LOD	14484	98349	<LOD	<LOD	<LOD	17149	<LOD	2771	<LOD	<LOD	923
Crabioules	2n	2.0	843	<LOD	235241	11543	98349	30009	1719	747	1459	41	3287	108	485	655
Crabioules	2n	2.0	<LOD	<LOD	247923	10825	98349	<LOD	<LOD	<LOD	<LOD	<LOD	4591	<LOD	1014	957
Crabioules	5n	2.0	834	1743	301558	13549	96382	<LOD	<LOD	<LOD	1447	34	1923	30	422	<LOD
Crabioules	5n	2.0	547	<LOD	154732	11309	96382	<LOD	<LOD	<LOD	4858	21	1866	<LOD	<LOD	<LOD

Crabioules	5n	2.0	<LOD	<LOD	603071	13520	96382	<LOD	<LOD	<LOD	<LOD	<LOD	2565	<LOD	<LOD	<LOD
Crabioules	5n	2.0	1706	<LOD	304358	5869	96247	<LOD	<LOD	<LOD	<LOD	<LOD	898	<LOD	<LOD	<LOD
Crabioules	5n	2.0	687	<LOD	167973	10981	96382	<LOD	<LOD	<LOD	<LOD	33	597	<LOD	<LOD	31
Crabioules	5n	2.0	687	<LOD	148897	10981	96382	<LOD	<LOD	<LOD	891	33	597	<LOD	<LOD	31
Crabioules	2n	3.0	13117	15756	<LOD	26471	98349	<LOD	<LOD	13804	<LOD	836	817	114	<LOD	13828
Crabioules	3b	3.0	<LOD	<LOD	<LOD	<LOD	103069	<LOD	<LOD	<LOD	100691	935	1869	<LOD	<LOD	<LOD
Crabioules	3n	3.0	766	<LOD	544493	14502	98349	16904	4465	1860	3774	135	5249	150	1492	1632
Crabioules	3n	3.0	1469	<LOD	745816	15709	98349	<LOD	3091	2149	7361	133	4677	198	704	2473
Crabioules	3n	3.0	<LOD	<LOD	671561	18297	98348	27192	6776	3621	8727	130	6208	120	2003	1235
Crabioules	3n	3.0	686	205	481996	18145	98349	14795	3470	2046	3751	146	5627	212	1369	987
Crabioules	4n	3.0	374	<LOD	414700	10128	98349	14965	417	309	3019	46	3695	31	490	69
Crabioules	4n	3.0	933	<LOD	619326	9085	98342	<LOD	<LOD	<LOD	<LOD	140	1882	<LOD	<LOD	<LOD
Crabioules	4n	3.0	737	246	301788	12982	98344	97513	87	343	1110	96	3453	141	513	296
Crabioules	5n	3.0	<LOD	<LOD	803038	8884	98349	<LOD	<LOD	<LOD	6759	<LOD	2375	85	<LOD	<LOD
Crabioules	6n	3.0	396	<LOD	660517	16029	98454	11297	500	<LOD	907	102	1650	69	379	41
Crabioules	6n	3.0	481	<LOD	486739	10151	98349	15377	<LOD	<LOD	2507	211	1785	512	340	24
Crabioules	6n	3.0	<LOD	<LOD	243276	5771	98349	17498	<LOD	<LOD	3041	26	2794	90	738	<LOD
Crabioules	6n	3.0	439	<LOD	296938	10723	98349	<LOD	<LOD	<LOD	9556	<LOD	1414	63	401	<LOD
Crabioules	7n	3.0	1338	<LOD	406739	10624	98349	<LOD	<LOD	<LOD	6488	117	1451	61	<LOD	<LOD
Crabioules	7n	3.0	<LOD	<LOD	<LOD	<LOD	98458	<LOD	<LOD	<LOD	<LOD	<LOD	524	<LOD	<LOD	<LOD
Crabioules	7n	3.0	<LOD	<LOD	<LOD	<LOD	98349	<LOD	<LOD	<LOD	26834	<LOD	6114	221	<LOD	<LOD
Crabioules	7n	3.0	<LOD	<LOD	<LOD	<LOD	98349	<LOD	<LOD	<LOD	<LOD	<LOD	1455	<LOD	<LOD	<LOD
Crabioules	7n	3.0	<LOD	<LOD	134007	<LOD	98246	63522	<LOD	<LOD	<LOD	<LOD	3292	<LOD	<LOD	<LOD
Crabioules	8n	3.0	1079	<LOD	233726	9711	98349	38710	2651	1063	1485	90	4912	145	400	837
Crabioules	8n	3.0	<LOD	<LOD	247616	11640	98334	16368	<LOD	<LOD	3072	<55.636	3452	98	404	601
Crabioules	8n	2.0	<LOD	<LOD	<LOD	14249	98353	<LOD	<LOD	<LOD	<LOD	<LOD	<LOD	50	<LOD	<LOD
Crabioules	9n	3.0	245	<LOD	314753	5742	98349	66696	789	<LOD	1372	<LOD	2035	25	274	<LOD
Crabioules	9n	3.0	<LOD	<LOD	481396	11768	98349	<LOD	<LOD	<LOD	10003	<LOD	1518	<LOD	<LOD	<LOD
Crabioules	9n	3.0	939	<LOD	453420	10297	98349	<LOD	<LOD	1642	5526	168	3267	167	<LOD	1148
Crabioules	9n	3.0	<LOD	<LOD	408985	7743	98349	<LOD	1727	<LOD	7093	124	2125	146	629	1099

Crabioules	9n	3.0	572	<LOD	247631	9727	98349	<LOD	241	<LOD	3187	87	1259	31	297	15
Arre	19n	5.0	443	<LOD	475203	11291	90481	14208	<LOD	623	2349	145	9274	232	1345	55
Arre	19n	5.0	1307	<LOD	677038	25133	90481	45615	<LOD	<LOD	10438	<LOD	14996	394	2580	<LOD
Arre	19n	5.0	389	829	414777	19441	1004560	51080	<LOD	<LOD	4166	95	6181	295	1753	157
Arre	19n	5.0	240	356	323218	17623	90481	88505	<LOD	145	1305	104	7822	240	1402	77
Arre	20n	5.0	271	<LOD	247510	12191	90083	<LOD	627	663	<LOD	<LOD	8531	86	2406	68
Arre	20n	5.0	<LOD	<LOD	<LOD	15022	90481	<LOD	<LOD	<LOD	16626	<LOD	16464	<LOD	2095	<LOD
Arre	20n	5.0	<LOD	<LOD	<LOD	25783	90481	24390	<LOD	<LOD	<LOD	<LOD	28166	441	6299	<LOD
Arre	20n	5.0	<LOD	813	303597	13735	90481	78794	559	<LOD	<LOD	86	11499	150	2577	61
Arre	20n	5.0	<LOD	<LOD	671195	12642	90147	<LOD	<LOD	<LOD	8383	203	6502	147	1702	<LOD
Arre	20n	5.0	<LOD	<LOD	343626	17165	90456	38914	<LOD	<LOD	<LOD	<LOD	8403	100	2310	<LOD
Arre	20n	5.0	<LOD	<LOD	<LOD	<LOD	90481	<LOD	<LOD	<LOD	<LOD	<LOD	9234	<LOD	1687	<LOD
Arre	21n	5.0	<LOD	<LOD	658684	9301	90481	9621	<LOD	<LOD	10698	105	9437	105	1703	105
Arre	21n	5.0	<LOD	<LOD	697834	8571	90481	<LOD	<LOD	<LOD	<LOD	<LOD	5779	254	734	243
Arre	21n	5.0	948	<LOD	<LOD	3786	105464	<LOD	<LOD	<LOD	<LOD	<LOD	7726	146	335	<LOD
Arre	21n	5.0	<LOD	<LOD	126237	13243	106464	12690	<LOD	<LOD	29724	<LOD	13867	275	2902	121
Arre	21n	5.0	<LOD	<LOD	450546	16555	90481	55042	<LOD	<LOD	5821	65	6486	164	1346	92
Arre	1n	6.0	456	<LOD	413927	15993	90481	109245	<LOD	<LOD	2506	100	4232	127	1719	53
Arre	1n	6.0	<LOD	<LOD	355635	18576	90481	<LOD	<LOD	<LOD	<LOD	115	2801	94	<LOD	192
Arre	2n	6.0	408	<LOD	384121	18812	1046547	111841	<LOD	2072	<LOD	68	4495	195	383	<LOD
Arre	2n	6.0	<LOD	<LOD	408120	21229	90481	62319	<LOD	<LOD	<LOD	93	5860	196	2309	119
Arre	2n	6.0	<LOD	<LOD	369328	16571	90481	55467	<LOD	<LOD	1057	126	4375	73	1286	99
Arre	2n	6.0	<LOD	<LOD	103508	29048	1046354	18282	<LOD	<LOD	6057	294	3995	221	<LOD	152
Arre	2n	6.0	<LOD	582	350779	14377	90481	77522	<LOD	<LOD	2691	79	2621	123	1115	24
Arre	3n	6.0	1602	<LOD	<LOD	35584	90481	<LOD	<LOD	<LOD	<LOD	197	4129	<LOD	<LOD	<LOD
Arre	3n	6.0	<LOD	<LOD	311592	26531	90481	<LOD	<LOD	<LOD	<LOD	155	3113	273	1002	<LOD
Arre	3n	6.0	<LOD	<LOD	209805	14567	1046354	<LOD	<LOD	<LOD	1467	43	2945	48	595	195
Arre	3n	6.0	<LOD	<LOD	402811	19093	90481	<LOD	<LOD	<LOD	<LOD	149	4031	244	1054	<LOD
Arre	4n	6.0	<LOD	<LOD	289110	14061	90481	11615	<LOD	<LOD	<LOD	207	7409	87	3013	<LOD
Arre	4n	6.0	<LOD	<LOD	396690	29171	90481	11653	<LOD	<LOD	<LOD	77	2842	187	601	<LOD

Arre	4n	6.0	<LOD	<LOD	245050	9648	90454	16974	<LOD	<LOD	6364	<LOD	3913	188	1707	115
Arre	5n	6.0	<LOD	<LOD	210550	12865	90481	<LOD	<LOD	<LOD	<LOD	144	4164	146	868	53
Arre	5n	6.0	275	<LOD	221746	15892	90481	66475	<LOD	<LOD	<LOD	<LOD	3653	132	994	42
Arre	5n	6.0	<LOD	<LOD	<LOD	27382	90481	<LOD	<LOD	<LOD	<LOD	<LOD	4598	228	1362	<LOD
Arre	5n	6.0	<LOD	<LOD	350764	19375	90481	<LOD	<LOD	<LOD	<LOD	146	6345	302	1956	<LOD
Arre	5n	6.0	<LOD	<LOD	587699	28295	1046354	<LOD	<LOD	<LOD	<LOD	241	3563	114	2102	125
Arre	6n	6.0	570	<LOD	357168	23554	90481	<LOD	<LOD	<LOD	5126	229	3575	233	1418	<LOD
Arre	6n	6.0	<LOD	<LOD	576327	18039	90481	<LOD	<LOD	<LOD	7231	117	4717	41	976	82
Arre	6n	6.0	<LOD	<LOD	213654	23424	90481	<LOD	<LOD	<LOD	<LOD	230	9825	149	1636	<LOD
Arre	7n	6.0	1207	7747	250195	11666	90481	<LOD	<LOD	12808	5893	2838	3987	182	15448	4535
Arre	7n	6.0	<LOD	<LOD	<LOD	16818	101497	<LOD	<LOD	5567	<LOD	748	6728	246	3790	678
Arre	7n	6.0	<LOD	<LOD	411183	4399	90481	10538	<LOD	<LOD	4480	113	4423	162	1032	83
Arre	8n	6.0	542	897	320415	27403	90481	<LOD	<LOD	<LOD	3276	109	5305	69	1482	36
Arre	8n	6.0	<LOD	861	399001	15729	101495	14689	<LOD	<LOD	4620	73	10398	161	3618	30
Arre	9n	6.0	<LOD	<LOD	120566	19867	101014	<LOD	<LOD	11691	20617	923	5706	286	4031	<LOD
Arre	10n	6.0	<LOD	<LOD	<LOD	24914	101496	<LOD	<LOD	2056	<LOD	<LOD	4096	81	1895	83
Arre	10n	6.0	263	<LOD	444092	22334	90481	54334	<LOD	<LOD	5758	93	2875	93	1520	57
Arre	11n	6.0	<LOD	<LOD	118723	<3370.67	90481	<LOD	<LOD	<LOD	<LOD	<LOD	8428	138	3497	234
Arre	12n	6.0	<LOD	<LOD	<LOD	28163	101496	12455	1214	15134	<LOD	460	4204	280	<LOD	461
Arre	13n	6.0	<LOD	<LOD	420905	<LOD	90481	18615	<LOD	3027	<LOD	<LOD	10212	144	519	<LOD
Arre	13n	6.0	<LOD	<LOD	385105	<LOD	90481	<LOD	<LOD	<LOD	<LOD	<LOD	10267	79	<LOD	<LOD
Arre	13n	6.0	<LOD	2548	298353	14685	90481	<LOD	<LOD	1545	<LOD	44	2315	101	388	126
Arre	14n	6.0	891	<LOD	494016	30441	90481	<LOD	<LOD	1482	7403	133	2784	211	<LOD	<LOD
Arre	14n	6.0	348	<LOD	224685	20920	101496	<LOD	<LOD	<LOD	1455	103	3387	91	1283	45
Arre	15n	6.0	496	<LOD	194385	14350	90481	67153	<LOD	1107	<LOD	48	4533	84	1030	130
Arre	15n	6.0	1806	<LOD	<LOD	20109	90481	<LOD	<LOD	10174	14316	903	1345	<LOD	6543	789
Arre	16n	6.0	<LOD	<LOD	535397	20327	90481	<LOD	<LOD	<LOD	<LOD	131	3321	107	1322	<LOD
Arre	16n	6.0	<LOD	484	239235	16623	90481	96481	<LOD	<LOD	1213	84	4221	78	1794	18
Arre	16n	6.0	1035	<LOD	529176	3549	90481	<LOD	<LOD	<LOD	4088	<LOD	2926	<LOD	1724	122
Arre	17n	6.0	<LOD	<LOD	433068	12584	101496	21244	<LOD	12020	3601	165	13476	153	1977	757

Arre	17n	6.0	<LOD	<LOD	246955	6323	90481	76867	<LOD	<LOD	<LOD	<LOD	4547	162	1495	<LOD
Arre	17n	6.0	<LOD	<LOD	288471	12251	90481	70368	410	1466	<LOD	71	3950	162	1791	131
Arre	17n	6.0	458	<LOD	419584	8783	90447	<LOD	<LOD	<LOD	5312	<LOD	5460	65	645	44
Arre	17n	6.0	<LOD	<LOD	419854	28982	101481	<LOD	<LOD	<LOD	<LOD	<LOD	3520	150	631	203
Arre	17n	6.0	<LOD	500	545442	12012	90447	16398	<263.308	960	1787	93	11815	122	2397	55
Arre	4b	3.0	<LOD	<LOD	<LOD	35395	98742	<LOD	<LOD	<LOD	<LOD	<LOD	3504	407	2731	9395
Arre	4b	3.0	<LOD	<LOD	<LOD	29300	98742	<LOD	<LOD	<LOD	<LOD	982	10059	633	<LOD	<LOD
Arre	10b	3.0	<LOD	<LOD	781883	18369	101496	<LOD	<LOD	<LOD	228	<LOD	7311	134	2624	<LOD
Arre	10b	3.0	<LOD	<LOD	449922	14740	101447	<LOD	<LOD	<LOD	<LOD	<LOD	9245	449	<LOD	<LOD
Arre	10b	3.0	304	<LOD	327257	17590	101496	95701	<LOD	<LOD	1099	103	8660	210	1492	9
Arre	9b	3.0	<LOD	<LOD	<LOD	<LOD	105036	<LOD	<LOD	<LOD	<LOD	<LOD	13747	<LOD	<LOD	1127
Arre	3b	3.0	<LOD	<LOD	192842	<LOD	105036	<LOD	<LOD	<LOD	<LOD	<LOD	<LOD	626	<LOD	<LOD
Arre	5b	3.0	<LOD	<LOD	<LOD	13049	108184	<LOD	<LOD	<LOD	<LOD	<LOD	<LOD	<LOD	1309	<LOD
Arre	5b	3.0	<LOD	<LOD	<LOD	28095	108184	<LOD	<LOD	<LOD	<LOD	5298	<LOD	<LOD	<LOD	<LOD
Arre	6b	3.0	<LOD	<LOD	200653	21502	106217	<LOD	819	<LOD	<LOD	<LOD	4792	143	944	<LOD
Arre	6b	3.0	<LOD	<LOD	335686	20386	106217	<LOD	<LOD	<LOD	<LOD	<LOD	7640	146	<LOD	<LOD
Arre	6b	3.0	<LOD	6332	<419260.8075	23145	106217	<LOD	<LOD	<LOD	<LOD	<LOD	8342	385	<LOD	346
Arre	11b	3.0	438	<LOD	<LOD	13025	91661	23701	<LOD	8524	<LOD	<LOD	21345	211	5651	<49.1293
Arre	11b	3.0	<LOD	<LOD	<LOD	<LOD	91661	<LOD	<LOD	<LOD	<LOD	<LOD	<LOD	<LOD	<LOD	<LOD
Arre	1c	4.0	152	674	171167	18336	101102	83443	504	<LOD	<LOD	129	6529	132	1309	146
Arre	8c	4.0	<LOD	<LOD	<LOD	24331	87334	<LOD	<LOD	<LOD	<LOD	133	4161	83	1406	<LOD
Arre	8c	4.0	<LOD	<LOD	<LOD	18053	87334	<LOD	<LOD	<LOD	<LOD	86	3992	104	1284	<LOD
Arre	8c	4.0	<LOD	<LOD	736524	18687	87334	<LOD	<LOD	<LOD	<LOD	249	6123	383	1276	<LOD
Arre	4c	4.0	<LOD	<LOD	<LOD	<LOD	88120	<LOD	<LOD	<LOD	<LOD	<LOD	2797	433	<LOD	<LOD
Arre	4c	4.0	359	288	343401	22086	88120	10317	<LOD	129	486	119	8384	228	1433	28
Arre	2c	4.0	<LOD	1357	175982	24024	94021	89668	371	1506	1821	156	5731	248	1396	159
Arre	2c	4.0	<LOD	<LOD	244943	24940	94021	<LOD	<LOD	<LOD	2855	195	8372	223	1606	113
Arre	3c	4.0	<LOD	13837	<LOD	24367	94808	<LOD	<LOD	<LOD	<LOD	<LOD	7682	516	2134	650
Arre	3c	4.0	<LOD	<LOD	286304	24414	94808	12249	556	11259	<LOD	115	6434	159	1463	41
Arre	3c	4.0	<LOD	<LOD	<LOD	21957	94808	<LOD	<LOD	<LOD	<LOD	<LOD	4925	<LOD	1672	<LOD

Arre	3c	4.0	444	<LOD	416682	17507	94808	<LOD	<LOD	<LOD	4461	108	3633	160	851	94
Arre	18n	4.0	330	629	166386	14864	101496	100427	231	<LOD	928	92	7608	99	1553	33
Arre	18n	4.0	409	519	282402	19976	101496	71290	258	<LOD	3551	99	5602	246	1150	<LOD
Arre	9c	4.0	188	80	322668	14437	88120	12933	35	98	1233	75	12665	154	3131	22
Arre	9c	4.0	1485	<LOD	631369	20932	88120	<LOD	3451	<LOD	<LOD	<LOD	11575	162	2231	435
Arre	1a	1.0	233	332	309223	20525	96775	83651	<LOD	<LOD	387	97	7144	95	1923	13
Arre	1a	1.0	365	385	241886	27458	96775	83429	221	8006	623	135	6746	97	2202	72
Arre	1a	1.0	332	<LOD	395761	25691	96775	89873	<LOD	386	2888	116	6512	96	2098	72
Arre	7a	1.0	568	<LOD	380022	23113	92054	<LOD	<LOD	<LOD	<LOD	144	12266	137	3901	<LOD
Arre	7a	1.0	568	<LOD	380022	29113	92054	<LOD	<LOD	<LOD	<LOD	144	12266	137	3901	<LOD
Arre	7a	1.0	568	<LOD	233712	19113	92054	<LOD	<LOD	<LOD	<LOD	144	12266	137	3901	<LOD
Arre	7a	1.0	196	282	241701	14490	92054	65628	72	<LOD	525	67	5148	73	1614	20
Arre	4a	1.0	312	294	285174	24636	96382	71928	171	<LOD	962	102	5990	256	1987	49
Arre	4a	1.0	312	294	282583	24636	96382	71928	171	<LOD	905	102	5990	256	1987	49
Arre	4a	1.0	312	294	267263	24636	96382	71928	171	<LOD	<LOD	102	5990	256	1987	49
Arre	4a	1.0	<LOD	6156	<LOD	10446	96775	<LOD	<LOD	<LOD	<LOD	314	7959	127	2267	<LOD
Arre	4a	1.0	<LOD	6156	<LOD	20475	96775	<LOD	<LOD	<LOD	<LOD	314	7959	127	2267	<LOD
Arre	4a	1.0	<LOD	6156	<LOD	20459	96775	<LOD	<LOD	<LOD	<LOD	314	7959	127	2267	<LOD
Arre	4a	1.0	<LOD	<LOD	274054	21547	96775	84519	258	<LOD	<LOD	106	5950	75	1814	20
Arre	4a	1.0	<LOD	<LOD	257610	24784	96775	<LOD	<LOD	<LOD	<LOD	112	6153	<LOD	2334	101
Arre	4a	1.0	<LOD	<LOD	441373	1655	96775	<LOD	<LOD	<LOD	<LOD	<LOD	8149	37	1832	<LOD
Arre	5a	1.0	1040	<LOD	536736	12896	102283	<LOD	<LOD	<LOD	<LOD	219	1842	151	<LOD	192
Arre	5a	1.0	1040	<LOD	390790	9896	102283	<LOD	<LOD	<LOD	<LOD	219	1842	151	<LOD	192
Arre	5a	1.0	<LOD	<LOD	132614	15894	102283	<LOD	<LOD	<LOD	<LOD	157	4229	<LOD	1170	120
Arre	5a	1.0	391	608	294186	26447	102283	106353	173	251	1227	106	9961	84	2288	53
Arre	5a	1.0	146	355	319965	27622	102283	95581	<23.4514	56	380	147	8395	147	2146	18
Arre	5a	1.0	<LOD	<LOD	590882	20878	102283	<LOD	<LOD	<LOD	<LOD	<LOD	8284	<LOD	3360	323
Arre	3a	1.0	544	1155	430697	34534	92054	102812	700	3941	23554	79	4164	112	592	441
Arre	3a	1.0	<LOD	<LOD	448055	18149	92054	<LOD	<LOD	<LOD	17144	61	2251	87	1824	<LOD
Arre	3a	1.0	<LOD	<LOD	288731	21950	92054	<LOD	<LOD	<LOD	<LOD	115	5169	57	1833	56

Arre	6a	1.0	179	1929	83512	11439	94808	58542	2591	9103	341	28	1257	22	426	302
Arre	6a	1.0	144	1212	52169	5816	94808	63855	589	14504	609	47	895	<LOD	270	128
Arre	6a	1.0	<LOD	<LOD	424723	7160	94808	<LOD	<LOD	<LOD	5507	<LOD	4454	82	1228	<LOD
Arre	6a	1.0	161	<LOD	289031	16757	96775	91159	<LOD	<LOD	1818	41	6848	200	1201	38
Arre	6a	1.0	161	<LOD	302332	16757	96775	91159	<LOD	<LOD	1916	41	6848	200	1201	38
Arre	6a	1.0	<LOD	<LOD	217910	26822	96775	<LOD	<LOD	<LOD	<LOD	109	5665	58	1216	<LOD
Arre	6a	1.0	381	258	289939	26371	96775	76082	67	51	866	108	6286	114	1926	42
Arre	6a	1.0	159	<LOD	197929	13524	96775	65790	131	152	2795	51	6982	99	743	31
Arre	1b	2.0	<LOD	590	124398	23908	96775	111375	<LOD	534	<LOD	244	11815	219	3906	103
Arre	1b	2.0	266	<LOD	481319	31082	96775	13229	<LOD	10387	3006	31	8272	127	2756	555
Arre	1b	2.0	4501	<LOD	<LOD	<LOD	96775	<LOD	<LOD	18261	<LOD	<LOD	11269	<LOD	3518	429
Arre	8b	2.0	<LOD	<LOD	<LOD	15755	96775	<LOD	1497	<LOD	17912	<LOD	14744	190	4073	166
Arre	8b	2.0	<LOD	<LOD	<LOD	15755	96775	<LOD	1497	<LOD	<LOD	<LOD	14744	190	4073	166
Arre	8b	2.0	<LOD	<LOD	539915	13914	96775	<LOD	3726	<LOD	<LOD	<LOD	16002	134	6319	<LOD
Arre	8b	2.0	<LOD	<LOD	637249	8993	96775	<LOD	<LOD	<LOD	27096	<LOD	14049	133	2885	<LOD

11.14 Fluid inclusions – Limit of detection of LA-ICP-MS analyses (quartz host)

Table 27. Limit of detection for fluid inclusion analyses acquired with LA-ICP-MS on quartz (ppm) for Victoria (VIC12), Pale Bidau (BO10-BO12), Crabioules (CRA02), Arre (ARR06) deposit. Abbreviations: FI: fluid inclusions.

Deposit	FI n°	FI assemblage	Li7	B11	Cl35	K39	Na23	Ca43	Mn55	Zn66	Br79	Rb85	Sr88	Cs133	Ba137	Pb208
Victoria	1n	5	263	930	69544	933	157	52631	483	604	2157	25	15	14	118	36
Victoria	1n	5	653	2017	173263	2447	380	133820	1212	1378	5267	62	47	36	289	78
Victoria	1n	5	153	474	32345	569	89	31291	282	324	986	15	11	9	70	18
Victoria	1n	5	4279	15275	1094555	15441	2602	909998	7827	9513	33561	502	388	197	2332	590
Victoria	1n	5	911	3159	234072	3274	577	183417	1699	2010	6988	108	92	66	498	133
Victoria	1n	5	240	819	68745	884	151	48419	455	524	2048	25	21	16	116	34
Victoria	1n	5	2044	7086	745448	7343	1293	411405	3811	4508	22255	242	207	148	1118	297
Victoria	2n	4	953	3164	287091	3668	593	193170	1865	2042	8520	75	64	48	347	124
Victoria	2n	4	353	1228	98995	1390	210	73294	706	793	2926	13	11	17	104	45
Victoria	2n	4	667	2349	182726	2560	399	137859	1310	1509	5411	34	29	38	240	89
Victoria	2n	4	581	2031	161075	2259	347	120272	1152	1308	4765	25	21	30	188	76
Victoria	2n	4	791	2790	216459	3032	474	163531	1552	1791	6411	41	35	45	289	106
Victoria	2n	4	197	663	52987	735	119	44061	384	457	1547	23	18	12	87	28
Victoria	2n	4	622	2099	2412215	2328	377	139491	1216	1446	70761	74	58	39	276	89
Victoria	2n	4	262	896	71137	963	160	58609	506	614	2080	34	27	18	130	39
Victoria	2n	4	182	591	51506	718	108	41211	370	415	1497	16	12	8	53	24
Victoria	2n	4	2944	9651	773362	10945	1773	638695	5686	6656	22958	252	356	195	1137	423
Victoria	2n	4	240	831	2998126	1010	160	52831	521	596	86581	16	19	13	35	30
Victoria	2n	4	1336	4611	393084	5630	891	293921	2905	3314	11289	89	106	69	181	168
Victoria	2n	4	2113	7416	650433	8636	1415	462302	4492	5279	18735	179	199	130	474	280
Victoria	2n	4	2148	7569	769255	8724	1440	469579	4545	5376	22272	191	210	137	522	288
Victoria	2n	4	900	2961	210078	3410	549	197595	1798	2035	5960	90	95	62	276	120

Victoria	2n	4	2958	10470	803329	11670	1890	622831	6168	6766	23284	284	243	104	1668	375
Victoria	2n	4	1506	4952	410434	5899	913	317421	3115	3472	11758	203	87	56	886	181
Victoria	2n	4	304	1064	112248	1218	200	64272	644	734	3144	40	32	17	95	44
Victoria	2n	4	2043	6985	593649	8509	1333	433595	4451	4865	16519	222	176	86	410	278
Victoria	2n	4	1034	3579	301473	4215	677	218844	2217	2479	8413	125	100	51	271	145
Victoria	4	1	2	7	2045809	7	1	356	4	4	27	56758	0	0	1	0
Victoria	4	1	2	6	924040	6	1	323	4	4	25	25614	0	0	1	0
Victoria	4	1	4	12	2470371	12	2	623	7	7	45	68623	0	0	2	0
Victoria	4	1	4	14	753806	13	2	690	8	8	52	20827	0	0	2	0
Victoria	2	1	2	6	187651	6	1	311	3	4	21	5169	0	0	1	0
Victoria	2	1	1	5	725756	5	1	255	3	3	18	20013	0	0	1	0
Victoria	2	1	2	6	553270	6	1	325	3	4	22	15251	0	0	1	0
Victoria	2	1	1	5	224863	4	1	240	2	3	17	6191	0	0	0	0
Victoria	2	1	2	7	347889	6	1	347	3	4	23	9583	0	0	1	0
Victoria	2	1	2	6	89739	6	1	314	3	4	22	2469	0	0	1	0
Victoria	1	1	2	6	282059	5	1	303	3	4	20	7682	0	0	1	0
Victoria	1	1	2	6	110616	6	1	330	3	4	22	3006	0	0	1	0
Victoria	1	1	1	5	279152	5	1	253	3	3	17	7599	0	0	1	0
Victoria	1	1	2	6	161098	6	1	314	3	4	21	4385	0	0	1	0
Victoria	1	1	1	5	17896	5	1	254	3	3	18	485	0	0	1	0
Victoria	5	1	1	4	118287	3	1	188	2	2	13	3237	0	0	1	0
Victoria	5	1	1	4	311178	3	1	192	2	2	13	8530	0	0	1	0
Victoria	7	1	0	2	66256	2	0	90	1	1	6	1758	0	0	0	0
Victoria	7	1	0	1	125301	1	0	69	1	1	5	3329	0	0	0	0
Victoria	7	1	0	1	25169	1	0	71	1	1	5	666	0	0	0	0
Victoria	7	1	1	2	192191	2	0	100	1	1	6	5089	0	0	0	0
Victoria	7	1	1	3	151916	3	1	175	2	2	11	4026	0	0	0	0
Victoria	8	1	1	4	30047	3	1	192	2	2	13	808	0	0	1	0
Victoria	8	1	1	3	52795	2	0	136	1	1	9	1422	0	0	0	0
Victoria	8	1	1	3	43656	3	0	144	1	2	10	1177	0	0	0	0

Victoria	9	1	1	3	249880	3	1	188	2	2	12	6609	0	0	0	0
Victoria	9	1	1	4	17407	4	1	212	2	2	14	459	0	0	0	0
Victoria	9	1	2	5	257843	5	1	283	3	3	18	6821	0	0	1	0
Victoria	2b	2	5	17	426907	13	3	841	8	9	50	11788	1	0	4	1
Victoria	2b	2	2	5	198377	5	1	282	3	3	18	5468	0	0	1	0
Victoria	2b	2	2	7	12524	6	1	351	3	4	22	344	0	0	1	0
Victoria	2b	2	2	6	17797	6	1	312	3	3	20	490	0	0	1	0
Victoria	2b	2	2	6	86316	6	1	323	3	3	21	2381	0	0	1	0
Victoria	2b	2	2	8	27835	7	1	396	4	4	25	767	0	0	1	0
Victoria	2b	2	2	7	635852	7	1	372	4	4	24	17568	0	0	1	0
Victoria	1c	3	2	6	192303	7	1	367	4	4	23	5299	0	0	1	0
Victoria	1c	3	2	5	304476	6	1	321	3	4	21	8376	0	0	1	0
Victoria	1c	3	2	8	630460	8	1	451	4	5	28	17325	0	0	1	0
Victoria	2c	3	2	6	81975	7	1	327	4	4	22	2213	0	0	1	0
Victoria	2c	3	3	13	31984	12	2	668	7	8	42	865	1	0	2	0
Victoria	2c	3	6	23	376775	22	3	1159	12	14	74	10176	1	0	3	1
Victoria	3c	3	1	2	63947	2	0	102	1	1	7	1742	0	0	0	0
Victoria	3c	3	1	2	64822	2	0	106	1	1	7	1773	0	0	0	0
Pale Bidau-PB12	18	1	1605	5949	383714	5686	960	311714	3171	3294	11031	220	143	111	642	203
Pale Bidau-PB12	18	1	190	695	46527	692	113	36797	382	383	1334	22	13	11	60	23
Pale Bidau-PB12	18	1	1010	3721	244430	3628	602	196016	2014	2056	7018	129	81	65	364	124
Pale Bidau-PB12	2	2	50	186	13150	196	29	10680	103	108	372	5	5	3	20	6
Pale Bidau-PB12	2	2	240	898	61824	918	139	51060	487	520	1751	27	27	18	107	30
Pale Bidau-PB12	2	2	506	1901	130174	1931	295	107871	1027	1101	3688	59	58	38	232	63

Pale Bidau-PB12	2	2	566	2122	146051	2168	329	120623	1151	1228	4136	64	63	42	254	70
Pale Bidau-PB12	19	2	1032	3341	250796	3710	556	200331	2013	1934	7056	122	114	34	267	117
Pale Bidau-PB12	19	2	1032	3341	250796	3710	556	200331	2013	1934	7056	122	114	34	267	117
Pale Bidau-PB12	19	2	6218	20107	1514760	22415	3346	1207438	12153	11642	42610	724	682	200	1568	703
Pale Bidau-PB12	19	2	6962	22761	1671781	24692	3773	1353291	13461	13192	47104	889	832	268	2095	815
Pale Bidau-PB12	20	2	2556	9141	633421	9357	1410	508856	5122	5390	17955	281	248	185	1252	293
Pale Bidau-PB12	20	2	2974	10589	742766	10983	1635	591874	5995	6242	21037	308	272	207	1385	334
Pale Bidau-PB12	1	2	105	367	26931	395	64	21137	218	234	746	14	11	4	47	13
Pale Bidau-PB12	1	2	35	123	9078	133	21	7105	74	79	252	5	3	1	16	4
Pale Bidau-PB12	11	2	513	1934	125159	1832	284	105719	1024	1179	3593	50	61	39	197	59
Pale Bidau-PB12	11	2	550	2051	137200	2014	301	113317	1117	1251	3930	43	57	37	170	59
Pale Bidau-PB12	11	2	534	1966	136741	2013	289	110078	1107	1200	3907	30	46	30	119	54
Pale Bidau-PB12	13	3	447	1508	107736	1593	227	90092	892	937	3104	52	46	34	232	57
Pale Bidau-PB12	13	3	460	1544	116440	1735	228	92435	952	923	3343	34	30	26	165	54
Pale Bidau-PB12	13	3	460	1544	116440	1735	228	92435	952	923	3343	34	30	26	165	54

Pale Bidau-PB12	17	2	248	960	64511	959	127	50796	519	545	1815	23	12	7	91	32
Pale Bidau-PB12	17	2	1105	4298	281956	4183	572	225913	2279	2445	7946	118	68	38	467	145
Pale Bidau-PB12	19	2	1982	6850	486894	7136	1055	398675	3924	4164	13748	276	197	73	875	210
Pale Bidau-PB12	22	2	17	64	3896	58	10	3371	33	36	110	3	2	2	11	2
Pale Bidau-PB12	22	2	339	1308	81024	1200	199	69260	676	729	2288	54	36	31	214	49
Pale Bidau-PB12	22	2	1545	5510	496484	5809	796	299126	3261	3315	14178	144	151	108	337	170
Pale Bidau-PB12	22	2	3705	13586	1616526	13687	1932	727240	7662	8256	46026	341	305	198	1578	400
Pale Bidau-PB12	22	2	670	2287	173456	2517	354	143186	1374	1451	4986	96	67	19	155	84
Pale Bidau-PB12	22	2	3972	13887	991802	14330	2140	847859	7930	8777	28612	674	498	175	1394	529
Pale Bidau-PB12	22	2	702	2384	183456	2665	370	150164	1451	1513	5270	96	66	18	141	86
Pale Bidau-PB12	22	2	977	3272	242923	3645	523	201220	2035	2068	6837	111	86	30	441	109
Pale Bidau-PB12	22	2	1128	3784	280087	4201	605	232428	2348	2392	7885	130	101	35	516	126
Pale Bidau-PB12	22	2	339	1138	83965	1259	182	69813	704	719	2364	40	31	11	157	38
Pale Bidau-PB12	7	3	1737	6103	424485	6251	975	352789	3585	4051	12021	160	242	80	988	199
Pale Bidau-PB12	10	2	77	250	18586	277	38	14633	154	160	526	9	9	2	19	8

Pale Bidau-PB12	10	2	1359	4895	236806	4761	710	273970	2723	2935	6655	116	105	92	658	163
Pale Bidau-PB10	4a	1	202	782	49516	663	120	35859	357	376	1449	23	18	12	104	22
Pale Bidau-PB10	4a	1	204	784	50477	677	120	36128	363	377	1476	22	17	11	98	22
Pale Bidau-PB10	4a	1	77	295	19317	259	45	13673	138	142	564	8	6	4	35	8
Pale Bidau-PB10	5a	1	23	91	5914	78	14	4215	42	43	168	2	2	1	9	3
Pale Bidau-PB10	5a	1	126	491	30873	407	73	22604	220	233	880	15	12	7	56	16
Pale Bidau-PB10	6a	1	20	71	4793	63	11	3609	34	40	136	3	2	1	10	2
Pale Bidau-PB10	1a	1	35	137	9079	122	20	7097	65	70	262	2	4	2	16	4
Pale Bidau-PB10	1a	1	62	242	15254	205	36	12294	111	124	442	6	8	4	34	8
Pale Bidau-PB10	1a	1	12	47	3193	43	7	2463	23	24	92	1	1	1	5	2
Pale Bidau-PB10	1a	1	70	271	18159	245	40	14109	131	139	524	4	8	4	30	9
Pale Bidau-PB10	7a	1	115	429	29220	392	69	20549	207	214	830	8	11	7	59	15
Pale Bidau-PB10	5b	2	216	720	54322	731	120	39479	384	392	1534	13	17	7	124	27
Pale Bidau-PB10	5b	2	528	1759	132632	1784	292	96393	938	957	3746	31	41	17	302	66
Pale Bidau-PB10	6b	2	103	359	26035	345	59	18690	186	196	744	10	9	5	27	12

Pale Bidau-PB10	6b	2	2637	9263	663350	8785	1524	480394	4747	5058	18971	279	245	135	769	321
Pale Bidau-PB10	7b	2	4640	16784	1151028	15451	2744	871282	8438	9069	32403	533	440	254	1873	527
Pale Bidau-PB10	12b	2	357	1271	91418	1248	192	66190	676	662	2600	36	15	17	123	39
Pale Bidau-PB10	11b	2	490	1881	128831	1741	294	95570	944	904	3570	46	40	38	202	60
Pale Bidau-PB10	11b	2	7173	27518	1891589	25570	4305	1399871	13859	13219	52402	664	581	553	2903	881
Pale Bidau-PB10	2b	2	209	790	52864	727	122	42133	384	428	1507	22	14	16	67	23
Pale Bidau-PB10	2b	2	50	184	13364	185	29	10118	96	100	379	3	1	3	7	5
Pale Bidau-PB10	8b	2	842	3000	218621	3016	455	162251	1582	1570	6100	80	63	33	311	91
Pale Bidau-PB10	1b	3	69	248	17527	245	39	13089	131	131	498	6	7	3	24	8
Pale Bidau-PB10	4b	3	34	120	9458	130	20	7000	70	69	276	10	9	5	41	7
Pale Bidau-PB10	4b	3	586	2088	155944	2135	340	119157	1170	1198	4562	175	154	93	732	123
Pale Bidau-PB10	4b	3	5120	18484	1331963	18186	2998	1040206	10043	10587	39037	1586	1389	841	6626	1087
Pale Bidau-PB10	4b	3	2128	7526	574337	7874	1228	433170	4295	4320	16781	624	546	331	2603	442
Pale Bidau-PB10	3b	3	641	2395	164573	2285	361	125563	1221	1264	4633	75	40	35	277	75
Pale Bidau-PB10	3b	3	312	1158	81409	1132	175	61176	602	610	2288	33	16	15	120	35

Pale Bidau-PB10	13b	2	272	985	72924	1018	149	52982	537	538	2058	30	23	16	126	34
Pale Bidau-PB10	13b	2	34	126	9052	126	19	6736	67	69	256	4	3	2	18	4
Pale Bidau-PB10	9b	2	2	8	589	8	1	446	4	4	16	0	0	0	1	0
Crabioules	1a	1	3	12	1619364	10	2	578	6	7	45893	1	0	0	2	0
Crabioules	3a	1	1	3	420740	3	1	184	2	2	11807	0	0	0	1	0
Crabioules	2a	1	1	3	1623915	3	0	143	1	2	44573	0	0	0	0	0
Crabioules	4a	1	1	5	1195447	5	1	263	3	3	33046	0	0	0	1	0
Crabioules	1b	2	1	3	230163	3	1	176	2	2	6206	0	0	0	0	0
Crabioules	1b	2	1	5	5335	5	1	284	3	3	143	0	0	0	1	0
Crabioules	1b	2	2	6	35817	6	1	355	3	4	937	0	0	0	1	0
Crabioules	1b	2	1	3	581097	3	0	150	2	2	15246	0	0	0	0	0
Crabioules	1b	2	1	3	40150	4	1	196	2	2	1048	0	0	0	1	0
Crabioules	1b	2	2	5	-996653	5	1	293	3	4	-26109	0	0	0	1	0
Crabioules	1b	2	1	4	235752	4	1	237	2	3	6185	0	0	0	1	0
Crabioules	1b	2	1	4	12223	4	1	213	2	2	320	0	0	0	1	0
Crabioules	2b	2	2	6	780163	6	1	357	3	4	20436	0	0	0	1	0
Crabioules	2b	2	1	3	49635	3	1	180	2	2	1306	0	0	0	0	0
Crabioules	2b	2	1	3	11562	4	1	186	2	2	302	0	0	0	0	0
Crabioules	2b	2	1	4	149369	5	1	264	3	3	3917	0	0	0	1	0
Crabioules	2n	2	1	3	122348	3	1	181	2	2	3298	0	0	0	0	0
Crabioules	2n	2	1	2	457373	3	0	157	2	2	12333	0	0	0	0	0
Crabioules	2n	2	1	2	16488	3	0	145	1	2	445	0	0	0	0	0
Crabioules	2n	2	1	3	1531495	3	1	171	2	2	41442	0	0	0	0	0
Crabioules	5n	2	1	3	42217	3	1	161	2	2	1109	0	0	0	0	0
Crabioules	5n	2	1	3	96870	4	1	192	2	2	2548	0	0	0	1	0
Crabioules	5n	2	1	4	511583	4	1	227	2	3	13196	0	0	0	1	0
Crabioules	5n	2	1	4	289593	4	1	230	2	3	7618	0	0	0	1	0

Crabioules	5n	2	1	5	30590	5	1	269	3	3	802	0	0	0	1	0
Crabioules	5n	2	1	5	22526	5	1	269	3	3	593	0	0	0	1	0
Crabioules	2n	3	2	5	802546	5	1	298	3	3	21069	0	0	0	1	0
Crabioules	3b	3	2	6	1506934	7	1	367	4	4	40007	0	0	0	1	0
Crabioules	3n	3	1	3	24406	3	1	165	2	2	642	0	0	0	0	0
Crabioules	3n	3	1	3	189137	3	1	180	2	2	4977	0	0	0	0	0
Crabioules	3n	3	1	2	217386	3	0	146	1	2	5716	0	0	0	0	0
Crabioules	3n	3	1	2	7865	2	0	125	1	1	206	0	0	0	0	0
Crabioules	4n	3	1	2	23213	3	0	141	1	2	603	0	0	0	0	0
Crabioules	4n	3	1	2	178213	3	0	155	2	2	4624	0	0	0	0	0
Crabioules	4n	3	1	2	1662	3	0	150	2	2	43	0	0	0	0	0
Crabioules	5n	3	1	4	161527	4	1	224	2	2	4054	0	0	0	0	0
Crabioules	6n	3	106	332	25420	429	64	22358	231	242	730	7	6	3	27	12
Crabioules	6n	3	177	565	45485	688	108	37046	375	408	1185	15	13	8	62	22
Crabioules	6n	3	350	1070	105473	1450	210	73677	777	787	2737	15	13	8	61	37
Crabioules	6n	3	360	1106	116011	1484	216	75785	796	811	3011	17	14	9	68	39
Crabioules	7n	3	432	1281	156188	1934	287	94389	1035	878	4129	69	49	25	194	53
Crabioules	7n	3	1544	4679	433362	6708	1030	335935	3616	3191	11482	272	199	104	807	200
Crabioules	7n	3	3367	10060	961105	14903	2241	734136	7996	6882	25433	559	401	206	1603	422
Crabioules	7n	3	1718	5025	502515	7812	1140	375763	4164	3454	13273	259	181	90	700	205
Crabioules	7n	3	2814	8362	808110	12539	1871	613938	6716	5727	21374	456	325	166	1291	348
Crabioules	8n	3	132	417	32562	554	74	28555	296	273	871	19	7	4	53	17
Crabioules	8n	3	350	1127	76263	1429	198	75419	770	734	2055	56	23	14	167	48
Crabioules	8n	2	1167	3762	307186	4741	659	251123	2557	2451	8261	188	81	48	569	161
Crabioules	9n	3	172	565	44157	808	111	39586	421	399	1172	18	19	9	73	24
Crabioules	9n	3	773	2635	216352	3385	503	175674	1794	1837	5757	113	111	59	457	118
Crabioules	9n	3	544	1805	162388	2495	352	124469	1307	1270	4311	64	65	33	259	78
Crabioules	9n	3	580	1930	188608	2646	375	132580	1388	1356	5004	70	71	37	283	84
Crabioules	9n	3	96	323	27424	426	62	21816	225	226	729	13	13	7	53	14
Arre	19n	5	1	3	75666	4	1	214	2	2	2016	0	0	0	0	0

Arre	19n	5	1	3	280233	4	1	214	2	2	7467	0	0	0	0	0
Arre	19n	5	1	2	80634	4	1	177	2	2	2140	0	0	0	0	0
Arre	19n	5	1	4	7007	5	1	270	3	3	187	0	0	0	1	0
Arre	20n	5	1	3	66067	4	1	210	2	2	1729	0	0	0	1	0
Arre	20n	5	1	3	615421	3	0	176	2	2	16097	0	0	0	1	0
Arre	20n	5	1	2	1353870	3	0	146	1	2	35455	0	0	0	0	0
Arre	20n	5	1	2	62362	2	0	118	1	1	1632	0	0	0	0	0
Arre	20n	5	1	2	252398	3	0	150	1	2	6595	0	0	0	1	0
Arre	20n	5	1	2	215438	3	0	148	1	2	5642	0	0	0	0	0
Arre	20n	5	1	3	4327587	4	1	203	2	2	113524	0	0	0	1	0
Arre	21n	5	1	2	255837	3	0	140	2	2	6813	0	0	0	0	0
Arre	21n	5	1	2	303125	3	0	128	1	1	7997	0	0	0	0	0
Arre	21n	5	1	2	183574	3	0	135	1	2	4895	0	0	0	0	0
Arre	21n	5	1	2	283196	3	0	145	2	2	7436	0	0	0	0	0
Arre	21n	5	1	2	59554	3	0	145	2	2	1578	0	0	0	0	0
Arre	1n	6	172	628	49163	689	128	31195	375	371	1315	20	20	12	86	23
Arre	1n	6	443	1647	141784	1708	330	80197	939	966	3803	60	59	35	259	63
Arre	2n	6	294	1022	115293	1097	190	54424	598	612	3065	31	16	16	166	40
Arre	2n	6	316	1142	82314	1122	209	58629	620	674	2199	42	25	22	217	46
Arre	2n	6	97	348	25703	351	64	18054	193	206	686	12	7	6	63	14
Arre	2n	6	957	3432	217343	3462	632	177998	1904	2031	5803	119	67	64	622	135
Arre	2n	6	150	515	66268	588	98	28133	317	310	1767	13	5	7	71	19
Arre	3n	6	1220	4352	322874	4411	786	221684	2469	2688	8609	113	127	109	892	171
Arre	3n	6	329	1167	87783	1200	211	59797	670	723	2339	29	33	29	234	45
Arre	3n	6	171	591	39396	655	109	31194	361	371	1051	11	14	13	104	22
Arre	3n	6	611	2160	217838	2249	392	111193	1253	1340	5802	51	59	52	425	84
Arre	4n	6	335	1061	94597	1307	215	67532	695	746	2534	34	16	11	93	42
Arre	4n	6	430	1376	146921	1662	277	86682	886	962	3937	47	23	16	132	55
Arre	4n	6	526	1694	132574	2006	339	105640	1073	1179	3548	60	31	22	176	68
Arre	5n	6	240	849	73137	923	143	43657	490	492	1910	20	11	12	99	26

Arre	5n	6	217	783	52228	806	131	39436	432	452	1370	22	13	13	108	25
Arre	5n	6	922	3344	247404	3388	556	167339	1821	1925	6482	99	60	59	480	108
Arre	5n	6	434	1573	108072	1594	262	78733	857	906	2834	47	28	28	226	51
Arre	5n	6	843	3092	222131	3035	513	152927	1641	1775	5828	99	62	59	480	103
Arre	6n	6	399	1344	175971	1425	249	71352	793	796	4601	54	43	30	218	51
Arre	6n	6	320	1036	106758	1211	196	57356	665	621	2767	35	27	18	130	37
Arre	6n	6	867	2863	514994	3176	536	154946	1756	1705	13407	106	83	58	417	107
Arre	7n	6	598	2018	171653	2410	397	114638	1252	1337	4423	22	38	27	218	65
Arre	7n	6	818	2828	281118	3180	547	156345	1668	1848	7272	47	66	45	372	95
Arre	7n	6	368	1264	96633	1448	246	70449	757	829	2496	19	28	19	157	42
Arre	8n	6	260	840	84155	1126	177	52259	587	537	2170	20	21	18	95	27
Arre	8n	6	194	624	54460	842	132	38959	439	399	1403	14	15	13	69	20
Arre	9n	6	2183	7823	766187	8702	1384	402715	4680	4880	19680	283	190	132	1079	263
Arre	10n	6	680	2375	206858	2863	448	130015	1513	1504	5330	71	23	16	346	66
Arre	10n	6	221	785	67894	900	146	42075	479	493	1755	27	11	7	128	23
Arre	11n	6	951	3022	306628	3371	550	174868	1788	1965	7866	105	90	62	511	122
Arre	12n	6	562	1997	244836	2235	353	104698	1176	1154	6226	52	35	28	272	67
Arre	13n	6	688	2208	201057	2757	445	135790	1444	1516	4995	37	32	22	359	78
Arre	13n	6	1318	4327	374718	5125	858	259172	2705	2931	9333	92	79	55	781	157
Arre	13n	6	688	2195	203067	2787	444	136137	1456	1513	5041	33	29	20	345	76
Arre	14n	6	691	2254	172814	2584	410	133507	1359	1388	4452	86	45	51	368	86
Arre	14n	6	191	615	44414	728	112	36995	381	381	1143	22	11	13	93	23
Arre	15n	6	226	788	62951	874	144	42352	463	472	1591	23	17	7	60	26
Arre	15n	6	1397	4930	465937	5271	891	260843	2808	2936	11796	158	119	55	452	169
Arre	16n	6	255	958	126721	1018	185	49603	541	536	3206	30	31	18	162	34
Arre	16n	6	107	397	31464	435	77	20831	230	223	795	12	12	7	63	14
Arre	16n	6	544	2055	155859	2149	396	105766	1146	1150	3946	67	68	40	359	73
Arre	17n	6	469	1420	132758	1975	307	91770	1072	1084	3473	62	54	29	261	47
Arre	17n	6	204	648	55783	773	142	35777	413	429	1423	23	19	12	110	21
Arre	17n	6	188	591	51542	715	130	32847	382	393	1314	20	17	11	98	19

Arre	17n	6	322	1010	161301	1238	202	63097	657	609	4021	31	34	24	153	42
Arre	17n	6	705	2286	192117	2598	448	137476	1393	1365	4806	84	87	60	405	98
Arre	17n	6	127	392	36705	499	79	24975	263	238	913	11	12	9	54	16
Arre	4b	3	6124	21650	1552938	21961	3723	1733102	11657	13059	65956	356	519	184	1480	721
Arre	4b	3	6319	23021	1507148	21167	3911	1839301	11491	13844	65067	665	779	343	2763	840
Arre	10b	3	1578	5582	377097	5442	870	449608	2866	3314	16164	197	137	81	743	192
Arre	10b	3	1882	6663	446282	6431	1104	558231	3426	4143	19486	291	199	131	677	249
Arre	10b	3	60	213	14504	209	33	17172	110	127	621	7	5	3	28	7
Arre	9b	3	6953	24337	1818040	26216	3884	2068093	13919	15428	75986	722	562	144	2209	813
Arre	3b	3	5699	20415	1426251	20466	3244	1724140	11032	12861	60307	771	620	221	2585	729
Arre	5b	3	1483	5393	332324	4755	939	464602	2618	3323	14804	213	226	133	1247	234
Arre	5b	3	11096	40365	2487252	35590	7031	3477271	19594	24868	110800	1595	1693	992	9331	1751
Arre	6b	3	246	909	62950	914	144	70016	483	572	2656	11	18	11	114	30
Arre	6b	3	1277	4743	324494	4705	748	365320	2493	2978	13721	66	101	59	622	160
Arre	6b	3	1664	6200	419261	6073	978	477640	3227	3889	17765	97	141	82	849	211
Arre	11b	3	311	1191	80146	1150	179	91599	609	741	3377	62	40	32	186	49
Arre	11b	3	2430	9376	615175	8809	1411	721460	4697	5820	26040	513	339	260	1578	393
Arre	1c	4	85	325	22198	319	50	24556	170	176	935	9	7	4	26	9
Arre	8c	4	1383	5431	370554	5300	811	432201	2830	3179	15424	72	63	80	293	172
Arre	8c	4	1179	4662	310636	4435	696	370737	2382	2728	12987	78	68	76	316	152
Arre	8c	4	2108	8388	544838	7763	1251	666568	4196	4907	22890	170	150	150	692	280
Arre	4c	4	6326	23951	1691809	24479	3585	1965900	12672	14449	70612	459	799	349	2769	915
Arre	4c	4	28	101	7769	113	16	8537	58	63	322	1	3	1	9	4
Arre	2c	4	88	359	23798	350	54	27757	182	208	1003	5	7	4	38	12
Arre	2c	4	248	1001	68055	1004	151	77356	519	579	2854	10	17	10	92	32
Arre	3c	4	3410	12448	922128	13371	2121	1059340	6911	7692	38427	360	207	209	946	496
Arre	3c	4	264	951	73302	1066	163	81286	546	590	3035	23	11	14	51	37
Arre	3c	4	2415	8701	668761	9721	1493	743655	4984	5395	27703	211	106	126	483	339
Arre	3c	4	316	1130	88420	1287	195	96794	657	702	3653	25	11	15	51	43
Arre	18n	4	97	352	25075	362	48	28341	190	191	1031	4	3	4	15	13

Arre	18n	4	98	357	25029	361	49	28719	191	194	1032	5	4	4	18	13
Arre	9c	4	16	65	4411	63	9	5046	33	35	179	1	1	1	5	2
Arre	9c	4	1421	5784	377850	5392	791	450935	2843	3169	15490	143	125	83	569	190
Arre	1a	1	11	45	2839	42	7	4352	20	30	99	1	1	1	4	1
Arre	1a	1	33	134	8599	128	20	13079	62	89	299	4	2	2	13	4
Arre	1a	1	90	353	22925	343	53	35734	165	246	804	9	6	5	38	12
Arre	7a	1	494	1855	118825	1791	294	180910	829	1296	3974	62	34	20	205	66
Arre	7a	1	494	1855	118825	1791	294	180910	829	1296	3974	62	34	20	205	66
Arre	7a	1	494	1855	118825	1791	294	180910	829	1296	3974	62	34	20	205	66
Arre	7a	1	24	89	5648	85	14	8641	39	62	189	3	2	1	10	3
Arre	4a	1	55	217	13094	193	33	20566	94	135	438	6	5	2	20	7
Arre	4a	1	55	217	13094	193	33	20566	94	135	438	6	5	2	20	7
Arre	4a	1	55	217	13094	193	33	20566	94	135	438	6	5	2	20	7
Arre	4a	1	1513	6056	367739	5620	937	597346	2695	3839	12560	173	136	63	641	198
Arre	4a	1	1513	6056	367739	5620	937	597346	2695	3839	12560	173	136	63	641	198
Arre	4a	1	1513	6056	367739	5620	937	597346	2695	3839	12560	173	136	63	641	198
Arre	4a	1	142	571	34173	522	88	56029	251	362	1169	17	14	6	64	19
Arre	4a	1	428	1731	102308	1560	266	169019	753	1096	3502	55	44	21	204	58
Arre	4a	1	378	1534	89956	1370	235	149328	663	971	3082	50	40	19	185	51
Arre	5a	1	770	3425	187227	2784	502	298074	1380	2065	6180	140	70	59	440	121
Arre	5a	1	770	3425	187227	2784	502	298074	1380	2065	6180	140	70	59	440	121
Arre	5a	1	439	1944	107380	1598	286	169657	790	1171	3540	77	37	32	241	68
Arre	5a	1	92	401	23236	347	59	35491	169	241	762	14	6	6	41	14
Arre	5a	1	13	54	3237	49	8	4829	23	32	106	2	1	1	5	2
Arre	5a	1	1467	6459	365108	5446	953	567330	2674	3889	12009	240	108	99	736	224
Arre	3a	1	211	859	52498	788	132	77968	384	553	1737	19	21	14	42	27
Arre	3a	1	388	1596	94842	1419	243	143587	696	1026	3145	41	43	29	101	51
Arre	3a	1	127	525	30631	458	80	46993	226	337	1018	15	15	10	38	17
Arre	6a	1	7	29	1742	26	4	2583	13	20	57	1	1	0	5	1
Arre	6a	1	9	35	2116	32	5	3165	16	24	70	2	1	1	6	1

Arre	6a	1	318	1254	74458	1117	195	112017	550	866	2455	61	51	23	231	49
Arre	6a	1	118	468	27890	415	70	43892	204	298	890	16	6	6	42	16
Arre	6a	1	118	468	27890	415	70	43892	204	298	890	16	6	6	42	16
Arre	6a	1	203	810	47082	699	121	75386	345	516	1506	30	14	12	82	28
Arre	6a	1	17	65	3986	60	10	6158	29	42	128	2	1	1	6	2
Arre	6a	1	46	192	11461	171	30	16539	84	133	367	11	10	4	30	8
Arre	1b	2	139	584	34751	518	91	50211	255	404	1112	34	29	13	92	23
Arre	1b	2	240	942	58904	888	142	85151	424	611	1881	22	21	16	91	28
Arre	1b	2	3163	12715	748020	11213	1894	1130008	5441	8243	24022	392	361	258	1573	402
Arre	8b	2	753	2713	187708	2810	457	274594	1401	1950	5949	89	37	21	298	104
Arre	8b	2	753	2713	187708	2810	457	274594	1401	1950	5949	89	37	21	298	104
Arre	8b	2	1685	6162	411958	6151	1028	615695	3091	4411	13093	225	107	62	766	240
Arre	8b	2	1816	6762	428373	6394	1108	662557	3277	4827	13754	272	154	90	1006	268

11.15 Fluid inclusions – LA-ICP-MS analyses (sphalerite host)

Table 28. LA-ICP-MS data on fluid inclusions in sphalerite (ppm) for Arre (ARR06) deposit. Abbreviations: FI: Fluid inclusions.

Deposit	IF n°	IF assemblage	Li7	B11	Cl35	K39	Na23	Ca43	Mn55	Br79	Rb85	Sr88	Cs133	Ba137	Pb208
Arre	1s	1.0	3560	<LOD	498606	<LOD	98349	<LOD	11485	13324	<LOD	2937	<LOD	807	478
Arre	1s	1.0	789	<LOD	236118	7262	98349	<LOD	6823	2450	<LOD	2633	<40.9112	357	<LOD
Arre	1s	1.0	1061	111	287289	9254	98349	45319	432	2042	44	3285	32	495	<LOD
Arre	1s	1.0	1276	77	247663	7403	98349	33212	460	1248	29	2327	21	436	13
Arre	1s	1.0	1059	<LOD	297789	2161	98349	<LOD	<LOD	1429	22	29	<11.078	<LOD	<LOD
Arre	1s	1.0	5561	<LOD	215394	<LOD	98349	<LOD	<LOD	15076	<LOD	1749	185	<LOD	<LOD
Arre	1s	1.0	<LOD	<LOD	516653	<LOD	98349	<LOD	<LOD	<LOD	<LOD	<LOD	<LOD	<LOD	<LOD
Arre	1s	1.0	<LOD	<LOD	694771	<LOD	98349	<LOD	<LOD	24384	<LOD	6257	<LOD	<LOD	<LOD
Arre	1s	1.0	857	<LOD	333887	9523	98349	83270	<LOD	1544	29	3171	24	465	47
Arre	1s	1.0	1486	<LOD	436913	8661	98349	<LOD	<LOD	1808	<LOD	3422	<LOD	<LOD	<LOD
Arre	1s	1.0	1288	<LOD	370422	13555	98349	13439	<LOD	1406	92	2682	<LOD	295	<LOD
Arre	1s	1.0	1104	<LOD	340991	10072	98349	59458	2538	2183	55	3229	29	448	232
Arre	1s	1.0	1780	<LOD	166391	2185	98349	8726	82	578	8	216	3	<LOD	<LOD
Arre	1s	1.0	1201	<LOD	253034	9012	98349	49817	288	1663	117	5035	51	446	73
Arre	1s	1.0	5647	<LOD	306777	2357	98349	11155	785	593	<LOD	1498	<LOD	<LOD	30
Arre	1s	1.0	1048	<LOD	194795	2237	98349	<LOD	265	448	<LOD	178	<LOD	<LOD	13
Arre	1s	1.0	1337	<LOD	440455	<LOD	98349	<LOD	<LOD	357	<LOD	2439	<LOD	<LOD	<LOD
Arre	1s	1.0	1074	<LOD	335281	10636	98349	65539	<LOD	2088	62	2360	36	738	<LOD
Arre	1s	1.0	268	<LOD	167525	64296	98349	47897	3587	753	83	706	<LOD	55	303
Arre	1s	1.0	1130	<LOD	308476	24973	98349	<LOD	4017	1158	103	2165	16	480	335
Arre	1s	1.0	2094	<LOD	476960	13893	98349	<LOD	<LOD	3546	<LOD	3837	<LOD	838	235
Arre	1s	1.0	2023	589	288304	20309	98349	65792	942	685	110	5072	129	1606	299
Arre	1s	1.0	1297	<LOD	282761	15253	98349	62807	<LOD	1902	40	3054	32	431	<LOD

Arre	1s	1.0	1126	<LOD	279370	2829	98349	<LOD	<LOD	947	<LOD	269	<LOD	<LOD	93
Arre	1s	1.0	6830	<LOD	166872	<LOD	98349	<LOD	12280	8243	295	3065	<LOD	<LOD	486
Arre	1s	1.0	<LOD	<LOD	621002	5076	98349	20990	6089	11438	<LOD	7910	<LOD	<LOD	818
Arre	1s	1.0	<LOD	<LOD	100751	<LOD	98349	<LOD	<LOD	12852	<LOD	6678	176	<LOD	<LOD
Arre	1s	1.0	<LOD	<LOD	533097	21500	98349	<LOD	<LOD	8650	138	5460	120	1190	<LOD
Arre	1s	1.0	1326	<LOD	285147	13497	98349	<LOD	<LOD	5549	139	2345	24	717	<LOD
Arre	1s	1.0	1326	<LOD	495826	13497	98349	<LOD	<LOD	5755	139	2345	24	717	<LOD
Arre	1s	1.0	1078	146	243319	9272	98349	65531	556	2900	94	4996	31	775	139
Arre	1s	1.0	1078	146	242467	9272	98349	65531	556	2795	94	4996	31	775	139
Arre	1s	1.0	1163	<LOD	225982	9012	98349	51172	<LOD	3239	113	5999	35	807	26
Arre	1s	1.0	624	<LOD	104995	6083	98349	<LOD	1315	1442	29	2066	30	240	185
Arre	1s	1.0	<LOD	<LOD	315322	<LOD	98349	<LOD	<LOD	13172	<LOD	3827	<LOD	<LOD	597
Arre	1s	1.0	1079	<LOD	326425	11966	98349	<LOD	<LOD	2506	84	3910	32	693	160
Arre	1s	1.0	923	<LOD	346550	12233	98349	<LOD	4550	2556	103	3321	32	428	150
Arre	1s	1.0	1491	<LOD	202862	9140	98349	<LOD	<LOD	2542	203	3856	<LOD	643	<LOD
Arre	1s	1.0	1135	<LOD	298081	11576	98349	<LOD	4856	681	<LOD	2723	<LOD	516	<LOD
Arre	1s	1.0	<LOD	<LOD	106158	47351	98349	<LOD	8965	4176	471	4049	<LOD	2988	3350
Arre	1s	1.0	2125	717	291665	20258	98349	61235	290	1304	106	5611	112	1688	<LOD
Arre	1s	1.0	1981	<LOD	330751	22973	98349	53781	<LOD	1445	152	6532	137	1671	207
Arre	1s	1.0	1559	1453	304416	20032	98349	<LOD	3604	1455	58	4706	143	1735	838
Arre	1s	1.0	2030	<LOD	512284	18920	98349	<LOD	<LOD	2549	160	2939	<LOD	1315	953
Arre	1s	1.0	1511	<LOD	312873	20437	98349	88026	2972	1606	94	5901	109	1897	249
Arre	1s	1.0	1610	<LOD	258148	20691	98349	34688	667	1258	65	4290	70	781	73
Arre	1s	1.0	<LOD	<LOD	481172	40450	98349	<LOD	3115	3083	<LOD	7914	283	1631	<LOD
Arre	1s	1.0	2386	<LOD	491497	24471	98349	<LOD	5350	4130	214	6538	165	1158	<LOD
Arre	1s	1.0	1797	535	285728	19188	98349	49550	1136	1423	65	4807	138	1330	18
Arre	1s	1.0	867	<LOD	292560	20417	98349	<LOD	4175	1744	<LOD	4519	111	1781	<LOD

11.16 Fluid inclusions – Limit of detection of LA-ICP-MS analyses (sphalerite host)

Table 29. Limit of detection for fluid inclusion analyses acquired with LA-ICP-MS on sphalerite (ppm) for Arre (ARR06) deposit. Abbreviations: FI: Fluid inclusions.

Deposit	FI n°	FI assemblage	Li7	B11	Cl35	K39	Na23	Ca43	Mn55	Zn66	Br79	Rb85	Sr88	Cs133	Ba137	Pb208
Arre	1s		2529	10215	227374	10769	1614	390559	2125		51170	281	140	185	729	369
Arre	1s		560	2262	50342	2384	357	86472	470		11329	62	31	41	161	82
Arre	1s		15	62	1363	64	10	2365	13		307	2	1	1	5	2
Arre	1s		15	63	1191	59	10	2486	12		271	2	2	1	5	2
Arre	1s		193	812	16028	799	136	32511	161		3640	20	18	11	55	22
Arre	1s		2824	11909	234111	11660	1997	476144	2357		53180	297	262	165	822	327
Arre	1s		6391	26512	545487	27297	4505	1073038	5346		123801	549	484	305	1257	692
Arre	1s		3147	11434	247689	12610	2034	559248	2506		55844	230	203	198	1039	346
Arre	1s		158	561	12835	657	102	28095	126		2891	8	7	8	37	16
Arre	1s		1416	5070	113275	5784	911	251288	1127		25525	87	77	80	392	150
Arre	1s		411	1353	35557	1789	275	83083	372		7707	18	16	25	203	35
Arre	1s		151	499	12982	653	101	30477	136		2814	7	6	9	77	13
Arre	1s		8	29	701	35	6	1689	8		152	1	0	1	5	1
Arre	1s		51	170	3738	196	31	10210	46		824	8	5	3	32	6
Arre	1s		202	659	15357	811	123	40882	183		3382	29	15	9	112	24
Arre	1s		53	172	3997	211	32	10641	48		880	8	4	2	29	6
Arre	1s		696	2201	54159	2874	418	140827	632		11917	88	41	25	332	79
Arre	1s		451	1590	34340	1853	275	95072	410		7217	61	70	22	264	65
Arre	1s		66	227	5125	278	40	13910	60		1076	8	9	3	34	9
Arre	1s		254	902	19238	1036	156	53563	231		4044	35	40	13	154	37
Arre	1s		762	2701	57632	3105	466	160459	691		12115	106	121	40	460	111
Arre	1s		18	56	1396	76	11	3525	15		294	1	1	1	6	2
Arre	1s		133	408	9143	506	77	25665	116		1918	18	14	10	84	15

Arre	1s		493	1492	34356	1905	286	95326	430		7205	63	49	33	297	56
Arre	1s		3323	9599	240335	13215	1924	644273	2902		49690	200	346	206	1848	347
Arre	1s		1043	2846	69760	3836	544	197359	827		14511	77	103	40	564	114
Arre	1s		2174	6166	142079	7767	1150	412158	1727		29592	203	250	106	1338	252
Arre	1s		1409	3956	92610	5070	742	266914	1119		19283	124	156	65	840	161
Arre	1s		855	2215	58857	3260	437	161379	676		12224	42	67	22	380	86
Arre	1s		855	2215	58857	3260	437	161379	676		12224	42	67	22	380	86
Arre	1s		34	95	2492	140	18	7224	28		519	4	3	2	8	4
Arre	1s		34	95	2492	140	18	7224	28		519	4	3	2	8	4
Arre	1s		24	71	1737	96	14	4743	21		352	1	2	1	12	3
Arre	1s		376	1087	25253	1475	208	76429	317		5368	26	37	21	171	37
Arre	1s		2165	6342	144048	8395	1205	439844	1825		30632	168	225	131	1052	220
Arre	1s		120	341	8174	479	66	24436	101		1737	7	11	6	50	11
Arre	1s		317	900	21557	1263	175	64447	267		4581	19	28	16	131	30
Arre	1s		875	2704	58761	3335	488	168701	747		11919	63	56	69	259	95
Arre	1s		756	2398	49711	2806	426	145971	645		10095	68	60	66	280	86
Arre	1s		8147	25945	533346	28225	4783	1385265	6102		124633	425	374	572	2024	902
Arre	1s		26	74	1698	90	15	4402	20		395	2	2	1	10	3
Arre	1s		203	587	13172	700	118	34502	155		3067	17	15	12	83	21
Arre	1s		396	1143	25658	1363	231	67209	303		5975	34	30	23	162	41
Arre	1s		1482	4470	93515	4932	876	252314	1134		21810	155	137	101	739	165
Arre	1s		301	892	19240	1018	177	51244	231		4484	29	26	19	139	32
Arre	1s		116	346	7386	390	68	19747	89		1722	11	10	8	55	13
Arre	1s		1953	5935	122577	6456	1157	332577	1494		28597	211	186	137	1006	220
Arre	1s		600	1786	38181	2018	353	102079	459		8900	59	52	39	283	65
Arre	1s		85	244	5552	295	50	14460	65		1293	7	6	5	33	9
Arre	1s		575	1762	35850	1885	342	97902	439		8367	64	57	41	307	66

11.17 Geochronology methodology and instrumentation

Table 30. LA-ICP-MS U-Th-Pb dating methodology (LMV, Univ. Clermont-Auvergne, France)

Laboratory & Sample Preparation		
Laboratory name	Laboratoire Magmas & Volcans, Univ. Clermont-Auvergne, France	
Sample type/mineral	Zircon, Monazite and Xenotime	
Sample preparation	Conventional mineral separation, 1 inch resin mount, 0.25µm polish to finish	
Imaging	CL, FEI QUANTA 450w, 15 kV, 19mm working distance (Université Bourgogne-Franche Comté)	
Laser ablation system		
Make, Model & type	Resonetics/M-50E 193nm, Excimer	
Ablation cell & volume	Laurin Cell ® two volumes cell, Laurin Technic Ltd., volume ca. 1-2 cm^3	
Laser wavelength	193 nm	
Pulse width	< 4 ns	
Fluence	*Zircon :* 5 $J.cm^{-2}$	*Monazite* 8 $J.cm^{-2}$, 15 $J.cm^{-2}$ and 9 $J.cm^{-2}$
Repetition rate	3 Hz	1 Hz
Spot size	separated : 33µm	in situ in thin section : 12 µm
Sampling mode / pattern	Single spot	
Carrier gas	100% He, Ar make-up gas and N_2 combined using the Squid® device from RESOlution Instruments.	
Background collection	30 secs	
Ablation duration	60 secs	
Wash-out delay	30 secs	
Cell carrier gas flow	0.75 l/min	
ICP-MS Instrument		
Make, Model & type	Agilent 7500cs, Q-ICP-MS	
Sample introduction	Via conventional tubing	
RF power	1350W	
Make-up gas flow	0.87 l/min Ar	
Detection system	Single collector secondary electron multiplier	
Masses measured	204, 206, 207, 208, 232, 238	
Integration time per peak	10 ms	

Total integration time per reading	130 ms *(should represent the time resolution of the data)*	
Sensitvity / Efficiency	20000 cps/ppm ^{238}U (44µm, 10Hz)	
Dead time	35 ns	
Data Processing		
Gas blank	30 second on-peak	
Calibration strategy	*Zircon :* GJ-1 used as primary reference material, 91500 used as secondary reference material (Quality Control)	*Monazite*: Trebilcock used as primary reference material, Bananeira used as secondary reference material (Quality Control)
Reference Material info	91500 (Wiedenbeck et al., 1995) GJ1 (Jackson et al., 2004)	Trebicock (Tomascak et al., 1996) Bananeira (Gonçalves et al., 2016)
Data processing package used / Correction for LIEF	GLITTER ® (van Achterbergh et al., 2001)	
Mass discrimination	Standard-sample bracketing with $^{207}Pb/^{206}Pb$ and $^{206}Pb/^{238}U$ normalized to reference material GJ-1 or Trebilcock	
Common-Pb correction, composition and uncertainty	No common-Pb correction. Analyses discarded when discordance >10%	
Uncertainty level & propagation	Ages are quoted at 2sigma absolute, propagation is by quadratic addition according to Horstwood et al. (2003). Reproducibility and age uncertainty of reference material are propagated.	
Quality control / Validation	*Zircon :* 91500 : Concordia age = 1064.1 ± 5.1 Ma (2SD, $MSWD_{(C+E)}$ = 0.18, N = 39) *Monazite :* Bananeira: Concordia age = 506.8 ± 3.6 Ma (2SD, $MSWD_{(C+E)}$ = 1.3, N= 27)	
Other information	For detailed method description see Paquette et al. (2014) and Hurai et al. (2010).	

Abstract

Rare metals are essential to the development of the green technologies that are at the core of emerging low-carbon societies. Germanium is a rare element considered critical by the European Union and the U.S. Geological Survey due to its several uses in optical and electronics devices. Non-deformed sphalerite crystals (ZnS) commonly contain Ge and other critical elements (In, Ga) which may grade up to a few thousands of ppm. Only few studies have described specific minerals with Ge contents above wt.%, because these are apparently rare in Pb-Zn(-Cu) deposits. These Ge-minerals appear to be more abundant in deformed and metamorphosed Pb-Zn(-Cu) deposits. This raises the question of the impact of deformation and metamorphism on Ge and other rare metals mobility. This type of orogenic deposits constitutes the largest known zinc concentrations on Earth and their potential for rare metal is yet to be assessed.

The Pb-Zn deposits in the Pyrenean Axial Zone are an ideal target to study the impact of deformation and metamorphism on rare metals mobility as sphalerite is only locally recrystallized. A structural field study allows to discriminate four Pb-Zn mineralization types. Type 1 is a minor syngenetic and stratiform disseminated mineralization. Type 2a is an epigenetic stratabound mineralization, concordant to the S_1 Variscan foliation. Type 2b ore are parallel to the S_2 cleavage. Sphalerite ore is highly deformed by a late cleavage sub-parallel to S_2 probably Pyrenean-Alpine in age. Fluid inclusions study shows the presence of two Type 2b fluids with a low salinity (<20 wt.% NaCl eq.) and high temperatures (200-350 °C) typical of Late-Variscan fluids whereas Mesozoic Type 2b ore exhibits high salinity (15-35 wt.% NaCl eq.) and low temperature (< 200 °C).

Germanium and related elements such as Cu, In and Ga are present in the deformed Pyrenean vein mineralizations and are heterogeneously distributed. Electron Backscattered diffraction (EBSD) analyses and chemical investigations allow to define distinct sphalerite textures with specific chemical contents: i) Dark-brown patchy or stripped zonations in coarse parent grains exhibit high Ge-content (up to 600 ppm Ge) in the lattice. ii) Light-brown zonations in coarse parent grains contain low Ge-contents mostly below 100 ppm Ge. iii) Light-brown small recrystallized daughter grains (below ~ 100 μm) present systematically low to very low Ge-contents (~ 20 ppm Ge). Copper contents (up to 1265 ppm) are highly correlated to Ge in sphalerite and Ga only occur in coarse sphalerite crystals (below ~100 ppm). Ge-minerals, such as brunogeierite, carboirite, briartite and argutite (up to ~ 70 wt. % Ge) are mainly hosted in recrystallized sphalerite domains or close to twin boundaries in coarse grains. These observations demonstrate that recrystallization of sphalerite has led to the redistribution of Ge from the sphalerite lattice into Ge-minerals. We suggest that the interactions between intra-granular diffusion and fluid assisted processes are responsible for the formation of patchy-stripped zonations and the crystallization of Ge-oxides, sulfides or chloritoids. A large variability of sphalerite chemistry and texture is frequently reported from other orogenic world-class deposits: these may have been affected by similar recrystallization and redistribution processes. The redistribution of rare metals in sulfide environments must have induced the concentration of rare metal in accessory minerals. These tiny minerals may be missed by punctual chemical analyses without prior detailed textural investigation. Understanding how rare metals concentrate through metamorphism and syntectonic recrystallization at mineral scale is essential to emphasize their spatial redistribution and localization at deposit scale. This study highlights the importance of coupling *in situ* and mapping chemical analyzes with macro- and microtextural characterization when targeting rare metals in deformed ore.

Keywords: Germanium; Pb-Zn mineralizations; Critical metals; Pyrenees; Remobilization; Recrystallization.

Résumé

Les métaux rares sont essentiels au développement des technologies vertes qui sont maintenant au cœur de nos sociétés. Le germanium est un élément rare considéré critique par l'Union Européenne et l'US Geological Survey, du fait de ses nombreux usages dans l'industrie de l'optique et de l'électronique. Les cristaux non déformés de sphalérite (ZnS) sont souvent porteurs de Ge et d'autres métaux rares (In, Ga) avec des concentrations pouvant atteindre quelques milliers de ppm. Seulement peu d'études décrivent des minéraux avec des concentrations en Ge au-dessus du % poids, du fait de leur apparente rareté dans les gisements Pb-Zn(-Cu). En fait, ces minéraux à Ge semblent plus fréquents dans les gisements Pb-Zn(-Cu) déformés ou métamorphisés ce qui soulève la question de l'impact de la déformation et du métamorphisme sur la mobilité du Ge et d'autres métaux rares. Ce type de gites contient les plus grandes ressources de zinc sur Terre and actuellement leur potentiel en métaux rares reste à évaluer.

Les gites Pb-Zn de la Zone Axiale des Pyrénées sont une cible idéale pour étudier l'impact de la déformation et du métamorphisme sur la mobilité des métaux rares car la sphalérite est seulement localement recristallisée. Une étude structurale de terrain a permis de discriminer quatre types de minéralisations Pb-Zn. La minéralisation Type 1 est disséminée, syngénétique et stratiforme. La minéralisation Type 2a est épigénétique et stratabound. Les minéralisations Type 2b tardi-Varisque et Mésozoïque sont parallèles à la schistosité S_2. La sphalérite est largement déformée par une schistosité tardive, probablement Pyrénéenne (S_p). L'étude des inclusions fluides montre la présence d'un fluide de faible salinité (<20 %poids eq. NaCl) avec de relative haute température (200-350 °C) typique d'un fluide tardi-Varisque tandis que le Type 2b Mésozoïque montre de forte salinité (15-35 %poids eq. NaCl) et des faible températures (< 200 °C). Le germanium est distribué de manière très hétérogène dans les minéralisations en veines. Des analyses texturales et chimiques permettent de définir différents domaines dans la sphalérite : i) des zonations marron sombres en patches ou rayées dans les gros grains parents présentent des concentrations en Ge élevées dans la maille cristallographique (jusqu'à 600 ppm Ge). ii) des zonations marron claires dans les gros grains parents contiennent des concentrations en Ge faibles, le plus souvent en-dessous de 100 ppmGe. iii) des petits grains clairs recristallisés (en dessous de ~100 μm) presentent de très faibles concentrations en Ge (~20 ppm Ge). Les concentrations en Cu sont corrélées à celles du Ge tandis que le Ga est zoné que dans les gros grains. Les minéraux à Ge, comme la brunogéiérite, la carboirite, la briartite et l'argutite (jusqu'à ~70 %poids Ge) apparaissent dans les domaines de sphalérite recristallisée ou plus rarement proche des limites maclées dans les gros grains. Ces observations démontrent que la recristallisation de la sphalérite a permis la redistribution du Ge depuis la maille de la sphalérite jusqu'à la formation des minéraux à Ge. Nous suggérons que les intéractions entre des fluides et la diffusion intra-granulaire sont responsable de la redistribution du Ge. Des hétérogénéités chimiques et texturales sont fréquemment reportées dans d'autres gisements et ont pu être affectés par des processus similaires de redistributions dans des minéraux accessoires. Ces petits minéraux peuvent avoir été manqués par des analyses chimiques ponctuelles sans contrôle textural préalable. Comprendre comment les métaux rares se concentrent à travers la déformation et la recristallisation syn-tectonique à l'échelle du minéral est essentiel pour surligner leur localisation à l'échelle du gisement. Cette étude met en évidence l'importance de coupler les analyses chimiques in-situ et cartographiques avec la caractérisation macro- et micro texturale lors de l'exploration des métaux rares dans des minerais déformés.

Mots-clés : germanium ; minéralisation Pb-Zn ; métaux critiques ; Pyrénées ; remobilisation ; recristallisation.